

Preparation for a Measurement of Charge Asymmetry  
in the Bethe-Heitler Process

Haoyu Chen  
Changsha, Hunan, China

B.S., Nanjing University, 2012

A Dissertation Presented to the Graduate Faculty  
of the University of Virginia  
in Candidacy for the Degree of Doctor of Philosophy

Department of Physics  
University of Virginia  
August, 2022

## Abstract

We have prepared a measurement of the energy asymmetry in wide- and medium-angle electron/positron pair production off protons and heavy targets. This asymmetry is caused by the interference between the first- and second-order Born diagrams and the Compton scattering diagram. It directly probes aspects of QED, as well as providing a direct measurement of the real part of the Compton amplitude. It will be conducted at the HI $\gamma$ S facility at Duke University, using a 60 MeV photon beam. This dissertation serves as documentation of the preparation stage of the Bethe-Heitler experiment. The major was the recommissioning of the vertical drift chambers previously used in the Q-weak experiment at the Jefferson Lab. Cosmic test runs were conducted, drift time data were collected and efficiency plateaus were measured. We made modifications to the JLAB Hall A analyzer to suit the geometry and drift characteristics of these wire chambers. The analyzer was used for the reconstruction of the trajectories of cosmic ray test runs with the results confirmed by direct measurement of trigger geometry. Spatial and angular resolution is estimated to  $\sim 300\mu\text{m}$  and  $0.17^\circ$  respectively. Geant 4 simulations with generated Bethe-Heitler pairs satisfying theoretical differential cross sections. It was used to check detector acceptance, optimize apparatus layout, and estimate measurable energy asymmetry. The measurable asymmetries from electron/positron pairs with polar angles around between approximately  $5^\circ$  and  $8^\circ$ , azimuthal angles differing by  $180^\circ$ , and energy differing by approximately 9 MeV to 15 MeV are predicted to be above 10%. The kinematics of primary vertices are reconstructed using the data from wire chambers in the simulation. The energy resolution is determined to be better than 1MeV.

## Contents

<b>Abstract.....</b>	<b>i</b>
<b>Contents .....</b>	<b>ii</b>
<b>List of Figures .....</b>	<b>v</b>
<b>Part I Theory.....</b>	<b>1</b>
<b>1 Physics Intro .....</b>	<b>1</b>
<b>2 Cross section and Asymmetry Calculation .....</b>	<b>3</b>
2.1 Diagrams .....	3
2.2 Calculation of cross section .....	3
2.3 Special cases .....	4
2.4 Asymmetry.....	5
<b>Part II Apparatus .....</b>	<b>7</b>
<b>1 Beam .....</b>	<b>7</b>
<b>2 Target .....</b>	<b>8</b>
<b>3 Magnet.....</b>	<b>9</b>
<b>4 Vertical drift chamber .....</b>	<b>12</b>
4.1 Introduction.....	12
4.2 Design and construction.....	13
4.3 Commissioning .....	16
<b>5 Hodoscopes.....</b>	<b>37</b>
5.1 Elements of the Hodoscope.....	37
5.2 Preparations of hodoscopes.....	46
5.3 Test run trigger setup .....	53
5.4 Scintillator setup in BH experiment.....	56
<b>Part III Analyzing test run data.....</b>	<b>58</b>
<b>1 Basics of JLab Hall A analyzer .....</b>	<b>58</b>
1.1 JLab Hall A analyzer .....	58
1.2 Users utilize the analyzer .....	58
1.3 Using analyzer for BH experiment .....	58

1.4 Contents in this part .....	59
<b>2 VDC database file setup.....</b>	<b>60</b>
2.1 The use of database file.....	60
2.2 Four main categories of parameters .....	61
2.3 Determine parameters in database file .....	61
<b>3 Cluster finding and fitting .....</b>	<b>83</b>
3.1 Introduction.....	83
3.3 Visualizing events.....	87
3.4 Cluster fitting .....	89
3.5 Misc. issues .....	96
<b>4 Time to distance conversion .....</b>	<b>99</b>
4.1 Origin of the problem.....	99
4.2 Time to distance function.....	101
4.3 Preliminary TTD function calibration and results .....	106
4.4 Integration of drift time distribution density function.....	120
4.5 Time to distance conversion parameters fitting .....	123
<b>5 Analyzer track finding, fitting and efficiency .....</b>	<b>133</b>
5.1 Introduction.....	133
5.2 Track finding and fitting .....	134
5.3 Test run setup.....	138
5.4 Track fitting results .....	148
5.5 Changes for improving efficiency.....	171
5.6 Misc. topics .....	176
<b>6 Other items required for replay.....</b>	<b>180</b>
<b>7 Decoder results and their applications.....</b>	<b>181</b>
<b>Part IV Simulation.....</b>	<b>185</b>
<b>1 Generate BH pairs.....</b>	<b>185</b>
1.1 Introduction.....	185
1.2 Pair generation procedure .....	186
1.3 Modifications on pair generator code .....	194
1.4 Applications .....	198
<b>2 Geant 4 simulation .....</b>	<b>202</b>



2.1 Introduction.....	202
2.2 Setup of Geant 4 simulation.....	203
2.3 Geant 4 simulation Results .....	210
2.4 Track finding and fitting using Geant 4 results.....	230
2.5 Additional transformations of wire chambers.....	241
<b>3 Simple acceptance simulation .....</b>	<b>248</b>
3.1 Introduction.....	248
3.2 Calculation of tracks .....	249
3.3 Basic results .....	257
3.4 Applications.....	264
<b>4 Reduce data dimension by principal component analysis.....</b>	<b>274</b>
4.1 Introduction.....	274
4.2 Principal component analysis (PCA).....	275
4.3 Application of PCA to Geant 4 simulation data.....	281
4.4 Energy reconstruction results via applying PCA to data .....	297
<b>Part V Conclusion.....</b>	<b>306</b>
<b>Appendices.....</b>	<b>308</b>
Part III Appendix A 4.3.1 Determine number of divisions for each iteration.....	308
Part III Appendix A 4.6 Quick sort algorithm .....	309
Part III Appendix A5.2.1 Track reconstruction derivation from geometry point of view ...	311
Part III Appendix A5.2.2 Calculation of track $(x, y, \tan\theta, \tan\varphi)$ from crossover point coordinates $(u_1, v_1, u_2, v_2)$ .....	313
<b>Part III Appendix A1 Angles in track reconstruction .....</b>	<b>315</b>
A1.1 Coordinate system used in Hall A analyzer .....	315
A1.2 Definitions of angles related to track reconstruction. ....	316
A1.3 Deriving relation from $(\theta, \varphi)$ to $(\delta_u, \delta_v)$ .....	317
A1.4 Deriving relation from $(\delta_u, \delta_v)$ to $(\theta, \varphi)$ .....	318
A1.5 Applications .....	318
Part IV Appendix 2.5 Coordinate transformations .....	321
Part IV Appendix 3.2: Derivation of projected radius $R_H$ .....	324
<b>References.....</b>	<b>325</b>
<b>Acknowledgements .....</b>	<b>330</b>

## List of Figures

### Part I Theory

I Fig2. 1 Diagram of BH pair production.....	3
I Fig2. 2 The dependence of asymmetry $A$ on $\delta_p$ .....	6
I Fig2. 3 The dependence of asymmetry $A$ on $\eta = Z\alpha$ .....	6

### Part II Apparatus

II Fig 1. 1 Gamma ray source. ....	8
II Fig 3. 1 SAL pair spectrometer magnet. ....	10
II Fig 3. 2 Field map of the magnet. ....	11
II Fig 4. 1 A pair of Q-weak drift chambers. ....	13
II Fig 4. 2 Cross section of one VDC.....	14
II Fig 4. 3 Wire chamber HV supply and HV distributor. ....	17
II Fig 4. 4 Diagram for HV supply on VDC cathodes. ....	18
II Fig 4. 5 Diagrams for discriminator cards threshold and power supplies. ....	19
II Fig 4. 6 Diagram of gas flow inside wire chambers.....	21
II Fig 4. 7 Return bubbler diagram. ....	22
II Fig 4. 8 Full set of labeled cards in chamber 1 or 2. ....	23
II Fig 4. 9 Locations of 12 cards implemented in U wire planes. ....	23
II Fig 4. 10 Fixation of cables on wire chamber. ....	24
II Fig 4. 11 A single ribbon cable holder for TDC. ....	25
II Fig 4. 12 Full implementation of holders and hanger of ribbon cables on TDC side. ....	25
II Fig 4. 13 MAD card attached on adaptor board. ....	26
II Fig 4. 14 Diagram for the signal transmission for both MAD card and Nano card. ....	27
II Fig 4. 15 TDC time distribution of all data from 3 discriminator cards.....	27
II Fig 4. 16 Two adjacent MAD or Nano Card channels TDC time comparison. ....	29
II Fig 4. 17 Cross talk on two adjacent MAD Card channels. ....	30
II Fig 4. 18 Grounding setup for Nano cards. ....	31
II Fig 4. 19 2D histogram showing the time dependent data rate of a test run. ....	33
II Fig 4. 20 Nano card efficiency plateau scan of high voltage dependence.....	35
II Fig 4. 21 Active U/V wires in chamber 1 or 2. ....	36

II Fig 5. 1 Scintillation material for BH experiment.....	38
II Fig 5. 2 Light emission spectral for a typical plastic scintillator.....	39
II Fig 5. 3 Diagram for a typical PMT with linear focused configuration.....	40
II Fig 5. 4 Spectral response of R7725.....	42
II Fig 5. 5 Typical test PMT pulse shape.....	44
II Fig 5. 6 Hodoscopes assemble used for wire chamber test run.....	47
II Fig 5. 7 Normal and light leak pulse from PMT.....	49
II Fig 5. 8 Configuration of gain match.....	50
II Fig 5. 9 Pulse shape of two PMTs before and after gain match.....	52
II Fig 5. 10 Diagram of trigger setup of for wire chamber cosmic ray detection test run.....	53
II Fig 5. 11 Trigger paddles placement on chambers after gain match.....	55
II Fig 5. 12 Schematic proposed assembly of hodoscopes for the experiment.....	57

### Part III Analyzing test run data

III Fig 2. 1 An example of a cluster.....	63
III Fig 2. 2 Relation between drift time difference and drift distance difference.....	64
III Fig 2. 3 Coordinate system illustrated for HRS chambers.....	66
III Fig 2. 4 Coordinate system and wire dimensions of wire chamber.....	67
III Fig 2.5 $U$ -axis and computation of absolute value of wire.spacing.....	68
III Fig 2. 6 Computation of wire.start and determine sign of wire.spacing.....	70
III Fig 2. 7 Nine inactive channels from card U9 of chamber 1,2.....	72
III Fig 2. 8 Full set of labeled cards in chamber 1 or 2.....	72
III Fig 2. 9 Schematics of active U/V wires in chamber 1 or 2.....	73
III Fig 2. 10 Six discriminator cards have to be reverse their channels.....	74
III Fig 2. 11 Chamber 1,2 U wire mapping.....	75
III Fig 2. 12 Drift time vs hit wire indices of matched clusters.....	77
III Fig 2. 13 Copy of Fig A1.4 Relation between drift distance $\Delta d$ and $\delta_u$ .....	78
III Fig 2. 14 Typical drift time distribution for a wire plane.....	79
III Fig 2. 15 TDC time distribution for 16 channels in the same discriminator card.....	81
III Fig 2. 16 Linear least chi square fit result for TDC time offset.....	81
III Fig 3. 1 A typical cluster of thits in a VDC plane.....	84
III Fig 3. 2 A typical event by event display in 2D view.....	88
III Fig 3. 3 Geometry of cluster fitting.....	90
III Fig 3. 4 Pivot wire drift distance sign.....	93
III Fig 3. 5 Illustration of resolving up-down ambiguity.....	94
III Fig 3. 6 One directional search of clusters in the JLAB analyzer.....	97
III Fig 3. 7 Drift time difference between adjacent wires.....	98
III Fig 4. 1 Drift time distribution of wire chamber.....	100
III Fig 4. 2 Time to distance conversion function.....	102
III Fig 4. 3 Graph of function $d(t)$ .....	103
III Fig 4. 4 Ideal $d$ and $t$ distribution.....	104

III Fig 4. 5 $U-U$ and $V-V$ matched clusters. ....	105
III Fig 4. 6 Distribution of angle difference squared between cluster fit and track fit squared. ...	108
III Fig 4. 7 Converted distance distribution after finding $C$ which minimize $f(C)$ .....	109
III Fig 4. 8 Effect of different $a_2$ values in TTD. ....	110
III Fig 4. 9 Drift distance distribution of each wire plane.....	113
III Fig 4. 10 Signed drift distance distribution.....	113
III Fig 4. 11 Analyzer fitted track $(\theta, \varphi)$ distribution.....	114
III Fig 4. 12 Signed drift distance of parallel tracks with 5-wire cluster. ....	115
III Fig 4. 13 Simulated crossover points $u$ coordinate and drift distance distribution.....	116
III Fig 4. 14 Geometry explanation of peaks in drift time distribution.....	118
III Fig 4. 15 Simulated signed distance distribution. ....	119
III Fig 4. 16 TTD plot. ....	122
III Fig 4. 17 TDC time offset from length of sense wire. ....	124
III Fig 4. 18 Drift distance distribution by applying TTD function.....	125
III Fig 4. 19 Drift distance distribution from applying the TTD function. ....	126
III Fig 4. 20 Drift distance vs incident angle $(d, \theta)$ distribution of each wire plane. ....	127
III Fig 4. 21 Drift distance distribution from interpolation of TTD table.....	129
III Fig 4. 22 Drift distance distribution of wire plane $u1$ with incident angle $\theta$ from $35^\circ$ to $36^\circ$ . .....	132
III Fig 4. 23 Drift distance distribution of wire plane $u1$ with incident angle $\theta$ from $35^\circ$ to $55^\circ$ . .....	132
III Fig 4. 24 Quick sort algorithm.....	310
III Fig 5. 1 Thin scintillator paddles labeling conventions and their channels on TDC. ....	139
III Fig 5. 2 Upper chamber trigger and reference scintillators.....	140
III Fig 5. 3 Bottom chamber trigger and reference scintillators.....	140
III Fig 5. 4 Z positions of paddles affect projection locations on wire planes. ....	142
III Fig 5. 5 Outer and inner projection boundaries. ....	143
III Fig 5. 6 Projection of a square should be also a square. ....	144
III Fig 5. 7 Hall C event display of a good event.....	145
III Fig 5. 8 Angle ranges for individual scintillator trigger telescopes. ....	147
III Fig 5. 9 Crossover point $(x' = -y, y' = x)$ of all tracks in wire plane $u1$ (lower chamber, upper histogram) and wire plane $u2$ .....	149
III Fig 5. 10 Upper $v$ plane hit index distribution.....	151
III Fig 5. 11 Track crossover point distribution $(x' = -y, y' = x)$ on $u$ wire planes.. ....	152
III Fig 5. 12 Separated crossover points coordinate distributions.....	153
III Fig 5. 13 Cluster span distribution for all wire planes.....	154
III Fig 5. 14(1) Simulated and test run cluster span $(\theta, \varphi)$ .....	155
III Fig 5. 15(1) Simulated cluster span $(nu, nv)$ distribution of trigger $(2,0)$ .. ....	156
III Fig 5. 16 Analyzer track reconstruction efficiency.....	160
III Fig 5. 17 The copy of Fig. 5.12.....	164
III Fig 5. 18 Calculated trigger outer projection on lower chamber wire planes. ....	166
III Fig 5. 19 Wrong $uv$ association cases.....	166
III Fig 5. 20 Missing wire plane $u1$ hits leads to loss of efficiency.....	168

III Fig 5. 21 Redraw of III Fig. 3.6. ....	169
III Fig 5. 22 Fitted tracks crossover points on $u$ wire planes, using default hit collection iteration direction for cluster finding. ....	170
III Fig 5. 23 Fitted tracks crossover points on $u$ wire planes, using reversed hit collection iteration direction for cluster finding ....	170
III Fig 5. 24 Difference histogram of fitted tracks between default and reversed cluster finding. ....	170
III Fig 5. 25 Illustration of premature ending of cluster finding.....	174
III Fig 5. 26 Illustration of new cluster finding method.....	175
III Fig 5. 27 Illustration of translation invariance of standard deviation of $\sigma u$ . ....	177
III Fig 5. 28 Track crossover point coordinates $x, y$ in $u$ planes of both wire chambers.....	179
III Fig 5. 29 Difference histogram of Fig 5.23 and Fig 5.29.....	179
III Fig 5. 30 $xy$ projection illustration of track reconstruction. ....	312
III Fig 7. 1 Cumulated hit time for all channels.....	182
III Fig 7. 2 Cumulated hit time when the wire has more than one hit in the event.....	183
III Fig 7. 3 Hit distribution of all wires.....	184
III Fig A1. 1 $x, y, z, u,$ and $v$ axis. ....	315
III Fig A1. 2 Direction relation between $u$ axis and $u$ wires. ....	315
III Fig A1. 3 Definition of $\delta_u$ or $\delta_v$ . ....	316
III Fig A1. 4 Relation between drift distance $\Delta d$ and track projection angle $\delta_u$ . ....	316
III Fig A1. 5 All vectors in section A1.3 computation.....	317
III Fig A1. 6 “Up/down” ambiguity of a wire plane. ....	320
<b>Part IV Simulations</b>	
IV Fig 1. 1 Energy distribution of electrons at primary vertex.....	188
IV Fig 1. 2 Electron $\varphi$ distribution for the simulation. ....	189
IV Fig 1. 3 $\tan\theta'$ (abscissa) vs $\tan\varphi'$ (ordinate) from simulation. ....	190
IV Fig 1. 4 Polar angle $\theta$ distribution of all generated events at target. ....	192
IV Fig 1. 5 Difference of the polar angle $\theta_p - \theta_q$ . ....	192
IV Fig 1. 6 $\varphi_{q-p}$ distribution.....	193
IV Fig 1. 7 1-dimension illustration of generating events satisfying certain distribution $f(x)$ ...	195
IV Fig 1. 8 Result and comparison between modified and standard pair generation code. ....	198
IV Fig 2. 1 Geant 4 global coordinate system $y$ - $z$ projection.....	207
IV Fig 2. 2 Transformations of holder of two wire chambers. ....	208
IV Fig 2. 3 Construction of one wire plane.....	209
IV Fig 2. 4 Input electron kinetic energy distribution.....	211
IV Fig 2. 5 Input (primary vertex) $\tan\theta$ vs $\tan\varphi$ distribution. ....	211
IV Fig 2. 6 Monitor 1 electron energy distribution.....	212
IV Fig 2. 7 Monitor 1 electron $x$ vs $y$ distribution.....	213

IV Fig 2. 8 Monitor 3 (electron detectors side) electron energy distribution.....	213
IV Fig 2. 9 Monitor 3 (electron detectors side) $x$ vs $y/\cos 45^\circ$ .....	214
IV Fig 2. 10 $\tan \theta$ vs $\tan \varphi$ distribution of electrons hit monitor 3.....	214
IV Fig 2. 11 Electron side wire plane distribution of all wire hits.....	216
IV Fig 2. 12 Electron side wire plane time of flights plot.....	217
IV Fig 2. 13 Electron side wire plane 0 and 2 $x$ vs $y$ distribution.....	217
IV Fig 2. 14 Electron side wire plane 0 $z$ coordinate (perpendicular to wire plane) distribution.....	218
IV Fig 2. 15 Hit wire number distribution of wire plane 0 and 1.....	218
IV Fig 2. 16 Kinetic energy distribution of wire plane 0 and 2.....	219
IV Fig 2. 17 Energy deposited of hits in wire plane 0, unit MeV.....	219
IV Fig 2. 18 Charge asymmetry at $\theta_{bin} = 5^\circ, 6^\circ, 7^\circ, 8^\circ$ .....	222
IV Fig 2. 19 Input $\theta$ difference, and input $\varphi$ difference.....	222
IV Fig 2. 20 Illustration: a straight track through 6 wire volumes of a wire plane.....	224
IV Fig 2. 21 Electron side detector hit $(x, y)$ coordinates distribution.....	225
IV Fig 2. 22 Projected coordinate $x_p$ on $v$ axis.....	226
IV Fig 2. 23 Electron track wire spans.....	227
IV Fig 2. 24 Projection of intersection of 56 MeV electron track on monitor.....	228
IV Fig 2. 25 Track horizontal projection coordinate $x$ (ordinate, in $cm$ ) on monitor (black), front (red) and back (green) chambers.....	229
IV Fig 2. 26 Track horizontal projection angle $\theta_o$ (ordinate, in $degrees$ ) when particles exit magnet.....	230
IV Fig 2. 27 Illustration of a 6-wire cluster.....	233
IV Fig 2. 28 Fit track intersection coordinates $x, y$ distribution.....	235
IV Fig 2. 29 Cluster span distribution of each wire plane on electron side wire chambers, using definition (1).....	237
IV Fig 2. 30 Cluster span distribution of each wire plane on electron side wire chambers, using definition (2).....	238
IV Fig 2. 31 Difference between fit track angle and Geant 4 monitor track $x$ projection ( $x$ is the beam axis) angles.....	239
IV Fig 2. 32 Difference between fit track and Geant 4 monitor track $x$ projection.....	239
IV Fig 2. 33 Difference between fit tracks and tracks extrapolate from monitor data.....	240
IV Fig 2. 34 All transformations in sequence and transformation $B, \eta$ .....	243
IV Fig 2. 35 Fit track intersections on wire chambers with rotation angle $\varphi = -15^\circ, 0^\circ, 15^\circ$ ....	246
IV Fig 3. 1 Coordinate system of the simple simulation.....	250
IV Fig 3. 2 Geometry of particle tracks till it exits uniform magnetic field, in $xy$ projection.....	254
IV Fig 3. 3 $yz$ projection view of track after it exits magnetic field.....	256
IV Fig 3. 4 Electron energy distribution at each check point.....	258
IV Fig 3. 5 Electron primary vertex polar angle vs azimuthal angle $(\theta, \varphi)$ distribution.....	259
IV Fig 3. 6 Energy $E$ vs detectors local horizontal coordinate $x'$ distribution.....	260
IV Fig 3. 7 Comparison of $xy$ distribution of positron intersection at front chamber between simple and Geant4 simulation.....	262
IV Fig 3. 8 Effect of Fringe field on tracks.....	263
IV Fig 3. 9 Energy asymmetry as a function of $E_e - E_p$ summing over all solid angles.....	264

IV Fig 3. 10 Conversion of e- direction in simulation coordinates $(x, y, z)$ to analyzer VDC coordinates $(x', y', z')$ .....	265
IV Fig 3. 11 Wire span $(n_u, n_v)$ distribution.....	267
IV Fig 3. 12 Intersection of e- track with wire planes. ....	268
IV Fig 3. 13 Calculation of amount of translation in $+x'$ direction.....	268
IV Fig 3. 14 Wire span $(n_u, n_v)$ distribution with tilt angle $60^\circ$ .....	269
IV Fig 3. 15 Track intersections on wire chambers at $60^\circ$ tilt angle. ....	270
IV Fig 3. 16 Difference of $xy$ coordinates of track on back chamber by changing $E$ by $0.1\text{MeV}$ . .....	272
IV Fig 3. 17 Difference of $xy$ coordinates of track on back chamber by changing $\theta$ by $0.1^\circ$ .....	272
IV Fig 3. 18 Difference of $xy$ coordinates of track on back chamber by changing $\varphi$ by $0.1^\circ$ . ...	273
IV Fig 4. 1 Projection $P\mathbf{x}$ of vector $\mathbf{x}$ onto 1D subspace spanned by vector $\mathbf{b}$ . ....	277
IV Fig 4. 2 Intrinsic projection coordinates (on standardized data $\mathbf{x}'$ ) $(z_0, z_1)$ distribution by PCA.....	284
IV Fig 4. 3 Distribution of $z_0, z_1, z_2$ of $e^+$ . ....	285
IV Fig 4. 4 Distribution of $z_0, z_1, z_2$ of $e^-$ . ....	285
IV Fig 4. 5 Data $\mathbf{x}$ before and after projection with number of principal components 1,2,3.....	287
IV Fig 4. 6 Standardized data $\mathbf{x}'$ before and after projection with number of principal components 1,2,3. ....	287
IV Fig 4. 7 $(z_0, z_1)$ of $e^+$ distribution, under $Ee$ cut. ....	291
IV Fig 4. 8 $(z_0, z_1)$ of $e^+$ distribution, under $\tan\theta_{et}$ cut. ....	293
IV Fig 4. 9 $(z_0, z_1)$ of $e^+$ distribution, under $\tan\theta_{et}$ cut, vacuum background.....	294
IV Fig 4. 10 Conditional distribution of e- $P(z_0, z_1   29\text{MeV} < E < 31\text{MeV})$ . ....	297
IV Fig 4. 11 $P(z_0, z_1)$ , after rotation $R$ . ....	298
IV Fig 4. 12 $P(z_0, z_1   E)$ , after rotation $R$ . ....	298
IV Fig 4. 13 $(z_0, z_1)$ distribution under energy cut.....	301
IV Fig 4. 14 $(z_0, z_1)$ distribution under energy cut and cut $(ZL_{e0} \leq z_{e0} \leq ZU_{e0}$ AND $ZL_{e1} \leq z_{e1} \leq ZU_{e1}$ AND $ZL_{p0} \leq z_{p0} \leq ZU_{p0}$ AND $ZL_{p1} \leq z_{p1} \leq ZU_{p1})$ .....	301
IV Fig 4. 15 Electron's $P(z_0   E)$ and $P(z_1   E)$ distribution, and fit function $F(z_0   E)$ and $F(z_1   E)$ . ....	303
IV Fig 4. 16 Target $E_e$ (from Geant 4 simulation data file) as abscissa vs reconstructed $E_e$ as ordinate. ....	305
IV Fig 4. 17 Target $E_e$ (from Geant 4 simulation data file) minus reconstructed $E_e$ . ....	305

## Part I Theory

### 1 Physics Intro [1]

The Gerasimov-Drell-Hearn (GDH) sum rule [2] [3] relates the total cross section of circularly polarized photons on a longitudinally polarized target to the anomalous magnetic moment of the target:

$$\int_{thr}^{\infty} (\sigma_{1/2} - \sigma_{3/2}) \frac{d\nu}{\nu} = -2\pi^2 \alpha \frac{\kappa^2}{M^2}$$

This sum rule has been shown to hold for all targets, both point-like and compound. The sum rule follows from the dispersion relation for forward Compton scattering, along with the optical theorem and the low energy theorem. The forward Compton amplitude may be written in terms of two scalar functions of  $\nu$ :

$$f(\nu) = f_1(\nu) \vec{\epsilon}'^* \cdot \vec{\epsilon} + \nu f_2(\nu) i \vec{\sigma} \cdot \vec{\epsilon}'^* \times \vec{\epsilon}$$

where  $\vec{\epsilon}$  and  $\vec{\epsilon}'$  are the transverse polarization vectors of the incident and forward-scattered photon. Due to the  $1/\nu$  weighing of the integrand, the sum rule is expected to be dominated by the low energy region.

The Bethe-Heitler [4] (BH) process  $\gamma Z \rightarrow e^+ e^- Z$ , lepton pair photoproduction in a Coulomb field, is one of the most well-studied processes in quantum electrodynamics. In a remarkable calculation, Bethe and Maximon [5] [6] evaluated the total cross section analytically to all orders in  $Z\alpha$ , providing one of the few nonperturbative all-orders results known in quantum field theory. Samuel C.C. Ting's group at DESY [7], showed that the differential cross section for wide-angle electron-positron pair production is in good agreement with the QED predictions, providing an important verification of fundamental theory.

The electron-positron charge asymmetry in either energy or angle measures the interference of first Born and second Born contributions to the BH amplitude, or more generally, the interference of an even and odd number of Coulomb exchanges. A simplified calculation is given by Brodsky and Gillespie [8], predictions of which are in fair agreement with the measurements of Asbury *et al.* [7] The analogous process in QCD is pomeron-odderon interference which leads to a charm-anti-charm asymmetry in the diffractive process  $\gamma p \rightarrow c\bar{c}p$ .

At low energies, one can use the BH charge asymmetry to check the low energy theorem for Compton scattering, extended to time-like virtuality. The first correction to the low energy limit of the forward Compton amplitude [9] [10] [11] has the spin-dependence  $\vec{S} \cdot \vec{\epsilon} \times \vec{\epsilon}'$  and is proportional to the anomalous magnetic moment squared  $\mu_A^2 = \left[ \frac{\mu - eS^2}{M} \right]^2$  for any particle of charge  $e$ , mass  $M$ , and spin  $S$ . This amplitude is the key input for the dispersion relation underlying the Drell-Hearn-Gerasimov sum rule [2] [3], generalized for any spin, due to the dominance of low energy processes in the integrand. For additional references and discussion see ref. [12].



The interference of the two-photon and one-photon exchange amplitudes is the primary cause of the electron-positron asymmetry in BH pair production. The two-photon BH amplitude is closely related to the two-photon exchange amplitude in  $ep \rightarrow ep'$  which is believed [13] [14] to cause the breakdown of the Rosenbluth separation. It may be much easier to measure two-photon exchange effects to high precision in  $\gamma p \rightarrow e^+e^-p'$  than to measure the electron-positron asymmetry in  $e^\pm p \rightarrow e^\pm p'$  elastic scattering.

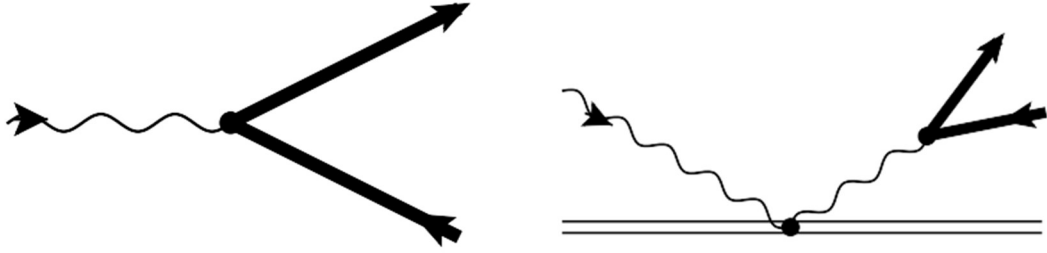
The electron-positron charge asymmetry in  $\gamma p \rightarrow e^+e^-p'$  also is sensitive to the interference of the real part of the virtual Compton amplitude  $T(\gamma p \rightarrow \gamma p^* \rightarrow e^+e^-p')$  with the Born contribution to BH pair production from one-photon exchange [15] [16]. This is particularly interesting at high photon energies where the real part of the Compton amplitude measures the  $J = 0$  fixed pole [17] due to the local coupling of the two photons to the fundamental carriers of the electromagnetic current [16] [18]. This is also called the ' $D$  term' in the deeply virtual Compton scattering (DVCS) literature [19].

## 2 Cross section and Asymmetry Calculation

The following is a summary of the calculation of corrections to the BH cross section which give rise to an asymmetry [20]. The main contribution comes from next-to-leading correction with respect to  $m/\omega$  ( $m$  the electron rest mass,  $\omega$  the photon energy). This is an odd function of  $\eta = Z\alpha$  ( $Z$  the atomic number of the nucleus,  $\alpha$  the fine structure constant) which causes asymmetry. The contribution of the Compton-type amplitude to the pair production cross section also leads to an asymmetry but is relatively minor so won't be elaborated on here.

### 2.1 Diagrams

The diagrams of both contributions are shown below:



I Fig2. 1 Diagram of BH pair production.

(Left) FIG. 1 of ref. [20] Diagram of pair production by a photon in a strong Coulomb field. Thick lines correspond to the positive- and negative-energy solutions of the Dirac equation in the Coulomb field. (Right) FIG. 3 of ref. [20]. Compton-type diagram for pair production by a photon in a strong Coulomb field. Thick lines correspond to the positive- and negative energy solutions of the Dirac equation in the Coulomb field. Double lines denote nucleus.

### 2.2 Calculation of cross section

The cross section of  $e^+ e^-$  pair production in external field is given by [21]:

$$d\sigma = \frac{\alpha}{(2\pi)^4 \omega} d\mathbf{p} d\mathbf{q} \delta(\omega - \varepsilon_p - \varepsilon_q) |M_{\lambda_1 \lambda_2}|^2 \quad (2.1)$$

where  $\varepsilon_p = \sqrt{\mathbf{p}^2 + m^2}$ ,  $\mathbf{p}$  and  $\mathbf{q}$  are the electron and positron momenta, respectively. The matrix element  $M_{\lambda_1 \lambda_2}$  has the form:

$$M_{\lambda_1 \lambda_2} = \int d\mathbf{r} \bar{u}_{\lambda_1 \mathbf{p}}^{(out)}(\mathbf{r}) \boldsymbol{\gamma} \cdot \mathbf{e} v_{\lambda_2 \mathbf{q}}^{(in)}(\mathbf{r}) \exp(i\mathbf{k} \cdot \mathbf{r}) \quad (2.2)$$

where  $\bar{u}_{\lambda_1 \mathbf{p}}^{(out)}(\mathbf{r})$  is a positive-energy solution and  $v_{\lambda_2 \mathbf{q}}^{(in)}(\mathbf{r})$  is a negative-energy solution of the Dirac equation in the external field,  $\lambda_1 = \pm 1$  and  $\lambda_2 = \pm 1$  enumerate the independent solutions of the Dirac equation,  $\mathbf{e}$  is the photon polarization vector,  $\mathbf{k}$  is the photon momentum,  $\boldsymbol{\gamma}^\mu$  are the Dirac matrices. The leading term and the first order correction of Born approximation for  $\bar{u}_{\lambda_1 \mathbf{p}}^{(out)}(\mathbf{r})$  and  $v_{\lambda_2 \mathbf{q}}^{(in)}(\mathbf{r})$  are derived by utilizing the asymptotic form of the Green function of the Dirac equation in the Coulomb field. ((14),(15) in [20])  $\bar{u}_{\lambda \mathbf{p}}^{(in)}(\mathbf{r})$  and  $v_{\lambda \mathbf{p}}^{(out)}(\mathbf{r})$  can be represented by integration of:

$$u_{\lambda p} = \sqrt{\frac{\varepsilon_p + m}{2\varepsilon_p}} \left( \frac{\phi_\lambda}{\varepsilon_p + m} \frac{\boldsymbol{\sigma} \cdot \mathbf{p}}{\varepsilon_p + m} \phi_\lambda \right), v_{\lambda p} = \sqrt{\frac{\varepsilon_p + m}{2\varepsilon_p}} \left( \frac{\boldsymbol{\sigma} \cdot \mathbf{p}}{\varepsilon_p + m} \chi_\lambda \right) \quad (2.3)$$

The matrix element represented by the leading term and the first order correction is:

$$M_{\lambda_1 \lambda_2} = \phi_{\lambda_1}^\dagger ((a_0 + a_1) + \boldsymbol{\sigma} \cdot (\mathbf{b}_0 + \mathbf{b}_1)) \chi_{\lambda_2} \quad (2.4)$$

where  $a_0$  and  $\mathbf{b}_0$  are represented by  $\mathbf{e}$ ,  $\mathbf{v}$ ,  $\mathbf{v} \times \mathbf{e}$ ,  $g$  and  $\mathbf{g}^{(\pm)}$ . In addition to those terms,  $a_1$ ,  $\mathbf{b}_1$  are also represented by  $(\boldsymbol{\theta}_p \pm \boldsymbol{\theta}_q)$ .  $a_0$  and  $\mathbf{b}_0$  are linear in  $\boldsymbol{\theta}_p = \hat{\mathbf{p}}_\perp$ ,  $\boldsymbol{\theta}_q = \hat{\mathbf{q}}_\perp$ , which are the  $\perp$  components of unit vectors  $\hat{\mathbf{p}}$  and  $\hat{\mathbf{q}}$ , where the notation  $\mathbf{X}_\perp = \mathbf{X} - (\mathbf{v} \cdot \mathbf{X})\mathbf{v}$ ,  $\mathbf{v} = \mathbf{k}/k$ .  $a_1$  and  $\mathbf{b}_1$  are quadratic in these variables.  $g$  and  $\mathbf{g}^{(\pm)}$  are integrations over  $d\mathbf{r}$  with terms  $F_A^{(\pm)}$ ,  $\tilde{F}_B^{(\pm)}$ , which can be expressed by integration of  $S_A(x_p, pr)$  and  $S_B(x_p, pr)$ , where  $x_p = \frac{r \cdot \mathbf{p}}{rp}$ .  $S_A(x, \rho)$  and  $S_B(x, \rho)$  are represented by infinite sums of Bessel functions and Legendre polynomials. Taking the leading terms of  $S_A$  and  $S_B$  one then integrates to get  $F_A^{(\pm)}$ ,  $\tilde{F}_B^{(\pm)}$ . Writing  $g = g_0 + \delta g$  and  $\mathbf{g}^{(\pm)} = \mathbf{g}_0^{(\pm)} + \delta \mathbf{g}^{(\pm)}$  yields  $g_0$  represented by  $N = -i \frac{2\pi}{mQ^2} \left( \frac{\varepsilon_q \xi_q}{\varepsilon_p \xi_p} \right)^{i\eta} |\Gamma(1 - i\eta)|^2$ ,  $\eta$ ,  $\xi_p = \frac{1}{1 + \delta_p^2}$ ,  $\xi_q = \frac{1}{1 + \delta_q^2}$ ,  $u = 1 - \frac{Q^2}{m^2} \xi_p \xi_q$ , ( $\mathbf{Q} = \mathbf{p} + \mathbf{q} - \mathbf{k}$ ),  $\mathcal{F} = F(-i\eta, i\eta, 1, u)$  (here  $F(a, b, c, x)$  is the hypergeometric function), and  $\mathcal{F}' = \frac{\partial \mathcal{F}}{\partial u}$ . In addition to those terms,  $\mathbf{g}_0^{(\pm)}$  is also represented by  $\omega$ ,  $\boldsymbol{\delta}_p = \frac{\varepsilon_p \boldsymbol{\theta}_p}{m}$ ,  $\boldsymbol{\delta}_q = \frac{\varepsilon_q \boldsymbol{\theta}_q}{m}$ .

The first corrections,  $\delta g$  and  $\delta \mathbf{g}^{(\pm)}$  are in addition represented by integration over  $d\lambda$  of their expression with above terms and  $\mathcal{G} = F\left(\frac{1}{2} - i\eta, i\eta, 1, z\right)$ ,  $\mathcal{G}' = \frac{\partial \mathcal{G}}{\partial u}$ ,  $z = 1 - \frac{Q^2 \xi_p \xi_q (1 + \lambda)}{m^2 (1 + \xi_p \lambda) (1 + \xi_q \lambda)}$ . Total amplitude of matrix elements is:

$$\begin{aligned} \sum_{\lambda_{1,2}} |M_{\lambda_1 \lambda_2}|^2 &= 2[|a_0 + a_1|^2 + |\mathbf{b}_0 + \mathbf{b}_1|^2] \\ &= 2[|a_0|^2 + |\mathbf{b}_0|^2 + 2\text{Re}(a_0 a_1^* + \mathbf{b}_0 \cdot \mathbf{b}_1^*)]. \end{aligned} \quad (2.5)$$

In the next-to-leading order approximation, terms  $|a_1|^2$  and  $|\mathbf{b}_1|^2$  are neglected and  $2\text{Re}(a_0 a_1^* + \mathbf{b}_0 \cdot \mathbf{b}_1^*) = 0$  for any photon polarization. Restricting the discussion to unpolarized photons for simplicity, the cross section is given by:

$$d\sigma = \frac{\alpha m^4 d\varepsilon_p d\delta_p d\delta_q}{2\pi^4 \omega^3} \left[ (\varepsilon_p^2 + \varepsilon_q^2) |\mathbf{g}^{(-)}|^2 + \omega^2 |g|^2 \right]. \quad (2.6)$$

Writing  $d\sigma = d\sigma_s + d\sigma_a$ , the leading term,  $d\sigma_s$ , and 1<sup>st</sup> correction,  $d\sigma_a$ , can be expressed with leading terms  $g = g_0 + \delta g$  and  $\mathbf{g}^{(\pm)} = \mathbf{g}_0^{(\pm)} + \delta \mathbf{g}^{(\pm)}$  shown above.

### 2.3 Special cases

Only the special cases relative to our experiment are listed here:

(1) If  $\eta \ll 1$  (applies for most lighter nucleus), the leading term  $d\sigma_s$  and correction  $d\sigma_a$ :

$$d\sigma_s = \frac{2\alpha m^2 \eta^2 d\varepsilon_p d\delta_p d\delta_q}{\pi^2 \omega^3 Q^4} \times \left[ \frac{Q^2}{m^2} \xi_p \xi_q (\varepsilon_p^2 + \varepsilon_q^2) + 2\varepsilon_p \varepsilon_q (\xi_p - \xi_q)^2 \right] \propto \eta^2 \quad (2.7)$$

$$d\sigma_a = -\frac{\alpha m^2 \eta^3 d\varepsilon_p d\delta_p d\delta_q}{2\pi\omega^3 Q^3} \{(\xi_p - \xi_q) \left[ 4 \left( \varepsilon_p \xi_p + \varepsilon_q \xi_q + \frac{\omega(\varepsilon_p^2 + \varepsilon_q^2)}{\varepsilon_p \varepsilon_q} \right) \right] + (\varepsilon_p - \varepsilon_q) \frac{(\varepsilon_p^2 + \varepsilon_q^2) Q^2}{\varepsilon_p \varepsilon_q m^2} \xi_p \xi_q \} \quad (2.8)$$

(2) In the limit  $\delta_p \gg 1$  and  $\delta_q \gg 1$  with  $\boldsymbol{\delta}_p = \frac{\varepsilon_p}{m} \boldsymbol{\theta}_p = \frac{\varepsilon_p \mathbf{p}_\perp}{m p}$ , then  $\delta_p \gg 1$ ,  $\varepsilon_p \sim p$  and  $\delta_p \sim \frac{p_\perp}{m} \propto p_\perp$ , or  $\delta_p$  is proportional to the electron transverse momentum, and  $\delta_p$  is proportional to positron transverse momentum:

$$\begin{aligned} d\sigma_a &= -\frac{\alpha \eta^3 (\varepsilon_p^2 + \varepsilon_q^2) d\varepsilon_p d\delta_p d\delta_q}{2\pi \varepsilon_p \varepsilon_q \delta_p^2 \delta_q^2 \omega^3 Q^3} [m^2 (\delta_p^2 - \delta_q^2) \omega + (\varepsilon_p - \varepsilon_q) Q^2] \\ &= -\frac{\alpha \eta^3 (\varepsilon_p^2 + \varepsilon_q^2) d\varepsilon_p d\delta_p d\delta_q}{2\pi \varepsilon_p \varepsilon_q \delta_p^2 \delta_q^2 \omega^3 Q^3} (\boldsymbol{\theta}_p - \boldsymbol{\theta}_q) \cdot \mathbf{Q}. \end{aligned} \quad (2.9)$$

For instance, with  $\varepsilon_p = 30 \text{ MeV}$  and polar angle  $\theta = 9^\circ$  at the primary vertex, we have  $p_\perp \sim \varepsilon_p \sin\theta \sim 4.7 \text{ MeV}/c$  and  $\delta_p \sim \frac{4.7}{0.511} = 9.18 \gg 1$  is satisfied. However, it's not convincing with a lower energy of  $\sim 18 \text{ MeV}$  and  $\theta = 5^\circ$ . Equation 2.9 can also be applied to case  $|\boldsymbol{\delta}_p + \boldsymbol{\delta}_q| \ll |\boldsymbol{\delta}_p - \boldsymbol{\delta}_q|$ , which can be satisfied if we measure azimuthal angle difference  $\varphi \sim 180^\circ$  and the two particles have similar  $\delta_p$  and  $\delta_q$  values.

## 2.4 Asymmetry

The cross section of  $e^+e^-$  pair photoproduction satisfies:

$$d\sigma(\mathbf{p}, \mathbf{q}, \eta) = d\sigma(\mathbf{q}, \mathbf{p}, -\eta) \quad (2.10)$$

And the charge asymmetry  $A$  is defined as:

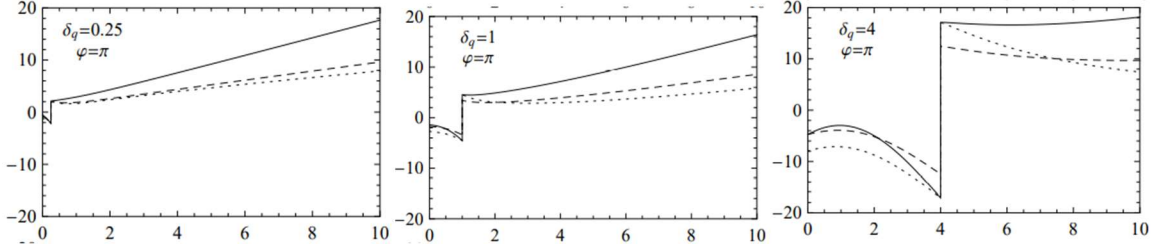
$$A = \frac{d\sigma(\mathbf{p}, \mathbf{q}, \eta) - d\sigma(\mathbf{p}, \mathbf{q}, -\eta)}{d\sigma(\mathbf{p}, \mathbf{q}, \eta) + d\sigma(\mathbf{p}, \mathbf{q}, -\eta)} = \frac{d\sigma(\mathbf{p}, \mathbf{q}, \eta) - d\sigma(\mathbf{q}, \mathbf{p}, \eta)}{d\sigma(\mathbf{p}, \mathbf{q}, \eta) + d\sigma(\mathbf{q}, \mathbf{p}, \eta)} \quad (2.11)$$

If we now write  $d\sigma = d\sigma_s + d\sigma_a$ , then  $d\sigma_s$  is an even function in  $\eta$  and  $d\sigma_a$  is odd in  $\eta$ . Then, eq. 2.11 turns into:

$$A = \frac{d\sigma_a(\mathbf{p}, \mathbf{q}, \eta)}{d\sigma_s(\mathbf{p}, \mathbf{q}, \eta)} \quad (2.12)$$

Outside the narrow region  $Q_\perp \lesssim |Q_\parallel| = |\mathbf{v} \cdot \mathbf{Q}| \sim m^2/\omega$ , the approximation  $Q^2 \cong Q_\perp^2 = m^2 (\boldsymbol{\delta}_p + \boldsymbol{\delta}_q)^2$  can be applied. In addition, if we fix  $\boldsymbol{\delta}_p, \boldsymbol{\delta}_q$  and  $x = \frac{\varepsilon_p}{\omega}$  (portion of  $\varepsilon_p$  out of total energy), it can be verified that the asymmetry  $A$  scales with  $m/\omega$ . Fig 2.2 below shows the asymmetry  $A$  in units of  $m/\omega$  as a function of  $\delta_p$  with different fixed  $\delta_q$  and  $x$  when  $\varphi = \pi$  ( $\varphi$  is the angle difference between  $\boldsymbol{\delta}_p$  and  $\boldsymbol{\delta}_q$  or, in the Geant 4 simulation, the azimuthal angle difference between electron and positron).

In addition, if we make the  $\eta \ll 1$  approximation and use equations 2.7 and 2.8 to compute asymmetry, we find that the asymmetry is proportional to both  $m/\omega$  and  $\eta$ . Fig 2.3 shows the dependence of asymmetry on  $\eta$  in units  $m/\omega$  for  $\delta_p = 2, \delta_q = 4, \varphi = \pi$  and a few values of  $x$ .

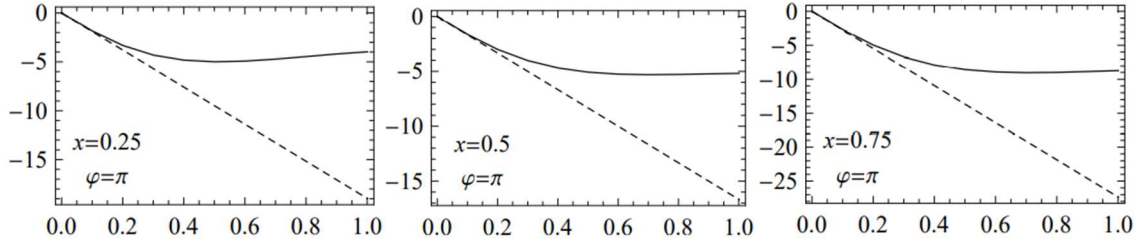


I Fig2. 2 The dependence of asymmetry  $A$  on  $\delta_p$ . Ordinate: asymmetry  $A$  in  $\frac{m}{\omega}$ , abscissa:  $\delta_p = \frac{\varepsilon_p}{m} \theta_p = \frac{\varepsilon_p p_{\perp}}{m p}$  no unit.

(Right side of FIG. 4 in Ref. [20]) Drawn for  $\varphi = \pi$  and a few values of  $\delta_q$  and  $x$ .  $x = 0.25$  (solid curves),  $x = 0.5$  (dashed curves), and  $x = 0.75$  (dotted curves),  $\eta = 0.54$  (tungsten).

A few observations:

- (1) the curves are all discontinue at  $\delta_p = \delta_q$ ,  $\varphi = \pi$  which means  $Q_{\perp} \sim 0$  and approximation  $Q_{\perp} \lesssim |Q_{\parallel}| = |\mathbf{v} \cdot \mathbf{Q}| \sim m^2/\omega$  cannot be satisfied.
- (2) Since we have fixed  $m$  for electron and positron, the asymmetry  $A$  then is inversely proportional to  $\omega$ . Thus, the lower the photon energy, the larger the asymmetry.
- (3) An estimate for the proposed experimental configuration:  $\omega = 60 \text{ MeV}$ , and  $\frac{m}{\omega} = \frac{0.511}{60} \cong 1/117.4$ . The largest value in plots is about 18, then asymmetry at  $\omega = 60 \text{ MeV}$  could be about  $18/117.4=15.3\%$ .



I Fig2. 3 The dependence of asymmetry  $A$  on  $\eta = Z\alpha$ . Ordinate: asymmetry  $A$  in  $\frac{m}{\omega}$ , abscissa:  $\eta = Z\alpha$  no unit.

(Right side of Fig. 5 in Ref. [20]) Drawn for  $\delta_p = 2, \delta_q = 4$ ,  $\varphi = \pi$  and a few values of  $x$ .

Observations:

- (1) For the proposed experimental configuration,  $\omega = 60 \text{ MeV}$ . Thus,  $x = 0.25$  means  $\varepsilon_p=15 \text{ MeV}$ ,  $x = 0.5$  means  $\varepsilon_p=30 \text{ MeV}$ , and  $x = 0.75$  means  $\varepsilon_p=45 \text{ MeV}$ . All energies here are within the detector acceptance.
- (2) The curves flatten at about  $\eta = 0.6$ . With an asymmetry value  $x = 0.75$ , about 9 in the plot, the asymmetry is about  $9/117.4=7.7\%$  for  $\omega = 60 \text{ MeV}$ .

## Part II Apparatus

### Introduction

The BH experiment will measure the charge asymmetry of electron-positron pairs produced from high energy photons scattered from the Coulomb field of various nuclei via the Bethe-Heitler process. The apparatus of proposed measurement from upstream to downstream includes:

The beam - we will use high intensity photon beam provided by the HI $\gamma$ S (High Intensity Gamma Source) in the Duke Free Electron Laser Laboratory (DFELL) located on the campus of Duke University.

Targets – we plan to use square thin foils of various materials.

Magnet – we will use a dipole magnet to analyze the electron-positron pairs.

Detectors – we will use two pairs of vertical drift chambers and two arrays of plastic scintillators to measure tracks of the electrons and positrons.

Data acquisition system (DAQ) – we will use a system based on the CODA system in use at Jefferson Lab.

In this part, all components of the apparatus will be introduced in the above order. No significant development work is required for the beam and targets; only their suitability for the requirements of the experiment is discussed. Preparation of the drift chambers and scintillators preparation is emphasized, with results from the tests shown. Further off-line track reconstruction results are presented in Part III Analyzer.

### 1 Beam

The beam is provided by the High Intensity Gamma Source (HI $\gamma$ S) in the Duke Free Electron Laser Laboratory (DFELL) located on the campus of Duke University. It utilizes Compton backscattering to generate a mono-energy gamma beam. As seen from the diagram (Fig 1.1) below, wigglers (or undulator) are magnets placed periodically with opposite polarizations. They cause the transverse acceleration of the electrons to result in photons (synchrotron radiation) being emitted. The mirrors at each end create an optical cavity with a length of half the circumference of the storage ring, causing the radiation to form standing waves. The multi-layered mirrors can achieve a reflectivity of  $\sim 0.9995$  for the laser which results in an intense beam of photons being stored. The electrons in the storage ring are synchronous with the photons in the optical cavity. On each pass the electrons interact with the transverse electric field of the synchrotron radiation, making electrons clump into microbunches within a period of one optical wavelength. The bunched electrons are in phase. [22]

There are two bunches in the storage ring. One generates the free electron laser beam. The other, half the storage ring circumference away, intersects with the photons in the optical cavity with each going in opposite directions. Some photons Compton backscatter from the electrons to generate a high intensity beam of  $\gamma$ 's. At our proposed photon beam energy of 60 MeV, a rate of  $1.2 \times 10^7 \text{ Hz}$  with an energy spread of 5% FWHM can be delivered. [23]

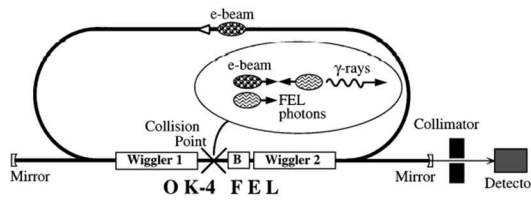


FIG. 1. Schematic of the OK-4/Duke storage ring FEL and  $\gamma$ -ray source. Two electron bunches spatially separated by one-half the circumference of the ring participate both in lasing and  $\gamma$ -ray production via Compton scattering of intracavity photons. A collimator installed downstream selects a narrow cone of quasimonoenergetic  $\gamma$  rays.

II Fig 1. 1 (Fig. 1 from Ref. [23]) Gamma ray source.

## 2 Target

The targets for the BH experiment will consist of  $4\text{cm} \times 4\text{cm}$  foils of  $\text{CH}_2$ ,  $^{12}\text{C}$ , and  $^{238}\text{U}$ . They will be mounted in frames and attached to a movable horizontal support structure. The structure will be moved using a remotely controlled stepping motor. The structure will have positions for five frames; one for each of the target materials; an empty one; and a multi-foil carbon optics target. [24]

There are several parameters of the targets that must be considered for the planning of the experiment. The materials of the targets determine the differential cross section and thus the angular distribution of the emerging electrons and positions. The cross section combines with the thickness of the target to determine the event rate. The distance between the target and the magnet is the major factor in determining the detector acceptance:

- (1) The opening angle from target to downstream of the yoke hole determines the maximum polar angle of primary particles;
- (2) The distance from target to center of magnet, along with the diameter of magnet and the gap between the magnet pole faces determines the vertical angle acceptance; and
- (3) A tungsten cone shaped baffle will be placed between the magnet poles to block high rate and low-resolution portion of the primary particles.

Referencing the Geant 4 simulation results, the targets will be placed perpendicular to the beam 42.3 cm upstream from magnet and 13.4 cm upstream from the back side of the yoke hole. This gives maximum polar angle of  $14.7^\circ$  with respect to the target center. The thickness of the targets will be  $25\mu\text{m}$  which, based on computation utilizing theoretical differential cross sections code, the raw data rate considering yoke hole and cone shaped baffle with polar angle  $4^\circ$  to  $7^\circ$  will be between 1.2 Hz to 13 Hz, see Part IV 1.4.

One possible issue caused by the thickness and density of the target is the multiple scatter of primary particles inside the target volume. Since the cross section dependence on polar angle is very sensitive, the measurable region lies between  $5^\circ$  and  $10^\circ$ , based on a balance of rate and resolution considerations. (*c.f.* Part IV Simulation, Figs. 1.4 and 2.18) A  $^{238}\text{U}$  target with a thickness of  $25\mu\text{m}$  could cause change of primary particle direction on the order about  $1^\circ$ , which would hamper the asymmetry extraction. A lighter nucleus such as Cu is being considered to replace  $^{238}\text{U}$ .

### 3 Magnet [25]

The electron-positron pairs will be analyzed using the magnet from the pair spectrometer constructed at the Saskatchewan Accelerator Laboratory (SAL). [26] The magnet was mapped at Jefferson Lab. The field map was consistent with that measured at SAL more than twenty years ago indicating no degradation of the magnet coils. The results of the field map are shown in Fig. 3.1. The SAL pair spectrometer was calibrated at a photon energy of 60 MeV by J.R. Sigurdson *et al.* [26]. The range of energies for the detected positrons and electrons was from 26 MeV to 34 MeV, close to the range of energies we will use: 22 MeV to 38 MeV. Our simulations, performed using the program DIMAD, were matched to the SAL results and then extended to the wider energy range. [27]

The acceptance of the system is constrained by the pole tip separation and physical constraints of where the detectors can be placed. The vertical acceptance is constrained by the pole tips to about  $\pm 3^\circ$ . The horizontal acceptance is constrained by the optics to between  $+ 30^\circ$  and  $- 15^\circ$  for the highest energy (40 MeV) particles and between  $+ 15^\circ$  and  $- 30^\circ$  for the lowest energy (20 MeV) particles. Inasmuch as both particles can be expected to come out at approximately the same angle (measured with respect to opposite sides of the photon beam), this means the effective overall horizontal acceptance will be  $\approx \pm 15^\circ$ . Based on our later Geant 4 simulation, the horizontal acceptance is more constrained by the rear wire chamber. Inasmuch as the magnet was powered and performed stably for the magnetic field measurements, we anticipate no significant development work on it will be required.

The magnet has three major roles for the experiment:

- (1) to separate the BH electron and positron pair from an event;
- (2) to provide energy and momentum dependent spectrum of BH electron or positron;
- (3) to be the major component which determines the acceptance.

Our collaborator, Prof. Rob Pywell of the University of Saskatchewan, has interpolated the field map and integrated it into the Geant 4 simulation. In the simulation, the magnetic field pointed vertical down, the electrons going to the right side of the beam, and the opposite for the positrons. Most of the behavior of the BH pair acquired through the simulation is discussed in detail in the Geant 4 simulation chapters.

Here list some principal results:

- (1) The existence of the cone baffle blocks particles with polar angle from target less than the cone angle. In addition, it blocks electrons with initial direction to the left side of the beam; the opposite for positrons.
- (2) When approximated by a uniform field, the charged particles have helical trajectories inside the magnet. The radius of the horizontally projected circle of the helix is proportional to  $1/B$ . Thus, the bending effect is less for higher energy particles. As a consequence, the lower energy acceptance measured at the detectors drops first and continuously to zero before the high energy particle on the other side does.
- (3) In addition to (2), the  $1/B$  dependent radius causes the horizontally projected angle at the exit of magnetic field,  $\theta_{out}$ , is not a monotonic function of the horizontal entering angle,  $\theta_{in}$ , for certain energies. This is different than visible light being separated by a prism where transformations through refractions make  $\theta_{out}$  always a monotonic function of  $\theta_{in}$  for monochrome.



- (4) The vertical acceptance is constrained by the pole tips to about  $\pm 3^\circ$ . This is the cause of the greatest loss of incident particles.
- (5) The side opening of the magnet frame spans a much larger vertical acceptance than the magnet pole tip. Thus, it has no effect on the acceptance. Meanwhile, the horizontal acceptance has major effect on the energy acceptance. According to (2), most particles can be accepted with energies even higher than 50 MeV, but many with low energy, and therefore small bending radius and energy loss through multiple scattering are lost. However, the major loss of acceptance of low energy particles is from the back wire chamber, where almost all 9 MeV particles are lost.



II Fig 3. 1 SAL pair spectrometer magnet.

SAL pair spectrometer magnet for BH experiment, currently at UVA.

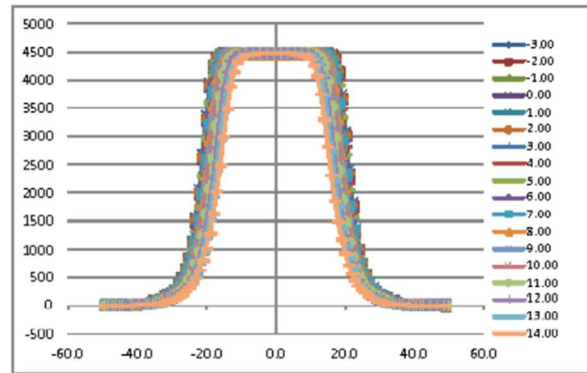


Fig. 3. Midplane magnetic field (in Gauss) of the SAL pair spectrometer dipole as measured at JLAB as a function of horizontal displacement from center.

II Fig 3. 2 Field map of the magnet. Ordinate: Magnetic field in *Gauss*, abscissa: horizontal displacement from center of the magnet in *cm*.

Fig. 3 from [25].

## 4 Vertical drift chamber

### 4.1 Introduction

Region III *vertical drift chambers (or wire chambers, abbr. VDC)* from the Q-weak experiment will be used in the BH experiment. The functioning components of drift chambers are composed of a plane with parallel thin conducting wires (called sense wires) and two conducting foil planes (with equi-distance) lies above and below the wire plane, which has been made gas tight. During operation, the wire chambers are supplied with high negative voltage applied to the foils as cathodes, and wires connected to ground. In addition, the gas mixture with inert gas is constantly flowing through the wire plane. When an ultra-relativistic charged particle passes through the active region of the chamber, electron-ion pairs are created along its path. Electrons drift to anode and ions drift to the cathode due to the electric field. These primary electrons drift at constant speed when they are away from sense wires and the electric field is essentially constant. When they are very close to wires (within a few wire diameters), the electric field strength increases dramatically. The electrons gain such energy that they cause ionization, and so can these secondary electrons. This phenomenon, which is called avalanche or cascade, produces gains of the order of  $10^5$  to  $10^6$ . [28] The induction from avalanche ions causes a measurable pulse on the corresponding sense wire where the electrons are collected. The pulse is pre-amplified and discriminated by a discriminator card attached to the wire chamber, then transmitted through ribbon cables to a *time to digital converter (abbr. TDC)*. The drift time of the first primary electron to reach a sense wire is converted to drift distance (c.f. Part III Analyzer, section 2.4 Time to distance conversion). All drift distances from all sense wire intersecting the track of the ultra-relativistic charged particle inside the wire chamber are fitted to reconstruct its track.

In this chapter we only discuss the hardware part of the preparation of VDC for BH experiment. Track reconstruction using Jlab Hall A analyzer is discussed in Part III Analyzer, section 2.3 to 2.5. The basics of design and construction of the VDC are discussed in 4.2, and the commissioning test of the VDC is discussed in 4.3.



II Fig 4. 1 A pair of Q-weak drift chambers.

Fig. 4 from [1].

## 4.2 Design and construction [29]

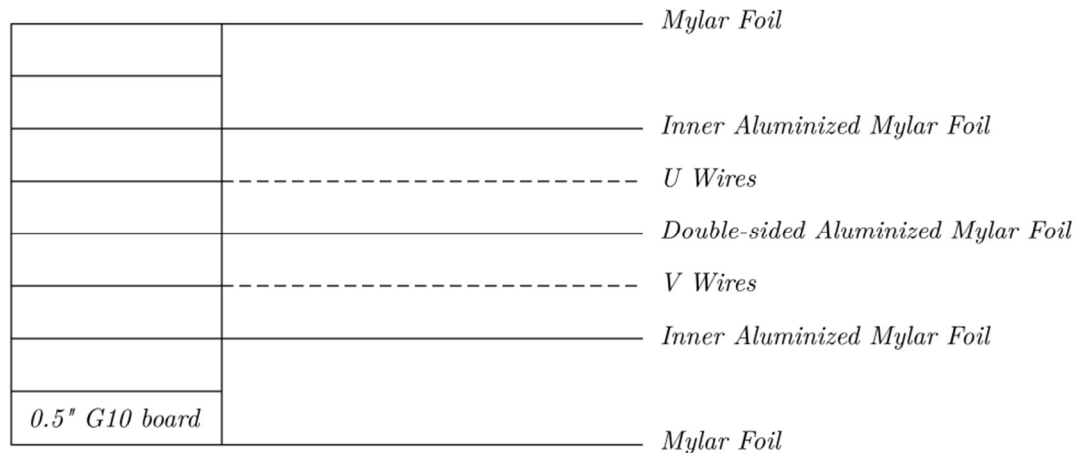
### 4.2.1 Overview

There are four wire chambers, identical in dimensions to be used in the BH experiment. One pair is placed on either side of the beam to provide tracking information of the primary Bethe-Heitler electron-positron pairs. The overall dimensions of a wire chamber are 3 feet by 8 feet by 5.5 inches. Two wire planes lie within with parallel wires oriented at different directions lies within, each with dimension 21 inches by 80.5 inches by 1 inch. The particle tracks are designed to cross wire planes at  $\sim 45^\circ$  angle to give spatial resolution about  $200\mu m$ . Thus, the wire chambers will tilted at  $45^\circ$  to the horizontal plane. The original high voltage applied to cathode planes for the Q-weak experiment was  $-3800V$ , and  $0V$  at wires. At the last cosmic test run in March 2020, the HV was set to  $-3900V$ . The chambers are gas tight, with 50% (by volume) argon and 50% ethane flowing through all wire planes.

## 4.2.2 Design

The design of the wire chambers is based on the JLAB HRS chambers, with two wire planes in each chamber. Due to the requirement of multiplexing 9 channels for the Q-weak experiment, there are 279 (as multiple of 9) wires per plane to provide the required resolution. [29]

The chambers were designed such that ultra-relativistic charged particles would hit each plane with a minimum of 4 wires to provide sufficient resolution and a maximum of 8 matching the readout design. Only single-track events were allowed. The wire stringing angle (angle between wires and long axis of the wire plane) was designed to maximize number of wire hits under the above requirements. Garfield [30] and Geant 4 simulations [31] suggested an angle of  $30^\circ$  was optimal. An angle of  $26.45^\circ [= \arctan(0.5)]$  [29] was chosen to make for easier wire stringing design and fabrication. It should be noted for comparison that the JLAB Hall A High Resolution Spectrometer (HRS) chambers use an angle of  $45^\circ [= \arctan(1)]$ . Material to support and hold frames is chosen to be G10-FR4 circuit board material [29]. It fulfills the requirement of holding shape under tension of wires and cathode foil, gas tight and strong dielectric. The complete structure of the frames is shown in the Fig 4.2 below.



II Fig 4. 2 Cross section of one VDC.

(Modified version of Ref. [29] Fig. 4.6) Eight 0.5-inch thick G10 boards holds wires and Mylar foils. The outside Mylar foils of wire frame are aluminized on side facing wires, and the center Mylar foil is double side aluminized to provide conduction. U, V wire frames are flipped by  $180^\circ$  to each other. U, V wires indicated are using dash lines since they're not parallel or perpendicular to sides of the frames.

## 4.2.2 Construction

While we were not involved in the construction of these chambers relevant details of their construction are included here as they are important to their use in the Bethe-Heitler Asymmetry measurements to be performed.

Wires: Each 0.5" thick G10 frame shown in Fig 4.2 is constructed by gluing 4 rectangle pieces.  $25\mu\text{m}$  gold-coated tungsten wires are used, all electrically connected outside through custom boards. They are tensioned to ensure flatness and resistance to repulsion between wires. Wire spacing on the long side of the frame was measured to be  $11.074 \pm 0.078\text{mm}$ . [29] Thus, the perpendicular wire spacing is:

$$11.07 \sin[\arctan(0.5)] = 4.95 \text{ mm} \quad (4.1)$$

The Mylar foils are 0.0005" thick [29] and also stretched and secured. Two 0.75" thick aluminum frames are secured on both sides of G10 frames, making 5.5" the total thickness of one VDC 5.5". [29]

Gas handling system: Holes drilled in aluminum frames and G10 frames allow gas to travel freely. Gas flows from one short side of the frame to the other and returns in the next frame. To illustrate in Fig 4.1, gases go left in uppermost gas frame, then right in U wire frame, left in V wire frame, and back to the right side of the frame in bottommost gas frame. Gases are slightly over pressured to ensure a steady flow which is monitored using a bubbler for each chamber. The purpose of the filling gas is to provide electrons and ions, and prevent electron absorbing molecules, oxygen, etc. The gases used in the Q-weak experiment was 50 % argon and 50 % ethane. [29] Noble gases are used since they have the lowest electric field intensity for avalanche, and argon is the cheapest. Ethane absorbs high energy photons created from Argon to prevent continuous discharge before primary electrons reach the wires, which would reduce the gain. In this usage, gain means the average number of avalanche electrons from a single primary ionization. With ethane, the gain improved from  $10^3 \sim 10^4$  to  $\sim 10^6$ . The gas composition during my cosmic ray tests are different due to the flammable nature of ethane. [28]

High voltage supply: HV is delivered to the aluminized Mylar foils using a custom-built distribution/safety circuit. Bertan 377N power supplies are used, one for each chamber. One constraint is that they must be ramped up slowly to prevent discharge by a larger avalanche, tripping the supply. Dark current is about 50nA. [29]

Gain: The number of ionizations is 94 per cm for Ar, 111 per cm ethane at atmospheric pressure. In these chambers, one primary electron can generate  $10^5 - 10^6$  secondary electrons, making wire hit signal a measurable quantity.

Chamber current:  $current = ionization \times rate \times gain + backgrounds$ . Here, background means background radiation from cosmic rays. Ultra-relativistic charged particles through chambers at  $45^\circ$  angle, one wire plane is 5.08 cm thick, which leads to path length  $\sim 8$  cm and  $\sim 816$  ionizations. A 75 kHz incident particle rate draws  $\sim 2.25 \mu\text{A}$  giving a gain of  $\sim 2.3 \times 10^5$ . [29]

## 4.3 Commissioning

The purpose of the commissioning of the VDC is to set up the wire chambers and test if they are fully operational for the purpose of the BH experiment. This includes:

- 1) Setting up the gas system.
- 2) Preparing high voltage supplies for cathodes of the wire chambers.
- 3) Implementing front end electronics. This includes preparing and testing pre-amp discriminator cards, their installation, and testing.
- 4) Signal cable management.
- 5) Grounding improvement and noise reduction.
- 6) Setting up scintillator triggers for cosmic tests. This includes logic operation for combined PMT signals, and its connection to TDC.
- 7) Setting up the data acquisition. This includes collecting the wire drift time raw data into “evio” formatted raw data file. The program was set up by Dr. Brad Sawatzky of JLAB.
- 8) Analyzing the VDC data using a modified wire chamber code derived from the Jlab Hall A analyzer to reconstruct particle tracks.
- 9) Performing test runs to find efficiency plateaus in terms of HV applied on chambers, to determine discriminator cards threshold voltages, and to confirm the good efficiency of the chambers.

Since this chapter is introducing the hardware preparation of the VDC, above items 1) through 5) and 8) and 9), will be discussed here. Items 6) and 7), which concern software will be discussed elsewhere. Except for grounding, which has been integrated into the discussion of the preparation of each individual component, each of these topics are discussed separately here.

### 4.3.1 Power supplies.

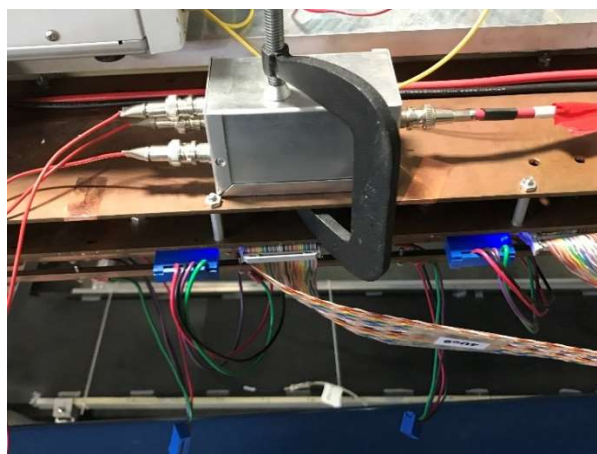
There are two types of power supplies used for the VDC: one provides high negative voltage for the Mylar foil cathodes of the wire planes, the other provides power and threshold settings for the discriminator cards.

1) HV supply for VDC: The wire chambers operate at a very high voltage, 3900V for the current Nanometric discriminator card setup (100V higher than in their original use in the Q-weak experiment) and very low current ( $\sim \mu A$ ). The Bertan 377N HV supplies are the same as in Q-weak experiment. It has a maximum voltage of 7.5 kV and the trip currents can be set from 0.1  $\mu A$  to 100 mA with 10x change at each step, which is adequate for the wire chambers. Each Bertan 377N has two channels to provide HV for one wire chamber each. The HV was applied to the foils using a custom-built distribution/safety circuit.

The procedure to setup the HV operating the chambers is as follows. After each change of gas cylinder for the chambers, a day or two wait was required to give the gas flow time to settle. HV cables were connected to the distribution circuit attached on the wire chamber. The HV dial was set to 0V, the trip current to 100 $\mu A$ , but was overridden while the HV was turned on. Both high voltages for the pair of wire chambers were set to the low 3 kVs, then dialed up even slower one chamber at a time. The HV supply had to be monitored carefully as it was common for the current to become very unstable for voltages above 3700 V. A few minutes after the desired voltage was reached the trip current was set to 10 $\mu A$ , the normal trip level for the VDC.



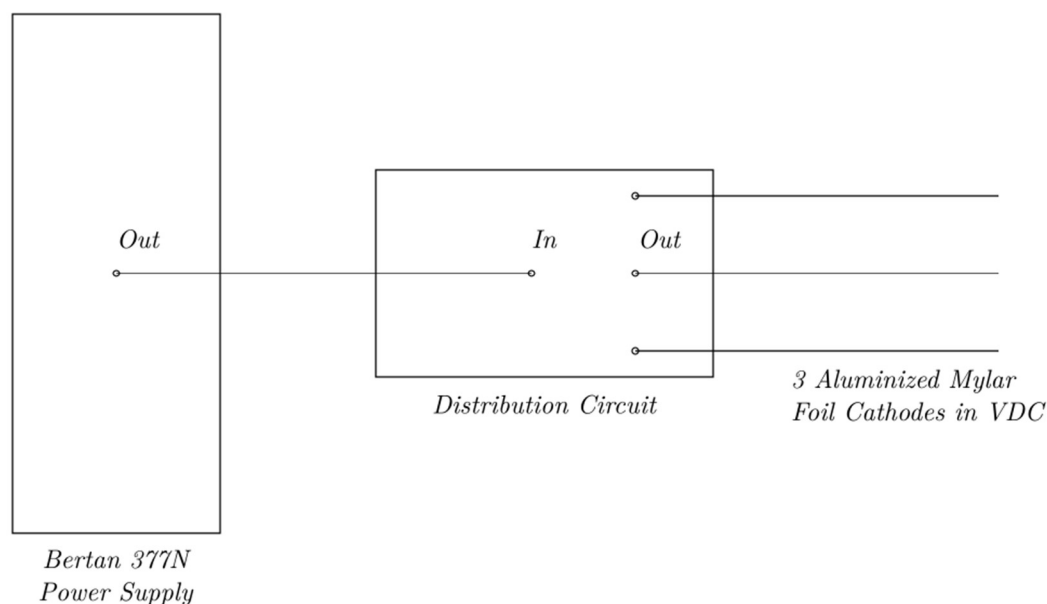
There are three points to be noted: 1) Due to the high sensitivity to change of voltage for the VDC mentioned above, the grounding has to be good for the HV supply. However, the power in ESB building of Jlab is not clean. HV supplies were easily tripped during unmonitored test runs, especially during thunderstorm weather in the summer. 2) The HV wires which connect the 3 aluminized Mylar foils of a wire chamber (c.f. Fig 4.1) from the shorter side of the wire chamber are very thin and much smaller than the connector on the HV distributor. In addition, a few original distributors attached to the chamber are had arcing issues which caused trips. Some better made distributors with thicker and better insulation materials replaced those. 3) The stability of the chamber current also depends on the gas mixture. Since ethane is flammable, 75% Argon and 25%  $CO_2$  was used. This was not as good as an argon-ethane mixture and could cause avalanches before drift electrons get very close to the sense wires, resulting in a larger region of discharge and current. This also affects the stability of the HV supply.



II Fig 4. 3 Wire chamber HV supply and HV distributor.

Here HVs are set to 3900V and trip current level to  $100\mu A$ . However, the right channel current is high for the normal chamber operation. Right, replacement of the HV distributor on the VDC.



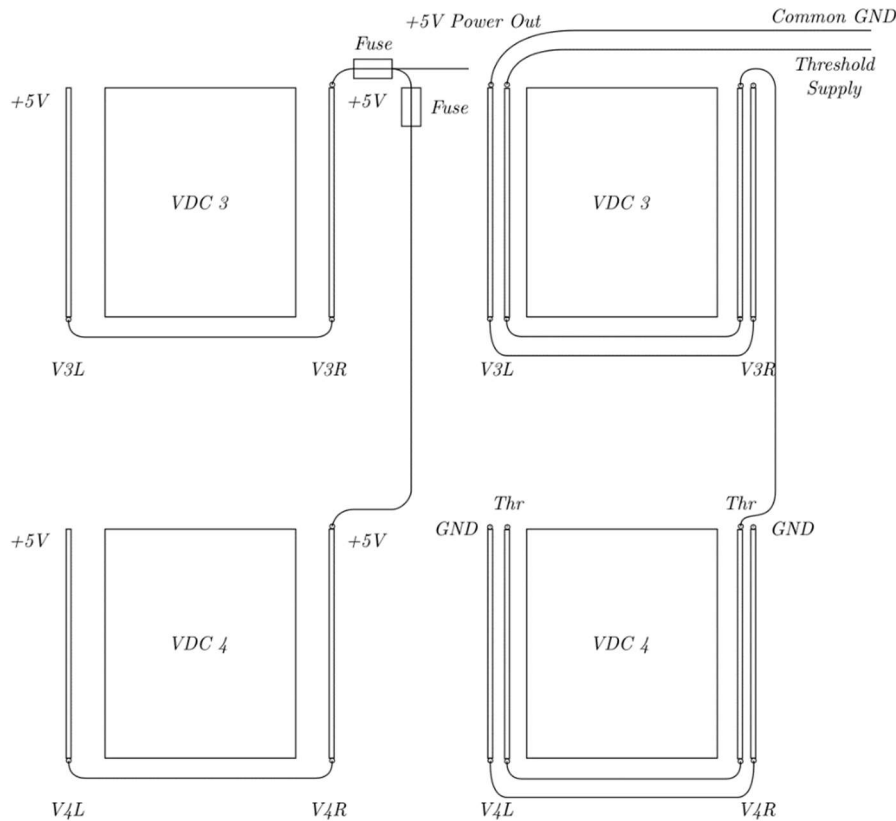


II Fig 4. 4 Diagram for HV supply on VDC cathodes.

2) Low voltage supplies for the discriminator cards: The low voltage supplies provide power and threshold to discriminator cards plugged onto each VDC through  $0.25" \times 0.25"$  copper bars attached parallel to the chamber. [29] Four parallel bars are reserved to be used, 4 crimp connectors are screwed onto the copper bars and the other sides are merged into a pigtail connector to the cards. The *MAD* cards (discriminator cards with MAD chips) used in the original Q-weak experiment were observed to have an unidentified false signal issue. Thus, they were replaced by *Nano N-277-C(CD)* cards (abbr. Nano card). These proved to be reliable during cosmic test runs. Detailed discussion of the MAD card is in discriminator card section 4.3.4. This change required updates of low voltage power and threshold supplies. There're two major reasons: 1) the way of supplying power to the cards are different, and 2) Nano cards have much higher power consumption.

The MAD cards have pins connected to +6 V power, positive and negative thresholds, and ground in that order. Nano cards have positive +5 V, -5 V, thresholds, and ground, in that order. The diagram showing connections to copper bars for both power supplies and thresholds of a pair of wire chambers is shown in Fig 4.4. In short, both +5 V or -5 V power supplies connect to the cards in parallel for each wire chamber, and in series for cards inside one chamber, while a threshold supply connects to chambers in series. The  $\pm 5$  V power supplies are Acopian model 5PH60, providing 5 V voltage and maximum 60 A current. The full 96 implemented Nano cards for all four chambers draw currents of more than that for -5V power, resulting in a drop of voltage for the cards, which in turns cause unexpected results. Thus, two -5V power supplies are used for four wire chambers, while one +5V supply is enough for the total 20A draw. Due to the high current compared to MAD cards, the power lines from power supplies and between copper

bars from opposite side of wire chamber have been replaced by heavy duty cables. For MAD cards, powers are connected through 1 gauge wire, and thresholds through 18-gauge wire. The connectors with crimp connectors on the copper bar and integrated plastic connectors on discriminator cards connect power and threshold directly to the cards, so bad crimp connectors are a common cause of strange behavior of discriminator cards. Unlike the MAD cards, if the crimp connector causes disconnection there is no LED light indicator of power on with Nano cards; the bad connector might only be identified when analyzing the data during test run. In 2018, all crimp connectors on copper bars were overhauled. To find bad crimp connectors, simply tried to pull them out from wires by hand. In total about 70 bad connectors found, the high failure rate was due to lack of twisting threads of wires before crimping, and having the threads spread out into thin layers during crimping. After the re-crimping, connectors were screwed back onto the copper bars parallel to the bars for better electric connection. It should be noted that there are 18 discriminator card slots for each wire plane, but only 12 are used for our tests and are necessary for the BH experiment. Thus, there is significant redundancy.



II Fig 4. 5 Diagrams for discriminator cards threshold and power supplies.

Left Diagram for +5 V power supply. Right: Diagram for threshold supply and ground on discriminator cards on wire chamber. The V3, V4 means chamber 3,4; L, R means Left and Right side of the chamber.

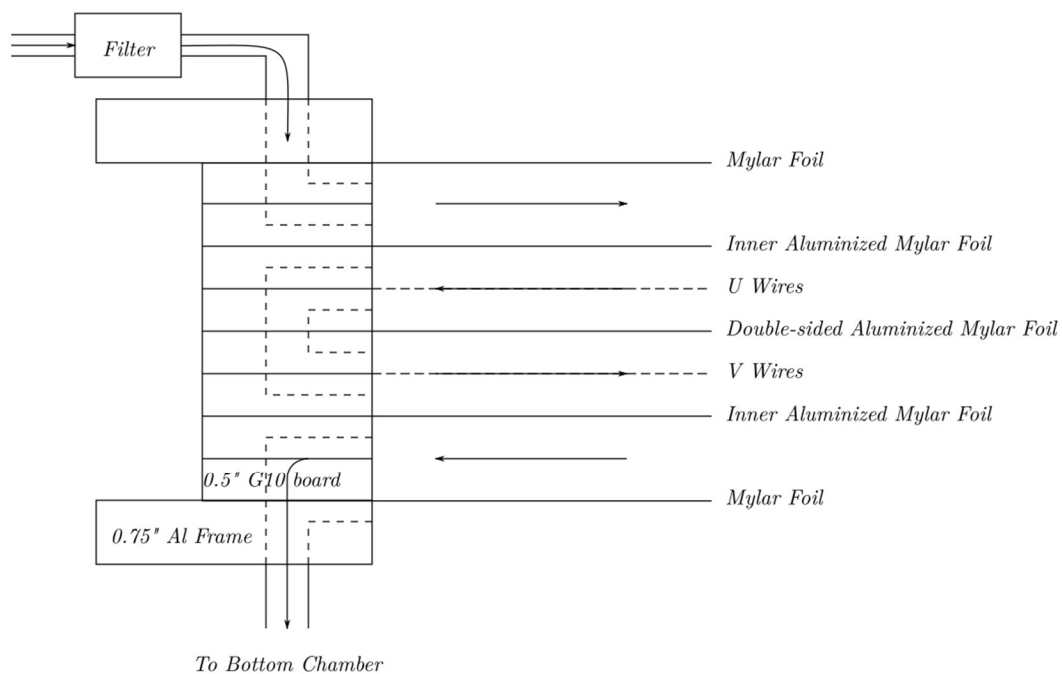
### 4.3.2 Gas type and flow regulation

Gas mixtures are essential for the operation of drift chambers. As mentioned in the overview, gas used for VDC usually is composed of a mixture of two components. An inert gas, usually argon, provides electron-ion pairs creating avalanches; the other provides quenching for photons emitted from excited argon ions to control the region of the avalanches to within several diameters of the sense wires. This produces pulses useful to extract drift time data from primary electrons. In addition, these gases prevent humidity and *electronegative gases* [28] (which capture free electron) such as  $O_2$  into the chamber. Thus, gases flow constantly through chambers even they're not under high voltage.

During our tests, 75% Argon and 25%  $CO_2$  were used. They were slightly overpressured (20 psi at outlet of gas cylinder) to ensure flow inside chamber. During our tests one gas cylinder was used for two wire chambers. The gas system is composed of the following components from upstream to downstream: gas cylinder, flowmeter and bubbler, gas filters into and out of wire chambers, and lastly the return bubbler. Each full gas cylinder went from 2500 psi to 500 psi within about two weeks. The flowmeter can be dialed to control the flow. The bubbler helps to visualize the return gas and prevents back-flow of gas.

A diagram of the gas flow inside a pair of wire chambers is shown in Fig 4.5 below. Gases flow in series from the top chamber to the bottom chamber. Each wire chamber consists of two gas entrance holes and two exit holes to aid smoother flow to prevent pocket gas build up in the corners. From top to bottom, there are four layers of chamber separated by Mylar foils (c.f. Fig 4.1), of which the middle two are under high voltage. Gases flow through each layer along the long axis from one side to the other, then return to the same side of chamber in the layer below. After two repetitions of the gas flowing to the other end of a chamber then returning to the same side, it exits the chamber on the opposite face to the entrance hole.

During testing in 2019 the return bubbler of chamber 1 and 2 showing much less frequency of bubbling. In addition, chamber 1 on the top showed a lower wire hit frequency when operated at the same HV as chamber 2. This indicated a gas leak along the line. Gas leak detection sprays were used on all joints of the gas line and no bubbles were seen. Dr. Sawatzky suggested the possibility of a gas leak from the wire chambers, which could be hard to fix. Instead, gas flow was increased from 90 (unit) to the maximum 150 at the flowmeter. Consequently, the efficiency of the chamber 1 was restored.



II Fig 4. 6 Diagram of gas flow inside wire chambers.

Diagram of gas flow inside the wire chambers with arrows indicating flow direction. The entrance and exit holes drilled into the chamber are all on one side. Here only the top chamber is shown and the bottom chamber follows the same pattern due to the identical construction. There is only one gas filter for the two chambers.

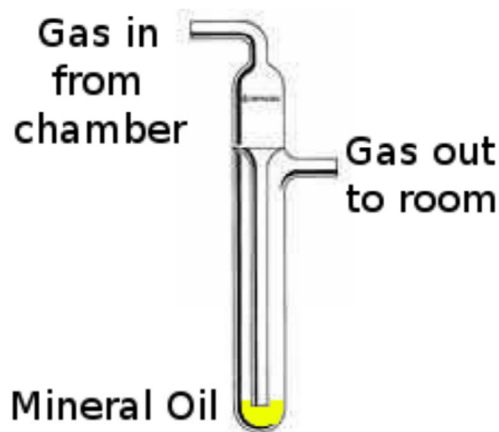


FIG. 4.17: Bubbler used to prevent back-flow of atmospheric gasses into the chamber and keep the chamber slightly overpressure. The gas starts at the top, is pushed through the mineral oil with the constant gas flow, and out through the exit on the side, maintaining the chamber at a slightly higher pressure than the room even if the pressure in the room changes.

II Fig 4. 7 Return bubbler diagram.

Fig 4.17 from [29].

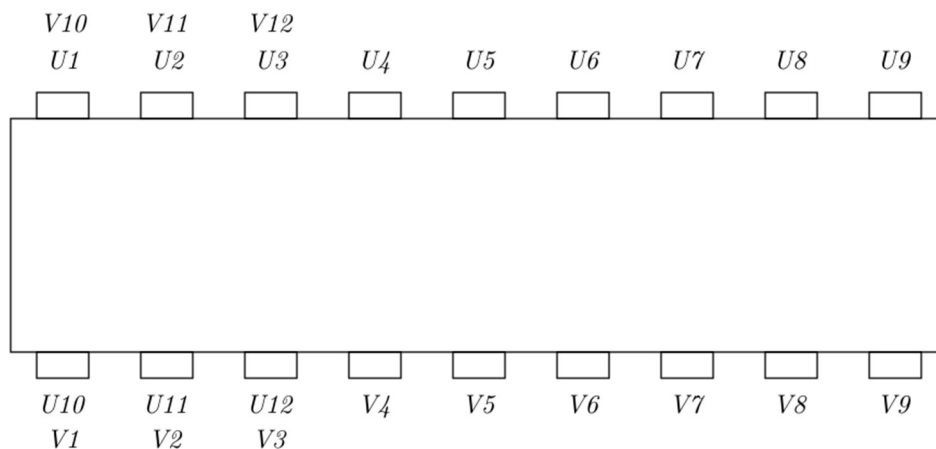
### 4.3.3 Cable management

Several different types of cables were used during the wire chamber tests. The HV cables for wire chambers and PMTs, the LEMO cables for trigger electronics and oscilloscope input, and the most heavily used ribbon cables for transmitting discriminator card signals to TDCs. Here we only discuss the ribbon cable management.

Since the wire chambers have a lot of wires, there are a lot of ribbon cables needed for signal transmission. Each wire chamber has 279 wires per wire plane. With each discriminator or TDC slot containing 16 channels, it needs 18 cards to fill up a wire plane leaving  $16 \times 18 - 279 = 9$  channels empty. The disconnected channels are all inside one discriminator card, but located in either 9<sup>th</sup> or 10<sup>th</sup> card counting from one end based on the wire plane orientation. [29] We only implemented 12 cards per wire plane, which leads to  $16 \times 12 - 9 = 183$  channels implemented. See Fig. 4.8 and Fig. 4.9 below for implemented discriminator cards on one wire chamber. The TDC module we use is the Lecroy 1877, with 96 channels (for 6 cards) each. Thus, for each wire plane we need 2 TDC modules or 16 modules for all 4 wire chambers. The actual number of TDC modules used is 18. Two are for spares and for reference trigger channels from PMTs to provide software cuts on trigger geometry. In total, there're  $16 \times 6$  batches of ribbon cables, and the management of those includes:

- 1) Prepare cables in group of 6 batches, to match one TDC module.
- 2) Print and tape labels on both ends of the cables.
- 3) Fix cables on the wire chambers to provide strain relief for connectors on cards.
- 4) Organize cables on TDC module side.

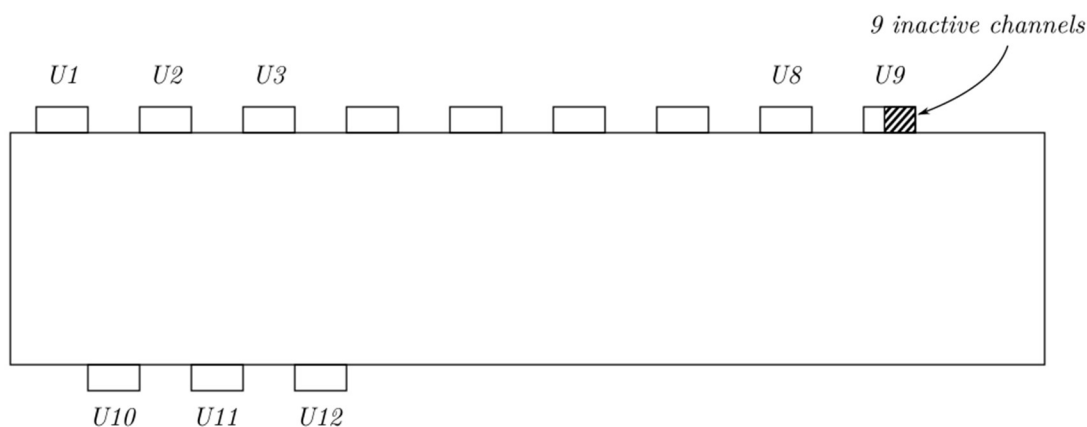
We'll expand upon the procedures following this order.



*Active card labeling for chamber 1,2 where  
V plane cards locate right above U cards*

II Fig 4. 8 Full set of labeled cards in chamber 1 or 2.

(Same as Part III Analyzer, Fig 2.2.8) Every 6 cards spatially located close to each other are bundled together to ribbon cables, thus from this diagram, U4 to U9 as group 1; V10 to V12 and U1 to U3 as group 2; V4 to V9 as group 3; U10 to U12 and V1 to V3 as group 4 of 6 cards plugged into 4 modules in TDC.



*Inactive channels in U wire planes of chamber 1,2.*

II Fig 4. 9 Locations of 12 cards implemented in U wire planes.

(Same as III Fig 2.7) The rest of the 6 cards U13 to U18 are not drawn. All 9 inactive channels lie on the last 9 channels of card U9.

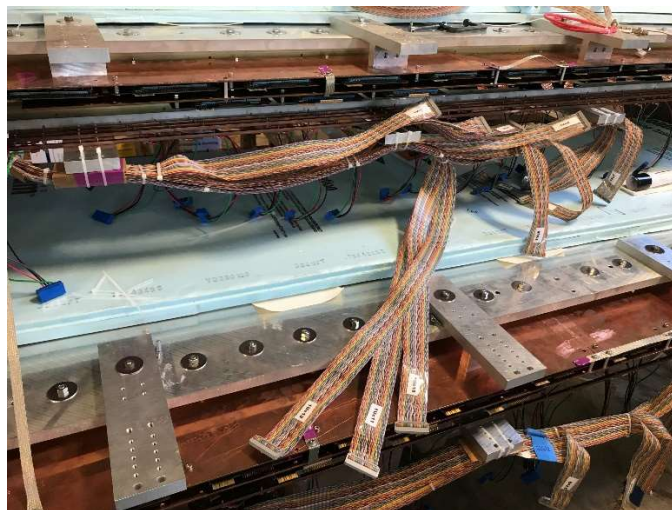
The U wires are oriented from lower left to higher right direction. Refer to Fig 4.8, for V wire plane, they're constructed identical as U wire plane, but flipped 180° around short axis of the chamber, and thus the first 9 channels of card V10 is inactive.

1) Prepared cables in group of 6 batches, to match one TDC module. All connectors on each side of the cables were checked and damaged ones were cut off and replaced by newly made ones. The distances from discriminator cards plugged onto a chamber to the TDC varies. As mentioned in Fig 4.8 above, a group of 6 ribbon cables should connect to 6 adjacent card slots on wire chamber. Thus, the lengths of all cables in a group should match in a batch. To make lengths match means all cables in the group with the same number of periods. Once a group of 6 cables was picked they were made as flat as possible, laid on top of each other, and then cable tied with connector ends offset to match the spacings between locations of the corresponding card on the chamber.

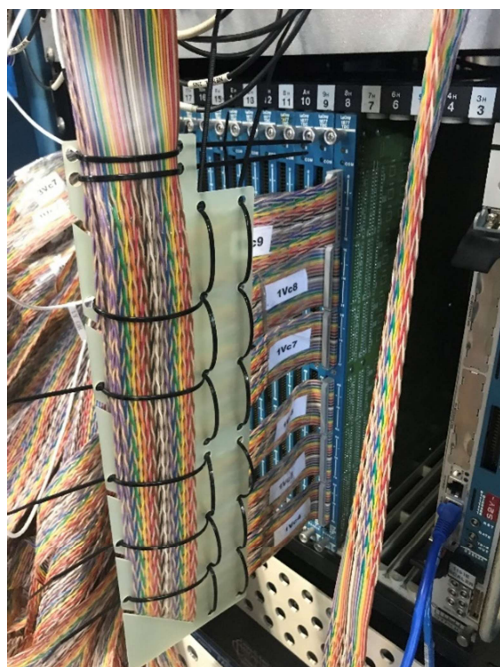
2) Print and tape labels on both ends of the cables.

3) Fix cables on the wire chambers to provide strain relief for connectors on cards. There are original rectangle tooled aluminum pieces with holes drilled attached to the main aluminum frame to hold copper grounding plates. Ribbon cables are attached to them after being wrapped with cardboards. See Fig. 4.10 below.

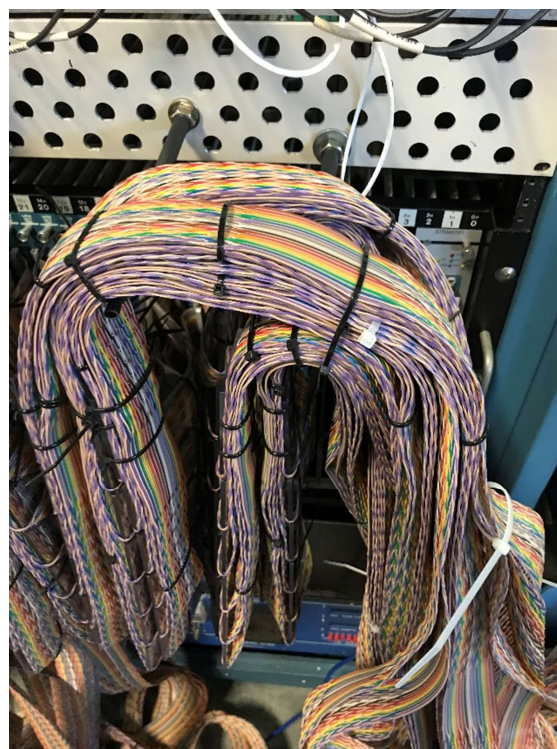
4) Organize cables on TDC module side. A TDC module with 6 slots is vertically slid into the crate. All ribbon cables had to be neatly inserted into and remove from TDC in groups. The solution was to hang cables on rods above the TDC, and use machined plastic holders to hold a group of 6 ribbon cables for a single TDC module. These holders have 45° slots to insert cables and make them turn 90° to change orientation from vertical to horizontal. The slot locations are set based on measurements of TDC connector slots, and cables have enough length to allow some flexibility. In such a way cables are neatly organized so that searching for connectors from a single TDC is like flipping a book. Check Fig 4.11 and Fig 4.12.



II Fig 4. 10 Fixation of cables on wire chamber.



II Fig 4. 11 (Left) A single ribbon cable holder for TDC.



II Fig 4. 12 (Right) Full implementation of holders and hanger of ribbon cables on TDC side.

#### 4.3.4 Discriminator cards.

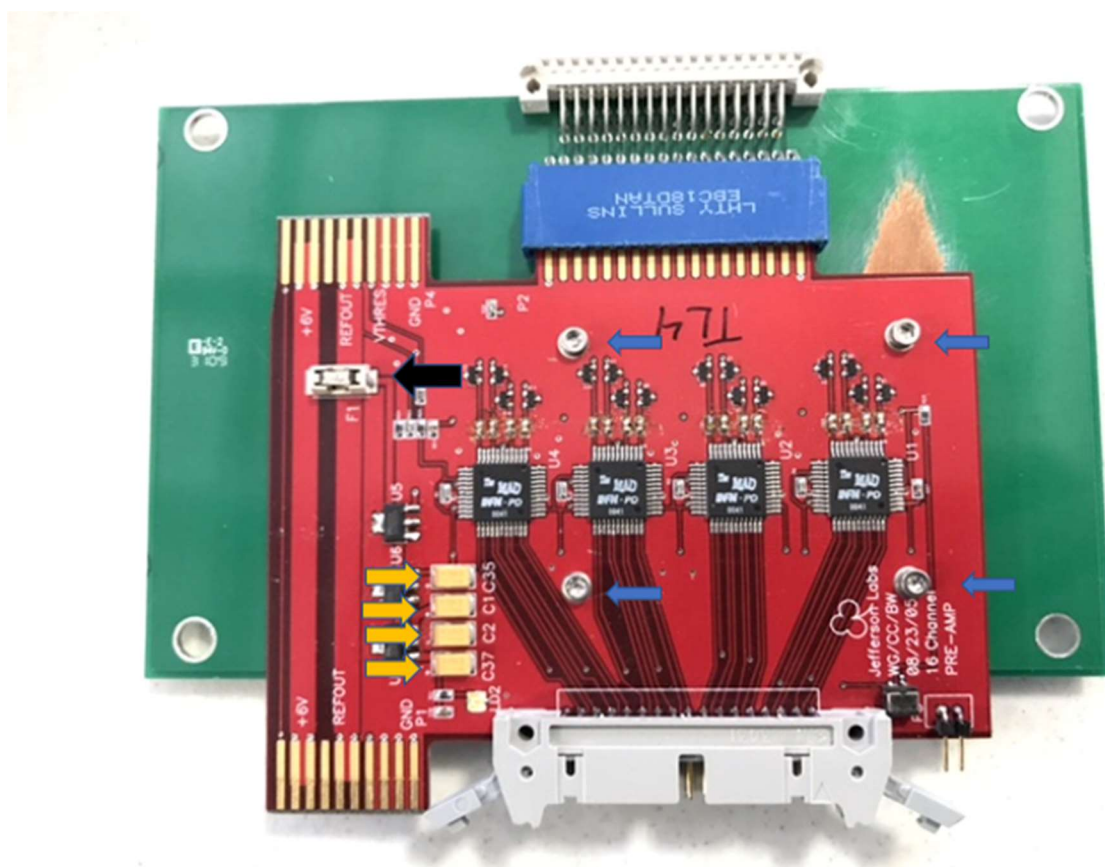
Discriminator cards are inseparable parts of the wire chambers. The cards accept signal pulses from sense wires, pre-amplify and discriminate them into signals with certain standard shapes before the signal is transmitted to the TDC. From the preceding section, there were a total of 96 discriminator cards prepared and confirmed to be in good condition from cosmic test runs. Also from section 4.3.1, all discriminator cards on one wire chamber are driven by the same power and threshold supplies through the copper bars on the chamber. Thus, all should be the same type. Initially the plan was to use MAD cards for the BH experiment. The plan to use MAD cards was aborted due to a serious issue found on drift TDC time distribution after analysis of test run data.

##### 4.3.4.1 MAD card test and issue

The power connection of the MAD cards is described in section 4.3.1. Each card takes 16 single input channels and outputs, 16 dual (one twisted pair on a ribbon cable) channels. The output signal is a low-voltage differential signal (LVDS) logic pulse. [29] In order to convert it to an acceptable signal for a TDC, the LVDS pulse must be converted to an ECL signal by a translator board. [32] A photo of a MAD card is shown in Fig. 4.13 and the diagram for the signal transmission is shown in Fig. 4.14. The MAD cards were initially picked due to their prior success on other experiments, predicted lower noise level due to lower power consumption, and low voltage signal output. See Chapter 2.4 Time to Distance Conversion in Part III Analyzer for

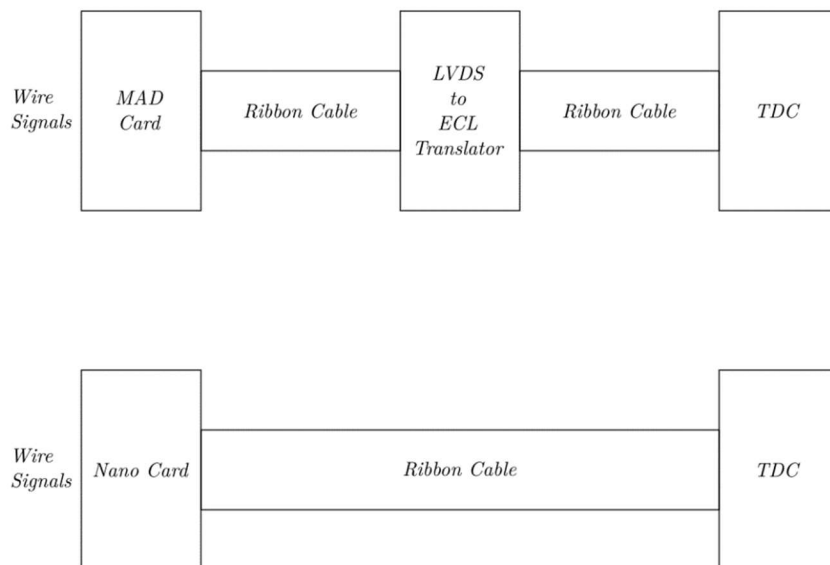


a detailed description of a typical TDC time distribution. Typically, the drift time distribution was composed of two regions. The frequency is higher (a peak in the distribution) at lower drift time due to increased electron drift speed in the higher electric field strength region near the sense wires. There is also a plateau of longer drift times due to the constant and lower electric field away from sense wires. Eventually the plateau falls off indicating the boundary of the wire plane. For the MAD card data, a 2<sup>nd</sup> peak was found where the plateau falls off, at about a 250 ns drift time. Fig 4.15 shows a comparison of TDC time distributions obtained using MAD cards and Nano cards from the same test run with the Nano cards inserted on the chamber between the two MAD cards. Power and thresholds were supplied individually.

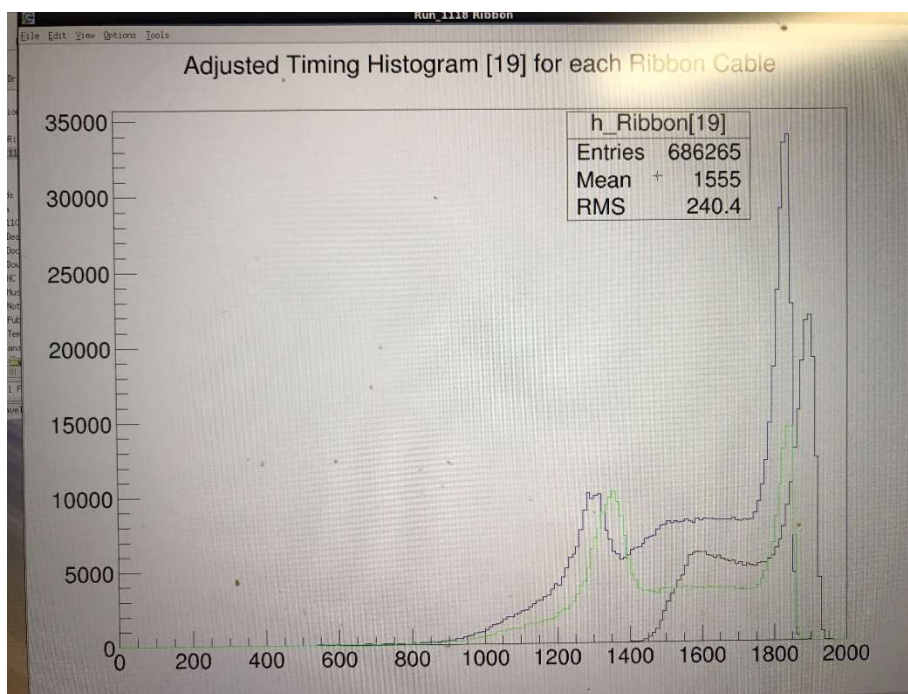


II Fig 4. 13 MAD card attached on adaptor board.

The blue arrows point to standoff screws for support on the adaptor board, black arrow to a fuse, and yellow to voltage dividers. The potentiometer is located on the lower right to the left of the 2-test pin, which can be adjusted slightly by screw driver. The threshold voltage will be divided by 20. (e.g., 5 V on copper bar converted to 250 mV on card.)



II Fig 4. 14 Diagram for the signal transmission for both MAD card and Nano card.



II Fig 4. 15 TDC time distribution of all data from 3 discriminator cards. Ordinate: counts no unit, abscissa: TDC time in TDC time unit ( $0.5 \text{ ns}$ ).

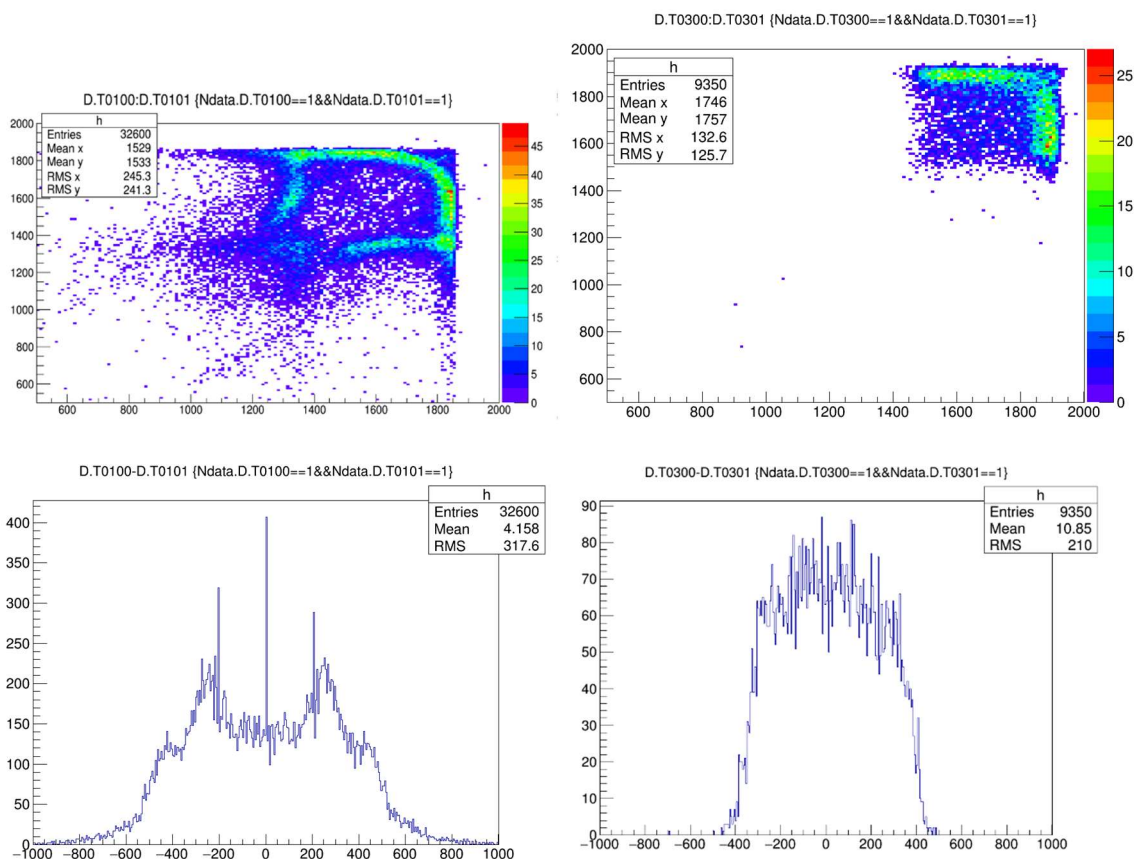
Two MAD cards (Green and Blue), one Nano card (Black) which connects to the chamber in between the two MAD cards. It should be noted that TDC times are in reverse order of real time,

0.5ns per TDC time unit. It's clearly seen the MAD cards TDC time distribution has 2<sup>nd</sup> peak (lower peak).

Apart from the obvious distinction between MAD and Nano cards for any normal TDC time distribution, there are some additional descriptions of the 2<sup>nd</sup> peak and explanation of why it's not from physical events:

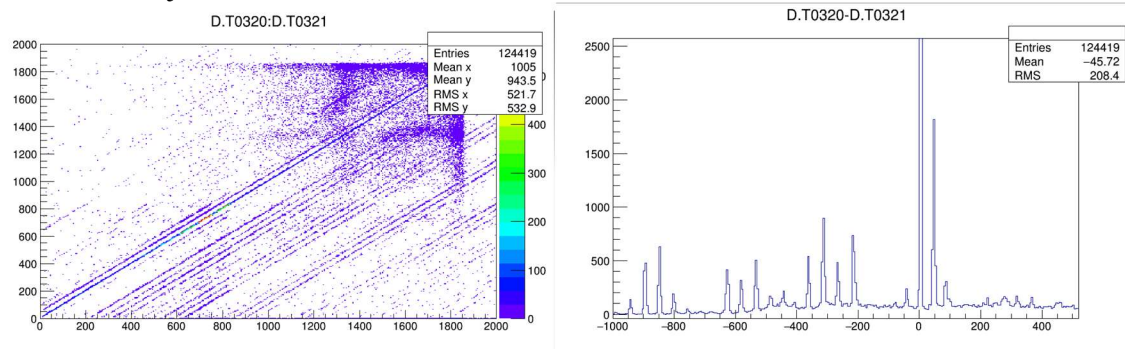
- 1) All 2<sup>nd</sup> peaks lie around a single time: 250ns.
- 2) The 2<sup>nd</sup> peak appears all TDC time data obtained using MAD cards.
- 3) We cannot confirm if it is the MAD cards or the LDVS to ECL level translators or the combination because the origin of the 2<sup>nd</sup> peak is inseparable with the MAD card setup. When MAD cards were replaced by Nano cards, there were no TDCs which could accept LDVS signals as direct input available.
- 4) The relative 2<sup>nd</sup> peak height compared to the 1<sup>st</sup> peak depended on the threshold voltage. Thus, the on-board potentiometer which makes small corrections to actual thresholds requires calibration. Since there shouldn't be any drastic change in TDC time distribution when a discriminator card is operating under the threshold voltage within the plateau of efficiency, this indirectly showed that data in 2<sup>nd</sup> peak arise from unphysical events.
- 5) For the same MAD card, the 2<sup>nd</sup> peak height depended on the card location on chamber. That is, if we inserted the card into another slot on the wire chamber under the same threshold voltage, the 2<sup>nd</sup> peak height changed. If the chamber is uniformly illuminated within the active area of the wire chamber, the drift time distribution should not change much except for statistical fluctuations. This also shows invalidity of the 2<sup>nd</sup> peak data.
- 6) See Fig 4.16 below. It shows more characteristics of the 2<sup>nd</sup> peak in a plot of the 2D histogram of two adjacent wires' TDC time distributions, along with their difference, with the comparison of the same location on wire chamber with the MAD card replaced by a Nano card. The additional green region in the histogram of the MAD card time compared to Nano card represents the 2<sup>nd</sup> peak. In addition, the TDC time difference shows two distinct peaks, very similar in shape and amplitude but with the opposite signs, corresponding to the effect of 2<sup>nd</sup> peak. Those two peaks in the TDC time difference shows some degree of correlation between the two adjacent channels, while Nano card data doesn't show such peaks and the time differences are much more uniform. Since the cosmic tracks cross the wire chamber at random angles, the drift distance between adjacent channels is close to uniformly random, where drift time difference is similar. The distribution obtained using MAD cards did not follow this pattern.
- 7) See Fig 4.17. Additional correlation between two neighboring channels of MAD card signals showed up for some test runs. There are two effects shown, none of which happens for Nano card runs:
  - 1) the time differences are sharply peaked at multiple values suggesting cross talk.
  - 2) there is a sharp peak of drift time at 700 unit for both channels.

Note: All the heights of 2<sup>nd</sup> peaks above are relative to the height of the 1<sup>st</sup> peak, or the height from normalized distribution.



II Fig 4. 16 Two adjacent MAD or Nano Card channels TDC time comparison. Top left figure ordinate: MAD card TDC time of channel 100 in TDC time unit ( $0.5\text{ ns}$ ), abscissa: MAD card TDC time of channel 101 in TDC time unit ( $0.5\text{ ns}$ ). Top right figure ordinate: Nano card TDC time of channel 300 in TDC time unit ( $0.5\text{ ns}$ ), abscissa: Nano card TDC time of channel 301 in TDC time unit ( $0.5\text{ ns}$ ). Bottom left figure: difference between MAD card TDC time of channel 100 and MAD card TDC time of channel 101 in in TDC time unit ( $0.5\text{ ns}$ ). Bottom right figure: difference between Nano card TDC time of channel 300 and Nano card TDC time of channel 301 in in TDC time unit ( $0.5\text{ ns}$ ).

Top: 2D histogram of two adjacent MAD or Nano Card channels TDC time. Bottom: TDC time difference of adjacent MAD or Nano card channels.



II Fig 4. 17 Cross talk on two adjacent MAD Card channels. Left figure ordinate: MAD card TDC time of channel 320 in TDC time unit ( $0.5 \text{ ns}$ ), abscissa: MAD card TDC time of channel 321 in TDC time unit ( $0.5 \text{ ns}$ ). Right figure: difference between MAD card TDC time of channel 320 and MAD card TDC time of channel 321 in in TDC time unit ( $0.5 \text{ ns}$ ).

Left: 2D histogram of two adjacent MAD card channels from another run. Right: TDC time difference of the two channels. The TDC time spectrum has a 3<sup>rd</sup> peak, the tiny red region around 700 TDC time. Cross talk between adjacent channels shows up as peaks in the time difference histogram.

The possible reasons could cause 2<sup>nd</sup> peak are:

- 1) Poor grounding.
- 2) Cross talk between neighboring channels. A copper strip crossing the input traces on a different layer by construction in all MAD cards. If this is the reason, it cannot be fixed. [14]
- 3) LVDS to ECL Level translator issue.
- 4) Some components of the MAD cards were damaged during previous experiments. MAD cards with burnt fuses and/or missing MAD chips were replaced and determined not to be the cause of the 2<sup>nd</sup> peak.

Extensive tests have been done to mitigate the 2<sup>nd</sup> peaks. The most common ones include:

- 1) test one MAD card only on a wire chamber.
- 2) use a VME crate to hold one level translator for a single MAD card.
- 3) add aluminum wrap around ribbon cables for MAD card to increase shielding.

None of them were effective. Due to the inability to conduct some other tests, which included using a TDC able to accept LDVS signals, a convincing idea of origin of the 2<sup>nd</sup> peak, as well as the more reasonable results from the Nano cards, dictated the choice of the Nano cards.

#### 4.3.4.2 Nano card setup.

Due to the reasons mentioned in the last section, Nano cards are used to replace MAD cards for VDCs. The setup changes include:

- 1) There is no LVDS to ECL level translators. The signals from Nano cards are directly transmitted to TDC through ribbon cables. Thus, longer ribbon cables are prepared and installed.
- 2) Power supplies changed, as mentioned in 4.3.1., four copper bars on wire chambers are now using +5V power, -5V power, threshold, ground.
- 3) Changes in grounding of the cards.

(1) As shown in Fig 4.13, for each MAD card and the adaptor board (green, below the card), there're four holes (indicated by the blue arrows in the figure) drilled through with metal coating. Sets of small screw, spacer, and nut combined to keep MAD cards fixed on the board, while providing grounding for card to the board. In addition, the grounding from adaptor board to copper plate on chamber is also provided by standoff screws with spacers.

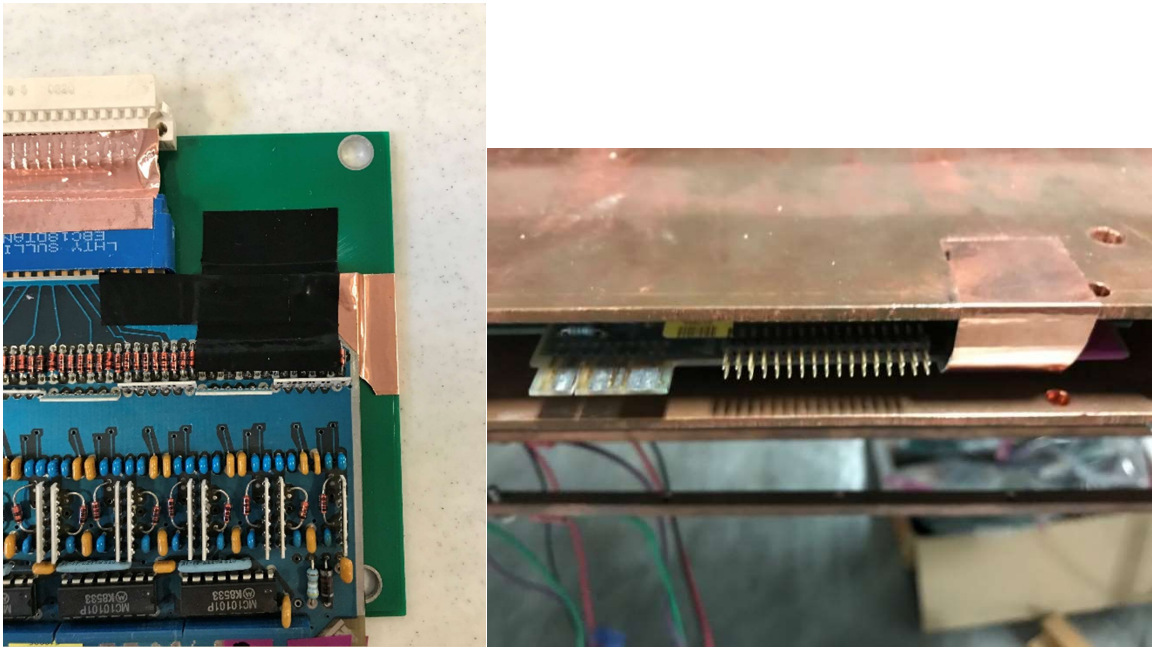
(2) The adaptor boards for MAD cards are not replaced, and paired again for Nano cards. Since Nano cards has completely different dimensions and layout,



the spacers for grounding is not applicable here. Instead, copper tapes are used, there're three places copper tapes used for grounding: (1) Covering all the grounding pins of the adaptor board on its wire chamber side. (2) Linking the upper left corner of Nano card to the back of the adaptor board after sanding to make copper layer exposed. (3) Linking the back side of the adaptor board to copper plates on wire chamber. For pictures, see Fig 4.18. It should note that, there is significantly amount of heat generated from long term operations of nano cards, causing the deterioration of copper tapes stickiness and detachment on Nano cards. For this reason, those tapes are remade and additional electric tapes are added to cover them, see left of Fig 4.18.

- 4) The different dimensions of Nano card to MAD card causes mismatches in mounting alignments. This is easily seen by comparing Fig 4.13 and Fig 4.18 Left, seeing how much Nano card boundary shift to the right of the plate. In addition, Nano cards also block some standoff screws between upper and lower copper plates of the chamber, new holes are drilled for relocation.

This sums up all the changes made for the setup change from MAD cards to Nano cards. It is proven to be quite robust for the test period besides the heating issue of the tapes, which are replaceable.



II Fig 4. 18 Grounding setup for Nano cards.

Left: Copper tape grounding on Nano card. Right: Copper tape grounding from adaptor board to copper plates on chamber. Paper cover of the original tape reel are unpeeled within the gap between tape on plate and tape on card to prevent electric connection on other places.

#### 4.3.4.3 Nano card trouble shooting and noise reduction.

In order to make the efficiency for detecting charged particles high for the wire chambers, we first had to ensure that all discriminator cards were working properly; then, try to find the best operating parameters, i.e., HV for the chambers and threshold voltages for the cards, etc. Extensive test runs were conducted to identify issues of noisy/bad channels, etc., and then the defect components were fixed or replaced. The general procedure was:

1. After replaying the data using the JLAB Hall A analyzer, we checked the generated ROOT file, which included raw TDC hit data for each of the TDC channels and the track reconstruction results. Through data mapping we located the physical locations of the defective channels. (c.f., Part Analyzer for how to generate ROOT file)
2. If the all channels on the adjacent card are good, the easiest way is to swap components between the good and the bad from upstream to downstream and rerun. Based on the result, the general rule of thumb is 1) if the bad channels is swapped along with the swap of the component (e.g. discriminator card, ribbon cable, TDC module) in the rerun ROOT file, the component is bad; 2) Any good components swapped upstream or downstream of the bad component won't change the location of the bad channel.
3. Once the bad component is identified the easiest way is to swap in a spare, then rerun to check if it's good or bad.

For the most common issues related to Nano cards, the description, effect, and fix are listed below:

1. Low efficiency card. When checking the cumulative hit distribution of each channel, those cards have significantly fewer counts, resulting in discontinuity in the distribution. This results in loss of real data, and the solution is to replace.
2. Bad channel, no data from the channel at all, self-explanatory.
3. Discriminator card ringing.

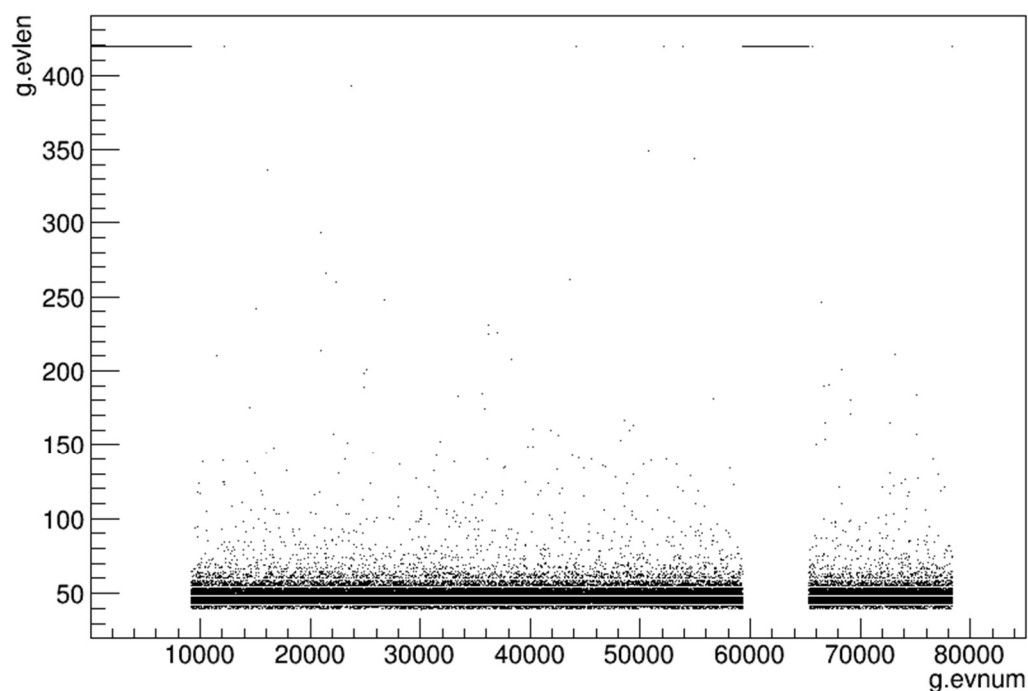
All cards start to ring when the threshold voltage is low enough. The lower the threshold for ringing ring, the higher the Nano cards efficiency due to more signal from event being transmitted safely to the TDC. Certain cards ring at much higher thresholds than others and identifying their location is crucial for the entire system. The ringing frequency is high, around the order of  $10^7 Hz$ . As long as one channel starts ringing, TDC data from ringing overwhelms actual hit signals and the data rate will easily hit its limit, resulting in completely useless data.

Some different forms of ringing are observed. The most common situation is when a group of cards starts ringing at the same time. With the same threshold supply for all cards in a chamber, usually a certain card drives the ringing of all these cards. Swapping a good card for one of the ringing cards, one at a time until ringing is suppressed for the same threshold, can eliminate the problem. In a second case, a less frequent occasion is that an isolated channel rings during a particular test run. When this happens, signals from other channels in the card are completely suppressed and no data are shown for those channels. The cause of this effect is unknown, it could come from TDC feedback.

There are two major sources of loss of efficiency that we could not change during the tests: (1) the gas mixture used,  $CO_2$  although used for absorbing photon energies from argon, is known to be electronegative, which lowers the gain; (2) the JLAB ESB building, where tests were conducted does not have clean power. Constant efforts to improve grounding to mitigate card ringing were made throughout the period of wire chamber hardware preparation and tests. Despite the setback of unclean power, a decent solution was to improve global grounding of the entire system. This improvement included: (1) linking all copper plates on the left and right, up and down, and through the gaps by copper braids; (2) linking all grounds from all wire chambers,

power supplies, and the TDC crate to a common ground through heavy duty cables; and (3) improve the grounding of the Nano cards as described in 4.3.2 3. Due to the higher voltage signal output and higher power consumption, the heat and noise levels of Nano cards are naturally higher than those of the MAD cards. Currently the threshold at which the cards start ringing is about 6.5 V.

g.evlen:g.evnum



II Fig 4. 19 2D histogram showing the time dependent data rate of a test run. Ordinate: count for the event no unit, abscissa: event number no unit.

The abscissa is the event number and ordinate are the total number of TDC data from all channels for the event. As seen the strip averaged near 50, shows the number of about 50 wires hit from all 4 wire planes for the normal events. When cards start ringing due to the unstable power in the ESB building in Jlab, the rate will be seen constant at the cap 420.

#### 4.3.6 Efficiency.

The efficiency is generally defined as the number of events detected by the detector divided by number of events triggered under certain conditions. Based on different situations, the specific definition of efficiency will be different. First let's examine how to define efficiency of the wire chambers. Since only a pair of wire chambers fastened together through a Z-shaped plate is designed to detect individual particle tracks, the efficiency must be defined for each such pair (referred as a *package* by the original constructor). When all the components working properly through prior preparation described above the data are credible. The replayed ROOT



file through raw TDC time includes (1) hit time (in TDC time) from each event of each channel and (2) modified Jlab Hall A analyzer wire chamber class calculated from the results of the track reconstruction. For (2), during the hardware test the Hall A analyzer code was not thoroughly understood, thus the full analysis of track reconstruction efficiency is not described here but later in Part III Analyzer, Chapter 5 Analyzer track finding fitting and efficiency.

Here we only use (1), the raw TDC hit time data to calculate efficiency. We don't have beam data to give a reliable reference for tracks so had to rely on data from cosmic rays which arrive from widely varying directions. In addition, cosmic rays often shower, producing multiple tracks which do not satisfy the requirement of detecting a single track with the number of hit wires per wire plane ranging from 4 to 8. In order to utilize data at hand under this condition, there is the efficiency definition 1:

$$Eff = \frac{\text{Number of events for which a wire plane has TDC hit-time data}}{\text{Number of scintillator triggered events}} \quad (4.2)$$

The events in the denominator in (4.2) means scintillators on top of both top and bottom wire chambers are triggered. This efficiency is well defined for cases of a single-track event and a shower where a large range of wires should be hit. The only exception is that at least two uncorrelated tracks, one track hitting the top chamber and corresponding scintillator but missing the bottom scintillator, while the other coming from an extreme angle triggers the bottom scintillator but not the wire chamber. This case should be rare considering the timing window of the TDC.

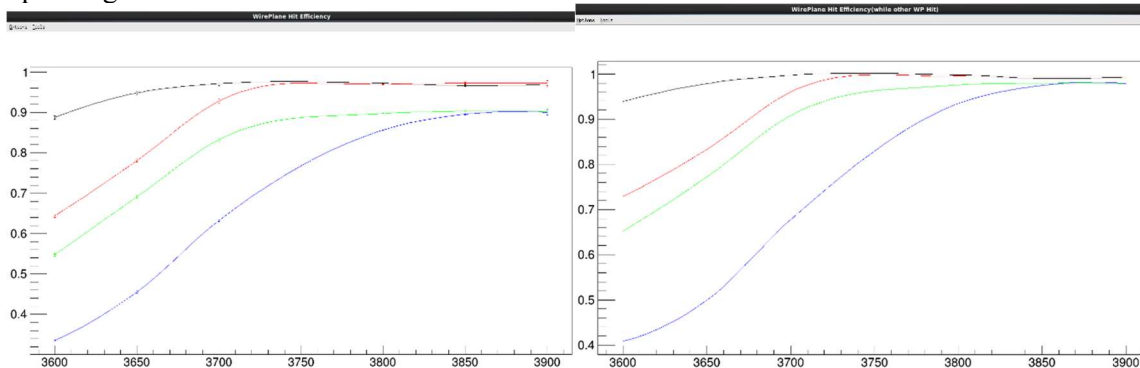
Dr. Sawatzky suggested another efficiency definition which is independent of scintillator trigger and only based on wire chamber TDC time data. Efficiency definition 2:

$$Eff = \frac{\text{Number of events for which a wire plane has TDC hit-time data}}{\text{Number of events when other 3 wire planes all have TDC hit-time data}} \quad (4.3)$$

For instance, denote wire planes from a pair of wire chambers by U1, V1, U2, and V2. If U1, U2, V2 planes are hit, then a track should also through wire plane V1.

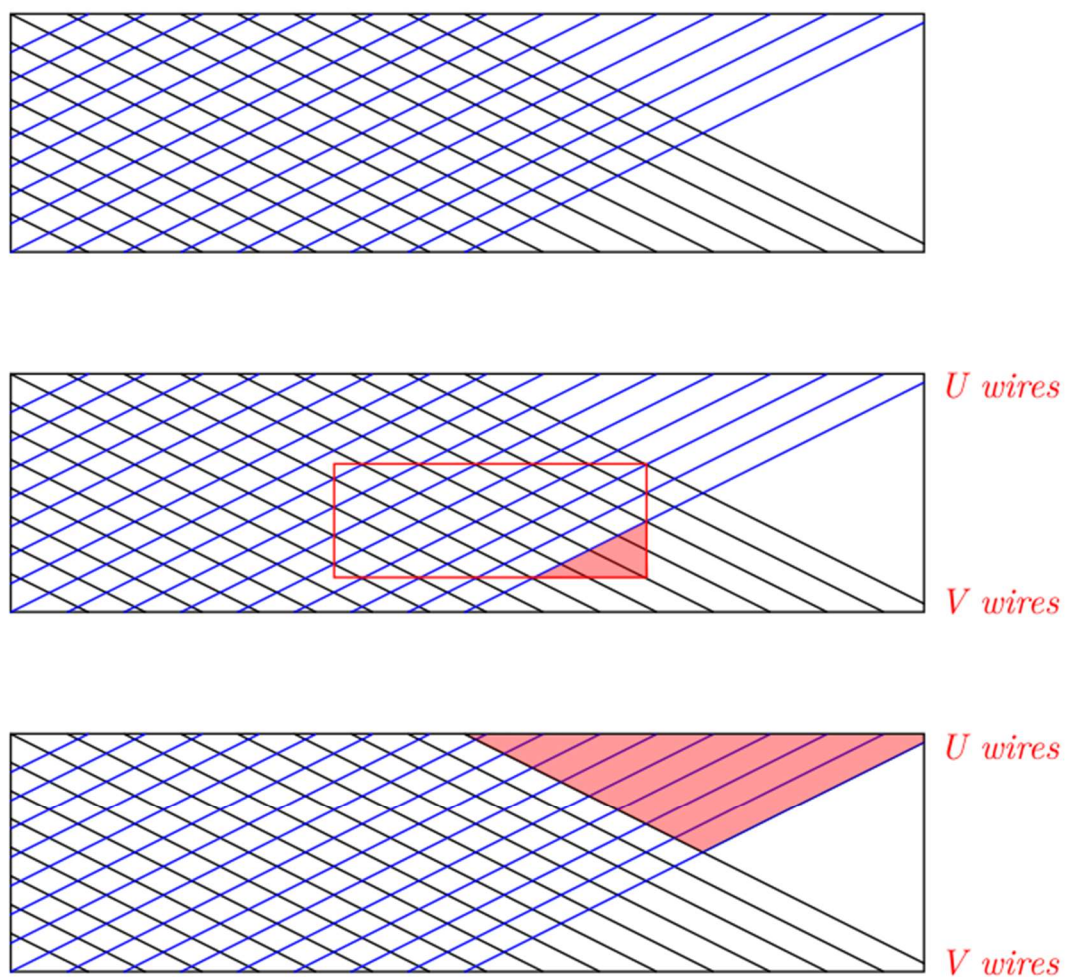
*Efficiency plateau* scanning test runs were conducted. The efficiency depends on two main parameters: (1) the high voltage applied to the wire chamber; (2) the threshold voltage applied to the discriminator card. No matter which definition of efficiency is used, by varying one parameter at a time, a plateau shows up when plotting the efficiency as a function of that parameter. By operating the wire chambers in the center of these plateaus, the system is the most robust when subjected to fluctuations of power supplies. It is most pronounced when changing (1) the high voltage applied to the wire chamber. When the HV is low, the electric field strength is not high enough to cause avalanches and/or the gain is not high enough to pass the threshold of discriminator card. When the HV is too high, the avalanche can happen in a much larger region of the wire plane and the discharge can cause a trip of the HV supply. The plateau should be seen in between. Different effects are seen when changing (2) the threshold voltage applied to the discriminator card. When it is at the low end cards start ringing; at the high end the chance of a signal passing the threshold drops significantly. Since changing (1) causes a larger change in efficiency, we scanned through the high voltage first, then fixed the high voltage and scanned through the threshold voltage. The results of plateaus obtained using efficiency definitions 1 and 2 are shown in Fig. 4.20 (through HV scan) and Fig. 4.21 (through threshold scan). Based on the

efficiency results below, under the setup for the corresponding pair of wire chambers, the efficiency plateau for HV is reached at about 3750V except for wire plane represented by the blue line. The plateau based on card threshold is reached at about 7.0 to 9.0V. As a result, the operating HV was set to 3900V and threshold of Nano card is set to 8.0V.



II Fig 4. 20 Nano card efficiency plateau scan of high voltage dependence. Figure ordinate: efficiency no unit, abscissa: high voltage to the chambers in unit  $V$ . Efficiency in the left figure is defined by definition 1, right by definition 2.

For wire chamber 1,2 package. Different colors indicate 4 different wire planes. The scan run through high voltage from 3600V to 3900V.



II Fig 4. 21 Active U/V wires in chamber 1 or 2.

Top: Illustration of active U/V wires in chamber 1 or 2. Black lines represent U wires, blue lines V wires. The wire plane is scaled, wire directions are the same as real chamber, and region covered is close to implementation region. Middle: Flaw of efficiency definition 1 as a result of scintillator projection on wire planes outside area of common region of wire planes in the chamber. Bottom: Flaw of efficiency definition 2 as a result of the common implementation region of both wire planes being smaller than one wire plane.

## 5 Hodoscopes

### Introduction

[33] Hodoscopes in the BH experiment provide trigger and crude position information for the events. The *hodoscopes* are composed of *scintillation material (scintillator)*, *photomultiplier tubes (PMTs)*, and *light guides* coupling the last two. When a charged particle passes through the scintillator, it deposits energy and excites the energy states of the scintillation material. Light is emitted during deexcitation. Light is then collected and transmitted through the light guide to the *photocathode* of the PMT, which causes emission of photoelectrons through photoelectric effect. The PMT then collects and amplifies the current signal which is later amplified and discriminated to provide the trigger for an event. The reasons to use hodoscopes as coincidence trigger for BH experiment are:

- (1) the whole process above is extremely fast, around dozens of nanoseconds. The overall variation in transition time is much smaller, providing precise timing.
- (2) The efficiency is very high. When a charged particle passes through scintillation material there is almost always some energy deposited, near 100% probability of providing enough light to produce a trigger.

In this chapter, the principle and characteristics of each hodoscope component is discussed first in section 5.1. Then the preparation of the hodoscopes for wire chamber test runs is explained in section 5.2. How the test run trigger were set up is elaborated on in 5.3. To end the chapter, the plan of the final experiment set up is shown in 5.4.

### 5.1 Elements of the Hodoscope

#### 5.1.1 Scintillator

The scintillator [33] has the property of *luminescence*. That is, when exposed to certain forms of energy, it absorbs and emits visible light. The most important features of scintillation material for our purpose are:

- 1) sensitivity to energy; the total light emitted depends linearly with energy deposited.
- 2) fast time response, on the order of nanoseconds; this gives great timing precision. In addition, both the fast response and recovery time greatly reduce dead time.

The time evolution of reemission can be formulated as:

$$N = \frac{N_0}{\tau_d} \exp\left(-\frac{t}{\tau_d}\right) \quad (5.1)$$

where  $N$  is the number of photons emitted at time  $t$ ,  $N_0$  total number of photons emitted,  $\tau_d$  is the *decay constant*. Rise time is much shorter than the decay time. The requirements for a good scintillator are:

- 1) high efficiency for conversion of excited energy to fluorescence radiation;
- 2) *transparency* to its fluorescent radiation so as to allow transmission of the light;
- 3) emission in a spectral range consistent with the spectral response of coupled PMT;
- 4) a short decay constant  $\tau_d$ .

Fluorescent radiation is the immediate reemission after absorption, within 1ns.

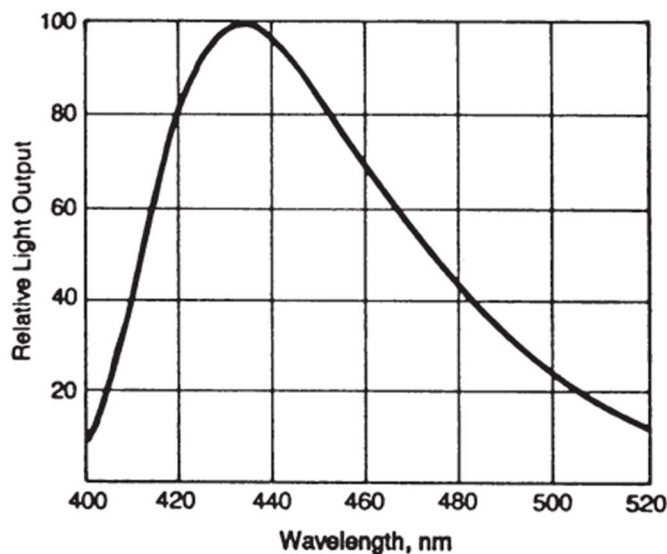
We use plastic scintillator, which is a type of organic scintillator. It is composed of aromatic hydrocarbon compounds, in a solid plastic solvent. The transparency above can be explained by the deexcitation energy being less than the excitation energy. plastic scintillators emit light with wavelengths between 400 and 500 nm, which is in the most efficient range of the photosensitive material on the photocathode of the PMT. It produces a fast signal with a decay constant about 2 to 3 ns. The scintillation material that will be used in the BH experiment is shown below in Fig 5.1.



II Fig 5. 1 Scintillation material for BH experiment.

Bicron BC412. The piece shown is longer than the wire chamber active area width 80.5". This was chosen since it has the longest attenuation length (210cm) within the BC400 family of scintillators.

## BC-412 & BC-416



II Fig 5. 2 Light emission spectral for a typical plastic scintillator. [34] Ordinate: relative light output no unit, abscissa: wavelength of scintillated photons in unit  $nm$ .

[33]The detection efficiency depends on:

- 1) mechanisms by which the radiation interacts with the molecules of the particular scintillator material;
- 2) probabilities that these interactions occur in the scintillator volume, given by the *mean free path* of the radiation in the scintillator material;
- 3) response in light output, governed by the luminescence mechanisms in the scintillator.

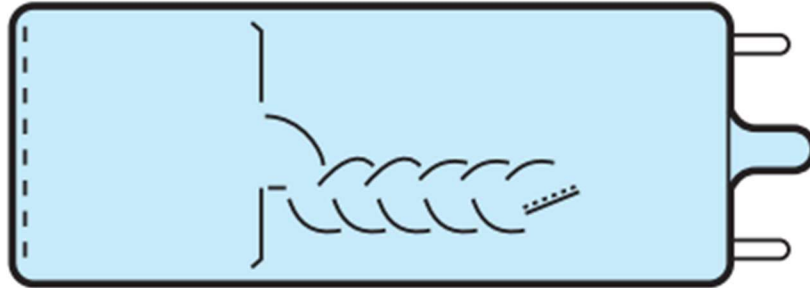
For the purpose of the BH experiment, we are detecting electrons and positrons with moderate energies. The mean free path is at microscopic level and it is nearly certain that a particle will lose some energy in any scintillator. In addition, the light weight of organic material in plastic scintillator reduces the effect of backscatter, which would make electrons exit the material prematurely.

### 5.1.2 Photomultiplier (PMT) [33]

Photomultiplier tubes [33] convert light into a measurable electric current. They are composed of (from upstream to downstream):

- (1) *Photocathode* emits electrons when struck by light through photoelectric effect;
- (2) *Electron-optical input system* accelerates electrons and focuses the cathode current to the 1<sup>st</sup> dynode;
- (3) *Electron-multiplier section* consists of a series of *dynodes (secondary emission electrodes)* which make a weak photocurrent into a measurable current;
- (4) *Anode*, which collects the current;
- (5) Voltage dividers which stabilize voltages between dynodes;

with all enclosed in a vacuum glass tube. The photomultiplier we are planning to use in the BH experiment is the Hamamatsu R7725. Below are simple illustrations of each of these components (with Hamamatsu R7725 as an example):



## Linear-focused type

II Fig 5. 3 Diagram for a typical PMT with linear focused configuration. [35]

The photocathode.

The cathode is composed of photosensitive material inside of the PM window. From the Einstein's formula, the kinetic energy of the electrons from photoelectric effect is:

$$E = h\nu - \phi \quad (5.2)$$

Here,  $E$  is the kinetic energy of the electron,  $\nu$  the frequency of the light, and  $\phi$  the work function. The conversion efficiency is far from 100%, it depends on the frequency of the light. One of the commonly used quantities to describe spectral response is the *Quantum efficiency*:

$$\eta(\lambda) = \frac{\text{number of photoelectron released}}{\text{number of incident photo on cathode}(\lambda)} \quad (5.3)$$

For the Hamamatsu R7725, the photosensitive material used is Bialkali, with a spectral response range of 300 to 650 nm, which is well matched to the light emission spectrum of the plastic scintillator. The  $\lambda$  at maximum response is 420 nm and at this wavelength  $\eta(\lambda) = 26\%$ . See Fig 5.4 for spectral response.

The Electron-optical input system

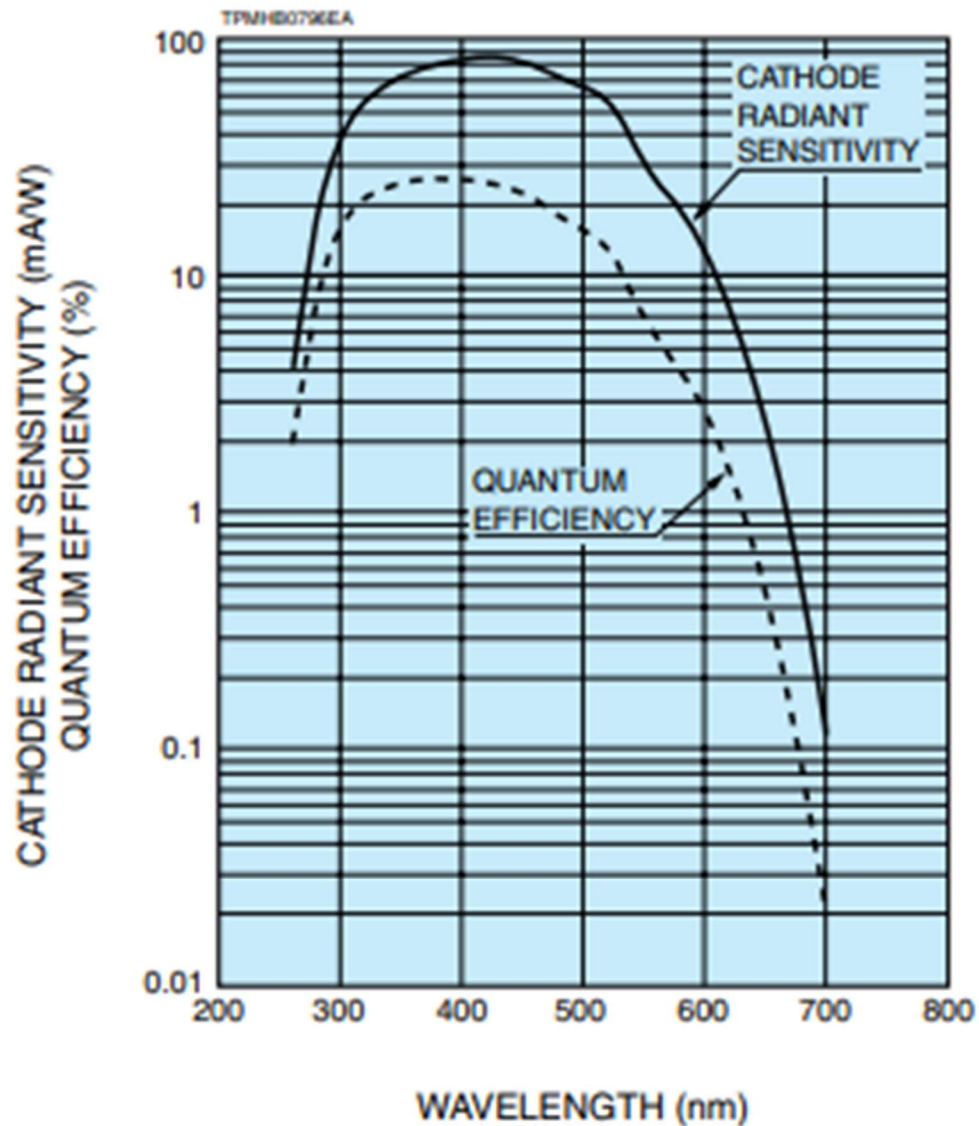
The system provides electric field, which accelerates and focuses the electrons emitted at the cathode to the 1<sup>st</sup> dynode. It is composed of accelerating electrodes, with the same potential as first dynode, and a focusing electrode on the sidewall of the glass housing. The requirements for the system are (1) efficiency and (2) time to travel independent of point of emission.

## The electron-multiplier section

It is composed of a series of dynodes (secondary emission electrodes) to increase the weak primary photocurrent into a measurable current. The *secondary emission factor*  $\delta$  is defined as the gain of each electrode, or the ratio between the number of emitted electrons and incident electrons on a dynode. The factor depends on the secondary emission material and the voltage applied on the dynode. For the Hamamatsu R7725, the number of stages is 12 and the total gain under the suggested HV is  $6.7 \times 10^6$ .

There are different configurations of dynodes. For the Hamamatsu R7725 it is linearly focused, the advantages of which are (1) space is efficiently used, (2) it provides a well isolated cathode and anode, (3) it is *linear*, and (4) it has less deviation in its *single electron spectrum*. Here linearity means the direct proportion between current at the cathode and anode. The more linear a configuration of dynode is means the linearity is maintained across wider range of anode current. The *single electron spectrum* is the measured pulse height distribution from the entry of a single electron. In addition to the configuration of dynodes, it also depends on the secondary emission factor  $\delta$ .





II Fig 5. 4 Spectral response of R7725. Ordinate: Cathode radiant sensitivity in unit  $mA/W$  or quantum efficiency in unit %, abscissa: wavelength of incident photon in unit  $nm$ .

As the scintillators has light in range around 400 to 520 nm, it's nicely coupled with the PMT's cathode photosensitive material. [36]

### Operational parameters

- 1) Voltage dividers: Gain and voltage supply. The relation is approximately:

$$G = \delta^n = (KV_d)^n \quad (5.4)$$

where  $\delta$  is secondary emission factor,  $n$  the number of stages,  $K$  a constant, and  $V_d$  the potential difference between dynodes. For the Hamamatsu R7725 at suggested gain  $6.7 \times 10^6$  and 12 stages,  $\delta \cong 3.7$ . The number of stages that minimize total voltage (supply voltage)  $nV_d$  for a given overall gain  $G$  is given by:

$$n = \ln G \quad (5.5)$$

When applied to Hamamatsu R7725,  $n = 15.7$ . It can be derived from (5.4) that the relation between the relative variation of the gain and corresponding supply is:

$$\frac{dG}{G} = n \frac{dV_d}{V_d} = n \frac{dV_b}{V_b} \quad (5.6)$$

where  $V_b$  is the supply voltage. Thus, a stable supply is required.

Voltage dividers: In addition to a stable voltage supply, an additional chain of resistors is added to stabilize voltage on the dynodes, with capacitors added on later stages to handle the high currents.

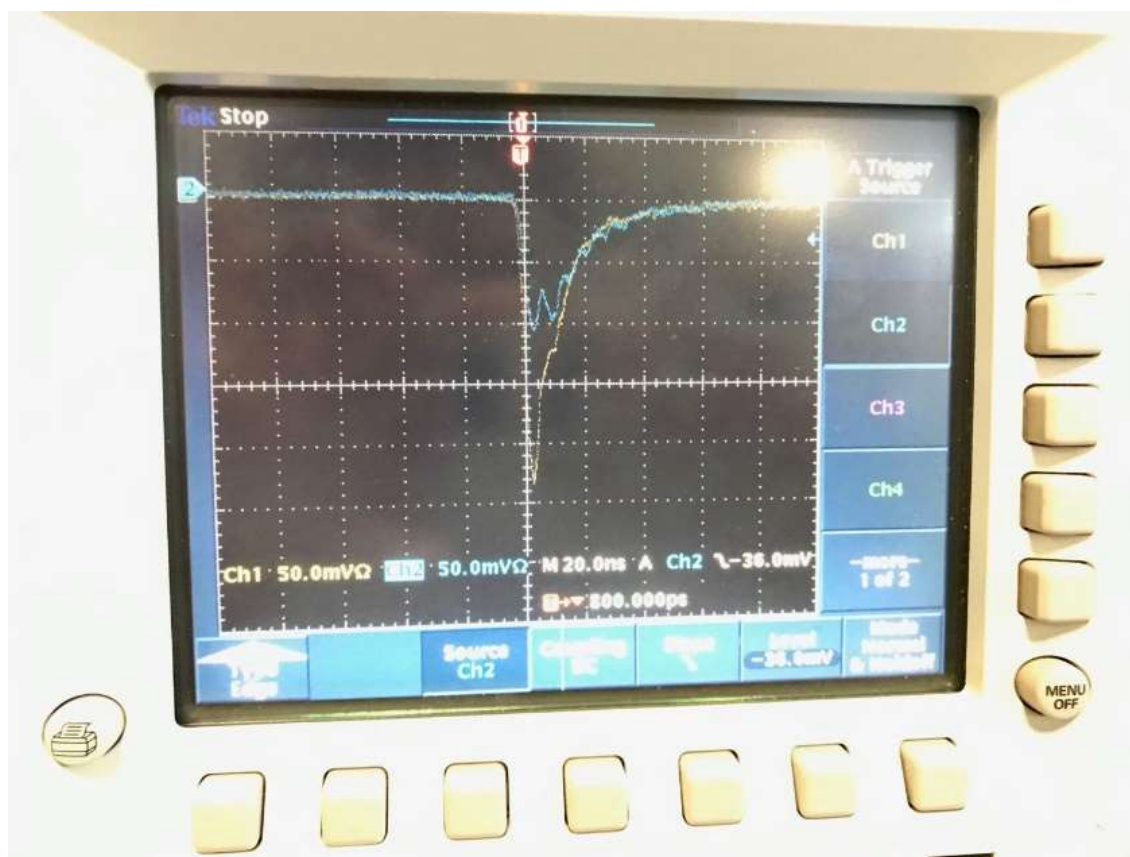
- 2) Linearity: As mentioned, linearity means the direct proportion between current at cathode and anode. It requires that near all of the electrons from previous stage has been collected on current stage. Sufficiently high voltage is required for compensating space charge formed in between dynodes, which hinders electron collection. When operating above the high voltage linearity will be well maintained.
- 3) Pulse shape: Assuming exponential decay of scintillator light, the anode current is:

$$I(t) = \frac{GNe}{\tau_s} \exp\left(\frac{-t}{\tau_s}\right)$$

Using the equivalent circuit:  $I(t) = \frac{V}{R} + C \frac{dV}{dt}$

$$V(t) = -\frac{GNeR}{\tau - \tau_s} \left[ \exp\left(\frac{-t}{\tau_s}\right) - \exp\left(\frac{-t}{\tau}\right) \right] \quad (5.7)$$

where  $\tau_s$  is the scintillator decay constant,  $\tau = RC$ , where  $R, C$  are equivalent resistance and capacitance of the voltage dividers. For plastic scintillators,  $\tau_s \cong 2 \sim 3ns$ . Thus, in our application  $\tau \gg \tau_s$ , the rising edge is determined by  $\tau_s$ , and falling edge is by  $\tau$ . This is called voltage mode; signal amplitude is much higher than current mode when  $\tau \ll \tau_s$ . A typical pulse shape is shown in Fig 5.5 below.



II Fig 5. 5 Typical test PMT pulse shape. Ordinate: pulse height in unit  $50\text{ mV}$ , abscissa: time in unit  $20\text{ ns}$ .

### Time response and resolution

Principle factors causing time variation in PMTs are:

- 1) variation in the transit time of the electrons through the PMT and
- 2) fluctuation due to statistical noise.

Of the two, 1) is the main factor. The *transit time difference* from cathode to the 1<sup>st</sup> dynode depends on the initial kinematics of the electron, the path, and electric field. Among them, the time difference caused by variation of initial electron velocity component perpendicular to cathode is called *transit time spread*. For R7725, it's about 1.3ns.

Noise is mainly composed of the following: (1) Dark current which is the small current flowing when the PMT is not illuminated. It should be small compared to the signal, on the order of nA. For the R7725, the typical value is about 9 nA. (2) After pulses which result from ionization of residue gas inside the PMT. Positive ions drift backwards to the previous stage of the dynode, causing secondary emission at times ranging from a few hundred ns to microseconds after the actual signal. (3) Statistical noise, which is measured by the variance of the fluctuations about the mean anode current.

## Environmental factors

These include:

- 1) Expose to ambient light. Since the PMTs are extremely sensitive to light, exposure will cause high current and fatigue. It can increase dark current and even destroy the PMT. The identification and prevention of light leaks will be discussed in section 5.2.
- 2) Operating under a magnetic field.
- 3) Temperature effect. It causes (1) dark noise, (2) changes in spectral sensitivity of the cathode of about 0.5% per °C, and (3) variation of the gain in the PMT.

### 5.1.3 Coupling of scintillation material to PMT

Neither the scintillator nor the PMT can work individually for the purpose of detecting charged particles. We already understand the light emission process and transit of electrons in PMT. The missing part of coupling scintillation material and PMT to function as a hodoscope for particle detection are the light collection and transportation from location of scintillation to PMT cathode window.

#### Light collection

There are two ways to lose light during light collection: (1) escape from the scintillator boundary and (2) absorption by the scintillator material. For latter the light intensity as a function of path length is:

$$L(x) = L_0 \exp\left(\frac{-x}{l}\right) \quad (5.8)$$

where  $l \cong 1m$  or more is the *attenuation length*. For the BH experiment, the scintillator length should cover the wire chamber, which is 81 inches  $\cong 2m$ . Thus, the absorption can be significant. The former is still the more important loss. If incident angle is larger than critical angle of total internal reflection:

$$\theta_c = \text{asin}\left(\frac{n_{out}}{n_{scint}}\right) \quad (5.9)$$

All light will stay inside scintillator, when  $\theta < \theta_c$  but can diminish quickly after multiple reflections. Total internal reflection can be maximized by reducing  $\theta_c, n_{out} \sim 1$  and making  $n_{scint} \sim 1.58$ ; for our scintillator  $\theta_c \sim 39.3^\circ$ . There is another problem: non-uniformity in pulse height response over the volume of the detector—depending on point of emission. That is, different fractions of the total light output will reach the photocathode. This can be partially compensated for by using multiple PMT as described below. We will loosely wrap external reflection materials around the scintillator to return some light to the scintillator. There're two surface type: specular (mirror like), diffuse, following Lambert's cosine law:  $\frac{dI}{d\theta} \propto \cos\theta$ . We plan to use specular reflector; Al foil and Mylar are two of the most common choices. It should be noted that their reflectivity is wavelength dependent. In order to improve light collection and transportation for plastic scintillator, the follow steps were taken: 1) polish surface, 2) wrap with

Al foil loosely to allow a thin layer of air to be in contact with the scintillator, which facilitates internal reflection, and 3) apply a light-tight layer of black tape.

## Coupling to PMT

The material used must maximize the light transmission. Thus, it should be made from material whose index of refraction is as close as possible to that of scintillator and PM window. We can also use silicone grease and “cookies”, which are flexible plastics to improve the coupling of uneven faces of PMT and scintillators.

## Multiple Photomultipliers

Placing PMTs on both ends of a scintillator and then summing the two signals increases the effective light collection. This is particularly useful for large scintillator.

## Light guides

Scintillator light may be conducted to a PMT via a *light guide*. These are optical quality plexiglass, lucite, or perspex, which can be made in any shape and length for desired geometry. This is very useful for adapting inconvenient scintillator shapes to the circular face of the PM. Common setups for light guide: (1) the “fish tail” light guide which is shaped such that slow changes in form make for a smooth transition from the long rectangular scintillator edge to the round face of the PMT. (2) twisted light guide, use separate strips of Lucite. We’ll use the “fish tail” setup. The maximum efficiency is achieved by configuring as adiabatic light guide, which changes shape gradually without any sharp bent. These light guides are computer machined with the shape computed using optimization programs.

## 5.2 Preparations of hodoscopes

In the following the preparation of the hodoscopes is discussed. Since the hodoscopes to be used in the BH experiment have not yet been constructed, here we describe only the preparation of hodoscopes for the wire chamber test runs. Procedures will be similar for the actual BH experiment hodoscopes. We first discuss the assembling of the hodoscopes, then the handling and cleaning to make each hodoscope ready for test runs. There is a brief description on setting up the test, followed by light leak check. The last step as to set up the HV applied to hodoscopes to ensure that they were all operating at the same count rate for the BH electrons and positrons we will be detecting. Unlike wire chambers, for which the HV on the sense wires and discriminator cards thresholds is the same for an entire chamber, hodoscopes are prepared as individual scintillator, light guide, and PMT units; the HV for each PMT is applied separately. This requires gain matching of all scintillators used for the same measurement.

### 5.2.1 Assemble

The assembling of the hodoscope to be used in BH experiment follows the same scheme of scintillator, light guide, and PMT. Scintillators will be cut into rectangle shape with

appropriate dimensions, followed by sanding and polishing the surface to improve light transmission. Light guides will be machined to fit the shape of scintillator and PMT on its ends. Silicone grease or optical cements can be used for binding the scintillator-light guide and light guide-PMT surfaces. They are chosen to be close to index of refraction of the scintillator and glass window of PMT for better optical transmission. It also should be noted that the optical transmission is depend on the wavelength of the lights and thickness of the grease or cement. In addition, setting aside then apply the binding material and pressing carefully to prevent any formation of air bubbles and/or air gaps forming between the hodoscope components. For scintillators and light guides, as mentioned before, to improve external reflection, a layer of Al foil or mylar are loosed wrapped around the entire scintillator and light guide. Since the scintillators used will be large, instead of black tape, black plastic or rubber wrap will be wrapped around the entire surface of both components to make them light tight. Still, additional black tape will be used at joints, edges, and corners, as well as for fixing light leaks. For PMTs, in addition to the light-tight requirement, magnetic shielding (MuMetal products) and a protective shell will be added. The Fig 5.6 below shows a pair of assembled huge hodoscopes used for wire chamber test runs.

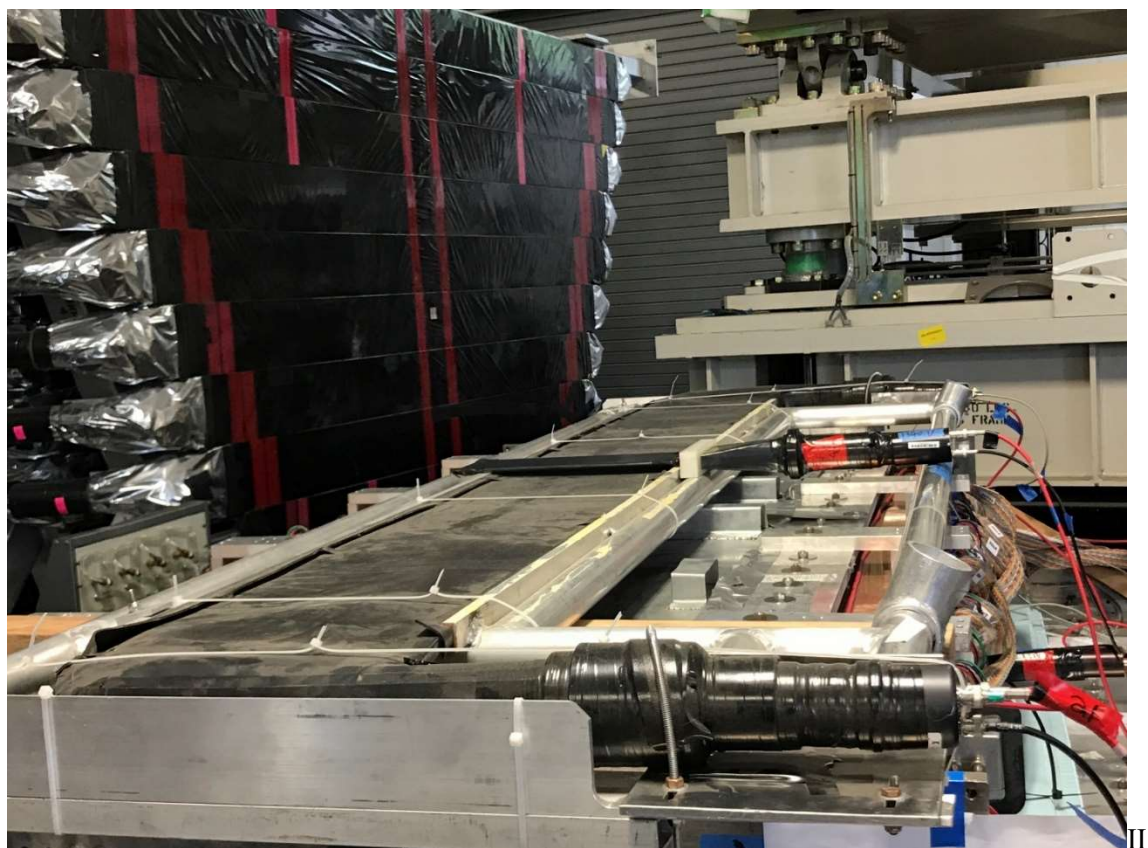


Fig 5. 6 Hodoscopes assemble used for wire chamber test run.

It lies on the top of upper wire chamber, with two PMT attached on its sides and metal support frame. A small scintillator paddle lying across the huge scintillator is used as a reference channel for timing.

## 5.2.2 Handling and cleaning [37]

Plastic scintillators are relatively strong under external forces, but are easily damaged by certain chemicals. Care must be taken during handling and cleaning:

- 1) Handling: When handling bare scintillator, one must wear clean soft cotton gloves, or wash hand to remove any oils as body oils can damage the scintillator.
- 2) Cleaning: Plastic scintillators are susceptible to most organic solvents, their vapors and other aromatic compounds. The exceptions are lower alcohols, such as methanol, ethanol, and isopropanol. Isopropanol is preferred as it causes less cooling during evaporation. Alcohols are best around epoxy joints (e.g. optical cement) but wiping motions must be avoided. Clean water/soapy water followed by a clean rinse are best; a solution of 10g of Alconox/ a gallon of water is recommended.
- 3) Drying: Oil-free compressed air is recommended. Gently patting must be done with clean, soft, non-abrasive cloths/ paper towels (Kimwipes).
- 4) Sanding: Each step of sanding must be at right angle to the previous one. Waterproof sand paper, with grit 240, 400, 600 should be used.
- 5) Hand Polishing: Polishing alumina, size 9 microns, on flannel cloth form paste with water must be used. Scintillators should be rinsed with general purpose non-abrasive plastic polishing liquid.

PMTs are a lot more fragile than scintillators due to the glass housing and light sensitive cathode window. Thus, preventing impact and ensuring light tightness are top priorities. The same applies to all the optical joints of the hodoscope. When handling the hodoscopes, hands must be placed near the joints to prevent bends. Also use cushioning, when possible, when laying hodoscopes.

## 5.2.3 Light leak check

Since PMTs are extremely light sensitive, when exposed to ambient light the current induced is much higher than the light from the excitation of charged particles to be detected. In addition, operating PMTs with a light leak present causes fatigue of light sensitive materials on the cathode and dynodes, which can increase dark current, damage, or even destroy the PMT. [33] Light-leak checks must be made of all components before using them with PMTs as such leaks can develop during handling. Analog oscilloscopes are better than digital counterparts for checking light leaks due to the sensitivity of currents on display. To test for light leaks, we applied HV to a PMT and connected the PMT anode output to oscilloscope. As cosmic rays, BH electrons or positrons excite multiple photons in nanoseconds the pulse heights from these particles are much higher than those of ambient light. Thus, to check signals on oscilloscope, lower (negative) threshold of oscilloscope is applied. For a typical test, HV was applied such that the pulse height from particles averaged around -150mV, where threshold has been set about -50mV on the oscilloscope. To test for light leaks the threshold was lowered to around -10mV.

Big light leak spots can be identified easily if the high intensity display on the oscilloscope screen is reduced when turning off the light in the room. For wire chamber tests in the ESB building at JLAB making the room dark was impractical and black cloths was used. To check for light leaks, we covered the entire hodoscope with the cloth and used a flash light inside and scanned slowly across the surface of the hodoscope. A sudden change in intensity of oscilloscope display was caused by light leak. To pinpoint the leak spot, we ran a finger slowly



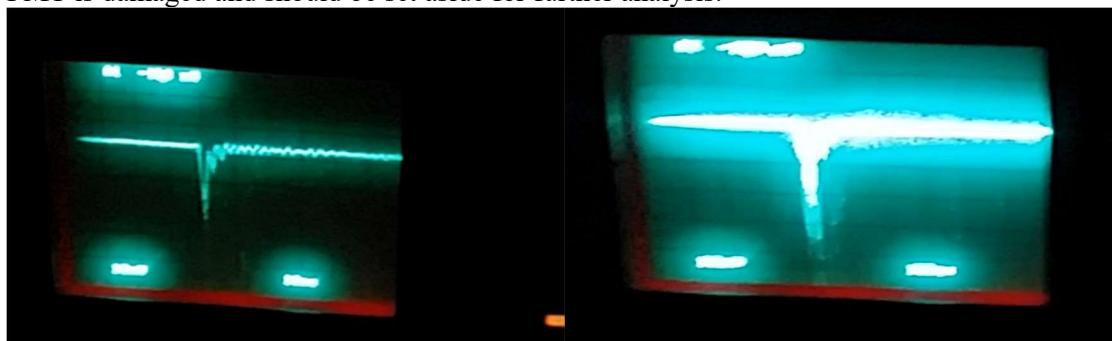
across the lit area to see if the oscilloscope screen signal darkens. Fig 5.7 below shows a light leak displayed on oscilloscope.

Common light leak spots are corners and edges of scintillator as well as the optical joints when sharp corners exist. It is also very common that holes at folds of black tapes are leak spots. Although only light with very constrained direction could leak into the scintillator or light guide, they still needed to be fixed. Flat surfaces of scintillators should also be checked in case of pinch holes.

To fix a light leak, clean the surface around the leak spots, remove the old tape if there is any near the spot and apply black tape. There're three good practices to follow when applying tapes on the leak spot:

- 1) Cut open or shape the tape around the sharp corners of the assembly to match near the zero curvature of the tape surface. Use force to cover with tape the kinks that could lead to folds or excess tension of the tape as these can easily cause a loss of light tightness.
- 2) Put the tape center on leak spot and slowly spread it to each side to prevent fold and tension.
- 3) It's usually a good idea to add additional layer of tape on the boundary of the tape over the leak spot.

Once the leak spot is taped, the spot should again be lighted with a flash light to determine if the fix was successful. It should also be noted that occasionally high currents persist even after the hodoscope is fully covered in black cloth and the HV on PMT is reasonable. This could mean the PMT is damaged and should be set aside for further analysis.



II Fig 5. 7 Normal and light leak pulse from PMT. Ordinate: pulse height, abscissa: time.

Left: Normal pulse from a PMT in hodoscope. Right: PMT signal with flash light lit the light leak spot. Ringing (small secondary pulses behind the main pulse) can be tolerated as long as it's smaller than the discriminator threshold.

#### 5.2.4 Gain match

After the previous steps were completed, PMTs were gain matched before being used in trigger and count cosmic ray events. It is seen in section 5.1.2 that the overall gain of the PMT depends on the HV applied. The manufacturer has provided suggested HV values and gains associated with it, but the gain versus voltage relation varies between individual PMTs. It is allowed to have PMTs operating at different voltage provided:

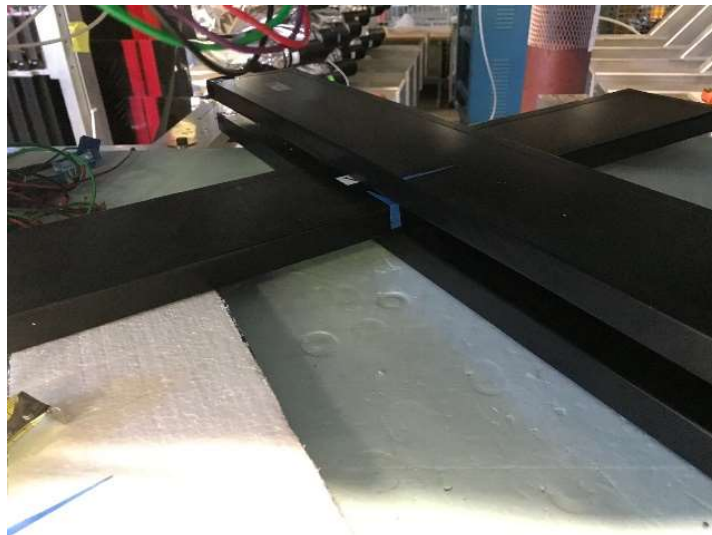
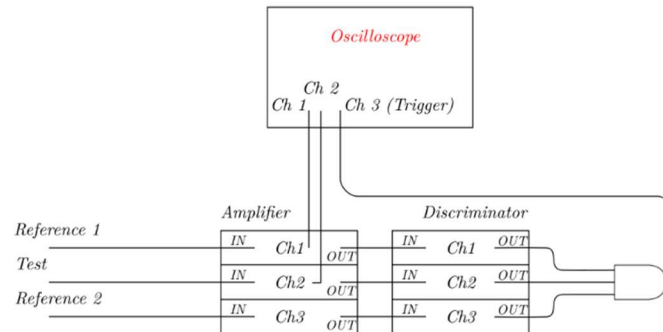
- (1) the voltage applied exceeds a certain value necessary to overcome space charge and make the PMT have a linear response;



(2) the voltage is within the range (about 1000V near recommended value for many PMTs) that gain is large enough and current is not so high that it can damage the dynodes. Since the PMT efficiency is determined by the portion of the current signals with pulse heights above the counter threshold, let's investigate the factors causing the variation of pulse height. According to pulse shape formula (5.7, eq. 8.3):

$$V(t) = -\frac{GNeR}{\tau - \tau_s} \left[ \exp\left(\frac{-t}{\tau_s}\right) - \exp\left(\frac{-t}{\tau}\right) \right]$$

the pulse height is proportional to gain the  $G$  and the number of photoelectrons  $N$ .  $N$  is ultimately proportional to the energy deposited in the scintillator. The cosmic rays and BH pairs are in the energy region of minimal ionization where,  $dE/dx$ , the rate of energy deposited over a particle track inside scintillation material is almost the same for individual particles with different energy. Then the total energy deposited is proportional to the length of the particle trajectory inside the scintillator. This, and additional random factors causing loss of light during collection and transmission are the two main factors causing variation of pulse height for fixed gain. Thus, when the PMTs have enough gain to make most pulses after amplification comfortably larger than the threshold voltage of the discriminator, the efficiency of detecting an event is nearly 100%. The goal of gain match is to find HV for each PMT for the required gain and making them have nearly the same efficiency.



II Fig 5. 8 Configuration of gain match.

Up: Configuration diagram of gain match. A threefold AND logic applied to two reference paddles and the one to be gain matched after amplifier and discriminator are triggered (3-fold AND) for oscilloscope channel 3. The oscilloscope displays its channel 1 and 2 from one reference paddle and the paddle to be gain match. Then the HV on the paddle is adjusted to match the gains match. Right: Placement of hodoscopes for gain matching. Two hodoscope paddles are laid perpendicular to each other below the one to be matched. That one is placed parallel to the bottommost paddle and above the middle paddle. The trigger is set by connecting the two reference paddles to an amplifier, discriminator, and logic unit with AND condition, then to the oscilloscope. All 3 PMTs are also connected to the oscilloscope through matched impedance. Thus, only pulses from tracks through the square common surface of bottom two paddles will be shown on oscilloscope, which shape and height varies from track to track. The distance of paddles trigger area, which is located near the center region of the scintillators, to PMTs were measured to be the same. The setup has two major benefits:

- 1) the coincidence trigger almost ensures pulses come from the same particle track and
- 2) the distance from scintillation location to PMT cathode is constrained, thereby reducing attenuation effects of light collection and transportation (c.f., 5.1.3). As a result, variation of pulse height from event to event is small.

To match the gains, we adjusted the HV on the PMT to be matched using a single pulse display on the oscilloscope and checked snap shots of pulse shapes and heights from PMT to be gain matched and bottommost reference PMT (these two paddles are placed parallel and pulse height should be similar) by eye. The pulse height of the paddle to be matched could be larger or smaller than the reference paddle from event to event, but if on average they are almost the same, then it's considered to be gain matched. A result of pulses shown after gain matching is shown in Fig 5.9.



II Fig 5. 9 Pulse shape of two PMTs before and after gain match. Ordinate: pulse height in unit  $V$ , abscissa: time in unit  $40 ns$ .

Pulse shape of two PMTs before (Up) and after (down) gain match, channel 2 pulse is not showing up here.

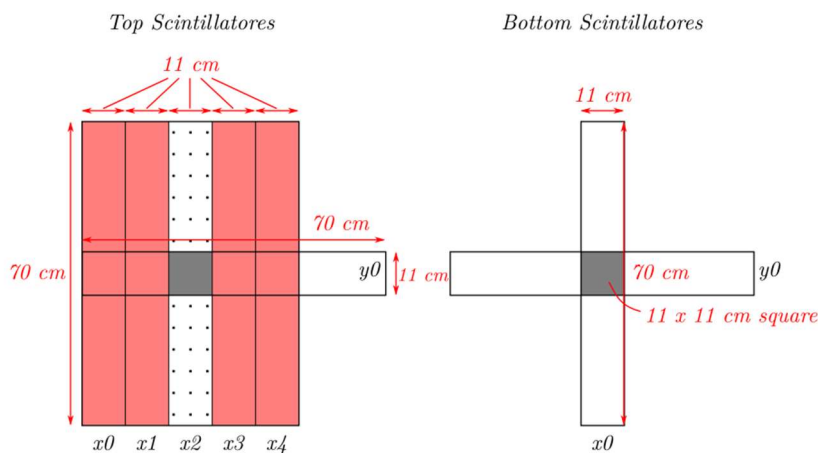
### 5.3 Test run trigger setup

Once a number of hodoscopes have been gain-matched, they were ready for setting up as triggers for the wire chamber TDCs. First, hodoscopes were usually placed in an array in contact with each other to cover an area. Next, the PMTs are powered with their outputs going through electronics and undergoing certain logic tests. The output of the logic unit was used to trigger the TDC. Thus, both the geometry of the hodoscope placement and the logic of PMT signals determine the allowable particle tracks of an event.

#### 5.3.1 Trigger setup diagram

Fig 5.10 below shows a simple diagram of the trigger setup of the hodoscopes. PMT anode pulses are first amplified by the 10-time amplifier, then passed to the discriminator. If their amplitude is higher than the discriminator threshold, the signals will be passed to the logic unit and, after certain logic operations, the output will be the input to TDC trigger. The additional added operations include:

- 1) another output of the logic unit will be connected to counter, which can be used to check count rate etc. and
- 2) all outputs of the discriminators from any hodoscope as part of the trigger are translated to pulse standard by the translator, then connected to the TDC as reference channels. Those individual triggers are handy when analyzing the data after the raw data have been replayed and stored as ROOT files.



II Fig 5. 10 Diagram of trigger setup of for wire chamber cosmic ray detection test run.

Top (lying on top of the upper chamber) has 5 parallel scintillator paddles, represented by  $x_0$  to  $x_4$ , and one ( $y_0$ ) perpendicular to all of them. Bottom (lying on top of the bottom chamber) has a pair of perpendicular paddles. In order to trigger common areas of paddles shown in black (top  $x_2$  and  $y_0$ , bottom  $x_0$  and  $y_0$ ), the top has logic ( $x_2$  AND  $y_0$ ) AND (AND (NOT  $x_0, x_1, x_3, x_4$ )) to prevent triggering multi-track events with one track in black shade region, but some other tracks through red shade region.

### 5.3.2 Trigger logic and count rate, pics in replayed file

Since we need to place scintillators such that particle tracks through them are also through both wire chambers of a set, it is good to have scintillators lie above both wire chambers and use the AND condition in defining the trigger. To be specific, we had 9 small hodoscope paddles with dimension of about 11 by 70 cm and a larger one with dimension about 30.8 by 73.5 cm prepared (the exact volume of scintillation area is unknown since light guide-scintillator joints have not been marked). Fig 5.11 shows the physical placement of all mentioned paddles. Five parallel small paddles placed above the top wire chamber are subjected to an OR logic, then to AND logic with the larger hodoscope which is placed above bottom wire chamber. Thus, the set of triggered events can be formulated as:

$$(\cup (5 \text{ top paddles hit})) \cap (\text{Bottom large paddle hit}) \quad (5.10)$$

There are still 4 small paddles left, 3 of which are used as additional reference channels whose trigger times are stored in the TDC raw data. One was placed on top of and oriented perpendicular to the 5 paddles and the other two are placed on top the large paddle with one parallel to the 5 paddles and the other perpendicular to them. Such placement gave a very limited solid angle constraint selected with certain cuts applied to 4 paddles (two pairs placed perpendicular to each other). Detail analysis is contained in “part 3 Analyzer, Chapter 2.5 Analyzer track finding, fitting and efficiency, section 2.5.1”.

Here we only give a quick estimation of the ratio of count rate of a 4-paddle “telescope” and the total count rate by taking product of the ratio of one square area of the “telescope” scintillation area to top square and 5 top paddles  $R_1$  and the ratio of one square area of the “telescope” scintillation area to the bottom large paddle  $R_2$ . As all dimensions are specified above:

$$R_1 = \frac{11 \times 11}{70 \times 55} \cong 3.14\%, R_2 = \frac{11 \times 11}{73.5 \times 30.8} \cong 5.35\% \quad (5.12)$$

Thus,  $R_1 \times R_2 \cong 0.168\%$  and it is estimated that about one “telescope” trigger per every 595 total triggers. The actual value from a test run with about 1.07 million events shows the measured number is 1 per 562.7 events. The lesser measured value is mainly caused by regions which are defined by light guides instead of the scintillator material in the measurement above.





II Fig 5. 11 Trigger paddles placement on chambers after gain match.

Up: top chamber Down: bottom chamber.

### 5.3.3 Test trigger setup compare to BH experiment

Although there are similarities, there are some fundamental differences between the test trigger setup and trigger to be used in the BH experiment. Due to these differences, we cannot possibly set up a real experimental trigger during our tests. This is discussed below.

In terms of similarity, the trigger logic is similar in that coincidences of scintillator signals from two different planes in space are required. For the test setup, one of these planes belongs to paddles above the top wire chamber, and the other belongs to the large paddle above bottom wire plane. For the experiment, the two planes will belong to scintillator arrays one on the left side of the magnet and the other on the right side. So, instead of the logic formulated in formula (5.10), there is only a slight change needed for experiment trigger:

$$(one\ of\ left\ paddles\ hit) \cap (one\ of\ right\ paddles\ hit) \quad (5.11)$$

Where “one of a set of paddles hit” can be implemented by a logic operation: For convenience, hit from arrays of paddles are labeled by  $P_i$ ,  $i = 1, 2, \dots, n$  if paddle  $i$  hit. Then:

$$one\ of\ left\ paddles\ hit = \cup_{i=1}^n (P_i \cap_{j=1, j \neq i}^n P_j) \quad (5.12)$$

One setback may be that  $P_i \cap_{j=1, j \neq i}^n P_j$  is not usually easy to implement using a logic unit rather than using code after replay, although still doable.

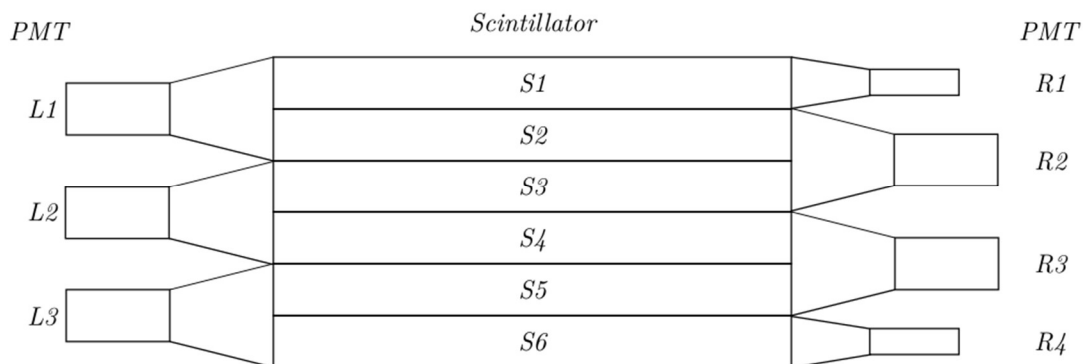
There're two major differences:

- (1) Cosmic particles cannot produce situation with a coincidence of a pair of charged particles as in the experiment. We cannot layer 4 wire chambers, with  $45^\circ$  to horizontal plane and two arrays of scintillators one above all wire chambers and one below all to setup coincidence from one cosmic particle. However, even this is the case, it doesn't prevent us to successfully setting up the trigger for the experiment since trigger (5.11) can be set up successfully with our prepared hodoscopes. The only major issue is that we must take signal transmission time into account; the two arrays of hodoscopes are placed about 1.5 m away from the magnet center. Thus, cuts on the timing difference to identify a BH event must be carefully calibrated.
- (2) The scintillators are horizontally placed to match the wire chambers' long axis lengths. Thus, the light collection and transmission is different. Due to the length of those paddles ( $\sim 2m$ ), attenuation of light intensity is significant (For reference, pulse height ratio from the two PMTs of the same scintillator in Fig 5.6 can be as large as 5). Thus, PMTs are attached on both sides of the scintillators and pulses are summed before amplification.

### 5.4 Scintillator setup in BH experiment

Fig 5.11 below shows a sketch of the proposed assembly of hodoscopes. The assembly of hodoscopes followed the standard scintillator, light guide and PMT scheme described in 5.1.3. Scintillators will cut into dimension about 4 inch by 2 meters with 6 of them aligned in an array for one side of the magnet. Six scintillators provide a coverage width of 24 inches which is enough to cover the short axis dimension of a wire chamber, which is 21 inches. Similarly, the length of the scintillators is enough to cover the long axis dimension. There will be 3 PMTs on

one end of the scintillators, and 4 on the other end. PMTs on each end of scintillators are offset by one scintillator to reduce the number of PMTs needed while still providing coincidence information from signals of PMTs from both ends. For example, if there is a particle that illuminates scintillator  $S_2$  in Fig 5.11, then PMT  $L_1$  and  $R_2$  will render signals. Due to the light attenuation along the long scintillators, their pulses will then be summed up as an event trigger. The mount of hodoscopes will also be constructed to serve as support. They will be built so that all paddles are secured, and stresses on optical joints are prevented. In addition, unlike the wire chambers, which are placed with  $45^\circ$  to the vertical plane to ensure enough wires are to reconstruct tracks, scintillators can be placed vertically as no precise location information is needed to be extracted from them.



II Fig 5. 12 Schematic proposed assembly of hodoscopes for the experiment.

Two of such assemble will be constructed and placed parallel to and behind wire chambers on left and right side of the beam.



## Part III Analyzing test run data

### 1 Basics of JLab Hall A analyzer

#### 1.1 JLab Hall A analyzer

The JLAB Hall A *analyzer* (abbreviated *analyzer* in what follows) was mainly contributed by Prof. Ole Hansen for users to have a common and easy-to-use framework for calculating and storing experimental data. The analyzer has software analysis objects that correspond to hardware of JLAB Hall A. Parameters of individual detectors are embedded inside *apparatus/spectrometers*. By combining apparatus, users can build objects called *physics modules* that make calculations for their desired results: kinematics calculations, vertex finding, etc.

#### 1.2 Users utilize the analyzer

For users there are a few codes to write or modify to customize the analyzer for their own application:

1. A *replay script* that defines detectors/apparatus to be analyzed, physics modules, and the calculation(s) needing to be done, and file/variable names;
2. Set of *database files*: (1) *detector database files* that contain parameters and hardware mapping information for individual detectors, (2) *run database files* which define beam energy, etc., and (3) *crate/scaler mapping database* defines *decoder* parameters which, for example, maps individual hardware channels onto analyzer channels;
3. *Output definition file* that defines which physical quantities are to be calculated and stored on disk; and
4. *Raw data* (CODA file), which is a standardized form of binary data file.

Once the above files are complete, the replay script and analyzer can be run, and the root file storing the calculation results will be generated.

#### 1.3 Using analyzer for BH experiment

For our purpose, one of the most important tasks in preparing for the BH experiment is extracting reliable track information from *Q-weak drift chambers* (will be called *VDC* as *vertical drift chamber*, or *wire chamber* in what follows) being used. Once the BH electron/positron pair's tracks are calculated and combined with the magnetic field we can *ray trace* back to *primary vertex* to obtain all kinematic quantities (energies and scattering angles) of the pair, the distribution of which is essentially what we need to calculate *BH charge asymmetry*.

Our application is a bit different from that at JLAB since the BH experiment has a much simpler spectrometer than HRS. Another program besides the *analyzer* will perform the ray tracing; this will be discussed in Part IV Simulation. What we need from the analyzer is to calculate particle tracks from raw data from VDCs. Dr. Sawatzky has already set up a data

acquisition system (*DAQ*) for the VDCs, the output of which the analyzer accepts. Thus, we had raw data files ready after cosmic test runs provided the VDC hardware worked properly. Once we set up the replay script, database files, and output definition file, the analyzer will calculate *VDC tracks* (particle tracks that have been simplified as straight lines) for us, assuming its *track finding* algorithm also applies for our VDC as well as for those in the HRS. There is also a bonus that the analyzer will convert raw binary data (i.e. raw *drift time* of VDC from TDC, for individual channel, into .evio format) into root file branches for easy access.

## 1.4 Contents in this part

In the following chapters we will discuss:

Chapter 2 VDC database file setup - how the VDC database file for the analyzer is modified from HRS chamber geometry and channel mapping to the Q-weak wire chamber setup. Then, after a brief explanation of how our replay script and output/cut definition files were written, raw VDC drift-time results of cosmic ray test runs are shown. We use the raw VDC drift time distribution to determine *TDC time offsets* of each channel in VDC database file. Once this is done, we can get tracking results by running our replay script. (2.3.4 Determine TDC time offset in wire chamber database file)

The main goal of the analyzer is to reconstruct tracks from the TDC time of each wire on which a hit is registered. The next three chapters discuss this issue, the algorithms are illustrated and test run results are shown.

Chapter 3 Cluster finding and fitting - a sequence of hit wires along with their drift times within a wire plane representing the response of the wire chamber to a charged particle is called a cluster. The algorithm for finding individual clusters from collections of hits is explained. The cluster fitting algorithm computes the track crossover point coordinates for the corresponding wire plane, which serves as input of track fitting.

Chapter 4 Determination of time to distance conversion parameters - Drift times are converted into drift distances to be used for cluster fitting. The determination of the time to distance conversion function, however, is independent of the analyzer and is treated separately. Two algorithms based on differing minimization criteria are described. Then, a more commonly used algorithm is chosen, based on the uniformity of the distance distribution through the conversion. Then the conversion function is represented by either a fitting function and its parameters or an interpolation through a generated (drift time, incident angle, drift distance) table.

Chapter 5 Analyzer track finding and fitting algorithm - Test run track fitting results from a specific trigger setup is shown, with the validity of the fitted tracks confirmed by checking geometrical constraints of the trigger. The track fitting efficiency of single-track events from the test run is computed, along with suggestions for its improvement. The end of the chapter discusses two misc. topics, estimation of track reconstruction (angular and position) resolution and the effect of a bad wire.

Chapter 6 Other files that are required to generate root file are briefly introduced.

Chapter 7 Other rudimental results analyzed from root file are shown as a credibility check.

## 2 VDC database file setup

For more information about VDC hardware, see Part I Apparatus Chapter 5 Wire chamber.

### 2.1 The use of database file

When a particle propagates through a VDC, it ionizes the inert gas inside the wire plane along its track. Ions then drift to cathode wires of the wire plane under high voltage within wire plane of the VDC. In the process capacitance of the wire plane is changed and signal pulses are generated at sense wires. Since there is a one-to-one correspondence between drift time and drift distance (non-linear), by knowing the drift time from a *TDC* of the VDC we can compute *drift distance*, which is the distance (measured perpendicular to VDC wire planes) from where the particle track passed the corresponding sense wire. By fitting the drift time of a *cluster* we can reconstruct the projected angle between track and the line linking sense wires (in the plane perpendicular to all sense wires in a wire plane). That determines one component of the direction vector, to get another component we need another wire plane parallel to the first wire plane with sense wires oriented in a different direction to wires in the first plane. The complete track fitting process determines both projection of the track on the 1<sup>st</sup> wire plane, represented by  $(x, y)$  coordinates of the track intersection on the 1<sup>st</sup> wire plane, and the track direction, represented by *projection angles* (tangents of which are change of  $(x, y)$  over distance between front and back chamber)  $(\theta, \varphi)$ . In summary, by using the analyzer we acquire track fitting results using the following sequence of steps:

- (1) decode TDC raw time data to get a collection of all *hit* (sense wire indices, raw time) pairs in each wire plane;
- (2) through *cluster finding*, clusters of (sense wire, drift time) pairs in each wire plane as candidates for track calculation;
- (3) through time to distance conversion, convert drift time to drift distance to get (sense wire, drift distance) pairs of each cluster;
- (4) fit each cluster of each wire plane to find their intersection on the wire plane. The intersections are represented as either  $u$  or  $v$  coordinates (wires in wire planes lie in different directions than  $x, y$  directions, thus been represented as  $u$  or  $v$  coordinates which lie along the direction perpendicular to its corresponding wire direction) depending on which wire plane is being calculated; and
- (5) use  $(u_1, v_1)$  and  $(u_2, v_2)$  coordinates from each wire plane to solve for pairs defining particle tracks  $(x, y)$   $(\theta, \varphi)$ , and store track fitting results in a ROOT file.

The role of database file here is to provide necessary information for the analyzer (its THaVDC and THaVDCPlane classes) to reconstruct the tracks described above. That information includes: (1) mapping of sense wires to TDC channels, (2) some cuts as part of criteria for determining cluster, (3) *raw time offset* of each channel, (4) time to distance conversion parameters, and (5) wire plane geometry. For example, wire angle entry in database file specifies angle between  $x$  axis and  $u$  or  $v$  axis, thus wire locations and track intersection on wire planes can be determined. Thus, setting the VDC database file parameters is crucial to the analyzer's ability to render correct track reconstruction results. In the process of assigning correct parameters for the database, multiple checks were conducted before and after replaying test run data, until all values and results were consistent.

## 2.2 Four main categories of parameters

1. Physical parameters: they are usually applied for all physical components in the individual VDC. For example, these include *drift velocity*, *TDC time resolution*, parameters which determine cuts on finding clusters, and *time to distance conversion parameters*.
2. Geometric parameters: parameters that uniquely determine the spatial location of each wire in each wire plane. These include *wire plane locations*, *wire angles*, *wire spacing*, etc.
3. Detmap: it generates a one-to-one mapping of each (wire plane#, wire#) to (crate#, module#, channel#) of a TDC. That is, it maps each hardware channel to a software channel.
4. VDC raw time offset of individual channel: for different channels, it takes a different time for signals to propagate through read-out electronics (partially resulting from different lengths of ribbon cables connecting discriminator cards and TDC). Setting raw time offsets will eliminate real time offsets for each channel which could affect the values of reconstructed track coordinates since drift time and drift distance are related.

## 2.3 Determine parameters in database file

The analyzer finds parameters in database this way: 1) In the replay script, initiates a THaHRS object, and name the instance "B" 2) Add a VDC type detector to the THaHRS object 3) in the default database directory DB/ write VDC database file and set filename to db\_B.vdc.dat 4) run the replay script in analyzer (ReadDatabase() function in THaVDC class will read the database) and VDC related tracking result will be stored in root file with root tree branch with prefix "B."

### 1.3.1 Global physical parameters

All units used in database files are SI units.

- 1) B.vdc.driftvel = 55000, (unit m/s) is the *drift velocity* of argon ions in wire plane. The wire chamber has 1 inch (2.54cm) thick wire plane filled with test gas; thus, maximum drift distance will be 1.27cm. Drift time data collected in TDC is about 225 ns. Thus 55,000 m/s is a good approximation for current use, it obeys relation  $d \cong v_{drift} \times t$ . (Drift velocity depends on electric field of wire plane, thus depends on high voltage applied to VDC and location of the ion inside wire plane, here the driftvel is approximation of drift velocity when it is enough far from sense wires that electric field is uniform)
- 2) B.vdc.tdc.min/max = 0/4096, are the lower/upper limit of raw time (in TDC unit) will be registered as a wire hit. They have been set to min/max possible values the analyzer allowed.
- 3) B.vdc.tdc.res =  $5 \times 10^{-10}$ , (or 0.5 ns) is one TDC time unit.
- 4) B.vdc.ttd.param, time to digital conversion parameters, 9 floating numbers. (FIXME: Will be discussed in time to distance conversion section)
- 5) B.vdc.t0.res =  $6 \times 10^{-9}$ , (or 6 ns) is the average resolution of cluster time offset fit.

The parameters below are related to criteria applied when analyzing collections of (sequence of wire index, drift time) pairs of all hits from all wire planes in an event of each wire

plane. They are used to separate the clusters into continuous pieces and to determine if each piece is a full cluster in the context of 2.2.1; Fig. 2.1 is an illustration.

6) B.vdc.clust.minsize = 3, is the minimum *size* of the wire sequence to qualify as a cluster, i.e., the number of channels with raw-time data. As a particle propagates through a wire plane, the distances between the track of a particle and the corresponding sense wires are first decreasing then increasing as the track passes through the midplane. Thus, drift times will also first decrease then increase. The drift time vs wire-index graph will be a V shape. Since time data from 3 wires is the minimum required to define the time vs index V shape, that's how the minimum cluster size has been set.

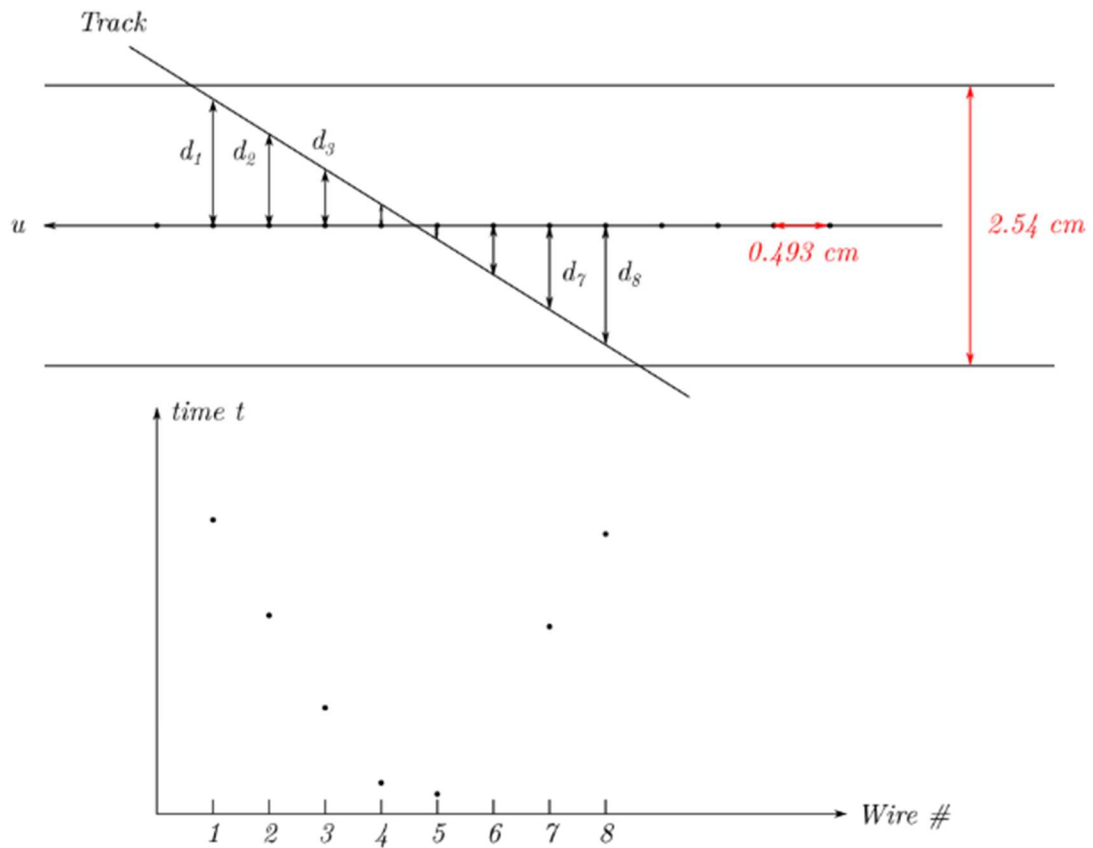
7) B.vdc.clust.maxspan = 12, the maximum *span* (max index of wire minus min index of wire +1) of a cluster. Span is somewhat different than size, since there could be a situation when a certain wire in the cluster provides no signal. Such wires are regarded as a *gap* in the cluster. They will be included in the *span* of a cluster but not in the *size* of the cluster.

8) B.vdc.maxgap = 1, the maximum number of *gaps* of wires allowed in a single cluster. This takes defects in the wire chamber into account as some wire(s) could be bad or have abnormally low efficiency and thus render no signal in certain events even if they should. Here it means allowing gap of one wire within cluster. It should be noted that there could be multiple gaps in a cluster.

9) B.vdc.tdiff.min/max = 0.0/  $3.0 \times 10^{-7}$  s, the minimum/maximum drift time difference between adjacent wires in a cluster. Below is the approximate formula for tdiff: (see Fig. 2.2, also see Appendix A 1.2 for the definition of  $\delta_u$  or  $\delta_v$  if considering  $v,z$  plane; in the appendix  $d_{diff}$  is denoted by  $\Delta d$ ):

$$t_{diff} = \frac{d_{diff}}{v_{drift}} = \frac{s}{v_{drift}} \tan \delta_u \quad (2.1)$$

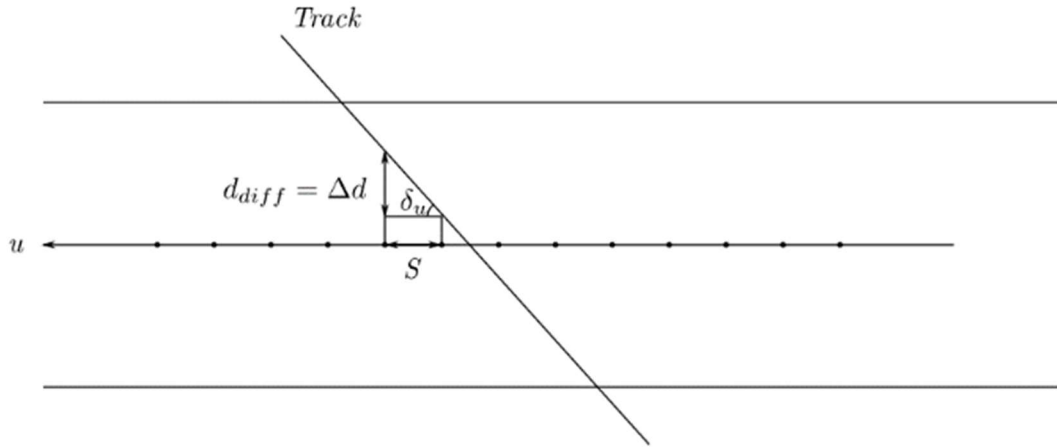
$d_{diff}$  is the drift distance difference between adjacent wire,  $v_{drift}$  is the drift velocity,  $s$  is the wire spacing, and  $\delta_u$  is the angle between a track and the line linking wires in the projected plane perpendicular to the wires.



*An example of a cluster with size 7 (7 wires have signal) with span of 8 wires. Wire with #6 is not counted in the cluster size since it has no signal but will be included in the cluster span. Maximum gap set to 1, so it allows gap at wire #6.*

III Fig 2. 1 An example of a cluster.

An example of a cluster with size of 7 (7 wires have signal) and a span of 8 Wires. Wire with #6 is not counted in cluster size since it has no signal, but is included in cluster span. Maximum gap set to 1, so it allows the gap at wire #6.



$$t_{diff} = \frac{d_{diff}}{V_{drift}} = \frac{S \tan \delta_u}{V_{drift}} \text{ is valid where}$$

*electric field and drift velocity is uniform.*

III Fig 2. 2 Relation between drift time difference and drift distance difference.

Or between drift time difference and the slope of the track in projection plane perpendicular to all wires.

As an approximation, in the Q weak chambers we use:  $s \approx 0.5\text{cm}$ ,  $v_{drift} \approx 55000 \left(\frac{\text{m}}{\text{s}}\right) \Rightarrow t_{diff} \approx 9.1 \times 10^{-8} \tan \delta_u (s)$ . For examples, (1)  $\delta_u = 45^\circ$ ,  $t_{diff} \approx 9.1 \times 10^{-8} = 91(\text{ns})$  and (2) in an extreme case,  $d_{diff} = 0.5'' = 1.27\text{cm}$ , which is half a wire plane thickness. In this case the maximum possible  $t_{diff} = \frac{d_{diff}}{v_{drift}} = \frac{1.27\text{cm}}{55000(\text{m/s})} = 2.31 \times 10^{-7} (s)$ , which is still less than  $t_{diff,max} = 3.0 \times 10^{-7} (s)$ . It means that  $t_{diff,max}$  is a pretty relaxed condition, only to exclude abnormal time difference values, such as in the case of noise.

### 2.3.2 Geometry parameters

We assign geometric parameters to uniquely determine the location and direction of each individual wire in each wire plane. Since 1) all wires in a wire plane are parallel, we only need one parameter (i.e. *wire angle*) to determine their direction and 2) the (absolute value of) *wire spacing* is also the same for all adjacent wires in all wire planes. Thus, the only coordinate (including  $x, y, z$ ) of the 1<sup>st</sup> wire in each wire plane is left to be designated and the geometry is completely determined. The analyzer utilizes this coordinate system for HRS wire chamber as well. The following notation is used:

1. wire spacing in the analyzer is defined as the perpendicular distance between adjacent wire;
2. in the analyzer, wire spacing is assumed to be the same for all wire planes but in practice the wire spacing varies slightly from wire to wire;

3. the analyzer regards all wires as having ‘infinite’ length. Thus, invalid track can result in a track intersection point on the  $u$  or  $v$  plane lying outside the active area of the wire plane. Such events were eliminated by an added cut.

## Coordinate system

### Coordinate axes

**X:** (Primary) projected direction of tracks, parallel to short side of drift chamber. In projected plane parallel to wire plane, the  $+x$  direction points from the center of the bottom wire chamber to the center of the top wire chamber. Since there is a shift in projection between two wire chambers within a pair of wire chamber, a line segment linking the two wire chambers is at  $45^\circ$  to wire planes. Unlike the case of the HRS, our  $x$ -axis is parallel to the side of spectrometer’s non-dispersive direction.

**Z:** Perpendicular to wire planes, pointing from the bottom wire chamber to the top, larger  $z$ -position is further from target.

**Y:** Chosen to make  $x$ - $y$ - $z$  right hand orthogonal coordinate system.

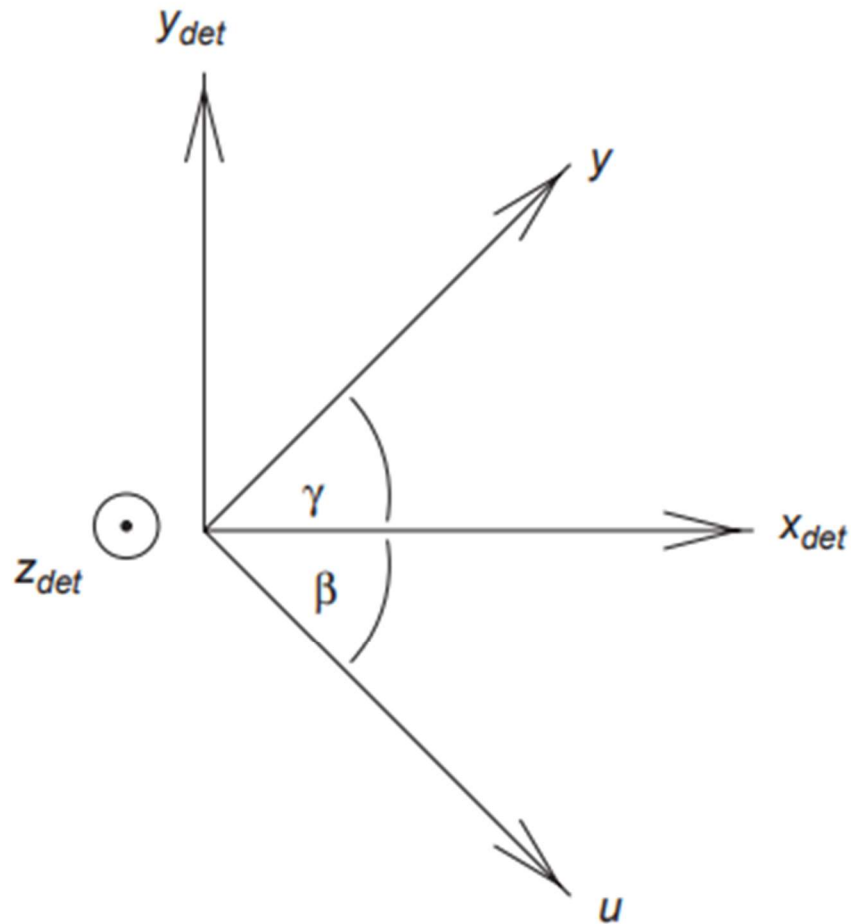
### Wire axes

U, V axis:

- (1) Wire plane axes are perpendicular to wires in corresponding wire plane.
- (2) Parameters in the database file such as `wire.spacing` and `wire.start` are measured along these axes.
- (3) Angle  $\beta$  and  $\gamma$  are in `wire.angle`. `wire.angle` is measured from  $x$  axis in and lie in the  $x$ - $y$  plane.

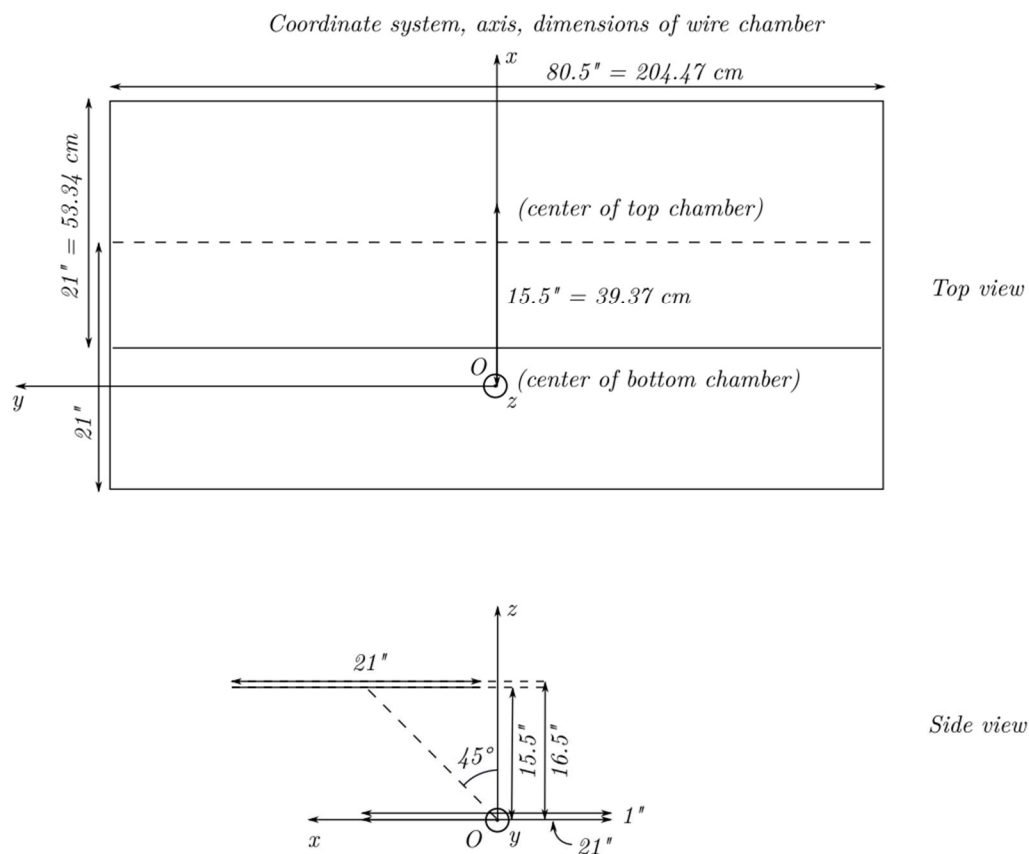
If the axis ( $u$  or  $v$ ) has acute angles with respect to the  $x$ - and  $y$ -axes, then `wire.angle` of the  $u/v$  axis is positive. If the axis has an acute angle to w.r.t. the  $x$ - and  $-y$ -axes, then `wire.angle` of the  $u/v$  axis is negative. The origin of  $u$ ,  $v$ ,  $x$ , and  $y$  axes coincides with the center of the 1<sup>st</sup> wire plane; it is the origin of the whole coordinate system in  $x$ ,  $y$  projection plane. For the analogous HRS coordinate system see Fig. 2.2.3. For BH coordinate system see Fig. 2.2.4 and Fig. 2.2.5.





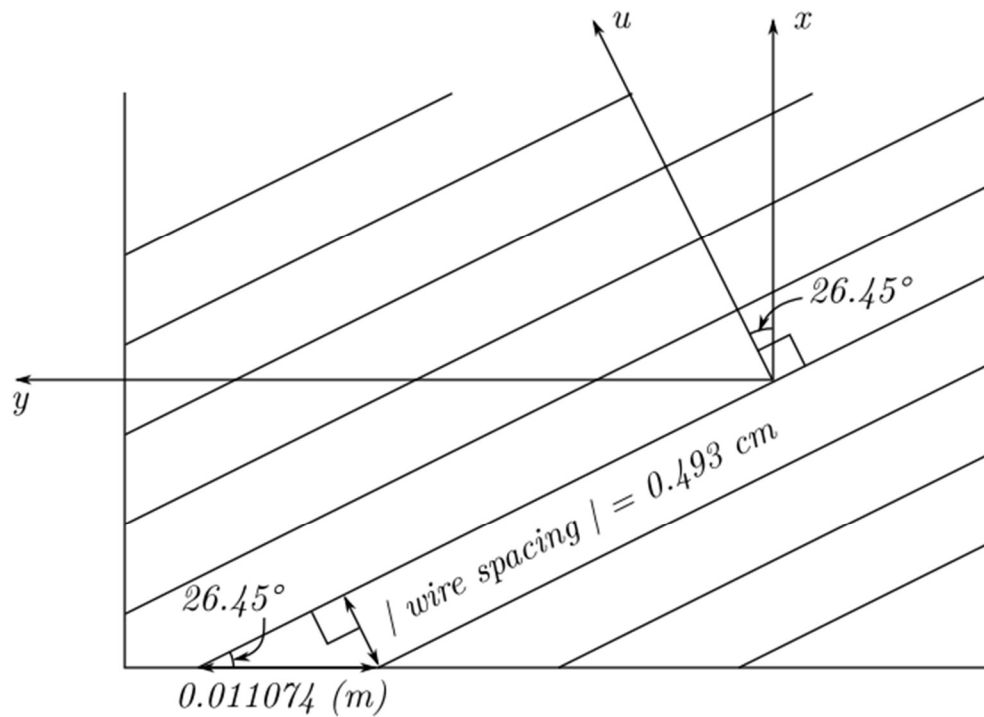
III Fig 2. 3 Coordinate system illustrated for HRS chambers.

[38] p. 338, Fig. 27. Shown is the top view of the wire plane and VDC detector coordinate system. The  $u$  and  $v$  (mis-labeled as  $y$ -axis in the figure) axes are perpendicular to wires of the U and V planes respectively and point in the direction of increasing wire index. The  $x$ -axis lies in the wire plane and points along the spectrometer dispersive direction (parallel to the long side of HRS VDC frame, and short side of BH VDC frame) such that  $x_{det}$  increases as momentum increases.  $z_{det}$  points in the vertically upwards direction and  $y_{det}$  is oriented along the non-dispersive direction (HRS chambers) to form a right-handed coordinate system. The  $u$  and  $v$  axes form angles  $\beta$  and  $\gamma$  with respect to VDC  $x$ -axis. For all VDCs,  $\gamma = 45^\circ$ , and  $\beta = -45^\circ$ . (HRS setup, as shown above)



III Fig 2. 4 Coordinate system and wire dimensions of wire chamber.

In the top view the  $z$ -axis is pointing out of page; in the side view the  $y$ -axis is pointing out of page. All lengths are in inches, but in database file they will be converted to meters. The dashed line represents the upper side of the bottom wire chamber.



$$| \text{ wire spacing } | = 0.011074 \text{ (m)} \times \sin (26.45^\circ) = 0.00493254 \text{ (m)}$$

*Note: 1. x, y, u axis here only indicate their direction not origin*

*2. As seen from the sketch:*

*x is short axis of chamber*

*y is long axis of chamber*

*u is perpendicular to all wires*

III Fig 2.5 U-axis and computation of absolute value of wire.spacing.

The average wire spacing along long axis of wire plane is 11.07 mm. The wire angle of 26.45° was measured during construction of the chambers.

### Database file units:

- (1) all lengths are in meters;
- (2) all angles are in degrees; database naming convention for wire planes from bottom to top:  $u1$ ,  $v1$ ,  $u2$ ,  $v2$  for the test run setup. In the experiment,  $u1$  will be the frontmost wire plane.

### Database file entries

- (1) B.vdc.nwires = 279 is the number of wires in a single wire plane;
- (2) B.vdc.u1/2.wire.angle = 26.45, B.vdc.v1/2.wire.angle = -26.45. B.vdc.u1/2.wire.angle corresponds to angle  $\beta$  in Figure 2.3 and B.vdc.u1/2.wire.angle corresponds to angle  $\gamma$  in Figure 2.3.
- 3) wire.spacing = -0.00493 (m); its absolute value is the perpendicular wire distance and is also the wire coordinate difference between adjacent wires along  $u$ - or  $v$ -axis. The reason for choosing the negative sign is because the 1<sup>st</sup> wire (wire with index 0) in each wire plane is chosen such that it has largest  $u$  or  $v$  coordinate of all wires in corresponding wire plane.
- 4) B.u1/v1/u2/v2.wire.start and B.vdc.u1/v1/u2/v2.position are determined simultaneously. The center of bottommost wire plane is the origin of the coordinate system. Position and wire.start combine to determine location of the 1<sup>st</sup> wire (wire with index 0) in each wire plane. For example, assume the unit base vectors are  $\hat{x} = (1,0,0)$ ,  $\hat{y} = (0,1,0)$ ,  $\hat{z} = (0,0,1)$ ,  $\hat{u} = (\cos\alpha, \sin\alpha, 0)$ ,  $\hat{v} = (\cos\alpha, -\sin\alpha, 0)$ , where  $\alpha = 26.45^\circ = \beta = -\gamma$  (see wire.angle entries). If the wire plane position gives three values  $(x, y, z)$  and the wire.start gives one value  $u$  (or  $v$ ), then a point on the 1<sup>st</sup> wire in each wire plane has coordinate:

$$\mathbf{r} = x\hat{x} + y\hat{y} + z\hat{z} + u\hat{u} \quad (2.2)$$

For all wire planes when  $x = y = 0$ ,  $z$  equals to 0, 0.0254 m, 0.3937 m, 0.4191 m for  $u1/v1/u2/v2$  (c.f. side view in Fig 2.2.4). In terms of database file entries:

B.vdc.u1.position = 0 0 0

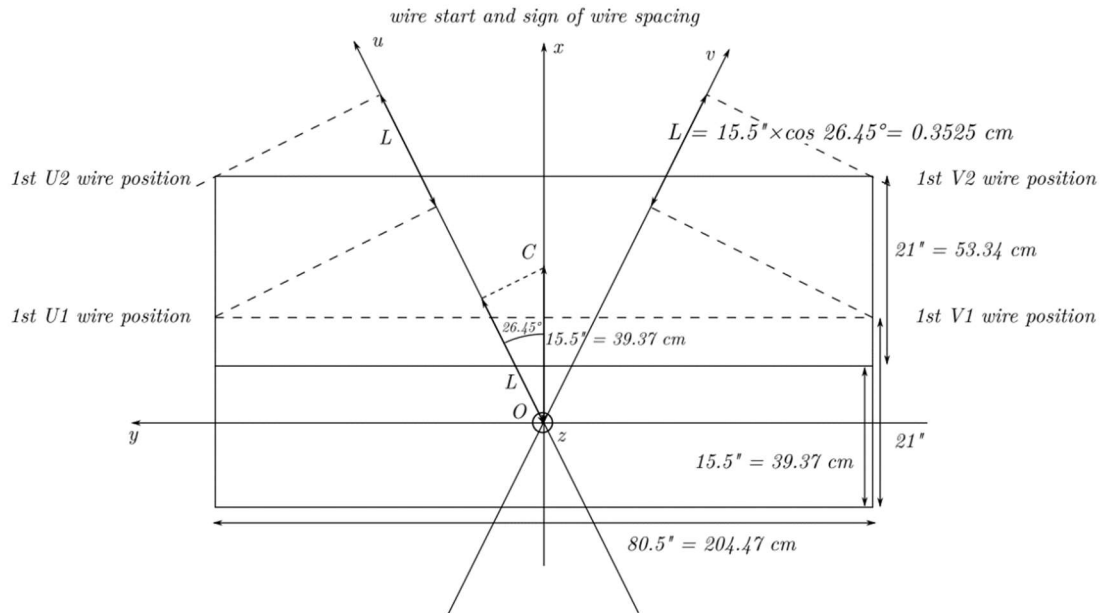
B.vdc.v1.position = 0 0 0.0254

B.vdc.u2.position = 0 0 0.3937

B.vdc.v2.position = 0 0 0.4191

(See Fig. 2.2.6)

For the bottom wire chamber's wire.start: There are 279(nwires) wires in bottom wire plane, with its center at  $U = V = 0$ . The  $U/V$  coordinate of the 1<sup>st</sup> wire B.u1/v1.wire.start = wire.spacing\*(B.vdc.nwires-1)/2 = 0.00493 \* (279-1)/2 = 0.686 (m). The center of the bottommost wire plane is the origin. For B.u2/v2.wire.start, 0.3937 m shift in the  $x$  direction induces a shift in the  $u$  direction of 0.3937 \*  $\cos 26.45^\circ = 0.35249$  m): B.u1/v1.wire.start = B.u1/v1.wire.start+0.35249 = 1.03811 m. All geometry database entries are thereby determined.



III Fig 2. 6 Computation of wire.start and determine sign of wire.spacing.

### 2.3.3 Determine wire mapping in wire chamber database file

The purpose of wire mapping is to map each physical wire in each wire chamber to an indexed wire in the analyzer. Since there is only a finite number of wires, all the mapping here is a finite, discrete one-to-one map. There are three sets needs that must be mapped to each other:

Set 1: Sense wires in wire chambers.

Set 2: Channels on TDC.

Set 3: Wire indices in each wire plane in analyzer.

These three sets are directly or indirectly mapped to each other by:

Set 1 is mapped to set 2 by physically connected wires through discriminator cards to ribbon cables into TDC.

Set 2 is mapped to set 3 through "B.vdc.u1/v1/u2/v2.detmap" entries in VDC database file.

Set 1 and set 3 also mapped each other by wire indexing conventions of wires in the analyzer as described in the last section.

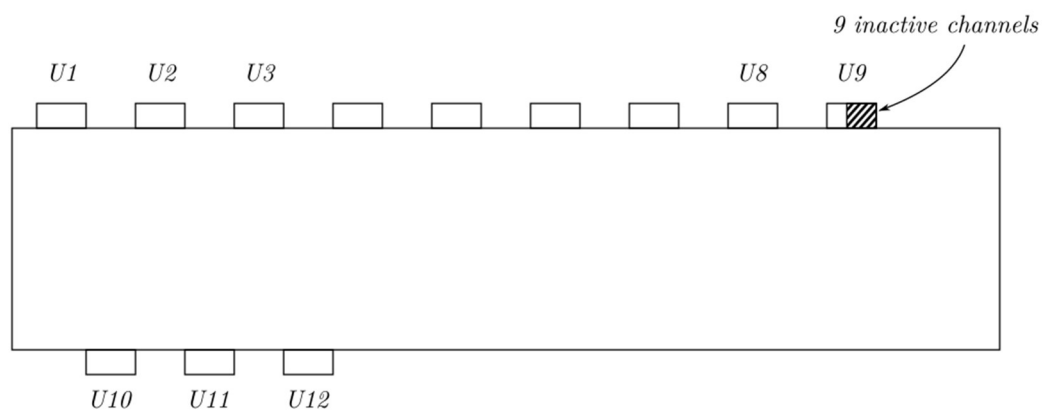
The last mapping is trivial since wires in a wire plane can be set from 0 to 278 (279 wires in a wire plane) by their increment or decrement of the  $u/v$  coordinate on the wire chamber. The other two are not trivial, since channels in each wire plane are divided into smaller sets of

channels; for example, into 16 channels per discriminator card, or into 96 channels per TDC module. This introduces some reordering and flipping. Thus, here we only describe how the first two mappings are deduced.

In this section, we will first discuss the main factors to consider to ensure the correct mapping, then the systematic procedure to determine the “detmap” entries in database file, followed by an example. Before we continue, the format of the wire mapping in the database followed by “B.vdc.u1/v1/u2/v2.detmap =” are lines (number of lines is not fixed) with 5 non-negative integers separated by spaces. Their meanings are: (1) crate index of TDC, (2) module index of TDC, (3) starting channel index of the TDC module, (4) ending channel index of the TDC module, (5) corresponding index of wire in analyzer corresponding to channel in (3). In short, the first four numbers represent a set of consecutive channels on a wire chamber mapped onto a TDC, the last number is the analyzer wire index mapped to first of the channels represented by the first four numbers. For example: a line 21 10 32 47 0 means TDC crate 21, module 10, begin from channel 32 to channel 47, will correspond to channel 0 (to channel 15) in the wire plane.

#### Factors under consideration:

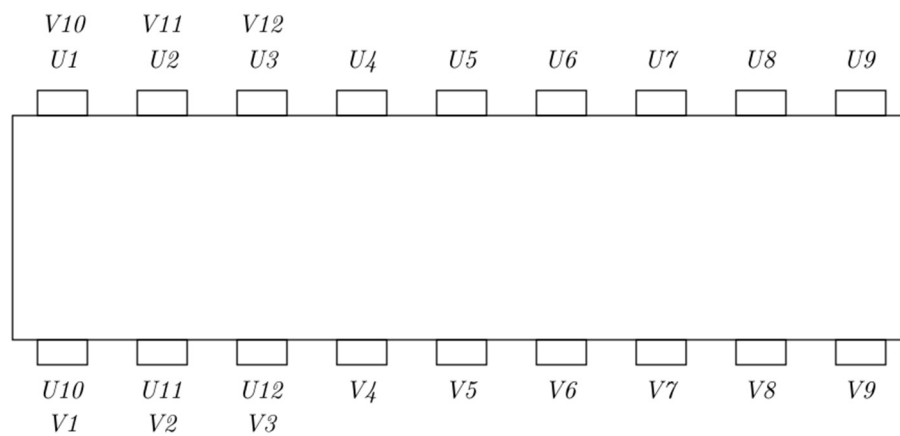
1. there are 279 wires in a wire plane, thus number of channels contained in a “detmap” for a wire plane should also be 279;
2. Only  $183 = 16 \times 12 - 9$  channels are active. Since  $279 = 16 \times 18 - 9$ , there are 18 discriminator cards for each wire plane, with one card having 9 inactive channels. However, we currently connect 12 cards per wire plane based on the acceptance investigation using a Geant 4 simulation. In addition, the 9 inactive channels are located in the middle wires (in card 9 or 10 of the plane, not on either end) so -9 is always presented in 12 consecutive discriminator cards. Thus, a slot of a TDC only contains 7 channels for “detmap”, before or after the line (in context of last page) so the last number won't be divisible to 16. (Fig. 2.7) The remaining 6 cards/ 96 inactive channels will be mapped into non-existing channels on the TDC. This is acceptable since there are no drift time data coming from them to affect track calculations from the active wires;
3. There are 12 ribbon cables connecting discriminator cards to TDCs, with printed labels. They facilitate checking of mapping wires to TDCs. The labeling was done before the study of the analyzer wire indexing convention. Thus, the 1<sup>st</sup> cable might correspond to last 16 channels rather than the first 16 channels as in the analyzer convention.
4. The active area of wires starts from the corners on the short sides of a wire chamber, but in analyzer coordinate convention 1<sup>st</sup> wires on both wire planes lie on a long side of wire chamber. Thus,  $V$  wire planes have active wires as wire 96 to 278 rather than wire 0 to 182 in analyzer convention. (Fig 2.9)



*Inactive channels in U wire planes of chamber 1,2.*

III Fig 2. 7 Nine inactive channels from card U9 of chamber 1,2.

They are at the corner of the chamber, but in the middle of wires.

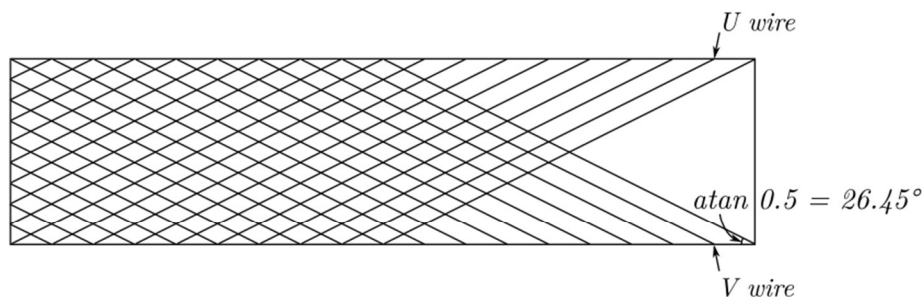


*Active card labeling for chamber 1,2 where  
V plane cards locate right above U cards*

III Fig 2. 8 Full set of labeled cards in chamber 1 or 2.

Every 6 cards spatially located close to each other are bundled together to ribbon cables, thus from this diagram, U4 to U9, V10 to V12 and U1 to U3, V4 to V9, U10 to U12 and V1 to V3 are 4 groups of 6 cards plugged into 4 modules in TDC.

5. The active area of wires starts from corners on short side of wire chamber, but in analyzer coordinate convention 1<sup>st</sup> wires on both wire planes lie on a long side of wire chamber. V wire planes has active wires as wire 96 to 278 rather than wire 0 to 182 in analyzer convention. (Fig 2.9)



*Active U and V wires in wire chamber 1,2  
 Active U wires correspond to wire 0 to 182 in analyzer U wire plane.  
 Active V wires correspond to wire 96 to 278 in analyzer V wire plane.*

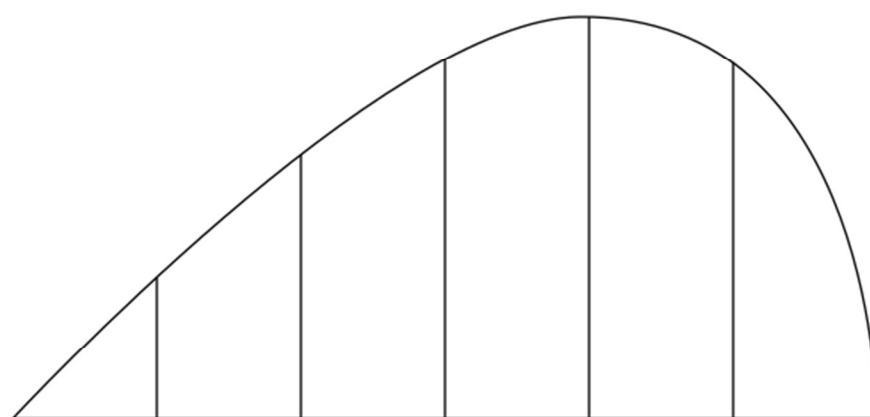
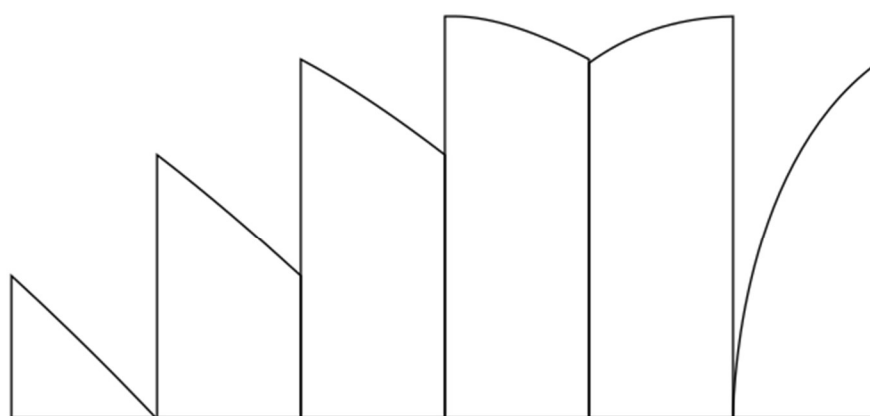
III Fig 2. 9 Schematics of active U/V wires in chamber 1 or 2.

Since U/V wire with index 0 defined in analyzer is on top left/right corner of their corresponding wire plane.

Thus, active U wires correspond to wire 0 to 182 in analyzer U plane, and V wires correspond to wire 96 to 278 in analyzer V plane. (c.f. Fig 2.6)

6. Polarity of ribbon cable connector result in the need of reversing inner channels of half of the discriminator cards in database file to make wire continuous (Fig 2.10): all TDC modules are facing one side, makes right side of card with smaller label (with higher indices in the module) always adjacent to left side of card with larger label. However on wire chamber, connectors are facing opposite direction, makes cards on one side of wire chamber has same relative location as cards on TDC, but on the other side of the chamber left of smaller labeled card will adjacent to right of larger labeled card.(See Fig 2.11 example) In database file, if a group of consecutive labeled cards are making wires continuous, they will be grouped together in one line of “detmap” entry, otherwise, all channels within each slot needs to reverse inner channels to make continuous wire.



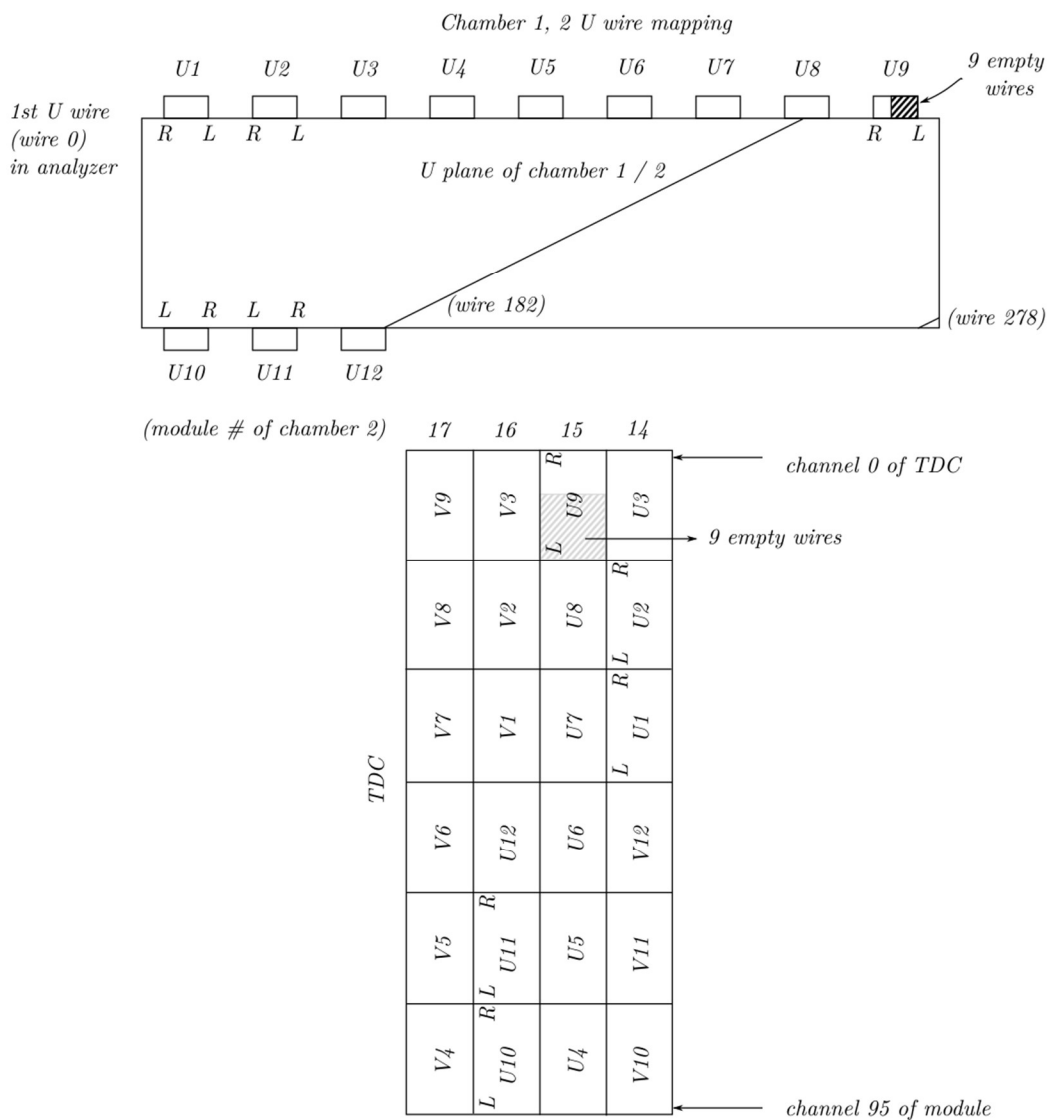


*Card 1      2      3      4      5      5*

*Reversing inner channels within each discriminator card.*

III Fig 2. 10 Six discriminator cards have to be reverse their channels.

Reverse internally to make hit counts vs wire indices continuous.



III Fig 2. 11 Chamber 1,2 U wire mapping.

Top: *U* cards on *U* plane. L, R indicate the polarity of how the ribbon cables are connected to chamber. Upper left is wire 0, wire drawn in the middle of *U* plane is the last wire of card *U12* as last active wire (wire 182) of the *U* plane. Bottom: Cards plugged into TDC slots. Upper numbers 17, 16, 15, 14 indicate module number of TDC, *V1* to *V12*, *U1* to *U12* for a total of 24 cards on the of bottom wire chamber 2 which are plugged into the 4 modules of TDC. L, R indicate the polarity of how ribbon cables are connected into the TDC. Note: Shaded regions in card *U9* of both top/bottom diagrams indicates location of the 9 inactive channels on wire chamber/TDC. They should be excluded in “detmap” line including card *U9* channels.

## Systematic mapping procedure

1. Identify active wires in the wire plane corresponding to wire 0 to 182 or wire 96 to 278 in the analyzer wire plane. Set the remaining unconnected channels to nonexistent modules.
2. Match cards (1 to 12 for each wire plane) in incremental order as analyzer wire indices.
3. If polarity (explained on last page) of how a ribbon cable is plugged into a TDC is the same as how the cable is plugged into a wire chamber, group these cards together and note that all cards in the group will be represented by continuous wires in the analyzer. Otherwise, reverse the first/last channels inside TDC start/end channel number entry in database file for each card.
4. While writing database file, also note the 9 inactive channels in the middle of each wire plane and exclude corresponding channels on TDC from the database file. Then, the starting index of the next card will be +7 (7 active channels in the card) of this card instead of +16.

Example: Chamber 1,2 *U* wire mapping (See Fig 2.11)

1. All implemented cards (*U1* to *U12*) will map to wire 0 to 182 in the database file.
2. Compare to TDC card map (Note: when plugging into a TDC, an arbitrary card (either *U* or *V* card) *N* is always below card *N+1*, so R(ight) side of card *N* is always adjacent to L(ef) side of card *N+1*. If a ribbon cable is plugged into the chamber following the same pattern (polarity), they will be continuous in the meaning described before, and vice versa. Also note that the right side of each card will be a smaller channel of the TDC module. In chamber 2: Card *U1* to *U9* are discontinuous (For example Left side of card *U1* is adjacent to Right side of card *U2* when ribbon cables plugged from top. While Right side of card *U1* is adjacent to Left side of card *U2* when they're plugged on TDC module 14) while cards *U10* to *U12* are continuous.
3. nine empty cards are at the Left side of *U9*. (Indicated by shaded area)

### 2.3.4 Determine TDC time offset in wire chamber database file

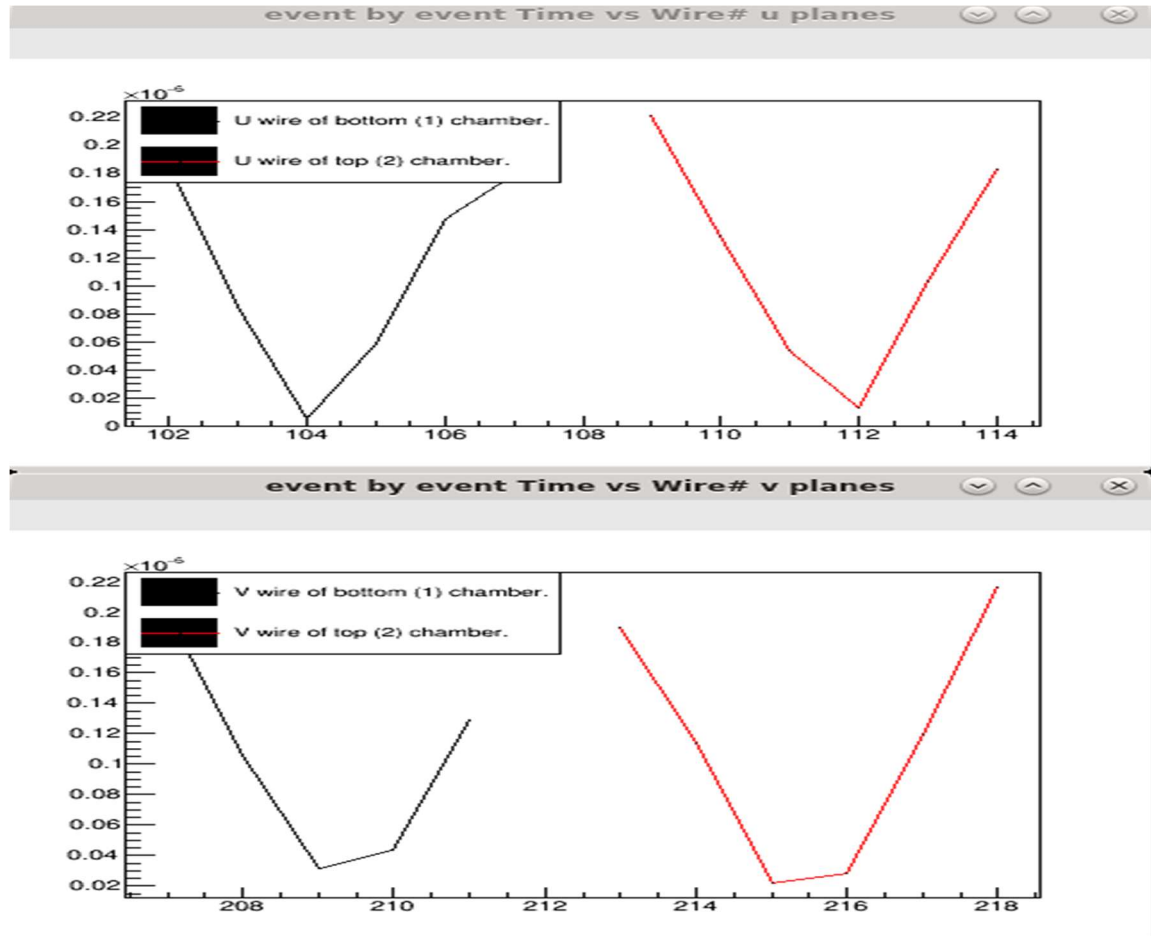
#### Significance of TDC time offsets

We have described the following entries in the wire chamber database file: 1) physical parameters, 2) geometric parameters that define coordinate systems and location of each individual wire, and 3) the mapping that mapping of every TDC channel to a wire in the analyzer. For track fitting, we need location of each wire and *drift distance* of each hit wire. The location of each wire is determined by geometric parameters, while drift distances to wires are computed from *drift time* data.

Without knowing the details of the *time to distance conversion function*, one can still deduce that: 1) greater drift times correspond to greater drift distances; thus, the function is monotonically increasing and 2) zero drift time corresponds to zero drift distance. Drift time is computed from TDC time (or *raw time* as named in analyzer). The TDC starts counting time, in TDC units, after the trigger, and stores the time when the signal from a sense wire reaches a TDC. Thus, TDC stores time in reversed order from real time and the conversion formula from TDC time *T* to real time *t* is:

$$t = -(T - T_{offset}) \times unit \quad (2.3)$$

This is a simple linear relation, much simpler than the time-to-distance conversion. The TDC *raw time offset*  $T_{offset}$  of each TDC channel is the only parameter left to be determined. These offsets can be defined as time (in TDC unit) taken for a signal propagating from a sense wire to a TDC. There are multiple sources of this offset, for instance length of ribbon cable linking discriminator card to TDC varies (see TDC raw time data in Fig. 2.15).



III Fig 2. 12 Drift time vs hit wire indices of matched clusters. Ordinate: Drift time in  $\mu s$ , abscissa: channel index no unit.

Of each wire plane of a given event. For example: if all hit wires in a cluster have drift time shifted the same amount to be larger, then all drift distances will go up. As a result, during track fitting, (absolute value of) slope fitted will increase. Thus, calibrating raw time offset is necessary for accurate track fitting.

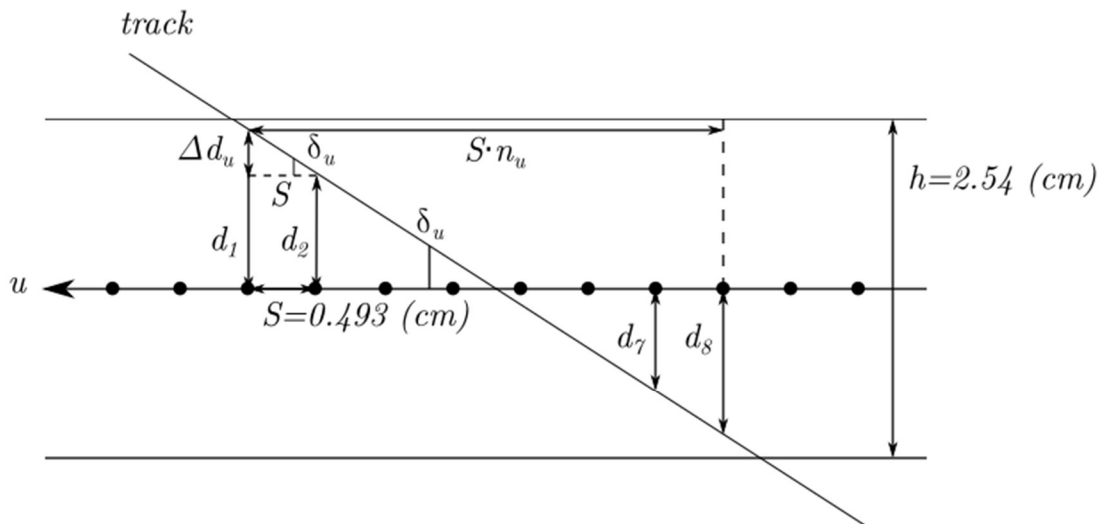
### Determination of TDC time offsets

We define the TDC time offsets as follows: assuming a drift distance distribution of a large number of events/tracks for all wires is uniform (see Fig. 2.13). To justify this assumption

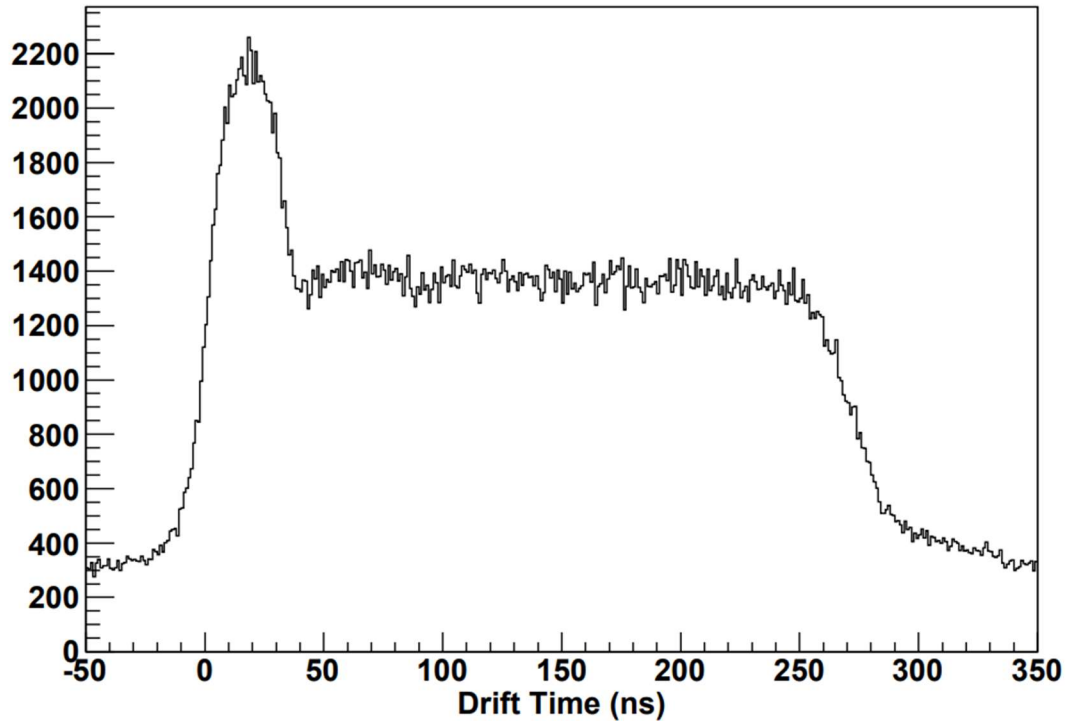
consider a single track. Drift distances have equal intervals and therefore contribute a number of equal interval points in the distribution. For the 8 wire (spanning 7 wire distances of the  $u$  or  $v$  coordinate) hit track in the figure, with wire plane thickness 1 inch, an example of drift distances can be 1.25, 0.90, 0.55, 0.20, 0.15, 0.50, 0.85, and 1.20 cm. For a large number of tracks, we can assume a track with same direction as this track but with a translation will also contribute to drift distance distribution, and result in a uniform distribution. In addition, different tracks will have different number of hit wires and drift distance intervals. Similarly, they with all have translations of their tracks which also make uniform contributions to the drift distance distribution.

According to above assumption, the real drift time distribution can be approximately separated into two regions (see Fig. 2.14):

- 1) where the track is away from sense wires, the electric field is approximately uniform and perpendicular to wire planes, and drift speed will be approximately uniform. Drift time distribution will be approximately uniform in this region since drift time and distance are linearly related, and
- 2) where the tracks are close to wires, the electric field is nonlinear and becomes much stronger closer to the wire, resulting in increased drift velocity. Since drift speed increases, electrons drift through same distance in shorter time. Thus, the drift time distribution in this region will have a distinct peak (higher frequency in distribution) in this region.



III Fig 2. 13 Copy of Fig A1.4 Relation between drift distance  $\Delta d$  and  $\delta_u$ .



III Fig 2. 14 Typical drift time distribution for a wire plane. Ordinate: counts no unit, abscissa: drift time in *ns*.

(Data from HRS chamber U1 plane), non-zero counts at 0 drift time here are due to background noises.

As mentioned earlier [formula (2.3)], TDC time is closely related to real drift time. Since all TDC channels share the same ending trigger, the TDC times are reversed with respect to real time, shifted by an offset, and scaled by its unit (0.5ns per TDC unit); larger TDC time corresponds to smaller real time and vice versa (see Fig. 2.15 for cumulative TDC time distribution of one discriminator card). According to the previous definition of TDC time offset, time (in TDC units) is that taken for the signal to propagate from the sense wires to the TDC. TDC time offset can also be defined as: *TDC time where the peak in TDC time distribution of the channel drops down to zero (excluding background noise), in TDC time units*. Remark: The definition is not strictly defined. Based on different shape of the peak in drift time distribution from different wire chambers, some adjustment can be made. Remark: Credibility check of TDC time unit is done by recording TDC time differences in a data file using a pocket pulse generator as signal, and comparing the corresponding time difference between consecutive pulses on an oscilloscope.

## Procedure to determine TDC time offset

1) We first acquire the TDC time distribution. To access the TDC time, we utilize the decoder portion of the analyzer to convert raw binary data of TDC time into ROOT format. The TDC time data are stored by channel in a ROOT file with each channel indexed. This is different from detmap entries in the VDC database file, which maps (crate, slot, group of channels) numbers on a TDC to (wire plane, group of wires) numbers. Here we use a decoder database file called db\_D.dat to map all (crate, slot, channel) numbers on TDC to just channel indices.

T1144 crate 21 14 88

means TDC crate 21, slot 14, channel 88 raw time data will be stored in analyzed ROOT file entry D.T1144)

2) Perform cosmic ray test runs for a pair of chambers to collect enough raw time data to make the raw time distribution histogram smooth when bins are finely divided for fitting of the peak. Since the data rate from cosmic ray is low, we collected enough data for every 16 channels, which is the number of channels per discriminator card. Offsets for all channels in each discriminator card are the same to a good approximation.

3) Run replay script to convert all raw data file into a ROOT file which contains all TDC time data for each wire.

4) Fill each discriminator card raw time data into a ROOT histogram.

5) Extract counts in each bin in those histograms. Perform a linear fit of all histograms from peak to bottom of the TDC time distribution. The calculated intersection between the fitted line and the abscissa is the TDC time offset (Fig 2.16).

Weighted least chi square fitting was used for finding the offset, that is if we have entries of histogram bins with TDC time and counts  $(t_i, C_i)$  with error for counts as  $\sigma_i$  and negligible error for TDC time. Assuming linear relation between  $t_i, C_i$  in the portion of TDC time distribution falling from peak to bottom. Assuming linear relation  $C = at + b$ , then fit parameters are:

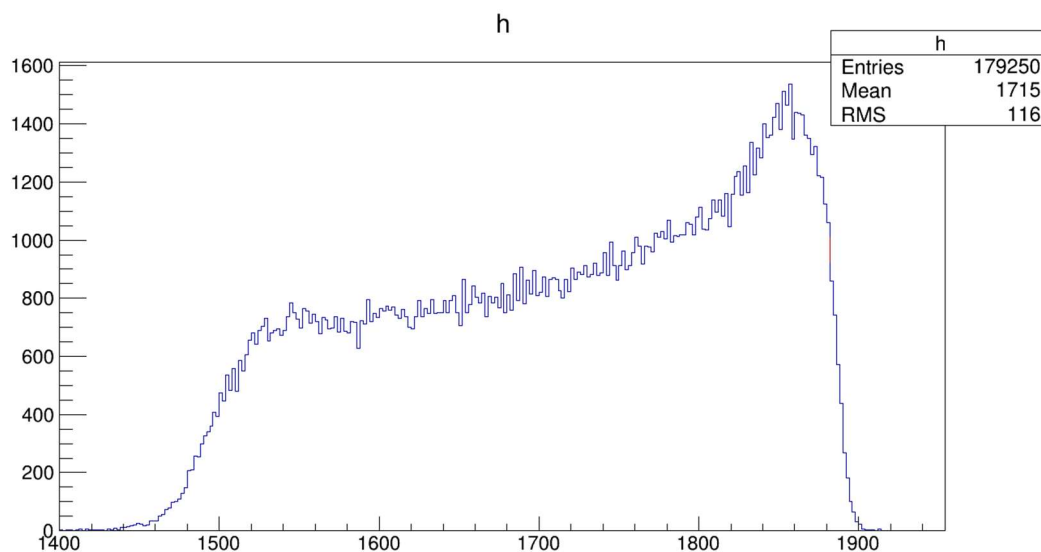
$$a = \left( \sum \frac{t_i^2}{\sigma_i^2} \sum \frac{C_i}{\sigma_i^2} - \sum \frac{t_i}{\sigma_i^2} \sum \frac{t_i C_i}{\sigma_i^2} \right) / \Delta \quad (2.4)$$

$$b = \left( \sum \frac{1}{\sigma_i^2} \sum \frac{t_i C_i}{\sigma_i^2} - \sum \frac{t_i}{\sigma_i^2} \sum \frac{C_i}{\sigma_i^2} \right) / \Delta \quad (2.5)$$

$$\Delta = \sum \frac{1}{\sigma_i^2} \sum \frac{t_i^2}{\sigma_i^2} - \left( \sum \frac{t_i}{\sigma_i^2} \right)^2 \quad (2.6)$$

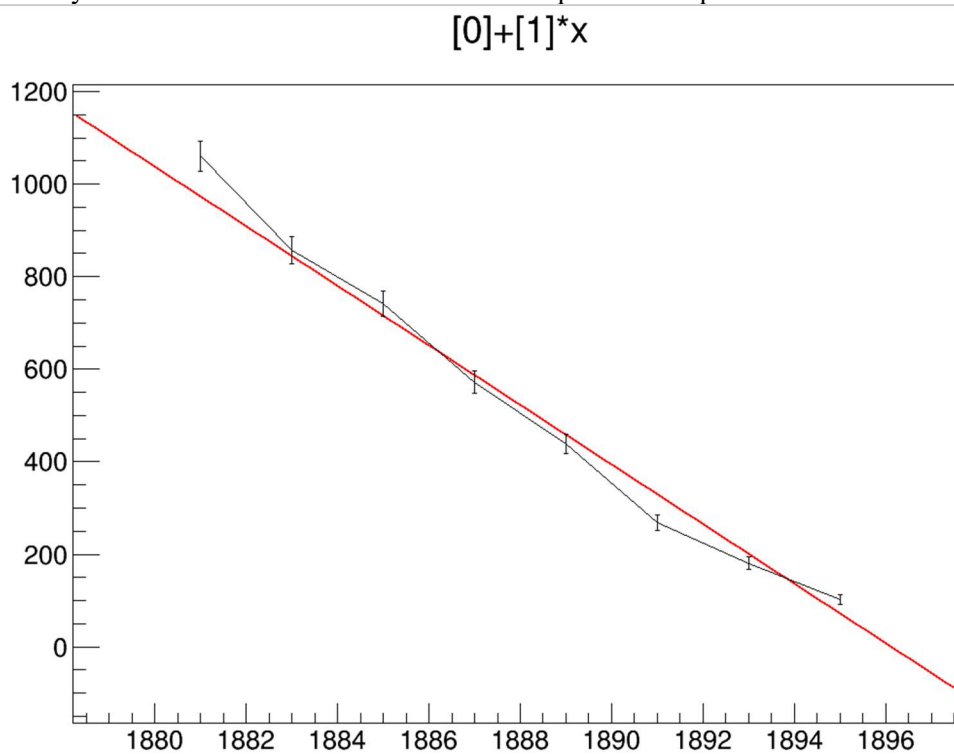
$$\begin{aligned} offset &= -\frac{b}{a} = -\frac{\left( \sum \frac{1}{\sigma_i^2} \sum \frac{t_i C_i}{\sigma_i^2} - \sum \frac{t_i}{\sigma_i^2} \sum \frac{C_i}{\sigma_i^2} \right)}{\left( \sum \frac{t_i^2}{\sigma_i^2} \sum \frac{C_i}{\sigma_i^2} - \sum \frac{t_i}{\sigma_i^2} \sum \frac{t_i C_i}{\sigma_i^2} \right)} \\ &= -\left( \sum \frac{1}{\sigma_i^2} \sum \frac{t_i C_i}{\sigma_i^2} - N \sum \frac{t_i}{\sigma_i^2} \right) / \left( N \sum \frac{t_i^2}{\sigma_i^2} - \sum \frac{t_i}{\sigma_i^2} \sum \frac{t_i C_i}{\sigma_i^2} \right) \end{aligned} \quad (2.7)$$

$N$  is the number of bins used in fit.



III Fig 2. 15 TDC time distribution for 16 channels in the same discriminator card. Ordinate: counts no unit, abscissa: TDC time in TDC unit ( $0.5 \text{ ns}$ ).

From data of a cosmic ray run, using a bin size of 2 TDC unit ( $1 \text{ ns}$ ) for fit. The time offset is defined by intersection of linear fit of the down slope from the peak.



III Fig 2. 16 Linear least chi square fit result for TDC time offset. Ordinate: counts no unit, abscissa: TDC time in TDC unit ( $0.5 \text{ ns}$ ).



The starting and ending bin centers are 1881 and 1895, which were manually picked. The reason for manually picking the starting/ending bin rather than using the code to find bin with maximum count and fit between bin with values between a high percentage and a low percentage of maximum counts is if the discriminator card is noisy the maximum count value could be higher than the maximum of the “real” peak.

## 3 Cluster finding and fitting

### 3.1 Introduction [39]

When a charged particle passes through a wire chamber, a sequence of adjacent wires register hit signals. This is called a *cluster*. From the wires of the cluster, viewed in the *projection plane* perpendicular to all wires, a straight-line segment perpendicular to the wire in the projection plane can be drawn and intersect the track projection. Thus, ions from ionized inert gas atoms will drift to wires of the cluster due to the potential difference generated by the cathode plane on upper and lower side of the gas layer. See next page for a typical cluster (Fig. 3.1 or Fig. 25. from Ref. [39]). It should be noted that the concept of *wire plane* has two related meanings here. One is the entire volume of the gas layer with thickness 1 inch for the wire chamber and the other is a geometric plane that passes through all sense wires' central axes. It's easy to distinguish them in context.

Here are some additional concepts relative to clusters. The *pivot wire* of a cluster is the wire which is the closest to particle trajectory and also with the least drift time. The *crossover point* is where the particle track intersects the wire plane. *Drift distance*  $d_i$  and *drift cell*  $C_i$  are defined in description of the Fig 3.1. Thus, to specify a cluster with all drift information it contains, we only need to specify pairs  $(n_i, d_i)$  of all wires in the cluster, where  $n_i$  is the wire index (of the wire plane) of the  $i^{\text{th}}$  wire of the cluster.

*Cluster finding* is the process of identifying all individual clusters of each wire plane in a triggered event from *hit collection*. As a particle passes through the wire plane, from the first wire in the cluster to the last, the drift distances  $d_i$  first decrease then increase, same as drift times  $t_i$ . Thus, when plotted the data points  $(n_i, t_i)$ , will define a V shape, as we'll visualize later in 3.3. This is the key point of cluster finding.

*Cluster fitting* is the process immediately after cluster finding and *time to distance conversion* that converts pairs  $(n_i, t_i)$  into  $(n_i, d_i)$  and which fits  $(n_i, d_i)$  to a "straight line". A straight line is the fitted result of particle trajectory inside the projection plane (the plane perpendicular to all wires in the wire plane; see Fig. 3.1). We obtained two important pieces of information from the fit: 1) the crossover point's  $u$  or  $v$  coordinate and 2) the slope  $\tau = \tan(\alpha_u)$  or  $\tan(\alpha_v)$  based on the wire plane in Fig. 3.1. The crossover point coordinates of all 4 wire planes will be used to calculate particle trajectory and the slope  $\tau$  will be used to compute the local track direction, which can be further compared with the global track direction  $(\tan\theta, \tan\phi, 1)$  to estimate the cluster span.

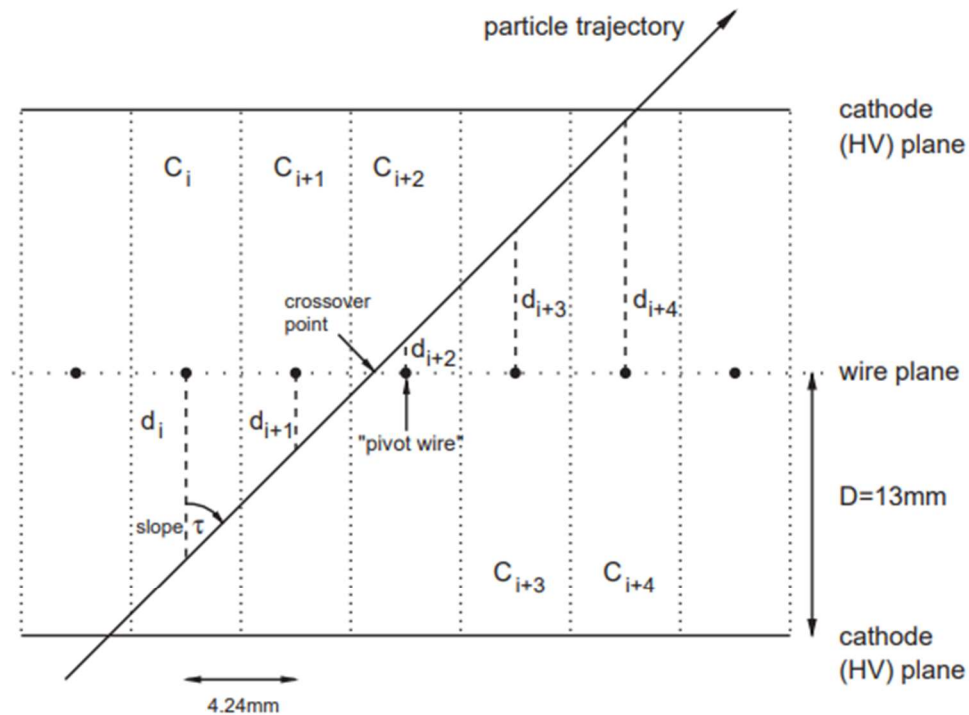


Fig. 25. A typical cluster of hits in a VDC plane.  $C_i$  denotes the  $i$ th wire cell, and  $d_i$  represents the perpendicular (effective) drift distance within that cell. The  $i$ th cell is defined as the region within which ions drift to the  $i$ th wire. By symmetry, the cell boundaries lie halfway between wires. The wire spacing is 4.24 mm. The separation between cathode high-voltage and wire planes is approximately 13 mm. The HV planes are held at a potential of approximately  $-4$  kV, while the wires are effectively grounded.

III Fig 3. 1 A typical cluster of thits in a VDC plane.

From *Basic instrumentation for Hall A at Jefferson Lab (Hall-A-NIM)* (Fig. 25. from Ref. [39])

Thus, the cluster finding and fitting process provides results as direct input for track fitting. In this chapter, we first explain cluster finding (section 3.2), then after briefly introduce JLAB Hall C *event display* (section 3.3) as a tool to visualize individual events we explain cluster fitting (section 3.4) with results of some examples shown. To end the chapter, we talk about some miscellaneous topics related to cluster finding and fitting.

## 3.2 Cluster finding.

### 3.2.1 Hall A analyzer wire plane class cluster finding

In the introduction, it was shown that identifying the  $V$ -shape drift time  $t_i$  vs wire index  $n_i$  relation in the  $(n_i, t_i)$  graph is the key to find a cluster. The analyzer algorithm is straight forward; that is, when searching through the wire index in the hit collection if the drift time value first falls then rises, it indicates a V shape and is identified as a cluster. [40] (Note, all wire chamber tracking algorithms are included in THaVDC\*.h or THaVDC\*.cxx source file) There are some conditions that will determine the end point of a cluster: 1) during the rising part of the  $V$ -shape, a gap in the wire index over the set gap limit (1 or 2 in wire chamber database file), 2) the estimated drift distance which was computed by drift velocity (calibrated, as a parameter in database file) times drift time is more than 1.1 times or less than -0.1 times the wire plane half-thickness, or 3) drift time starts falling again after rising. The end points are then set as limits of the new cluster and the new cluster will be registered and written in the ROOT file. There are some conditions that will end a cluster candidate as a cluster prematurely, and the wires will not be included in any cluster: 1) only falling and no rising before a large enough gap in the wire index or 2) only rising. These wires will be skipped, etc.

There are certainly some defects and some special cases for which this algorithm doesn't work since there are always some special cases a simple falling then rising concept the algorithm does not take into consideration. An obvious one is that the searching is one directional (at the moment searching from lower wire index to higher wire index in hit collection, also see Fig 3.6). Then if two adjacent clusters create a  $W$  shape, the middle local maximum drift time of the  $W$  shape will always be assigned to the lower indexed cluster. In addition, if the middle local maximum time is the only hit on left part of the V shape the right cluster cannot complete a  $V$  shape and will be discarded. It's been found that changing the searching direction will give about 1% difference in final fitted track result. We'll come back to this when fit track results are displayed in track fitting chapter.

### 3.2.2 An alternative cluster finding algorithm

The one directional search routine in the analyzer cluster finding code introduces an artificial asymmetry because it focuses on the falling then rising structure of drift time in a sequence of wires. In order to correct this an alternative algorithm was developed. Although it has not yet replaced the algorithm in the analyzer, it does provide a useful credibility check of the analyzer results.

For this algorithm, instead of focusing on the falling and rising timing structure of hit wires in the cluster, it searches for the local minimum times first. In other words, we find the pivot wire first. Once this pivot wire is found, we start to iterate wires in the hit collection on both sides of the pivot wire. The cluster end wires are determined when: 1) a gap appears that is larger than the database file limit, 2) a drift time starts to decrease again, or 3) the drift time difference of adjacent wires is outside the limits set in the database file. (Also see Fig 5.27) This cluster finding algorithm will keep the middle wire with local maximum drift time for both

clusters it shared. It can eventually be discarded from both clusters but we keep it anyway so that it won't generate spurious error in local cluster fitting. Thus, this algorithm will usually render similar cluster finding results as the original analyzer algorithm since a  $V$  shape structure is the basic unit. However, since the asymmetry of falling and rising of drift time in analyzer algorithm is replaced by only rising of drift time when searching from the pivot wire, this alternative algorithm is simpler and much less error prone. Moreover, it allows us to introduce more cuts to ensure a good cluster. For example, since the time difference between adjacent wires in a cluster are related to the cluster span, a constraint can be imposed on the drift time of the pivot wire.

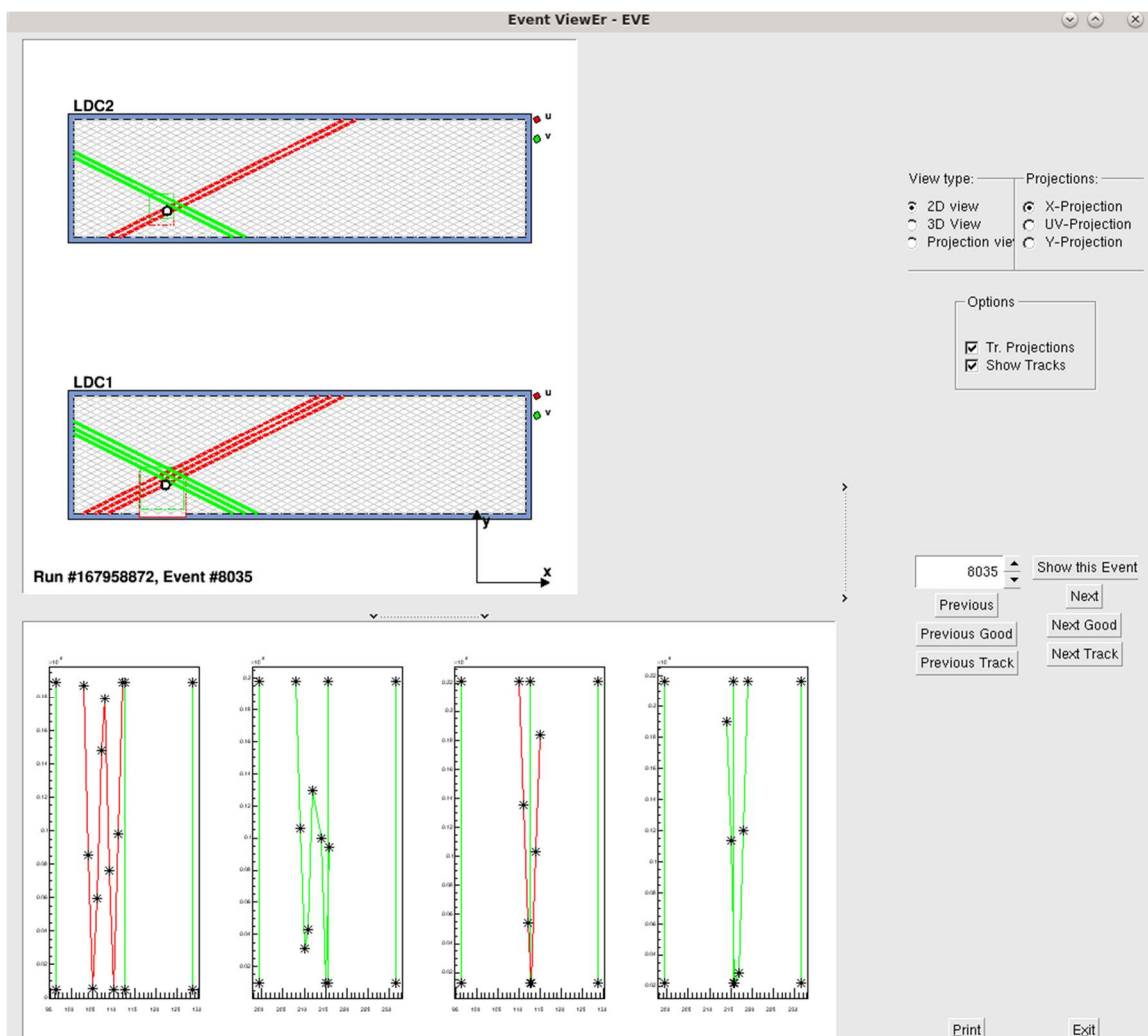
### 3.3 Visualizing events

An event-by-event display program called EveHallC ([24] by ?) displays track information event by event. It has been modified to suit our wire chamber geometry and channel mapping. After the analyzer has replayed a full test run and generated the ROOT file, the event display program reads the hit collection and fitted track information and visually displays the tracking and clustering information event by event.

There are two displays (see Fig. 3.2 below) that are most useful for our purpose:

- 1) a 2D projection of two wire chambers. It illustrates track geometry information, displaying wire locations. Wires that have been hit are highlighted. In addition, the track crossover point on wire planes have also been drawn. Due to the limited space on canvas, one line on the wire plane represents 5 wires in actual wire plane; and
- 2) drift time vs hit wire indices or  $(n_i, t_i)$  graph on each wire plan It displays the entire hit collection of the event, and thus cluster information.

Thus, the event display program's main application is to check track reconstruction results. For example, if the track intersection on a wire plane is not located on one of the "intersections" ("Intersection" is not a precise word. Since the  $U$  and  $V$  wire planes are different planes, with a 1 inch offset from one to the other,  $U$  and  $V$  wires cannot intersect each other. Thus, to be more precise the track intersection on one wire plane must lie between two adjacent wires of the hit wires and as does its intersection on the other wire plane.) between  $U$  wire and  $V$  wire of the same wire chamber, then the fitted track is incorrect and the reason must be investigated. The drift time vs wire index graph will give a general idea of number of clusters, cluster span, and its slope, maximum and minimum drift time information, etc., which can also be used as confirmation of results of cluster finding or indicate necessary improvements.



III Fig 3. 2 A typical event by event display in 2D view. Bottom figures ordinate: drift time in  $\mu\text{s}$ , abscissa: wire number in the corresponding wire plane, no unit.

This is an event with a good track reconstructed. The upper diagram shows the active area of the top wire chamber (LDC2) and bottom wire chamber (LDC1) with red and green wires indicate  $U$  and  $V$  wires respectively. The dots are track intersection on  $U$  wire plane and thus should lie on one of the  $U$  wires and close to one of the  $V$  wires that lie above it. The red and green squares are the boundaries of the trigger scintillator projection on each wire plane computed by projecting intersection area to wire planes. The lower diagrams are drift time vs wire index plots for each wire plane. From left to right, they represent  $U$  of LDC1,  $V$  of LDC1,  $U$  of LDC2, and  $V$  of LDC2.

## 3.4 Cluster fitting

### 3.4.1 Procedure of cluster fitting

After finding clusters with indices and drift times  $(n_i, t_i)$  associated with each wire the drift times,  $t_i$ , we convert them into drift distances,  $d_i$ , through time to distance conversion, which will be discussed in next chapter. The relation we want to fit is either the relationship between the local distance,  $d_i$ , vs local wire number,  $n_i$ , the  $(n_i, d_i)$  or the  $(u_i, d_i)$   $(v_i, d_i)$  relation, where  $u_i, v_i$  are  $U, V$  coordinates of wires in the cluster. For fitting  $(n_i, d_i)$  we use the least square fit without weight. The relation is:

$$d = A + Bn \quad (3.1)$$

Denoting  $|s|$  as the (unsigned) wire spacing, we can also find slope  $\tan(\delta_u)$  or  $\tan(\delta_v)$  of the track in projection plane (also see Fig. 3.3. below for definition of  $\delta_u$  or  $\delta_v$ ):

$$B = \tan(\delta_{u/v}) \times |s| \quad (3.2)$$

Denote  $h = 1(\text{inch}) = 2.54(\text{cm})$  as the wire plane thickness. From  $\tan(\delta_{u/v})$  we can also compute the cluster span (unitless):

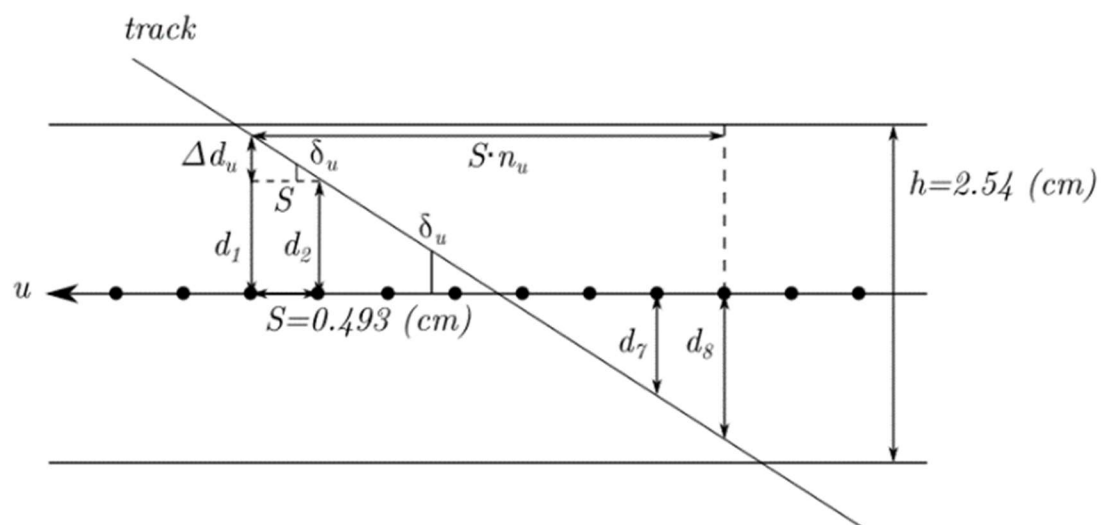
$$n_{u/v} = \frac{h}{|s \times \tan(\delta_{u/v})|} = \frac{h}{|B|} \quad (3.3)$$

In addition, if we want to check the hit crossover point in terms of wire plane  $U, V$  coordinates all we need to do is to convert them from intersection  $n_{int} = -A/B$ :

$$u_{int} = u_0 + n_{int} \times s \quad (3.4)$$

Here  $u_0$  is the  $U$  coordinate of 0<sup>th</sup> wire in  $U$  plane,  $s$  is the signed wire spacing, which is the same for both  $U$  and  $V$  planes. Same formalism for  $V$  plane by replacing  $u$  by  $v$ . According to the setup in the database file, we obtained parameters for (3.4), 279 wires per wire plane and  $s = -0.493(\text{cm})$ , thus  $u_0 = (279 - 1) \frac{|s|}{2} = 68.527(\text{cm})$ .





III Fig 3. 3 Geometry of cluster fitting.

(Redraw of Fig 2.13) projection view in  $uz$  plane. A fitted cluster is shown, with all the notations the same as on last page. In addition, the wire spacing  $s$  in the figure is its absolute value.

$n_i$	$d_i$ (cm)
102	1.098
103	0.540
104	0.0420 (Pivot point)
105	-0.397
106	-0.884
107	-1.057
$A$ (cm)	$B$ (cm)
46.1	-0.442
$-A/B$ (Intersection $n_{int}$ )	$\delta_u$ (°)
104.3	41.86
$n_u$ by $(n_i, d_i)$	$n_u$ by $(\theta, \varphi)$
$5.74 = (2.54/0.442)$	4.39

Table 3.1. A typical cluster fitting result. The cluster consists of wires  $n_i$  from  $i = 102$  to  $107$  without a gap, and associated drift distance,  $d_i$ . The least square fit got  $A$  and  $B$ . Then, the intersection is  $-A/B$ , and complement of the incident angle  $\delta_u = 90^\circ - \alpha_u = 41.86^\circ$ , and the wire span  $n_u = \frac{h}{|s \times \tan(\delta_u)|} = \frac{h}{|B|} = (2.54/0.442) = 5.74$ . It has been compared with cluster span computed from track direction angle  $(\theta, \varphi)$ , by relations:  $\tan(\alpha_u) = \cot(\delta_u) = \tan\theta \cdot \cos\alpha + \tan\varphi \cdot \sin\alpha$  (Formula (4) in appendix A1.3)  $\alpha = \arctan(0.5) \cong 26.45^\circ$  is the angle between analyzer  $y$ -axis and  $U$  wires inside the wire plane.

We made a quick explanation of the notation  $\delta_{u/v}$  and  $\alpha_{u/v} = 90^\circ - \delta_{u/v}$ . [39]  $\alpha_u$  and  $\alpha_v$  are the global track angles in the  $u$ - $v$  coordinate system, i.e., the angles between the  $z$ -axis and the projection of the track onto the  $u$ - $z$  and  $v$ - $z$  planes, respectively.  $\alpha_{u/v}$  is a better representation of the track direction under  $u, v$  coordinate system, which is converted from track direction  $\vec{t}$  in the analyzer coordinate system as shown below.

The track direction in analyzer coordinate system is represented by

$$\vec{t} = (\tan\theta, \tan\varphi, 1) = \left( \frac{\Delta x}{\Delta z}, \frac{\Delta y}{\Delta z}, \frac{\Delta z}{\Delta z} \right) \quad (3.5)$$

while  $\Delta x$  can be computed from  $\Delta x = x - x_0$ , where  $x$  is the  $x$  coordinate of any point on track,  $x_0$  is the  $x$  coordinate of the track crossover point in the 1<sup>st</sup> wire plane, and similarly for  $\Delta y$  and  $\Delta z$ . We have the linear transformation of track angles  $\theta, \varphi$  from coordinates system  $xyz$  to track angles  $\alpha_u, \alpha_v$  from coordinates system  $uvz$  (Formula (4) in appendix A1.3):

$$\begin{aligned} \tan(\alpha_u) &= \cot(\delta_u) = \tan\theta \cdot \cos\alpha + \tan\varphi \cdot \sin\alpha = \vec{t} \cdot \hat{u} \\ \tan(\alpha_v) &= \cot(\delta_v) = \tan\theta \cdot \cos\alpha - \tan\varphi \cdot \sin\alpha = \vec{t} \cdot \hat{v} \end{aligned}$$

Notice that unit base vector  $\hat{u} = (\cos\alpha, \sin\alpha, 0)$  is similar to (3.5):

$$\tan(\alpha_u) = \frac{\Delta u}{\Delta z}, \tan(\alpha_v) = \frac{\Delta v}{\Delta z}$$

The track angles  $\theta, \varphi$  are essentially  $\alpha_x, \alpha_y$  while  $\delta_{u/v} = 90^\circ - \alpha_{u/v}$  is better to represent the slope of the cluster fitting (see formula (3.2)).  $\delta_{u/v}$  and  $\alpha_{u/v}$  describe the same issue, the choice of which to use depends on the situation just explained.

### 3.4.2 Up-down ambiguity and disambiguation

In the cluster fitting result shown in Table 3.1. the drift distance  $d_i$  is signed so the projected track is a straight line. However, the measured drift time  $t_i$  values from the TDC are always positive. This introduces an up-down ambiguity (see Appendix A1.5.3). Thus, determining the signs of drift distances  $d_i$  is a must for resolving this ambiguity and performing accurate cluster fitting. We resolve signs for drift distance of each wire in two steps:

1. determine side of pivot point; and
2. determine signs of distances on each side.

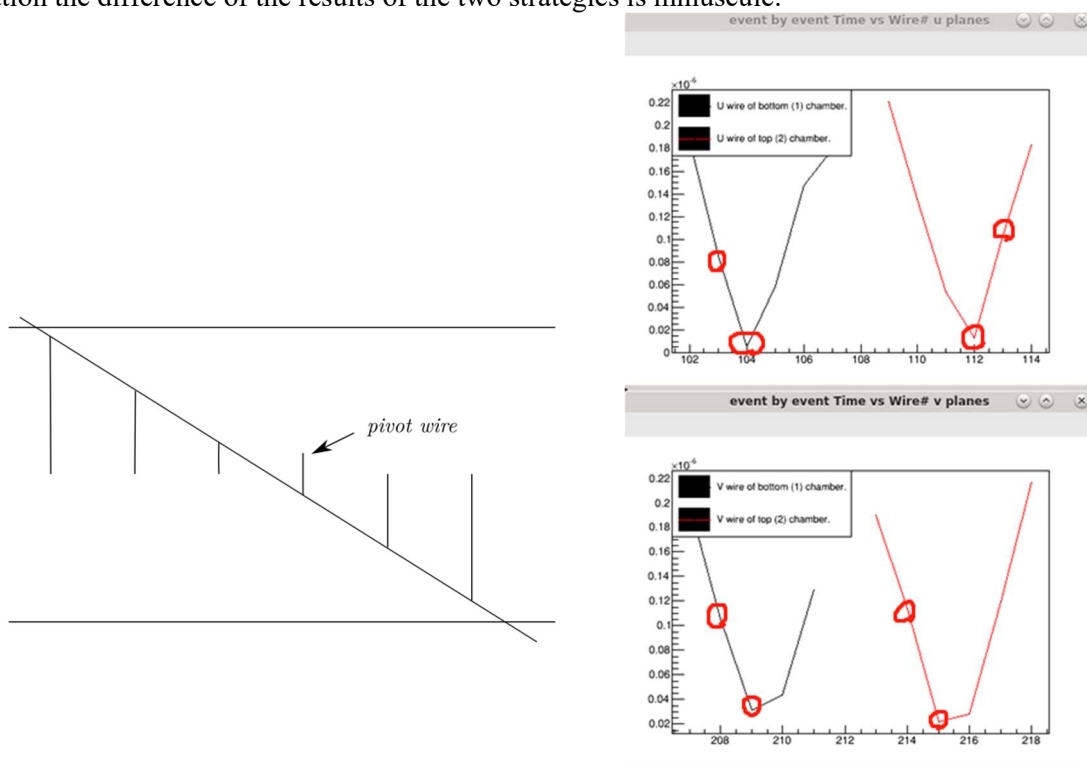
For step 1, which has been explained before, as a particle travels through a wire plane, the track gets closer to sense wires, intersects wire plane at crossover point (see Fig. 3.1), then gets further away from sense wires. This results in clusters with index and drift time  $(n_i, t_i)$  having a  $V$ -shape structure as shown in Fig. 3.2. Wires on opposite sides of a  $V$  shape in an  $(n_i, t_i)$  graph have different signs of drift distance  $d_i$ . Recall that the wire with the least drift time and drift distance at the bottom of  $V$  shape is called pivot wire. Since the pivot wire belongs to both sides, the sign of its drift distance needs additional analysis.

There are two ways to resolve the side of drift distances (see Fig 3.4 below):

- 1) (Fig. 3.4 Left) assign all wires on one side of the pivot wire one sign and those on the other side the opposite sign. Then, fit a straight line from cluster data  $(n_i, d_i)$  twice, with the pivot point drift distance being either positive or negative. Calculate  $\chi^2$  for both fits with the one with the lower  $\chi^2$  indicating the correct pivot point  $d_i$  sign. [39]

2) (Fig. 3.4 Right) compute drift time difference between pivot wire and wires adjacent to it. The wire with larger time difference means it has the same sign as pivot wire, and thus the sign of pivot wire is determined.

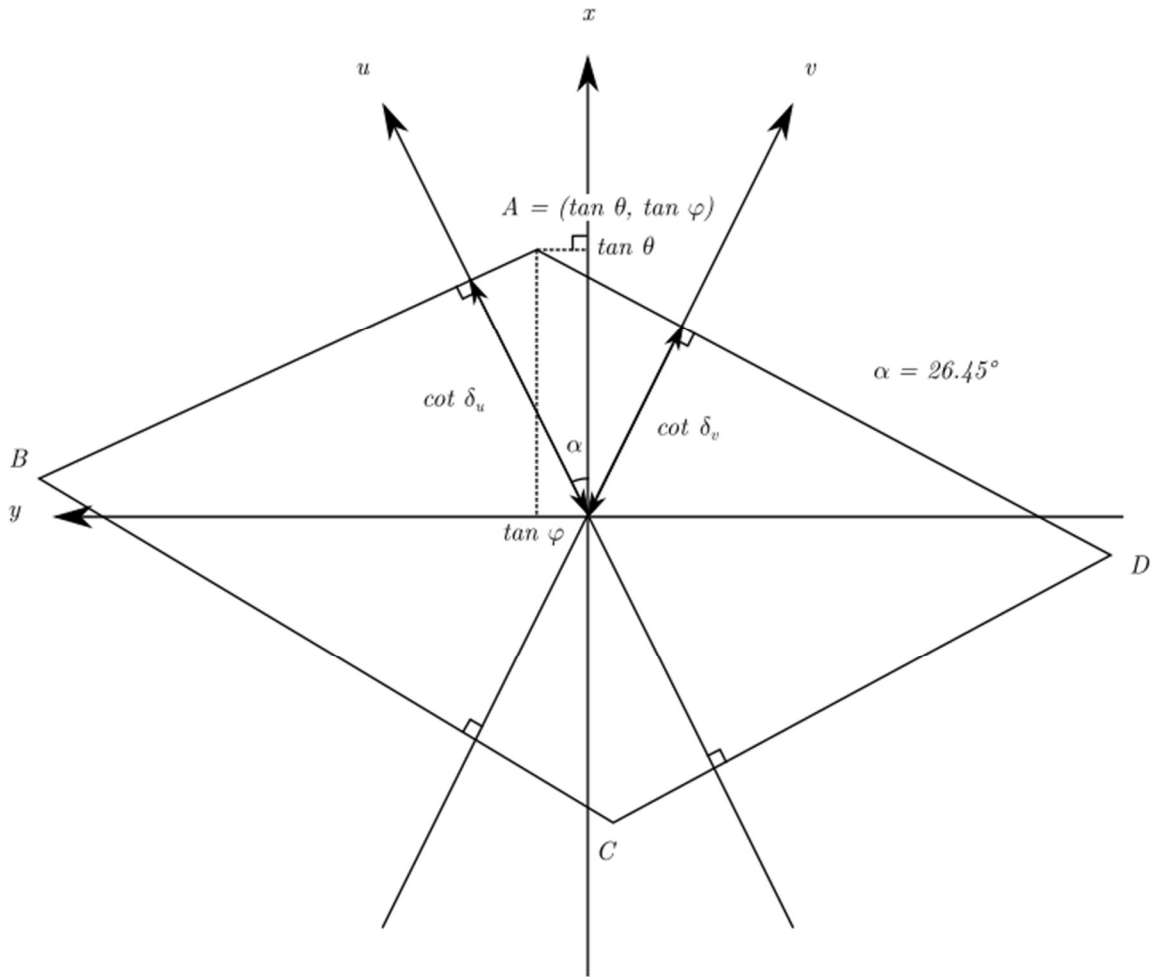
Generally, the results of methods 1) and 2) in last paragraph are the close to the same except in a few cases when the drift distance is very close to 0 or, equivalently, the drift time difference between pivot wire and both wires adjacent to it are almost the same. In either situation the difference of the results of the two strategies is minuscule.



III Fig 3. 4 Pivot wire drift distance sign. Right figure ordinate: drift time in  $\mu\text{s}$ , abscissa: wire number in the corresponding wire plane, no unit.

Pivot wire is the wire with the least drift time. We know the signs of the drift distance of wires with index larger than that of the pivot wire and wires with index less than that of the pivot wire are opposite, but the sign for pivot wire is unknown.

- 1) fit distances twice with pivot wire assigned a different sign in each case; the fit with the lower  $\chi^2$  corresponds to the best choice of sign for drift distance of the pivot wire. (Left)
- 2) compare drift time differences between pivot wire and its neighbor wires, one with larger difference is the side where the pivot wire belongs. (Right)



III Fig 3. 5 Illustration of resolving up-down ambiguity.

For step 2 we refer to appendix A 1.5.3. In short, we need to determine if the track enters wire plane from lowest indexed wire in the cluster or the highest indexed wire. That is, we acquired  $|\cot(\delta_u)|$  or  $|\cot(\delta_v)|$  but its sign is undetermined. (see Fig. A 1.6)

The track direction  $\vec{t} = (\tan\theta, \tan\varphi, 1)$  has its projection in the  $x$ - $y$  plane to be  $(\tan\theta, \tan\varphi)$ , while its projection on  $U/V$  axes are  $\cot(\delta_{u/v})$  by the formula, and noting  $(\cos\alpha, \sin\alpha)$  and  $(\cos\alpha, -\sin\alpha)$  are  $\hat{u}$  and  $\hat{v}$  in  $xy$  plane respectively:

$$\begin{aligned} \cot(\delta_u) &= \tan\theta \cdot \cos\alpha + \tan\varphi \cdot \sin\alpha \\ \cot(\delta_v) &= \tan\theta \cdot \cos\alpha - \tan\varphi \cdot \sin\alpha \end{aligned}$$

Since the sign of  $\cot(\delta_{u/v})$  can be either + or -, there will be 4 possible track directions computed by drift distance information. These 4 directions are represented by ABCD above (For example, point B has positive  $\cot\delta_u$  and negative  $\cot\delta_v$ ). Forming a parallelogram, each end point is in a quadrant divided by both U and V axis.

To disambiguate: compare differences of these 4 directions to global fit direction ( $\tan\theta$ ,  $\tan\varphi$ ) in the  $x$ - $y$  plane (uses intersections of track on each wire plane in global track fitting), and pick the direction with the smallest angle difference. Note: A much quicker disambiguation method is to check formulas below (3.5):

$$\cot(\delta_u) = \tan(\alpha_u) = \frac{\Delta u}{\Delta z} \text{ and}$$

$$\cot(\delta_v) = \tan(\alpha_v) = \frac{\Delta v}{\Delta z}.$$

When  $\Delta u = u_2 - u_1 > 0$ ,  $u_2$  is the cluster fit intercept for upper u plane,  $u_1$  for lower u plane, then  $\alpha_u > 0$ , and vice versa. A similar argument applies for  $\alpha_v$ .

## 3.5 Misc. issues

### 3.5.1 Time to distance conversion

After cluster finding (3.2) we have clusters containing information on indices and drift times  $(n_i, t_i)$ , the time to distance conversion convert drift time to  $t_i$  into absolute value of drift distance  $|d_i|$ , then we resolve up-down ambiguity of the cluster by determining sign of drift distance  $d_i$ , and converted cluster  $(n_i, d_i)$  is used in cluster finding. The missing part time to distance conversion (abbr. as TTD) will be discussed in detail in chapter 4.

Here we list some basic properties of TTD. First, the TTD relation is incident angle  $\alpha_u$  or  $\alpha_v$  dependent. Second, for fixed incident angle TTD is a monotonically increasing function  $d(t; \alpha_{u/v})$ ; that is, a larger drift time corresponds to a larger drift distance. Thus, TTD is a function to be fitted with incident angle dependent parameters, to make resulting the  $(n_i, d_i)$  relation to be as straight as possible, and result in local tracks from  $(u_i, d_i)$  or  $(v_i, d_i)$  relations as close to charged particle tracks as possible. The fitting procedures will be the main content in chapter 4 Time to distance conversion.

### 3.5.2 Improving Hall A analyzer cluster finding algorithm

The goal of the cluster finding algorithm is to find correct clusters from primary charged particles in BH process. Note that the cluster finding result will eventually affect the track fitting result, so we should avoid the mistake of aiming for high efficiency. Based on these factors the actual algorithm will fulfill the goal to a decent degree.

There were aspects of the Hall A analyzer that required improvement; some major defects were found during examination of wire chamber test data.

For the algorithm itself:

1) (See Fig. 3.6) As explained in 3.2.1. the falling then rising search method to find the  $V$  shape structure is one directional and “common” hit wires from both cluster candidates will be always assigned to the one with lower indices. This leads to about 1% difference when compared to searching in the both directions.

2) Uncategorized wires during the previous search will be interpreted as the starting wire of the new cluster candidate after finding a cluster. This can be unnecessary and can result in a redundancy of wires in the new cluster.

For cuts:

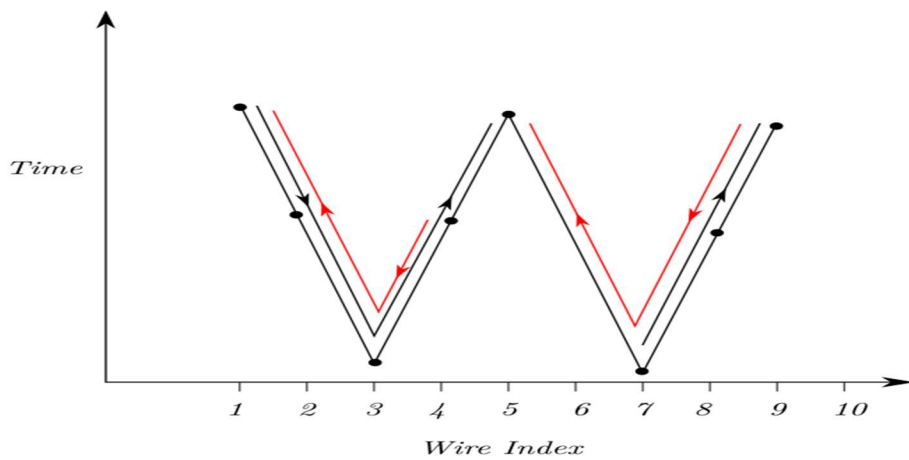
1) Some cut parameters were determined while entirely overlooking difference between wire planes. For example, the time distribution of hits is different between wire planes, and so should TTD parameters.

2) Cluster span  $(n_u, n_v)$  limits neglect differences between  $u$  and  $v$  wire planes. Since the orientations of the wire planes are different, the possible allowed cluster spans depend on both  $u$  and  $v$  orientation. It is actually better if we can assign limits of ordered pairs  $(n_u, n_v)$  by enumeration as this will allow better conditional efficiency analysis. The 2D region of allowed

$(n_u, n_v)$  pairs from detector acceptance can be estimated by simulation. We will revisit this topic later in Part IV Simulation, section 3.4.2 Wire span  $(n_u, n_v)$  distribution.

3) (See Fig. 3.7) The parameters for minimum and maximum time differences between adjacent wires in a cluster is useful to cut off clusters with abnormal time data. However, they will be much better to designate these parameters based on cluster size, since larger clusters correspond to smaller time differences between neighboring wires, and vice versa.

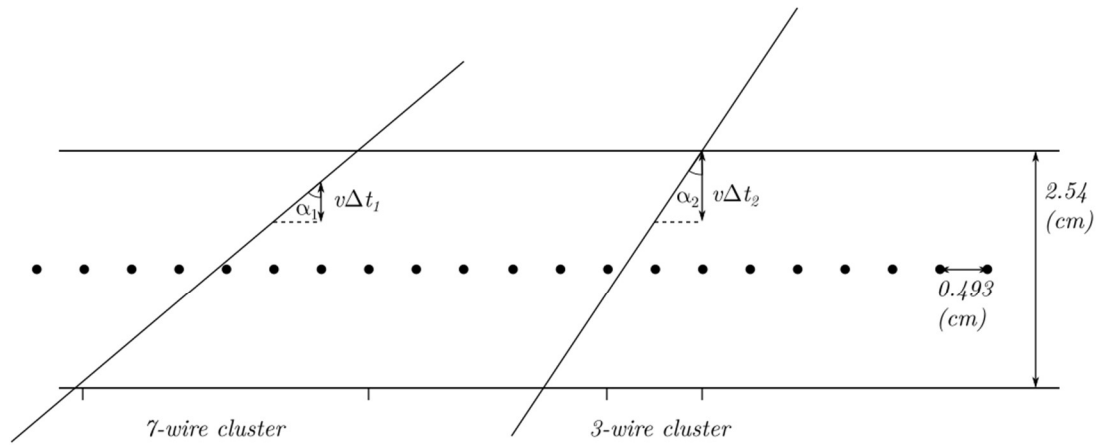
4) Wires are regarded as infinitely long according to the analyzer source code, that even a pair of  $u$  and  $v$  clusters from one wire chamber don't have any intersection inside active area of the wire chamber, they could still be paired and used in track fitting, resulting in tracks outside a wire chamber.



III Fig 3. 6 One directional search of clusters in the JLAB analyzer.

Dots in the graph are  $(n_i, t_i)$  data point. Assume a gap of 1 wire in cluster finding is allowed. Now suppose wire 6 doesn't have data (might be the result of a bad wire). The arrow indicates iterative direction of cluster finding; if the search starts from the smallest wire index, then the only found cluster found includes wires (1,2,3,4,5) while the group of wires (7,8,9) is not a cluster since there's no V shape structure. If search starts from largest wire index, two clusters will be found: wires (1,2,3,4) and wires (5,7,8,9).





III Fig 3. 7 Drift time difference between adjacent wires.

From wires in a cluster should be cluster size dependent. In the two clusters illustrated, cluster 1 has 7 wires and cluster 2 has 3 wires. Thus, the incident angle  $\alpha_1 > \alpha_2$ . The difference in drift time between two adjacent wires in the cluster can be approximated by  $\Delta t_1 = \frac{ws}{v \tan \alpha_1} < \frac{ws}{v \tan \alpha_2} = \Delta t_2$ , here  $ws$  is wire spacing and  $v$  is drift velocity. Thus, drift time difference between adjacent wires in a cluster will decrease as cluster size increases.

### 3.5.3 More on ambiguities

We have already considered two ambiguities: 1) the sides of the pivot wire and 2) the sign of drift distances. For 2), the ambiguity is resolved once we have picked correct set of clusters belonging to the same track, one in each wire plane. This leads to 3), the  $u$ - $v$  association. [41] That is, to choose one cluster from the  $u$  wire plane and one from the  $v$  wire plane of one wire chamber, both of which belong to the same particle track. Determining this association is only required for a case of multiple clusters, when all wire planes have cluster(s) and at least one of them has more than one cluster. Since the number of possible ways of the  $u$ - $v$  association equals the product of the number of clusters from all wire planes, this number can get large and computation time will increase significantly.

During our wire chamber test runs using cosmic rays, the probability of multi-clusters produced by a shower is very high, and the  $u$ - $v$  association algorithm in the analyzer had difficulty finding correct result. In our experiment, based on projected event rates, detector acceptances, and the pulsed nature of the beam, coincident two-pair production in the same drift time window is negligible and single cluster events will be our principal concern. Nevertheless, we will give a short explanation of  $u$ - $v$  association when discussing track finding.

## 4 Time to distance conversion

### 4.1 Origin of the problem

Once we obtained cluster, we acquired the wire index and drift time  $(n_i, t_i)$  of each wire in the cluster. In order to fit the cluster and reconstruct the local track projection inside the wire plane, we have to convert  $(n_i, t_i)$  to  $(n_i, d_i)$ , where  $d_i$  is the drift distance of  $i^{\text{th}}$  wire of the cluster. This operation is called *time to distance conversion* and can be abbreviated by TTD, and the conversion function that converts any  $t$  to a  $d$  is called the TTD function. Our objective in this chapter is to establish and calibrate the time to distance conversion function that converts  $(n_i, d_i)$  data can be used in cluster fitting to produce local tracking results.

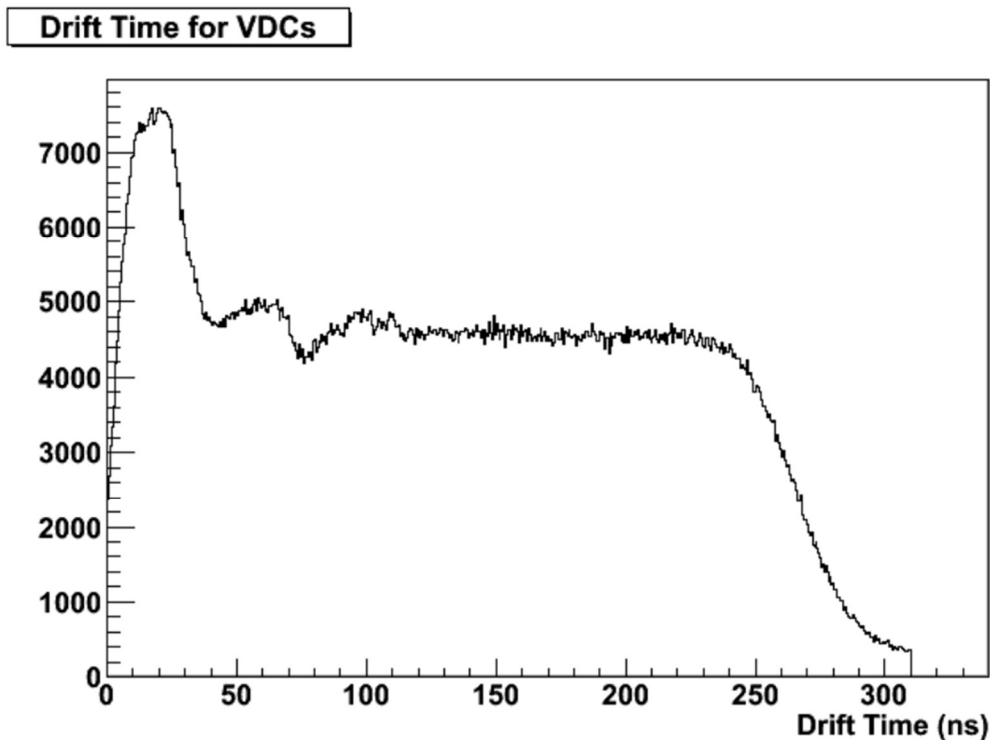
#### 4.1.1 Drift time data for a single event

The spatial volume containing all electric field lines leading to a single sense wire is called a *drift cell*. Due to the large area of the wire plane compared to the ionized region of a single particle track and equally spaced sense wires, drift cells have translation symmetry and the center plane between two adjacent sense wires separates them. Thus, one drift cell contains volume that extends half a wire plane thickness ( $1.0''/2$ ) above and below a sense wire, and half a wire spacing ( $\sim 0.493\text{cm}/2$ ) to the left and right of the sense wire [29]. The signal of a single sense wire is only generated from ionized electrons within the corresponding drift cell. The drift time data from the TDC corresponds to the time of the 1<sup>st</sup> drift electrons that reach its corresponding wire. If all sense wires are efficient enough, the drift time data for a single event contains times from all sense wires that the charged particle crosses in all wire planes (see Fig. 3.2. for visualization of single event data). For a single cluster of a single wire plane the data are  $(n_i, t_i)$ .

#### 4.1.2 Distribution of drift time and drift distance

The distributions of drift times and drift distances are the most direct results reflecting time to distance conversion. We discuss drift distance 1<sup>st</sup> since it is directly related to trajectory of particles inside wire plane. The drift time collected in the TDC corresponds to the 1<sup>st</sup> bunch of ionized electrons that reach the sense wire. The corresponding drift path is not necessarily the straight line directly above or below the sense wire, which represents the reconstructed drift distance. We assume that the actual and reconstructed drift distance are the same to a 1<sup>st</sup> order approximation. In addition, the drift distance distribution is uniformly distributed from around 0 to half wire plane thickness if certain assumption is satisfied: for each set of tracks with the same incident angle, their crossover point coordinate is uniformly distributed (translation symmetry). This can be further relaxed to assuming that the crossover point coordinate is uniformly distributed between the coordinate of two adjacent wires. The assumption can be easily satisfied when the active area of wire chambers are large enough to retain translation symmetry. A detailed discussion of the condition of uniform distance distribution appears in section 4.3.4 3).

Under the assumption that we have uniformly distributed drift distances, we consider the drift time distribution. Since the TTD function  $d(t)$  is also incident angle  $\theta = \alpha_u$  or  $\alpha_v$  dependent and should be represented as  $d(t; \theta)$ , we constraint our discussion below to tracks with nearly the same incident angle. As discussed in 4.1.1, when a track is away from sense wire in the corresponding drift cell, the drift velocity is constant due to the uniform electric field, thus we have uniformly distributed drift time in this region. And when track is close to sense wire, the increased electric field will result in increased drift velocity and for same interval of time more drift distance is covered. Due to the uniformly distributed drift distance, drift time distribution has higher frequency in the sense wire region.



III Fig 4. 1 Drift time distribution of wire chamber. Ordinate: counts, no unit, abscissa: drift time in unit  $ns$ .

(Fig. 4.19 in Ref. [29]) As described above, it has a peak near 0, and is nearly uniform when the drift time is sufficiently large.

## 4.2 Time to distance function

### 4.2.1 Properties of TTD function

There are several properties of that TTD function that we can utilize to simplify its determination process:

- 1) The function is incident angle  $\alpha_u$  or  $\alpha_v$  dependent. There are several reasons for this: incident angle determines where the particles will cross the region close to a sense wire with increased electric field and drift velocity. The drift path with the least drift time will also be different for different incident angle. It should be noted that the incident angles are only determined after a track has been fully fit. The input in TTD function in analyzer is an estimated incident angle  $\tan(\alpha_u) \cong \frac{|u_0 - u_N|}{v(t_0 + t_N)}$  [42], which takes the absolute value of the coordinate difference over the estimated sum of the drift distance of the 1<sup>st</sup> and last hit wire in the cluster. It will be a further improvement to implement an iterative routine to use fit track incident angles as arguments for the TTD function.
- 2) At fixed incident angle TTD function is a monotonic increasing function of drift time.
- 3) To a good approximation, the TTD function goes through the origin. In the real data acquisition process, there is some fluctuation due to the length of the sense wire. The longest wires have length  $\frac{21''}{\sin 26.45^\circ} \cong 4 \text{ feet}$  and we observed a fluctuation in drift time data on the order of 4 ns with same drift distance during testing. Here 21'' is the short axis length and 26.45° is the angle between wire and long axis for active area of a wire plane.
- 4) As shown in Fig 4.2 below, the TTD function can be approximated by 3 pieces: (1) where the particle tracks close to sense wire, (2) where there is a constant drift velocity in uniform electric field region away from sense wire, and (3) where the particle track crosses the corners while entering or exiting the drift cell of a wire and the reconstructed drift distance is beyond height of drift cell or cathode plane. Thus, they are virtual distances. For cluster fitting purpose, the piece (3) is of less importance and we could already fit good tracks from converted drift distances within regions (1) and (2). In addition, any drift time corresponding to piece (3) or a virtual distance will be discarded since the TTD function formula in the analyzer (4.1) did not describe piece (3).

### 4.2.2 TTD function in analyzer

Based on 3) 4) above the analyzer uses two straight line segments to represent time to distance function:

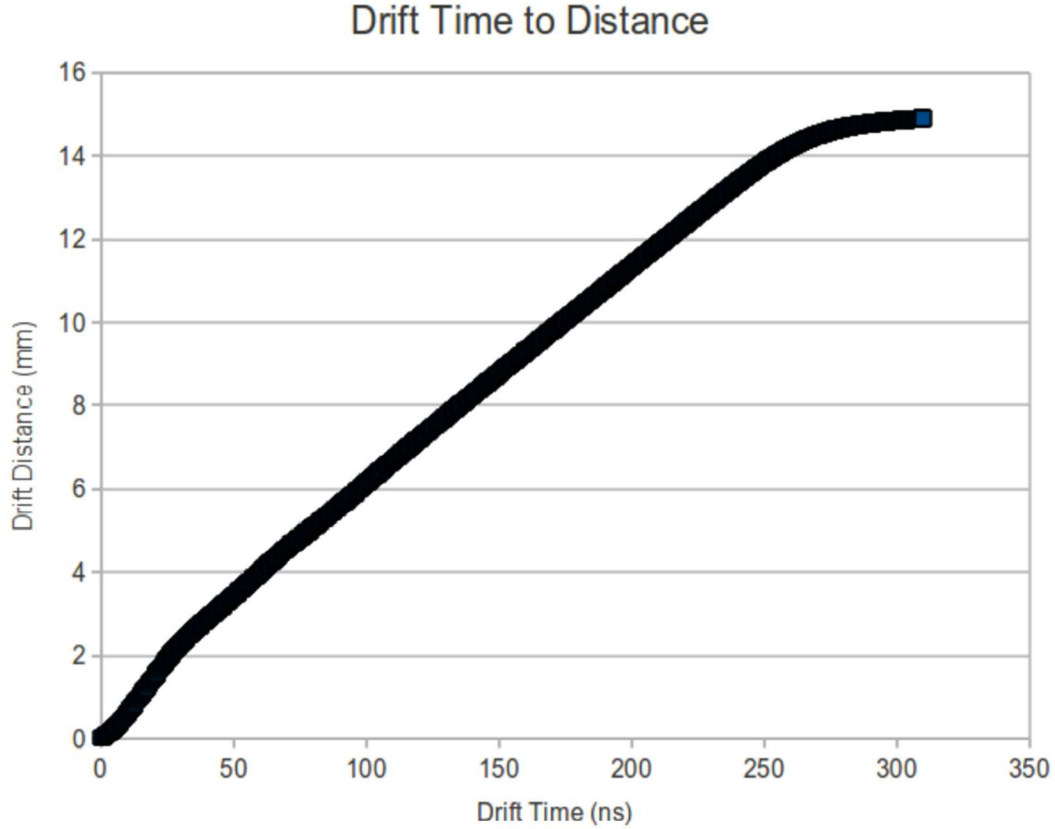
$$\begin{aligned} d(t; \theta) &= v \cdot t \cdot \left(1 + \frac{a_2(\theta)}{a_1}\right), & v \cdot t \leq a_1 \\ d(t; \theta) &= v \cdot t + a_2(\theta). & v \cdot t > a_1 \end{aligned} \quad (4.1)$$

Here  $\theta$  represents either  $\alpha_u$  or  $\alpha_v$  based on the wire plane. And, for the angular dependence, the default choice is a 2<sup>nd</sup> order polynomial of  $\tan(\theta)$  for  $a_2$ :

$$a_1 = A_{10}$$

$$a_2 = A_{22}\tan^2(\alpha_{u/v}) + A_{21}\tan(\alpha_{u/v}) + A_{20} \quad (4.2)$$

However, the wire chamber database file supports parameter  $A_1, A_2$  from 0<sup>th</sup> to the 3<sup>rd</sup> order of polynomial [43]. In addition, the drift velocity  $v$  is also a parameter, representing the constant velocity in piece (2) of the TTD function.



III Fig 4. 2 Time to distance conversion function. Ordinate: drift distance in unit  $mm$ , abscissa: drift time in unit  $ns$ .

(Fig. 4.20 from [29]) This function is mapped by assuming uniform distance distribution and relates the time distribution by conservation of probability. That is for each drift time in each event, by applying this TTD function, the resulting drift distance distribution will be uniform.

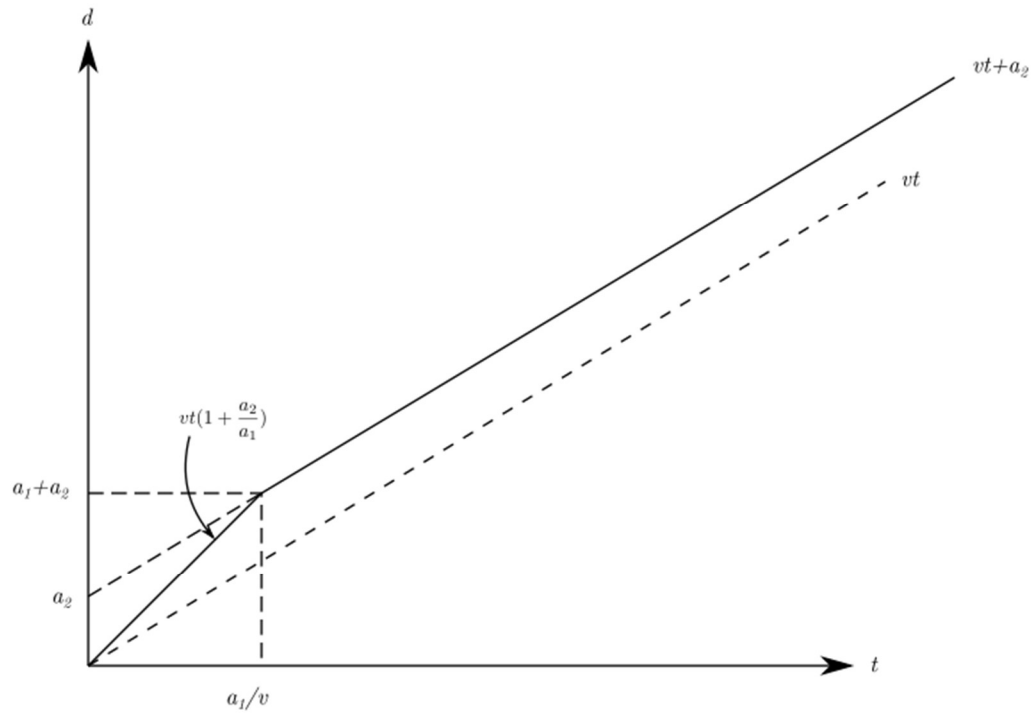
#### 4.2.4 Meaning of analyzer TTD function parameters

As illustrated in Fig 4.3. below the meaning of TTD function parameters is:

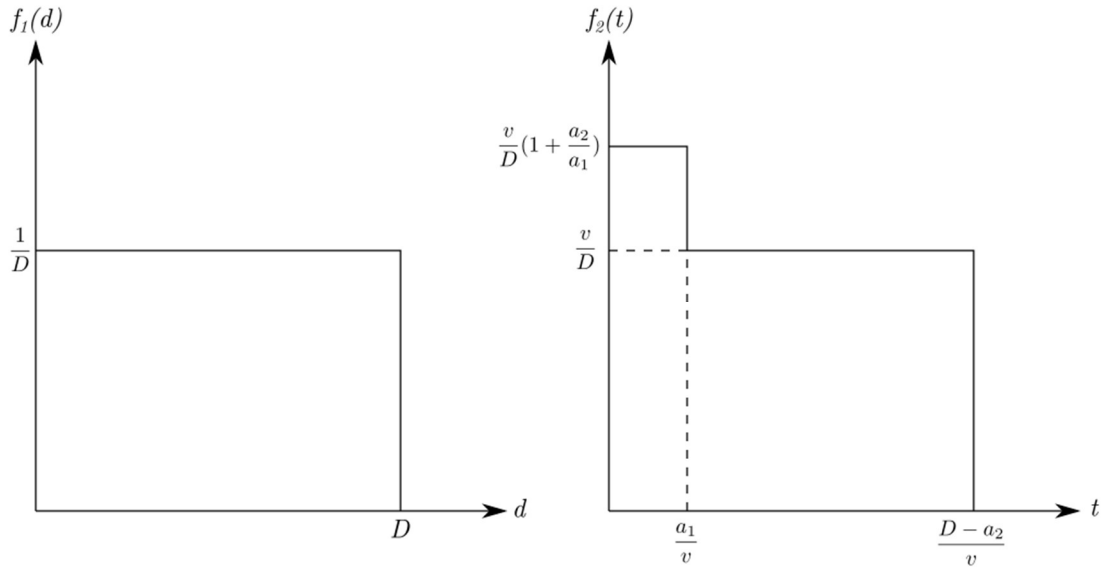
1.  $v$  (constant) drift speed of ionized electrons in the region of a drift cell where there is sufficient distance to the sense wire that the electric field is nearly uniform. We assume  $v$  is only depend on the HV applied to the cathode plane of the wire chambers, and independent of incident angle.
2.  $a_1/v$  ( $a_1 + a_2$ ) is the drift time (distance) at the intersection of the straight-line segment representing the region in drift cell with lower drift speed and higher drift speed. In

addition,  $1 + \frac{a_2(\theta)}{a_1}$  is the ratio between the higher and the lower drift speeds.  $a_2$  is also the intercept of piece (2) of the TTD function and the distance axis, which means the additional drift distance added due to the higher drift speed in the region.

In short, the analyzer TTD function uses two straight line segments to represent the (curved) calibrated TTD function in Fig 4.2.



III Fig 4. 3 Graph of function  $d(t)$ .



III Fig 4. 4 Ideal  $d$  and  $t$  distribution.

Assume the drift distance uniformly distributed from 0 to a upper limit  $D$  (half wire plane thickness), thus the probability density function of distance is:

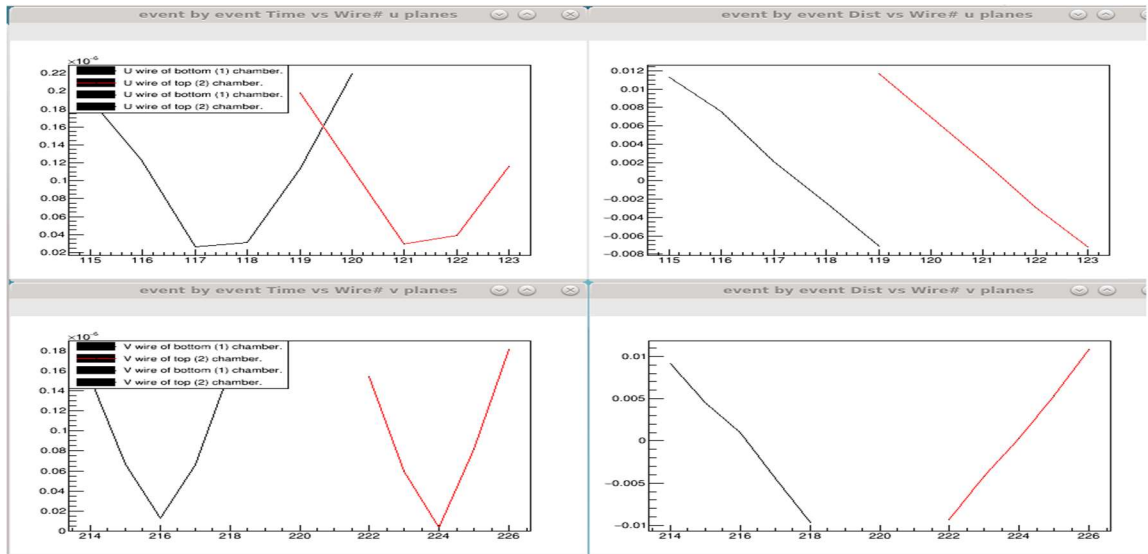
$$f_1(d) = \frac{1}{D}, 0 \leq d \leq D; f_1(d) = 0 \text{ elsewhere} \quad (4.3)$$

By coordinate transformation using the relation (4.1) and equating the probabilities by integrating  $f_1(d)$  we find corresponding time distribution:

$$\begin{aligned} f_2(t) &= \frac{v}{D} \left( 1 + \frac{a_2(\theta)}{a_1} \right), 0 \leq t \leq \frac{a_1}{v}; 0 \text{ elsewhere} \\ f_2(t) &= \frac{v}{D}, \frac{a_1}{v} \leq t \leq \frac{D-a_2}{v}; f_2(t) = 0 \text{ elsewhere} \end{aligned} \quad (4.4)$$

#### 4.2.5 Analyzer TTD function applied to single cluster

Figure 4.5 shows an example of applying the analyzer TTD function formula (4.1) to a set of UV associated clusters in an event from a test run. On the left side are the wire index and drift time ( $n_i, t_i$ ) for  $u_1$  cluster (black line, upper left graph),  $u_2$  cluster (red line, upper left graph),  $v_1$  cluster (black line, lower left graph),  $v_2$  cluster (red line, lower left graph). The corresponding converted wire index and drift distance (signed) ( $n_i, d_i$ ) graph are shown on the right plots. Here the up-down ambiguity is not resolved, thus the lower right lines are parallel only when all signs of distances  $d_i$  for one of the lines are reversed.



III Fig 4. 5  $U-U$  and  $V-V$  matched clusters. Left figure ordinate: drift time in unit  $\mu s$ , abscissa: wire number, no unit. Right figure ordinate: drift distance in unit  $m$ , abscissa: wire number, no unit.

Left:  $(n_i, t_i)$  graph. Right:  $(n_i, d_i)$  graph.



## 4.3 Preliminary TTD function calibration and results

### 4.3.1 Introduction

The default TTD function parameter values  $A_{1i}$  and  $A_{2i}$ , for  $i = 0 - 3$  in the analyzer have to be recalibrated because of the difference between wire chambers, HV applied, composition of the inert gas, etc. The approximated value for  $a_1$  can be estimated by noticing  $a_1/v$  is the width of time distribution peak in Fig. 4.4. Based on the default values in the analyzer  $a_1 = A_{10}$  is fixed, and we started with this in initial calibrations. For  $a_2 = A_{22}\tan^2(\alpha_{u/v}) + A_{21}\tan(\alpha_{u/v}) + A_{20}$ , we are not changing the relative ratio between  $A_{20}$ ,  $A_{21}$ , and  $A_{22}$ , but are adding a new parameter scale  $C$  to the new  $a_2$  value:

$$a_2 = C(A_{22}\tan^2\alpha_{u/v} + A_{21}\tan\alpha_{u/v} + A_{20}) \quad (4.5)$$

As seen in Fig 4.3, calibration essentially using  $a_2$  alone only changes the slope (drift velocity) of the first segment of the TTD function. In addition, parameter  $v$  can be determined by using (4.1) and setting the drift distance  $d$  and drift time  $t$  at the point where the ionization happened at cathode plane. In Leckey's test, according to Fig 4.1, the drift time from ionized electrons at cathode plane  $d = 1.27\text{cm}$  should be about  $t = 250\text{ns}$  based on the plot, where the uniform drift time plateau starts to drop. If  $a_2$  is ignored in (4.1), then  $v \cong \frac{d}{t} = 50800(\text{m/s})$ . During our tests, the HV and inert gas compound were different and, therefore,  $v$  is different, about  $60000(\text{m/s})$ . Thus, the only parameter left to be determined is the scale factor  $C$ . In this section, based on the physical meaning of TTD function, we are minimizing certain statistical errors of the resulting drift distance distribution by using an iterative method. With each change of  $C$  or any TTD parameters in the database file, the analyzer should replay the test run events again, which would lead to long computation time and large consumption of disk space. Thus, determining the number of divisions in each iteration is crucial to reduce the total number of iterations needed to reach our final result. This will be discussed in appendix A 4.3.1. In the following sub-sections 4.3.2 and 4.3.3 of this section we devise two different determinations of statistical errors and determine value of  $C$ , respectively. Sub-section 4.3.4 will give an explanation for the shape of resulting drift distance distribution due to the constraints imposed by a certain trigger condition.

### 4.3.2 Minimize local and global track direction angles difference squared.

There are two sets of track direction angles:

- 1) One is from fitting of local clusters, which fit straight lines  $(u_i, d_i)$  or  $(v_i, d_i)$  which include TTD converted drift distances  $d_i$  in form

$$d = A + Bu \quad (4.6)$$

The slope  $B$  is related to incident angle  $\alpha_u$ :

$$B = 1/\tan\alpha_u \quad (4.7)$$

Exchange  $u$  and  $v$  for the results in  $v$  wire planes. A pair of local fit incident angles  $\alpha_u$  and  $\alpha_v$  in one wire chamber can be converted to track direction angles  $\theta, \varphi$  by relation (slightly modified formula (5) and (6) in appendix A 1.4):

$$\tan\theta = \frac{1}{2\cos\alpha} (\tan\alpha_u + \tan\alpha_v) \quad (4.8)$$

$$\tan\varphi = \frac{1}{2\sin\alpha} (\tan\alpha_u - \tan\alpha_v) \quad (4.9)$$

- 2) On the other hand, the track direction by  $\alpha_u$  and  $\alpha_v$  can be solved by crossover point coordinates  $(u_1, v_1)$  and  $(u_2, v_2)$  directly (Eq. (20) (21) from [38]):

$$\tan\alpha_u = \frac{u_2 - u_1}{d_u} \quad (4.10)$$

$$\tan\alpha_v = \frac{v_2 - v_1}{d_v} \quad (4.11)$$

Here  $u_2, v_2$  are crossover point coordinates on the top wire chamber, while  $u_1, v_1$  for bottom wire chamber in analyzer coordinate system, which origin is center of the lowest ( $u_1$ ) wire plane.  $d_u$  and  $d_v$  are distances (separation in the  $z$  coordinate in the analyzer coordinate system) between two  $u$  wire planes or two  $v$  wires planes respectively; for our Q-weak chamber  $d_u = d_v = 15.5'' = 39.37(\text{cm})$ . Then use the same formula (4.8) (4.9) to get  $\theta, \varphi$ .

We compare track direction  $\vec{d} = (\tan\theta, \tan\varphi, 1)$  calculated from method 1), which utilized TTD function to get  $d_i$ s as data for fitting, and method 2) which can be regarded as the true value since there are very small errors from (4.8) and (4.9) for each fitted track from analyzer, by scalar product of vectors:

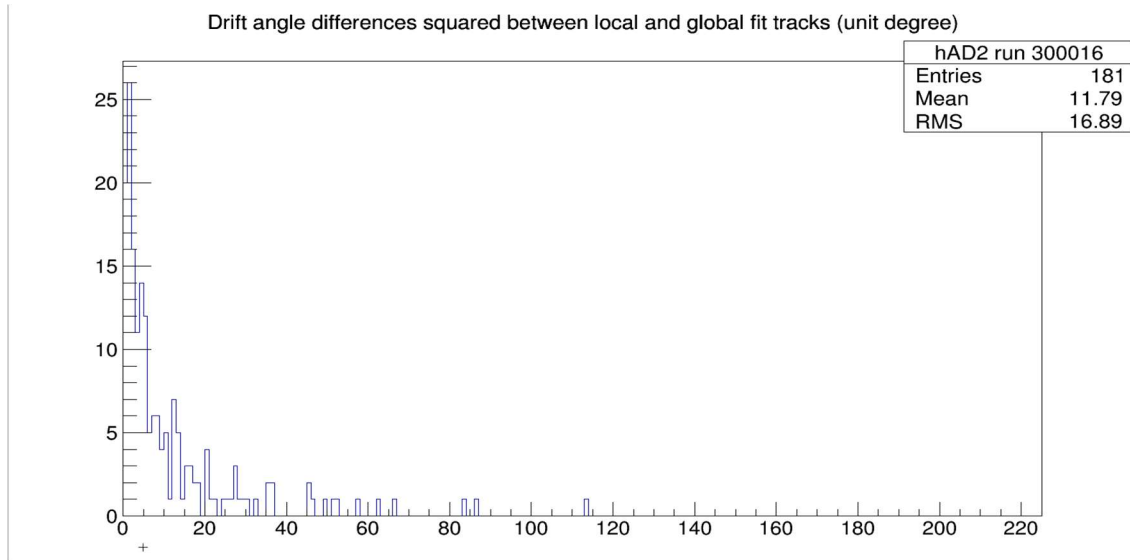
$$\cos(\frac{\vec{d}_l \cdot \vec{d}_g}{|\vec{d}_l| |\vec{d}_g|}) \quad (4.12)$$

Here  $\vec{d}_l$  and  $\vec{d}_g$  represents local and global fit track direction angles. Our criterion to calibrate  $C$  in (4.5) is to minimize sum of all track direction angular differences squared from all events in the test run data. This will indicate that local fit tracks  $d = A + Bu$  are close to the real track, and thus drift distances  $d_i$  in  $(u_i, d_i)$  or  $(v_i, d_i)$  have been converted correctly.

The result of minimizing the average of squares of angular differences in (4.12) is

$$f(C) = \frac{1}{N} \sum_{\text{all\_tracks}} [\cos(\frac{\vec{d}_l \cdot \vec{d}_g}{|\vec{d}_l| |\vec{d}_g|})]^2 \quad (4.13)$$

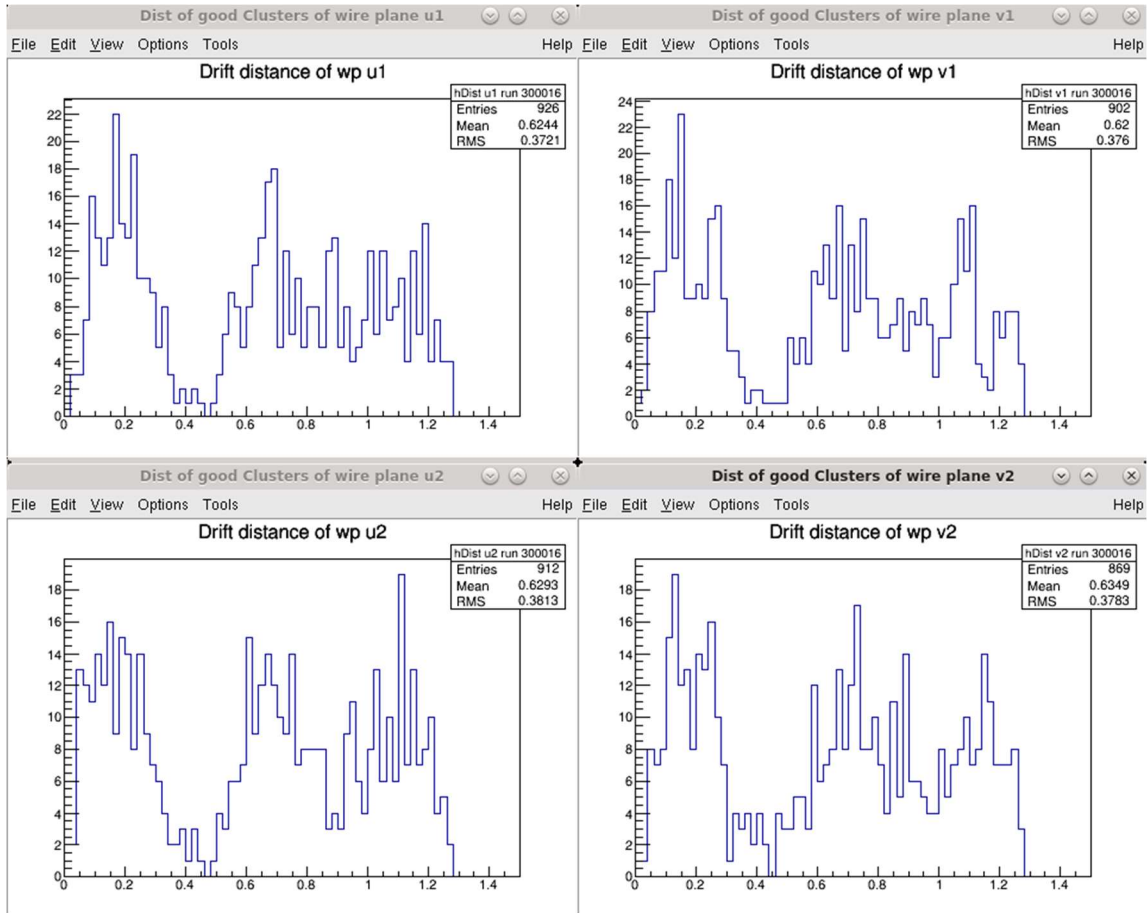
For each trial, we set a value  $C$  to change TTD parameter  $a_2 = C(A_{22} \tan^2(\alpha_{u/v}) + A_{21} \tan(\alpha_{u/v}) + A_{20})$ . After the analyzer found all tracks, it computed the statistics quantity in (4.13) for selected events (the reason of manual selection of events or tracks in sum (4.13) will be explained in the next chapter 5). Following the algorithm in Appendix A 4.3.1. we expect to find value of  $C$  converging to within a specified accuracy. Fig. 4.6 shows a histogram of a distribution of difference of angle squared  $[\cos(\frac{\vec{d}_l \cdot \vec{d}_g}{|\vec{d}_l| |\vec{d}_g|})]^2$  for selected events:



III Fig 4. 6 Distribution of angle difference squared between cluster fit and track fit squared. Ordinate: counts, no unit, abscissa: angle difference squared in unit degree squared.

From a trial run of the minimization algorithm (ordinate units degree squared). From the replay of test run data using  $C$  with the smallest value of (4.13).

This calibration of  $C$  is invalid when the assumption that the function  $f(C)$  in (4.13) with  $C$  as parameter has one minimum is incorrect. During the minimum searching on the last iteration, the value of  $f(C)$  at 9 end points of 8 divisions (see Appendix A 4.3.1 for reason that 8 division was chosen) are 12.34, 12.11, 11.98, 11.92, 11.94, 11.86, 11.79, 12.02, 12.13 with units of degree squared, gave local minima: 11.92 and 11.79. During further investigation the cause was found. The reason is that for small changes of  $C$ , for certain events the matched clusters used for track fitting changed. The reason of the use of different clusters could be that the previous clusters didn't satisfy a particular cut during the cluster finding or that a particular hit wire was removed from original cluster due to its being out of range, etc. These can result in a huge difference in angle for the individual event, which makes its impact even greater when squared. Those isolated events cause the jump in  $f(C)$  value and a discontinuity. To make matters worse, during the last division of interval for minimum searching, events with changes in clusters that contribute the most to  $f(C)$  in (4.13) are random and display almost no discernable pattern. Thus, in addition to changing  $C$ , eliminating these events that cause a jump in  $f(C)$  are too time consuming and leads to a small subset of events could be used in the summation in (4.13). Thus, using this criterion is quite impractical. The converted distance distribution for each wire plane from these selected events is shown in Fig. 4.7.



III Fig 4. 7 Converted distance distribution after finding  $C$  which minimize  $f(C)$ . Ordinate: counts, no unit, abscissa: drift distance in  $cm$ .

It's easy to see that the distance distribution is quite uniformly distributed, but having gaps with low counts in certain distance region, the cause will be explained in section 4.3.4.

### 4.3.3 Modified cluster fit

#### Motivation

Comparing the TTD function by integration in drift time distribution (section 4.4) in Fig 4.2 and Fig 4.3 which approximated by two straight line segments. Since the near 0 drift time or drift distance near sense wire is highly non-linear, 1<sup>st</sup> part of analyzer TTD function (4.1) will never accurately describe this region. On contrary the TTD in region away from wires are well behaved. If we assume that in these regions the electric field is uniform, then the drift velocity is constant, thus drift time and distance distribution are uniform.

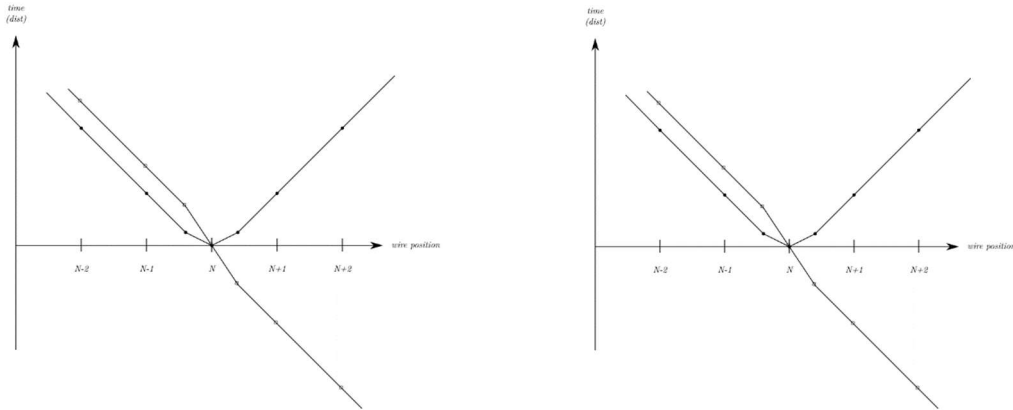
#### Analyzing the cluster $(n_i, d_i)$ graph shape

For cluster fitting, the hit data we use  $(u_i, d_i)$  or  $(v_i, d_i)$  are highly accurate in region away from sense wire because of the well-behaved TTD relation in this region. While the case is not so

good for hit data point near sense wire from the highly non-linear electric field, which for most clusters it correspond to the pivot wire.

Since we essentially only change TTD parameter  $a_2$  in TTD function (4.1) in this section while keeping all other TTD parameter fixed. Let's check the effect when  $a_2$  is too small or too large. Referring to Fig 4.8 below, it draws the  $(n_i, t_i)$  and  $(n_i, d_i)$  converted from TTD function (4.1) graphs in the same canvas. Since  $a_2$  is always positive (near wire drift velocity is always higher than the away from wire region), Fig 4.8 illustrate two cases:  $a_2 = 0$  and  $a_2$  is large.

When  $a_2 = 0$  the drift velocity is constant in the entire region from (4.1) and absolute drift distance  $|d|$  is proportional to drift time  $t$ . Thus, if we have the  $(n_i, t_i)$  of a cluster, the converted  $(n_i, d_i)$  graph is coincided with  $(n_i, t_i)$  on one side of pivot wire and for the other side is the reflection of  $(n_i, t_i)$  over  $t = 0$  line, when scale is chosen as the constant drift velocity  $v$ . Since the higher drift velocity near sense wire, the drift time distribution near sense wire has a peak (c.f. Fig 4.1),  $(n_i, t_i)$  relation shrunk near  $t = 0$  and so does the converted  $(n_i, d_i)$ . As a result, the entire  $(n_i, d_i)$  graph is a bent straight line with near  $t = 0$  region having less slope (Left plot Fig 4.8). When  $a_2$  is too large, compare to  $a_2 = 0$  case, the only change is the slope becomes large in the near  $t = 0$  region, which results in again a bent straight line (Right plot Fig 4.8).



III Fig 4. 8 Effect of different  $a_2$  values in TTD.

For left illustration  $a_2 = 0$ , for right illustration  $a_2$  is too large. For both plots, blue lines represent  $(n_i, t_i)$  graph of the cluster, while black line in left illustration represents fit line of  $(n_i, d_i)$  relation, and black line in right illustration represents  $(n_i, d_i)$  data of the cluster after TTD conversion.

If  $a_2$  is chosen that its value is between two extreme cases in Fig 4.8 and making TTD conversion totally accurate, then the bent straight line becomes a straight line. However, because the TTD relation represented by formula (4.1) is linear instead of non-linear shown in Fig 4.1 in drift time distribution, the TTD conversion by (4.1) will never making those bent straight line to straight line in all different cases.

As a results, we accept this effect that for all converted  $(n_i, d_i)$  graphs are more or less deviate from a perfect straight line due to inaccuracy near  $t = 0$  region. We change the fit accordingly to fit two line segments, one on the same side as pivot wire while the other on the opposite side, with a shift  $\Delta y$  as an additional parameter. Hoping the combined two lines segment to be as straight as possible. We use the slope  $B$  from this fit to compute track incident angles  $\alpha_u$  and  $\alpha_v$  as local cluster fit result to compute track direction angles  $\theta, \varphi$ , and compare it to global fit track directions.

## Derivation of slope $B$ in modified cluster fit

First, we relabel our independent variables  $(n_i, d_i)$  or  $(u_i, d_i)$  or  $(v_i, d_i)$  to  $(x_i, y_i)$ . Once we disambiguate the side of pivot wire,  $x_i$ 's are grouped as above, with indices  $(x_1, y_1), (x_2, y_2), \dots, (x_n, y_n)$  having one sign, and  $(x_{n+1}, y_{n+1}), (x_{n+2}, y_{n+2}), \dots, (x_{n+m}, y_{n+m})$  having the opposite sign. Also, we assume all that all  $x_i$ 's have negligible  $\sigma_x$ 's compared to  $\sigma_y$ 's, and all drift distances  $y_i$ 's have the same  $\sigma_y$  value. From the principle of maximum likelihood, the fit will be to minimize:

$$\sum_1^n (y_i - A - Bx_i)^2 + \sum_{n+1}^{n+m} (y_i + \Delta y - A - Bx_i)^2 \quad (4.14)$$

where  $A$ ,  $B$ , and  $\Delta y$  are to be fitted.  $\sum_1^n$  will be abbreviated by  $\sum_{(1)}$  and  $\sum_{n+1}^{n+m}$  will be abbreviated by  $\sum_{(2)}$  during the derivation. Taking partial derivatives of  $A$ ,  $B$ , and  $\Delta y$  in equation (4.14), gives three equations respectively:

$$\sum_{(1)+(2)} y = \sum_{(1)+(2)} A + \sum_{(1)+(2)} Bx + \sum_{(2)} \Delta y \quad (4.15)$$

$$\sum_{(1)+(2)} xy = \sum_{(1)+(2)} Ax + \sum_{(1)+(2)} Bx^2 + \sum_{(2)} x\Delta y \quad (4.16)$$

$$\sum_{(2)} \Delta y = \sum_{(1)+(2)} A + \sum_{(1)+(2)} Bx - \sum_{(1)+(2)} y \quad (4.17)$$

where in equations  $x, y$  without suffices should not cause confusion. The solution for  $B$  of these simultaneous linear equations (4.15) to (4.17) with unknown variables  $A$ ,  $B$ , and  $\Delta y$  is

$$B = \frac{\left[ \sum_{(1)+(2)} xy - \frac{\sum_{(1)} x \sum_{(1)} y}{\sum_{(1)} 1} - \frac{\sum_{(2)} x \sum_{(2)} y}{\sum_{(2)} 1} \right]}{\left[ \sum_{(1)+(2)} x^2 - \frac{(\sum_{(1)} x)^2}{\sum_{(1)} 1} - \frac{(\sum_{(2)} x)^2}{\sum_{(2)} 1} \right]} \quad (4.18)$$

where  $\sum_{(1)} 1$  and  $\sum_{(2)} 1$  can be abbreviated as  $N_1$  and  $N_2$ . For reference, compare the slope result of standard linear fit:

$$B = \frac{N \sum xy - \sum x \sum y}{N \sum x^2 - (\sum x)^2} \quad (4.19)$$

When all terms with sums  $\sum_{(1)}$  or  $\sum_{(2)}$  are totally omitted in (4.18), it will reduce to the same form as (4.19).

## Some properties of the slope $B$ formula

1) From the symmetries in equation (4.19), it can be seen that if all  $y_i$ 's in formula (4.19) are added by the same  $\Delta$ , the resulting  $B$  will be unchanged, while the intersection  $A$  will shift by  $\Delta$ . In addition, equation (4.18) will have more symmetry:

- (1) Result of  $B$  is symmetric under exchange of  $\sum_{(1)}$  and  $\sum_{(2)}$ .
- (2) Rewriting  $\sum_1^n (y_i - A - Bx_i)^2 + \sum_{n+1}^{n+m} (y_i + \Delta y - A - Bx_i)^2$  as  $\sum_1^n (y_i + \Delta y_1 - A - Bx_i)^2 + \sum_{n+1}^{n+m} (y_i + \Delta y_2 - A - Bx_i)^2$ , while keeping  $\Delta y = \Delta y_1 - \Delta y_2$  constant, results in  $B$  being unchanged.

2) An improved result of intersection  $A$  on the  $y$ -axis of the fit can be found by setting  $\Delta y_1 = -\Delta y_2$ . Then, the estimated intersection on the  $x$ -axis ( $-\frac{A}{B}$ ) (crossover point of track and wire plane) can be computed accordingly.

As for the result of using the new fit (4.18), it's not much of the improvement over the standard straight line fit (4.19) when minimizing the squared angle difference (4.13). The reason could be that we did not remove the pivot wire data point which is non-linear. However, removing the pivot wire could lead to a lack of data points for the fit, especially for clusters with low number of wires, e.g., 3 or 4.

#### 4.3.4 Making all fit track as straight as possible

The goal of cluster fitting is to fit TTD converted  $(n_i, d_i)$  data of each found cluster as a straight line. Thus, the premise of the cluster fitting is that the  $(n_i, d_i)$  data indeed represent a straight line. As we already saw in Fig. 4.8, the  $(n_i, d_i)$  graph lines are more or less bent near the  $t = 0$  region. Following the same idea of (4.13), we want to formulate a function of  $C$  to quantify the linear relation of  $(n_i, d_i)$  data, then minimize it to optimize value of  $C$ . The coefficient of linear correlation is used to quantify the linear relation:

$$r = \frac{\sum(x_i - \bar{x})(y_i - \bar{y})}{\sqrt{\sum(x_i - \bar{x})^2 \sum(y_i - \bar{y})^2}} \quad (4.20)$$

Here  $(x_i, y_i)$  represent independent and dependent variables. We know that when  $|r|$  is close to 1 the  $x, y$  relationship is more linear. Defining the probability  $P(r_0; N) = P(|r| > r_0; N)$  to be that when considering  $N$  data points, the probability of  $|r| > r_0$ . As we can see here the probability is also dependent on the number of data points; the larger the  $N$  the less the  $r_0$  needed for same value of  $P(r_0; N)$ . When  $N$  is fixed, the larger the  $r_0$ , the less probable of  $P(r_0; N)$  and the data  $(x_i, y_i)$  relation is more probable to be linear. [44] Then, our criterion to optimize  $C$  is to minimize the average probability of  $P(r_0; N)$  squared:

$$f(C) = \frac{1}{N} \sum_{all\_tracks} P(r_0; N)^2 \quad (4.21)$$

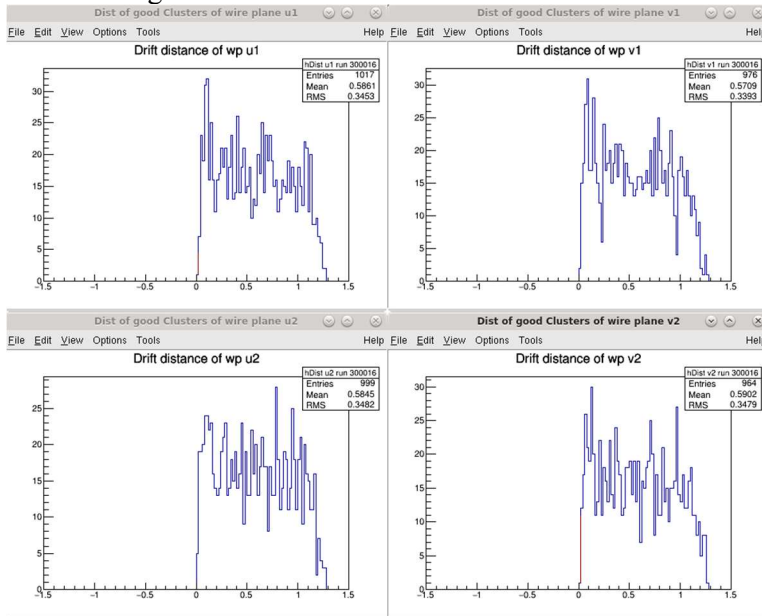
Since most of the events in the cosmic ray test run are showers, the sum of all tracks here are tracks manually picked from selected events to ensure a good single track. In addition,  $P(r_0; N)$  requires numerical integration so we utilized a table of  $P(r_0; N)$  values with a spline interpolation from a built-in ROOT function. Then we minimized (4.21) to optimize  $C$  through the iterative method explained in Appendix A 4.3.1.

The criterion for minimizing (4.21) is a lot better behaved and we get a single minimum without indication of discontinuity in  $f(C)$  compared to minimizing the squared angular difference. We use the same manually picked events as in section 4.3.2. and add two additional cuts:

- (1) Only hits with the best matched slopes in the  $UU$  and  $VV$  clusters of these events are included in the histogram.

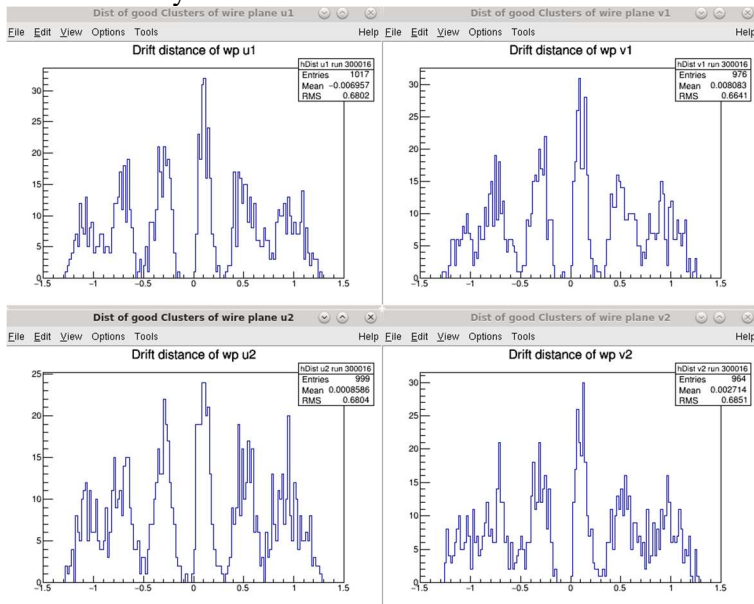
- (2) Events for which the TTD converted distance is larger than half wire plane thickness (0.5 inches) were omitted.

The resulting drift distance distribution is shown below:



III Fig 4. 9 Drift distance distribution of each wire plane. Ordinate: counts, no unit, abscissa: drift distance in *cm*.

From manually selected clusters with cuts described above.



III Fig 4. 10 Signed drift distance distribution. Ordinate: counts, no unit, abscissa: drift distance in *cm*.

It's derived from the same clusters as in Fig 4.9. That is flip sign of (absolute valued) drift distances if the hits are on the other side of the pivot wire.



### 4.3.5 Converted drift distance distribution and explanation

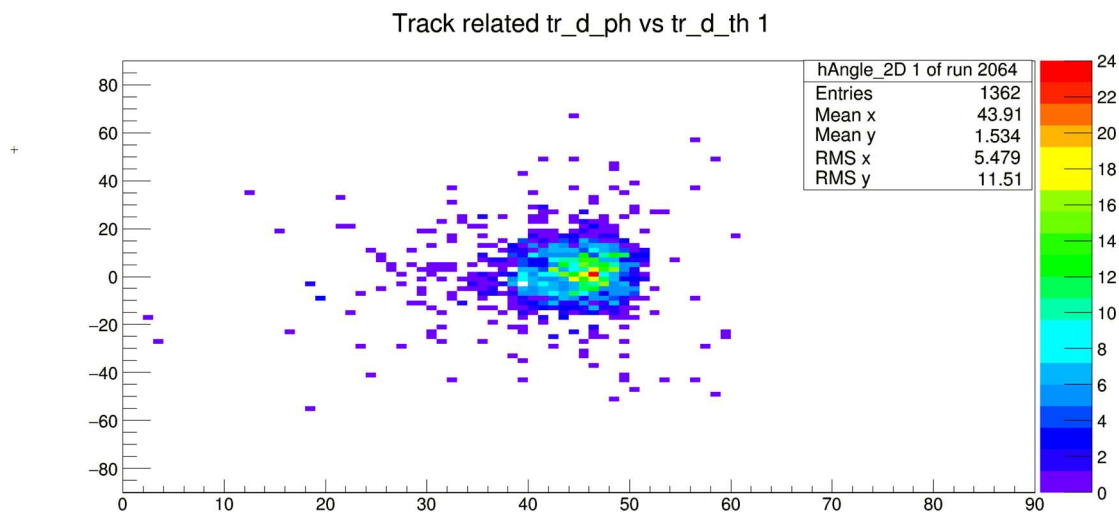
#### 1) The motivation of the discussion

As we seen from the distance distribution histograms Fig 4.7 and Fig 4.10. The distance distribution has multiple peaks, which leads to a question on one intuitively obviously correct statement: drift distance distribution is uniform. In this section we are trying to answer the question: What causes the peaks in distance distribution?

#### 2) Geometry of the trigger

**Trigger paddles placement:** The scintillator trigger used to test the wire chambers was not fully explained. We placed the scintillator paddles with widths of about 11 cm parallel to  $x$  or  $y$  axes above the top and bottom wire chambers. Above each wire chamber, at least a pair of paddles were placed perpendicular to each other forming an 11 cm by 11 cm square area defining the area through which particles can pass and generate tracks. They're placed above and on the center line (parallel to the long axis, or  $y$  axis) of the wire chamber. While along the long axis, the square areas formed by trigger paddles have the same  $x$  coordinate. The tracks are allowed only if they pass through the square areas above both wire chambers.

**Track direction angles:** Based on how the paddles are placed, the track direction angles  $\theta, \varphi$  to represent track direction as  $(\tan\theta, \tan\varphi, 1) = \left(\frac{\Delta x}{\Delta z}, \frac{\Delta y}{\Delta z}, \frac{\Delta z}{\Delta z}\right)$  through the centers of square areas are estimated to be  $\theta \sim > 45^\circ$  and  $\varphi \sim 0^\circ$ . By placing cuts such that only 4 paddles from 2 squares are hit, the  $(\theta, \varphi)$  distribution is shown below. It can be seen that the direction of tracks satisfying the trigger cut is quite well constrained. We hope to explain the cause of peaks in drift distance distributions under both direction and area constraint of the cut on the trigger.

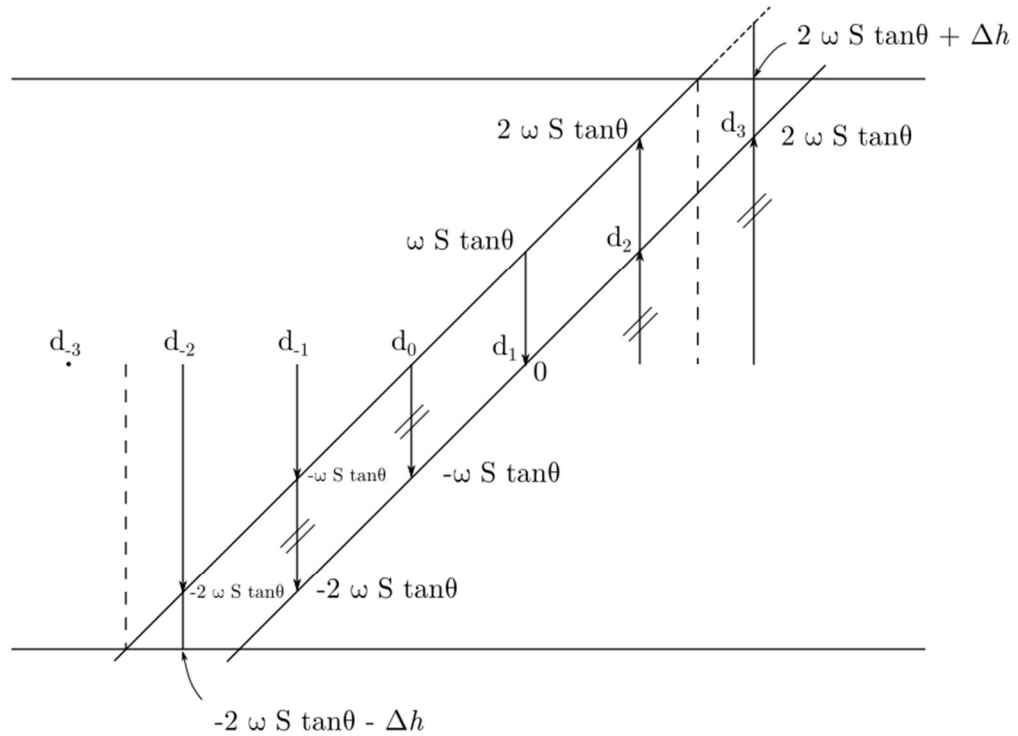


III Fig 4. 11 Analyzer fitted track  $(\theta, \varphi)$  distribution. Ordinate: track projection angle in  $x$  direction (short axis of chamber)  $\theta$  in unit degree, abscissa: track projection angle in  $y$  direction (short axis of chamber)  $\varphi$  in unit degree.

$(\theta, \varphi)$   $\theta$  as abscissa,  $\varphi$  as ordinate distribution with cut on trigger described above.

3) Conditions for uniform distance distribution.

Here we consider the condition which makes distance distribution uniform. Consider the following situation: assume incident angles  $\alpha_u$  or  $\alpha_v$  of the track be fixed; that is, in the  $u-z$  or  $v-z$  projection we consider the set of parallel tracks. Then, if the crossover point coordinate of the tracks are uniformly distributed, covering through integer number of wire periods (abbr. as translation symmetry) the drift distance distribution will be uniform, within half wire plane thickness range (0 to 1.27 cm). If we consider the signed drift distance distribution, it will be uniformly distributed from -1.27cm to 1.27cm instead. The reason is illustrated in Fig. 4.12:



III Fig 4. 12 Signed drift distance of parallel tracks with 5-wire cluster.

With crossover point uniformly distributed from wire 0 to wire 1. Notation:  $d_i$ ,  $i = -3, -2, 1, 0, 1, 2, 3$  are drift distances of the  $i^{\text{th}}$  wire;  $ws$  is the wire spacing;  $\theta = 90^\circ - \alpha_{u/v}$ ;  $\Delta h = \frac{h}{2} - 2ws \cdot \tan\theta$ , where  $h = 2.54\text{cm}$  is the wire plane thickness.

Let us consider drift distances between two parallel tracks. When the 2<sup>nd</sup> track has its crossover point shifted by  $\Delta u$  in the  $u$  coordinate, then the relation between the two sets of drift distances from the two parallel tracks will be  $+d'_i = d_i \Delta d = d_i + \Delta u \cdot \tan\theta$ . Thus, the change of drift distance is proportional to the change of crossover point  $u$  coordinate, and if  $u$  is distributed uniformly, so should  $d$ . However, there are more constraints in this case:

- (1) All drift distances  $d_i$  must be within the wire plane region:  $r - h/2 < d_i < h/2$ .
- (2) The drift distance distribution is filled with all wire hits having drift distances  $d_i$  from each cluster.
- (3) The translation symmetry, that is if a track translate along  $u$  by wire spacing  $ws$ , then the next wire in the original cluster will have the same drift distance as the current wire in the original cluster. This generates the same set of data point to be filled in the drift distance distribution.

As an example of the track and corresponding cluster with 6 wires, we translate the track uniformly along the  $u$  direction, with a crossover point from wire 0 translated to wire 1, as shown in Fig. 4.12. We denote

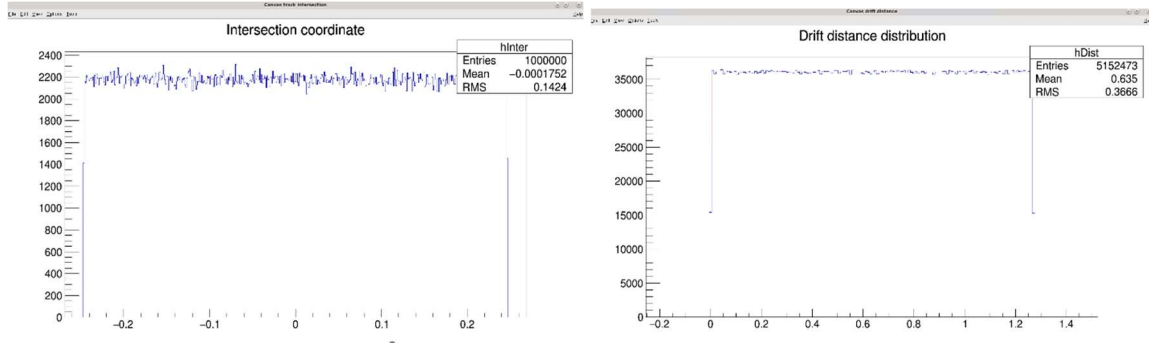
$$\Delta = ws \cdot \tan\theta \quad (4.22)$$

$$\frac{h}{2} = 2\Delta + \Delta h \quad (4.23)$$

Then drift distances of each wire in the clusters are:

$$\begin{cases} d_{-2} \in [-2\Delta - \Delta h, -2\Delta] \\ d_{-1} \in [-2\Delta, -\Delta] \\ d_0 \in [-\Delta, 0] \\ d_1 \in [0, \Delta] \\ d_2 \in [\Delta, 2\Delta] \\ d_3 \in [2\Delta, 2\Delta + \Delta h] \end{cases} \quad (4.24)$$

Based on the assumption (1) and noting the relation (4.23), the drift distances  $d_i$ ,  $i = -2, -1, 0, 1, 2, 3$  of all wires in the cluster are filling the drift distance  $d$  distribution from  $-h/2$  to  $h/2$  with no gap and no overlap. If we consider the absolute value of the drift distance  $|d_i|$  distribution, it can be seen that the distance distribution of  $d_{-2}$   $d_{-1}$   $d_0$  are exactly the negatives of  $d_1$   $d_2$   $d_3$ . Thus,  $|d|$  will be uniformly distributed from 0 to  $h/2$ . That illustrates the statement above Fig 4.12. A simple simulation is conducted and both crossover points coordinate and drift distance distributions are shown below.



III Fig 4. 13 Simulated crossover points  $u$  coordinate and drift distance distribution. Left figure ordinate: counts, no unit, abscissa: cross over point  $u$  coordinate in unit  $cm$ . Right figure ordinate: counts, no unit, abscissa: drift distance in unit  $cm$ .

Left, crossover point  $u$  coordinate distribution. Right, drift distance distribution. The geometry of the simulation was: wire spacing  $ws = 0.493$   $cm$ , track incident angle  $\alpha_u = 45^\circ$ , thus  $\Delta = ws =$

0.493 cm. Wire plane thickness  $h = 2.54\text{cm}$  and  $\Delta h = \frac{h}{2} - 2\Delta$ . Simulation setup: One million events generated with crossover point coordinates uniformly distributed in range  $[-\frac{ws}{2}, \frac{ws}{2}]$  and corresponding drift distance of wire 0 being  $d_0 \in [-\Delta/2, \Delta/2]$ ,  $d_1 = d_0 + \Delta \in [\Delta/2, 3\Delta/2]$  and so on. Results of the simulation: Take all distances from all wires in the cluster satisfying  $-h/2 < d_i < h/2$ , compute their absolute value then fill the drift distance histogram. The distribution is uniform in range  $[0, \frac{h}{2}] = [0, 1.27\text{cm}]$  in right Fig. As we can see from the number of entries of crossover point coordinates is 1,000,000, while drift distance distribution number of entries is 5,152,473. Note that the ratio of the number of entries to the number of trials is about  $5.1521 = \frac{h}{\Delta} = \frac{2.54\text{cm}}{0.493\text{cm}}$ .

#### 4) Explanation of peaks in distance distributions

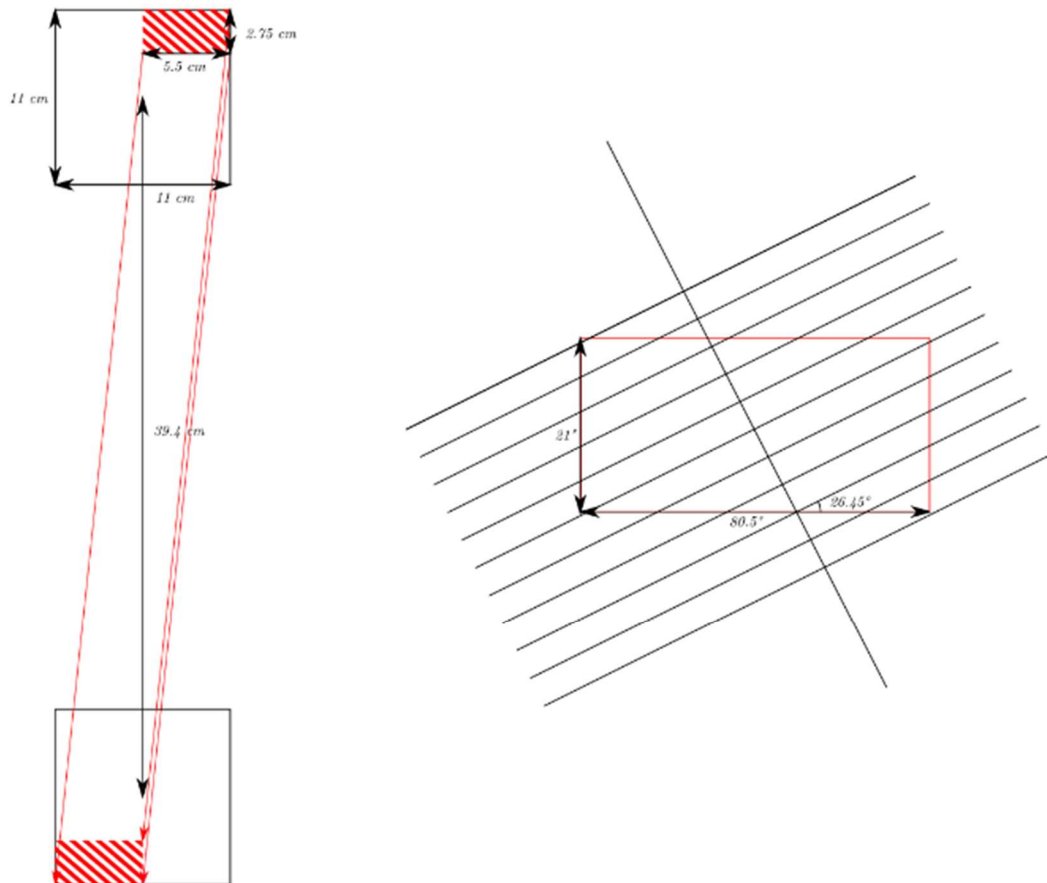
Following the discussion above, we will explain the peaks in distance distribution. First, we can partition all tracks passing the trigger cut when we analyze replayed ROOT files into small subsets, each containing particles with similar incident angle values, i.e., approximately parallel to each other. Then, if each subset satisfies the condition the “*crossover point coordinate of the tracks are uniformly distributed, covering an integer number of wire periods*” then “*the drift distance distribution will be uniform, within half wire plane thickness range*” as argued above. However, the translation symmetry of the tracks above is broken. From the geometric constraint of the trigger, for certain set of parallel tracks, their allowed sub-area inside the 11 cm-by-11 cm square of common area a pair of perpendicular trigger scintillator paddles could be far from translationally symmetric due to two factors illustrated in Fig. 4.14:

- 1) The parallel tracks for a certain direction can be seen as a set of parallel vectors pointed from the top square trigger to the bottom square trigger. Constrained by the boundaries of the squares, the allowed area for these sets of parallel tracks are rectangles (shaded red areas).
- 2) The locations of wires within the projection of the squares cannot be measured precisely and can be seen as somewhat random. Further analysis of the projection will be analyzed in the next chapter.

Combining with 1) and 2) we arrive at the following results:

- 1) The wires in the middle of the rectangle projection have longer lengths in the projection compared to the wires on the sides, and thus the distance distribution will have more events for these wires.
- 2) The translational symmetry is broken as wires on the sides have shorter lengths within the rectangle projection, since the probability of a track passing through these wires are no longer uniform for a period of wire spacing.

These breaks of translation symmetry will result in gaps and peaks for the set of parallel tracks. The result from a simple simulation demonstrating this is shown in Fig. 4.15. In addition, Fig. 4.15 also shows that the higher peak at the pivot wire could be a result of an error in the TDC time offset calibration.

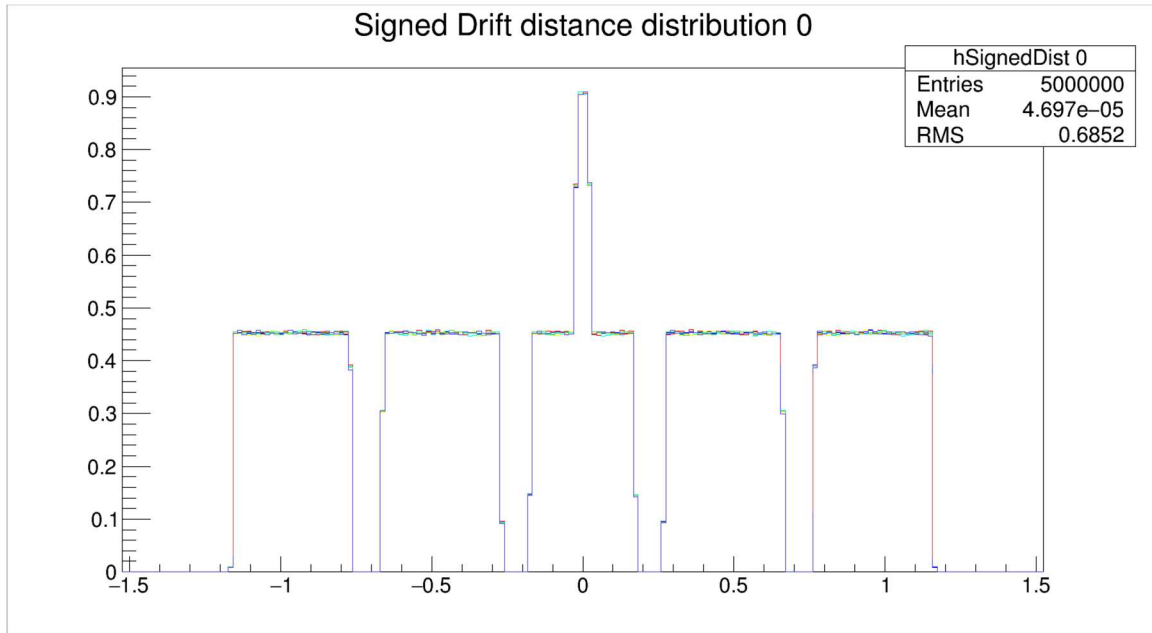


III Fig 4. 14 Geometry explanation of peaks in drift time distribution.

Left: allowed area (in red shade) for a set of parallel tracks within common trigger paddle area.  
 Right: projection of allowed area (enclosed by red rectangle) on  $u$  wire plane, with wires drawn.  
 For this set, the span in  $u$  coordinate is:

$$\begin{aligned} \Delta u &= (\Delta x, \Delta y) \cdot \hat{u} \cong (2.75\text{cm}, 5.5\text{cm}) \cdot \left( \frac{2}{\sqrt{5}}, \frac{1}{\sqrt{5}} \right) \\ &\cong 4.91\text{cm} \cong 9.97 \times 0.493\text{cm} = 9.97 \text{ wire spacings} \end{aligned}$$

Approximately 10 wires cross the rectangle. And, wires on the sides (upper left and lower right wires) have broken translation symmetry, with less length covered compared to middle wires.



III Fig 4. 15 Simulated signed drift distance distribution. Ordinate: counts, no unit, abscissa: signed drift distance in unit *cm*.

Compared to Fig 4.13, the crossover point coordinates are uniformly distributed in  $u$  for a 0.8 wire spacing, the rest of the region has 0 probability density. This break of translation symmetry within a wire spacing period of crossover points coordinates results in gaps and peaks in the distance distribution above.

Also, a shift of positively signed distances down by a small amount shifts negative signed events up a small amount to simulate the effect of error of the TDC time offset. This results in the higher peak in the center wire (pivot wire) distance distribution.

## 4.4 Integration of drift time distribution density function as time to distance function

### 4.4.1 Introduction

Now we change the procedure to determine TTD function based on the assumption that the converted distance distribution should be uniform. As we already saw in last section (4.3.5), this assumption is based on the translation symmetry of parallel tracks. If the trigger has a tight geometric constraint on track direction and small in area (dimension comparable to wire spacing), then the translation symmetry is broken for nearly parallel tracks. This results in peaks in the distance distribution, as seen in Fig. 4.7 and Fig. 4.10 as a result of previous TTD conversion. If we now consider all hit time data from a test run with enough statistics, considering the fact that each wire plane has 183 wires activated, then the translation symmetry for parallel tracks with reasonable angles should be approximately preserved. Thus, the uniformity of the drift distance distribution should be valid.

The TTD function can be derived from the drift time distribution through integration. The result is a TTD function curve, with discrete points  $(t_i, d_i)$  computed. Now we have two options:

- 1) Assuming the TTD function has certain functional form (e.g. the default TTD function (4.1)), we fit parameters of that function from data points  $(t_i, d_i)$ . This will be described in section 4.5.
- 2) We interpolate data points  $(t_i, d_i)$  to find drift distance  $d$  for certain drift time  $t$ . This will be described in section 4.6.

### 4.4.2 Derivation of TTD curve

Now when we have the following information:

- 1) the drift time distribution, from replay ROOT file entries from TDC raw data file and
- 2) the drift distance distribution is uniformly distributed, for tracks with fixed incident angle,

the derivation of the TTD curve is pretty simple, based on the transformation of variable of a probability distribution. [45]

The probability distribution for time  $t$  is:

$$F(t_0) \equiv Prob(t \leq t_0) = \int_0^{t_0} f(t) dt \quad (4.25)$$

where  $F(t_0)$  is the probability distribution function of drift time,  $Prob(t \leq t_0)$  is the probability of time  $t \leq t_0$ , and  $f(t)$  is the probability density function of drift time. The distribution drift distance  $d$  has form:

$$G(d_0) \equiv Prob(d \leq d_0) = \int_0^{d_0} g(d) dd = \frac{d_0}{D} \quad (4.26)$$

where  $G(d_0)$  is the probability distribution function of drift distance,  $Prob(d \leq d_0)$  is the probability of time  $d \leq d_0$ , and  $g(d)$  is the probability density function of drift distance.  $D$  is the upper bound on the value for  $d$  (could be larger than half of wire plane thickness due to virtual drift distance (see section 4.2.1). Now in order to determine the relation  $d(t)$ , we want to associate time  $t_0$  with drift distance  $d_0$ , thus

$$Prob(t \leq t_0) = Prob(d \leq d_0) \quad (4.27)$$

It should be noted that both the probability density functions  $f(t)$  and  $g(d)$  are non-negative, and thus both  $F(t_0)$  and  $G(d_0)$  are monotonically increasing. In addition, the function  $d(t)$  is monotonically increasing so the inverse function exists. We will have the relation  $t(d) = d^{-1}(d(t))$ . By equating (4.25) and (4.26) due to (4.27), we have:

$$\begin{aligned} G(d_0) &\equiv Prob(d(t) \leq d_0) = \int_0^{d_0} g(d) dd = \frac{d_0}{D} \\ &= Prob(t < t(d_0)) = \int_0^{t(d_0)} f(t) dt \end{aligned} \quad (4.28)$$

Alternatively:

$$d_0 = D \int_0^{t(d_0)} f(t) dt \quad (4.28')$$

If we utilize data from the histogram of the distribution of  $t$  which can be normalized, and if we then approximate the integration by the sum we can numerically compute time to distance conversion function  $d(t)$  by:

$$d_0 = d_0(t_0) \approx D \sum_{t_i < t(d_0)=t_0} f(t_i) \Delta t \quad (4.28'')$$

Then,  $D$  and the normalization of the  $t$  distribution will uniquely determine  $d$  as function of  $t$ .

#### 4.4.3 Practical procedure to obtain TTD function by integration

Before we apply equation (4.28) to compute the TTD function, we should note that for our experiment the range of BH pair particle directions is much larger than the situation in most JLAB experiments. Thus, the incident angles  $\alpha_u$  or  $\alpha_v$  dependence on drift distance, which is already shown in the parameter  $a_2$  in default analyzer formula (4.1), should not be overlooked. And, we should incorporate the incident angle dependence in our calculations. Instead of  $d(t)$  for all wire hit data, we calculate  $d(t; \theta)$  from the subset of data with incident angle close to  $\theta$  (the estimated slope  $\tan\theta$  instead of  $\theta$  could also be a choice). Convention: in this section and 4.5 we denote incident angle by  $\theta$  instead of  $\alpha_u$  or  $\alpha_v$  for simplicity.

The steps to follow to compute TTD function  $d(t; \theta)$  with fixed  $\theta$  :

- 1) (Analyzer) find clusters for each wire plane in each event.
- 2) Determine if a cluster has an estimated incident angle  $\theta$  within range  $[\theta - \Delta\theta, \theta + \Delta\theta]$  ( $\Delta\theta = 1^\circ$  during calculation)
- 3) Fill the drift time distribution histogram of clusters with selected incident angle.
- 4) Calculate the sum  $\sum_{t_i < t(d_0)=t_0} f(t_i) \Delta t$  for a set of time  $t_i$  till a cutoff value. Record each  $t_i$  then normalize the sum to 1.



5) Set the cutoff drift distance  $D$ .

6)  $d_i = D \sum_{t_i < t(d_0)=t_0} f(t_i) \Delta t$  and record data  $(t_i, d_i)$  and plot the graph.

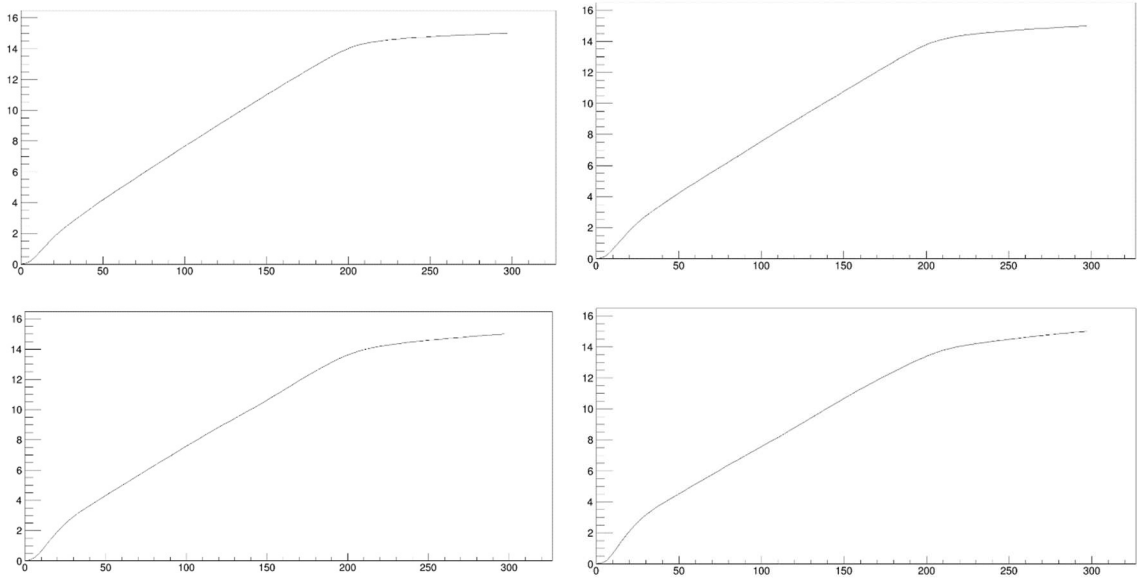
The cutoff time could be chosen for any time beyond the plateau of time distribution. For example, in Fig 4.1 it is 310 ns. A cutoff distance  $D$ , which corresponds to the cutoff time, should be close to the half wire plane thickness (1.27cm) at this point, since it's near the transition between a region with uniform electric field with uniform time distribution and a region outside the plane beyond cathode plane with a different drift distribution. The value of  $D$  can be fine tuned later based on the track reconstruction result, now we choose  $D = 15 \text{ mm}$  and cutoff time  $T = 300 \text{ ns}$ .

#### 4.4.4 Result

The resulting TTD curves, based on our test run data, are very similar to the TTD function in Fig 4.2. They're shown below in Fig 4.16. The function still can be approximated as 3 straight line segments (see section 4.2.1). In addition, we have the calculated result of different estimated incident angles. As for the estimated incident angles for a given found cluster is computed by:

$$\tan\theta \cong \frac{|u_0 - u_N|}{v(t_0 + t_N)} \quad (4.29)$$

or replace  $u$  by  $v$  for  $v$  wire planes. The meaning is interpreted as  $|u_0 - u_N|$  being the  $u$  coordinate difference between the 1<sup>st</sup> and last wire of the cluster, while  $v(t_0 + t_N)$  is the estimated absolute drift distance sum of the 1<sup>st</sup> and last wire of the cluster. As seen from the functions, the TTD functions are heavily dependent on incident angle  $\theta$ .



III Fig 4. 16 TTD plot. Ordinate: drift distance in unit  $mm$ . Abscissa: drift time in unit  $ns$ .

From sum of time probability density described in previous pages.  $\theta = 35^\circ, 40^\circ, 45^\circ, 50^\circ$ .  
Abscissa drift time, unit ns; ordinate drift distance, unit mm.

## 4.5 Time to distance conversion parameters fitting

We now have the TTD curve with some selected incident angles shown in Fig 4.16. Next we want to fit them to a single functional form for simpler representation of the TTD relation.

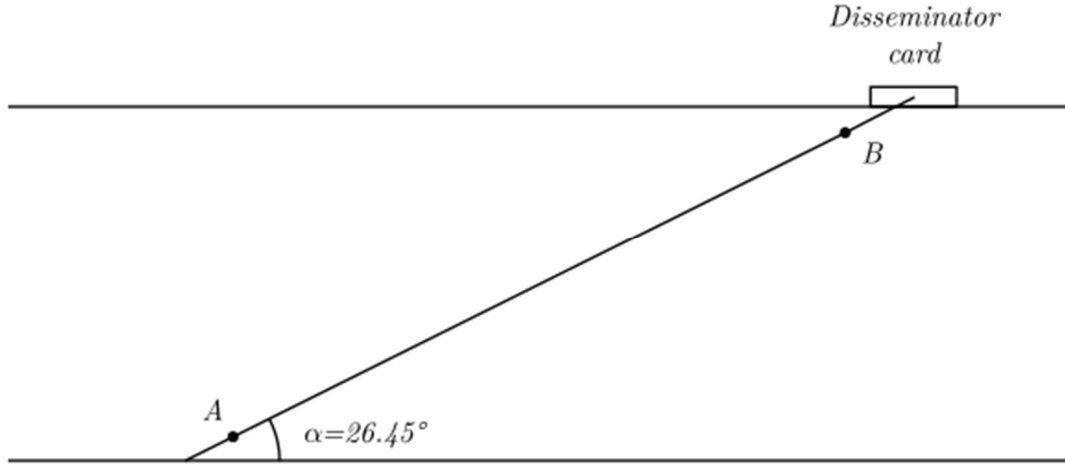
### 4.5.1 The TTD function

As with all the curves in Fig 4.16, as well as Fig 4.2., we can divide each curve by 3 pieces and approximate each by a straight line segment. That is:

$$\begin{aligned} d(t; \theta) &= A_1(\theta) + v \cdot t \cdot \left(1 + \frac{a_2(\theta)}{a_1(\theta)}\right) & , v \cdot t \leq a_1(\theta) \\ d(t; \theta) &= v \cdot t + a_2(\theta) & , v \cdot t > a_1(\theta) \end{aligned} \quad (4.30)$$

Here this is just a modified form of (4.1) with  $a_1$  now also incident angle dependent, and the intercept  $A_1(\theta)$  as a new term is added (ignored in some fit attempts). Here several points that need to be pointed out:

- (1) The 3<sup>rd</sup> piece has not been determined in this formula. The reason is that the hits in this region are beyond the cathode planes and represent virtual distances which need additional care. The data in the 1<sup>st</sup> and 2<sup>nd</sup> pieces are already sufficient to fit local track with high precision.
- (2) The incident angle dependence in (4.30) is much more than in the previous version. The reason is that for our experiment the solid angle range of primary particles are a lot larger and so does the incident angles range in different wire planes. The larger range requires the more general form of  $\theta$  dependence in the TTD function.
- (3) The additional incident angle dependent intercept  $A_1(\theta)$  results from the fact that TDC time offset for the wires are not perfectly calibrated. The insufficient calibration of TDC time offset will result in  $d(t=0) \neq 0$  and it is the reason that  $A_1(\theta)$  is needed for more accurate  $d(t; \theta)$  fitting. There are several reasons that at the current stage TDC time offsets cannot be calibrated precisely enough. First, the offset is sense wire or channel dependent but, due to the lack of statistics, they are calibrated per 16 channels from each discriminator card. Second, the propagation of signals within a wire takes time, so the time offset also depends on where the particles intersect the wires (see section 4.2.1 2). This results in a fluctuation of about 4 ns in the result. Also see Fig 4.17 below. The absolute nominal value of  $A_1$  is 0.64 mm, and for  $v = 6 \times 10^4 (m/s)$ , it results in about 10.7 ns offset in time, which is about 5% of the total range of drift time ( $\sim 200$  ns).
- (4) We treat  $v$  as constant and scale to the same  $v$  after the fit. During the TTD calculated from numerical integration the time distribution density function we used the condition  $D = d(T)$  with  $D = 15$  mm and  $T = 300$  ns to normalize the integration. However, due to the unknown incident angle dependence of the TTD function, the normalization condition failed. The drift velocity  $v$  in region sufficiently away from sense wires on the other hand should only depend on HV and inert gas properties due to the randomness of acceleration of the electric field and scattering by the gas molecules. In the most reliable fit result,  $v$  is kept as constant. And after each fit, all other parameters ( $a_1, a_2, A_1$ ) were scaled to keep  $v$  constant.



III Fig 4. 17 TDC time offset from length of sense wire.

Even though the time when the cosmic particle track intersects with the wire should represent 0 time, the sense wire has length (longest is about  $\frac{21''}{\sin 26.45^\circ} \cong 4 \text{ feet}$ ) and it will take different time to propagate the signal when the track intersects the wire in different locations.

#### 4.5.2 Procedure for fitting the TTD function

- 1) In order to extract discrete data points  $(t_i, d_i)$ , import the images of each graph in Fig 4.16 into a digitizer; [46] select sufficient data points from the 1<sup>st</sup> and 2<sup>nd</sup> pieces of the TTD curve, and specify maximum range on  $t$  and  $d$  axes. The digitizer will then export the values of points  $(t_i, d_i)$ .
- 2) Using separated data points from  $(t_i, d_i)$ , we fit them with straight lines with form:
 
$$\begin{aligned}
 d(t; \theta) &= A_1(\theta) + B_1(\theta)t \\
 &= A_1(\theta) + v(\theta) \cdot t \cdot \left(1 + \frac{a_2(\theta)}{a_1(\theta)}\right) \\
 &= A_2(\theta) + B_2(\theta)t = a_2(\theta) + v(\theta) \cdot t
 \end{aligned}
 \tag{4.31}$$

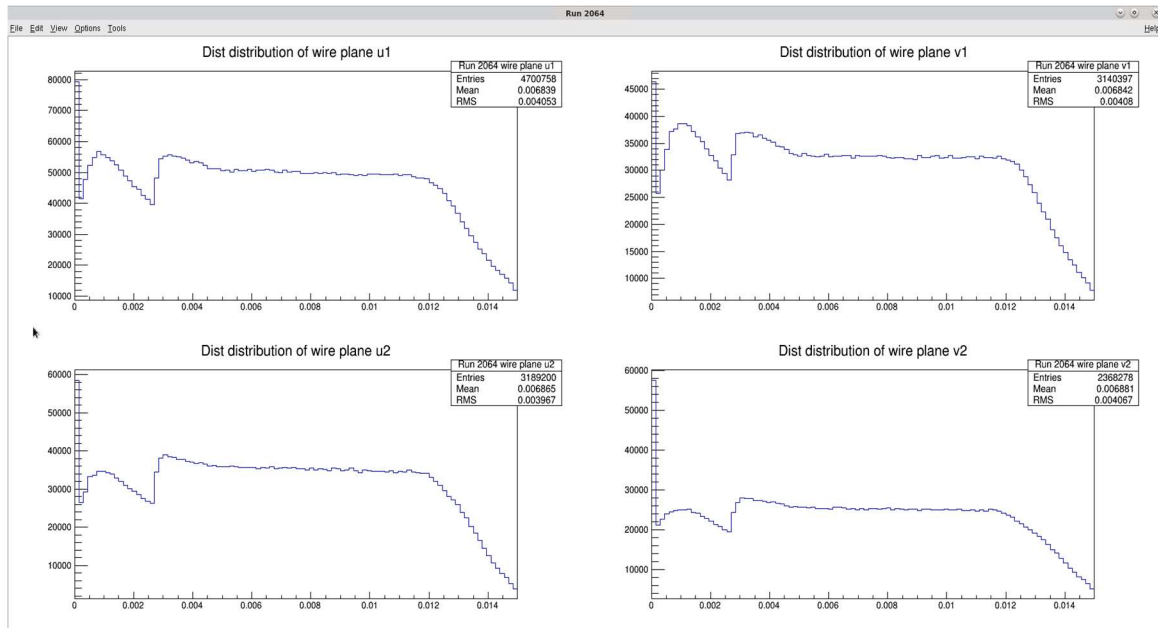
Write values of  $A_1(\theta), B_1(\theta), A_2(\theta), B_2(\theta)$  for each  $\theta$  into a table.

- 3) Compute  $a_2(\theta) = A_2(\theta)$  first, then use the  $a_2(\theta)$  value in  $B_1(\theta) = \left(1 + \frac{a_2(\theta)}{a_1(\theta)}\right)$  to determine  $a_1(\theta)$ .
- 4)  $B_2(\theta)$  is supposed to be  $v$  and should not have incident angle dependence, set  $v = 60000 \text{ m/s}$ , and scale  $A_1(\theta), A_2(\theta), a_1(\theta)$  accordingly to make  $B_2(\theta) = v = 60000 \text{ m/s}$  a constant.
- 5) Fit all TTD parameters  $A_1(\theta), A_2(\theta) = a_2(\theta), a_1(\theta)$  as polynomial functions of  $\tan\theta$ , and similarly for  $A_1(\theta)$  and  $a_1(\theta)$ .
- 6) Fill wire chamber database file TTD parameters with fit parameters  $A_1(\theta), a_2(\theta), a_1(\theta)$  and  $v$ . Replay the raw data file to generate a new ROOT file and check drift distance distribution.

### 4.5.3 TTD function fit results

The goal of the fit is to reproduce the drift distance distribution under the assumption that it is uniform. Alone from the generation process of TTD curves in section 4.4, if we directly apply the curved functions to drift time distribution, we expect to obtain a uniform distance distribution. The TTD function fit in this section approximated the curve by two straight line segments and it will never be making drift distance distribution fully uniform. The fit turns to find proper forms of TTD parameters  $A_1(\theta)$ ,  $a_2(\theta)$ ,  $a_1(\theta)$  and  $v$  that makes resulting distance distribution as uniform as possible. Our best attempt is to fit  $A_1(\theta)$ ,  $A_2(\theta) = a_2(\theta)$ ,  $a_1(\theta)$  as quadratic functions of  $\tan\theta$ . The result is shown below:

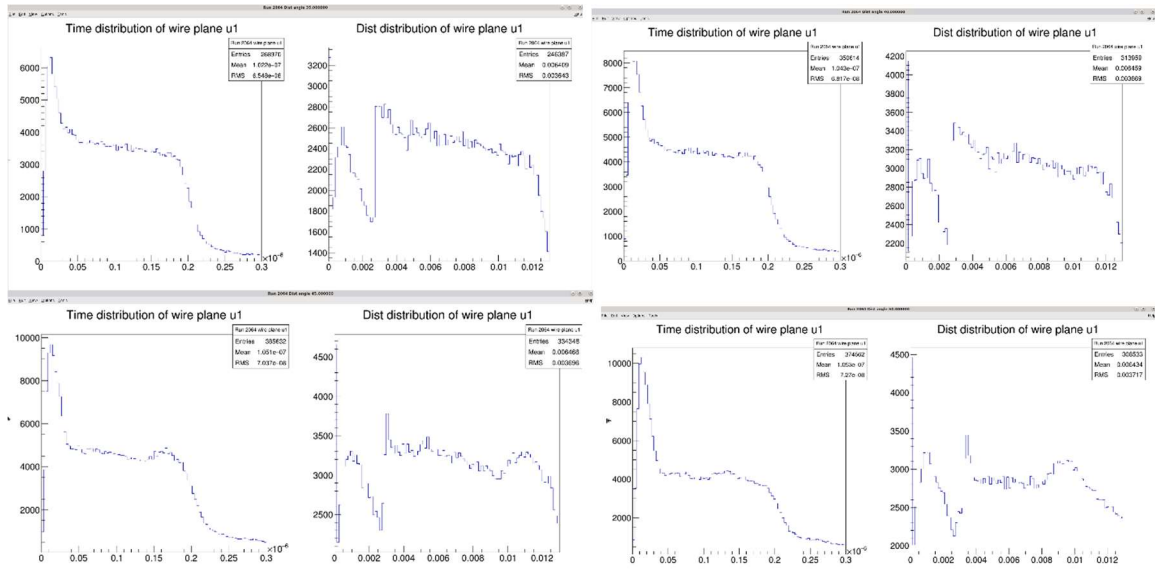
- 1) TTD function parameters.
 
$$\begin{aligned} A_1 &= -0.2190 - 0.2698\tan\theta + 0.09438\tan^2\theta \text{ (mm)} \\ a_2 &= 0.8712 - 0.7221\tan\theta + 0.9722\tan^2\theta \text{ (mm)} \\ a_1 &= 1.907 - 1.487\tan\theta + 0.7046\tan^2\theta \text{ (mm)} \\ v &= 60000 \text{ (m/s)} \end{aligned} \quad (4.32)$$
- 2) Drift distance distribution of each wire plane from a package of wire chambers.



III Fig 4. 18 Drift distance distribution by applying TTD function. Ordinate: counts, no unit, abscissa: drift distance in unit  $m$ .

From function (4.31) with incident angle  $\theta$  dependent parameters on drift times, unit meter. Here  $u1, v1$  are bottom wire chamber wire planes, and  $u2, v2$  are top wire chamber wire planes.

- 3) Drift distance distribution for each incident angle in wire plane  $u1$



III Fig 4. 19 Drift distance distribution from applying the TTD function. Each left figure ordinate: counts, no unit, abscissa: drift time in unit  $\mu s$ . Each right figure ordinate: counts, no unit, abscissa: drift distance in unit  $m$ .

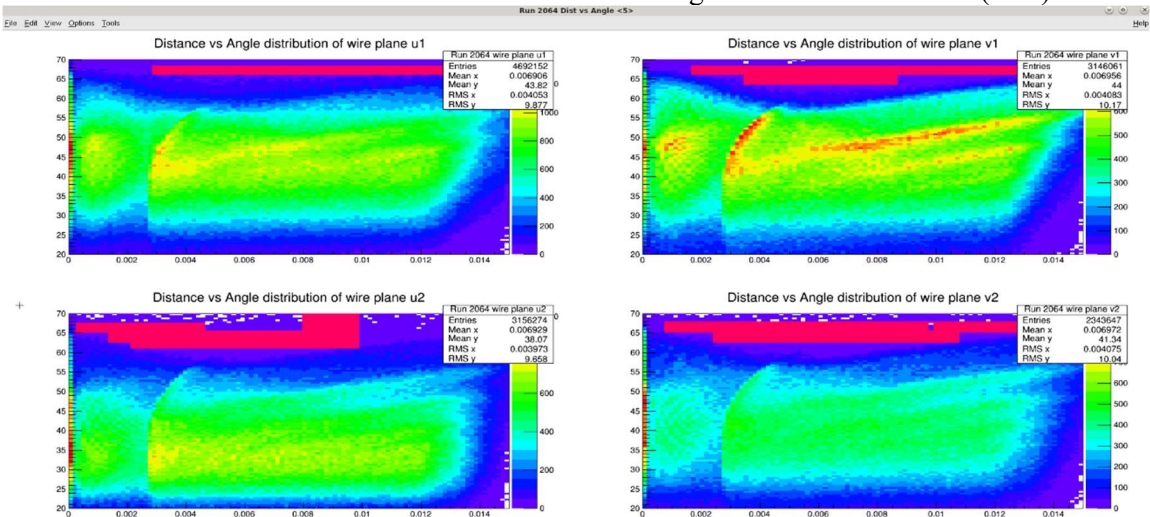
(4.31) with incident angle  $\theta$  dependent parameters on drift times in wire plane  $u_1$  (in meters). From upper left to lower right,  $\theta = 35^\circ, 45^\circ, 50^\circ, 55^\circ$  respectively.

### Discussion on the resulting drift distance distribution

The TTD function makes drift distances somewhat uniformly distributed, except the part where drift distance and time transits from the 1<sup>st</sup> to 2<sup>nd</sup> segment of the curve. This is understandable since two line-segments could never reproduce a curve with a nearly continuous transition. The TTD function (4.31) essentially shrinks the 1<sup>st</sup> segment of the drift time distribution uniformly (see Fig 4.4.), and we can see from all plots in Fig. 4.18 and Fig. 4.19 that near the  $d = 0$  the region has been shrunk to match the frequency of 2<sup>nd</sup> plateau segment. The time and distance at intersection of 2 segments in function (4.31) now is particularly important since it determines the region to shrink. The fitted values for the intersection parameters are shown below in Table 4.1.

	35°	40°	45°	50°	55°
$A_1$ (mm)	-0.4542	-0.5118	-0.5832	-0.6746	-0.7968
$a_1$ (mm)	1.211	1.155	1.125	1.136	1.221
$a_2$ (mm)	0.8422	0.9498	1.1213	1.3914	1.8228
$t = \frac{a_1 a_2 - A_1}{v a_2}$ (ns)	31.08	29.63	28.49	28.10	29.23
$d(t) = a_2 + \frac{a_1(a_2 - A_1)}{a_2}$ (mm)	2.704	2.933	2.831	3.078	3.577

Table 4.1 Fitted parameters  $A_1, a_1, a_2$  for selected incident angles.  $t$  is the drift time and  $d(t)$  is the drift distance at intersections between the 1<sup>st</sup> and 2<sup>nd</sup> segments in TTD function (4.31).



III Fig 4. 20 Drift distance vs incident angle ( $d, \theta$ ) distribution of each wire plane. Ordinate: track incident angle in each wire plane  $\theta$  in degrees, abscissa: drift time in  $m$ .

The drift distance  $d$  is on the abscissa in meters; the incident angle  $\theta$  is on the ordinate in degrees. We can clearly see the dividing lines between the 1<sup>st</sup> and 2<sup>nd</sup> segments. In addition, we can see the difference in the resulting distance distributions on different wire planes, especially for the  $v_1$  plane result, the dividing lines should be pushed to larger distances for larger  $\theta$ . This indicates that it might be necessary to fit a separate TTD function for each wire plane.

## 4.6 TTD function by interpolation

### 4.6.1 Introduction

Till now we have applied the formula (4.28") to generate the TTD curve for different incident angles with some results plotted in Fig. 4.16. There are different options for applying the result of (4.28") to the cosmic ray test run data. One is to approximate and fit a TTD function, then apply the function to the drift time data as discussed in section 4.5. Another reliable way to utilize the result is to interpolate to get drift distances from arbitrary drift times, which will be discussed in this section. The benefit of interpolation is the drift distance distribution is significantly more uniform than that obtained using a TTD function.

### 4.6.2 Procedure of interpolation and result

1) Calculate drift distance  $d(t; \theta)$  by applying formula (4.28")

$$d_0(t_0) \approx D \sum_{t_i < t(d_0)=t_0} f(t_i) \Delta t$$

for various incident angles and drift times. The result generates a 2-dimensional table of  $d(t; \theta)$ .

2) [47] During the analyzer replay process, once we get drift time  $t$  and estimate the cluster slope  $\tan\theta$  after cluster finding, we interpolate the drift distance linearly from nearest drift distance values from 4 data points  $(\theta_{i(+1)}, t_{j(+1)})$  enclosing our  $t$  and  $\theta$ :

$$\theta_i < \theta < \theta_{i+1} \text{ and } t_j < t < t_{j+1} \quad (4.33)$$

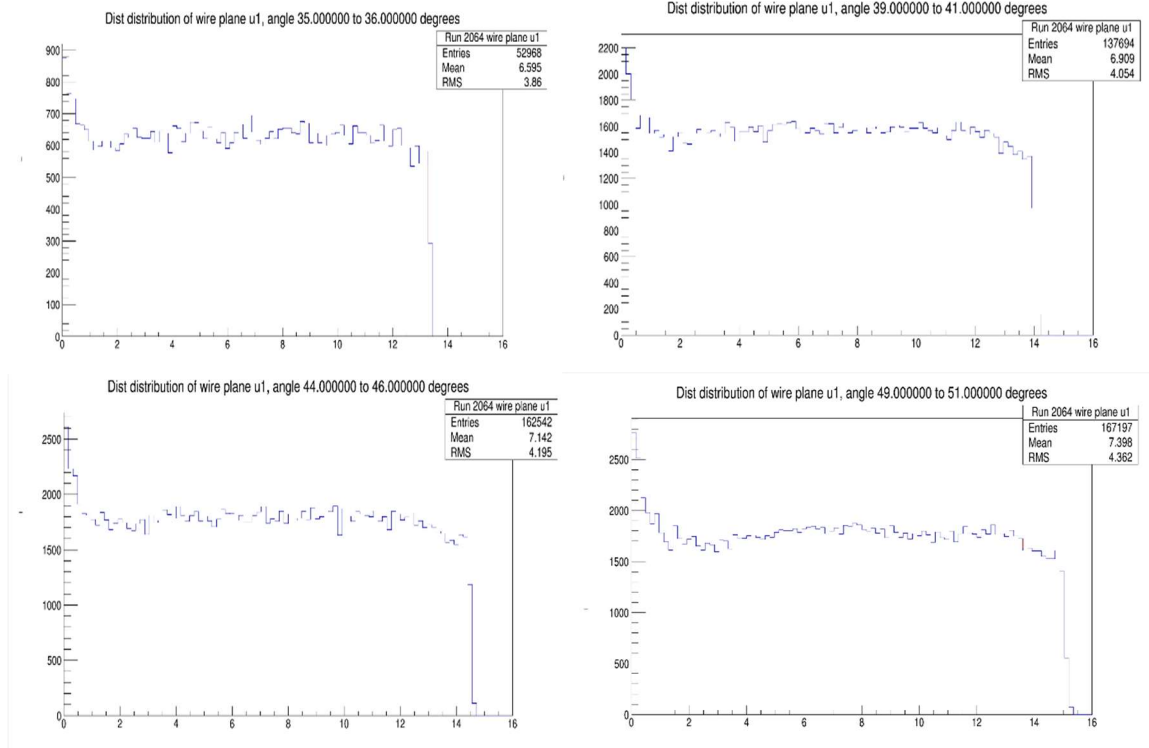
3) We 1<sup>st</sup> interpolate  $\theta$ :

$$d(\theta, t_i) = \frac{\theta_{i+1} - \theta}{\theta_{i+1} - \theta_i} d(\theta_i, t_i) + \frac{\theta - \theta_i}{\theta_{i+1} - \theta_i} d(\theta_{i+1}, t_i) \quad (4.34)$$

and get  $d(\theta, t_{i+1})$  similarly. Then we interpolate  $t$ :

$$d(\theta, t) = \frac{t_{j+1} - t}{t_{j+1} - t_j} d(\theta, t_j) + \frac{t - t_j}{t_{j+1} - t_j} d(\theta, t_{j+1}) \quad (4.35)$$

This 2D interpolation algorithm is simple and the resulting drift distance distributions are very close to uniform. A set of TTD results from this interpolation method is shown in Fig. 4.21 below.



III Fig 4. 21 Drift distance distribution from interpolation of TTD table. Ordinate: counts, no unit, abscissa: drift distance in  $mm$ .

Unit  $mm$ . With incident angle range indicated in the titles. As we can see there are still some problems in the result. This distance distribution has a peak in the initial small  $d$  region and a sharp drop in the large  $d$  region, both regions are where  $f(t)$  changes rapidly. The obvious flaw is in using the sum  $\sum_{t_i < t(d_0) = t_0} f(t_i) \Delta t$  in (4.28') to replace the integral  $\int_0^{t(d_0)} f(t) dt$  in eq. (4.28'), or replacing average value  $\int_{t_i}^{t_{i+1}} f(t) dt / \Delta t$  of each interval by its center value  $f(\frac{t_i + t_{i+1}}{2})$ .



### 4.6.3 Modified $d(t)$ calculation

It is suggested that by finding drift times  $t_i$  in the time distribution in which each interval  $[t_i, t_{i+1}]$  has the same number of time data points, then the resulting distance  $d(t_i)$  points should be equally spaced. This is proved by seeing that in interval  $[t_i, t_{i+1}]$  the change of drift distance is

$$d(t_{i+1}) - d(t_i) = D \int_{t_{i+1}}^{t_i} f(t) dt \quad (4.36)$$

and the integral is the probability of drift time in  $[t_i, t_{i+1}]$ , which is proportional to counts in interval  $[t_i, t_{i+1}]$ . Our goal is to get all drift time data from all clusters within a small incident angle range in a wire plane. Then group them into same counts in each interval so that all time data in one interval  $[t_i, t_{i+1}]$  should be larger than any interval on its 'left', and also for the 'right'. (Assuming finding median by sorting a data set, but now it's extended to sorting into 100 subsets, with any time  $t$  in the  $i^{th}$  set of data larger than all time  $t$  data in previous  $i-1$  sets, and less than all time  $t$  data in sets starts at  $i+1$ .) We don't have to sort inside each subset, that's called a *quick sort algorithm* and greatly increases computation speed. A brief discussion of the quick sort algorithm used is in Appendix A 4.6.

There are also changes in the interpolation, to use the previous 2D linear interpolation formula (4.33) to (4.35), we have 4 data points  $(\theta_i, t_j)$ ,  $(\theta_{i+1}, t_j)$ ,  $(\theta_i, t_{j+1})$ ,  $(\theta_{i+1}, t_{j+1})$  located at 4 corners of a rectangle in the  $\theta$ - $t$  coordinate system. Now, instead of numbers in  $(\theta, t, d(\theta, t))$  table being equally spaced  $\theta$  and  $t$  values, we have numbers in table  $(\theta, d, t(\theta, d))$  with equally spaced  $\theta$  and  $d$  values. The method of finding the interpolation formula using  $d$  and  $\theta$  is to find  $t(d, \theta)$  first, then solve  $d$  as  $d(\theta, t)$  from  $t(d, \theta)$ , as elaborated on below. We derive the formula for  $d(\theta, t)$  from the 2D table with numbers  $(\theta_i, d_j, t((\theta_i, d_j)))$ . For simplicity we use the notation  $\theta_1, \theta_2$  and  $d_1, d_2$  in the derivation.

1) At line  $d = d_1$  linear interpolate  $\theta$

$$t(d_1, \theta) = \frac{\theta_2 - \theta}{\theta_2 - \theta_1} t(d_1, \theta_1) + \frac{\theta - \theta_1}{\theta_2 - \theta_1} t(d_1, \theta_2) \quad (4.37)$$

Replace  $d_1$  by  $d_2$  in (4.37), then for  $d = d_2$

$$t(d_2, \theta) = \frac{\theta_2 - \theta}{\theta_2 - \theta_1} t(d_2, \theta_1) + \frac{\theta - \theta_1}{\theta_2 - \theta_1} t(d_2, \theta_2) \quad (4.38)$$

2) Interpolate  $d$  on line  $\theta = \theta$ :

$$t(d, \theta) = \frac{d_2 - d}{d_2 - d_1} t(d_1, \theta) + \frac{d - d_1}{d_2 - d_1} t(d_2, \theta) \quad (4.39)$$

3) We know time  $t = t(d, \theta)$  as a result value in the table, but not  $d$ . However, we can solve for  $d$  from equation (4.39):

$$d = \frac{(d_2 - d_1)t(d, \theta) - d_2 t(d_1, \theta) + d_1 t(d_2, \theta)}{t(d_2, \theta) - t(d_1, \theta)} \quad (4.40)$$

It should be noted that we don't expand  $t(d, \theta)$  in (4.40) by (4.39), the  $t(d, \theta)$  is the drift time from measurements so all the terms in (4.40) can be acquired.

In order to apply formula (4.40), the last issue is to determine which cell with 4 corners  $(d_1, \theta_1)$ ,  $(d_1, \theta_2)$ ,  $(d_2, \theta_1)$ ,  $(d_2, \theta_2)$  we use to apply the interpolation formulas (4.37) to (4.39). There are two pieces of information we can exploit:

- 1) We know the value of  $\theta$  (see eq. 4.29), here  $\theta$  is the arctangent of the estimated slope) so we only need to find two adjacent values of  $\theta$  for which  $\theta_i < \theta < \theta_{i+1}$  in the table.
- 2) When  $\theta$  is fixed, the function  $t(d, \theta)$  is a monotonically increasing function of  $d$ .

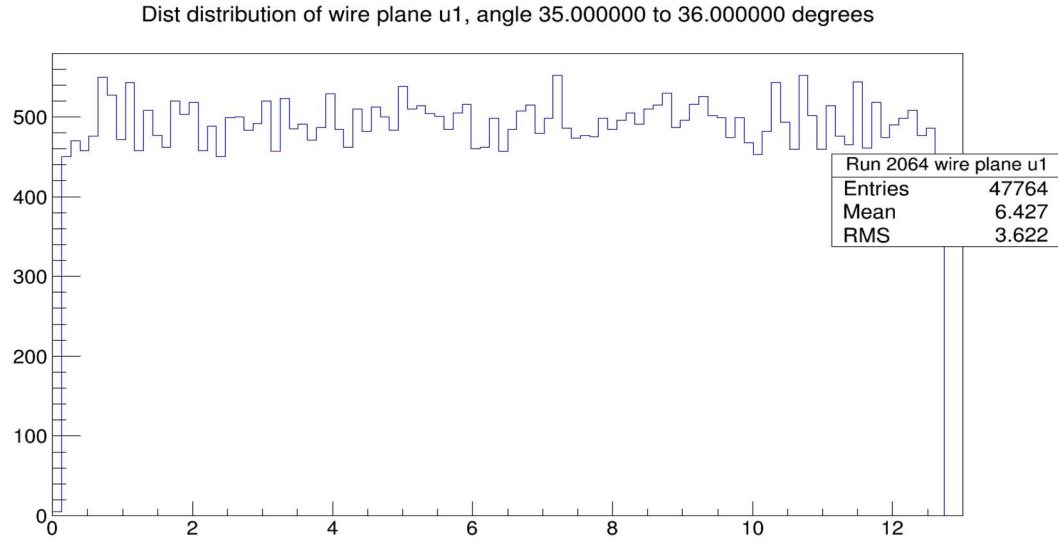
Thus from the  $\theta$  we use interpolation formulas such as (4.37) to get a sequence of interpolated drift time data:

$$t(d_j, \theta) = \frac{\theta_{i+1} - \theta}{\theta_{i+1} - \theta_i} t(d_j, \theta_i) + \frac{\theta - \theta_i}{\theta_{i+1} - \theta_i} t(d_j, \theta_{i+1}) \quad (4.41)$$

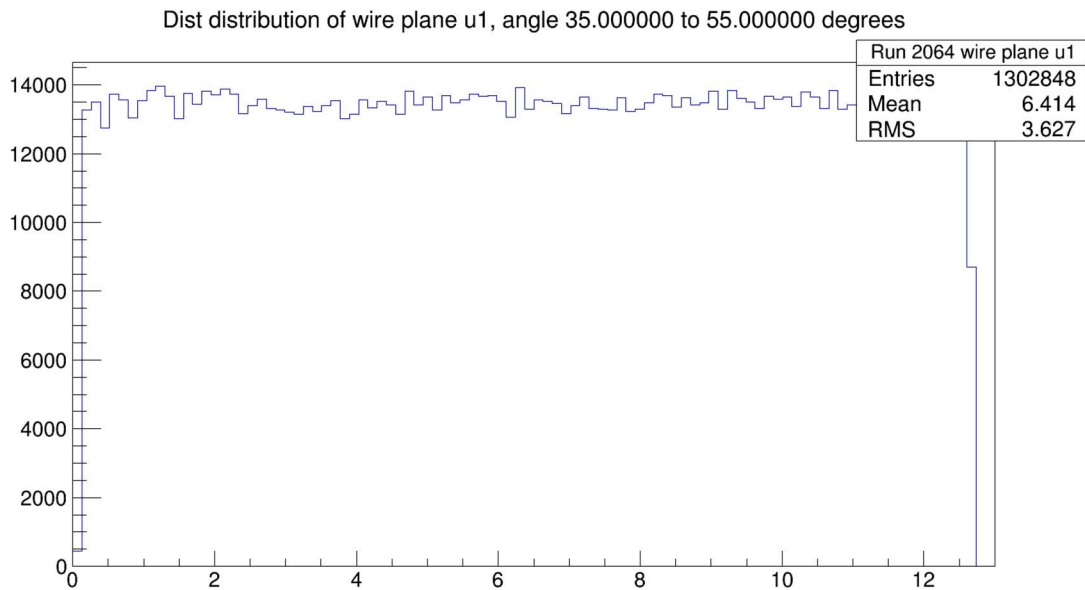
Since  $t(d, \theta)$  is a monotonically increasing function of  $d$ ,  $t(d_j, \theta) < t(d_{j+1}, \theta)$  is always satisfied. Thus, we can end our search for  $d_j$  and  $d_{j+1}$  once we have

$$t(d_j, \theta) < t(d, \theta) < t(d_{j+1}, \theta) \quad (4.42)$$

The resulting distance distributions from the modified  $d(t)$  calculation are shown in Fig. 4.22 and Fig. 4.23. As we see, the previously seen anomalies either in a narrow range in the incident angle  $\theta$  or a large range the distance distribution  $d(t)$ , are eliminated and the distribution shows only statistical fluctuations. The defect of using  $f(\frac{t_i + t_{i+1}}{2})\Delta t$  to approximate  $\int_{t_{i+1}}^{t_i} f(t)dt$  is solved.



III Fig 4. 22 Drift distance distribution of wire plane  $u1$  with incident angle  $\theta$  from  $35^\circ$  to  $36^\circ$ . Ordinate: counts, no unit, abscissa: drift distance in  $mm$ . Note the counting error with 500 counts is  $\sqrt{500} = 22.4$ .



III Fig 4. 23 Drift distance distribution of wire plane  $u1$  with incident angle  $\theta$  from  $35^\circ$  to  $55^\circ$ . Ordinate: counts, no unit, abscissa: drift distance in  $mm$ .

## 5 Analyzer track finding, fitting and efficiency

### 5.1 Introduction

In Chapters 3 and 4 we discussed how to find and fit clusters from wire chamber TDC time data. The most important results are found clusters and their crossover point coordinates  $(u_1, v_1, u_2, v_2)$ . In the analyzer replayed ROOT file, track information is stored as  $(x, y, \tan\theta, \tan\varphi)$  where  $x, y$  are the  $x, y$  coordinates of lowest wire plane and  $\tan\theta = \frac{\Delta x}{\Delta z}$  and  $\tan\varphi = \frac{\Delta y}{\Delta z}$  are track projection angles between in the  $x$ - $z$  axis and  $y$ - $z$  axis, respectively. In this chapter, we will discuss the analyzer track fitting algorithm and how the track position and direction information  $(x, y, \tan\theta, \tan\varphi)$  is obtained from the cluster fitting result  $(u_1, v_1, u_2, v_2)$  (Section 5.2). In order to check the validity of the current analyzer code track fitting result, we compare the analyzer track results with specific geometric constraints to the predicted range of tracks from direct measurement of the geometries of the trigger scintillator paddles. Thus, not only tracks should be found and fitted for these specified triggers, but also the track fitting result needs to lie within the bounds of the trigger geometry. The trigger setup will be discussed in 5.3. The results, including found tracks and efficiency are shown in 5.4. To end this chapter, suggestion of improvement of the track finding efficiency are proposed in 5.5. Some miscellaneous topics are discussed in 5.6.

There are two very important points to be made here:

- 1) The difference between JLAB experiment and BH experiment are mainly in the data rates and range of track directions. Experiments at JLAB have much higher rates and it is common that multi-cluster/track events emerge. Some aspects of the Hall A analyzer track finding and fitting code are written specifically to handle these situations. For the BH experiment this is not the case. From a Geant 4 simulation using a  $25\mu\text{m}$  thick Uranium-238 target, the rate of events at the yoke hole of the magnet not excluded by the tungsten cone baffle is on the order of 10 Hz (see Part IV Simulation, Section 1.4.2). Compared to typical drift time of ionized electrons in wire chamber 200 ns, this data rate should rarely result in a multi-track situation. Thus, the main focus of the test run results is on single-cluster/track events. On the other hand, the range of track directions in the BH experiment is much larger than in JLAB experiments. This gives some additional requirements on our wire chambers and tracking code to have good efficiency covering a wider range of track angles.
- 2) The main difference between cosmic ray tests and the BH experiment is the shower of cosmic particles, which result in very messy hit collections, both in terms of the number of wires hit and their hit time structures. This inevitably results in the domination of multi-cluster/track events. In order to compensate for this, small sized scintillator paddles were placed to constraint track crossover location on wire chamber and direction for easier handling of the tracking results. The downside is just as mentioned, the constraint geometry of these triggers cannot fully cover the area and angles of track in BH experiment. However, if we assume that the untested regions of the wire planes perform at similar efficiency as the tested regions, then the test runs are good indications of successful tracking in experiment.

## 5.2 Track finding and fitting

The condition for an event rendering a track is simple; each wire plane has at least one cluster found. Once this condition is satisfied, each wire plane will have at least one crossover coordinate  $(u_1, v_1, u_2, v_2)$  calculated. The next step is to calculate track info  $(x, y, \tan\theta, \tan\varphi)$ , which are defined in 5.1. This calculation is called track fitting and will be discussed in 5.2.2, Appendix A5.2.1, and Appendix A5.2.2.

The analyzer handles track finding and fitting based on two cases [38]:

- (1) One and only one cluster per wire plane for the event; a single-cluster event.
- (2) Each wire plane has a cluster, and at least one wire plane has more than one cluster for the event; a multi-cluster event.

For case (1), it's simple in that there is only one crossover coordinate per wire plane, so one and only one track is found and fitted. For case (2), even only two tracks will result in a much more complex situation. It will be only briefly discussed in 5.2.1, since it is expected to rarely be the case for the BH experiment but frequently appears in test run replays. The effects of cuts which will change the result of track finding and fitting results will be discussed in 5.2.3.

### 5.2.1 Track identification by path analysis ([38])

Let's consider a 2-track event to illustrate the challenge of track finding and fitting in multi-cluster or multi-track events. It should be noted that:

- 1) two tracks in the trigger timing window won't cross wire chambers at the exactly the same time, in other word one track will cross the wire chambers earlier than the other. If this time separation is large enough (e.g., larger than the maximum drift time), then the time difference between two tracks can be observed from their corresponding cluster drift time distribution off trigger timing. That is, the 1<sup>st</sup> track starts the trigger, the 2<sup>nd</sup> and later track will have uniform drift times offset to the 1<sup>st</sup> track time.
- 2) For a single hit wire, only the 1<sup>st</sup> hit time will be stored in TDC and analyzed. Thus, if 2 tracks cross a wire plane on some common wires, only the 1<sup>st</sup> arrived track will have drift time info stored and 2<sup>nd</sup> track timing info on these wires are lost.

Disregarding the much rarer case when 2 tracks have overlapped hit wires on even one wire plane, we should observe 2 clusters on each wire plane. In total, there are total  $2^4 = 16$  combinations of clusters from 4 wire planes. So, we have to make 16 times of the number of fits compared to the 1 track case. In addition, comparisons of total  $\chi^2$  are need to find 2 tracks out of 16 combinations, which will greatly increase computation time.

Let's consider general case. Assuming that there are multiple tracks through wire chambers, and thus multiple clusters found on each wire plane. Let the numbers of clusters found in each wire plane be  $n_{u1}, n_{u2}, n_{v1}, n_{v2}$ . By choosing any combination from  $n_{u1}n_{u2}n_{v1}n_{v2}$  possible combinations of 4 clusters, one from each wire plane, a possible track can be calculated. Each such combination is considered a possible *path* of the track through the chambers. The process of identify tracks from all possible paths is called *track identification*. A *link* is a combination of two clusters from wire planes with same orientation; that is, a combination of  $u_1, u_2$  clusters or  $v_1, v_2$  clusters. The fundamental of path analysis is to fit all hits  $(u_i, d_i)$  in a link, that is a fit straight line from  $(u_i, d_i)$  data from both  $u_1, u_2$  clusters of the link together (note

$u_i$  should be replaced by  $v_i$  for  $v$  wire planes). All hits in the link should align in a straight line if both clusters in the link belong to the same track. Results associated with a link, including  $\chi^2$ , crossover position, timing offset  $t_0$ , and track slope are stored. Next comes path ordering: order all possible paths according to an error function that combines the quality of straight line fit of clusters in  $u, v$  links and the hit timing to give most probable tracks from multi-cluster events. There are two methods for doing this:

- (1) [38] All possible combinations of links that composed possible paths are connected by following order  $u_1-u_2, u_2-u_1$ , then  $v_1-v_2$  to form a path. The  $\chi^2$  of links  $u_1-u_2$  and  $v_1-v_2$  contains both  $\chi^2$  of straight line fit and difference in timing info while link  $u_2-u_1$  only contains difference in timing. According to equation (14) in [38]:

$$\chi_{tot}^2 = \chi_{u_1u_2}^2 + \chi_{v_1v_2}^2 + \left( \frac{t_{0,v_1v_2} - t_{0,u_1u_2}}{\min(\sigma(t_{0,v_1v_2}), \sigma(t_{0,u_1u_2}))} \right)^2$$

Here,  $\chi_{u_1u_2}^2$  and  $\chi_{v_1v_2}^2$  are the  $\chi^2$  values found in the U1-U2 and V1-V2 global cluster fits, respectively,  $t_{0,v_1v_2}$  and  $t_{0,u_1u_2}$  are the timing offsets obtained from these respective fits, and the  $\sigma(t_0)$  are the uncertainties in those offsets. This total  $\chi^2$  of all paths are sorted into increasing order, and  $\min(n_{u_1}, n_{u_2}, n_{v_1}, n_{v_2})$  paths with lowest total  $\chi^2$  and without common clusters are the identified tracks.

- (2) The Hall A analyzer code suggests another way of path ordering: sorting errors of all *point pairs*. A point pair is a pair of points, one from wire chamber 1 and the other from wire chamber 2, from crossover point coordinates of local cluster fits. Points undergo coordinate transformations  $(u_i, v_i) \rightarrow (x_i, y_i)$ ,  $i = 1, 2$  to the analyzer  $xyz$  coordinate system. When the track direction  $(\tan\theta, \tan\varphi, 1)$  is fit, we can propagate  $(x_1, y_1)$  with the track direction onto wire chamber 2 to get  $(x_{p2}, y_{p2})$ , then compute distance between  $(x_2, y_2)$  and  $(x_{p2}, y_{p2})$  squared. Do the same for the other way and the sum is the error of the point pair, which will be sorted as was done with path ordering.

This sums up the procedure of track finding. One last point that should be noted is that for our test run data, if the event corresponds to shower this algorithm for multiple-cluster usually won't give the correct result. Two main reasons are: first, due to there being too many clusters the chances that  $\chi^2$  values are close increases. The result of path ordering would not necessarily give correct answer, in addition wrong ordering results from lower  $\chi^2$  hinders higher  $\chi^2$  paths to find correct one that correspond a track. Second, if the shower is close to wire chambers, it is highly possible that the tracks on 1<sup>st</sup> wire chamber no longer reaches 2<sup>nd</sup> wire chamber and result is useless. We discard shower events when analyzing track fitting results.

## 5.2.2 Track fitting

It takes 4 linear equations to solve for  $(x, y, \tan\theta, \tan\varphi)$  from  $(u_1, v_1, u_2, v_2)$ . Thus, a unique solution almost always exists once we find at least one track from track finding. Since there is one and only one straight line intersecting with 4 straight lines in each of  $u_1, v_1, u_2, v_2$  wire plane with crossover coordinate  $(u_1, v_1, u_2, v_2)$  while having 0 distance to these 4 straight lines, *track fitting* is rather more precisely called *track reconstruction*. Once the equations are set, the calculational procedure is straight forward. Derivation of the linear equations to solve is in Appendix A5.2.2.

If we take geometric constraints such as  $u_1$  &  $u_2$  wires and  $v_1$  &  $v_2$  wires being parallel, and all  $u_1, v_1, u_2, v_2$  wire planes being parallel into consideration, then the solutions are greatly simplified and the result can be immediately obtained. The steps are as follows:

- 1) (see 4.3.2) The incident angles  $\alpha_u, \alpha_v$  (recall they're track direction angles in the  $u$ - $v$  coordinate system are defined as the angles between the  $z$ -axis and the projection of the track onto  $uz$  or  $vz$  plane.) are easy to compute (Eq. (20) (21) from [38]):

$$1) \tan(\alpha_u) = \frac{\Delta u}{\Delta z} = \frac{u_2 - u_1}{d_u} \quad (5.1)$$

$$2) \tan(\alpha_v) = \frac{\Delta u}{\Delta z} = \frac{v_2 - v_1}{d_v} \quad (5.2)$$

- 3) where  $d_u$  and  $d_v$  are distances between 2  $u$  wire planes or 2  $v$  wire planes.

Crossover coordinates  $u_1, v_1, u_2, v_2$  can be either computed from local cluster fit, or fit of a *link* as described in Section 5.2.1.

- 2) (see 4.3.2) The track direction angles are:

$$1) \tan\theta = \frac{\Delta x}{\Delta z} = \frac{1}{2\cos\alpha} (\tan(\alpha_u) + \tan(\alpha_v)) \quad (5.3)$$

$$2) \tan\varphi = \frac{\Delta y}{\Delta z} = \frac{1}{2\sin\alpha} (\tan(\alpha_u) - \tan(\alpha_v)) \quad (5.4)$$

which are solved from:

$$\tan(\alpha_u) = \tan\theta \cdot \cos\alpha + \tan\varphi \cdot \sin\alpha = \vec{t} \cdot \hat{u}$$

$$\tan(\alpha_v) = \tan\theta \cdot \cos\alpha - \tan\varphi \cdot \sin\alpha = \vec{t} \cdot \hat{v}$$

where  $\alpha \cong \text{atan}(0.5) \cong 26.45^\circ$  is the angle between  $u$ -axis and  $x$ -axis (short axis of wire chamber) of wire plane,  $\vec{t} = (\tan\theta, \tan\varphi, 1)$  is the track direction vector, and  $\hat{u} = (\cos\alpha, \sin\alpha, 0)$ ,  $\hat{v} = (\cos\alpha, -\sin\alpha, 0)$  are unit vector of  $u, v$  axes.

Remark: Note that

$$\begin{pmatrix} \frac{1}{2\cos\alpha} & \frac{1}{2\cos\alpha} \\ \frac{1}{2\sin\alpha} & \frac{-1}{2\sin\alpha} \end{pmatrix} = \begin{pmatrix} \cos\alpha & \sin\alpha \\ \cos\alpha & \sin\alpha \end{pmatrix}^{-1}$$

Which illustrates the relationship between (5.3), (5.4) and the formulas for  $\tan(\alpha_u)$ ,  $\tan(\alpha_v)$ .

- 3) As for track crossover point coordinate on wire plane  $u_1$  ( $x, y$ ):

$$x = \frac{1}{2\cos\alpha} (u + v) \quad (5.5)$$

$$y = \frac{1}{2\sin\alpha} (u - v) \quad (5.6)$$

Here ( $u, v$ ):

$$u = u_1 \quad (5.7)$$

$$v = v_1 - d_{uv} \tan\alpha_v \quad (5.8)$$

Is the  $u, v$  coordinates of track crossover point on wire plane  $u_1$ ,  $d_{uv} = 1(\text{inch})$  is the distance between  $u, v$  wire planes in the same wire chamber. Thus, by set  $\alpha = \text{atan}(0.5) \cong 26.45^\circ$  and  $d_{u1} = 0$ ,  $d_{v1} = d_{uv} = 2.54 \text{ cm}$ ,  $d_{u2} = d_u = 39.4 \text{ cm}$ ,  $d_{v2} = d_{uv} + d_u = 41.9 \text{ cm}$  in the wire chamber database file. The Hall A analyzer will successfully perform track fitting (reconstruction) for our wire chamber data. Equations (5.1) to (5.8) are all we need to solve ( $x, y, \tan\theta, \tan\varphi$ ) from ( $u_1, v_1, u_2, v_2$ ) for track reconstruction.

A simple geometric derivation of formula (5.3) to (5.6) presented in Appendix 5.2.1.

### 5.2.3 Effect of cuts on track fitting

The goal of cosmic ray test runs is to confirm that the wire chamber and analyzer produce accurate tracking results and have a high enough efficiency. The simple definition of analyzer efficiency:

$$Eff = \frac{\text{Number of events have track(s)}}{\text{Number of triggered events}} \quad (5.9)$$

is not meaningful if the fitted tracks are inaccurate. In addition, if we apply additional cuts the number in the numerator will decrease while denominator stays the same, and the efficiency also decreases. It should be noted that the triggered events do not always correspond to events in which a track intersects all four wire planes. For example, a track could miss one wire chamber but hit the other and the trigger scintillator. As a result, we still have a triggered event but no tracks *should* be found. To cope with this, we set up a new set of triggers using scintillators with a lot stricter geometric constraints. Such a trigger greatly increases the chance for a track to be real, and narrows down possible track positions and directions. In addition, if we measure and calculate geometric constraints on such a trigger, issues in the analyzer track reconstruction can be observed if the reconstructed tracks fails to pass these constraints. This trigger setup will be discussed in next section 5.3.

Besides the change in the denominator of (5.9) by changing trigger setup, we can also apply cuts on both denominator and numerator. For example, the tracks from BH experiment only have certain range of directions, so it limits the cluster spans, e.g., we shouldn't worry about tracks reconstructed from clusters with 20 wires. Thus, if apply cut, for example "u wire plane cluster size equals 5" on both denominator and numerator, the resulting conditional efficiency is a lot more meaningful.

Various cuts can change the result of all steps in the tracking, and have an impact not only on tracks being found but the results of the fit  $(x, y, \tan\theta, \tan\varphi)$  as well. We have already introduced certain cuts in previous chapters; for instance, cuts on cluster finding in 3.5.2, cuts on geometry of trigger in 4.3.5 2. These will certainly change the final track fitting result. The only cuts that need to be added here are on geometrical constraints. First, the analyzer treats all wires as having infinite length. Thus, (see Fig. 5.1) even the crossover point coordinate (e.g. on the  $u_1$  wire plane is  $(u, v) = (u_1, v_1 - d_{uv}\tan\alpha_v)$  in  $u, v$  coordinate system, or  $(x, y) = (\frac{1}{2\cos\alpha}(u + v), \frac{1}{2\sin\alpha}(u - v))$ ) can lie outside of the active area of wire plane. A track which does not cross the wire plane will still be computed. Thus, a cut on  $(x, y)$  for all 4 wire planes should be added to limit the boundary of track. Second, if we use the more constrained trigger, we have to add a cut requiring that the reconstructed track's crossover point on all wire planes is also within the projection of the trigger.



## 5.3 Test run setup

The only setup change compared to the preparation discussion in the hardware chapters is the placement of trigger scintillator, we only discuss trigger setup in this section. As was introduced previously, the goal is to constraint the geometry such that the range of straight lines within all triggers is so limited that we can be almost certain that the coincidence of all triggers having signals indicates the existence of a track. As a bonus, the triggers are purposely placed such that the track fitting result is much easier to be analyzed due to its simple geometry. The physical setup of trigger is discussed in 5.3.1 and the geometry of the trigger is discussed in 5.3.2. In the next section, 5.4, track reconstruction results are compared with the projection of the trigger scintillators on each wire plane.

### 5.3.1 Trigger setup

#### 1) Placement of trigger scintillators:

We have 8 tested and gain-matched thin scintillator paddles with lengths and widths of about 70 *cm* by 11 *cm*. Six of them are placed above the top wire chamber, with one vertically above the center line of the long axis of the wire chamber. The other 5 lie below this paddle, oriented perpendicular to it (so they're parallel to the short axis of the wire chamber), and touching each other. Two other thin paddles are placed above the bottom wire chamber, oriented perpendicular to each other, and parallel to the long and short axes of wire chamber respectively, and vertically above center line. Since the thin paddle has a small area, a medium sized scintillator was placed above bottom chamber as a trigger paddle.

#### 2) Trigger logic:

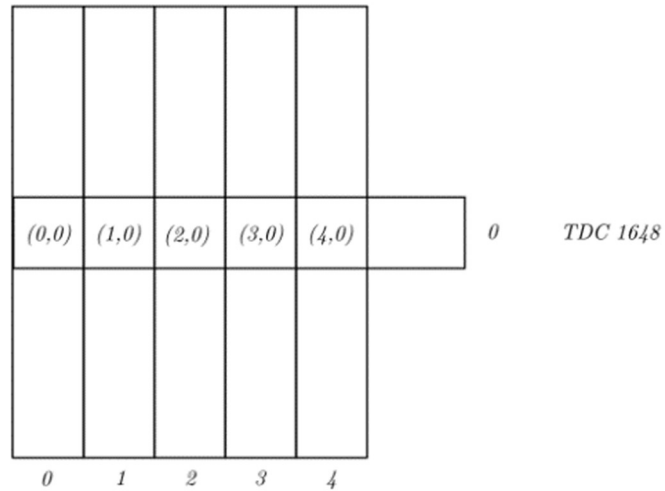
The 5 parallel scintillators on top of the top wire chamber comprise the trigger paddles; any one of them firing is considered a top trigger. The medium sized scintillator is the only trigger paddle on the bottom. An event is triggered and will be analyzed only when both top and bottom triggers fire. The active scintillation area for the top one is about 55 *cm* by 70 *cm* along the long and short axes of the wire chamber, respectively. The bottom scintillator is about 70 *cm* by 30 *cm*.

#### 3) Reference trigger logic:

A pair of perpendicularly oriented thin scintillator paddles above one wire chamber are touching each other on their largest surfaces, the shared area is a square shaped planar region with area 11 *cm* by 11 *cm*. Two of such pairs, one on the top chamber and one on bottom chamber allow only straight lines intersecting two 11 *cm* by 11 *cm* squares to constitute a reference trigger with a strict geometrical constraint. Five pairs on the top chamber are labelled as (0,0), ..., (4,0), the only pair on bottom chamber is labelled as (0,0). Thus, 5 combinations of a top square to bottom square shaped area firing is considered as a reference trigger. Each of those paddles are linked to a separate TDC module and the logic applied to the replayed ROOT file can implement reference trigger logic. As an example, if we want trigger top (2,0) to bottom (0,0) the pseudo code is: (Top (2,0) hit) AND (Top (0,0), (1,0), (3,0), (4,0) not hit) AND (Bottom (0,0) hit). The "not hit" is necessary. Since there're such a possibility that in a multi-track event, which is very common from a shower during our cosmic rays test runs, track 1 triggers top (2,0) but misses bottom (0,0),

track 2 triggers top (1, 0) and also bottom (0,0), then both top (2,0) hit AND bottom (0,0) hit but there is no valid track through both top (2,0) and bottom (0,0) reference trigger square areas. The schematic diagram of the reference triggers is shown in Fig. 5.2, the top and bottom scintillator placement photos are shown in Fig. 5.3 and Fig. 5.4, respectively.

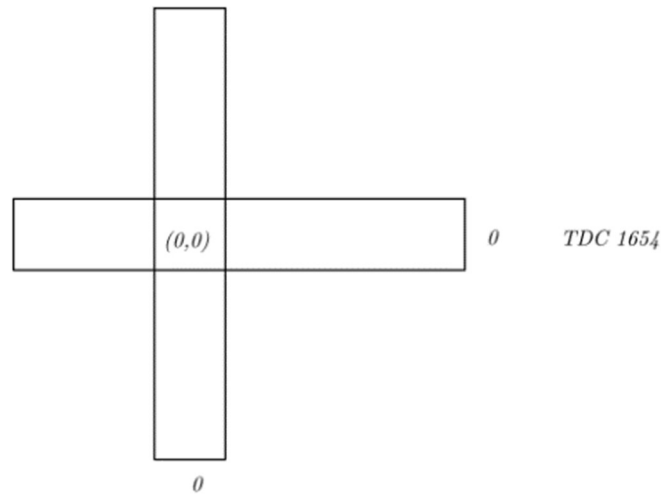
*Top paddles*



*TDC channel*

1632 1633 1634 1635 1636

*Bottom paddles*



*TDC channel*

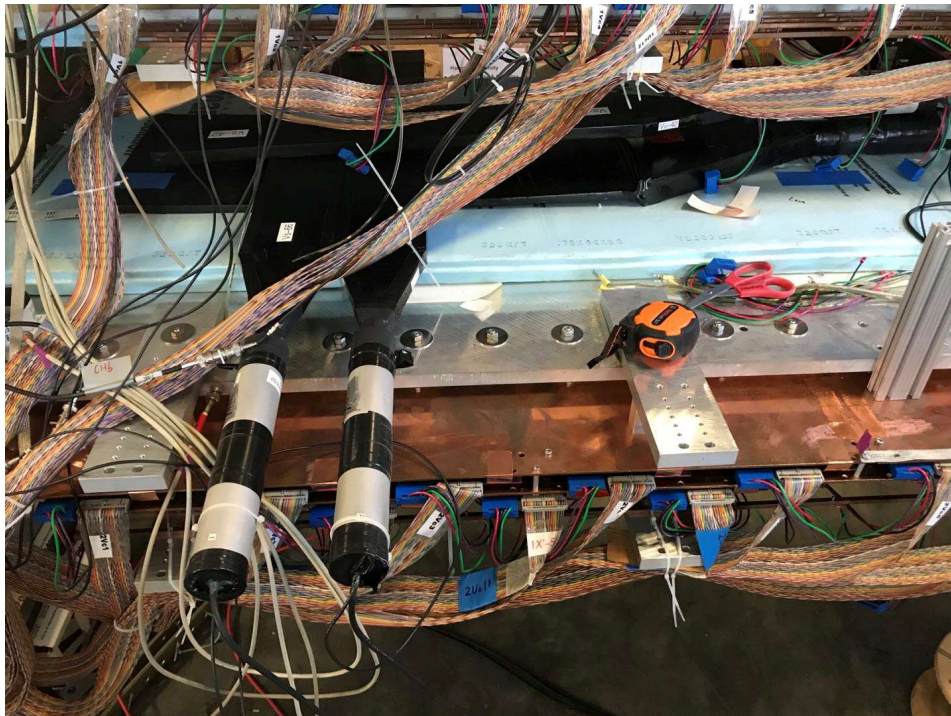
1652

*All rectangles 11 cm x 70 cm*

III Fig 5. 1 Thin scintillator paddles labeling conventions and their channels on TDC.  $(0,0)$  ...  $(4,0)$  indexing trigger with square shaped common area from left to right, 1st number indexes scintillators lie parallel to short axis of wire chamber, 2<sup>nd</sup> number indexes the only scintillator parallel to long axis of wire chamber.



III Fig 5. 2 Upper chamber trigger and reference scintillators.



III Fig 5. 3 Bottom chamber trigger and reference scintillators.

Only the one in the middle (within vertical projection from (2,0) trigger paddles on upper chamber) is linked to reference channel in TDC.

### 5.3.2 Trigger geometry, projection on wire planes

In this section, we are approximating all possible tracks through a fixed reference trigger by considering projection of two parallel squares in space. The contents include:

- 1) Establish some properties of such projection and identify the shape and dimension of projection on any plane parallel to these two squares.
- 2) Numerically compute the projections on each wire plane, and draw an event-by-event display.
- 3) Additional calculation of ranges of track angle ( $\theta = \text{atan}(\frac{\Delta x}{\Delta z})$ ,  $\varphi = \text{atan}(\frac{\Delta y}{\Delta z})$ ).
- 4) Properties of projection.

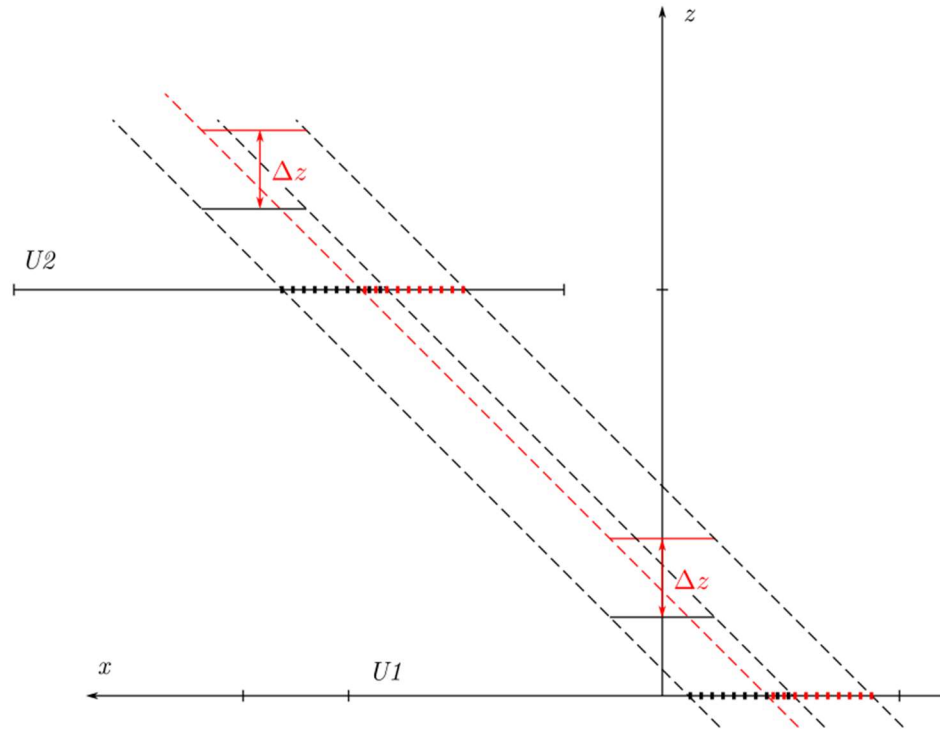
There are a few approximations to make:

- (1) Squares as shared surface regions of two oriented perpendicular thin scintillator paddles are parallel, and they also parallel to all wire planes.
- (2) The sides of any pair of squares are considered parallel to each other.

Now back to properties of projection:

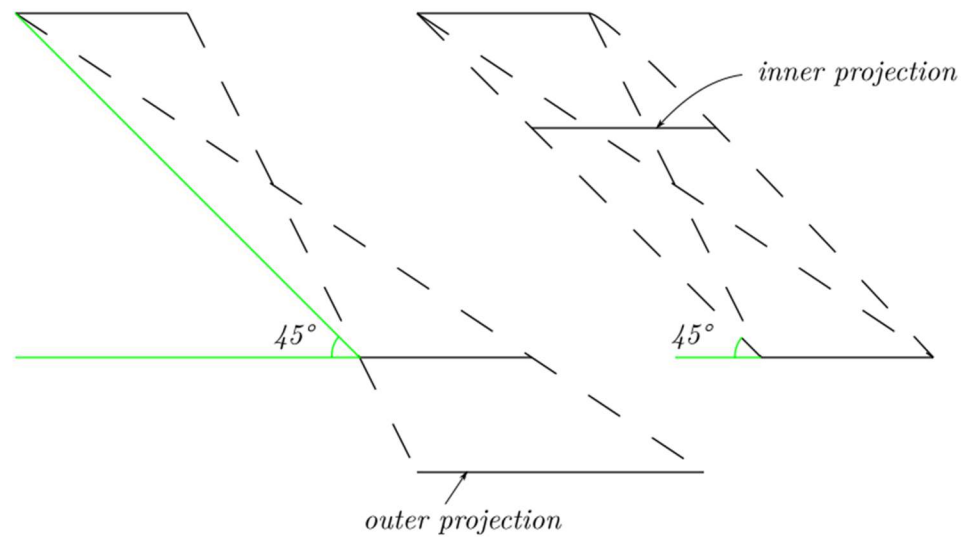
- (1) Placing paddles above wire chambers means they are shifting in the  $z$  direction in the analyzer coordinate system. If both planes of paddle squares (one lies above top chamber, one lies in between top and bottom chambers) shift in the  $z$  direction by  $\Delta z$ , the parallel projections of those squares will shift in  $x$  direction by  $-\Delta z$ . See Fig 5.5 for an illustration.
- (2) The shape of projection on any plane parallel to those two planes containing a square each. First the boundary of projection from two parallel squares should be lines linking from boundary of one square to boundary of the other square. Consider drawing a straight line from one side of one square to one of two sides which are parallel to it on the other square, the projection of all these straight lines on any plane parallel (wire planes as a special case) to the squares is also a straight line which is parallel to any sides of the square considered. Those projected straight lines meet each other at projections of corners of the squares, so the projection boundary is at least rectangle in shape. As for the length of sides, since the two planes containing squares and the plane considered for projection are all parallel, any ratio in length is the same no matter whether it is in the  $x$  or  $y$  direction. Thus, the boundary of a projection from two squares is always a square. (Fig. 5.6 and Fig. 5.7)

- (1) If the projected plane is a plane parallel and between the planes of squares, the boundary is determined by lines linking corresponding top and bottom square sides. Thus, the projection is square with same dimensions as a square from shared area of trigger paddles. This applies to the projection on the top chamber wire planes. (Fig 5.6, Right sketch)
- (2) If the projected plane is a plane parallel but lies above the top square or below bottom square, the boundary is square with corners determined by linking diagonal corners of squares of trigger paddles. They are always bigger than the original squares; the further away from original squares the larger the projected square. This applies to projection on bottom chamber wire planes. (Fig. 5.6 Left sketch and Fig. 5.7)



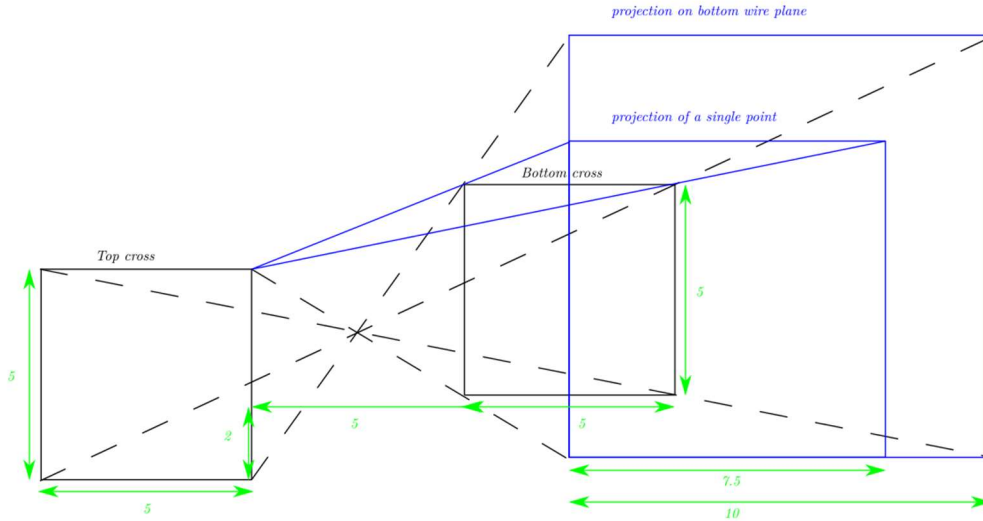
III Fig 5. 4 Z positions of paddles affect projection locations on wire planes.

Illustrated in  $x$ - $z$  projection in analyzer coordinates. A pair of square shaped paddle shared areas and their projections by linking corresponding sides on  $u1$  and  $u2$  wire plane. Two configurations are drawn in black and red lines. Both red squares are shifted in the  $z$  direction by  $\Delta z$  from the black squares, leading to a  $-\Delta z$  shift in the  $x$  direction on the wire planes.



III Fig 5. 5 Outer and inner projection boundaries.

Left: Outer projection is bounded by diagonal lines, and size is bigger than the original squares.  
 Right: Inner projection is bounded by parallel lines, and size is equal to the original squares. No matter which case, their solid angle coverages of tracks are the same.



III Fig 5. 6 Projection of a square should be also a square.

. The example here, suppose  $z = 0, -5, -7.5 \text{ cm}$  for top cross square, bottom cross square, and projected plane. Top and bottom cross both with side length  $5 \text{ cm}$ . Then, the square on the projected plane is of side length  $10 \text{ cm}$ . Since it is an outer projection (see Fig. 5.6 Left), the projected square is larger than the original squares and its corners are determined by linking diagonal corners of the two original squares, illustrated by black dashed lines. The projection of a single point is also a square. From the same assumption, the projection of a single point is a square with side length  $7.5/5 = 1.5$  times the original square side length. The projection of upper right corner of top square is drawn.

2) Numerically compute the projections on each wire plane, and draw in event-by-event display. What we need for calculating the boundaries of projection of trigger square areas are:

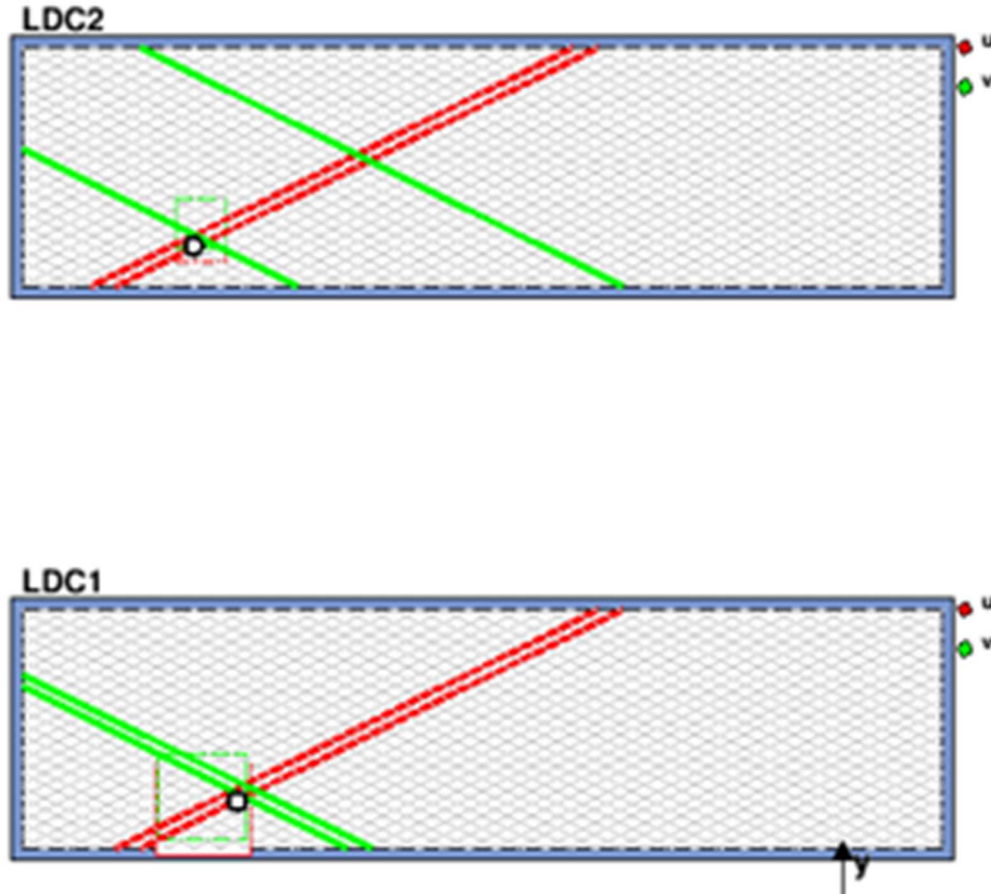
- (1)  $z$  coordinates of each wire plane, which are documented.
- (2)  $z$  coordinates of both top and bottom scintillators common square areas.
- (3)  $x, y$  coordinates of 4 corners of each square in (2).

For  $x, y$  coordinates of corners scintillators' common square areas, we measured them from lower left corners of wire chambers, then converted to  $(x, y)$  with center of the wire chamber as the origin. For  $z$  coordinates of scintillators, we can only measure their height above wire chamber, add half wire chamber height depth to find center plane of wire chamber first, then take offsets of sense wire planes  $z$  coordinate into consideration. The numerical calculation of square projection on each wire plane from trigger is straight forward (see Fig. 5.6):

- (1) For top chamber wire planes  $u_2, v_2$ , their projected square is computed by linking a straight line through corresponding corners of trigger squares. (Fig. 5.6 Right, inner projection)
- (2) For bottom chamber wire planes  $u_1, v_1$ , their projected square is computed by linking a straight line through diagonal corners of trigger squares. For instance, upper left corner (see in  $x, y$  projection) of square from upper trigger square to lower right corner of lower trigger square. (Fig. 5.6 Left, outer projection)



The intersection of those straight lines on each wire plane are the corners of projected squares. For visualization, draw polyline (TPolyLine in ROOT) in the Hall C Event display to indicate boundaries of projected squares on each wire plane, only for (2,0) trigger. Crossover points of reconstructed tracks by analyzer on each wire planes are examined to see whether they are inside projected squares. It is illustrated in Fig. 5.8.



III Fig 5. 7 Hall C event display of a good event.

LDC 2 is top wire chamber, LDC1 is bottom wire chamber. LDC2 is the top wire chamber, LDC1 is the bottom wire chamber. The highlighted lines are hit wires (one drawn wire represents 5 real wires), with red lines for  $u$  wires and green lines for  $v$  wires. Green and red squares are projected squares on  $u$  and  $v$  wire planes, respectively. Black dots are reconstructed track intersection on  $u$  wire planes. Thus, for a valid track, black dots should lie within green squares.

3) Additional calculation of ranges of track angles. As seen in Fig. 5.6, the outer projection will cover a larger track direction angular range. Thus, we compute:

$$\theta = \text{atan}\left(\frac{\Delta x}{\Delta z}\right), \varphi = \text{atan}\left(\frac{\Delta y}{\Delta z}\right) \quad (5.10)$$

from straight lines linking diagonal corners of trigger squares.

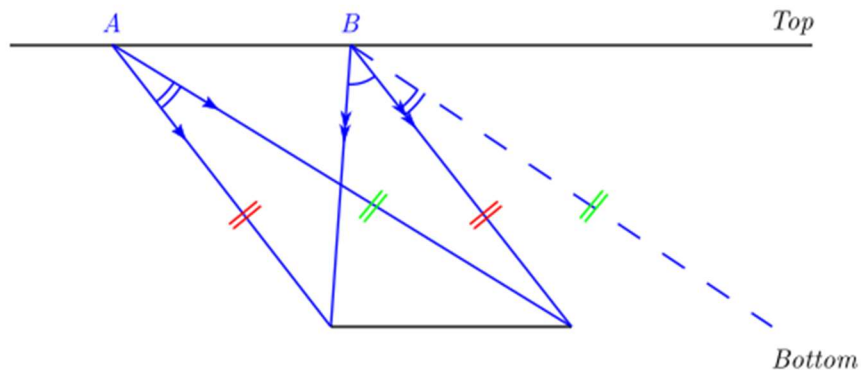
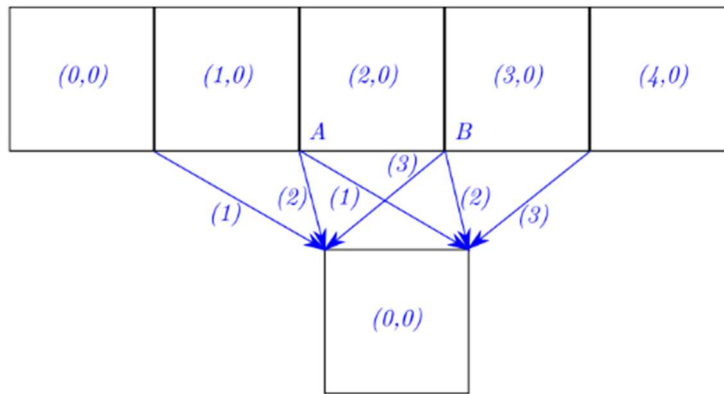
(1) It should be noted that all squares on the top are aligned in the  $x$  direction, and thus the range of  $\Delta x$  is the same for all triggers from (0,0) to (4,0). The measured range of  $\theta$  is  $[37.5^\circ, 53.6^\circ]$  for all triggers.



(2) The range of  $\varphi$  for different trigger are different but there have overlaps between adjacent trigger. From trigger (0,0) to trigger (4,0) the ranges of  $\varphi$  are:

Trigger	(0,0)	(1,0)	(2,0)	(3,0)	(4,0)
$\varphi$ range	[17.2°, 42.0°]	[0.8°, 31.2°]	[-15.8°, 17.2°]	[-30.0°, 0.8°]	[-41.2°, -15.8°]

There is a pattern here: for every trigger  $(i,0)$ , its lower limit of range of  $\varphi$  equals upper limit of range of  $\varphi$  in trigger  $(i + 2,0)$ . The common angles are 17.2°, 0.8°, and -15.8°. This can be seen in Fig. 5.9 below; the diagonal line going from the upper (0,0) trigger to the lower right corner is parallel to the diagonal line going from the upper (2,0) trigger to the lower left corner. The parallel lines are marked by (1), (2), and (3) in Fig. 5.9 Left. Another important observation from Fig. 5.9 is that in order to make the range of  $\varphi$  completely disjoint, we have to skip one trigger. This can be seen from Fig. 5.9 Right.



III Fig 5. 8 Angle ranges for individual scintillator trigger telescopes.

Up: Pairs of parallel diagonal straight lines link corners of trigger squares which have the same  $\theta$  and  $\varphi$  (in order words, they're parallel), indicated by (1), (2), and (3).

Down: The indicated points A and B are just disjoint in the  $\varphi$  range. Seen from the left figure, point A is the lower right corner of the square from upper trigger (1,0), and point B is the lower left corner of the square from the upper trigger (3,0). Thus, the  $\varphi$  range trigger (0,0) and (2,0), trigger (1,0) and (3,0), trigger (2,0) and (4,0) are just disjoint.

## 5.4 Track fitting results

### 5.4.1 Track geometry result

#### 1) Track crossover point on wire planes

Since reconstructed tracks are straight lines, we don't need to draw tracks in 3 dimensions.

Instead, the crossover points  $(x, y)$  coordinate on wire plane  $u_1, u_2$  are drawn. The Fig 5.10 below shows the distribution of  $(x, y)$  coordinate on wire plane  $u_1, u_2$ . We can extract following information:

(1) The active area of the wire chamber. Since only 183 channels out of 279 of all wire planes have been connected to TDC, only partial area of each wire plane would have reconstructed tracks covering. As seen in Fig 5.10, these area covers left side of the wire planes, with a "pencil" shape. (Also see the common area of U and V wires in Fig 2.9)

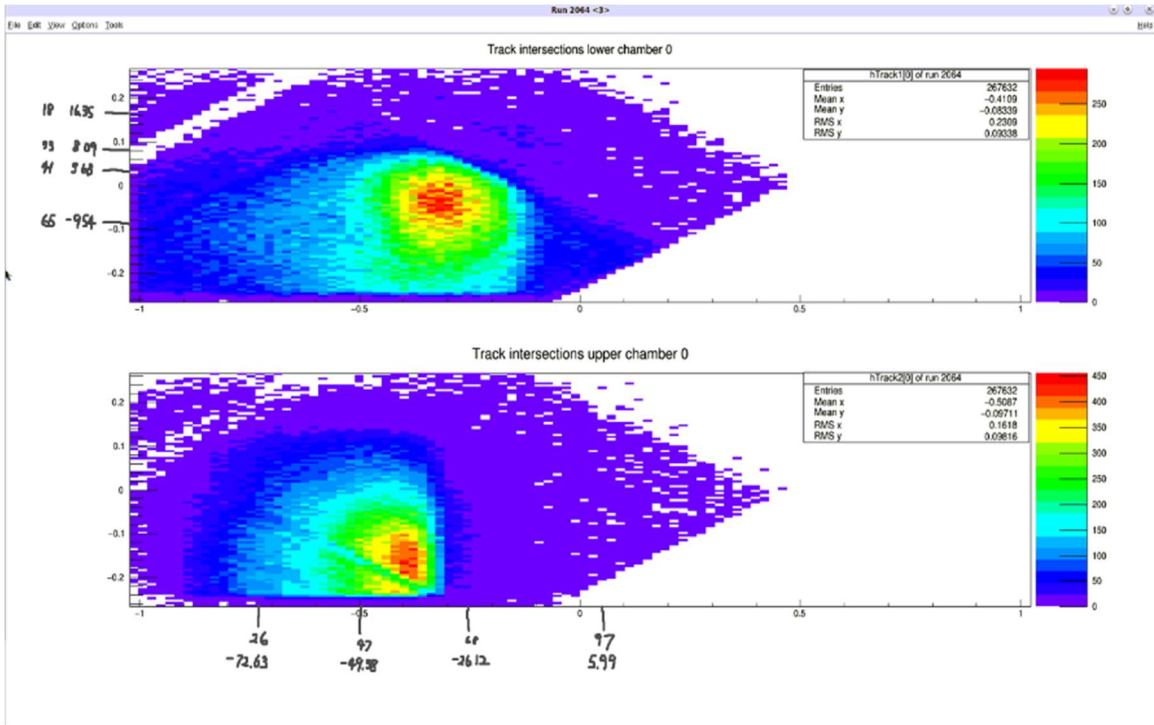
Let's estimate the location of the apex point of the "pencil" shape. Centers of wire planes are their origins. Note  $x$  axis is the short axis of the wire chambers and point up. Due to same amount of  $u, v$  wires implemented, based on symmetry:

$$x = 0(cm)$$

For the abscissa in Fig 5.10 is  $-y$  and its estimation is:

$$\begin{aligned} -y &= \left[ (80.5 + 21/\tan(\text{atan}(0.5))) \times \frac{183}{279} + 21 - 42 - \frac{80.5}{2} \right] (inch) \\ &= 48.5(cm) \end{aligned}$$

Here 80.5 *in* and 21 *in* are the length and width of the wire chamber and  $\text{atan}(0.5)$  is the angle between wires and the  $y$  axis in the wire plane. The estimation is very close to the apex point of the "pencil" shape in Fig. 5.10.



III Fig 5. 9 Crossover point ( $x' = -y, y' = x$ ) of all tracks in wire plane  $u_1$  (lower chamber, upper histogram) and wire plane  $u_2$ . Ordinate: short axis coordinate of wire plane in  $m$ , abscissa: long axis coordinate of wire plane in  $m$ .

Wire plane  $u_1$  (lower chamber, upper histogram) and (upper chamber, lower histogram). It's proportional to real wire plane shape.  $(x', y')$  is abscissa and ordinate of the histogram, and  $(x, y)$  are the horizontal coordinates in the analyzer coordinate system. The apex point location where the last active wires from both  $u, v$  wire planes meet is estimated above. The numbers on the sides below the upper chamber histogram are pairs indicating  $(n, x')$  as wire index and  $x'$  as coordinate of where bad  $v$  wires intersect the lower side of the wire plane in the figure. Similar numbers are placed on the left of lower histogram to indicate bad  $u$  wires on the lower chamber.

(2) There exist wires without TDC data. There are some straight strips in the histograms with much less hit frequency compared to their neighboring regions. These are caused by wires with no TDC data. The causes of no TDC data could be any disconnect between the wire chamber and the TDC, bad channels on discriminator cards or on TDC modules, etc. It is hard to eliminate all of them since they can also be caused by the threshold voltage of discriminator cards, which are uniformly applied to all cards of each wire plane. If the bad wires are located in a region where the wire is short, or the hit frequency is low, e.g. wires 33 to 41, then they won't affect the experimental result much due to the low hit density and small area the wires covered. On the other hand, if a bad wire with longest length is in a high hit density region, the loss of its drift time information could cause significant loss in track fitting efficiency.

An example of finding bad wires intersection coordinate on wire plane boundary:  $u$  wire planes, if using the same coordinate system in histogram  $((x, y)$  here is  $(x', y')$  in Fig. 5.10 description):

$$\vec{r} \cdot \hat{u} = -x \sin \alpha + y \cos \alpha = (140 - N) \cdot WS \tag{5.11}$$

Where  $\hat{u} = (-\sin \alpha, \cos \alpha), \alpha = \text{atan}0.5 \cong 26.45^\circ$ , 140 is half number of wires in each wire plane rounded up,  $N$  is the bad wire index (1 to 279) counting from upper left corner of  $u$  wire

planes, and  $WS = 0.493 \text{ cm}$ . Solve for the  $y$  coordinate from (5.11) where the bad wire intersects the left boundary of the wire plane:

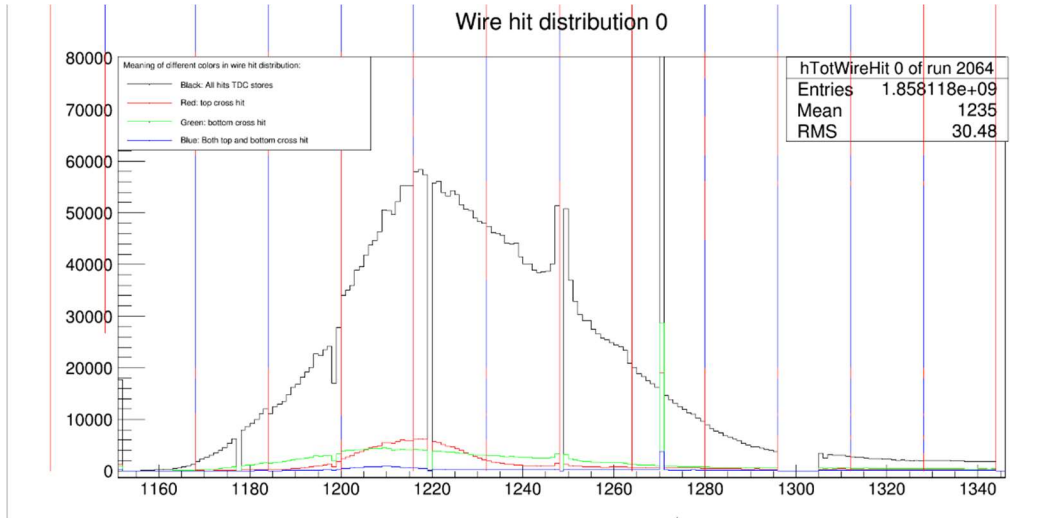
$$\begin{cases} y = xtana + \frac{(140-N) \cdot WS}{cosa} \\ x = -\frac{80.5}{2}(\text{inch}) = -102.235 \text{ (cm)} \end{cases} \quad (5.12)$$

The results of the lower chamber  $u$  wire plane bad wires are shown in Fig. 5.10 upper histogram. For  $v$  wire planes:

$$\vec{r} \cdot \hat{v} = -x\text{sin}\alpha - y\text{cos}\alpha = (140 - N) \cdot WS \quad (5.13)$$

where  $\hat{v} = (-\text{sin}\alpha, -\text{cos}\alpha)$ ,  $\alpha$ , 140, and  $WS$  are the same as for the  $u$  wire planes.  $N$  is the bad wire index (1 to 279) counting from lower left corner of  $v$  wire planes. Solve for the  $x$  coordinate from (5.13) where the bad wire intersects the left boundary of the wire plane:

$$\begin{cases} x = -y\text{cot}\alpha - \frac{(140-N) \cdot WS}{\text{sin}\alpha} \\ y = -\frac{21}{2}(\text{inch}) = -26.67(\text{cm}) \end{cases} \quad (5.14)$$



III Fig 5. 10 Upper  $v$  plane hit index distribution. Ordinate: counts, no unit, abscissa: TDC channel number, no unit.

Bad wire indices  $N$  (1 to 279) from lower left corner shown in lower histogram of Fig 5.10 are 26, 47 (low efficiency), 68, and 97. The channels indexed in this histogram start with  $192 \times 6 - 1 = 1151$ .  $1151+26=1177$  is the wire with empty hit in this histogram, same check applies for other bad wires.

## 2) Confirm by projective geometry

As discussed in 5.3, we placed trigger scintillators in specific locations. The projection from the trigger paddles on each wire plane is computed (see 5.3.2 and Fig. 5.7). We expect for events that trigger all 4 scintillators for a specific trigger and also not trigger other scintillators (see 5.3.1) tracks should intersect each wire plane inside the projection of the trigger paddles. As a reminder, we restate the cut used to constrain our track geometry:

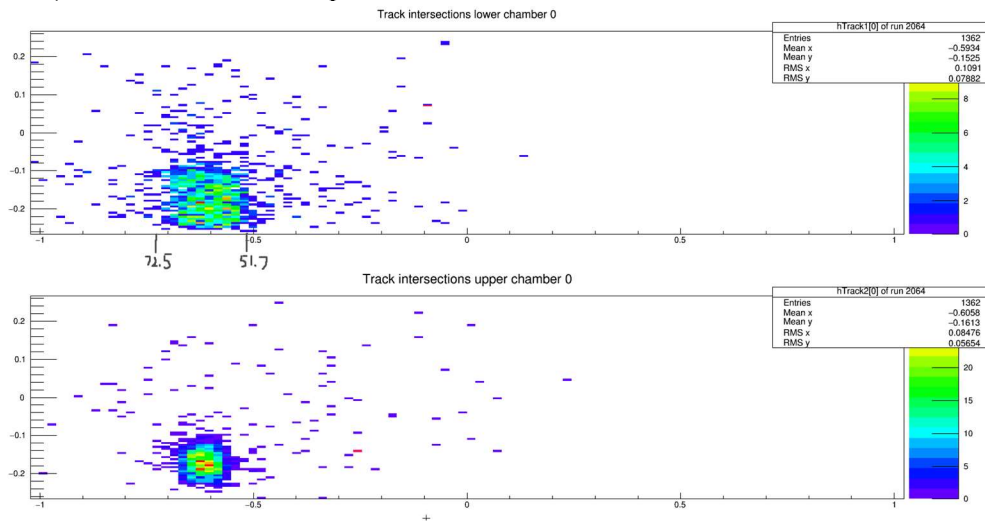
$$\begin{aligned} &(\text{Top } (2,0) \text{ hit}) \text{ AND } (\text{Top } (0,0),(1,0),(3,0),(4,0) \text{ not hit}) \\ &\text{AND } (\text{Bottom } (0,0) \text{ hit}) \end{aligned} \quad (5.15)$$

The check procedure is simple: apply trigger cuts for the replayed ROOT file, draw  $(x, y)$  histogram of track crossover points on wire plane, one from each wire chamber is enough, then check if  $(x, y)$  points in the histogram are within the projected squares from the geometrically constrained trigger. The result is shown in Fig 5.11 where we only marked the lower wire plane long axis coordinates with limits of the trigger projection.

Remarks:

1. The placement of trigger paddles can greatly reduce the chances that a multi-cluster event with one track through the top trigger but none in the bottom trigger, while another track has one track through bottom trigger but none in the top trigger. One way of applying a cut to reduce such events is to require other scintillators in the same layer to not have a hit, which is shown in (5.15). However, only the top layer has multiple scintillators to apply such a cut. Therefore, such multi-track events still exist. Fig 5.11 includes such multi-track events, so still a noticeable portion of track crossover points are outside the trigger projection.
2. There are discrepancies between the area covered by accumulated track crossover points on wire planes and trigger projections. The following causes of this discrepancy are:

1. Planes not being parallel; especially bottom trigger scintillators, due to the tilt of medium sized trigger paddle.
  2. Sides of squares not being parallel due to lack of a precision alignment tool. Thus, paddles are not perpendicular to each other and the geometry is irregular.
  3. Measurement error.
  4. The lack of location information of the relative locations of wire planes inside the wire chamber frame.
3. Due to the effect shown in Fig 5.5, the trigger projection on the bottom wire chamber is partially outside of wire plane active area. One suggestion regarding changing the positions of the crosses: move the paddles in the  $+x$  direction by about  $19.1\text{ cm}$ , then in the  $x$  direction, the projected square will lie somewhere on the center line of the wire planes. (i.e. the centers of the squares in the distribution below will shift to 0 in ordinate)



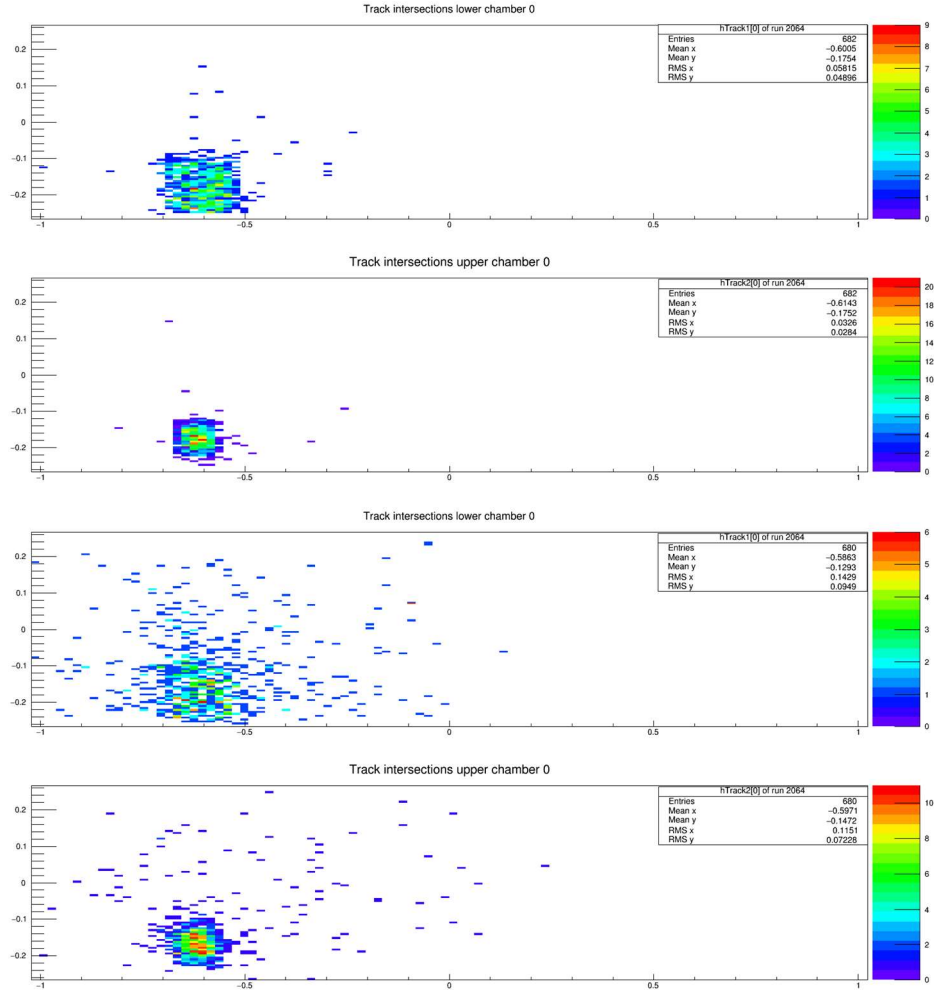
III Fig 5. 11 Track crossover point distribution ( $x' = -y, y' = x$ ) on  $u$  wire planes. Ordinate: short axis coordinate of wire plane in  $m$ , abscissa: long axis coordinate of wire plane in  $m$ .

Dimensions are in meters. The trigger cut is for the combination (2,0) (0,0) (see Fig. 5.2). The numbers below the upper histogram are the marked ranges of squares computed from outer projections (see Fig. 5.6 and Fig. 5.7) based on measured trigger locations. Most of the points are contained in squares, as predicted in 5.3.2.

#### 4. Additional cuts suggestion:

- (1) Use the number of clusters in each wire plane to isolate single track events. The cut should be: at least one wire plane contained only one cluster, and the others found at most two clusters.
- (2) Cluster spans of clusters in  $u$  wire planes and in  $v$  wire planes. This will be discussed later.

An improvement to Fig 5.11 is the separation of single-cluster events from all other events. The results are shown below in Fig 5.12 for crossover point coordinate distributions on  $u$  wire planes and in Fig 5.13 for cluster span distributions for all wire planes.



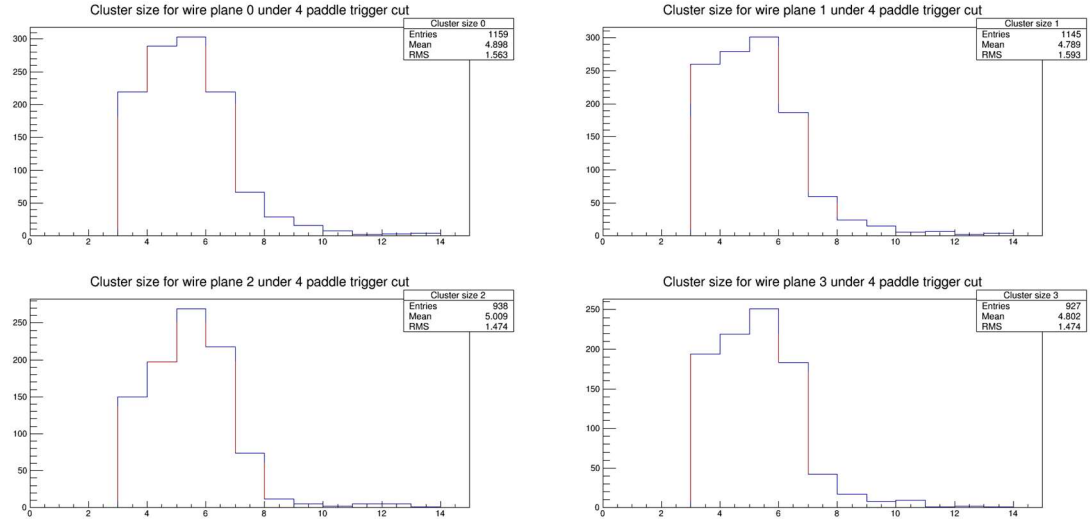
III Fig 5. 12 Separated crossover points coordinate distributions. Ordinate: short axis coordinate of wire plane in  $m$ , abscissa: long axis coordinate of wire plane in  $m$ .

On  $u$  wire planes Fig 5.12, separated by conditions:

- (1) only single-cluster event in top 2 plots.
- (2) all other events (all wire planes have cluster, and at least one wire plane has more than one cluster) in bottom 2 plots.

The top two plots have very distinct square shape boundaries with fewer than 30 tracks out of 682 out of square region. The bottom two plots contain events with multi-tracks. Due to the effect in remark (1) above, some events in these plots have tracks through only one side of the trigger but miss the other side, resulting in points outside a square region.





III Fig 5. 13 Cluster span distribution for all wire planes. Ordinate: counts, no unit, abscissa: cluster size of the corresponding wire plane, no unit.

For top 4 and bottom 4 histograms respectively:

- (1) only single-cluster events in top 4 histograms.
- (2) all other events (all wire planes have cluster, and at least one wire plane has more than one cluster) in bottom 4 histograms.

For a group of 4 histograms, left two are  $u$  wire planes cluster spans and right two are  $v$  wire planes cluster spans. As seen many times, the relationship between (non-integer) cluster span relationship to track angle in  $u, v$  coordinates  $n_{u/v} = \frac{h}{|s \times \tan(\delta_{u/v})|}$  (see formula (3.3)). We expect the (integer) cluster spans for wire planes with same orientation to have similar distributions, which has been confirmed here. The top 4 histograms have a much more constraining cluster span distribution since the clusters correspond to tracks with constrained geometry. The bottom 4 histograms have more spread in cluster span due to tracks being outside the constrained region, and there being clusters not belonging to the same track or simply being due to noise.

## 2) Simulation checking track direction angles $(\theta, \varphi)$ and cluster span $(n_u, n_v)$

A simple simulation was conducted to check the track incident angles and cluster spans by dividing trigger squares into smaller equally spaced squares, linking every possible center of one top smaller square to one bottom smaller square, and using measured data for the relative locations of the squares. The  $(\theta, \varphi)$  distribution of the results of the simulation is shown in Fig. 5.13, and the  $(\theta, \varphi)$  distribution of the data in the replayed ROOT file from a test run is shown in Fig. 5.14. The shape of the dense angular regions and average values are quite similar. The major factors generating discrepancies come from:

- (1) The difference of idealization of considering tracks bounded by two squares with the same size parallel to each other in space; see 5.4.1, 2 and remark 2,
- (2) The simulation generated direction angular distribution is different from the cosmic ray test run counterpart.

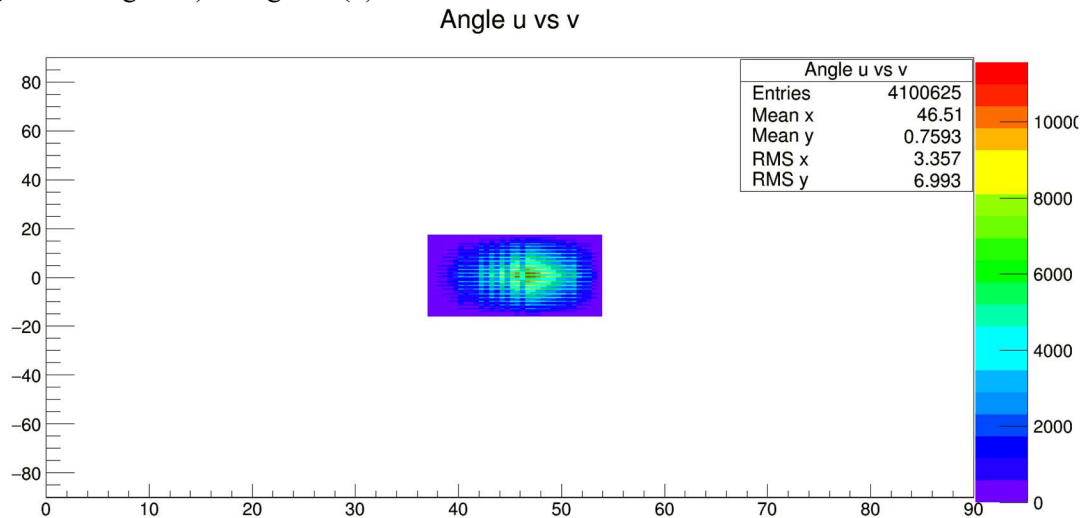
Simulated cluster spans  $(n_u, n_v)$  distributions are generated from converting track direction angles  $(\theta, \varphi)$  to track incident angles  $\alpha_u, \alpha_v$  in  $uz$  and  $vz$  plane by formulas below (5.4):

$$\begin{aligned} \tan\alpha_u &= \tan\theta \cdot \cos\alpha + \tan\varphi \cdot \sin\alpha \\ \tan\alpha_v &= \tan\theta \cdot \cos\alpha - \tan\varphi \cdot \sin\alpha \end{aligned}$$

Then (modified formula (3.3))

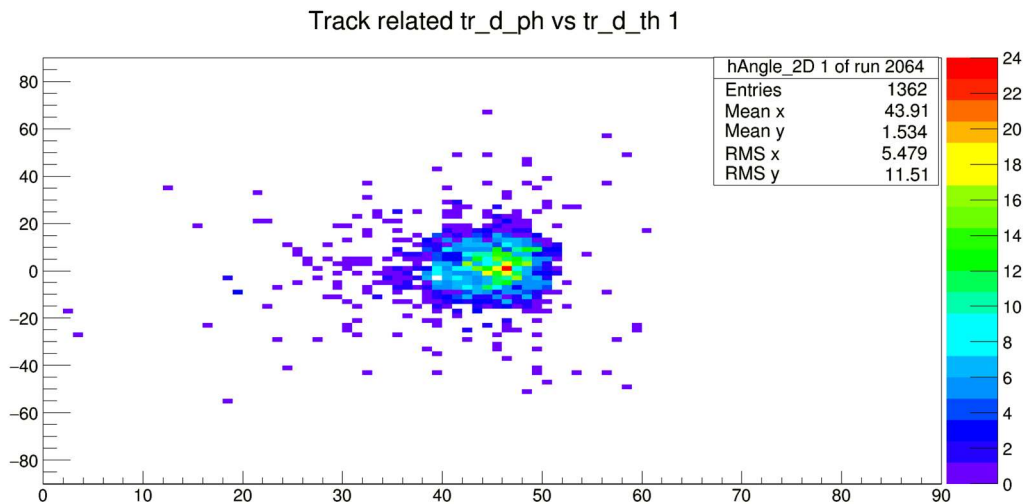
$$n_u = \frac{|h \cdot \tan\alpha_u|}{s} \text{ and } n_v = \frac{|h \cdot \tan\alpha_v|}{s}$$

The 2D  $(n_u, n_v)$  distribution is shown in Fig. 5.15 and the individual 1D  $n_u, n_v$  distributions from the simulation are compared with the single-cluster events  $n_u, n_v$  distribution (upper histograms in Fig 5.13) in Fig 5.16(2).



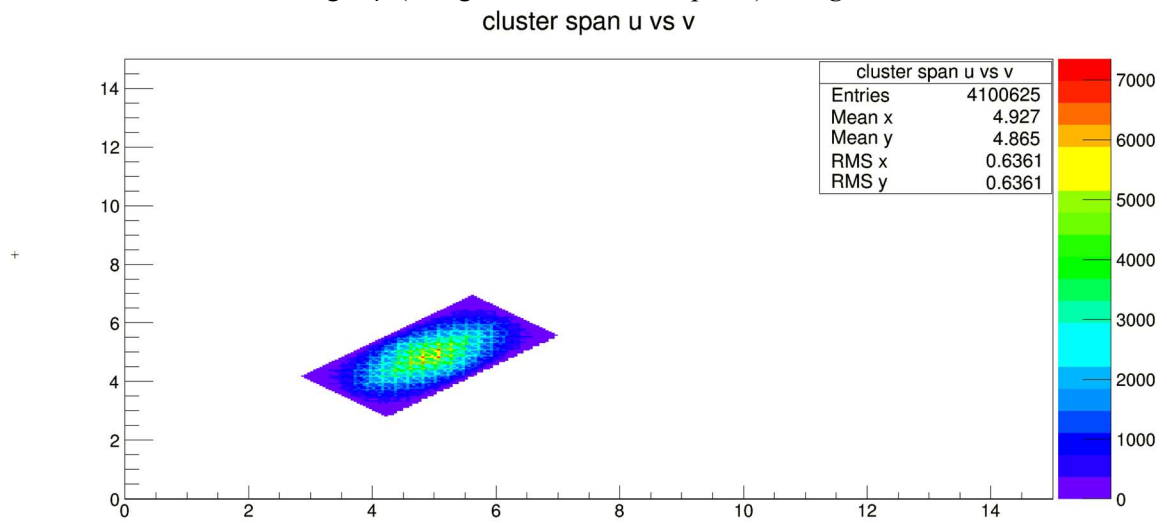
III Fig 5. 14(1) Simulated and test run cluster span  $(\theta, \varphi)$ . Ordinate: simulated track direction angle  $\theta$  (track projection angle along short axis of wire plane) in *degrees*, abscissa: simulated track direction angle  $\varphi$  (track projection angle long axis of wire plane) in *degrees*.

Simulated track direction angle  $(\theta, \varphi)$  (angles in degrees for track direction vector  $\vec{t} = (\tan\theta, \tan\varphi, 1)$ ) distribution. The trigger square location based on measured  $(2,0)$  trigger. See table 5.1 for ranges of  $\theta$   $[37.5^\circ, 53.6^\circ]$  and  $\varphi$   $[-15.8^\circ, 17.2^\circ]$  which match the purple square region here.

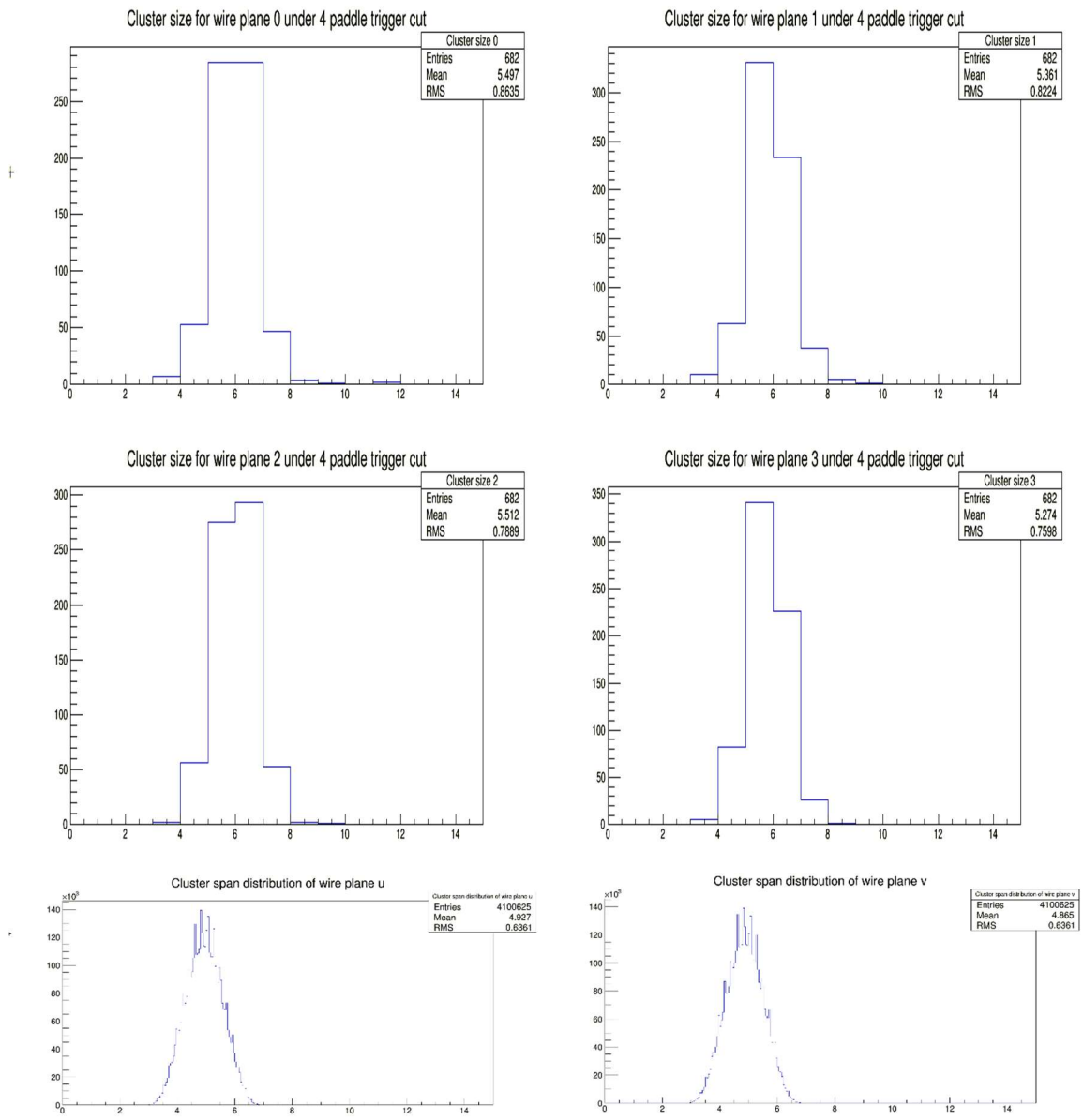


III Fig 5.14(2) Cosmic ray test run track direction angle ( $\theta, \varphi$ ). Ordinate: test run track direction angle  $\theta$  (track projection angle along short axis of wire plane) in *degrees*, abscissa: test run track direction angle  $\varphi$  (track projection angle long axis of wire plane) in *degrees*.

For track direction vector  $\vec{t} = (\tan\theta, \tan\varphi, 1)$ . The trigger square location based on the measured (2,0) trigger. Ordinate: track direction angle  $\theta$  (along short axis of wire plane) in *degrees*, abscissa: track direction angle  $\varphi$  (along short axis of wire plane) in *degrees*.



III Fig 5. 15(1) Simulated cluster span ( $n_u, n_v$ ) distribution of trigger (2,0). Ordinate:  $u$  cluster span, no unit, abscissa:  $v$  cluster span, no unit.



III Fig 5.15 (2) Simulated cluster span  $n_u$  (non-integer, lower left histogram) and  $n_v$  (non-integer, lower right histogram) of trigger (2,0), compared with integer cluster span  $n_u$  and  $n_v$  distribution (Upper, copies of upper histograms of Fig 5.13). Top 4 figures ordinate: counts, no unit, abscissa: cluster size of the corresponding wire plane, no unit. Bottom 2 figures ordinate: counts, no unit, abscissa: simulated cluster size (non-integer) of the corresponding wire plane, no unit. All left figures for wire span  $n_u$  and all right figures for wire span  $n_v$ .

### 5.4.2. Relative efficiency (events with track/triggered events). Counting events under certain trigger cut. Single, multiple cluster track results, cluster spans

As noted earlier, there are different ways to define the efficiency of track fitting. One of the easiest way is:

$$eff = \frac{\text{Number of events with track}}{\text{Number of triggered events}} \quad (5.16)$$

The definition is attractively simple but there are a few things to be noted:

- 1) It is expected that the efficiency defined here not only depends on both the analyzer code and the hardware. For example, the threshold voltage of discriminator card, the negative HV applied to cathode plane, the flow of inert gas inside wire chamber, etc. Thus by changing any parameters in the database file of the analyzer for a given test run, the efficiency will still hit a plateau with maximum value that is hardly close to 100%.
- 2) The placement and logic of the trigger is also very important to the resulting value of the efficiency. Every triggered event is expected to have at least one track through the geometric constraints on the trigger. Thus, any possibility of triggered events that cannot be detected by wire chambers or triggered events could lead to incorrect tracks reducing the efficiency. For example:
  - 1) If any straight line linking trigger scintillators misses a wire chamber active area, then if a track coincides with the line it won't be detected by the wire chamber. Our test run trigger setup has this issue and will be discussed in 5.4.3.
  - 2) There is the possibility of multiple tracks with trigger scintillators triggered by different particles. We expect very few wrongly computed track through all scintillators. As explained in Section 5.1 Subsection 1) we should avoid multi-cluster/track events in our experiment since the probability of multi-track events is negligible.
  - 3) The geometry of the trigger should avoid the possibility of extreme track angles and locations. The reason is that the efficiency for such tracks is irrelevant for the BH experiment.

The measured efficiencies under definition (5.16) with different triggers discussed in 5.1.3. 2) 3) are computed and tabulated below

Condition	Number of tracks from all events (Multiple tracks per event allowed and counted)	Event with all 4 wire plane cluster and 4 paddle trigger	Events with Trigger	Efficiency (%)
All paddles trigger	255039		1075300	23.7
(0,0) (0,0) trigger	938	882	1192	78.69/73.99
(1,0) (0,0)	1320	1227	1583	83.3/77.51
(2,0) (0,0)	1362	1287	1698	80.2/75.79
(3,0) (0,0)	1334	1241	1606	83.06/77.27
(4,0) (0,0)	1114	1040	1405	79.28/74.02

Table 5.2. Number of tracks in triggered events, number of events with trigger obeying (5.15) trigger logic, number of events with trigger, and relative efficiency.

Note: For example, efficiency numbers in row with (0,0) (0,0) trigger:  $78.69\% = 938/1192$ ,  $73.99\% = 882/1192$ .  $73.99\% = (\text{Number of event with track, under 4 paddles trigger})/(\text{Event with 4 paddles trigger})$  is the efficiency defined in (5.16).

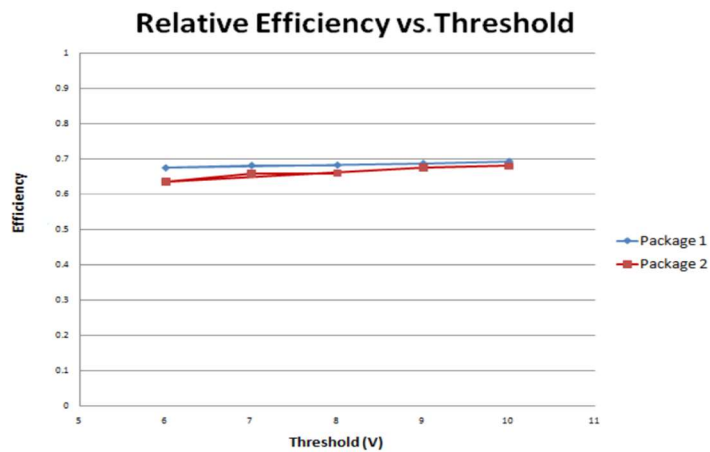


FIG. 4.31: Relative VDC efficiency vs. discriminator threshold where efficiency is defined as the percent of events containing a VDC track out of the total triggers from the scintillator. VDC HV was 3800 V for these these data and were taken at 50 pA of electron beam current. The VDCs have approximately the relative efficiency across the thresholds tested.

III Fig 5. 16 Analyzer track reconstruction efficiency. Ordinate: efficiency, no unit, abscissa: threshold voltage of discriminator card in  $V$ .

(Fig 4.31 from [29]) The efficiency with the same definition is a bit lower than our result in Table 5.2. The reason could be the different trigger setup been used, resulting in different levels of loss of efficiency defined in (5.16).

Condition	Events with track & with all 4 wire plane cluster and 4 paddle trigger	Event with all 4 wire plane cluster and 4 paddle trigger	Efficiency (%)
All paddles trigger	255039		23.7
(0,0) (0,0) trigger	882	882	100
(1,0) (0,0)	1227	1227	100
(2,0) (0,0)	1287	1287	100
(3,0) (0,0)	1241	1241	100
(4,0) (0,0)	1040	1040	100

Table 5.3. Efficiency under following condition:

$$eff = \frac{\text{Number of events with track}}{\text{Number of triggered events and with all 4 wire planes found cluster by analyzer}}$$

(5.17) The efficiency as shown in the table is always 100%. The result in the table means: As long as there are 4 paddles triggered, and all 4 wire planes each has at least 1 cluster found by analyzer. Then analyzer will fit a track for the event.

On the next page, we try to find out which wire plane is the least efficient in finding a cluster.



u1	v1	u2	v2	counts
0	0	0	0	11
1	0	0	0	7
0	1	0	0	5
0	0	1	0	0
0	0	0	1	0
<b>1</b>	<b>1</b>	<b>0</b>	<b>0</b>	<b>33</b>
1	0	1	0	7
1	0	0	1	0
0	1	1	0	2
0	1	0	1	9
<b>0</b>	<b>0</b>	<b>1</b>	<b>1</b>	<b>77</b>
<b>1</b>	<b>1</b>	<b>1</b>	<b>0</b>	<b>45</b>
<b>1</b>	<b>1</b>	<b>0</b>	<b>1</b>	<b>36</b>
1	0	1	1	12
<b>0</b>	<b>1</b>	<b>1</b>	<b>1</b>	<b>112</b>
1	1	1	1	1227

Table 5.4. For row “(1,0) (0,0) trigger” in table 5.2. Sort and count the number of events with different combinations of wire plane finding clusters. For example, the row with numbers 1, 1, 0, 0, 33 means for  $u_1, v_1, u_2, v_2$  the result was *find, find, not find, not find* a cluster, respectively.

There are only two cases:

- 1) As long as all 4 wire planes have a trigger and a cluster, it has a 100% chance to have a track. Thus, counts = 1227.
- 2) When there is at least one wire plane without a cluster, there will be no track for the event. Thus, counts =  $11+7+5+0+0+33+7+0+2+9+77+45+36+12+112 = 356$ .

The efficiency by definition (5.16) is  $1227/(356+1227) = 1227/1583=77.51\%$  is the same as row “(1,0) (0,0) trigger” in table 5.2. Bold rows cause large efficiency loss. It’s seen in the table that the  $u_1$  plane is the most unlikely to find cluster (row (0111)), since the trigger paddle projection is over the edge of wire plane  $u_1$ . It is better to move the trigger paddle to avoid this.

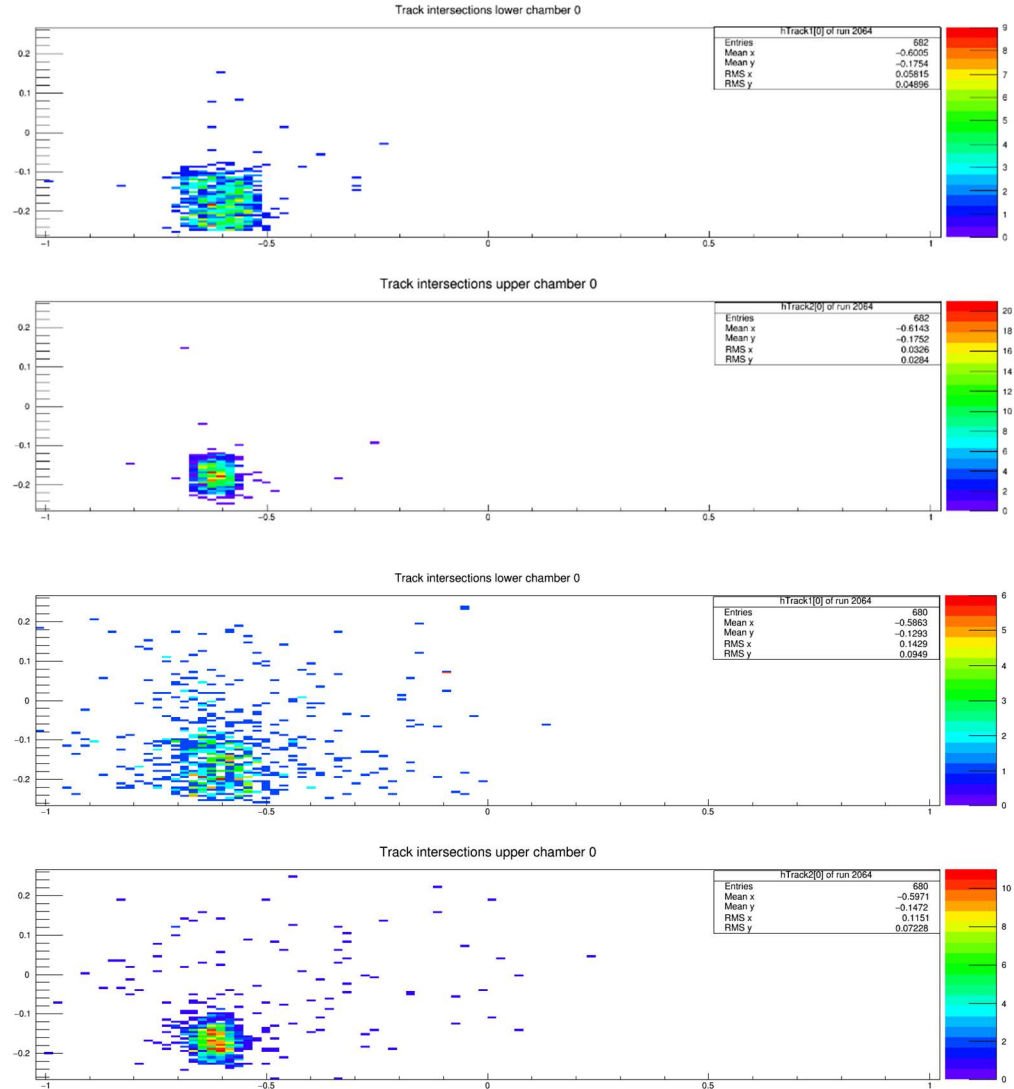
3) Separate single-cluster events and multi-cluster events. Single-cluster events will be almost the only events we expect to detect in the Bethe-Heitler experiment. The efficiency of such events need special care. Not only do we want the analyzer to be successful in finding tracks for these events, but we also want those tracks limited within the geometric constraint of the corresponding trigger discussed in section 5.3. Instead of efficiency:

$$Eff = \frac{\text{Number of events with single track}}{\text{Number of events triggered and have exactly one cluster per wire plane}} \quad (5.18)$$

which considers only a subset of events in (5.17) under the condition “exactly one cluster found per wire plane” and, as a result always yields an efficiency 100%, we should consider the following definition of efficiency:

$$Eff = \frac{\text{Number of events with single track}}{\text{Number of events triggered, have exactly one cluster found per wire plane, and lie within trigger geometry constraints}} \quad (5.19)$$

That is, (see Section 5.4.2. Subsection 2) Entry 3)) we not require that a track be found, but also that a found tracks be “correct”.



III Fig 5. 17 The copy of Fig. 5.12. Ordinate: short axis coordinate of wire plane in  $m$ , abscissa: long axis coordinate of wire plane in  $m$ .

The track crossover points on wire planes under the (2,0) (0,0) trigger divided into two cases:  
 1) (upper plots) single-cluster events where each wire plane has one and only one cluster found for the event.

2) (Lower plots) multi-cluster events where we focus on the counts and efficiency:

682+680=1362 is the count in column 2 for a (2,0) (0,0) trigger in table 5.2. As discussed above, our focus is single-cluster events, satisfying the geometric constraints on the trigger. The number of points outside the square area of the trigger projection in the top plot is about 29, and in 2<sup>nd</sup> top plot is about 21. Thus, the efficiency by the definition (5.19) above is at least about  $(682-29-21)/682=92.7\%$ .

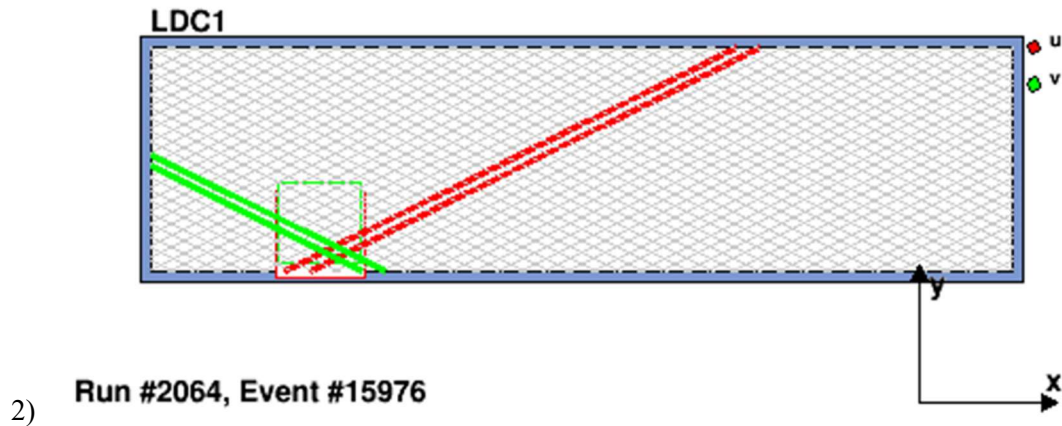
Trigger	(Single-cluster) Events with one and only one cluster per plane	(Multi-cluster) Events with all wire plane cluster, and at least one wire plane has more than one cluster. (Track count in bracket)	Event with all 4 wire plane cluster and 4 paddle trigger
(0,0) (0,0)	469	413 (469)	882
(1,0) (0,0)	662	565 (658)	1227
(2,0) (0,0)	682	605 (680)	1287
(3,0) (0,0)	620	621 (714)	1241
(4,0) (0,0)	547	493 (567)	1040

Table 5.5. Separated counts of single/multi-cluster events (2<sup>nd</sup> and 3<sup>rd</sup> columns). Since single and multi-cluster conditions are mutually exclusive, their sum will be the number of events satisfying geometrically constraint triggers where each wire plane has at least one cluster in the last column. This is just the numbers in the 3<sup>rd</sup> columns of Table 5.2.

#### 5.4.3. Cause of loss of efficiency

According to table 5.3., as long as there is at least one cluster on each wire plane, the analyzer will have track(s) found and fitted. This is also the subject of the discussion in section 5.2.2 on track fitting where it was noted that the crossover points of clusters  $(u_1, v_1, u_2, v_2)$  on each wire plane is sufficient to determine track information  $(x, y, \tan\theta, \tan\varphi)$ . Thus, there are two ways to lose track fitting efficiency: 1) At least one wire plane has no cluster found and 2) the track is computed from the wrong cluster  $(u_1, v_1, u_2, v_2)$  association. Some of the most common cases are explained with examples below.

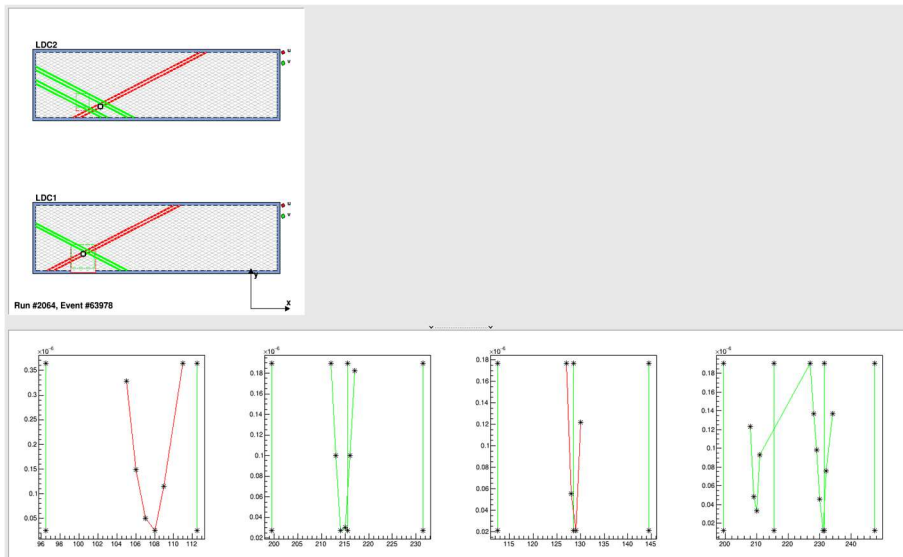
- 1) Placement of trigger paddles. We must place trigger paddles such that their projection on each wire plane is within the active area of the wire plane. The combination of effects shown in Fig 5.5 (higher placement of trigger paddles results in shift of projection on the short axis of wire planes) and in Fig 5.6 (lower chamber wire plane trigger projection is computed by outer projection with larger area than shared area of mutually perpendicular trigger scintillators in the same layer results in  $u_l$  wire plane projection outside its active area). No drift time data in  $u_l$  plane means no cluster found.



III Fig 5. 18 Calculated trigger outer projection on lower chamber wire planes.

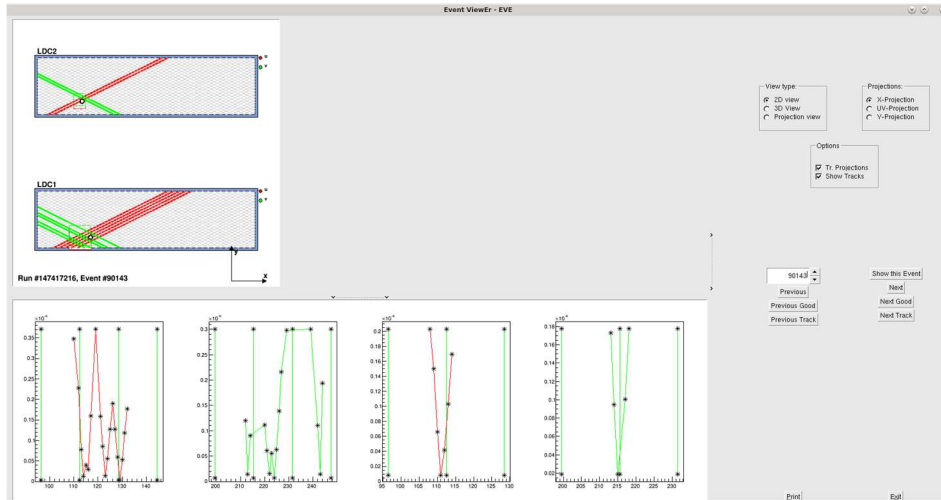
It's based on tape measure measurement of scintillator paddle locations. It's easy to see in Eve\_HallC event by event display, the projection of paddles on bottom u plane (red square) is just out of its active area and efficiency is lost accordingly. Furthermore, it can be noted that the calculated bottom  $u_1$  plane x coordinate in the analyzer coordinate system (-y coordinate in the figure) is  $-28.23 \text{ cm} < -26.67 \text{ cm}$  which is the lower bound of wire plane active area.

3) Wrong  $u-v$  association (ambiguity). This loss of efficiency only affects multi-cluster cases, where  $u-v$  clusters from different tracks are associated to fit tracks; see discussion in 5.2.1 With the track identification by path analysis all possible paths are paired and fitted and the ones with best fits chosen. In the cosmic ray test runs, a shower event would result in tracks with nearly the same timing and slope. Thus, a pair of adjacent clusters in the same wire plane would easily get similar  $\chi^2$  values and yet result in a wrong  $u-v$  association. Below, figures show several special cases where a wrong  $u-v$  association occur:

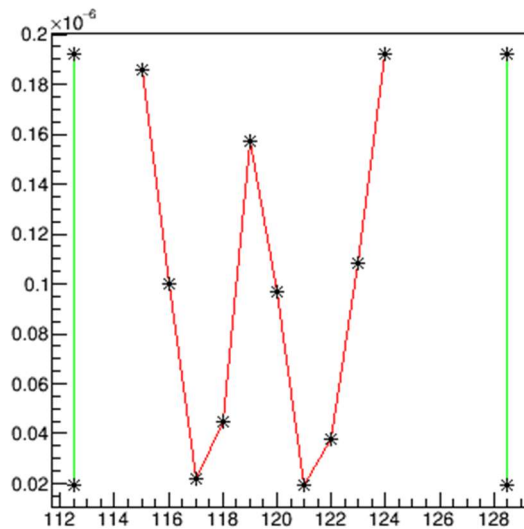


III Fig 5. 19 Wrong  $uv$  association cases. Bottom figures ordinate: drift time in unit  $\mu\text{s}$ , abscissa: wire number of wire plane  $u1, v1, u2, v2$  from left to right, no unit.

(1) Wrong  $u$ - $v$  association case 1. The top chamber  $v$  plane (LDC2 projection view green lines, and lower rightmost drift time graph) has two clusters, the analyzer track finding algorithm picked the wrong one, which resulted in the track crossover point missing the trigger projection on the top chamber.



III Fig 5.20 (2) Wrong  $u$ - $v$  association case 2. Bottom figures ordinate: drift time in unit  $\mu s$ , abscissa: wire number of wire plane  $u1, v1, u2, v2$  from left to right, no unit. In an event with close clusters and similar slope on bottom chamber LDC1, the  $u$ - $v$  association could easily pick an adjacent cluster of the cluster from the same track of top wire chamber clusters.



III Fig 5.20 (3). Wrong  $u$ - $v$  association case 3. Ordinate: drift time in unit  $\mu s$ , abscissa: wire number of a  $u$  wire plane, no unit. Hit wire indices vs drift time in seconds graph of a wire plane for an event. When clusters are adjacent to each other (in the sense of hit wire indices) with similar slope and timing, the current analyzer track finding algorithm is inadequate to resolve which cluster to choose in such case.

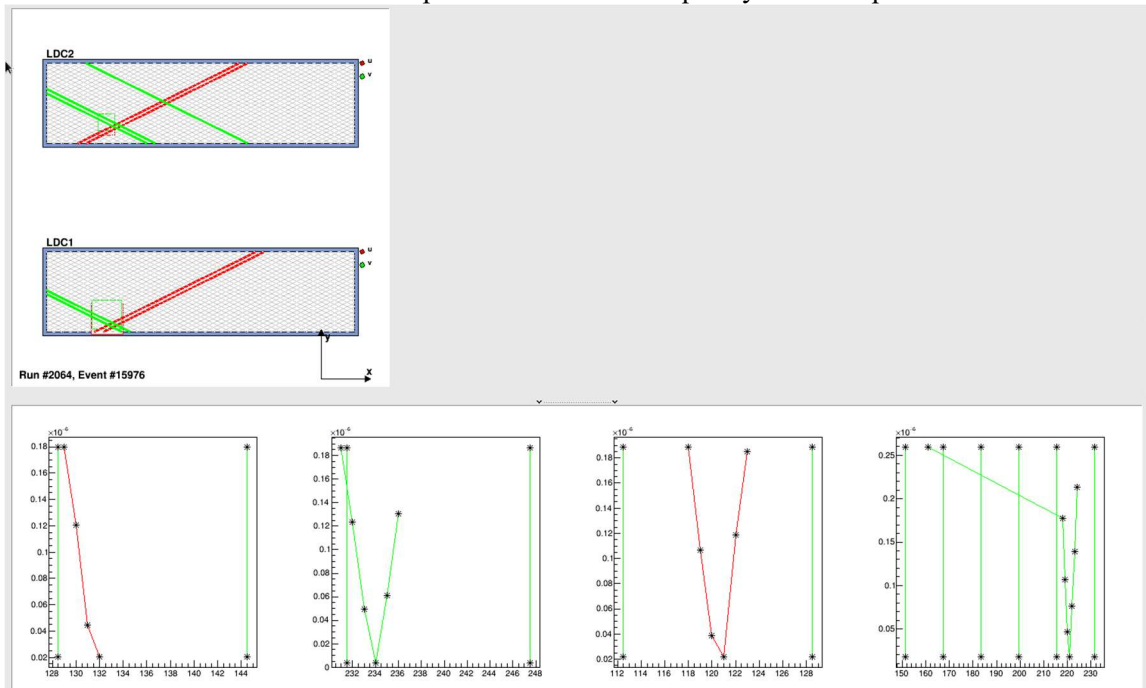
3) No clusters found in a wire plane. This results from the combination of algorithmic and hardware inefficiencies. The analyzer relies on the  $V$  shape drift time structure to identify a cluster. (Function THaVDCPlane::FindClusters() in [48] ) Anything causes incomplete  $V$  shape timing structure will make cluster identification failure. Some examples are shown in below figures.

Some cases causing incomplete  $V$  shape time structure. When one wire does not have drift time data, due to bad wire(s). From top to bottom:

Case 1: With a 3-wire cluster, eliminating any wire makes it a 2 wire cluster. Result is no  $V$  shape time structure and less than minimum cluster size.

Case 2: The eliminated wire is the only wire on one side of the cluster. Eliminating it will disqualify  $V$  shape.

Case 3: The eliminated wire is the wire with the minimum time and only one wire has the 2<sup>nd</sup> minimum time on one side of  $V$  shape. This will also disqualify the  $V$  shape.

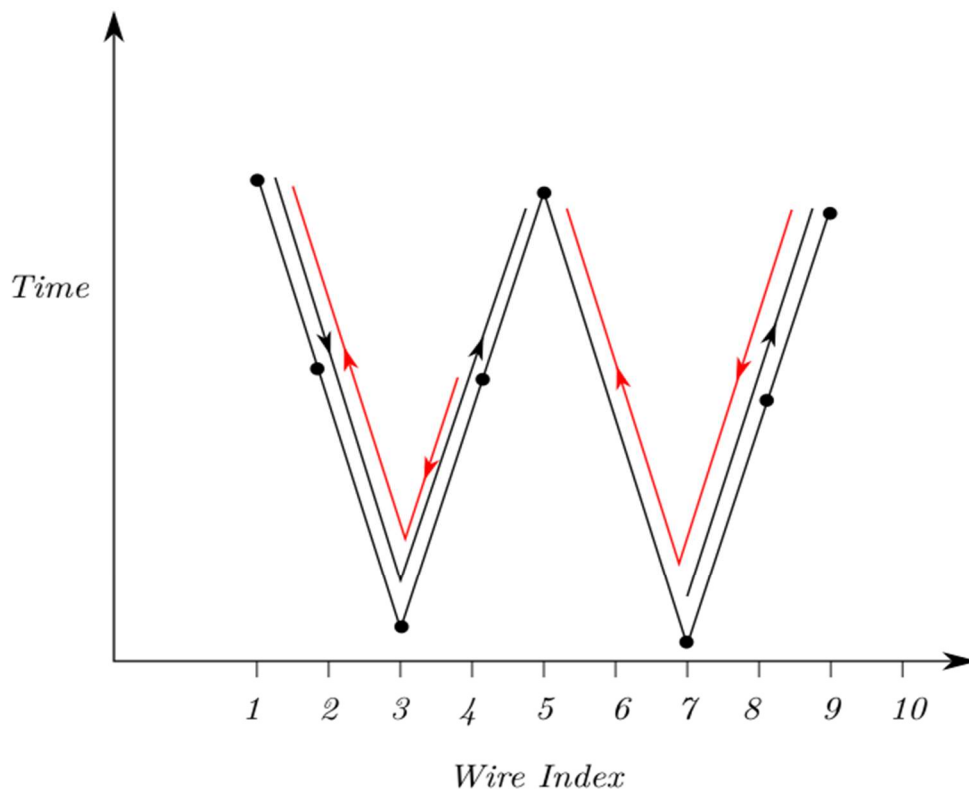


III Fig 5. 20 Missing wire plane  $u_1$  hits leads to loss of efficiency. Bottom figures ordinate: drift time in unit  $\mu s$ , abscissa: wire number of wire plane  $u_1, v_1, u_2, v_2$  from left to right, no unit.

Wire plane  $u_1$  (LDC1 red wires, and lower leftmost drift time graph) only has drift time data on one side of  $V$  shape. This disqualifies it in the analyzer cluster finding algorithm. As a result, no track is found.

4) Algorithm inefficiency.

The one orientation cluster finding (see 3.5.2 and Fig. 3.6) makes the common wire of two adjacent clusters always belong to the 1<sup>st</sup> cluster. This results in the elimination of a possible 1<sup>st</sup> wire for the adjacent cluster and possible disqualification of the cluster due to an incomplete  $V$  shape. This effect is due to the defect of the algorithm instead of a bad wire.

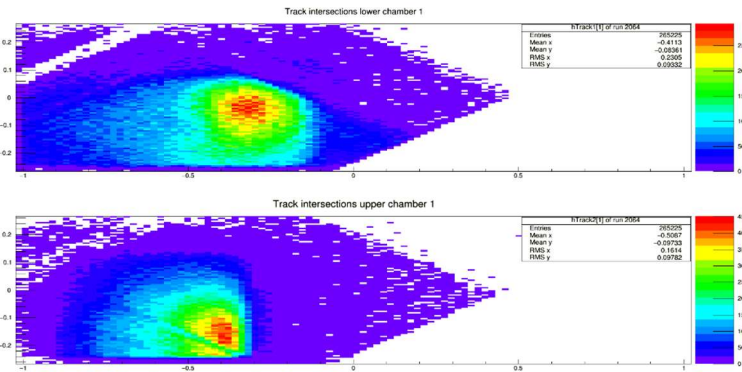


III Fig 5. 21 Redraw of III Fig. 3.6.

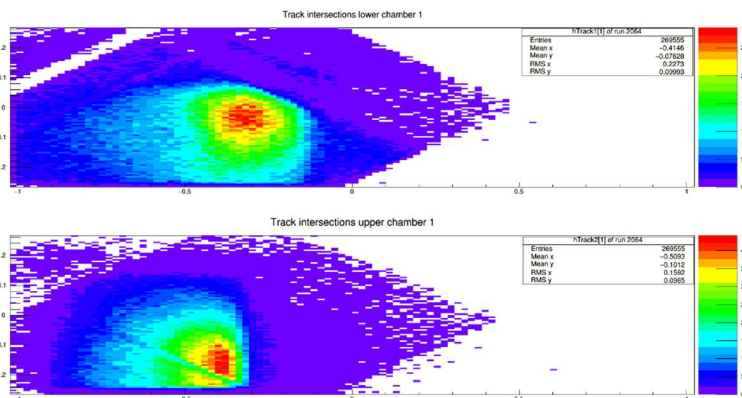
One directional search of clusters in the JLAB analyzer. Dots in the graph are  $(n_i, t_i)$  data point. Assume a gap of 1 wire in cluster finding is allowed. Now suppose wire 6 doesn't have data (might be the result of a bad wire). The arrow indicates iterative direction of cluster finding; if the search starts from the smallest wire index, then the only found cluster found includes wires (1,2,3,4,5) while the group of wires (7,8,9) is not a cluster since there's no V shape structure. If search starts from largest wire index, two clusters will be found: wires (1,2,3,4) and wires (5,7,8,9).

In order to estimate this effect on track finding efficiency, we compare the track fitting results by cluster finding with the default direction iteration method of hit collection and cluster finding with reversed direction iterations. A well-behaved algorithm will have the same result, regardless of the direction of iteration, which is not the case here.

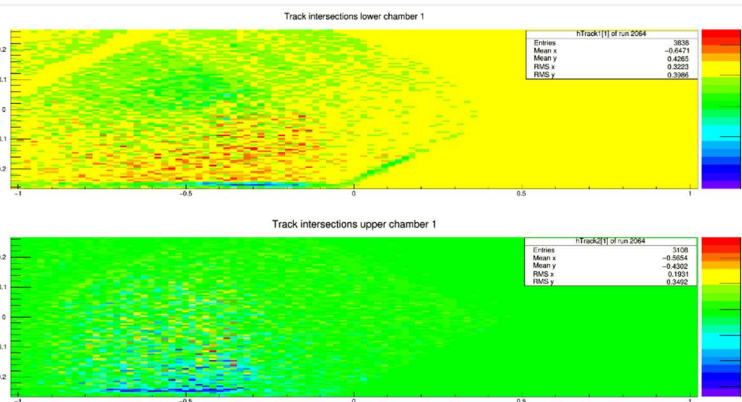




III Fig 5. 22 Fitted tracks crossover points on  $u$  wire planes, using default hit collection iteration direction for cluster finding.



III Fig 5. 23 Fitted tracks crossover points on  $u$  wire planes, using reversed hit collection iteration direction for cluster finding. Ordinate: short axis coordinate of wire plane in  $m$ , abscissa: long axis coordinate of wire plane in  $m$ .



III Fig 5. 24 Difference histogram of fitted tracks between default and reversed cluster finding. Ordinate: short axis coordinate of wire plane in  $m$ , abscissa: long axis coordinate of wire plane in  $m$ .

The difference of efficiency is about  $3108/269555 \sim 1.15\%$

## 5.5 Changes for improving efficiency

Based on the efficiency results shown in the last section, we propose a few methods which could improve the efficiency of the measurement either for the BH experiment or for test runs.

### 5.5.1 Conditional efficiency

The efficiency we measured with fewest constraints was very low (see Table 5.3). However, only efficiency under certain conditions is what we care about. The primary particles exiting the magnet in the BH experiment only have a certain range of direction and thus hit positions on the wire chambers. In order to have a successful measurement, the wire chambers and analyzer track finding algorithm only need to have good efficiency over this range.

One of the parameters in the analyzer that is well connected to wire chamber drift time data is the cluster span. Recall that simulated cluster span  $(n_u, n_v)$  distributions were generated from converting track direction angles  $(\theta, \varphi)$  to track incident angles  $\alpha_u, \alpha_v$  in the  $u$ - $z$  and  $v$ - $z$  planes by the formulas below (5.4):

$$\begin{aligned} \tan(\alpha_u) &= \tan\theta \cdot \cos\alpha + \tan\varphi \cdot \sin\alpha \\ \tan(\alpha_v) &= \tan\theta \cdot \cos\alpha - \tan\varphi \cdot \sin\alpha \end{aligned}$$

Then (modified formula (3.3))

$$n_u = \frac{|h \cdot \tan\alpha_u|}{s} \text{ and } n_v = \frac{|h \cdot \tan\alpha_v|}{s}$$

The non-integer cluster spans  $(n_u, n_v)$  have a linear relation to tangents of track angles  $\alpha_u, \alpha_v$  in  $u$ - $v$  coordinate system, and also have a linear relation to tangents of track angles  $\theta, \varphi$  in the analyzer  $xyz$  coordinate system. The integer cluster spans are larger than non-integer cluster spans. Their range is based on the acceptance of the spectrometer and wire chambers and has been estimated in Geant 4 simulations (see Chapter 4 Cluster finding and fitting using Geant 4 results; Fig. 4.3 and Fig. 4.4).

Thus, the efficiency under the condition for a certain range of cluster span is the one we need to investigate. For this we use concepts in conditional probability to establish the cuts we're applying in analyzer database file.

*Conditional probability* is defined as [49]:

$$P(B|A) = \frac{P(A \cap B)}{P(A)} \quad (5.20)$$

Here,  $P(B|A)$  is the probability that event  $B$  occurs under the condition that event  $A$  also occurs,  $P(A \cap B)$  is the probability of both event  $A$  and  $B$  occur, and  $P(A)$  is the probability of event  $A$  occurs.

*Total probability theorem*:  $B_i, i = 1, \dots, n$  are finite, mutually exclusive, and exhaustive event ( $\bigcap_i B_i = \Omega$  is the *sample space*) and  $A$  is any event. Then:

$$P(A) = \sum_i P(A \cap B_i) = \sum_i P(B_i)P(A|B_i) \quad (5.21)$$

The first equating sign means the probability of event  $A$  occurs over the entire sample space is the sum of the probability of both event  $A$  and  $B_i$  occur over  $i$ , when  $B_i$ s is mutually exclusive ( $B_i \cap B_j = 0$  for any  $i \neq j$ ) and exhaustive ( $\bigcap_i B_i$  is the *sample space*). It is the direct result of defining property of probability  $P(A \cap B) + P(A \cap C) = P(A \cap (B \cup C))$  if  $B \cap C = \emptyset$ . The 2<sup>nd</sup> equating sign is reached by applying the definition of conditional probability  $P(A \cap B_i) = P(B_i)P(A|B_i)$ .

Bayes' theorem:

$$P(B_k|A) = \frac{P(B_k)P(A|B_k)}{P(A)} = \frac{P(B_k)P(A|B_k)}{\sum_i P(B_i)P(A|B_i)} \quad (5.22)$$

Where  $B_k$ ,  $k = 1 \dots, n$  are the subsets of sample space under the same conditions of total probability theorem. The 1<sup>st</sup> equating sign uses the definition of conditional probability:

$$P(A)P(B_k|A) = P(A \cap B_k) = P(B_k)P(A|B_k)$$

The 2<sup>nd</sup> equating sign expands  $P(A)$  in the denominator using the total probability theorem (5.21). As an example:  $A$  represents event with tracks found by the analyzer, and  $B_k$  represents event with cluster with  $k$  wires hit. Then the conditional probability of  $k$  wires under the condition of tracks are found by the analyzer can be computed from knowing all  $P(B_k)$  (the probability of event occurs with cluster with  $k$  wires hit) and each conditional probability of event with tracks found by the analyzer under the condition of the event has cluster of size  $k$ .

Consider a procedure as below: Let  $B_i$  represent an event with a certain span of clusters,  $i = 3, \dots, 8$ . Let  $A$  represent an event with tracks. We can classify events by  $B_i$ . For example,  $B_5$  is event with cluster span of 5. When the analyzer is finding and fitting tracks, it reads an event, applies cuts to clusters, then uses the clusters after cuts to each wire plane to fit the track. Now we apply the total probability theorem. We expect it to be interpreted as: the probability of an event with track(s) found is the sum over cluster span  $i$  of the probability of an event with cluster span  $i$  times the conditional probability of finding tracks with certain cluster span  $i$ . Thus,  $P(B_i)$  and  $P(A|B_i)$  with  $i = 3, \dots, 8$  give complete information of the efficiency of track finding. In addition, if the wire chamber and analyzer combined don't have a good track finding efficiency for events with certain cluster spans, then we may discard such an event by adding a cut in the database file. Based on results from the Geant 4 simulations (see Part IV Simulation, section 2.4 Track finding and fitting using Geant 4 results; Fig. 2.29 and Fig. 2.30), the range of cluster spans during BH experiment is  $n_u \in [4, 8]$  and  $n_v \in [4, 7]$ . Thus, as long as in these range ( $n_u \in [4, 8]$  and  $n_v \in [4, 7]$ ), we expect high efficiency globally by the total probability theorem if efficiency  $P(A|B_i)$  is high, while any efficiency during test run with  $i = n_u$  or  $n_v$  is not in this range is irrelevant.

As for applying the total probability theorem to the current analyzer, the theorem relies on all  $B_i$  being mutually exclusive and exhaustive. However, in the database file, limits of cluster spans are applied to all wire planes and they cannot represent mutually exclusive events. For example, the minimum cluster size and maximum cluster span will limit the span of cluster in range  $[n_{min}, n_{max}]$ , if pick range of  $i$  for  $B_i$  to be  $(n_{min}, n_{max}) = (3, 7)$  and  $(n_{min}, n_{max}) = (8, 12)$  Their union set is not equal to the set of events corresponding to  $(n_{min}, n_{max}) = (3, 12)$ . Then a cluster span of  $u_1, v_1, u_2, v_2$  with span  $(n_{u1}, n_{v1}, n_{u2}, n_{v2}) = (8, 4, 8, 4)$  will not be included in each of the above cases, but it does apply to  $(n_{min}, n_{max}) = (3, 12)$ . Thus, the total probability formula does not apply.

Proposed improvement in defining track finding efficiency:

In order to correct the over generalized specification of range of cluster span in database file, cuts on wire spans for each  $u$ - $v$  wire plane  $(n_{umin}, n_{umax}, n_{vmin}, n_{vmax})$  should be separately specified. In other words, the conditional probability  $P(A|B_i)$  here should be interpreted as  $P(A|n_u, n_v)$ .

## 5.5.2 Placement of trigger paddles

Due to the current placement of trigger scintillator paddles, their projections on the bottom chamber  $u$  wire plane is partially outside of wire plane active area (see Fig 5.8). Based on the definition of efficiency (5.16):

$$eff = \frac{\text{Number of events with track}}{\text{Number of triggered events}}$$

which requires that every triggered event can be detected by the wire chamber, is not applicable in this situation. In addition, we can also observe in the second last row in Table 5.4, which shows the number of events for which the wire plane  $u_1$  does not find a cluster, while wire planes  $v_1, u_2, v_2$  have found cluster(s). This is the case with the most efficiency loss. However, an easy fix for this is to relocate trigger paddles.

## 5.5.3 Improvement on analyzer track fitting algorithm.

Since there are always special cases in drift time vs sense wire structure for hit collection it is impossible for an analyzer cluster finding or track finding algorithm to identify all of them. In addition, to deal with certain types of special cases in the timing structure new algorithms and parameters are often introduced, which complicate the issue. There are two ways to improve the efficiency of analyzer cluster and track finding:

- (1) Modify the algorithm and calibration of parameters for current method. The current analyzer cluster finding is based on identifying the V shape timing structure by searching for a falling then rising trend in drift time vs sense wire pattern. It has some obvious flaws which might not be easily resolved using current method. Thus
- (2) Invent a new algorithm from scratch, in which possible flaws are dealt with from the beginning. In this section both cases are discussed. It should be noted that the discussion here is more proposition than real implementation in the analyzer code. However, these improvements are expected.

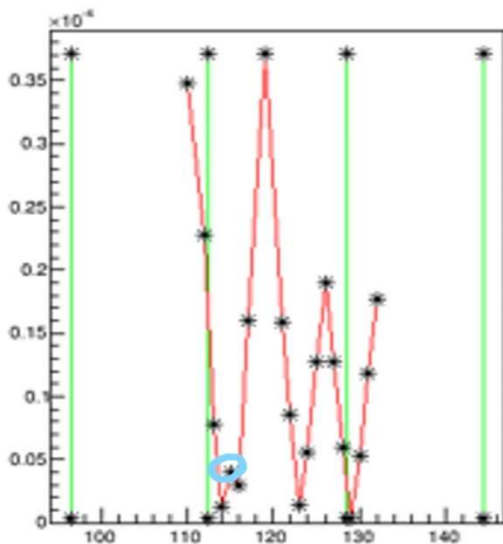
- 1) Identifying bad timing structure.

The current analyzer algorithm does not deal with the change from “falling” to “rising” with flexibility. For example, during “falling” a single wire eventually starts “rising” while the trend after the wire is still “falling”. The analyzer, by changing the flag to “rising”, and then detecting the 2<sup>nd</sup> time it starts “falling” ends because of the new “fall” and determines that the cluster is cut short. For such a case, the global trend is not properly dealt with since the code itself lacks the logics to consider the magnitude of change in drift times between adjacent wires. Such an example is shown in Fig 5.26.

- 2)  $UV$  association of similar slope cluster, compare local and global fit. As seen in 5.4.3 2) the incorrect  $u-v$  association of clusters leads to an incorrect track, which is a very common result from the current analyzer track finding algorithm. Additional cut or modified  $\chi^2$  will improve this.
- 3) Use data of clusters with bad timing structure. See Fig. 5.21. Losing timing information on one side of the  $V$  shape from hardware causes no cluster in one wire plane, which leads to no track being found. However, the information obtained from the hardware, which includes 3 full clusters in the other 3 wire planes and the half cluster in the disqualified wire plane, is more than enough to fit a track with good precision. We can easily fit the half cluster to a straight line, or combine it with the cluster with same

orientation in the other wire chamber (see 5.2.1 for path analysis) to find the crossover point. The real issue is how to identify such half cluster through a stable and reliable algorithm.

- 4) Two defects in cluster  $V$  shape identification. (Difference of results when searching clusters on hit collection through increasing/decreasing wire index, reuse of failed wires in previous cluster candidate) (c.f. 5.4.3 4) The “falling” to “rising” identification as criteria for a cluster is one directional and an asymmetry originates from iterating hit wire indices from different directions (see Fig 5.23 to Fig 5.25). However, identifying a real cluster should never depend on the direction of iteration of wire indices. In order to fix this, a new algorithm independent of iteration direction is devised below.



III Fig 5. 25 Illustration of premature ending of cluster finding. Ordinate: drift time in unit  $\mu s$ , abscissa: wire number of a  $u$  wire plane, no unit.

The circled hit wire will end the current new cluster build up, because the next wire hit time is falling instead of continue to rise. However, the real cluster should also include next 3 wires.

2) Another defect is in the classification of each wire in the hit collection in the analyzer algorithm. During the iteration of wires to build up a new cluster, a wire with bad hit time is removed in the current cluster and set aside. Then those wires will be re-examined again for new cluster candidate, this could cause a sequence of adjacent wires in the hit collection being identified as two clusters with common range mixed together. Such result is usually incorrect and has little use for track finding and fitting.

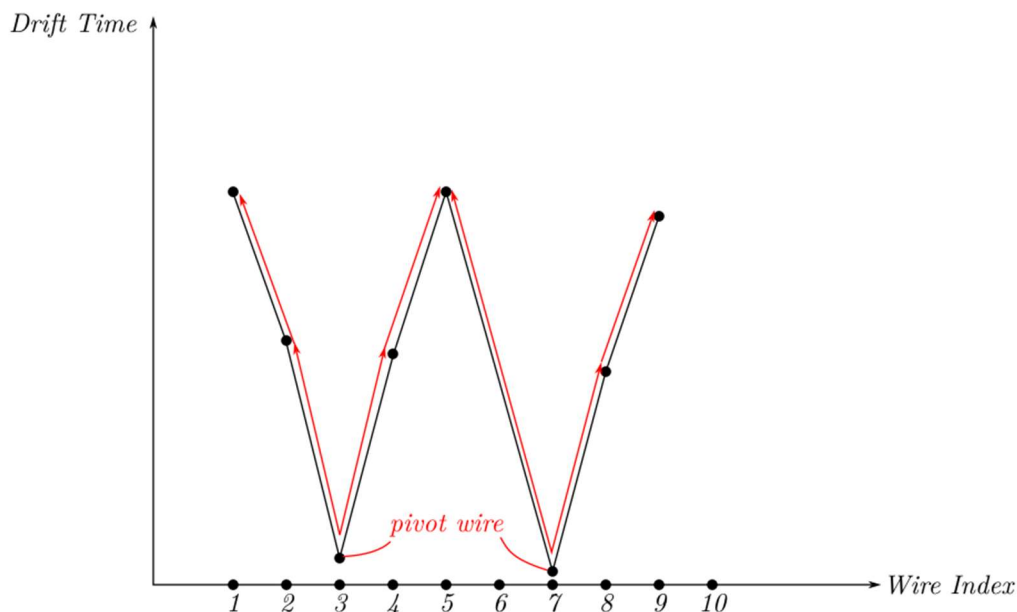
5) New cluster finding algorithm.

The new algorithm does not depend on the direction of iteration of wire indices during cluster finding, which eliminates the difference between results of clusters finding in different direction as shown in Fig 5.25.

The idea is also very simple: instead of first “falling” then “rising”, the V shape can also be interpreted as from a local minimum and “rising” on its both sides until reaches the local maximum or big wire gap. Thus, the steps to find clusters in this algorithm is:

- (1) Read entire hit collection. Search for wires with local minimum drift time; that is, drift times of hit wires on its both sides are larger than the time of current wire. Call those local minimum wires pivot wires.

- (2) Start with each pivot wire, iterate through wires on its lower index side, then add the wire into the new cluster if drift time is “rising”. Do not end the iteration until a maximum is found, a big wire gap appears, or other exceptions controlled by database file parameters.
  - (3) Do the same for wires on the higher wire index side of pivot wire.
  - (4) Combine both sides wires with “rising” time and the pivot wire as a new cluster.
- An illustration of this new algorithm is shown in Fig. 5.27.



III Fig 5. 26 Illustration of new cluster finding method.

First, find pivot wires, which are wires with local minimum in drift time. Then search from each pivot wire to the left and right, until drift time reaches local maximum.

#### 6) Suggestion on additional cuts.

- (1) Add maximum number of clusters in each wire plane, since the BH experiment rarely generate multi-cluster/track events.
- (2) As suggested in the last section 5.5.1, specify the maximum and minimum cluster span on  $u$  wire plane and  $v$  wire plane independently instead of maximum and minimum cluster span for both wire orientations.
- (3) The  $t_{\text{diff}}$  (drift time difference between adjacent wires in a cluster) could be cluster span dependent. For instance, if there are 3 wires hit for a cluster, 2 side wires ionization point at cathode, then  $t_{\text{diff}}$  in this case is  $\sim 200\text{ns}$ , which equals the maximum drift time. But, for a 7-wire cluster with side wires ionization point at cathode,  $t_{\text{diff}} \sim 200/3 \sim 70\text{ ns}$ .
- (4) Add the maximum of the smallest drift time of the  $V$  shape. For instance, if the pivot wire has a large drift time, the cluster associated to it should not be the one that triggers the scintillators, then a time offset should add to all wires. The cluster fit should be similar to that which has been discussed in 4.3.3.

## 5.6 Misc. topics

### 5.6.1 Track angle and location resolutions estimation

According to how the track is fitted in section 5.2.2, the track angle  $\theta, \varphi$  and location  $x, y$  resolution originates from the error of crossover point coordinates  $(u_1, v_1, u_2, v_2)$  in the wire chamber. Those coordinates are fit results from each cluster of the wire plane. Thus, the uncertainty/resolution ultimately originates from errors of drift distance or drift time. Now we estimate the resolutions with two different methods.

#### 1) Estimated by error propagation of fit parameters.

The crossover points coordinate  $u$  or  $v$  is fitted in form:

$$d = A + Bu \quad (5.23)$$

where  $d$  is the drift distance, and  $u$  or  $v$  is the position of wires in the cluster; replace  $u$  by  $v$  for  $v$  wire planes. The crossover point coordinates is then:

$$u_0 = -\frac{A}{B} \quad (5.24)$$

With

$$A = \frac{\sum u^2 \sum d - \sum u \sum ud}{\Delta}, B = \frac{N \sum ud - \sum u \sum d}{\Delta}, \Delta = N \sum u^2 - (\sum u)^2 \quad (5.25)$$

Thus, we can apply the error propagation formula

$$\sigma_u = \sqrt{\left(\frac{\partial u}{\partial A}\right)^2 \sigma_A^2 + \left(\frac{\partial u}{\partial B}\right)^2 \sigma_B^2} = \sqrt{\left(-\frac{1}{B}\right)^2 \sigma_A^2 + \left(\frac{A}{B^2}\right)^2 \sigma_B^2} \quad (5.26)$$

to find the resolution of the crossover point coordinate  $\sigma_u$  or  $\sigma_v$ . Here  $\sigma_A$  and  $\sigma_B$  are also need to be determined, and we are making some assumptions before proceeding:

- (1) Since both  $A$  and  $B$  are  $u$  and  $d$  dependent, we assume error of each data point's  $u$  coordinate is negligible compared to  $\sigma_d$ . The reason for this is that the sense wire locations in the wire chambers are fixed during construction, and their positions are constructed and measured with very high precision, compared to drift distance.

- (2) All drift distances have the same uncertainty  $\sigma_d \cong v \sigma_t \cong \frac{60000m}{s} \times 10ns = 0.6 mm$ .

Here  $v$  is the estimated drift velocity, and  $\sigma_t$  is the error of drift time.  $\sigma_t$  is combined from the drift time offset and random fluctuations of ionization and scattering processes.

Thus, by error propagation on drift distance  $d$  only. We have:

$$\sigma_A = \sigma_d \sqrt{\frac{\sum u^2}{\Delta}} \quad (5.27)$$

$$\sigma_B = \sigma_d \sqrt{\frac{N}{\Delta}} \quad (5.28)$$

Replacing  $\sigma_A$  and  $\sigma_B$  in (2.5.27) and (2.5.28) into (2.5.26)

$$\sigma_u = \frac{\sigma_d^2 N}{B^2 \Delta} \left[ \frac{\sum u^2}{N} + \frac{A^2}{2B^2} \right] \quad (5.29)$$

We have the crossover point resolution dependence on wire positions and drift distances  $(u_i, d_i)$  in the cluster, which can be pretty messy. We still have to impose a credibility check on the formula. The resulting formula should be invariant for translation of coordinate of  $u$ ; that is, if

we add a constant  $\Delta u$  to all  $u$  coordinates  $u_i$ , the formula (5.26) should still render the same results. See Fig 5.28 for illustration. Under translation:

$$\sum u^2 \rightarrow \sum (u + \Delta u)^2 = \sum u^2 + 2\Delta u \sum u + N(\Delta u)^2 \quad (5.30)$$

$$\sum u \rightarrow \sum (u + \Delta u) = \sum u + N\Delta u \quad (5.31)$$

$$\sum ud \rightarrow \sum (u + \Delta u)d = \sum ud + \Delta u \sum d \quad (5.32)$$

Which leads to

$$\Delta = N \sum u^2 - (\sum u)^2$$

$$\rightarrow \Delta' = N[\sum u^2 + 2\Delta u \sum u + N(\Delta u)^2] - (\sum u + N\Delta u)^2 = \dots = \Delta \quad (5.33)$$

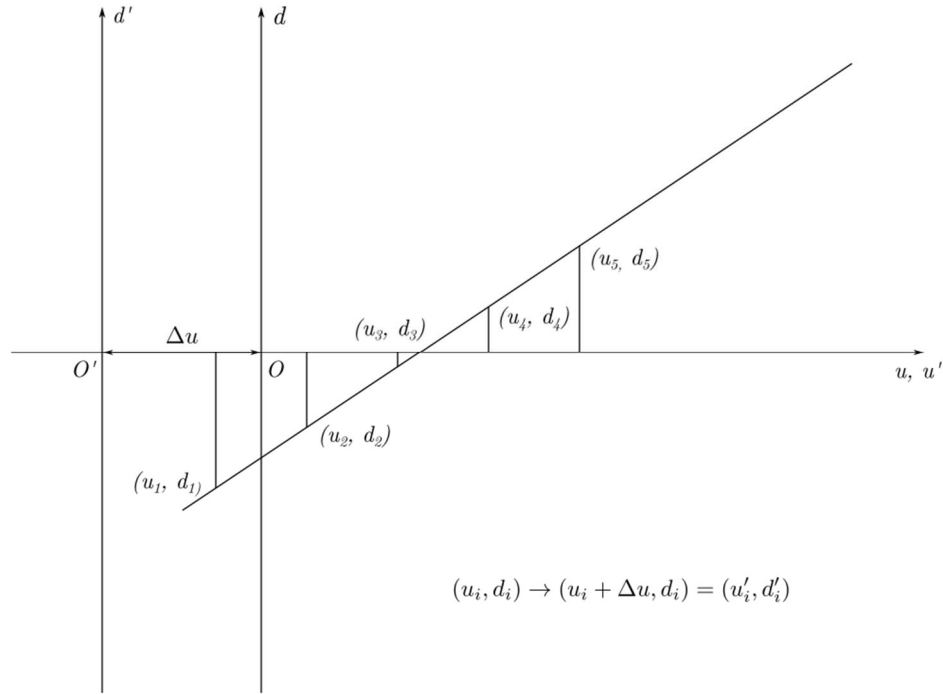
$$A' = \frac{[\sum (u + \Delta u)^2 \sum d - \sum (u + \Delta u)d \sum u]}{\Delta'}$$

$$= \dots = A + \frac{\Delta u}{\Delta} (\sum u \sum d - N \sum ud) = A - B\Delta u \quad (5.34)$$

$$B' = \frac{N \sum (u + \Delta u)d - \sum (u + \Delta u) \sum d}{\Delta'} = B \quad (5.35)$$

$$\sigma_{A'}^2 = \sigma_d^2 \frac{\sum u^2 + 2\Delta u \sum u + N(\Delta u)^2}{\Delta} = \sigma_A^2 + \sigma_B^2 \left( \frac{2\Delta u \sum u}{N} + (\Delta u)^2 \right) \quad (5.36)$$

$$\sigma_{B'} = \sigma_d \sqrt{\frac{N}{\Delta'}} = \sigma_B \quad (5.37)$$



III Fig 5. 27 Illustration of translation invariance of standard deviation of  $\sigma_u$ .

Here  $(u_i, d_i)$  to  $(u_i + \Delta u, d_i)$  with the same  $\Delta u$  to keep all distances and spacing of each  $u_i$  same, and drift distances same to represent the same track. However, the origin of coordinate system is shifted  $-\Delta u$  in  $u$  direction. When combined leads to

$$\sigma_u'^2 = \sigma_u^2 + 2 \frac{\sigma_B^2}{B^2} (\Delta u) \left[ \frac{\sum u}{N} - \frac{A}{B} + (\Delta u) \right] \quad (5.38)$$

which does not satisfy the invariance for translation of coordinate of  $u$ . The reason is that both  $A, B$  are  $u, d$  dependent, thus heavily correlated to each other. The formula (5.26) is for independent random variables, which cannot be applied here. Still we can estimate



by using (5.29), assuming (by translation)  $A = 0$ , for  $45^\circ$  track  $B = 1$ , cluster size  $N \cong 5$ . Also assume

$$\begin{aligned} \sum u &= 0, \text{ so by } \Delta = N \sum u^2 - (\sum u)^2 \Rightarrow \frac{\sum u^2}{\Delta} = \frac{1}{N}. \\ \sigma_u^2 &= \frac{\sigma_d^2}{B^2} \frac{N}{\Delta} \left[ \frac{\sum u^2}{N} + \frac{A^2}{2B^2} \right] \cong \frac{\sigma_d^2}{1^2} \frac{\sum u^2}{\Delta} \cong \frac{\sigma_d^2}{N} \end{aligned} \quad (5.39)$$

Which gives  $\sigma_u = \sigma_d/\sqrt{N} \cong 0.27 \text{ mm}$ .

## 2) A crude estimation

This is about the estimation of upper limit of  $\sigma_u$  or  $\sigma$  of intersection. This results from shifting all hits of the track up or down by  $\sigma_d$

$$\sigma_d = B\sigma_u \quad (5.40)$$

The range of slope  $B$  is approximately from  $\tan(30^\circ) = 1/\sqrt{3}$  to  $\tan(60^\circ) = \sqrt{3}$  so use  $45^\circ$  as estimate ( $\sim 5$  wire hit cluster), so  $\sigma_u \sim \frac{\sigma_d}{B} \sim \sigma_d \sim 0.6 \text{ mm}$  from previous result. To estimate the final track angle error, use a  $\theta = 45^\circ$  track and add  $0.6 \text{ mm}$  in the  $x$  direction (parallel to short side of wire chamber) as overestimate. With  $38.1 \text{ cm}$  apart from bottom to top chamber:

$$\begin{aligned} \tan\theta &= \frac{38.1 \text{ cm}}{38.1 \text{ cm}} = \frac{x}{z} = 45^\circ, \text{ then shift } \delta x = 0.6 \text{ mm} \text{ in the } x \text{ direction} \\ \delta(\tan\theta) &= \frac{\partial \tan}{\partial x} \delta x = \frac{\delta x}{z} = \frac{0.6 \text{ mm}}{38.1 \text{ mm}} \sim 1.6 \times 10^{-3} \end{aligned} \quad (5.41)$$

Error of track angle:

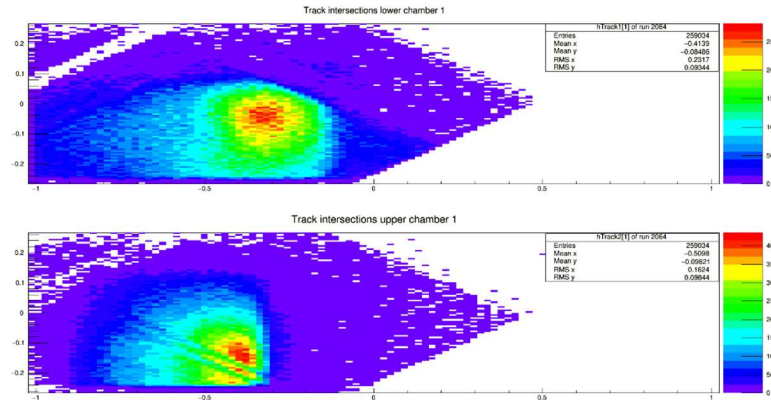
$$\delta\theta \cong \left( \frac{\partial \tan}{\partial \theta} \right)^{-1} \delta(\tan\theta) = \sec^2\theta \delta(\tan\theta) = 2\delta \tan\theta \sim 3 \times 10^{-3} \text{ rad} \sim 0.17^\circ \quad (5.42)$$

## 5.6.2 Location of bad wires, and their effect on loss of efficiency

We investigate the effect of removing all hit time data from one wire of a test run before analyzer cluster finding, which equivalently corresponds to a bad (broken?) wire situation. The result is shown in Fig 5.29 and Fig 5.30 below.

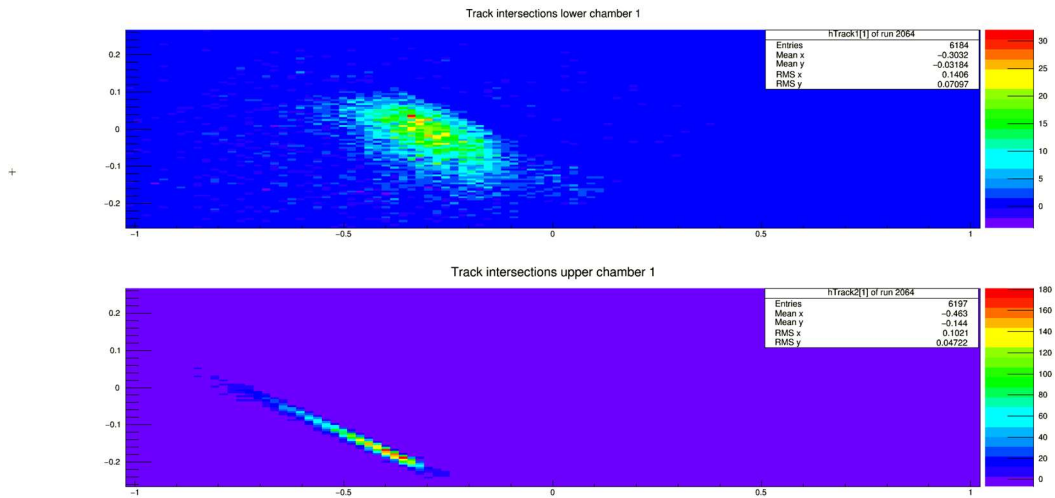
We have seen from the track crossover point distributions  $(x, y)$  on wire chambers that bad wires cause less tracks found and results in less density strip in the distribution of the wire plane bad wire lies. We should note:

- (1) Removing hit time data from a wire in a cluster will not necessarily result in the loss of the cluster found. See 5.4.3. 3) for some cases leading to loss of cluster.
- (2) The loss of efficiency is also heavily depended on the location of a bad wire. Wires with short lengths that lie on the corners of the wire plane with a small area covered or wires that lie in a region where the hit density is low will not have an effect as big as a long wire in densely hit region.



III Fig 5. 28 Track crossover point coordinates  $(x, y)$  in  $u$  planes of both wire chambers. Ordinate: short axis coordinate of wire plane in  $m$ , abscissa: long axis coordinate of wire plane in  $m$ .

Compare to Fig 5.23. Wire 204 in the  $v_2$  plane was “cut off” during replay (its data were removed by the code). The lower plot shows an extra low hit density strip in the upper chamber  $(x, y)$  coordinates, which correspond to tracks lost.



III Fig 5. 29 Difference histogram of Fig 5.23 and Fig 5.29. Ordinate: short axis coordinate of wire plane in  $m$ , abscissa: long axis coordinate of wire plane in  $m$ .

This shows the effect of loss of efficiency by one bad wire in the most densely hit region of test run. The relative loss is:

$$6184/259034 = 2.4\%$$

## 6 Other items required for replay

As mentioned before in the Introduction chapter 1, in order to replay the data we need following items:

1. A replay script that defines detectors/apparatus to be analyzed, physics module and calculation that need to be done, and file/variable names.
2. Set of database files: (1) Detector database files that parameters and hardware mapping info of individual detectors are stored. (2) Run database files which defines beam energy etc. (3) Crate/scaler mapping database defining decoder parameters which for example maps individual hardware channel into channel in analyzer.
3. Output definition file that defines which physical quantities to be calculated and stored in ROOT file.
4. Raw data (CODA file), which is a form of binary data.

We already have the following items determined: detector database files, run database file (even though it is irrelevant for our application), and raw data. In addition a database for the decoder that maps channels from TDC by format (crate, slot, channel) into integer channels which are used to convert raw time data to ROOT data is written for credibility checks and determination of the TDC offset. Now we still need following items: 1. Replay script. 2. Crate mapping database. 3. Output definition file. 4. Cut definition file.

### Files needed other than replay script

1. Crate mapping database: this is a simple database file that assigns info relevant to TDC crate, which includes crate number, type; and slot number, model, number of channels for each slot etc.
2. Output definition file: For now, all VDC class related data (including accumulated raw time, time, track direction etc. for each wire plane), all decoder data (raw time for each channel/wire converted from binaries), and global data (number of events, event length etc.) will be calculated and stored in ROOT file for test purpose.
3. Cut definition file.

### Replay script

Only two apparatuses (corresponding to two pairs of wire chambers) in our case are to be analyzed. Thus replay script is pretty straight forward:

1. We instantiate a THaHRS object since it includes VDC, and VDC database file has been rewritten in last section, and a THaApparatus object for decoder data.
2. The prefixes of these objects also included in these objects' constructor thus database file names are set accordingly.
3. Set raw data file (the CODA file includes binaries of raw time), output file (ROOT file stores results), output definition file and cut definition file names.

Once all above items set in replay script, run the replay script then we will get desired results.

## 7 Decoder results and their applications

Data stored in a replayed ROOT file after running replay script with other files properly set, as described in Chapter 2 and 6. They are divided into three categories:

- 1) Decoder data, which are raw time for each channel (possible multiple hits per channel per event). It has been used to determine raw time offset and various credibility checks.
- 2) Analyzer processed HRS object data, we will focus on its wire chamber class VDC track finding results. It requires a fully modified VDC database file to render reliable results, which was not the case in early stage of the BH experiment preparation.
- 3) Variables storing event number, event length, etc.

Usage of data in 1) will be discussed this chapter:

- (1) Make several basic plots to check if TDC working properly (believable raw time distribution, noise level is low, etc.).
- (2) Another important application is to determine TDC raw time offsets from them, already discussed in chapter 2 section 2.3.4.
- (3) Based on efficiency defined by wires hit over scintillator trigger, or other similar definitions we use with these data to compute efficiencies of wire planes using various definitions.
- (4) Use these data with definition of efficiency in (3) to scan efficiency vs threshold voltage of discriminator cards or vs high voltage applied on wire planes.

(1) will be discussed in this chapter. (4) was discussed in Part II Chapter 3 Wire chamber.

Usage of data in 2) will be mainly focus on credibility checks of the validity of fitted tracks and track finding efficiency. This efficiency will be lower than the efficiency defined in the last paragraph, which merely requires at least one wire hit in a wire plane coincident with a trigger. There are, however, some exceptions: the wire can be outside the area covered by scintillator paddles, or there may not be enough hit wires in a wire plane to form a cluster. When combining wire plane geometry, geometry of trigger scintillator paddles, fitted track direction/intersection, and event-by-event hit time vs wire graph, we can decide if a fitted track is valid. *Event-by-event display* was discussed in Chapter 3, section 3.3 “Visualizing events” as visualization of wire hits. Track finding related application of the data in 2) was discussed in Chapter 5, section 5.4 track fitting results and onward.

For decoder data, there are only two types of entries: (1) Prefix D.T followed by a 4-digit number, stores the TDC time data for individual channel. (2) Prefix Ndata.D.T followed by a 4 digit number, stores the number of hits for the channel for each event. The number of hits capped at 6 per event per channel to prevent high-rate noise from discriminator cards ringing to dominate the data file.

We generate three useful plots from these data:

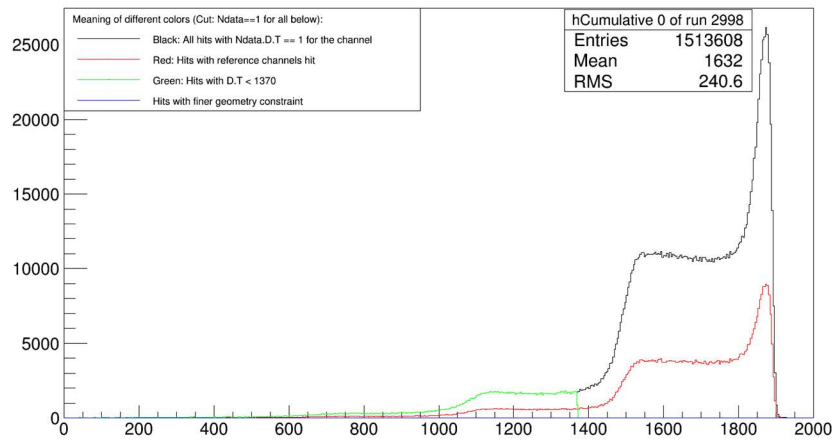
- 1) The cumulated TDC time distribution for all channels give us general ideal of the raw time distribution. It only uses the largest TDC time (correspond to the smallest real time, or from the 1<sup>st</sup> hit) entry for each wire for each event.
- 2) The cumulated hit time when the wire has more than one hit in the event, and only fill times indexed larger than 0. This indicates the noise level of the run when compared to the number of entries to plot 1), with some residue image of the raw time distribution.
- 3) The hit counts for each wire. The wire indices have been rearranged to make them follow the increment or decrement order of wires since when writing the crate map database file, the channel indices follow the positions of channels on the TDC from top to bottom, then left to right (since a single TDC module/slot arranges 96 channels from top

to bottom). The ordering of these wires can be in the same order as analyzer convention, or the opposite.

Remarks:

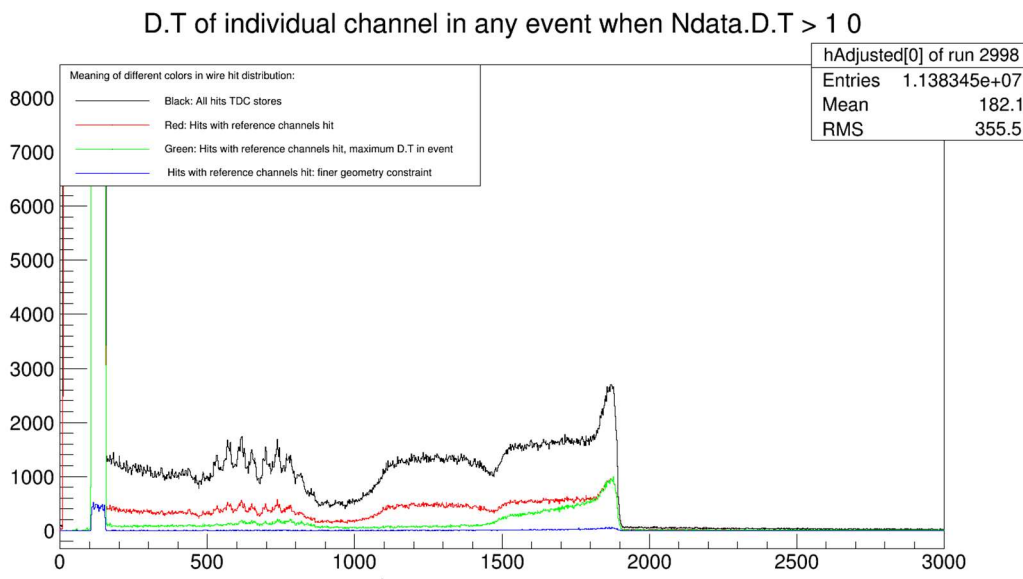
- (1)  $96 \times (2 \times 8 + 2) = 1728$  channels are implemented,  $2 \times 8$  means 2 TDC modules per wire plane, and 8 wire planes from 4 wire chambers, with 2 additional spares, thus 4 digits are needed to specify a channel.
- (2) Cuts could be easily applied to these histograms. D.T stores raw time, so applying cuts on raw time is natural. Another common cut is applying geometric constraints, usually accomplished by placing additional smaller (than trigger paddles) scintillator paddles above or below wire chambers and connecting output from these scintillators to TDCs as reference channels. Logic AND condition of these triggers will give geometric constraints for the tracks.

D.T of every hit channel that Ndata.D.T==1 0



III Fig 7. 1 Cumulated hit time for all channels. Ordinate: counts, no unit, abscissa: TDC time with corresponding cuts explained in legend in TDC unit ( $0.5 \text{ ns}$ ).

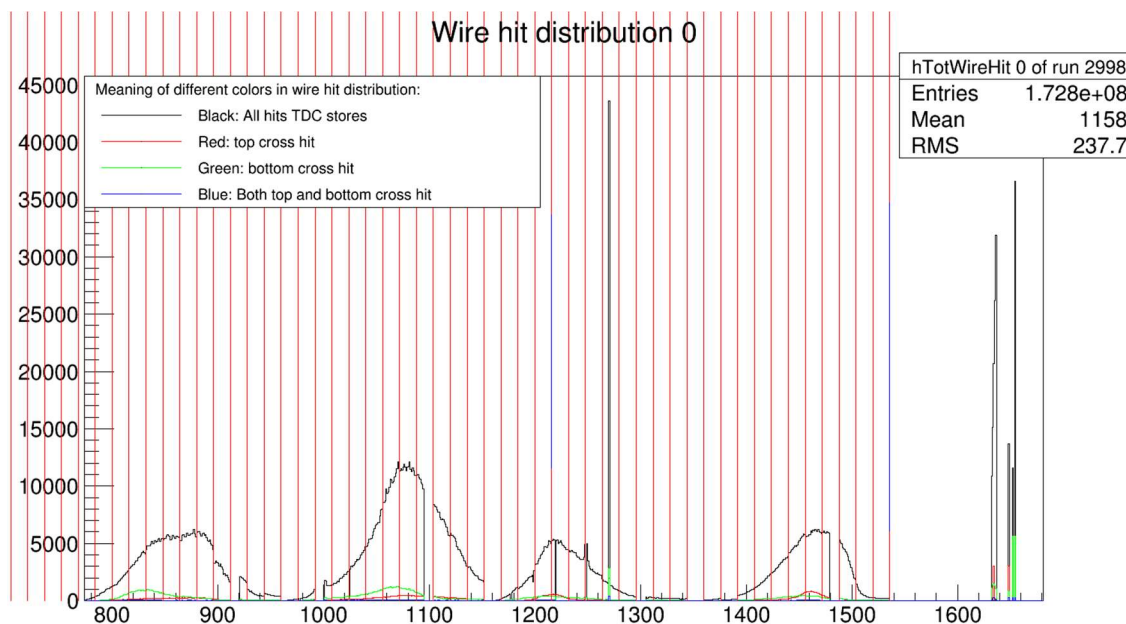
From all 4 active wire planes in the run of test run 2998. (From 1<sup>st</sup> 100k events, abscissa represents TDC time, ordinate represents counts.)



III Fig 7. 2 Cumulated hit time when the wire has more than one hit in the event. Ordinate: counts, no unit, abscissa: TDC time with corresponding cuts explained in legend in TDC unit (0.5 ns).

Using the same condition as Fig 7.1. Abscissa represents TDC time, ordinate represents counts. Note: for histogram with other colors, the cuts applied were different as described in legend. Remark:

1. It can be seen here the number of entries is 11.4 million, which is a lot more than 1.51 million entries from the last histogram. It means noise level were high in this run, as it can be seen in the much higher peak with low TDC time (about 150 TDC time and less). At most of the time it means for certain time interval certain discriminator card(s) was/were ringing.
2. Although the high noise rate is present, the data from this run are mostly valid when it is not ringing since comparing the peak and the plateau in comparison to the previous histogram in Fig. 7.1. Fig. 7.1 has about 7 times data in this TDC time region. Thus if we apply cut in TDC time to remove data in the noisy region that could not possibly be a real drift time, the rest of the data are mostly valid.
3. To pinpoint where the noise originated we will refer next histogram (Fig 7.3). Wires with noise usually have much higher hit counts. In some cases the ringing cards are on the other pair of wire chambers (usually when 4 wire planes not 8, are tested at a time), which were not holding high voltage during the run. The cards on the other pair of wire chambers were still powered to suppress noise, but sometimes they ring. It is exactly the case in this run. (Fig 7.3 is zoomed in and didn't show TDC time from the other 4 wire planes.)
4. To check if there is a power surge that triggers ringing of a certain discriminator card, we can draw event length vs event number, a jump of event length in a certain region of event number indicates the time region of the ringing.



III Fig 7. 3 Hit distribution of all wires. Ordinate: counts, no unit, abscissa: TDC channel, no unit.

Data of wire chamber 1,2 form run 2998 (chamber 3,4 are not active in this run). Red vertical lines are separating channels of different discriminator cards. Abscissa represents wire index, ordinate represents counts.

Remarks:

1. The 9<sup>th</sup> or 10<sup>th</sup> cards in each wire plane has a gap of 9 channels since they're not connected to any wires (see Fig. 2.7).
2. The right-most channels (with indices > 1600) with higher counts are reference channel counts from small scintillator paddles. Applying cuts of coincidence to these paddle triggers gives geometry cuts on tracks.

## Part IV Simulation

### 1 Generate BH pairs

#### 1.1 Introduction

The Geant 4 physics package does not have the Bethe-Heitler cross section built in. Positron and electron pairs produced from the BH process is required as primary vertex input for Geant 4 simulation. That is, a text file storing BH pair kinematics information has been read by our Geant 4 simulation program, as the primary vertex. The simulation then simulates these electron positron pairs by propagating them through background and detector materials as well as the magnetic field. The simulation then retrieves track information from preset simulation sensitive detector volumes that represents response of real detectors.

R.N Lee *et al.* have calculated the BH cross section and provided us the code to compute the BH cross section at any point in phase space. [20] Prof. R. Pywell has written a “wrapper” code that provides a C++ class `BH_cross_sections` and simplifies the use of Lee’s code along with the internal global variables needed within the code from any code written by the user. [50]. First, we provide atomic number of the target  $Z$ , and photon beam energy  $E_\gamma$ , then the code calculates differential the cross section:

$$d\sigma(E_p, E_q, \theta_p, \theta_q, \varphi_{q-p}) \quad (1.1)$$

where the subscripts  $p, q$  represent the electron and positron, respectively,  $E_{p,q}$  are total energy of the particle,  $\theta_{p,q}$  are polar angle, and  $\varphi_{q-p}$  is the difference of azimuthal angles between two particles. The dependence of the cross section on azimuthal angle is only one difference between the two particles, yet the azimuthal angles of both particles are to be specified for Geant 4 simulation.

The task left is to generate the BH pairs satisfying this distribution. Briefly speaking, the generation process starts with random (kinematics) pair generation, followed by Monte Carlo simulation selecting pairs satisfying distribution of the cross section. The resulting file stores the following information:

$$KE_p, KE_q, \theta'_p, \varphi'_p, \theta'_q, \varphi'_q, d\sigma \quad (1.2)$$

where  $KE$  are the kinetic energies of the particles,  $\theta'$  are the horizontal projection angles and  $\varphi'$  are vertical projection angles of particle velocity direction with respect to the beam direction.  $d\sigma$  is the differential cross section of this pair at this kinematics.

In this chapter we first discuss the procedure of the pair generation, showing the resulting pair energy, angle distributions at the end. Some modification of the code has been made, either to confirm the precision of the result or to increase the efficiency of the Monte Carlo simulation. In the end applications of the pair text file are discussed.



## 1.2 Pair generation procedure

### 1.2.1 Introduction

The first step of pair generation includes generating pairs random in energy and direction. The cross section calculation using the program provided by the R. Lee is the most time-consuming part of the routine, which is followed by the Monte Carlo simulation to select qualified BH pairs.

Thus, both energy and angle cuts before cross section calculation is essential for Monte Carlo simulation speed. Energy cuts are made based on how magnets bend the particles and the wire chamber acceptances. The solid angle acceptances are mainly constrained by the acceptance of the magnet, which provide the most opportunity for efficiency improvement. It includes: 1. Yoke hole of the magnet, which limits maximum spherical angles; 2. Inner cone shaped baffle, which places a limit on minimum spherical angles; 3. Magnet poles, which are circles in shape parallel to horizontal plane, and mainly limit azimuthal angles of the particles. In addition, kinematics constraints have also been considered.

The final step is to use Monte Carlo simulation to generate a text file with pairs distributed according to the cross section. The main reasons this part is so time consuming are: 1. Cross section code by Lee consists of numerical operations on special functions and interpolations. 2. the cross section is very sensitive to the difference in energies of the pair and to polar angles, which makes Monte Carlo simulation very inefficient. A modification has been made to improve greatly the Monte Carlo efficiency. It reduced computation time to 1/20 or even less based on beam energy, specific cuts used and randomness of the Monte Carlo process.

### 1.2.2 Uniform random pairs generation

The main methods used here include uniform random number generation and change of variables of random variables. A function  $R = randfloat()$  which generates random floating point numbers in the range  $[0,1]$  is coded based on the  $random()$  function from C++, which generates random non-negative integer from 0 to  $INT\_MAX \sim 2 \times 10^9$ .

To generate uniform random energy:

$$E_p = E_{min} + (E_{max} - E_{min})R \quad (1.3)$$

$$E_q = E_\gamma - E_p \quad (1.4)$$

where  $E_{max} = E_\gamma - E_{min}$ .

To generate uniform random solid angles between minimum polar angle  $\theta_{min}$  to  $\theta_{max}$  is a bit more complicated. The differential solid angle is:

$$d\Omega = \sin\theta d\theta d\varphi = d\cos\theta d\varphi \quad (1.5)$$

It's easy to see in order to have uniform random solid angle,  $\cos\theta$  and  $\varphi$  must be uniformly distributed. The one issue here is that  $\theta$  and  $\varphi$  are not necessarily generated in the entire range of solid angle. For  $\varphi$ , since the existing cone baffle with center axis coincide with beam, electron only propagate to right side detectors while positron to the left. In addition, limits on the angles are symmetric about horizontal plane as the beam lies in the symmetry plane of magnet pole.

Currently  $\varphi$  are generated in range:

$$\varphi_p \in [180^\circ - \varphi_0, 180^\circ + \varphi_0], \varphi_q \in [-\varphi_0, \varphi_0] \quad (1.6)$$

And  $\varphi_p, \varphi_q$  are generated using the uniform random number  $R$  by:

$$\varphi_p = 180^\circ + (2R - 1)\varphi_0, \varphi_q = (2R - 1)\varphi_0 \quad (1.7)$$

where  $\varphi_0$  is chosen as  $28^\circ$  and will be explained in next section.

In order to generate the angle  $\theta$  making  $\cos\theta$  uniformly distributed from  $\theta_{min}$  to  $\theta_{max}$ .  $\theta_{min}$  is determined by polar angle of the con baffle,  $\theta_{max}$  is determined by polar angle spanned from target center to bound of yoke hole. Using the change of variable formula for cumulative distribution function in probability theory [51]:

$$N(\cos\theta_{min} - \cos\theta) = P(\cos\theta < \cos\theta < \cos\theta_{min}) = P(0 < r < R) = R \quad (1.8)$$

$P(\cos\theta < \cos\theta < \cos\theta_{min})$  is the probability of random variable  $\cos\theta$  in range  $[\cos\theta, \cos\theta_{min}]$ , noting  $\cos\theta$  is monotonic decreasing function in region  $\left[0, \frac{\pi}{2}\right] \supset [\theta_{min}, \theta_{max}]$ .  $P(0 < r < R)$  is the probability of our uniform random variable  $r$  in range  $[0, R] \subset [0, 1]$ . Here  $N$  is the normalization factor, which is determined by:

$$\begin{aligned} P(\cos\theta_{max} < \cos\theta < \cos\theta_{min}) &= N(\cos\theta_{min} - \cos\theta_{max}) = 1 \\ N &= 1/(\cos\theta_{min} - \cos\theta_{max}) \end{aligned}$$

Thus, random angle  $\theta$ , with condition  $\cos\theta$  uniformly distributed in range  $[\cos\theta_{max}, \cos\theta_{min}]$  is:

$$\begin{aligned} (\cos\theta_{min} - \cos\theta)/(\cos\theta_{min} - \cos\theta_{max}) &= R \\ \theta &= \text{acos}[\cos\theta_{min} - R(-\cos\theta_{max})] \end{aligned} \quad (1.9)$$

Both  $\theta_p$  and  $\theta_q$  were generated this way.

### 1.2.3 Choosing cuts based on magnet and wire chamber acceptance

The purpose to using cuts on particle energy and direction angles is to improve pair generation efficiency. For current setup, it takes about a week to generate one million events on local machine. For example, the differential cross section dependence on polar angle  $\theta$  ranges over  $10^6$ , and it will greatly decrease the Monte Carlo simulation selection of the pairs.

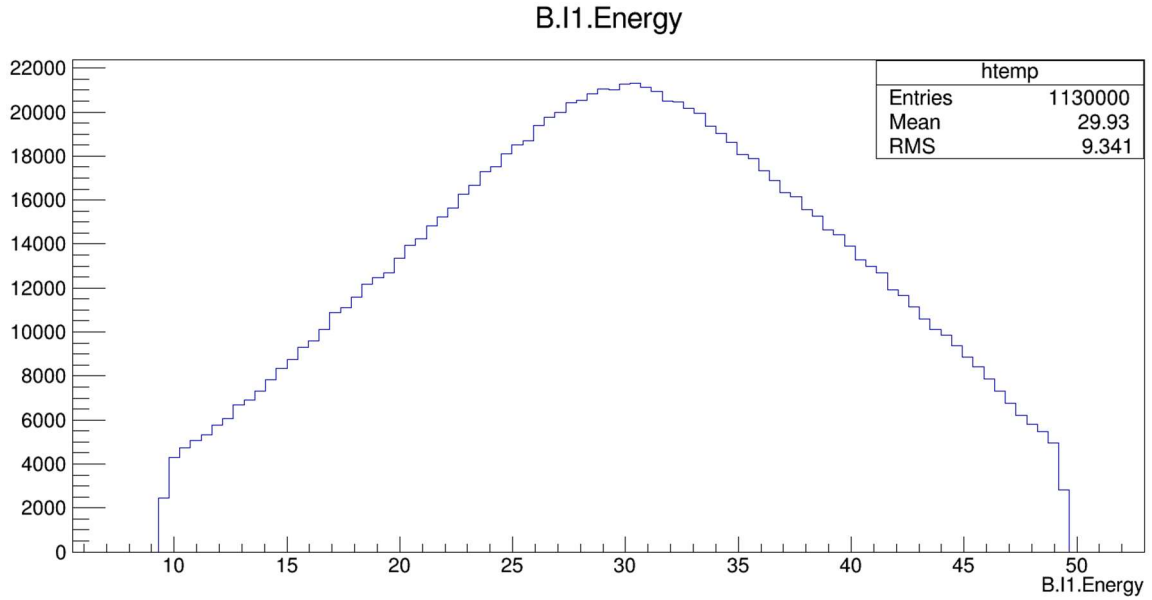
#### 1. Choosing energy cut

As seen in below figure, the electron energy distribution (from current simulation setup, which includes  $\varphi \in [-28^\circ, 28^\circ]$ ) is peaked near 30 MeV and density dropped to less than 1/5 of the peak value near 10 MeV and 50 MeV. By  $E_q = E_\gamma - E_p$  positron energy distribution is mirror image of electron energy about  $\frac{E_\gamma}{2} = 30\text{MeV}$ . The energy cut is:

$$10\text{MeV} \leq E_p, E_q \leq 50\text{MeV} \quad (1.10)$$

Since the trajectory of charged particles in uniform magnetic field is helix, the projected radius in horizontal plane is proportional to total energy  $E$  of the particle according to special relativity. Thus, particles with low energy the radius is very small that track direction has been bent too much, which will easily miss wire chamber. On the other end, the higher energy particles tracks have much larger radius in magnet, and could miss the wire chamber in downstream direction. In addition, the low or high energy particles intersect both front and back wire chambers but at some shallow angle to wire plane. In this situation, based on geometry of the wire planes (c.f. Part III, Appendix A1.5 formula (1)(2)), it always results in one of the u or v wire plane as high number of wires intersects the track and render signals, while the other wire plane has too few wires fired. This results in very low efficiency of track reconstruction from software by wire chamber.

It's proposed that the measurement of asymmetry will be between 18 to 42 MeV, the expanded energy range in simulation dealing with the effects of multiple scattering smearing the tracks, which needs to be taken into account in fitting BH pair kinematics from track information.



IV Fig 1. 1 Energy distribution of electrons at primary vertex. Ordinate: counts, no unit, abscissa: electron energy at primary vertex in  $MeV$ .

Using current planned experimental configuration.

## 2. Choosing the angle cuts

Spherical angles  $\theta$ ,  $\varphi$  are combined to determine tracks that could propagate through the magnet. The polar angle  $\theta$  range  $\theta_{min}$  to  $\theta_{max}$  are simple: tracks of the particles are straight lines before entering magnetic field and the geometric constraints prior to the magnet determine the range of  $\theta$ . For  $\theta_{min}$ , it is determined by the baffle cone aligned with the beam. The proposed polar angular limit for the cone is  $5^\circ$  and for Geant 4 simulations  $\theta_{min} = 4^\circ$  is set to approximate the effects of a finite beam radius and scattering of particles inside the target.  $\theta_{max} = 15^\circ$ , which is a bit larger than the polar angle spanned from center of target to back circumference of yoke hole:

$$\theta_{min} = 4^\circ \leq \theta \leq \theta_{max} = 15^\circ \quad (1.11)$$

Since the small gap (2'') of the magnet poles is the most constraining factor for  $\varphi$ . In addition, the smaller the value of  $\theta$ , the broader the range accessible for  $\varphi$ . To estimate the largest value of  $\varphi$  at the smallest  $\theta = 4^\circ$ , we assume straight line tracks to the back side of magnet poles. The target center to pole center distance is  $\sim 42$  cm, and pole radius is 19.7 cm. Thus, the distance  $d \cong 62$  cm from target center to back edge of magnet pole. If it hits the pole:

$$r \sin \theta \sin \varphi = h \quad (1.12)$$

$r \cong d$  is the straight track length to back upper or lower edge of the pole,  $h = 2.54$  cm is the half-gap between the two poles.

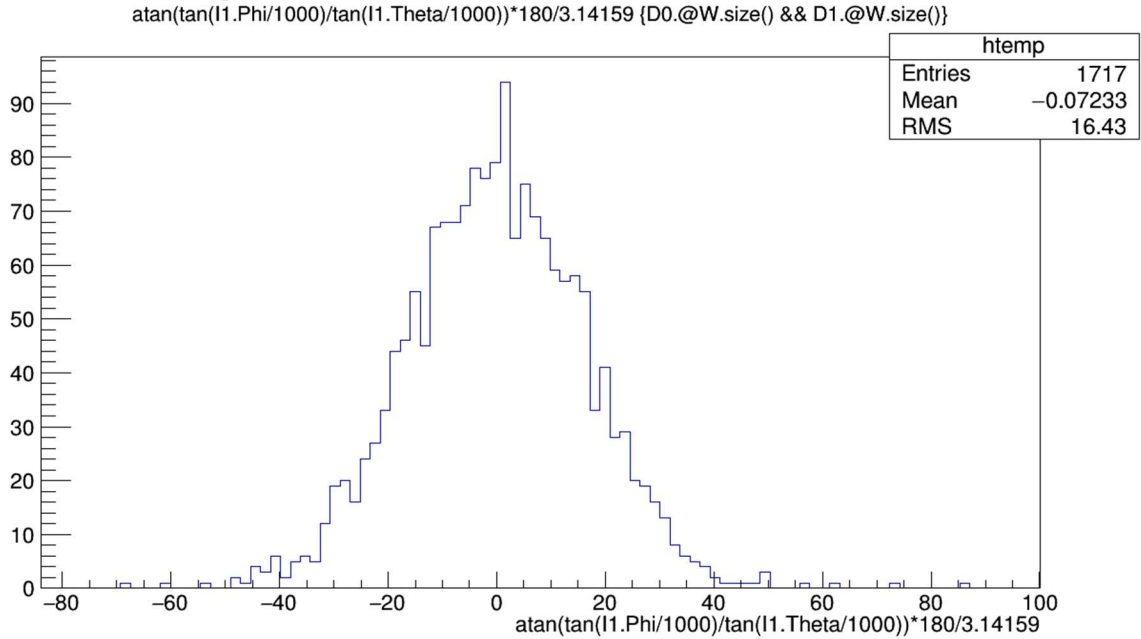
Solving (1.12)

$$\varphi = \arcsin\left(\frac{h}{r\sin\theta}\right) \quad (1.13)$$

It gives following typical values for max  $\varphi$  range:

$$\begin{aligned} \varphi &= 36.0^\circ \text{ at } \theta = 4^\circ \\ \varphi &= 28.0^\circ \text{ at } \theta = 5^\circ \\ \varphi &= 9.11^\circ \text{ at } \theta = 15^\circ \end{aligned}$$

For this reason,  $\varphi_0 = 28.0^\circ$  in formulas (1.6) and (1.7). The simulation results also support this estimate. The figures below show the  $\varphi$  distribution for a simulation using a generated pair file with range of  $\varphi \in [0^\circ, 360^\circ)$ , while particle energies were bounded at 10 MeV and 50 MeV:



IV Fig 1. 2 Electron  $\varphi$  distribution for the simulation. Ordinate: counts, no unit, abscissa: electron azimuthal angle  $\varphi$  at primary vertex in *degrees*.

With all possible values of  $\varphi$  at the primary vertex when wire chambers on both sides generate signals. In the description of the plot,  $\theta$  and  $\varphi$  are horizontal and vertical projection angles of the electron direction at the primary vertex. As it shows,  $\varphi_0 = 28.0^\circ$  is a reasonable estimate.

### 3. Additional cuts on track projection angles $\theta'_p, \varphi'_p, \theta'_q, \varphi'_q$ to constraint spherical angles

$\theta_p, \varphi_p, \theta_q, \varphi_q$ . Projection angles  $\theta'$  and  $\varphi'$  are defined as arctangents of the horizontal and vertical coordinate verses beam direction coordinate spanned from target. Since Geant 4 simulation uses direction vector to specify particle momentum directions, projection angles are convenient. While spherical angles are input for cross section calculation in code provided by theorists. The particle momentum direction can be represented in either way:

$$\mathbf{d} = (1, \tan\theta', \tan\varphi') \quad (1.14)$$

$$\hat{\mathbf{d}} = (\cos\theta, \sin\theta\cos\varphi, \sin\theta\sin\varphi) \quad (1.15)$$

By relating both equation above we can solve  $\theta', \varphi'$  by  $\theta, \varphi$  and vice versa:

$$\begin{cases} \tan\theta' = \tan\theta\cos\varphi \\ \tan\varphi' = \tan\theta\sin\varphi \end{cases} \quad (1.16)$$

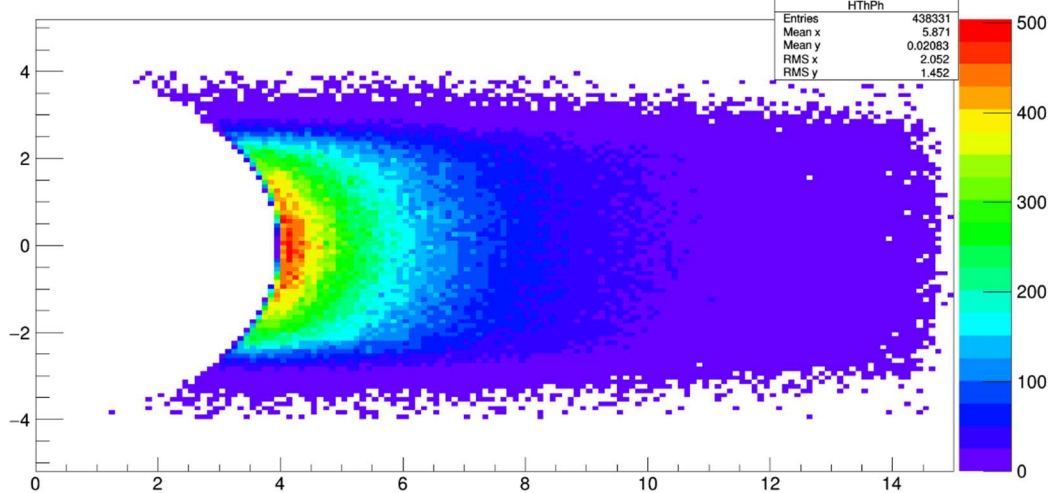
$$\begin{cases} \tan^2\theta = \tan^2\theta' + \tan^2\varphi' \\ \tan\varphi = \tan\varphi'/\tan\theta' \end{cases} \quad (1.17)$$

Due to the constraint on the yoke hole and upper/lower magnet pole the track projections seen from target center has a strip shape. The constraint on  $\theta'$  and  $\varphi'$  with maximum values will contain the strip shape in a rectangular box when projected onto a plane behind the magnet and perpendicular to the beam direction as seen in Fig. 1.3. For the current setup:

$$\theta'_{max} = 15^\circ = \theta_{max}, \varphi'_{max} \cong 4^\circ$$

$\varphi'_{max}$  cut makes  $\varphi$  much more constraint. Because of the variation of tracks for different energies and angles, the  $\varphi'$  range cannot be simply determined from analytic calculation as it requires relating tracks with certain energy and angle, propagate it into the magnet until it reaches the plane of the upper or lower pole's circle shaped boundary. By the result of simulation in figure below, we set  $\varphi'_{max} = 4^\circ$  to contain physically interested region.

t\_theta vs t\_phi distribution of detector accepted pairs



IV Fig 1. 3  $\tan\theta'$  (abscissa) vs  $\tan\varphi'$  (ordinate) from simulation. Ordinate:  $\tan\varphi'$ , no unit, abscissa:  $\tan\theta'$ , no unit.  $\theta'$  and  $\varphi'$  are horizontal and vertical projection angle of electron momentum direction at primary vertex. Under cut: BH pairs must reach detectors on both sides of the magnet.

The plot here has less constrained generated pair file that also required the wire chambers on both sides to detect particles.

### 1.2.4 Selection of random pairs by Monte-Carlo simulation

Once the randomly distributed  $e^+ - e^-$  pair has been specified by  $E_p, E_q = E_\gamma - E_p, \theta_p, \theta_q, \varphi_{q-p} = \varphi_q - \varphi_p$ , Monte Carlo simulation is used to determine if it will be written in to the generated pair data file. The procedure is simple. Calculate the differential cross section  $d\sigma$  with the kinematics, then generate a random number  $r \in [0, d\sigma_{max}]$ . If  $r < d\sigma$ , write the corresponding

$$KE_p, KE_q, \theta'_p, \varphi'_p, \theta'_q, \varphi'_q, d\sigma \quad (1.18)$$

into the data file, else discard the pair and start over.

The only parameter needs to be determined here is  $d\sigma_{max}$ , which is any value that is larger than the upper bound of  $d\sigma$  in the phase space considered. Since the dimension of phase space is 5, and as mentioned before the ratio of  $d\sigma$  values can be as large as  $10^6$  between two different regions of the phase space,  $d\sigma_{max}$  is hard to determined. However, from the previous resulting energy and angle distributions shown in the figures, instinct tells us the largest  $d\sigma$  should be near this setting:  $E_p \cong E_q, \theta_p \cong \theta_q \cong \theta_{min}$  and  $\varphi_{q-p} \cong 180^\circ$ . In our practice, the  $d\sigma_{max}$  value is determined by searching: comparing millions of random generated pair with relatively small  $\theta$  values and record the maximum value  $d\sigma'_{max}$ , which by no means will be the maximum  $d\sigma$  in the phase space, but it will be close. Then, set  $d\sigma_{max} = \alpha d\sigma'_{max}$  with a scaling factor  $\alpha > 1$ . There could be case that after assigned  $d\sigma_{max}$  be less than the  $d\sigma_{max}$  value during a simulation. However, the chance is very small and we can update the value for future runs, the factor  $\alpha$  compensates for this issue, and due to the interpolation nature [52] of look-up tables of the numerical code calculating  $d\sigma$  using current  $d\sigma_{max}$  is very dependable.

### 1.2.5 Pair generation results, and asymmetry

The result of pair generation is input to the Geant 4 simulation. Since the phase space dimension is 5, the distributions can only be shown with respect to one or two components while others are integrated out.

The pair data file shown is generated under setting:

Energy cut:

$$10MeV \leq E_p, E_q \leq 50MeV$$

Spherical angle cut:

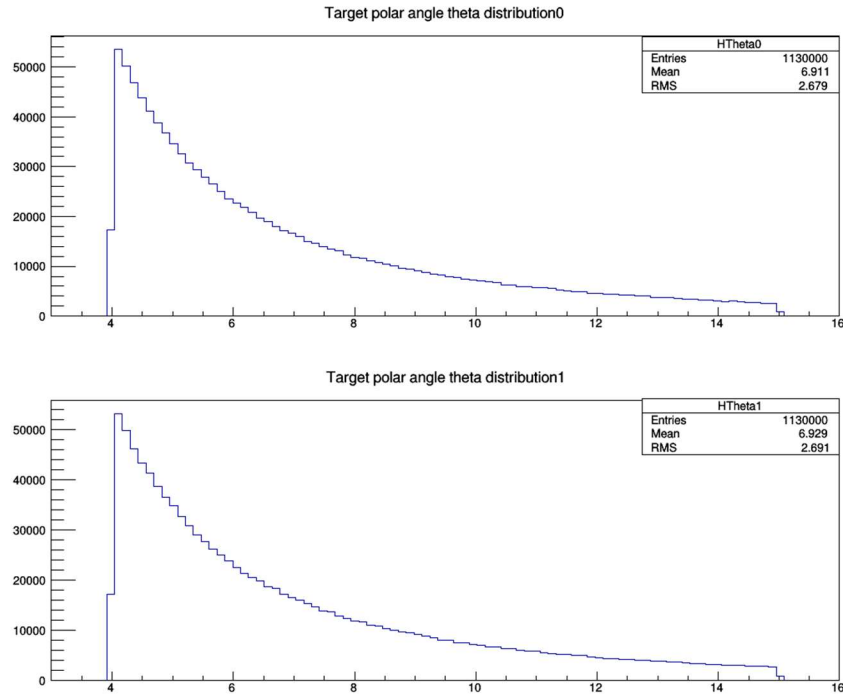
$$\theta_{min} = 4^\circ \leq \theta \leq \theta_{max} = 15^\circ$$

$$\varphi_p \in [180^\circ - \varphi_0, 180^\circ + \varphi_0], \varphi_q \in [-\varphi_0, \varphi_0], \varphi_0 = 28^\circ$$

Projection angle cut:

$$\theta' \leq \theta'_{max} = 15^\circ, \varphi' \leq \varphi'_{max} = 4^\circ$$

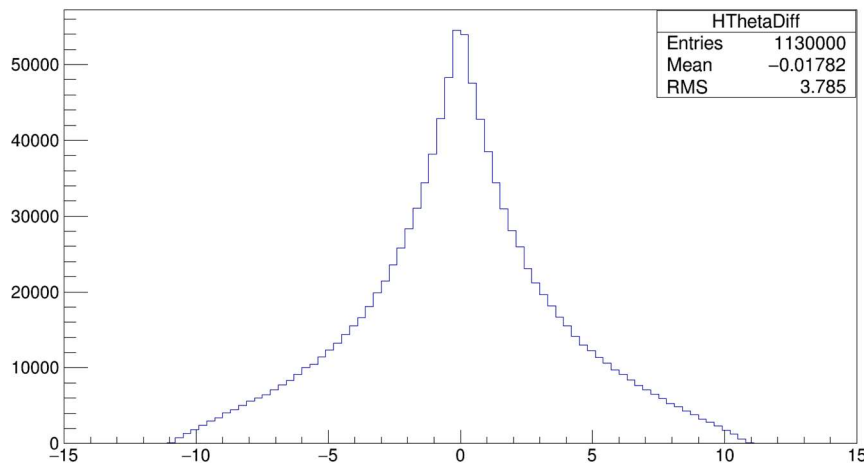
The electron (kinetic) energy distribution figure has been shown (In Fig 1.1). Counts are high near  $30 MeV$ , while decreasing when either energy increases or decreases. The peak count has about 5 times count as lowest/highest energy count. It is obvious that the energy asymmetry shown in the histogram, asymmetries between low/high energy pairs are much larger while counts are much less and wire chamber efficiency is low in the extreme regions. According to Lee [20], the asymmetry is 0 at an electron energy of  $30 MeV$  or when energy difference  $\delta$  between electron and positron is  $0 MeV$ . Only when particle energies are not close to  $30MeV$ , and not too low or high, is the asymmetry is measurable.



IV Fig 1. 4 Polar angle  $\theta$  distribution of all generated events at target. Ordinate: counts, abscissa: polar angle  $\theta$  at primary vertex in *degrees*. Top for positrons and bottom for electrons.

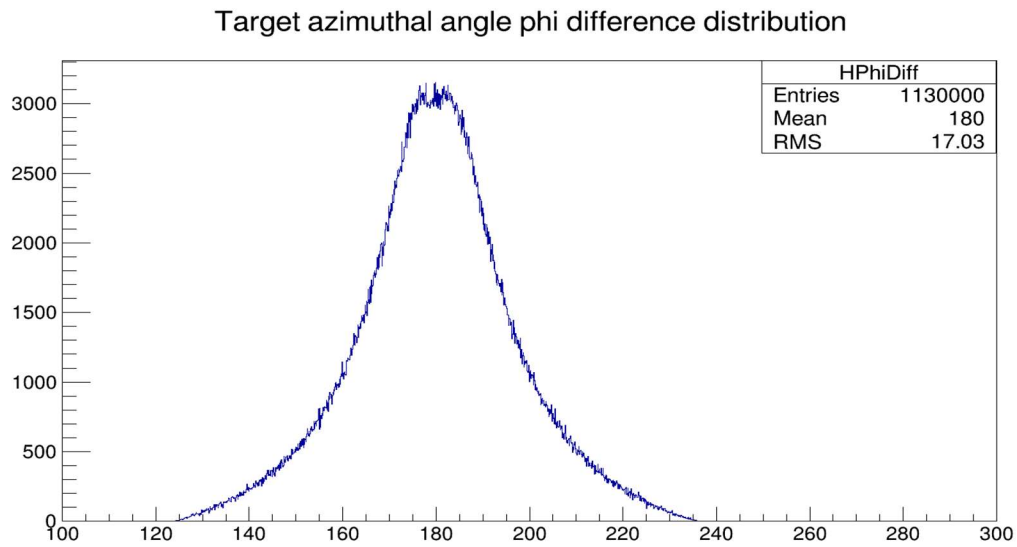
The Upper histogram is for the positron  $\theta_q$ , the Lower for electron  $\theta_p$ . The distributions are almost identical, and it is also seen that the cross-section dependence on  $\theta$  is a lot more sensitive than the dependence on  $E$ .

Target polar angle phi difference distribution



IV Fig 1. 5 Difference of the polar angle  $\theta_p - \theta_q$ . Ordinate: counts, abscissa: polar angle difference between the two particles in BH pair  $\theta_p - \theta_q$  at primary vertex, in *degrees*.

The kink at  $\theta_{diff} = 0^\circ$  comes from the cut  $\theta_{min} = 4^\circ \leq \theta$ .



IV Fig 1. 6  $\varphi_{q-p}$  distribution. Ordinate: counts, abscissa: polar angle difference between the two particles in BH pair  $\varphi_{q-p}$  at primary vertex, in *degrees*.

Unit degrees. The peak at  $180^\circ$  is expected. We constrained our

$$\varphi_p \in [180^\circ - \varphi_0, 180^\circ + \varphi_0], \varphi_q \in [-\varphi_0, \varphi_0], \varphi_0 = 28^\circ$$

And  $\varphi_{q-p_{max/min}}$  reaches  $180^\circ + 2\varphi_0 = 236^\circ$  and  $180^\circ - 2\varphi_0 = 124^\circ$ , respectively. If we loosen the  $\varphi_p, \varphi_q$  range,  $\varphi_{q-p}$  could be even larger.



## 1.3 Modifications on pair generator code

### 1.3.1 Solving 2<sup>nd</sup> particle energy $E_q$

As noted in previous sections, the recoil nucleus kinetic energy is ignored (or equivalently the rest mass of the recoil nucleus is approximated to be infinite), or  $E_q = E_\gamma - E_p$ . To confirm if this is the case, this energy is included in the calculation and compared with simple result

$$E_q = E_\gamma - E_p.$$

First, we derive formula for the recoil nucleus kinetic energy  $KE_r$ , without loss of generality set  $\varphi_p = 0^\circ$ , using energy-momentum relation:

$$\begin{aligned} p_p &= \sqrt{E_p^2 - m_e^2} \\ p_q &= \sqrt{E_q^2 - m_e^2} \\ \mathbf{p}_p &= (p_p \sin \theta_p, 0, p_p \cos \theta_p) = (p_{px}, p_{py}, p_{pz}) \\ \mathbf{p}_q &= (p_q \sin \theta_q \cos \varphi_q, p_q \sin \theta_q \sin \varphi_q, p_q \cos \theta_q) = (p_{qx}, p_{qy}, p_{qz}) \end{aligned}$$

Here  $z$  is the beam direction. From momentum conservation:

$$\mathbf{p}_r = (-(p_{px} + p_{qx}), -(p_{py} + p_{qy}), E_\gamma - p_{pz} - p_{qz})$$

And recoil nucleus kinetic energy will be:

$$KE_r = E_r - m_r = \sqrt{p_r^2 + m_r^2} - m_r$$

The notations above are consistent with previous ones, while  $\mathbf{p}'$ s are momentum vectors,  $m_e$  is electron rest mass,  $m_r$  is recoil nucleus rest mass.  $m_e = 0.511 \text{ MeV}$ ,  $m_r \cong 238 \times 931.5 \text{ MeV} \cong 4.34 \times 10^5 m_e$  for  $U^{238}$ , thus  $KE_r$  must be small. From the above formulas  $KE_r$  is analytically represent as a function:

$$KE_r(E_p, E_q, \theta_p, \theta_q, \varphi_q) \quad (1.19)$$

with  $E_\gamma$ ,  $m_e$ ,  $m_r$  as parameters. Next  $E_q$  is solved using the  $KE_r$  formula by a step searching method:

First, we set initial value of  $KE_{r(0)}$ , and step size  $\Delta E_{(0)}$ . Then using energy conservation:

$$E_{q(i)} = E_\gamma - E_p - KE_{r(i)} \quad (1.20)$$

We estimated  $E_q$  with known  $E_p$ . Using formula (1.19) to calculate  $KE_r$  using this estimated  $E_q$  value. Or:

$$KE_{r\_cal(i)} = KE_r(E_p, E_{q(i)}, \theta_p, \theta_q, \varphi_q) \quad (1.21)$$

Here  $i$  is the index of iteration. For each iteration,  $KE_{r(i)} = KE_{r(i-1)} + \Delta E_{(i)}$ .  $\Delta E_{(i)}$  is the set step size. Next compare difference of  $KE_{r(i)}$  and  $KE_{r\_cal(i)}$  with result of previous iteration, that is compare  $\Delta_{(i)} = KE_{r\_cal(i)} - KE_{r(i)}$  and  $\Delta_{(i-1)} = KE_{r\_cal(i-1)} - KE_{r(i-1)}$ .

- 1) If  $\Delta_{(i)} \Delta_{(i-1)} > 0$ : If  $|\Delta_{(i)}| < |\Delta_{(i-1)}|$ , means searching is in the correct direction, don't change  $\Delta E_{(i+1)} = \Delta E_{(i)}$  and continue. If  $|\Delta_{(i)}| > |\Delta_{(i-1)}|$ , means searching is in the wrong direction, set  $\Delta E_{(i+1)} = -\Delta E_{(i)}$
- 2) Else if  $\Delta_{(i)} \Delta_{(i-1)} < 0$ , it means the solution lies in between  $KE_{r(i)}$  and  $KE_{r(i-1)}$ , set  $\Delta E_{(i+1)} = -\Delta E_{(i)}/2$  and continue.

The solution search continues until  $|\Delta_{(i)}|$  is lower than the preset threshold. The current set of values are  $KE_{r(0)} = 0.1 \text{ (MeV)}$ ,  $\Delta E_{(0)} = 10^{-2} \text{ (MeV)}$ , and its typically takes about 30 iterations to reach the preset threshold value  $10^{-7} \text{ MeV}$ . The final  $KE_r$  result is at  $10^{-4} \sim 10^{-5} \text{ MeV}$  range.

For this much of  $KE_r$  or the discrepancy of  $E_q$ , there is hardly noticeable change in differential cross section  $d\sigma(E_p, E_q, \theta_p, \theta_q, \varphi_{q-p})$ . Thus, using simple formula  $E_q = E_r - E_p$  is justifiable.

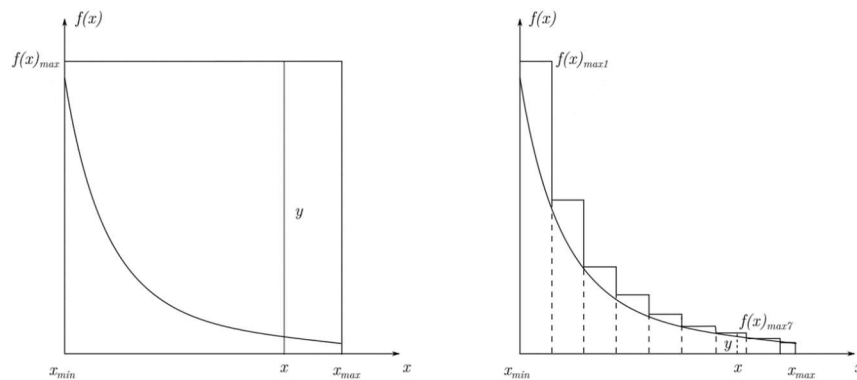
### 1.3.2 Monte-Carlo simulation improvement

One big drawback of the pair generation code lies in the efficiency. As mentioned before, it takes about 1 week to generate 1 million events on a local machine, and it varies based on the cuts on the phase space described on section 1.2.3. The main reason of this inefficiency is the very low selection rate of random pairs from the Monte-Carlo simulation: the differential cross section  $d\sigma$  is highly sensitive on the point in the phase space, and there are about 6 orders of magnitude variation in the phase space under current cut. It means a huge amount of time is used to compute  $d\sigma(E_p, E_q, \theta_p, \theta_q, \varphi_{q-p})$  but few of the pairs will be selected after the computation. The Monte-Carlo selection probability is based on a point in phase space, the lower the  $d\sigma$  corresponds to point  $(E_p, E_q, \theta_p, \theta_q, \varphi_{q-p})$  the lower the probability. Thus, the looser the cut, the larger the phase space region scrutinized by the Monte-Carlo simulation, and the slower the computation speed. Thus, the choice of cut in section 1.2.3 requires a balance of containing as large a phase space region as we are interested in to measure the asymmetry from and the pair generation computing speed. In order to tackle this special situation, a new version was written and the computation speed of pair generation was increased by about a factor of 50.

#### 1) Basic idea

To be precise, the notation  $d\sigma(E_p, E_q, \theta_p, \theta_q, \varphi_{q-p})$  should be  $\frac{d\sigma(E_p, E_q, \theta_p, \theta_q, \varphi_{q-p})}{d\theta_p d\theta_q d\varphi_p d\varphi_q dE_p dE_q}$ . In this section we just write it simply as  $d\sigma$  (See Fig 1.7 below for illustration of 1D case). Recall from the simple 1-dimensional case of Monte-Carlo simulation for computing the area under curve  $f(x)$  from limits  $x_{min}$  to  $x_{max}$ . We first generate a uniform random number  $x_{min} < x < x_{max}$ , then generate a second uniform random number  $0 < y < f(x)_{max}$ , and pick if  $y < f(x)$ . So, the Monte-Carlo simulation efficiency in the entire region is the ratio of the area under curve  $f(x)$  to area of the rectangle below  $f(x)_{max}$ :

$$Eff = \frac{\int_{x_{min}}^{x_{max}} f(x) dx}{\int_{x_{min}}^{x_{max}} f(x)_{max} dx} = \frac{\int_{x_{min}}^{x_{max}} f(x) dx}{f(x)_{max}(x_{max} - x_{min})} \quad (1.22)$$



IV Fig 1. 7 1-dimension illustration of generating events satisfying certain distribution  $f(x)$ .

Left: standard procedure described in the paragraph above. Right: modified procedure. Divide interval  $[x_{min}, x_{max}]$  into smaller subintervals, set individual upper bound  $f(x)_{\max(i)}$  for each subinterval, the random number  $y$  is generated  $0 < y < f(x)_{\max(i)}$  instead of  $f(x)_{\max}$ , if  $f(x)_{\max(i)} \ll f(x)_{\max}$  the efficiency is greatly increased.

And for our case  $f(x) \rightarrow d\sigma$ ,  $dx \rightarrow dV = \sin\theta_p d\theta_p \sin\theta_q d\theta_q d\varphi_p d\varphi_q dE_p$  as an infinitesimal volume of the phase space. Then, the efficiency of our Monte-Carlo simulation is:

$$Eff = \frac{\iint d\sigma dV}{\iint d\sigma_{\max} dV} = \frac{\iint d\sigma dV}{d\sigma_{\max} V} = \frac{\langle d\sigma \rangle}{d\sigma_{\max}} \quad (1.23)$$

Where  $d\sigma_{\max}$  is the maximum value of  $d\sigma$  in the phase space region,  $V$  is the total volume of the region, and  $\langle d\sigma \rangle$  is the average value of  $d\sigma$  in the region. Since the value of  $d\sigma$  drops drastically as  $E_p$  deviates from  $\sim 30$  MeV and as  $\theta_p$  or  $\theta_q$  increases, the  $\langle d\sigma \rangle$  is very small in most regions of the phase space and so is  $Eff$  in eq. (1.23).

The idea to increase computation speed is to improve the efficiency in (1.23). We cannot change  $\langle d\sigma \rangle$  once the phase space region is specified but we can modify the denominator in the formula. To do this, we split the region into smaller regions, indexed by  $i$ . For each region we search for the largest value  $d\sigma_{\max}(i)$  in the region. Thus, the denominator of (3.5) turns into:

$$\sum_i \iint d\sigma_{\max}(i) dV_i = \sum_i d\sigma_{\max}(i) \cdot V_i \quad (1.24)$$

In most regions  $d\sigma_{\max}(i) \ll d\sigma_{\max}$  so  $\sum_i \iint d\sigma_{\max}(i) dV_i \ll \iint d\sigma_{\max} dV$  and the efficiency improves.

## 2) Practical procedure of improved implementation

Now we use modified formula (3.5) for Monte-Carlo simulation with higher efficiency:

$$Eff = \frac{\iint d\sigma dV}{\sum_i \iint d\sigma_{\max}(i) dV_i} = \frac{\sum_i \iint d\sigma dV_i}{\sum_i \iint d\sigma_{\max}(i) dV_i} \quad (1.25)$$

Thus, two quantities are to be determined:

1. Maximum differential cross section  $d\sigma_{\max}(i)$  for each sub-region. The method to determine  $d\sigma_{\max}(i)$  is the same as  $d\sigma_{\max}$ , described in section 2.4. That is, generate random  $E_p, E_q, \theta_p, \theta_q, \varphi_{q-p}$ , compute the corresponding  $d\sigma$ 's, and take the largest value. This process can be very time consuming since each  $d\sigma_{\max}(i)$  costs about the same time as determining  $d\sigma_{\max}$ . The only change here is that it's found that if both  $\theta$  are selected to be the  $\theta_{\min}(i)$  for the subregion, the  $d\sigma_{\max}(i)$  are almost taken in these setting while only  $E_p, E_q, \varphi_{q-p}$  are subjected to change. It significantly reduced time for  $d\sigma_{\max}(i)$  searching.

2. Total cross section  $\sigma_i = \iint d\sigma dV_i$  of each region. While for the standard one region procedure, this is not a problem. Here, if we split into small regions, how many pairs need to be generated inside each region is proportional to the total cross section of the region. Monte-Carlo integration is a way to do it. Denote  $\sigma_i = \iint d\sigma dV_i$ , and  $\sigma = \iint d\sigma dV = \sum_i \iint d\sigma dV_i$ . If we want to generate  $N$  total number of events, then for each sub-region the number of events needs to be generated is:

$$N_i = \frac{N\sigma_i}{\sigma} \quad (1.26)$$

To compute  $\sigma_i$ , Monte-Carlo integration is used. First rewrite

$$\sigma_i = \iint d\sigma dV_i = \langle d\sigma_i \rangle V_i \quad (1.27)$$

where  $\langle d\sigma_i \rangle$  is the average differential cross section in the sub-region  $V_i$ . This is very similar to calculating mass of a volume by substitution  $\sigma_i \rightarrow M$ ,  $d\sigma \rightarrow \rho$ , and  $\langle d\sigma_i \rangle \rightarrow \langle \rho \rangle$  in the formula, or total mass of the volume  $M$  equals average density  $\langle \rho \rangle$  times the volume  $V$ . Thus, we generate  $n$  uniformly distributed pairs in phase space sub-region  $V_i$  of the phase space, by using exactly the same method in section 2.2 (Uniform random pairs generation). We compute

$d\sigma$  at each random point, and then the sample average  $\langle d\sigma_i \rangle$  of all  $n$  points, calculate  $V_i$  by converting integral into sum. Use (3.8) to get result of each  $\sigma_i$ .

Remarks:

1) If we split one of the sub-regions into smaller ones and apply the same method, that is finding the  $j^{\text{th}}$  sub-sub-region maximum differential cross section  $d\sigma_{max}(i, j)$ , etc., Then  $\iint d\sigma_{max}(i)dV_i \leq \sum \iint d\sigma_{max}(i, j)dV_{i, j}$ , and the result with finer partitioning is always better. The only issue is finding  $d\sigma_{max}(i, j)$  is time consuming, so we cannot make smaller sub-regions indefinitely.

2)  $N$  and  $N_i$  in formula (1.26) are integers, while  $\sigma_i$  and  $\sigma$  are real numbers. Thus, there is some roundoff error after turning  $N_i$  from (1.26) into integer, the sum of  $N_i$ 's will not be exactly equal to  $N$ . In addition, the greater number of subregions the more the discrepancies.

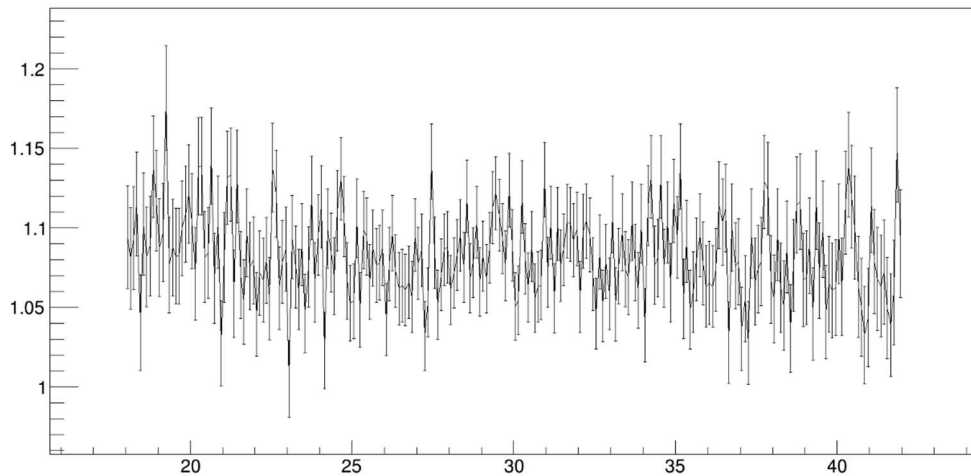
3) In order to use this improved code to Geant 4 simulation to simulate any number of events other than total number of events stored in the generated data file  $\sum N_i$ , it's necessary to shuffle the events in the generated pair data file before conducting Geant 4 simulation. The issue is that in the current setup, pairs are generated by sub-region, i.e., until all pairs in one sub-region is generated, then starts for the next sub-region. If the number of events in the Geant 4 simulation is set smaller than  $\sum N_i$ , then any events in higher indexed sub-regions will not be generated and the Geant 4 simulation input will not satisfy the distribution by the calculated cross section.

The current setup is: the cross section is most sensitive to change of polar angle  $\theta$ , so divide both  $\theta_p, \theta_q$  into 44 regions from  $\theta_{min} = 4^\circ$  to  $\theta_{max} = 15^\circ$ . Each sub-region contains  $(\theta_{max} - \theta_{min})/44 = 0.25^\circ$  spans, giving a total of  $44^2 = 1936$  sub-regions. Other cuts are the same as a standard generator. A pre-run file has been generated to store subregion bounds,  $d\sigma_{max}(i, j)$ ,  $\frac{\sigma_{i, j}}{\sigma}$  information.  $i, j$  are indices of subregions for  $\theta_p, \theta_q$  respectively. As a example of improvement of using  $d\sigma_{max}(i, j)$  instead of  $d\sigma_{max}$ :

$$\begin{aligned} d\sigma_{max}(1,1) &= 1232.3 \\ d\sigma_{max}(1,44) &= 13.22 \\ d\sigma_{max}(44,44) &= 0.0578 \end{aligned}$$

There is a quick comparison between the pair distributions generated by standard and the improved method as seen in Fig 1.8 below. Two root files are generated from different methods, with same cut, but different total number of events. Energy distributions are compared by taking the ratios of respective bins. To the accepted error, the ratios are the same.

Graph



IV Fig 1. 8 Result and comparison between modified and standard pair generation code. Ordinate: ratio of corresponding energy bin counts from electron energy distribution from ROOT files using different methods, no unit, abscissa: electron energy in  $MeV$ .

## 1.4 Applications

There are some very useful applications of the pair generation code. The most important one is for input to Geant4 simulations. The other applications include computing the ratio between total cross section that can be detected to total cross section, this will help us to improve the estimates of event rates and run times.

### 1.4.1 For Geant 4 simulation input

As mentioned before, each line (event) stored in the pair data file is of format (see formula (1.18)):

$$KE_p, KE_q, \theta'_p, \varphi'_p, \theta'_q, \varphi'_q, d\sigma$$

Primary vertices are generated in Geant 4 by specifying particle type, initial position, initial kinetic energy, and momentum direction. Kinetic energies are provided by  $KE_p, KE_q$ , and momentum direction is converted from  $\theta'_p, \varphi'_p, \theta'_q, \varphi'_q$  by (see (1.14)):

$$\mathbf{d} = (1, \tan\theta', \tan\varphi')$$

Based on the purpose of Geant 4 simulation, if any of the settings, cuts during pair generation and number of events are altered, new pair data files have to be generated from the beginning. What are subjected to change for pair generation include beam energy, target material, particles' energy range, solid angles cut, etc. The goal is to find which setup is the best for having the most detector acceptance and efficiency in the phase space range in which we are interested measuring the asymmetry.

### 1.4.2 Cross section within detector acceptance and estimation of experiment run time

Although this subsection doesn't have much relation to the generated pair data file, the numerical cross section  $d\sigma$  calculation and the same cut for phase space in section 1.2.3 is heavily used. These are closely related to pair generation.

The experiment run time  $t$  is calculated by total number of events to be measured  $N_{mea}$  divided by the data rate  $R$ :

$$t = \frac{N_{mea}}{R} \quad (1.28)$$

where  $N_{mea}$  is some number we can estimate from checking the statistics of pairs used to calculate asymmetry we want to measure. At the moment,  $N_{mea} = 10^6$  is a reasonable number for asymmetry calculation; we will elaborate on this in later chapters.

The data rate  $R$  is number of data can be detected per unit time, it is related to the total pair generation rate  $R_{target}$  at the target by:

$$R = R_{target} \cdot \frac{\sigma}{\sigma_{tot}} \cdot \frac{N_{det}}{N} \quad (1.29)$$

where  $\sigma$  is the total cross section within the cuts on phase space used in pair generation,  $\sigma_{tot}$  is the total cross section for the BH process. This includes all possible energies ( $m_e$  to  $E_\gamma - m_e$  for both particles) and solid angles (whole  $4\pi$  range) for both particles of the pair.  $\frac{\sigma}{\sigma_{tot}}$  gives an artificial acceptance. It is a compromise since we cannot reasonably generate pairs over the entire phase space. However, it's reasonable to use  $\frac{\sigma}{\sigma_{tot}}$  to simplify our calculation as long as the cut used in the calculation of  $\sigma$  covers acceptance of the magnet.  $N_{det}$  is the number of BH pairs

detected in the Geant 4 simulation, while  $N$  is the number of events from the Geant4 simulation, usually being the number of pairs in the pair data file.

If we replace  $\sigma$  and  $\sigma_{tot}$  by  $N$  and  $N_{tot}$ , respectively, (4.2) is changed to:

$$R = R_{target} \cdot \frac{N}{N_{tot}} \cdot \frac{N_{det}}{N} = R_{targ} \cdot \frac{N_{det}}{N_{tot}} \quad (1.30)$$

where  $\frac{N_{det}}{N_{tot}}$  is the ratio of the number of events detected to the total number of Bethe-Heitler events at the target, which could only indirectly be computed from (1.29).

### Calculating $R_{target}$

The beam rate  $R_{beam} = 1.2 \times 10^7 \text{ V/s}$ , the theoretical cross section  $\sigma_{tot} = 33 \text{ (barn)} = 3.3 \times 10^{-27} \text{ m}^2$  [38], the  $^{238}\text{U}$  target number density  $\rho_n = 4.8 \times 10^{28} \text{ m}^{-3}$ , and the target thickness  $h = 2.5 \times 10^{-5} \text{ m}$ . Thus, the total Bethe-Heitler pair production rate is:

$$R_{target} = R_{beam} \times \sigma_{tot} \times \rho_n \times h = 4.77 \times 10^4 \text{ Hz} \quad (1.31)$$

### Calculate the ratio $\frac{\sigma}{\sigma_{tot}}$

We calculate total cross section  $\sigma_{tot}$  and cross section for events surviving the cuts  $\sigma$  separately. Both use the same numerical integration formula:

$$\sigma = \sum \frac{d\sigma(E_p, E_q, \theta_p, \theta_q, \varphi_{q-p})}{d\theta_p d\theta_q d\varphi_p d\varphi_q dE_p dE_q} \sin\theta_p \Delta\theta_p \sin\theta_q \Delta\theta_q \Delta\varphi_p \Delta\varphi_q \Delta E_p \quad (\text{barn}) \quad (1.32)$$

The formula approximates integration by a sum. For the  $\sigma_{tot}$  calculation, the summation includes all possible energies ( $m_e$  to  $E_\gamma - m_e$  for both particles) and solid angles (whole  $4\pi$  range) for both particles. For the  $\sigma$  calculation, the summation only includes phase space for events surviving the cuts described in section 1.2.3.

Remarks:

1. Although in the numerical code to calculate  $\frac{d\sigma(E_p, E_q, \theta_p, \theta_q, \varphi_{q-p})}{d\theta_p d\theta_q d\varphi_p d\varphi_q dE_p dE_q}$  includes both  $E_p, E_q$  as arguments, the summation is only over  $E_p$  alone since the numerical code itself does not have any units. Dimensional analysis is used to determine the multiplicity of the sum. Since  $E_q$  can be represented as either  $E_q = E_\gamma - E_p$ , or be solved through solving recoil nucleus kinetic energy and be represented as a function  $E_q(E_p, \theta_p, \theta_q, \varphi_{q-p})$ , sum of  $E_q$  is redundant. On the other hand,  $\varphi_{q-p} = \varphi_q - \varphi_p$  and the summation over both  $\varphi_p$  and  $\varphi_q$  is needed.
2.  $\sigma_{tot} = 33 \text{ barn}$  is the official value, and has been used to calculate  $R_{target}$ . The numerically integrated  $\sigma_{tot}$  from the code provided by R. Lee does not need to be exactly the same as the rigorously obtained value due to certain approximations that been made and the look-up table which will not have perfect interpolation precision. Nevertheless, too much discrepancy will raise the question of the validity of (1.32) or the code computing  $d\sigma(E_p, E_q, \theta_p, \theta_q, \varphi_{q-p})$ .
3. Indeed, the computation of (1.32) is time consuming since  $d\sigma(E_p, E_q, \theta_p, \theta_q, \varphi_{q-p})$  is not simple and summing over 5 dimensions still requires a lot of sample points. To apply (1.32), instead of summing over  $(4\pi)^2$ , cuts are put to only contain points where  $d\sigma$  is reasonably large, which has been observed to be the case when: 1) one of  $\theta_p, \theta_q$  has a small value and 2)  $\theta_p \times \theta_q$  has a small value.
4. Mixing energy and angles in divisions in (1.32) can make some dimensions over or under-divided. Using Monte-Carlo integration can circumvent this issue. Because majority of the  $d\sigma$  range has very small values, Monte-Carlo integration could still lack efficiency. The  $\sigma$  and  $\sigma_{tot}$

result is shown below in table 1.1. different  $\theta_{min}$  (minimum polar angle in during summing (1.32), see section 1.2.3) are tried, while all other cuts are unchanged from section 1.2.3.

Angle cut	$\sigma$ (barn)	Raw data rate $R_{target} \cdot \frac{\sigma}{\sigma_{tot}}$ (Hz)
None	$\sigma_{tot} = 39.82$	$4.8 \times 10^4$
$\theta_{min} = 4^\circ$	$1.510 \times 10^{-2}$	18.2
$\theta_{min} = 5^\circ$	$5.838 \times 10^{-3}$	7.03
$\theta_{min} = 6^\circ$	$2.425 \times 10^{-3}$	2.92
$\theta_{min} = 7^\circ$	$1.072 \times 10^{-3}$	1.29

Table 1.1 Raw data rate dependency on minimum polar angle  $\theta_{min}$  cut during pair generation. It can be seen above that  $\sigma_{tot}$  from (1.32) is 39.82 barns, and there's obvious discrepancy to 33 barns. However, for rate estimation purposes, it is close enough to let us get a reasonable idea of the raw data rate.

### Calculating $\frac{N_{det}}{N}$

Due to the complexity of the magnet and detector acceptances, the number of events in which both particles reach their corresponding wire chambers are hard to determine by any analytic method. Geant 4 simulation has been used to find both  $N_{det}$  and  $N$  values.

For  $N$ , the number of events in the root file with same cut as  $\sigma$  as in the table above is used. If we have a simulated ROOT file with  $\theta_{min} = 4^\circ$ , we can put additional cut on  $\theta_{min}$  to count cases with  $\theta_{min} = 5^\circ, 6^\circ, 7^\circ, 8^\circ$  above. For  $N_{det}$ , in addition to cuts on counting  $N$ , we require that both particles reach their corresponding wire chambers in the simulation.

Table 1.2 below shows the values of  $N$ ,  $N_{det}$ ,  $\frac{N_{det}}{N}$  and the final data rate  $R$  (still an overestimate, since wire chamber efficiency is assumed to be 100% here).

Angle cut	$N$	$N_{det}$	$\frac{N_{det}}{N}$	$R = R_{target} \cdot \frac{\sigma}{\sigma_{tot}} \frac{N_{det}}{N}$ (Hz)
$\theta_{min} = 4^\circ$	1129990	679989	0.6918	12.6
$\theta_{min} = 5^\circ$	551123	283891	0.5151	3.62
$\theta_{min} = 6^\circ$	288464	120117	0.4164	1.21
$\theta_{min} = 7^\circ$	157184	52996	0.3372	0.428

Table 1.2 Detectable data rate estimation, with minimum polar angle  $\theta_{min}$  dependence. Thus, if we want total 1 million events for asymmetry calculation, total time it will take for  $\theta_{min} = 4^\circ$  case will be:

$$t = \frac{N_{mea}}{R} = \frac{10^6}{12.6} = 7.94 \times 10^4 s = 0.92 \text{ days}$$



## 2 Geant 4 simulation

### 2.1 Introduction

The Geant 4 simulation of the Bethe-Heitler pair generation, largely written by Prof. Pywell (available at [nucleus.usask.ca](http://nucleus.usask.ca)), serves the main purpose in the design of the experiment and estimating the result we could achieve in the experiment. The Geant 4 simulation is a tool to give us an approximated result of the experiment to guide us in setting up the actual experiment. The process of the Geant 4 simulation is to propagate the BH pairs generated through Monte-Carlo simulation following a theoretical calculation from primary vertex. The particles are sent through the magnetic field and the detection apparatus as well as the atmosphere. The setup of the Geant 4 simulation involves: Setting the particle kinematics at the primary vertex. Setting the magnetic field profile. Specifying the dimensions and placements of apparatus. Setting materials in each volume. Specifying certain volumes to be “sensitive detectors” for collecting intermediate particle kinematics information. The next part of the setup is storing the simulation results. This involves picking data either from user defined quantities (e.g., BH pair kinematics at primary vertex), to particle information at any point inside any sensitive detector. After some simple calculation such as coordinate transformations, these data are then stored in ROOT files.

To analyze the simulation data, an independent program is written. It reads data from ROOT files, making additional calculations utilizing these data to produce desired results. Those analyzed results include particle kinematics information, asymmetries, a detector hit map and acceptance information, particle track information, etc. They provide a preliminary estimate of experiment result. In addition, the results may suggest new changes in the simulation setup to improve detector acceptance, efficiency, resolution and reducing errors in the asymmetry extraction.

For the rest of this chapter, Geant 4 simulation has been introduced in the following order: a brief explanation of setup of the Geant 4 simulation (section 2.2), followed by basic results from analyzing data in ROOT file (section 2.3). Then two major applications of the Geant 4 simulation are shown: First, to simulate Jlab Hall A analyzer treatment of wire chamber track finding and fitting process, a counterpart is introduced to render wire chamber track fitting result from simulation data (section 2.4). Second, the additional transformation of wire chambers is added in order to optimized detector resolution with multiple scatter taking into account (section 2.5).

## 2.2 Setup of Geant 4 simulation

### 2.2.1 Introduction

In the general introduction, the setup of Geant 4 simulation involves defining the basic components of the experimental apparatus. The format/structure of the generated data to be stored in ROOT file should also be set up.

The data in the ROOT file will be read and analyzed using programs independent of the Geant 4 simulation so any change of data structure in the Geant 4 setup could result in problems if one is utilizing old versions of programs to analyze the data. Also, old ROOT files could become obsolete. Thus, data storage plan should be handled with care.

Since the setup of the geometry and data in the ROOT file are the most complicated, they are explained in separated sections, while all other setup is combined. Once the Geant 4 simulation is set, the simulation is run to produce a ROOT file storing raw simulation results. Analyzing these results is the content for the next section of the chapter.

### 2.2.2 Basic setup

#### 1) Set the magnetic field

The magnetic field of the dipole magnet is well measured and the field map is well understood. The magnetic field in the Geant 4 simulation takes the expansion of a dipole field to 4th order of  $z$  for  $z$  components and 3<sup>rd</sup> order of  $z$  for  $x$  and  $y$  components ( $z$  is the vertical coordinate off the horizontal plane), with field map measurements used for computing coefficients.

The only parameter left to be changed is the 0<sup>th</sup> order, which has been nominally set to  $B_0=0.4536\text{T}$  but other values may be used later.  $B_0$  is also the value of magnetic field to approximately make 30 *MeV* electrons or positrons along beam direction bend 90° and reach the wire chambers in the horizontal plane along a line from the center of the magnet perpendicular to beam direction.

For certain simulation runs the magnetic field strength value is set lower, since  $B_0$  in the last paragraph is the largest the magnet can comfortably reach. The benefit of a lower field strength could be the larger angle between higher energy particles to wire chambers and closer to perpendicular to wire chambers for low energy particles results from the reduced bend of the all tracks. For this setup the track length of lower energy particles to the wire chambers is less, resulting in a reduced effect from multiple scatter in the air, while the larger angle for higher energy particles, which are less susceptible to multiple scattering, will have larger spread of track intersections with the wire chambers, resulting in better resolution. The downside of this is that the detector acceptance should be carefully investigated to prevent loss of efficiency. In addition, larger incident angle ( $\alpha_u$  or  $\alpha_v$  in Part III Chapter 3,4,5) between high energy particles to wire chamber will result in less wire span for one of the wire planes thus lower efficiency. This effect will be elaborate in later sections (section 2.5.3 Figure 2.35(1) and the table below Fig 2.35 for the result).

## 2) Set the particle kinematics at primary vertex

The Geant 4 simulation physics package do not include the calculation of BH cross section. Thus, the BH pairs are generated using a theoretical calculation of the BH cross section and Monte-Carlo simulation (see last chapter “Generate BH pairs”).

Geant 4 simulation reads BH pair file, convert energies and the projection angles in the file to kinetic energy and momentum direction at primary vertex. For the volume of target, some different specification is used. It could be vacuum, air, or Uranium with  $25\mu\text{m}$  thickness. The location of primary vertices includes: at center of target, parallel to beam line with 0 radius with  $25\mu\text{m}$  long inside target, or within 0.5 cm radius as that is the estimated actual beam radius. After setting up the particle type, their kinetic energy and momentum direction, and location, the primary vertex is set.

Remark: the BH pair file has been generated such that the electron is bent to the right and positron to the left for all pairs, it is planned for the experiment that a tungsten cone shaped baffle will block electrons (positrons) generated to the left (right) from bending back to right (left) side of the beam by magnetic field. The purpose of the cone baffle is also to block any particles with polar angle less than  $4^\circ$  or  $5^\circ$ . Particles with polar angles less than the cone angle have a very high cross section and electrons and positrons coming from these angles have negligible asymmetries.

## 3) Set materials of each volume

The only meaningful materials that need to be set are those covering all the possible paths of the electron-positron pairs. These include target, background, windows of the wire chambers, gas inside the wire chambers and all metal frames.

There is a two-step procedure for defining materials:

- (1) Define the element composed of the material, specifying atomic number and mass per mole.
- (2) Define the density, number of components (elements), and the fraction of each element, either by number of atoms in the molecule or by fraction of mass.

For the most common simulation, the background has been set to air (30% mass by O, and 70% mass of N), while wire chamber window is set to mylar, and gas layer using ethane-argon. For the frames, the choice of metal is immaterial, however iron is chosen for magnet pole as well as magnet frames, while VDC frames are set to aluminum.

## 4) Set sensitive detectors

Certain physical volumes are set to “sensitive detectors.” These are “imaginary” detectors whose sole purpose is to allow particle information to be extracted. This includes (1) its type, (2) kinematics, (3) energy deposited, (4) time of flight, etc. at any step of the Geant 4 simulation. All sensitive detectors store selected data in ROOT files. It should be noted that inside a volume the number of steps of integration during simulation is unknown, while for some thin volume there would be usually one step, making handling of these data easier. In addition, any boundary of the physical volume will be a bound of the integral no matter how thin the volume is. Thus, if we want to monitor particle tracking information anywhere other than in the actual detectors to be used in the experiment, we add a thin physical volume with the same material as originally placed and set it to sensitive detector.

## 2.2.3 Geometry setup

### 1) Basics of Geant 4 geometry [53]

In order to completely specify a volume, there are three steps:

- (1) Specify its shape and dimensions. Geant 4 includes a wide set of common shapes, such as box, cone, cylinder etc. Different shapes have different sets of parameters to specify their dimensions. In addition, some binary operations can be done to generate new shapes, including unions, intersections and subtraction, etc. All shapes in our simulation are determined by one of the methods above.
- (2) Specify its material. By adding this attribute, the volumes are now called G4LogicalVolumes. There is only one material for each logical volume.
- (3) Specify its relative placement inside its mother volume. The basic information that must be provided here are the transformation of the daughter volume from the origin of the mother volume, the daughter volume in form as a logical volume, the mother volume, and copy number. There are rules to follow: (1) Since any normal motion is the combination of rotation and translation, the transformation is specified by them. (2) The daughter volume must be completely included inside mother volume. (3) There can be different types of logical volumes inside mother volume, for same type with different placement (transformation) they need to be specified by the copy number. (4) Overlap of volumes is not allowed. (5) This provides a hierarchy structure and method to specify a single volume, the copy number, along with a sequence of mother volumes are specified until reaches the world volume (an event will end of the primary particle kinetic energies drop below threshold, or reaches boundary of world volume).

There are two additional attributes are assigned under specific conditions:

- (1) Sensitive detectors, which are briefly explained in 2.2.2 4). They provide a snapshot as a particle track reaches the volume and particle information can be extracted.
- (2) Visual attributes, which only matters when visualization of the simulation is required. For this, visibility, color, and visual types can be set.

### 2) Specifics of dimension and placements of apparatus

The dimensions of each apparatus are explained in Chapters in hardware. Thus, we only describe the placement of the apparatus here:

- (1) Coordinate system: By the symmetry of the wire chamber placement, we set center of magnet as origin of the simulation.  $x$  is beam direction,  $z$  is vertical up direction perpendicular to beam,  $y$  is horizontal point from magnet center to the left perpendicular to beam to make right hand coordinate system.
- (2) Target: The orientation of the target is placed perpendicular to the beam, and is located just outside the magnet so that the polar angle spanned from target center to yoke hole is about  $14.7^\circ$ .
- (3) Magnet: Align the magnet to make center at origin, and yoke holes are aligned with beam.
- (4) Cone baffle inside magnet: The baffle is used to block electron positron pairs with small polar angle. The apex of the cone will be at center of the target, its center axis will be aligned with the beam. Holes with radius 0.75 cm in the magnet frame are aligned with the beam along the path to the beam dump. This radius constrains on how close the front (upstream side) surface of the cone can be located, since we need front surface with a larger radius compared to the inner hole radius of the cone to prevent a “kink” which

could scatter particles in too randomly. The upper and lower sides of the cone have also been “subtracted” by upper and lower magnet pole surface. It’s confirmed from Geant 4 simulation results that the cone will serve its purpose. Meanwhile we will lose some data rate but since the electron directed to the left will always be blocked by the cone when bent by magnet to the right side (same effect applies for positrons). Such events would be unusable anyway as their trajectories would be too complex to analyze.

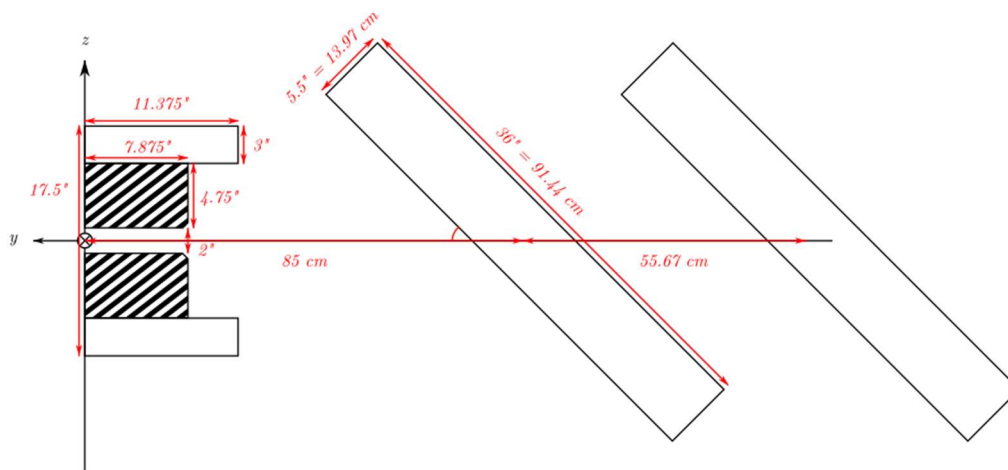
- (5) Monitors: Since the Geant 4 simulation is not real, we can set as many additional virtual detectors as we want to track particle at different key positions. The first monitor was placed just behind the target, with same cross sectional area as the target to track particles immediately after the target volume. Another two monitors are placed on each side of the magnet. They are set either parallel to side opening surfaces of the magnet, or parallel to the wire planes.
- (6) Wire chambers: since the nature of the complexity of the wire chambers as detectors compared to other volumes, there are three hierarchies of their volume placements: (1) one volume holds both wire chambers on one side of magnet, called wire chamber holder, (2) one volume holds individual wire chamber, (3) one volume of holds each individual wire, or volumes of other gas layers or Mylar sheets.

The reason for using a volume to hold both wire chambers is that z plates are used to fix the two chambers together. Thus, any transformation of the chambers involves rigid body motion for both chambers. This makes it simpler to transform two chambers as a unit. And, there will be two copies of individual chambers in the volume.

For each wire chamber, there are 6 layers of ethane-argon gas, the 4 outer layers with thickness 0.5 inch, while the center two layers with thickness 1 inch and active layers with sense wires, called wire planes.

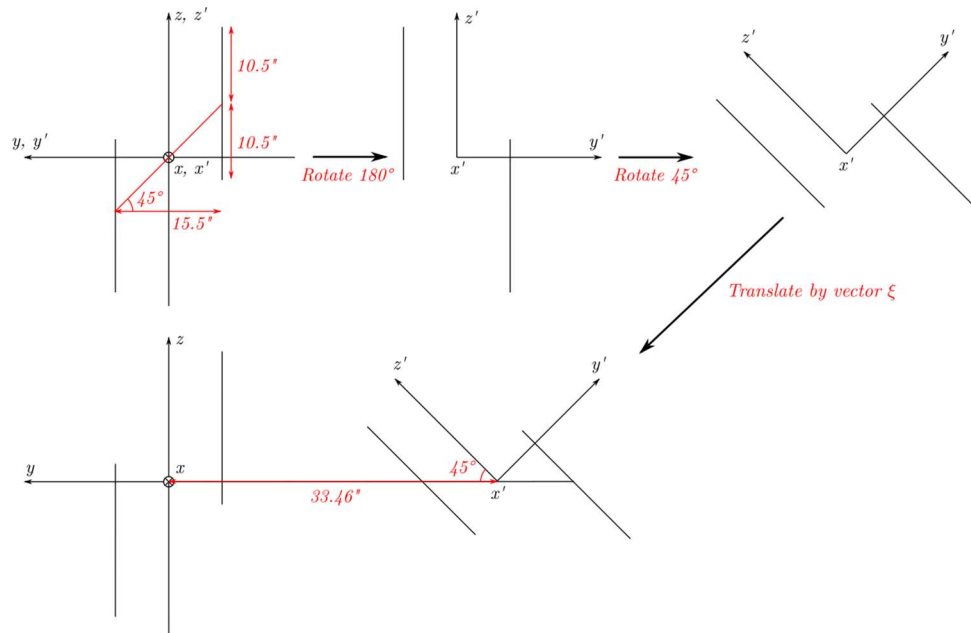
For individual wire plane, there are 279 parallel wires, each occupying a single wire volume.

Fig 2.1 below illustrates the geometry of the setup of the right half of the space of the simulation. The construction and placement of the wire chambers are illustrated in the next two figures (Fig 2.2, 2.3).



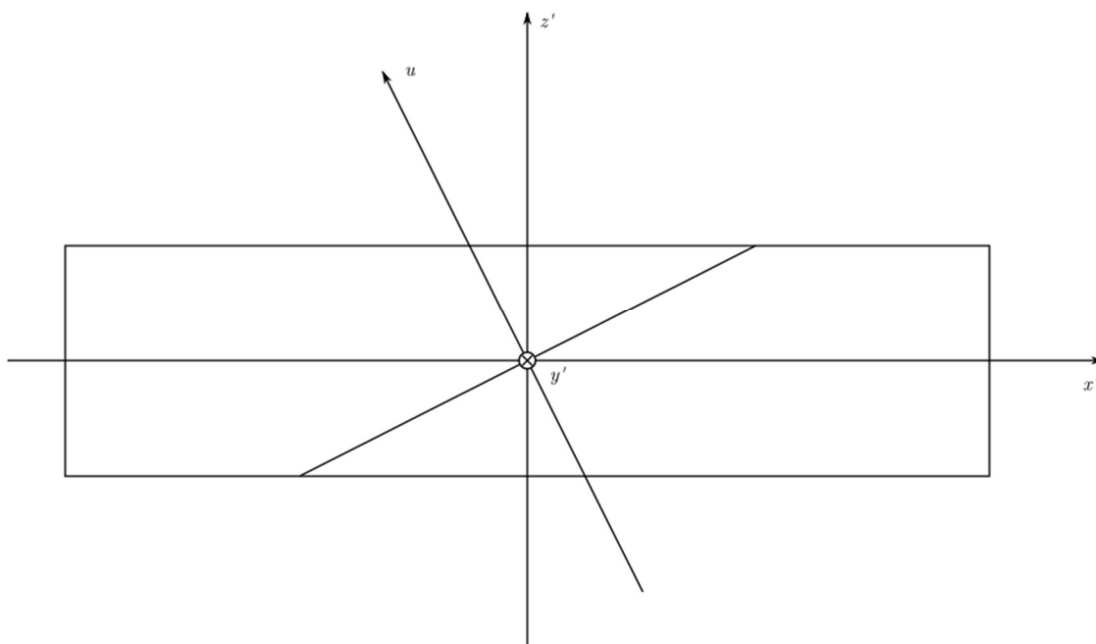
IV Fig 2. 1 Geant 4 global coordinate system  $y$ - $z$  projection.

Only right half of the space (electron side) is drawn; the left side magnet is a mirror image of the right, while wire chambers on the left are  $180^\circ$  rotations about  $z$  axis of right chambers. In the middle is the right half of the magnet. Shaded areas are the magnet poles, the right two rectangles represent the pair of wire chambers tilted  $45^\circ$  from vertical. The target, monitors, and tungsten cone along the beam ( $x$  axis) are not drawn.



IV Fig 2. 2 Transformations of holder of two wire chambers.

Shows transformations from origin to configuration of experiment setup. Only center planes of each wire chamber are drawn. The order of rotations is followed by arrows, all lengths are in inches. It starts with all three coordinate axes  $x, y, z$  from the Geant 4 global coordinate system and  $x', y', z'$  from local coordinate system coinciding. Shift in direction along wire chamber short axis and in direction perpendicular to chambers are the same, 15.5 inches. Thus, when the wire chambers are properly placed the holder is rotated by  $45^\circ$ , ensuring that the centers of both wire chambers are in the same horizontal plane.



IV Fig 2. 3 Construction of one wire plane.

$x', y', z'$  are in the same local coordinate system as Fig. 2.2. Total 279 wires lie in each wire plane, each occupies volume with gas layer thickness 1 inch, with vertical spacing 0.493cm to adjacent one. The  $u$  axis through the local coordinate system origin and perpendicular to  $u$  wires is drawn, along with the center  $u$  wire. The  $v$  axis and  $v$  wires are mirror images of the  $u$  axis and  $u$  wires about  $z'$  axis. Wires are translated from the origin to their corresponding locations according to the wire spacing and assigned ordered copy number. Next, since wires are at an angle of  $\text{atan}(1/2)$  to the long axis of the wire chamber, many of them are not equal in length due to the constraint of the wire plane boundary. Thus, it is best to use the intersection volume of longest wire volume and wire plane active area to construct these wires in the Geant 4 simulation.

#### 2.2.4 Setup data to store in ROOT file

Data to be stored in the ROOT file are aimed to be closely related to real experiment data. Data in the ROOT file is either an approximate representation of experiment data or snapshot at certain point in simulation for credibility checks. A user defined class is written, then converted into a ROOT class through `ClassImp()` function [54] ]. Data for each event has been set to the class then written into the ROOT file.

Data are either coming from variables set as input, or extracted from volumes set as sensitive detectors. All of these locations contain tracking information; i.e., position and direction of track intersection with a surface, and may have undergone coordinate transformations before they are written into the ROOT file. For sensitive detectors to represent real detectors in the experiment, additional information is extracted related to real detector characteristics, such as channel mapping information and energy deposited, etc.

Since the resulting data stored in the ROOT file is closely related to how data are set up, i.e., how they're processed before been written in the ROOT file, the coordinate system conventions etc., it is better to explain the setup along with plots of results, in next section 2.3.



## 2.3 Geant 4 simulation Results

### 2.3.1 Introduction

The results of the simulations are divided into two types: data stored during simulation and results after analyzing the data. Data are stored in ROOT files during simulation, and for those, we simply read the file and, using tools from ROOT, placed cuts on variables, plotted histogram, etc. For analysis of the data, additional calculations had to be made. Some of them were easy to implement, such as the charge asymmetry computation. There are several important applications for the analyzed data: (1) We need simulation result presented as close as possible for real detectors in the BH experiment, especially the wire chambers. Thus, an analog procedure of using simulation data to fulfil track finding and track fitting procedure in the Hall A analyzer was devised. The track result is then compared with results from the “monitor” (see next section 2.4) *Track finding and fitting using Geant 4 results*. (2) Additional change in Geant 4 simulation is made for optimizing the experiment setup, including change of magnetic field and wire chamber placement. For this new setup, see chapter 2.5 *Additional transformation of wire chambers*. We start with simple results which can be almost directly deduced from ROOT file data, in next section 2.3.2 *Data stored in ROOT files*. Then we show the result that need some simple analysis; see section 2.3.3 *Additional results with simple analyzation*.

### 2.3.2 Data stored in ROOT file

#### 1) Introduction

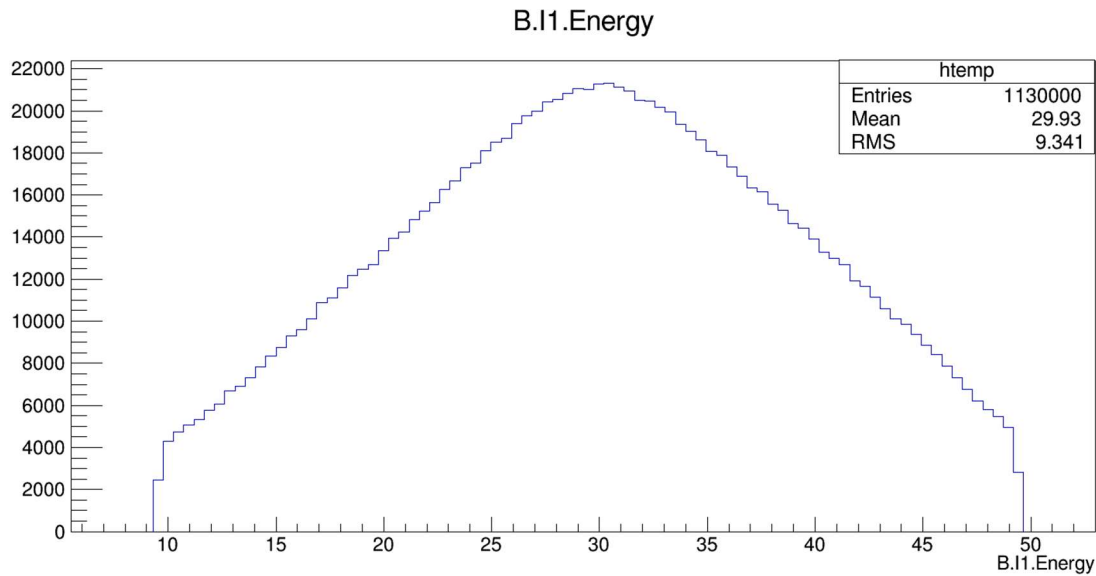
In following sections the meaning of data to be stored in the ROOT file and the conversion operations applied by them are explained for each individual detector. All the plots of results in this section were either directly drawn through clicking a TBrowser or using TTree::Draw() function after opening the ROOT file [55]

#### 2) Data by location

##### 1. Input:

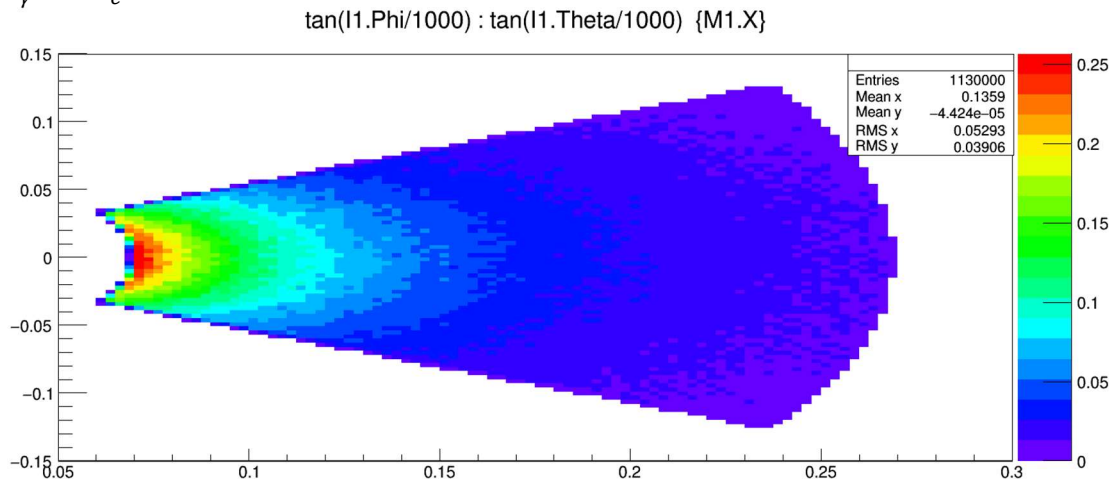
These are data from BH pair data file specifying the kinematics of the pair before they are set as a primary vertex in the simulation. Includes:

- (1) Kinetic energy  $KE$ .
- (2) Local position  $x, y$  in the plane perpendicular to the beam; that is, the view from upstream looking at the target, with the local  $x$  is the horizontal right direction, local  $y$  is the vertical up direction. At this point they're both set to 0.
- (3) Projection angle  $\theta, \varphi$  which makes the particle momentum direction vector to be  $(1, \tan\theta, \tan\varphi)$  in the global coordinate system. Thus, particles goes in straight lines, the projection in plane perpendicular to beam should be proportional to  $(\tan\theta, \tan\varphi)$ .



IV Fig 2. 4 Input electron kinetic energy distribution. Ordinate: counts, no unit, abscissa: input (primary vertex) electron kinetic energy in  $MeV$ .

And the mean of positron kinetic energy (not drawn) is 29.05 MeV, so  $\overline{E}_e + \overline{E}_p = 58.98 MeV = E_\gamma - 2m_e$ .



IV Fig 2. 5 Input (primary vertex)  $\tan\theta$  vs  $\tan\phi$  distribution. Ordinate: tangents of input (primary vertex) electron vertical projection angle  $\tan\phi$ , no unit, abscissa: tangents of input (primary vertex) electron horizontal projection angle  $\tan\theta$ , no unit.

This will be proportional to projection perpendicular to beam. Note the angles are stored in  $mrad$ .

## 2 Monitor

Monitors are the virtual detectors that only appear in the simulation to provide additional tracking information from primary particles. There are two sets of monitors, one placed directly after the target volume to provide information for effects of multiple scattering inside the target; two placed on left and right sides of the magnet in front of the front wire chamber, providing tracking information on the effects of the magnetic field and multiple scattering from the first monitor. Thus, the coordinate system of the two sets of monitors is quite different and will be explained separately.

Monitor 0, 1, placed behind target, touching the target:

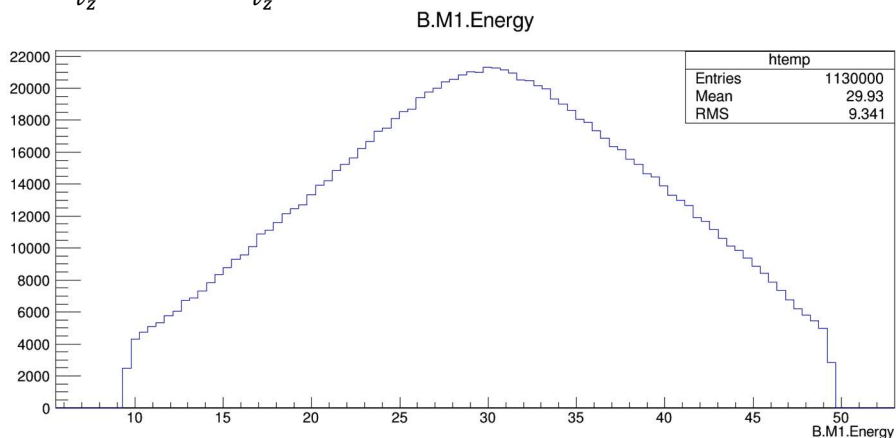
- (1) Kinetic energy.
- (2) Position: specified by  $x, y$  coordinate. Same convention as input data.
- (3) Spherical angles  $\theta, \varphi$  of the particle, relative to beam direction.  
( $\cos\theta, \sin\theta\cos\varphi, \sin\theta\sin\varphi$ ) is unit direction vector.
- (4) Charge of particle to identify positron, electron. Charge -1 particle electrons are stored in monitor 0, +1 particle positrons are stored in monitor 1.

Remarks: (1) There is only one monitor volume behind target, and it extracts data for both positron and electron. (2) For this monitor volume we want the electron and positron kinematics info where they just entered the monitor volume (or just exited the target volume). As we know when a new volume is constructed, the 1<sup>st</sup> step of a Geant 4 simulation inside the volume will be exactly at the boundary. (3) To find which hit is from the 1<sup>st</sup> step when particles just enter monitor volume, we order hits by time and the 1<sup>st</sup> in time with corresponding charge (or particle type) is the hit we are looking for.

Monitors 2,3, placed in between magnet and wire chambers:

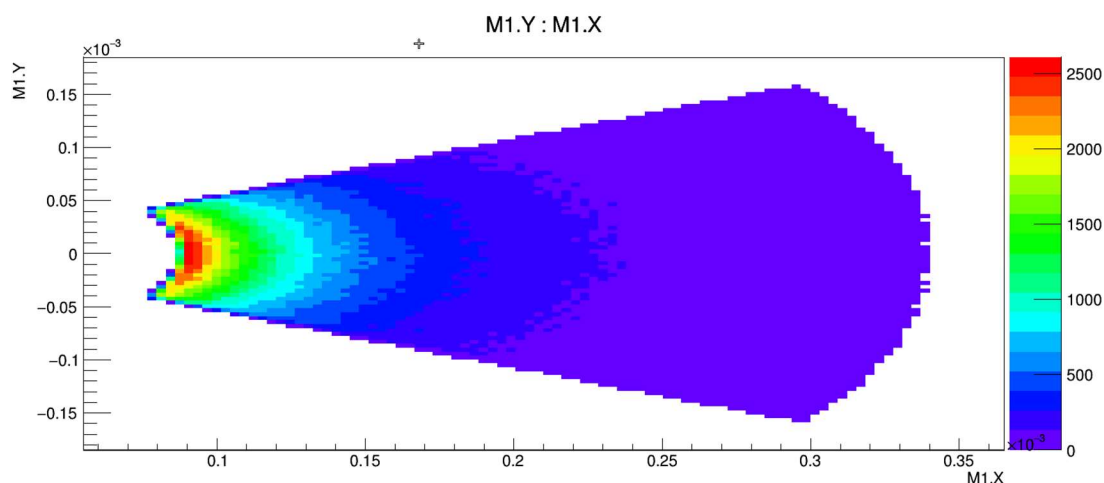
There are changes to positions and angles for these two monitors.

- (1) For positions: The local  $x, y, z$  coordinates convention is visualized by placing your eye at the center of magnet and look towards detectors;  $x$  is horizon right,  $y$  is vertical up,  $z$  is perpendicular to beam from center of magnet to detectors, so it is a left-handed coordinate system. Then tilt each by  $45^\circ$  to be parallel to wire chambers.
- (2) For angle  $\theta, \varphi$ : global coordinate system projection angles for momentum direction  $\theta = \text{atan}(\frac{v_x}{v_z})$ ,  $\varphi = \text{atan}(\frac{v_y}{v_z})$ .



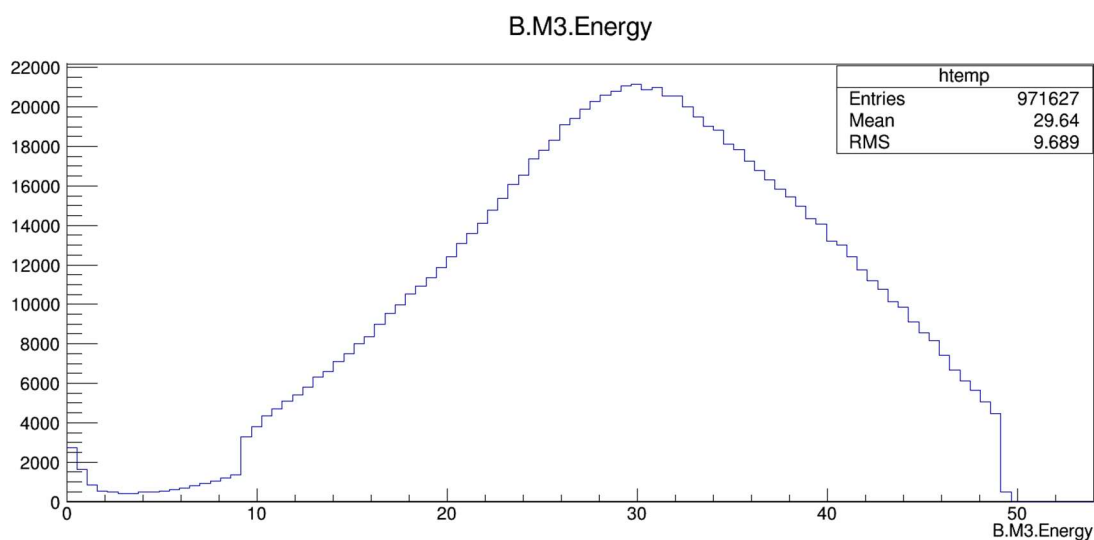
IV Fig 2. 6 Monitor 1 electron energy distribution. Ordinate: counts, no unit, abscissa: monitor 1 (behind target volume) electron kinetic energy in  $MeV$ .

There's almost no change from input energy when target material is set to air here.



IV Fig 2. 7 Monitor 1 electron  $x$  vs  $y$  distribution. Ordinate: electron vertical projection at monitor 1 in  $mm$ , abscissa: electron vertical projection at monitor 1 in  $mm$ .

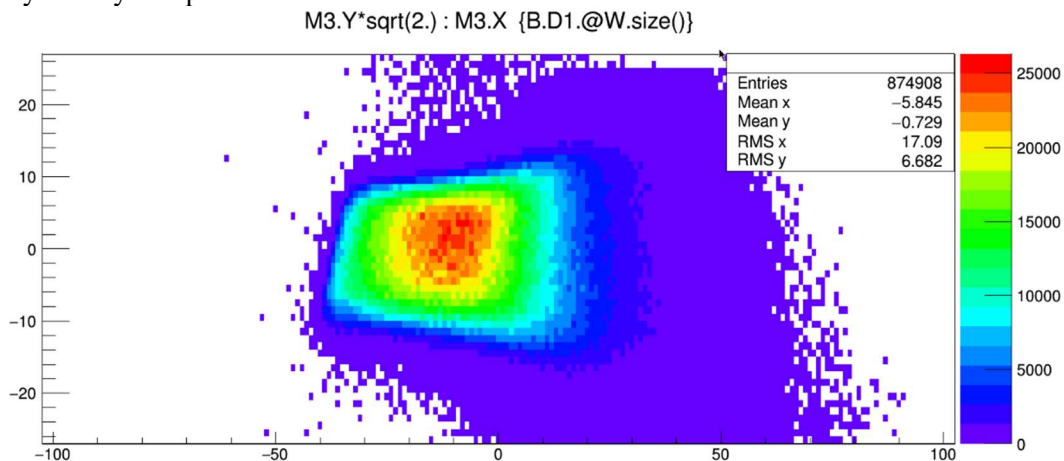
This is almost proportional to Fig 2.5 since all primary vertex positions are set to center of target in this simulation.



IV Fig 2. 8 Monitor 3 (electron detectors side) electron energy distribution. Ordinate: counts, no unit, abscissa: monitor 3 (between electron side wire chamber and magnet) electron kinetic energy in  $MeV$ .

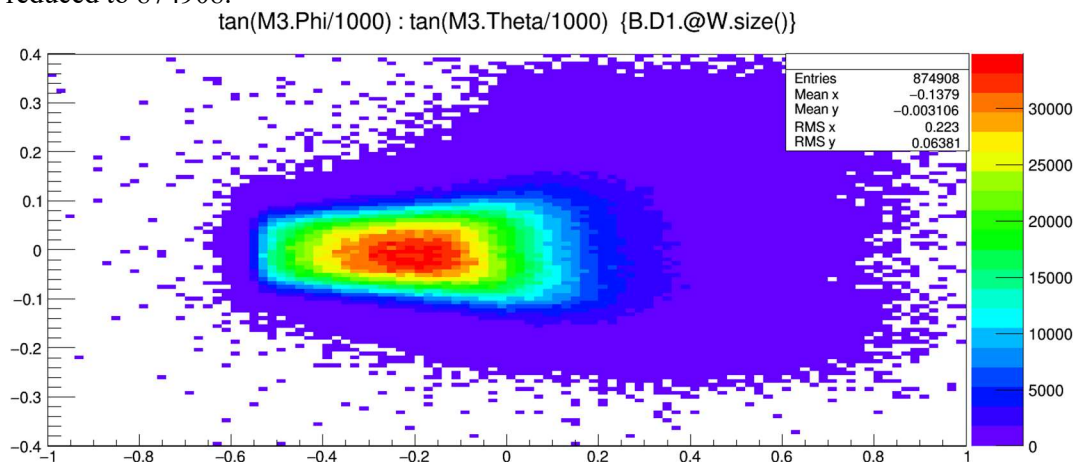
There are several observations to be made here: (1) there are electrons blocked at the yoke hole, cone baffle, magnet poles, and even magnet side frame. Thus, events are dropped from 1130000 at target to 971627, a loss of about 14%. (2) Due to multiple scattering, the average energy drops, and a tail of low energy electrons is seen in the histogram. (3) Although the hit stored for the monitor is from the 1<sup>st</sup> hit in time, there is no way to tell if it's from the primary particle. Although it's the 1<sup>st</sup> electron entering the monitor volume, but it can be a secondary particle with shorter track. etc. The only way the simulation could indicate it is by giving a secondary particle a new track ID, but during the experiment wire chambers cannot identify them. (4) Lower energy

electrons are more susceptible to multiple scattering. In addition, their direction ranges are much wider and thus their counts are generally less in lower energy region. This will affect statistics in the asymmetry computation.



IV Fig 2. 9 Monitor 3 (electron detectors side)  $x$  vs  $y/\cos 45^\circ$ . Ordinate: monitor 3 vertical coordinate  $y/\cos 45^\circ$  in  $cm$ , abscissa: monitor 3 horizontal coordinate  $x$  in  $cm$ .

In  $cm$ . The monitor is parallel to the wire planes which are tilted  $45^\circ$ , placed just in front of front wire chamber, and negligibly thin. Since  $y$  is stored in the monitor here its global  $z$  coordinate must accommodate the different tilt angle of monitor, thus the  $y/\cos 45^\circ$  is the coordinate of the track intersection on monitor local coordinate, and should be close to the result at the 1<sup>st</sup> wire chamber local  $x$  vs  $y$  distribution. Also, by constraining hits on the monitor they will also hit detectors behind (cut B.D1.@W.size() here) within wire chamber active area in this plot. Counts are reduced to 874908.



IV Fig 2. 10  $\tan \theta$  vs  $\tan \varphi$  distribution of electrons hit monitor 3. Ordinate: tangent of monitor 3 electron track vertical projection angle  $\tan \varphi$ , no unit, abscissa: tangent of monitor 3 electron track horizontal projection angle  $\tan \theta$ , no unit.

Based on the density of the hits, higher energy particles, with hits having much less spread, are on the left side. Thus, the particles will in general go in the downstream direction towards the back detectors. However, there will be low energy particles (purple region on the right side) covering the upstream side of the wire plane.

### 3. Wire chamber

From the complexity of the structure of wire chamber, its data are a lot more complicated. If we consider the detector on one side of the beam, there are two wire chambers. Each wire chamber consists of two wire planes oriented in different directions. Each wire plane has 279 wires. Thus, the smallest unit with data is a single wire, and the information being stored in ROOT files is a bit different from previous virtual detectors, either input or monitor. In addition, for each electron or positron track intersecting the chambers, on average there are about 16.4 wires hit per event. Thus, there are a lot more raw data for wire chamber hits compared with other sensitive detectors. Chamber data include:

- (1) A pair of numbers (wire plane, wire number) to identify a single wire.
- (2) The local coordinate of hit inside the wire:  $x, y$  is the coordinate in the wire plane, while  $z$  is the depth of the hit in the sense wire gas layer. While this is totally different than wire chamber data from hardware, which includes location of each wire (through hit wire indices) and drift time of the hit. We can use  $x, y$  to emulate the location of a wire, and the  $z$  as drift distance. And, tracking information can be extracted from these.

The overall direction of the particle (away from or towards the magnet) at each wire is omitted in the ROOT file data. The reason is that the wire chambers use intersections of tracks and wire planes to fit track and determine direction so there is no direct way to obtain the overall particle direction.

Other data: kinetic energy, energy deposit, time of flight, charge, and particle type. Time of flight and kinetic energy give hints on the order of wires been hit, if the particle is from a primary vertex, and also if wire hits are coming from the same particle.

Storing wire chamber data:

We take data generating process in Geant 4 carefully: for an event where there are multiple wires hit, for each wire there could be multiple tracks (particles) propagating through it. In addition, due to the integration algorithm of Geant 4, a single track could have multiple steps of hits inside a single wire. Thus, we need a systematic way to deal with the entire hit collection. Below is a step by step introduction to how to store data on wire chamber hits in a ROOT file. Since the information between different wire planes can be regarded as completely independent, we only consider all hits in a single wire plane of an event. An example is given parallel to the explanation.

- (1) Extract all hit wire labels (copy number of wires from sensitive detector), repetitively. For example, after this step all wires that have been hit in this wire plane are ordered as:

100, 50, 51, 51, 51, 50

- (2) Sort wire numbers in decrement order. Now the hits in the vector storing wire numbers look like:

100, 51, 51, 51, 50, 50

- (3) Remove repetition, for each hit wire, associate number of hit counts to it. Two vectors, one storing hit wire numbers, one stores number of hit counts:

Wire number vector: 100, 51, 50

Hit count vector: 1, 3, 2

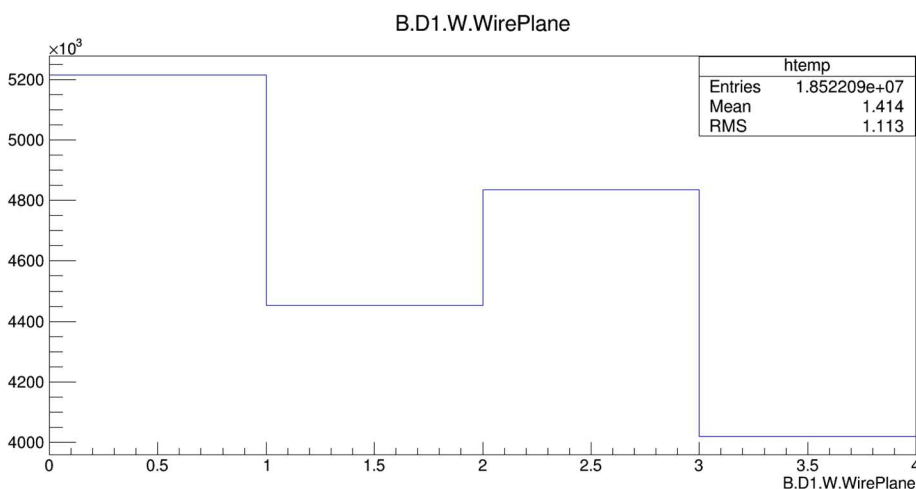
- (4) Loop over all hits in each single wire, store the data with cut:

(4.1) Find the largest kinetic energy hits in the wire, call it max KE. If the kinetic energy is larger than input kinetic energy minus 1 MeV, it means it's coming from primary particle, continue to next step.

(4.2) If the other hits in the wire have kinetic energy larger than max KE minus 0.1 MeV, it means they're also from the same particle, this is a candidate step.

(4.3) Store hits of the wire in ROOT file in this order: (1) The wire chamber, wire plane, and the wire number. (2) Position of the hit is the average position of all candidate steps, with position of each step as average of local pre-step and post-step position. (3) Energy deposited, sum of energy deposited in all candidate steps. (3) Kinetic energy, use max KE. (4) Time of flight, charge, particle type, use the hit data of step with max KE.

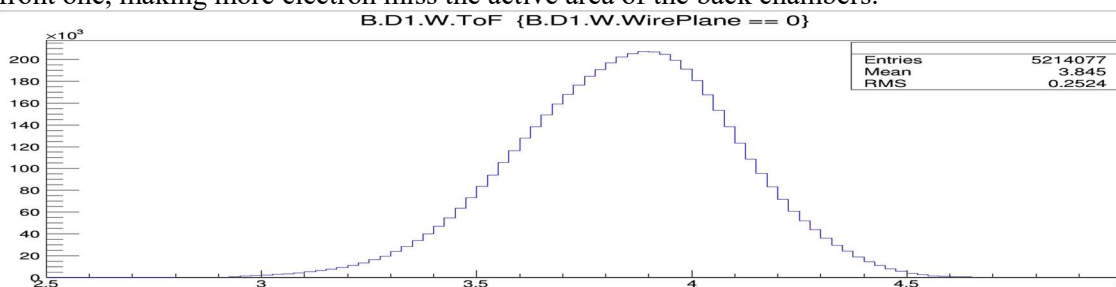
(4.3) Store hits of the wire in ROOT file in such order: (1) The wire chamber, wire plane, and the wire number. (2) Position of the hit is the average position of all candidate steps, with position of each step as average of local pre-step and post-step position. (3) Energy deposited, sum of energy deposited in all candidate steps. (3) Kinetic energy, use max KE. (4) Time of flight, charge, particle type, use the hit data of step with max KE.



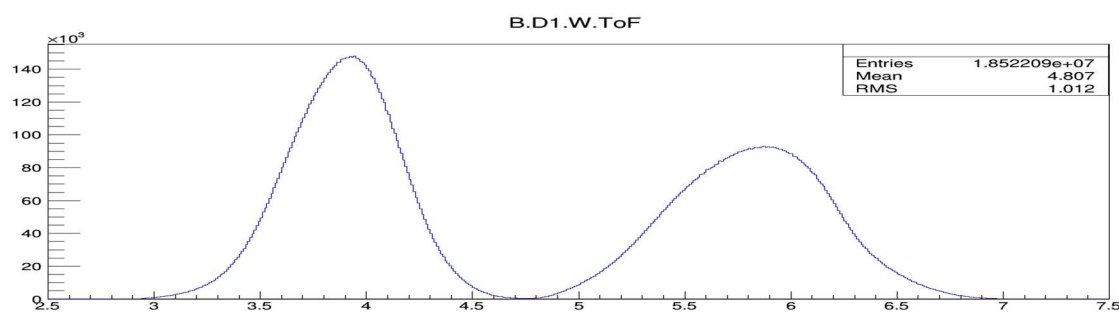
IV Fig 2. 11 Electron side wire plane distribution of all wire hits. Ordinate: counts, no unit, abscissa: wire plane number (0 2<sup>nd</sup> frontmost, 1 frontmost, 4 2<sup>nd</sup> backmost, 3 backmost wire plane to magnet).

abscissa is wire plane indices, ordinate are hit counts. The total number of events is 1,130,000, so in each wire plane, there are multiple wires hit in (almost) every event, making the counts much larger than 1,130,000. General observation: front wire chamber planes (0,1) have more hit wires than corresponding back chamber planes (2,3); for the same wire chamber, front planes (1,3) have less hits than back planes (0,2).

Purely from geometry, the orientation of wires in wire planes 0 and 2 (back wire planes of the chambers) are paired, so are wires in wire planes 1 and 3. The loss from wire plane 0 to 2 is due to both multiple scattering and the acceptance of the back wire chamber is less than that of the front one, making more electron miss the active area of the back chambers.

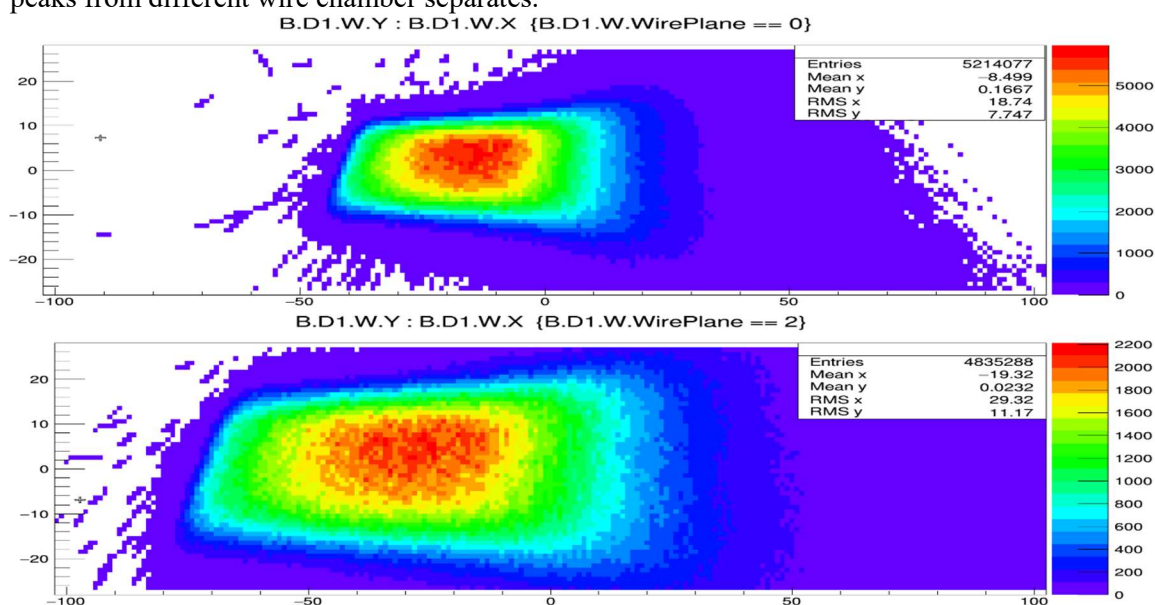






IV Fig 2. 12 Electron side wire plane time of flights (TOF) plot. Ordinate: counts, no unit, abscissa: time of flight, unit *ns*.

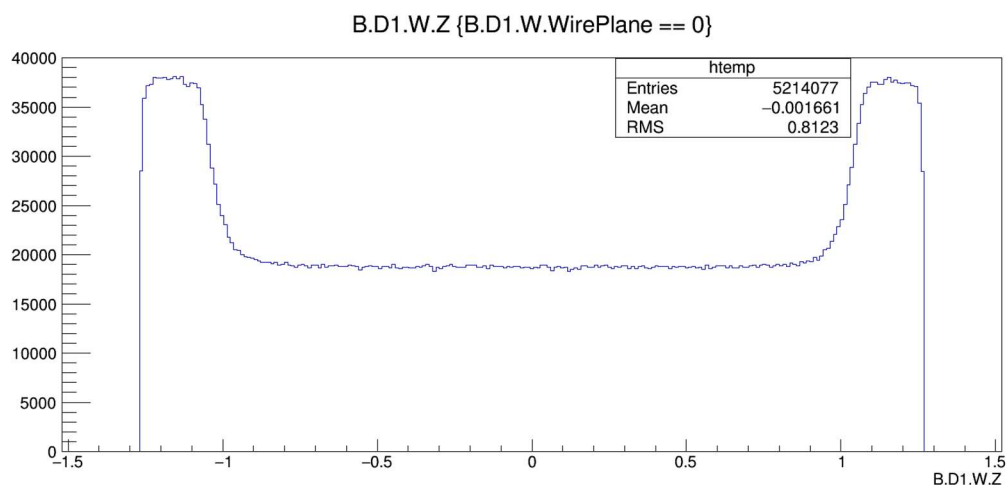
Upper histogram wire plane 0 hits time of flight, lower histogram time of flight plots from all wire planes. The time of flight from primary particles should be directly proportional to path length from target, which depends on both the track (which depends on initial direction and energy) and location of the wire plane. The two peaks in the lower plot result from adjacent volumes of wire planes in the same chamber, two wire planes in the same wire chamber TOFs are mingled together to a single peak. There is large distance between front and back chambers, so peaks from different wire chamber separates.



IV Fig 2. 13 Electron side wire plane 0 and 2  $x$  vs  $y$  distribution. Ordinate: wire plane vertical coordinate  $y$  in *cm*, abscissa: wire plane horizontal coordinate  $x$  in *cm*.

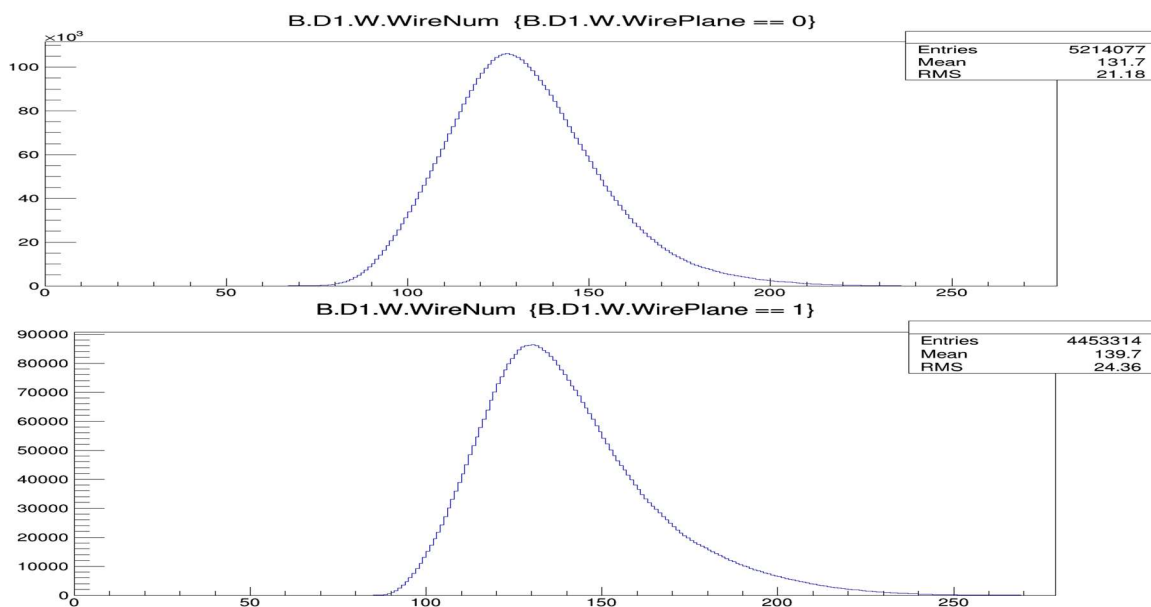
Units on both axes are *cm*. These are the wire chamber local coordinates,  $x$  as long axis and  $y$  as short axis of wire chamber. Since the tracks are dispersed at the target and through magnet, the wire plane 2 on the back chamber has a much larger area covered by hits. Although the hit distribution is similar to the Fig 2.9 monitor hits, the hit counts here are much larger than the monitor  $x$  vs  $y$  distribution, since there are on average 5.96 and 5.53 wires hit per event on wire chambers 0 and 2, respectively. It can also be seen here that the distance from the wire chambers to the magnet is as large as possible to have better resolution, with not much loss in acceptance.





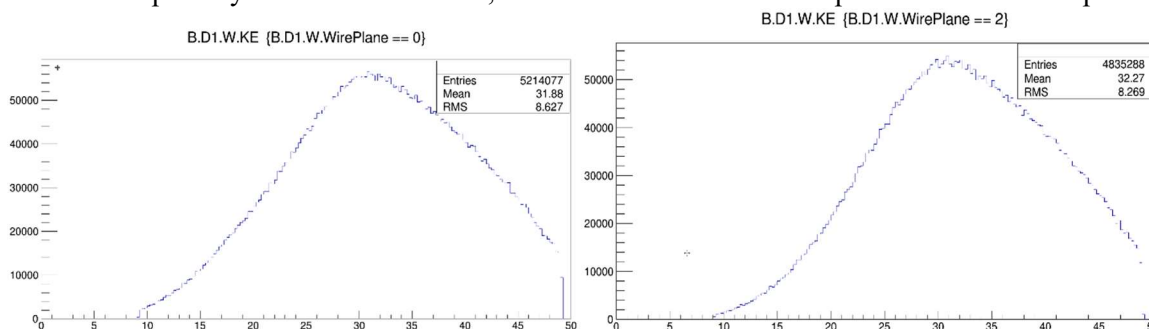
IV Fig 2. 14 Electron side wire plane 0  $z$  coordinate (perpendicular to wire plane) distribution. Ordinate: counts, no unit, abscissa:  $z$  coordinate (perpendicular to wire plane) at wire plane 0 in  $cm$ .

Remarks: (1) Local  $z$ -coordinates bounded at  $-1.27cm$  and  $1.27cm$ , as wire plane 0 thickness is 1 inch. (2) Since the tracks are almost straight lines through the wire plane, for each track, there is the same shift of  $z$  from one wire to the adjacent wire, due to the randomness of track,  $z$  distribution should be uniform. The deviation of  $z$  distributions on each side (edge) of the wire plane results from wire hits from end points of each track usually entering and leaving a single wire volume without cross the entire wire spacing. Those  $z$ 's are measured as the average coordinate of a hit inside the wire volume, which are not directly above and below corresponding wires. This results in more hits.



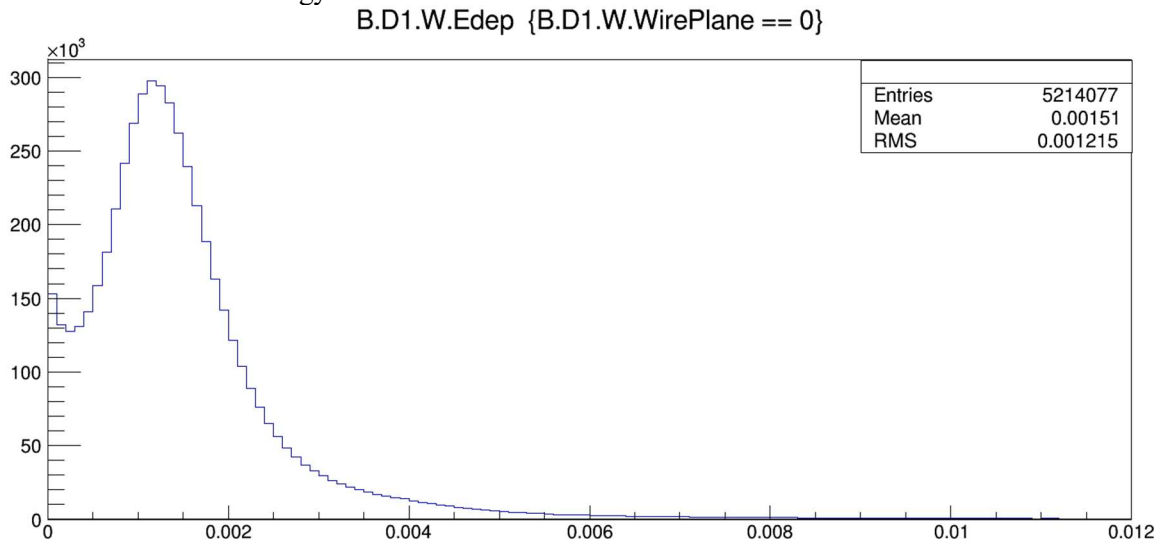
IV Fig 2. 15 Hit wire number distribution of wire plane 0 and 1. Ordinate: counts, no unit, abscissa: hit wire number at wire plane 0 and 1 in  $cm$ .

Even though the wire planes are adjacent to each other, the orientation is different, resulting in different wire hits. Also, the number of wires hit from same track and the average for all tracks are different. It's easy to see here we don't have to implement all wires in the front wire chamber to detect all primary electrons. However, the back wire chamber wire planes are more occupied.



IV Fig 2. 16 Kinetic energy distribution of wire plane 0 and 2. Ordinate: count, no unit, abscissa: electron kinetic energy at wire plane 0 and 1 in  $MeV$ .

Note that pairs are generated between 10 and 50  $MeV$  (total energy). On average, particles generating wire plane 2 events have 0.39  $MeV$  more energy than do those generating front wire plane 0 energy. The cause can be at least two-fold: (1) Fewer counts in wire plane 2, mean some lower energy electrons missed the back chamber but hit the front. (2) The lower energy electrons are more susceptible to multiple scattering effect, as cut requires kinetic energy of particles to be more than the energy at the target minus 1  $MeV$  as the cut for storing the hit in the ROOT file. Electrons lose more energy to reach back chamber than to front and missed the cut.



IV Fig 2. 17 Energy deposited of hits in wire plane 0 Ordinate: count, no unit, abscissa: electron deposit energy at wire plane 0 in  $MeV$ .

The estimate is 1.51 keV average loss in the wire plane with 1 inch thickness. On average, the electron time of flight of 5.85  $ns$  or about 175.4  $cm$  to reach back wire plane, so we can estimate the average energy loss until electron reaches back chamber to be 104.3 keV  $\sim$  0.1  $MeV$ .

Charge and particle distributions on wire chambers are not explained here. For the electron side 211 positron hits versus 18.5 million electron hits from the simulation; 374 electrons versus 18.5 million positrons on positron side wire chambers. Particles on the wrong side of the magnet are extremely rare. Thus, the cone baffle placed along the beam and the separation by magnetic field are effective.

#### 4. Hodoscopes

The data for the hodoscopes are not discussed here. The choice of hodoscopes is not the original ones planned to be used in the BH experiment. The main reason that they were discarded is that the areas covered (especially their span in the horizontal, longer direction) is too small compared to wire chambers, which seriously limited their acceptances. In addition, our asymmetry measurement is not concerned much with BH pairs where both energies are similar, each nearly half the beam energy. Given the short lengths of the original hodoscopes those pairs occupied a large portion of the old hodoscope setup.

##### 2.3.3 Additional results with simple analysis

In addition to the simple analysis using ROOT directly, code was written to render further results relative to the experiment.

Those scripts, compared to direct analysis in last section have the following advantages:

- (1) They can carry out more complicated calculations.
- (2) Multiple results are computed at the same time. Changes can be made in certain cuts so that all these related results are rendered simultaneously.
- (3) All ROOT files with same data structure and similar simulation conditions can be analyzed using the same code.

In the following sections, some of the most important results calculated from scripts are shown. Most of them are from the simulation with pairs generated obeying cross section calculation from theorists. Efforts are put into issues concerning the experiment, for example, asymmetry calculation, wire chamber hit data, track fitting, detector resolution estimation etc. Contents in this section:

Asymmetry calculation is presented in 1).

Some obvious differences between data obtained from simulation and from real wire chambers are posing new challenges for analyzing the simulation wire chamber hit data and using them as a mock track fitting regime. This issue will emerge in subsection 2) and will be further developed in 2.4 “Track finding and fitting using Geant 4 results”.

One of the calculations uses a customized simulation setup to check detector resolution, and will be explained in subsection 3).

For the last, another group of simple simulations are used to give some results on the dependence of detector data on the initial conditions of the primary particles. They are related to the reconstruction of those initial conditions using fitted tracks, see subsection 4).

##### 1) Charge asymmetry

The experiment is dedicated to determination of charge asymmetry of the BH pairs. Thus, obtaining an estimated asymmetry from a simulated result is useful for predicting experiment results. Asymmetries reflect the cross section of the BH process, since the cross section from theory provided is in the form:

$$d\sigma(E_p, E_q, \theta_p, \theta_q, \varphi_{q-p}) \quad (2.1)$$

The asymmetry can be defined on different levels based on which of the arguments in (2.1) are integrated out. Here, the asymmetry is still defined in terms of this complete form of differential cross section without any integrations, but with special constraints on points inside phase space to simplify the calculations. The asymmetry is defined as (Eq. (45) from [20]):

$$A(\mathbf{p}, \mathbf{q}) = \frac{d\sigma(\mathbf{p}, \mathbf{q}) - d\sigma(\mathbf{q}, \mathbf{p})}{d\sigma(\mathbf{p}, \mathbf{q}) + d\sigma(\mathbf{q}, \mathbf{p})} \quad (2.2)$$

Under the constraint that both polar angles are the same  $\theta_p = \theta_q = \theta$  and  $\varphi_{q-p} = 180^\circ$ , since sum of energies of both particles equals beam energy  $E_p + E_q = E_\gamma$ , we denote the energy difference between the two particles  $\delta = E_p - E_q$ , which uniquely determines the pair  $E_p, E_q$ :

$$\begin{aligned} d\sigma(\mathbf{p}, \mathbf{q}) &= d\sigma(E_p, E_q, \theta, \theta, \pi) = d\sigma(\delta, \theta) \\ d\sigma(\mathbf{q}, \mathbf{p}) &= d\sigma(E_q, E_p, \theta, \theta, \pi) = d\sigma(-\delta, \theta) \end{aligned}$$

And asymmetry:

$$A(\mathbf{p}, \mathbf{q}) = A(\delta, \theta) = \frac{d\sigma(\delta, \theta) - d\sigma(-\delta, \theta)}{d\sigma(\delta, \theta) + d\sigma(-\delta, \theta)} = \frac{N(\delta, \theta) - N(-\delta, \theta)}{N(\delta, \theta) + N(-\delta, \theta)} \quad (2.3)$$

From (2.3) we can see the usual property of asymmetry,  $A(\delta, \theta) = -A(-\delta, \theta)$ . For different fixed  $\theta$  value and varying  $\delta$  we obtain asymmetry curves of fixed  $\theta$ . For a Geant 4 simulation asymmetry calculation, we obtain counts  $N(\delta, \theta)$  for various values of  $\delta$  for a specific polar angle  $\theta$ . Then, we use formula (2.3) to compute the asymmetry. In order to find  $N(\delta, \theta)$  properly the following should be noted:

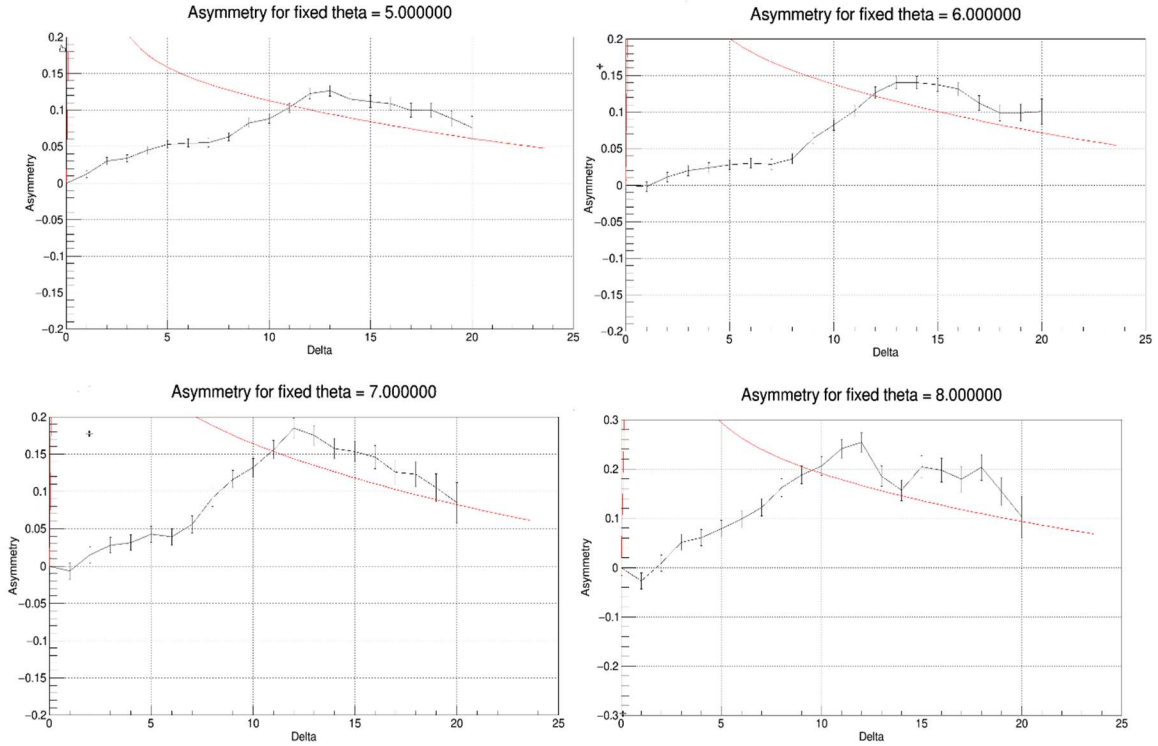
- (1) Due to the definition, all quantities  $\delta, \theta_p, \theta_q, \varphi_p, \varphi_q$  are the values at primary vertex inside target. During the experiment we only have track information measured at the wire chambers so we must rely on the algorithm to fit  $\delta, \theta_p, \theta_q, \varphi_p, \varphi_q$  from tracks, which is quite a complicated process. For simplicity here, we assume the fitting algorithm has full efficiency and no errors at the moment. We use the data at input or monitor behind target in the ROOT file in the asymmetry calculation. The only condition we impose here is that both sides of the wire chambers have wire hit data.
- (2) [50] Due to the finite nature of our simulation, the count  $N(\delta, \theta)$  are counted within a finite bin; that is, for each bin the energy difference,  $\delta_{bin}$ , for the bin center pairs satisfies

$$(1) \quad \delta = E_p - E_q \in \left[ \delta_{bin} - \frac{\Delta\delta_{bin}}{2}, \delta_{bin} + \frac{\Delta\delta_{bin}}{2} \right], \text{ or } |\delta_{bin} - \delta| < \Delta\delta_{bin}/2 \quad (2.4)$$

is accepted. In a real calculation  $\delta$  is calculated from  $\delta = KE_p - KE_q$

- (3) For spherical angles  $\theta = \theta_p = \theta_q$  and  $\varphi_{q-p} = 180^\circ$  cannot be exactly satisfied and following conditions are applied for selecting qualified BH pairs to contribute to  $N(\delta, \theta)$ :
  - (1) The difference of  $\theta_p, \theta_q$  is allowed within constraint  $|\theta_p - \theta_q| < \Delta\theta_{tol}$ , (2.5)  
 $\Delta\theta_{tol}$  is the tolerance of difference between  $\theta_p, \theta_q$ .
  - (2) The difference of  $\varphi_p, \varphi_q$  is allowed within constraint  $|\varphi_p - \varphi_q| < \Delta\varphi_{tol}$ , (2.6)  
 $\Delta\varphi_{tol}$  is the tolerance of difference between  $\theta_p, \theta_q$ .
  - (3) The measured  $\theta = \frac{1}{2}(\theta_p + \theta_q)$  is  $\left| \theta_{bin} - \frac{1}{2}(\theta_p + \theta_q) \right| < \Delta\theta_{bin}/2$  (2.7)
  - (4) During the asymmetry calculation, cut (2.5) and (2.6) must be applied before (2.4) and (2.7), while the order of cut between (2.5) and (2.6), or the order of cut between (2.4) and (2.7) is immaterial.

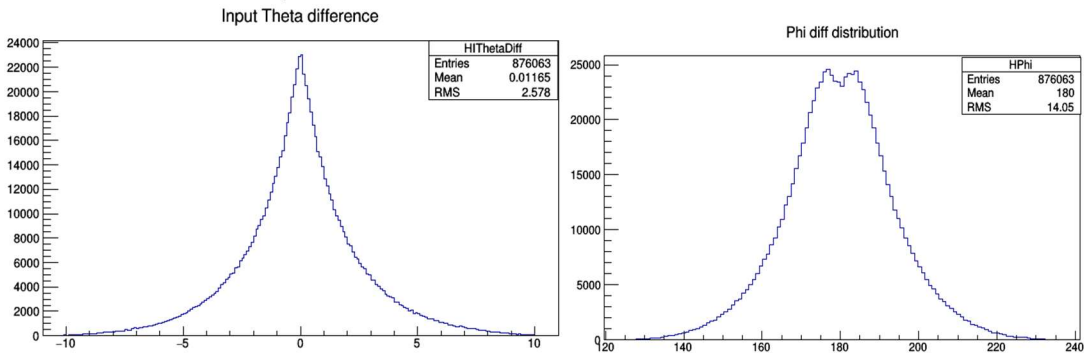
Setting  $\Delta\delta_{bin} = 2MeV$ ,  $\Delta\theta_{bin} = 2^\circ$ ,  $\Delta\theta_{tol} = 2.6^\circ$ ,  $\Delta\varphi_{tol} = 9^\circ$ , and performing the cuts in (1), (2), and (3) above, and then counting  $N(\delta, \theta)$ , we reach the asymmetry results  $A(\delta, \theta)$  for varying  $\delta$  with fixed  $\theta$  below:



IV Fig 2. 18 Charge asymmetry at  $\theta_{bin} = 5^\circ, 6^\circ, 7^\circ, 8^\circ$ . Ordinate: asymmetry, no unit, abscissa: energy difference between electrons and positrons in BH pairs in  $MeV$ .

Abscissa is energy difference  $\delta = E_p - E_q$  in  $MeV$ , and ordinate is asymmetry  $A(\delta, \theta)$  from eq. (2.3). The red line is the result from theory, calculated from  $A(\delta, \theta) = \frac{d\sigma(\delta, \theta) - d(-\delta, \theta)}{d\sigma(\delta, \theta) + d\sigma(-\delta, \theta)}$ . The uncertainties of the asymmetry are computed by error propagation (also see [56]):

$$\sigma_A = \sqrt{\frac{4N(\delta, \theta)N(-\delta, \theta)}{(N(\delta, \theta) + N(-\delta, \theta))^3}} \quad (2.8)$$



IV Fig 2. 19 Input  $\theta$  difference (left), and input  $\varphi$  difference (right). Ordinate: count, no unit, left figure abscissa: input (primary vertex) polar angle difference between particles in BH pair  $\theta_p - \theta_q$  in *degrees*, right figure abscissa: input (primary vertex) azimuthal angle difference between particles in BH pair  $\varphi_p - \varphi_q$  in *degrees*.

In *degrees*. There were 1 million events in this simulation, about 876k events having pairs reaching wire chambers on both sides. Only pairs satisfies both  $|\theta_p - \theta_q| < \Delta\theta_{tol} = 2.6^\circ$  and  $|\varphi_p - \varphi_q| < \Delta\varphi_{tol} = 9^\circ$  are candidates for pairs contributing to the asymmetry.

Remarks on the asymmetry result:

- (1) The setup of the simulation here is different from the real experiment: besides minor geometric and magnetic field differences, the primary vertex is a point instead of being within a cylindrical volume of beam, the BH pair data input file does not fully cover the acceptance, the target material is set to air thus multiple scatter is almost omitted within target, and kinematics reconstructed from detector tracks is assumed to be fully accurate and efficient.
- (2) It should be noted that due to the largeness of bin sizes  $\Delta\delta_{bin}$  and  $\Delta\theta_{bin}$  and to the fact that the differential cross section  $d\sigma$  depends sensitively on  $\delta$ ,  $\theta_p$ , and  $\theta_q$ , and  $d\sigma$  falls rapidly as  $\delta$  or  $\theta_p, \theta_q$  increases. Thus, the calculated asymmetry is not a fully faithful representation of the asymmetry at the bin center, and it can be quite different from the value obtained from theory. From the results seen in the Fig 2.18, we can see this effect:
  - 1) Within the small  $\delta$  region where the theoretical asymmetry varies rapidly from 0 to a maximum near 1, and back to value of about 0.2. The weighted average of the counts within a bin in rapidly changing differential cross section section, especially when  $\delta \cong 0$  with 0 asymmetry and cross section value high. Making asymmetry value small and way lower than theory curve. In these regions, we can hardly measure any asymmetry based on the parameter bin sizes and tolerance values  $\Delta\theta_{tol}, \Delta\varphi_{tol}$  set. The asymmetry in this region is immeasurable due to the detector resolution.
  - 2) When  $\delta$  is relatively large  $\delta \sim > 10MeV$ , the theory asymmetry is change much less dramatically and simulation asymmetry is consistently larger than the theory result at relatively large value. This is the region we are seeking to measure in the experiment. The asymmetry is biased to lower  $\delta$  and  $\theta_p, \theta_q$  values in the region where both asymmetry and cross section falls as  $\delta$  or  $\theta_p, \theta_q$  increases.
- (3) When particles within the phase space of a bin are not within acceptance, the pairs will not be added in counts  $N(\delta, \theta)$ , giving another bias in asymmetry calculation. Typically, it happens on two occasions:
  - 1) At low values of  $\theta$ , when one of  $\theta_p$  and  $\theta_q$  is less than the cone baffle polar angle.
  - 2) When particles miss the back wire chamber on one side at high  $|\delta|$  value, one of the particle energies is too low or high, and misses the detector.

Nevertheless, we are expecting the binned asymmetry value to be quite different compared to both theory and experiment result. But it gives us an idea of designing the experiment that when measuring asymmetry (2.3) with constraints (2.4) to (2.7), we should check region  $\delta \sim > 10MeV$  for measurable asymmetry.

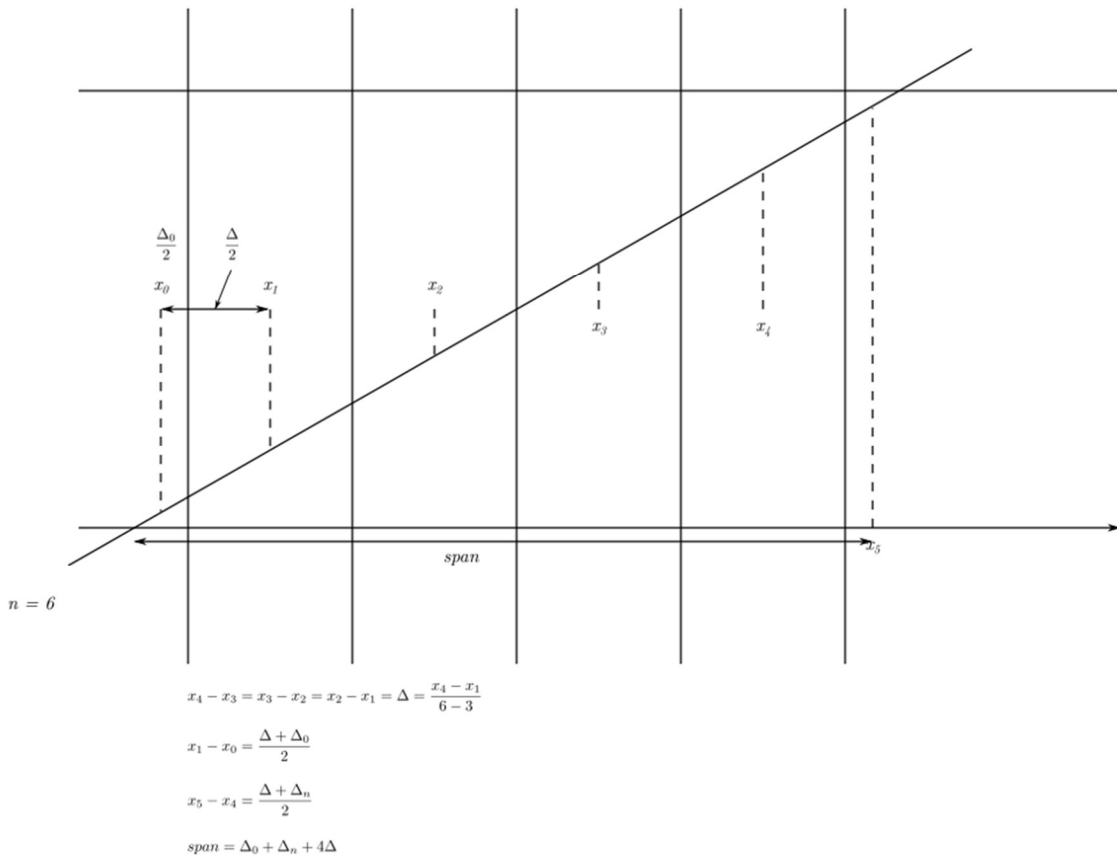
## 2) Wire chamber wire hit coordinates and wire spans.

Assume the track of a particle within each wire plane's wire volume (or drift cell volume of a wire) has minimum multiple scattering, which means it is close to a straight line track. By the way the Geant 4 simulation stores particle coordinates inside a wire, that is the average position

of all “steps” within the wire volume, the  $(x, y)$  coordinate in a simulation result in a ROOT file is approximated to be the value of one of the following cases (See Fig 2.20 in next page):

- (1) If the track transverses the entire wire volume, that is the particle exits an adjacent wire volume, then enters the wire volume we’ve set for measuring  $(x, y)$  coordinate, exits from its side and enters an adjacent wire volume, then the  $(x, y)$  stored in the ROOT file is taken to be the average  $(x, y)$  position of the track within wire, and should be approximately at the location of the sense wire.
- (2) If the wire we’re checking is where the wire enters or exits the wire plane gas layer, then only traverses part of the wire volume, by which  $(x, y)$  will be off sense wire location.  
( $x_0$  and  $x_5$  in Fig 2.20 below)

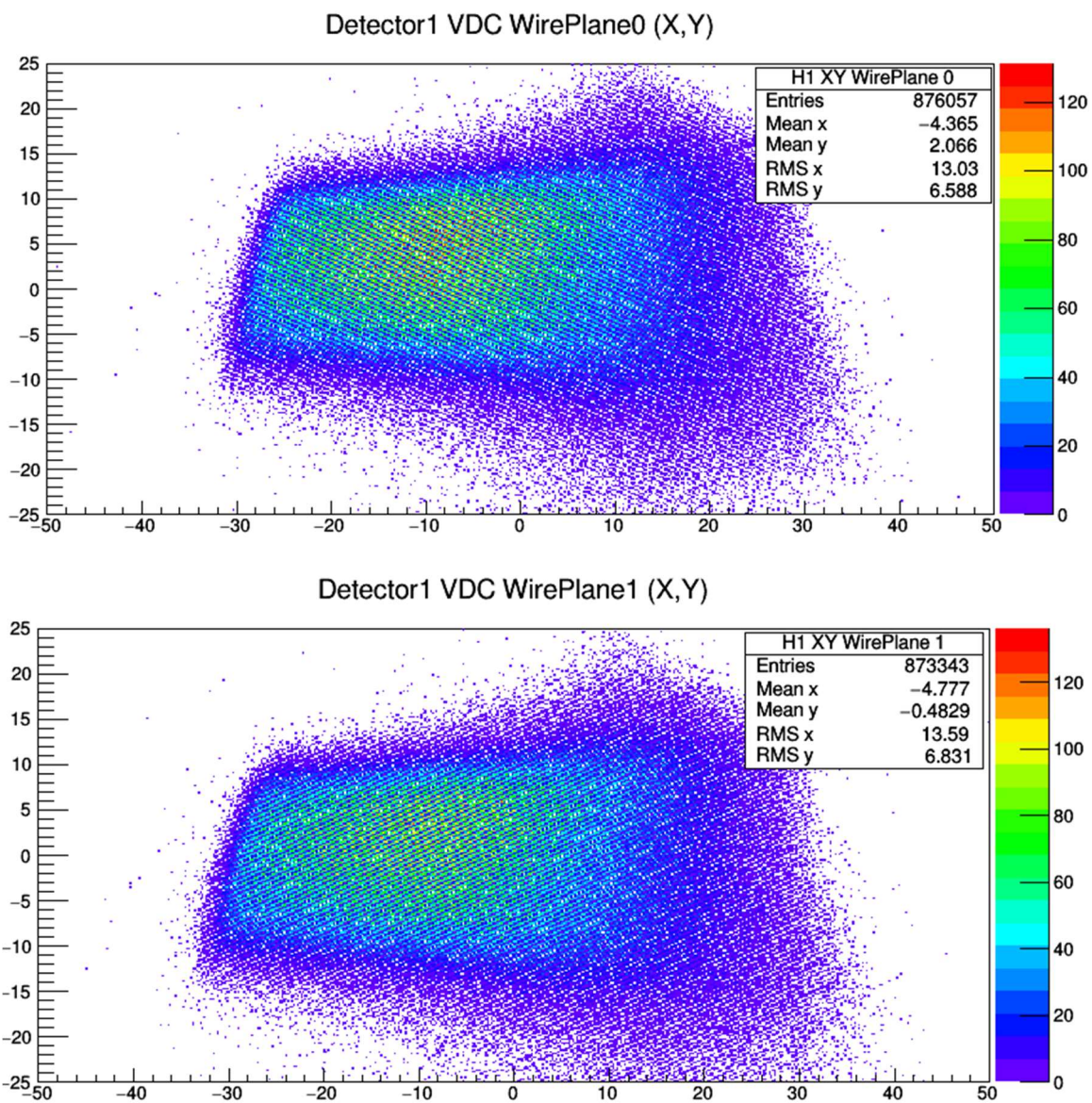
The number of wires of the cluster in the wire plane in cases (1) or (2) depends on the direction of track and orientation or placement of wire chambers. Because of the effect of (1), the  $(x, y)$  coordinates of the wire distribution should be peaked at sense wire locations (or precisely, the sense wire location projection in  $xy$  plane). The effect shows up again in Fig. 2.21 and Fig. 2.22.



IV Fig 2. 20 Illustration: a straight track through 6 wire volumes of a wire plane.

The average location of all integration “steps” in the simulation of each wire: 1) The wires 1,2,3,4 in the middle are fully traversed through the wire volume, and the  $(x, y)$  is the location of the track projection on the sense wire. 2) The wires 0 and 5 are the wire volumes where the track enters and exits the wire plane, but does not traverse the entire wire volume;  $(x, y)$  is not a sense wire location projection.

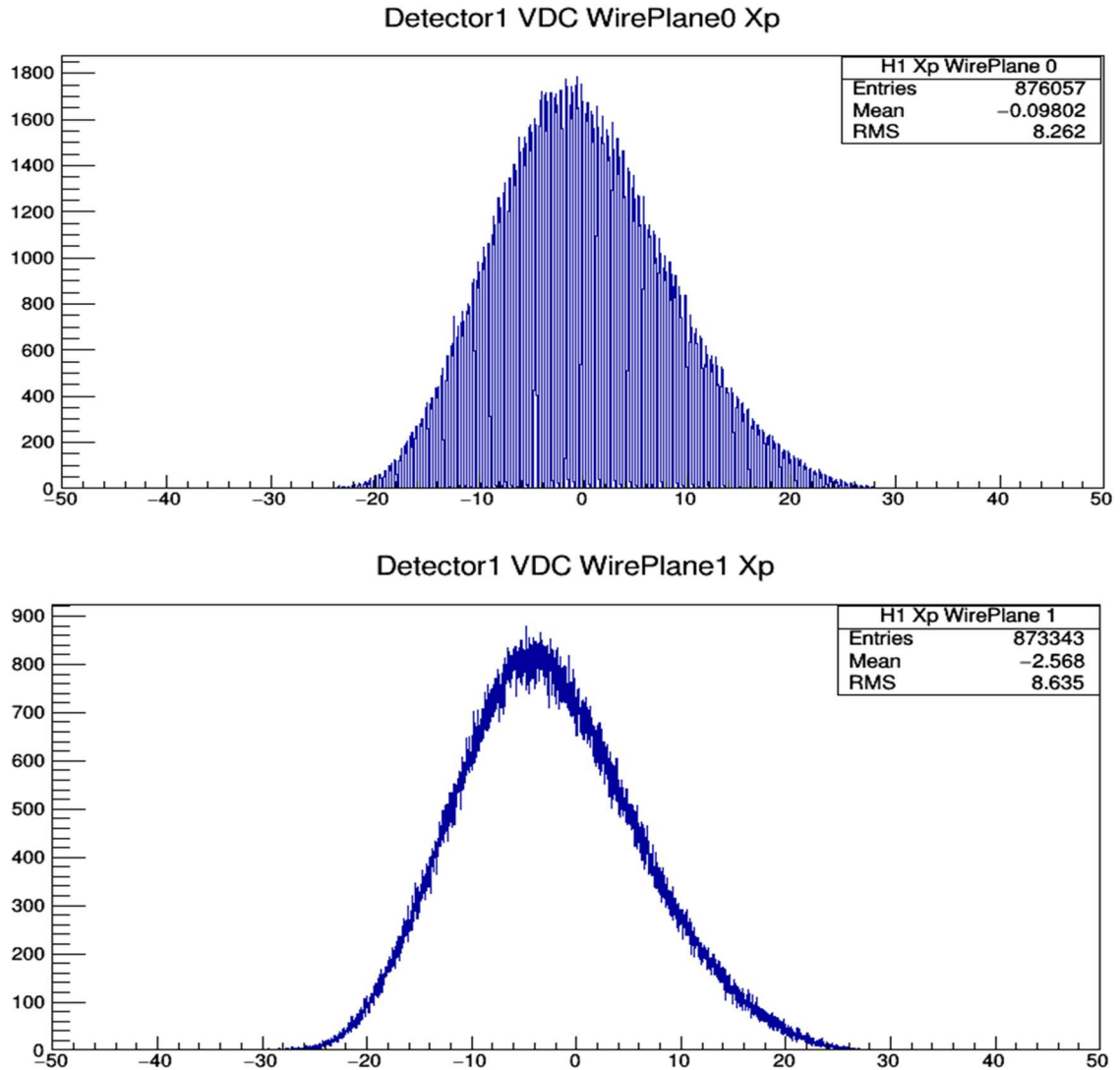




IV Fig 2. 21 Electron side detector hit  $(x, y)$  coordinates distribution. Ordinate: vertical coordinate of hit electron position on wire plane in  $cm$ , abscissa: horizontal coordinate of hit electron position on wire plane in  $cm$ .

For wire plane 0 ( $v$  wire plane), and wire plane 1 ( $u$  wire plane) of front wire chambers. We can see the pattern of the distribution; hits  $(x, y)$  are highlighted at where the sense wires located for wire plane 0 (sense wires are in upper-left to lower-right orientation), and the opposite is true for wire plane 1.



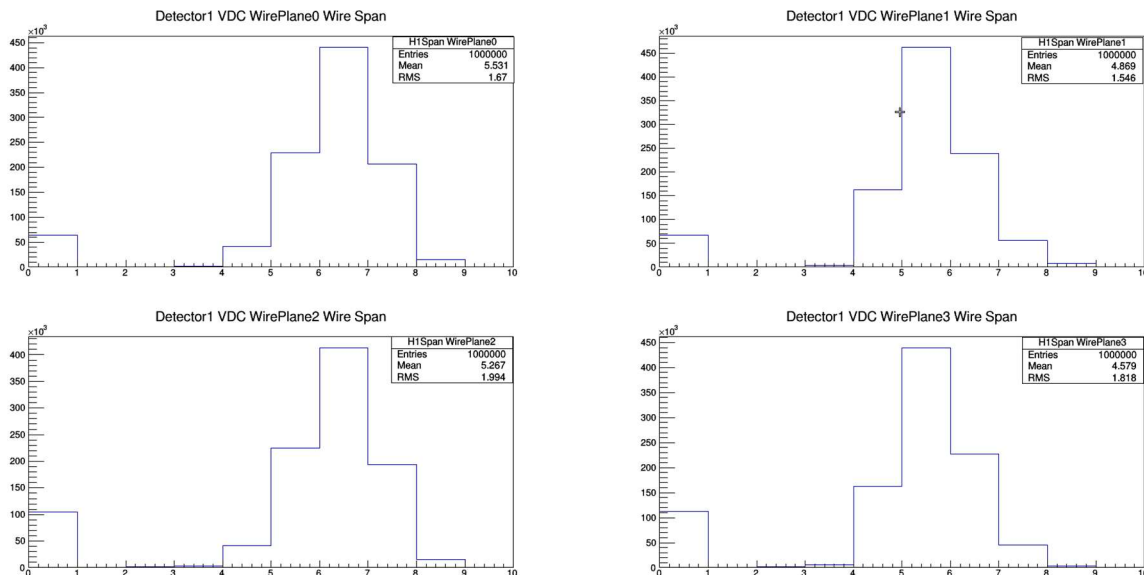


IV Fig 2. 22 Projected coordinate  $x_p$  on  $v$  axis. Ordinate: count, no unit, abscissa: projected coordinate  $x_p$  defined in equation (2.9) below in  $cm$ .

( $v$  axis direction is perpendicular to  $v$  wires) from  $(x, y)$  of the wire plane 0 ( $v$  wire plane, upper plot), and wire plane 1 ( $u$  wire plane, lower plot).  $x_p$  in the plots is simply the scalar product of  $(x, y)$  and unit vector  $\hat{v}$ :

$$x_p = x \cos \alpha + y \sin \alpha \quad (2.9)$$

where  $\alpha \cong \text{atan}(0.5)$  is the angle between  $v$  axis and  $y$  axis.



IV Fig 2. 23 Electron track wire spans. Ordinate: count, no unit, abscissa: number of hit wires in the event, no unit.

Or number of hit wires in an event of all wire planes on electron side wire chamber. The “mean” is inaccurate since a considerably large portion of the results are 0; a track missing the wire plane. Both left plots show wire spans of  $v$  planes, and distributions are similar since the projection angles between the tracks and the  $v$  planes inside the  $vz$  plane are the same for both  $v$  planes; the same applies for the right plots from  $u$  planes.

The results above in this section are not precise and might not be used as final wire chamber hit results and wire span results:

- (1) For tracking, the ROOT files stores values of  $(x, y)$  for all wires hit in the wire plane. However, for track finding and fitting, we need to find all clusters in the wire plane, then find the matched pairs of clusters from wire planes with the same orientation, fit their crossover points at the wire planes. Then the only useful  $(x, y)$  value is of the crossover points. Linking the one in the front wire chamber and the one in the back wire chamber we get the track of the particle, just as JLAB Hall A analyzer does. Figs. 2.21 and 2.22 above show the coordinates of all hit wires in a ROOT file with no further analysis conducted (no crossover point coordinate computed).
- (2) For the wire spans, they are only the result of counting the number of wires in the event for the wire plane having been hit without repetition. However, for the case when multiple clusters are presented in the wire plane, the numbers will be combined to the wire spans plotted, resulting in failure.

For a systematic way of cluster finding and track fitting using algorithms similar to JLAB Hall A analyzer, see section 2.4.

### 3) Simple monochrome electron simulation and track intersections on wire planes

What follows is an attempt to check the resolution of detectors in the Geant4 simulation for particle energy  $E$  and polar angle  $\theta$  at the primary vertex. A simulation which shoots isolated monochrome electron or positron in same direction repetitively is run. Then, we check the projection on each surface with a sensitive detector.

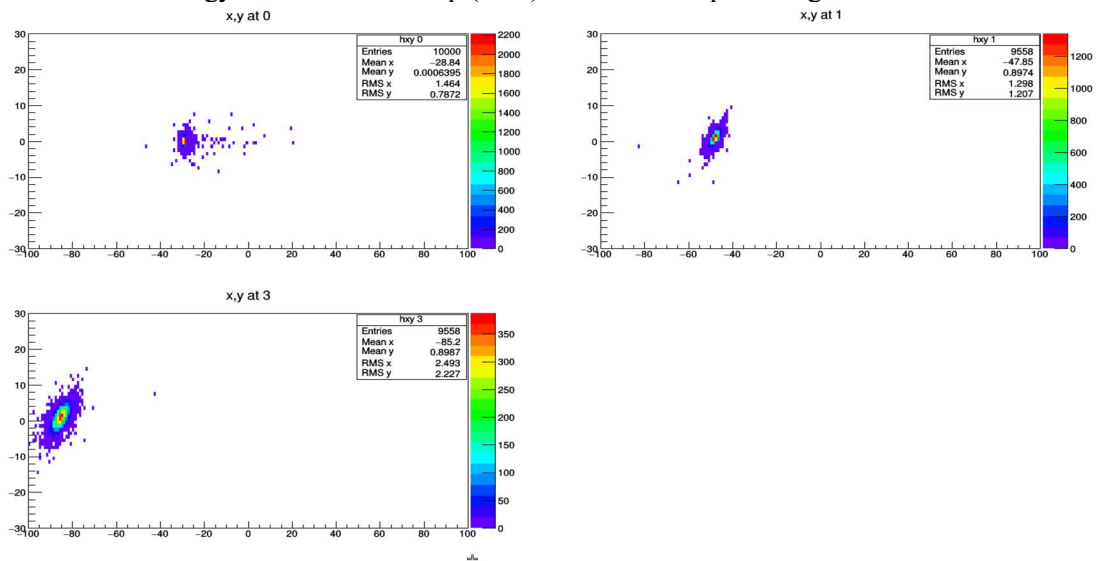
As for the initial condition of the simulation: polar angle  $\theta = 9^\circ$ , azimuthal angle  $\varphi = 0^\circ$ , particle kinetic energy  $KE = 18, 20, \dots$ , and  $56 \text{ MeV}$ , 10k events per energy. As we expect, the energy resolution (or polar angle resolution) is composed of two parts:

- (1) How much the magnet separates tracks of electrons with different energies.
- (2) How much of the effect of multiple scattering is for electrons with a specific energy.

Since the initial particle direction is fixed in this simulation, it estimates energy resolution only for the direction, comparing the shift in the  $x$  coordinate from change of energy  $E$ , we can get estimated value  $\frac{dx}{dE}$ . From the Geant 4 simulation, we get the multiple scattering effect on the wire or  $\sigma_x(E)$ . From

$$\begin{aligned} \sigma_x(E) &\cong \frac{dx}{dE} \sigma_E \\ \text{or } \sigma_E &\cong \sigma_x(E) / \left(\frac{dx}{dE}\right) \end{aligned} \quad (2.10)$$

we estimate the energy resolution as in eq. (2.10). See an example in Fig 2.24 below.



IV Fig 2. 24 Projection of intersection of 56 MeV electron track on monitor, front wire chamber plane, back wire chamber plane. Ordinate: vertical coordinate of hit electron in  $cm$ , abscissa: horizontal coordinate of hit electron in  $cm$ . From top left to lower right, in electron side monitor, front wire chamber, back wire chamber respectively,

In vertical plane parallel to beam, in  $cm$ . For coordinates of wire chambers, they're the average of all wires hit  $(x, y)$  coordinates in the wire plane. For the back chamber wire plane (in lower left plot), at  $KE = 56 \text{ MeV}$ ,  $\bar{x} = -85.2 \text{ cm}$ ,  $\sigma_x(E) = 2.49 \text{ cm}$ . At  $KE = 54 \text{ MeV}$  (Not shown here),  $\bar{x} = -80.8 \text{ cm}$ ,  $\sigma_x(E) = 2.495 \text{ cm}$ . Then using formula (3.10)

$$\sigma_{E|E=54M} \cong \frac{\sigma_x(E)}{\frac{dx}{dE}} \cong \frac{2.49 \text{ cm}}{\frac{4.4 \text{ cm}}{2 \text{ MeV}}} = 1.13 \text{ (MeV)}$$

It should be noted that this value is overestimated, since it is not guaranteed that for the event there is only one track reaching the wire chamber. In addition, even if there is only one track, the average of all wire hit coordinates is not the intersection in the plane of sense wires, since the entering and exiting hits should be weighted less.

#### 4) Energy vs horizontal coordinates of detectors

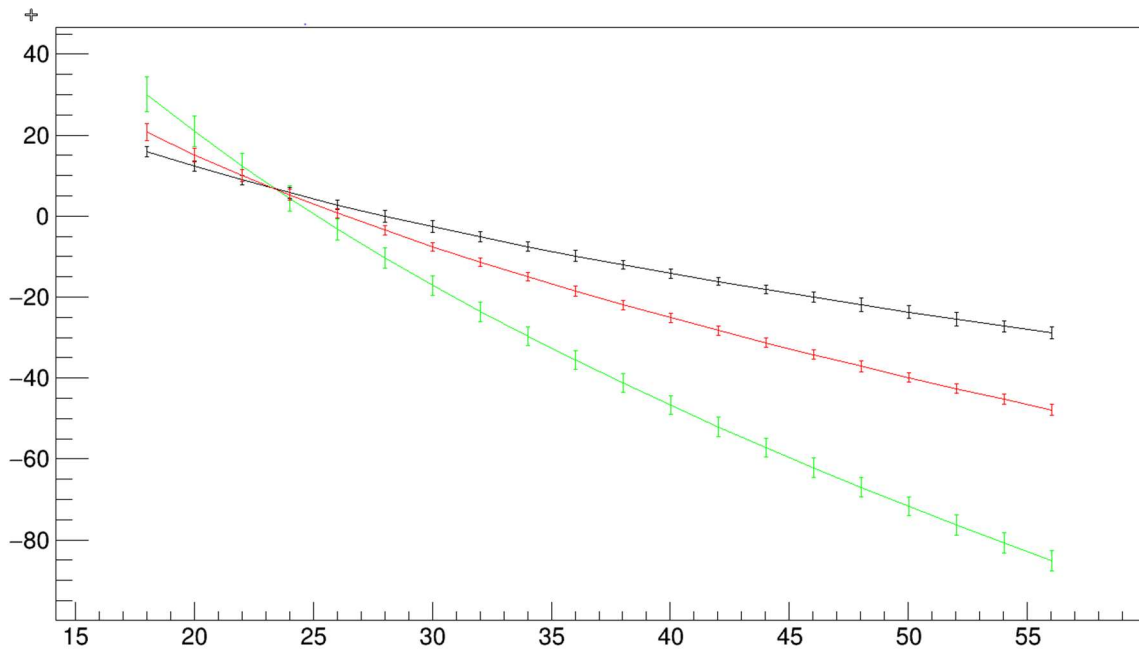
Continuing the method used above, we have for each particle energy  $E$ , coordinates on a monitor or one of the two wire planes:  $\overline{x(E)}$  and  $\sigma_x(E)$ , making this plot for the 3 surfaces. In addition, we also check the energy dependence of the track horizontal projection angle  $\theta_o$  after exiting the magnet (at input polar angle  $\theta = 9^\circ$ , azimuthal angle  $\varphi = 0^\circ$ ). Which is defined by:

$$\theta_o = \text{atan}\left(\frac{x_2 - x_1}{\Delta y}\right) \quad (2.11)$$

Here,  $x_1$  and  $x_2$  are horizontal coordinates of track intersections on front and back wire chambers, while  $\Delta y \cong 55.7 \text{ cm}$  is the distance between front and back wire chambers in the horizontal plane. From error propagation:

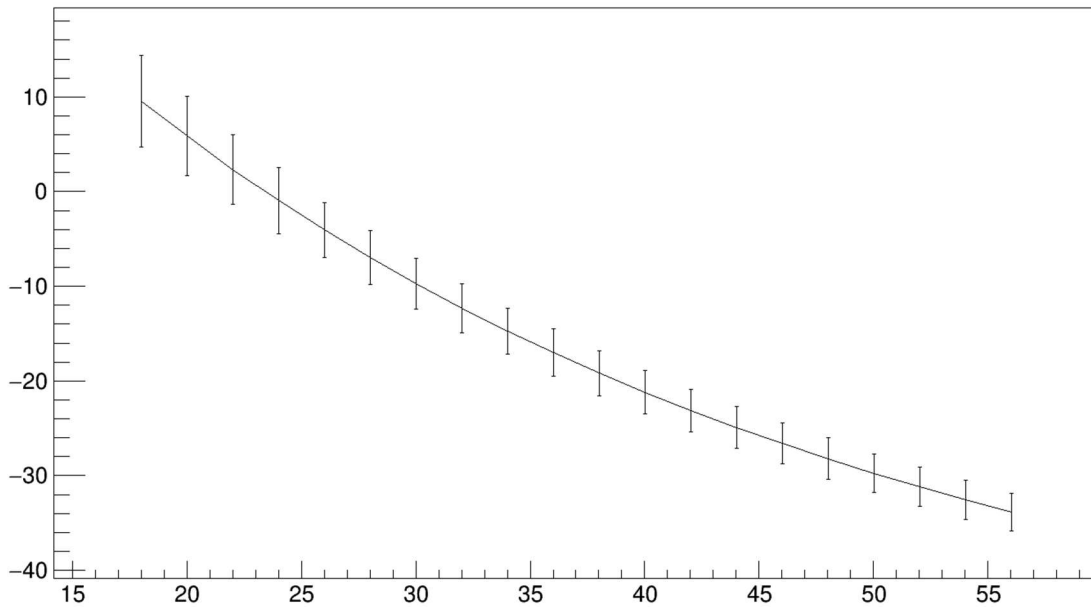
$$\sigma_{\theta_o} = \frac{\sqrt{\sigma_{x_2}^2 + \sigma_{x_1}^2}}{\Delta y \sqrt{1 + \left(\frac{x_2 - x_1}{\Delta y}\right)^2}} \quad (2.12)$$

where  $\sigma_{x_1}$  and  $\sigma_{x_2}$  come from the multiple scattering effect and are obtained by Geant 4 simulation.



IV Fig 2. 25 Track horizontal projection coordinate  $x$  on monitor (black), front (red) and back (green) chambers. Ordinate: track horizontal projection coordinate  $x$  in  $cm$ , abscissa: electron kinetic energy in  $MeV$ .

After particles exits magnet, with dependence on electron kinetic energy. At some value between 23 and 24MeV, the out-electron track is almost perpendicular to beam and detectors where the 3 curves intersect.



IV Fig 2. 26 Track horizontal projection angle  $\theta_0$  when particles exit magnet. Ordinate: track horizontal projection angle  $\theta_0$  in *degrees*, abscissa: electron kinetic energy in *MeV*.

Dependence on electron energy (abscissa, in MeV).

## 2.4 Track finding and fitting using Geant 4 results

As seen in 2.3.3 2), treating all hit wires in a wire plane as a single cluster is faulty. It didn't consider cases like noise and multi-track situations. A cluster finding and fitting routine has been written to imitate real wire chamber analyses. It starts with the hit collection of an event, finding cluster(s) and then fitting a cluster by linking track intersections on the wire plane from front and back chambers.

There is a big difference in data structure between Geant 4 simulations and Hall A analyzer wire chamber classes. The Geant 4 simulation can retrieve  $\mathbf{r} = (x, y)$  projection coordinates of tracks for all hit wires on a wire plane, while  $z$  has not been used for most of the simulations. The analyzer utilizes  $u$  and  $v$  coordinates of the wire plane based on wire plane orientation, and raw drift time which will eventually be converted into drift distance  $d = |z|$ . Thus, the Geant 4 simulation has complete information of wire plane projection for each wire plane, while for analyzer (see formula (2.9)) only  $u$  or  $v$  projection coordinates are given from the exact geometry of wires in the wire planes:

$$\begin{aligned} u &= \mathbf{r} \cdot \hat{u} = x \cos \alpha - y \sin \alpha \\ v &= \mathbf{r} \cdot \hat{v} = x \cos \alpha + y \sin \alpha \end{aligned} \quad (2.13)$$

and for drift distance  $d$  to determine sign of  $z$  needs additional treatment. However, for Geant 4 simulations, not knowing  $z$  also requires some special method to acquire the desired intermediate fit result:

$$(x_1, y_1) (x_2, y_2)$$

that is, the intersection of the track and wire planes with local  $z = 0$ , one on the front chamber and one on the back chamber. Then these two pairs are converted into:

$$(x_1, y_1) (x_2, y_2) \Rightarrow (x_1, y_1), (\theta, \varphi) \quad (2.14)$$

as data specifying a single track. In addition, by exploiting the track geometry in the wire chamber (analyzer) coordinate system, we can get from  $(\theta, \varphi)$  (projection angles of tracks in the analyzer coordinate system) to angles between tracks and wires, which eventually can be converted into wire spans (using formula (3.3)  $n_{u/v} = \frac{h}{|s \times \tan \delta_{u/v}|}$  in section 3.4 of Part III) of the track inside each wire chamber:

$$(\theta, \varphi) \Rightarrow (\alpha_u, \alpha_v) \text{ or } (\delta_u, \delta_v) \Rightarrow (n_u, n_v) \quad (2.15)$$

where  $n_u, n_v$  are cluster spans directly related to geometric effects of wire chamber track finding efficiency.

Prior to getting crossover point coordinates  $(x_1, y_1) (x_2, y_2)$ , we have to identify groups of wire hits as clusters, which is a set of all hit wires with adjacent indices from the same particle track, along with their location information (for the analyzer, it is drift time). The routine for identifying clusters for individual wire planes is called cluster finding. Once a cluster is found, fitting straight line to all hit wires yields the local track. This local (within each wire plane) fitting is different between analyzer and Geant 4 simulation. For the analyzer, we fit cluster data  $(u_i, z_i)$  or  $(v_i, z_i)$  from hit wires at locations  $u_i$  or  $v_i$ , and signed drift distance  $z_i$  after disambiguation. For Geant 4 simulations, we fit cluster of data  $(x_i, y_i)$ . The next step includes sorting clusters from different wire planes to find clusters, one from each wire plane belonging to the same particle track. This procedure involves comparing the local fitted track slopes from both  $U$  planes or both  $V$  planes, or checking the distance between the location of one cluster's intersection in the wire plane and the fitted track projection from cluster intersection from clusters belonging to the other wire chamber. This procedure can be called matching clusters, or  $U$ - $V$  association.

The local fits provide track crossover point coordinates. For the analyzer, they are  $u_1, v_1, u_2, v_2$ . For a Geant 4 simulation, they are  $(x_1, y_1) (x_2, y_2)$ , with  $(x_1, y_1)$  from one wire plane in the front chamber and  $(x_2, y_2)$  from one wire plane in back chamber (Two wire plane data are enough). By combining all 4 wire planes (or can be simplified by 2 wire planes for the Geant 4 simulation), we can solve for  $(x_1, y_1) (x_2, y_2)$  or equivalently  $(x_1, y_1), (\theta, \varphi)$  as representing the track.

In summary, for track finding and fitting, we handle the data in the following steps:

- (1) Cluster finding: Find all clusters in each wire plane.
- (2) (Local) Cluster fitting: Fit clusters locally to find slope and coordinate of crossover points.
- (3) Track finding: Matching clusters from all wire planes that belong to the same track.
- (4) Track fitting: Use coordinate of crossover points from matched clusters to compute track data  $(x_1, y_1), (\theta, \varphi)$ .

In this next chapter, we'll discuss the implementation of these steps in 2.4.1 and 2.4.2, then show the track fitting results  $(x_1, y_1) (x_2, y_2)$ , and  $(n_u, n_v)$  in 2.4.3.

### 2.4.1 Cluster finding

The main implementation of the cluster finding process is grouping hit wires in the same wire plane into an event with either adjacent wire indices, or close in distances. For the analyzer, the main criteria for regarding a set of wires to be cluster include: (1) It has at least 3 wires. (2) The drift time vs wire location or wire indices graph has a  $V$  shape, which means the track indeed crossed the wire plane by approaching sense wires first then moving away from the sense wire and leaving the wire plane.

The drift time is converted into a drift distance  $d$  which is the absolute value of the  $z$  coordinate. Since the Geant 4 simulation does not have  $d$  or  $z$  data, the criterion 2) is discarded, and other cuts ensure the validity of cluster. The following is a brief explanation of steps for cluster finding:

- (1) Read the data from the ROOT file, each wire plane with all hit wires along with array of data (wire number,  $x$ ,  $y$ ).
- (2) Sort wire number in increasing order.
- (3) Separate the hit collection into cluster candidates by continuity of wires (allow gap of one wire):

For example: hit wires for the wire plane (index in the hit collection) are

85(0), 86(1), 87(2), 89(3),  
 110(4), 111(5), 112(6), 112(7), 113(8), 113(9), 114(10), 115(11),  
 119(12), 120(13),  
 125(14), 126(15), 127(16), 128(17), 129(18)

Gaps exist from 89 to 110, 115 to 119, and 120 to 125, all larger than 2. Then cluster candidates are:

(85 - 89), (110-115), (119-120), and (125-129).

- (4) Remove clusters with less than 3 wires, thus the left candidates are:

(85 - 89), (110-115), and (125-129).

- (5) We can see here the cluster candidate (110-115) could be a combination of two clusters.

Starting from one side and checking the  $(x, y)$  distance between the wire and its adjacent wire hit, we compute following quantities:

sum of distance squared:

$$S = \sum_{i=0}^j [(x_i - x_{i+1})^2 + (y_i - y_{i+1})^2] \quad (2.16)$$

and the average distance squared:

$$\bar{d}^2 = S/j \quad (2.17)$$

and current distance squared:

$$d_j^2 = [(x_i - x_{i+1})^2 + (y_i - y_{i+1})^2] \quad (2.18)$$

If  $d_j^2 > 9\bar{d}^2$ , or approximately  $d_j > 3\bar{d}$ , the current cluster candidate is regarded as separated, and a new cluster candidate starts at wire  $j$  of the old cluster candidate.

- (6) Check if any cluster candidates after separation in step (5) have number of wires less than 3. Remove any that do.

What's left are identified as clusters.

Remark: Although there are systematic ways of finding clusters they use clustering which minimizes the sum  $\sum_i \sum_j |\bar{x}_{ij} - \bar{\mu}_i|^2$  [57] where,  $\bar{x}_{ij}$  are points in  $i^{\text{th}}$  cluster,  $\bar{\mu}_i$  is the average coordinate of  $i^{\text{th}}$  cluster if we know the number of clusters. It is not implemented here for simplicity.

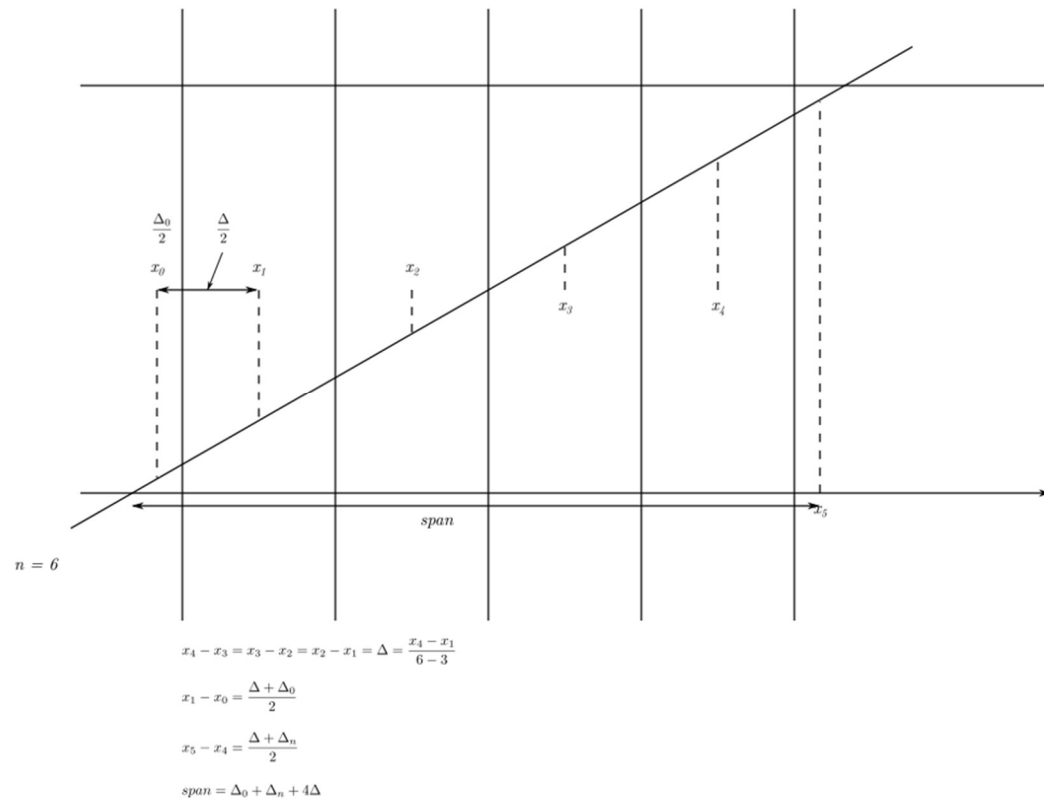
## 2.4.2 Cluster fitting and track fitting

### 1) Local cluster fitting

It's very easy to fit data  $(x_i, y_i)$  in the form:

$$y = A + Bx \quad (2.19)$$

for the coordinate  $(x_{avg}, y_{avg})$  as the intersection on a sense wire plane, which requires drift distance  $z = 0$ . Due to the lack of information about  $z$  coordinates, we have to circumvent it by the following approximation method: if the track fully traverses the hit wire, we assume the  $(x_i, y_i)$  as average coordinate inside the wire volume is vertically projected on the sense wire. When the track traverses the wire partially, it must be that the wire track enters or exits the wire plane, and  $(x_i, y_i)$  still denotes an average coordinate of the track inside the wire. However, they're not vertically above sense wire anymore. Below in Fig. 2.27 is an illustration of a 6-wire cluster case:



IV Fig 2. 27 Illustration of a 6-wire cluster.

The track traverses the wire plane with  $x_0$  to  $x_5$  as the coordinate of each wire. The total span of the track in length should be  $\Delta_0 + (6 - 2)\Delta + \Delta_{n-1}$  as illustrated.

Computing track crossover point coordinate  $(x_{avg}, y_{avg})$ :

(1) Number of wires in the cluster is denoted by  $n$ . If  $n \geq 4$ , by use symbols  $\Delta, \Delta_0, \Delta_{n-1}$  as previously. Then,

$$span = \Delta_0 + (n - 2)\Delta + \Delta_{n-1} \quad (2.20)$$



By noticing relations:

$$x_1 - x_0 = \frac{\Delta_0 + \Delta}{2}, \quad x_{n-1} - x_{n-2} = \frac{\Delta_{n-1} + \Delta}{2}$$

the span becomes

$$span = 2[(x_1 - x_0) + (x_{n-1} - x_{n-2})] + (n - 4)\Delta \quad (2.21)$$

Where  $\Delta$  is calculated from

$$\Delta = (x_{n-2} - x_1)/(n - 3) \quad (2.22)$$

Thus,  $(x_{avg}, y_{avg})$  is computed from:

$$\begin{aligned} x_{avg} &= \left(x_0 - \frac{\Delta_0}{2}\right) + \frac{span}{2} = (2x_0 - x_1) + (\Delta + span)/2 \\ y_{avg} &= A + Bx_{avg} \end{aligned} \quad (2.23)$$

Knowing  $x_0, x_1$ , and  $\Delta$  from (2.22), and  $span$  from (2.21), we can compute  $(x_{avg}, y_{avg})$ .

(2) If  $n = 3$ , the way to compute  $x_{avg}$  cannot be represented by the illustration, formula is altered: (2.23) still applies, thus:

$$\begin{aligned} x_{avg} &= \left(x_0 - \frac{\Delta_0}{2}\right) + \frac{span}{2} = x_0 + \frac{span - \Delta_0}{2} = x_0 + \frac{\Delta + \Delta_2 + \Delta_0 - \Delta_0}{2} \\ &= x_0 + \left(\frac{\Delta + \Delta_2}{2}\right) = x_0 + x_2 - x_1 \end{aligned} \quad (2.24)$$

Remark: When the slope  $B$  in (2.19) is large (this happens quite often, since wire chambers are designed to have better efficiency when the tracks hit the chambers almost vertically), then the “intercept”  $A$  has huge error. To compensate for this, we exchange  $x_{avg}$  and  $y_{avg}$  in the formula (2.20) to (2.23).

## 2) Track finding and track fitting

For track finding there are two major steps:

- (1) Find the clusters from the same track.
- (2) Apply cuts to select tracks which have fit clusters (represented by (2.19)) from both chambers sufficiently aligned.

For matching clusters from the corresponding wire planes (matching  $u_1, u_2$  planes or  $v_1, v_2$  planes), loop over all the combinations of pairs of wire chambers clusters, and minimize the angle differences of the two:

$$\Delta\beta(i, j) = \min \left\{ \begin{array}{l} \arctan(B_{0i}) - \arctan(B_{2j}), \\ \arctan(B_{0i}) - \arctan(B_{2j}) \pm \pi \end{array} \right\} \quad (2.25)$$

Here  $\arctan B$  is the track angle being compared. Indices  $i$  and  $j$  mean the  $i^{\text{th}}$  cluster of wire plane 0 (wire plane  $v_1$ ), and  $j^{\text{th}}$  cluster of wire plane 2 (wire plane  $v_2$ ). Eq. (2.25) can be applied to wire planes  $u_1$  and  $u_2$  by replacing subscripts 0, 2 to 1, 3. Thus, using the  $(x_{avg}, y_{avg})$ 's from the matched cluster, we can fit the global track by linking the  $(x_{avg}, y_{avg})$  of  $i^{\text{th}}$  cluster of wire plane 0 and  $j^{\text{th}}$  cluster of wire plane 2. The slope (with suffix  $avg$  and  $i, j$  omitted) equals:

$$B = \frac{y_2 - y_0}{x_2 - x_0} \quad (2.26)$$

Two cuts have been applied after (2.25) and (2.26) to ensure the clusters are from the same track:

- (1) Angular difference  $\Delta\beta(i, j)$ , and also the one from global fit ( $\arctan B$  in (2.26) replacing one of  $\arctan(B_{0i})$  or  $\arctan(B_{2j})$  in (2.25)) if it is less than  $0.5^\circ$ .
- (2) For difference between fit (2.19) intercepts on  $y$  axis  $|A_{0i} + 15.5'' - A_{2j}| < 1\text{cm}$ , here  $15.5''$  is the vertical distance between centers of wire chambers, and it's also the shift in origin of  $y$  axis between front and back chambers since the shift is  $45^\circ$ . Remark: when

atanB~90° the error of A's are large, and instead intercepts on x axis are compared, the cut is: |(A<sub>0i</sub> + 15.5'')/B<sub>0i</sub> - A<sub>2j</sub>/B<sub>2j</sub>| < 1cm.

Till now, using the (x<sub>avg</sub>, y<sub>avg</sub>)'s from the matched cluster, we uniquely specified the track we're looking for. They are:

$$(x_0, y_0) (x_2, y_2)$$

where (x<sub>0</sub>, y<sub>0</sub>) is abbreviated for the matched cluster's (x<sub>avg</sub>, y<sub>avg</sub>) in 0<sup>th</sup> wire plane; so is (x<sub>2</sub>, y<sub>2</sub>). We can also convert the data above to analyzer format to specify projection angles of the track. So, the track data will be represented as (x<sub>0</sub>, y<sub>0</sub>) (θ, φ), by using the conversion formula:

$$\tan\theta = \frac{(y_0 + \Delta z) - y_2}{\Delta z}, \quad \tan\varphi = -\frac{x_0 - x_2}{\Delta z} \tag{2.27}$$

Here Δz = 15.5'' is the vertical distance between center planes of two chambers, and (x, y) the direction from the analyzer corresponding to (y, -x) of the Geant 4 simulation data convention results in formula (2.27). Also, choosing a pair of wire planes 1, 3: (x<sub>1</sub>, y<sub>1</sub>) (x<sub>3</sub>, y<sub>3</sub>) is also an alternative for the representing the track data when using the Geant 4 simulation.

### 2.4.3 Results

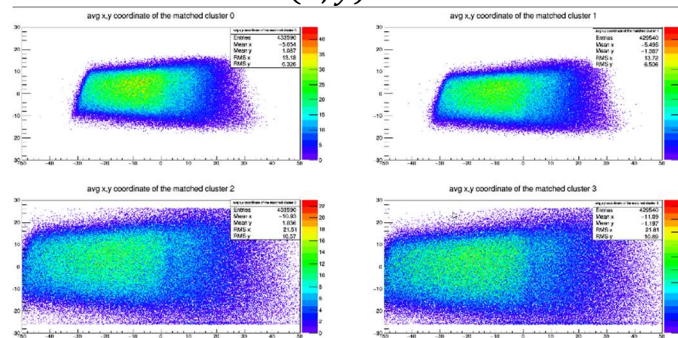
In this section results of track finding and fitting through procedure in last section is shown, they're representing the final results of analyzing wire chamber data of Geant 4 simulation. To some extent, they can be compared with results in section 2.3.3 2).

All the results shown here were analyzed from ROOT files from the same Geant 4 simulation as in the last chapter. The only difference is that only the first 500k events were analyzed instead of the 1 million events in the last chapter.

There are two different categories of results shown here:

- (1) Result of track, which includes the fit track crossover point in each wire plane, cluster spans, number of clusters etc.
- (2) Results reflecting the quality and efficiency of track finding and fitting, which include the differences between cluster angles defined in (2.25), the differences of cluster fit intercepts between fits of front and back chambers defined in (2.26), and the differences of projection coordinates between fit tracks on wire planes (x<sub>i</sub>, y<sub>i</sub>)s and tracks propagated from the monitor using monitor track data.

#### 1) Fit track intersection coordinates (x, y)



IV Fig 2. 28 Fit track intersection coordinates (x, y) distribution. Ordinate: vertical coordinate y in cm, abscissa: horizontal coordinate x in cm. On wire plane 0 to 3.

Plots distributions on all electron side wire planes, in cm.

It is quite obvious there is a quite straight strip parallel to  $y$  axis (at  $x \cong 2\text{cm}$ ) in Fig 2.28, which has lower density compared to its neighbor region. It is an inevitable effect of the fitting  $y = A + Bx$  or  $x = A' + B'y$ , the issue is that when  $B \cong 0$  or  $B$  is *large* the intercept error become large and it is hard for tracks in this region to pass cuts on the intercept difference in section 2.4.2 2), cut (2) below formula (2.26). This issue only originates with Geant 4 simulations, which didn't store  $z$  at each step of the simulation. Compared with the JLAB Hall A analyzer, which fits either  $u, z$  or  $v, z$  relation,  $z$  coordinate display good behavior since only tracks intersecting both front and back wire chamber will always have enough change in the  $z$  coordinate. Meanwhile, the  $u$  and  $v$  also have good behavior since we require a minimum number of wires in the cluster, which is equivalent to demanding a decent amount of change in the  $u$  or  $v$  coordinate. For fitting  $x, y$  in Geant 4 simulation, when change in  $x$  is near 0 then the track traverses the wire planes and the fitting of  $y = A + Bx$  or  $x = A' + B'y$  will result in ill behavior. In order to resolve this issue in the future, we can transform  $x, y$  into  $u, v$  coordinates before track fitting. Or, we can store the  $z$  coordinate in the ROOT file and use it as one of the variables for fitting.

## 2) Number of clusters in each wire plane

The cluster finding results have shown that all wire planes have only 1 or 2 clusters, while the probability of 2 clusters is very low, see the table below. Thus, the error in Fig 2.23 is small. Remark: We see in the table that the probability of events with 2 clusters in wire planes 0 and 2 are similar (0.295% and 0.291%). This also applies to wire planes 1 and 3 (0.380% and 0.379%). Here the larger probability of 2 cluster events in wire plane 1 and 3 might not mean there are actually more tracks in wire plane 1 and 3 than in 0 and 2. Given the geometry of the wire planes and the higher probable of abnormal angles of those track originating from scattering, the track in wire plane 0 and 2 might intersect fewer than 3 wires, and the cluster finding algorithm would have omitted them.

Wire plane	Total events with clusters	Events with 2 clusters	Probability of events with 2 clusters
0	467491	1381	0.295%
1	465943	1771	0.380%
2	445922	1298	0.291%
3	441712	1672	0.379%

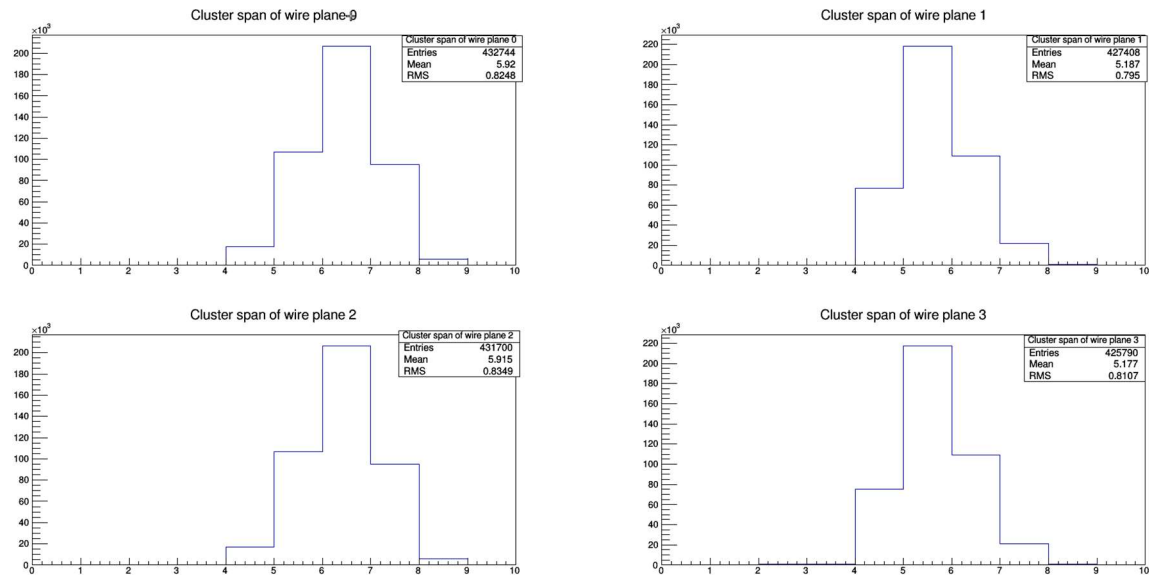
### 3) Cluster spans

There are two definitions for a cluster span:

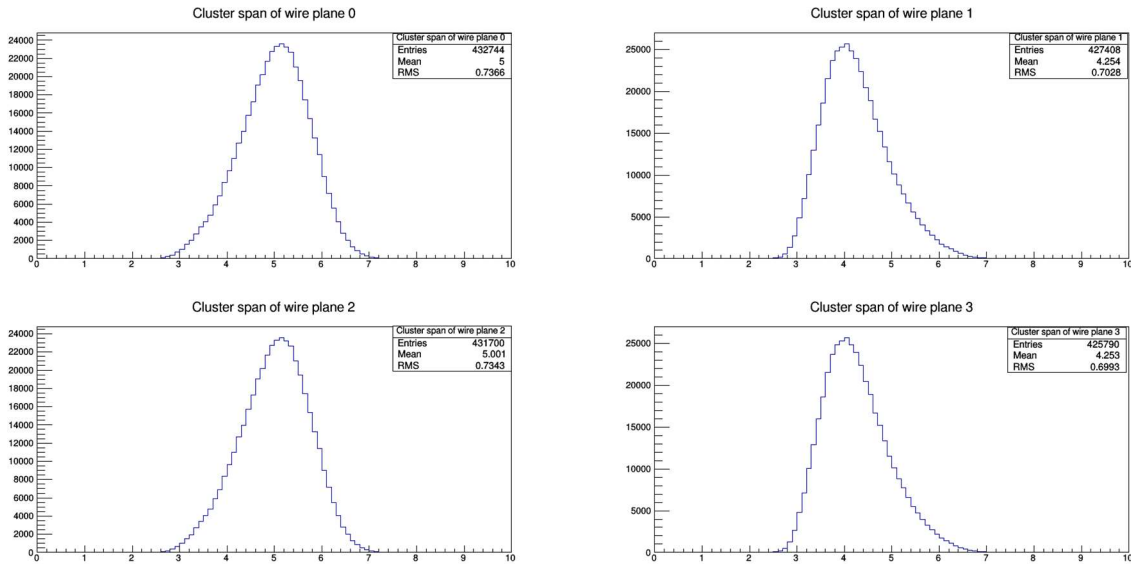
- (1) In the analyzer it is defined as the largest hit wire index in the cluster minus the smallest plus 1. If there is no gap between wires in the cluster (due to bad sense wires for example), it equals number of wires in the cluster.
- (2) The span of track in length within the wire plane thickness divided by wire spacing. They can be computed by formula (3.3)  $n_{u/v} = \frac{h}{|s \times \tan(\delta_{u/v})|}$  in section 3.4 of Part III.

There is obviously a difference between the definitions (1) and (2); while the span in (1) can only have an integer value, the span in (2) is not so constrained. The two definition are related as following: for example, a cluster with 5 wires hit 110, 111, 112, 114, 115 (Note wire 113 hit is missing here). By definition (1),  $span = 115 - 110 + 1 = 6$ . By definition (2) based on how much the track occupies space in wire 110 and 115, the span could be just 4 full wire spans from wire 111 to 114, up to 6 fully wire spans from wire 110 to 115; thus  $4 < span \leq 6$ . The span of definition (2) can be at most 2 wire spans less than definition (1).

Fig. 2.29 and Fig. 2.30 below show the cluster spans distribution from both definitions, only spans of matched clusters with minimum angle difference are filled. In addition, the cluster span of definition (1) helps to determine the corresponding parameters in the Hall A analyzer, which includes the minimum and maximum cluster span. However, the minimum cluster span has been set to 3 no matter the distribution below.



IV Fig 2. 29 Cluster span distribution of each wire plane on electron side wire chambers, using definition (1). Ordinate: count, no unit, abscissa: cluster span, no unit.



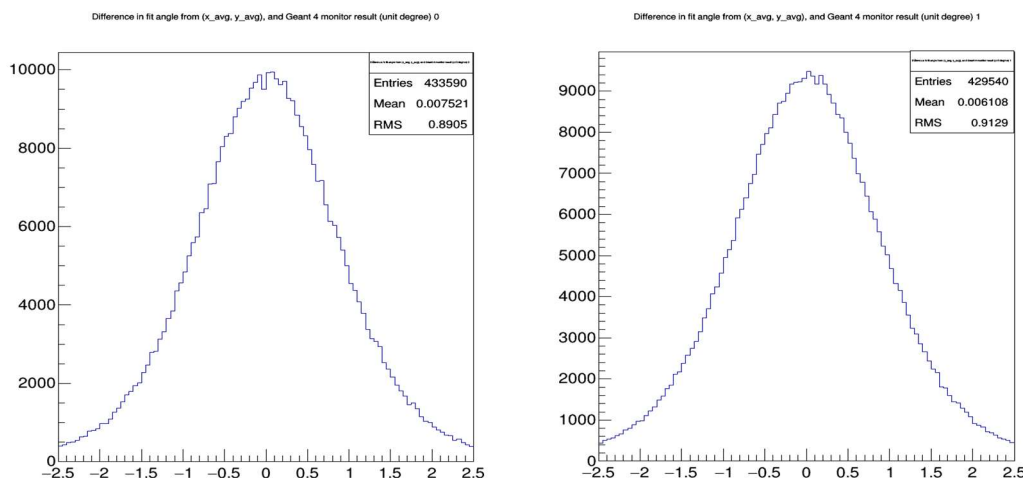
IV Fig 2. 30 Cluster span distribution of each wire plane on electron side wire chambers, using definition (2). Ordinate: count, no unit, abscissa: cluster span, no unit.

#### Remarks:

- (1) Since the wire chambers are parallel, the angle between the track and both  $u$  wire planes  $\delta_{u1}$  and  $\delta_{u2}$  are the same, so are the  $\delta_v$ 's. Thus, for cluster spans using definition (2) are the same for both  $u$  wire planes if they correspond to the same track. This rule also applies for both  $v$  wire planes. For cluster spans by definition (1) for a specific event, since the location of wires are discrete and the location where track enters front and back chamber are different, it may be different for a single event. However, this randomness of entering location is uniformly distributed and have much affect on the distribution of spans.
- (2) Comparing Fig. 2.29 and Fig. 2.23, we see that they are very similar. However, one noticeable difference in Fig. 2.23 is that the probability of larger span values (for example, clusters with a span 8) is larger than the counterparts in Fig. 2.29. The reason is that for the distribution in Fig. 2.23 the total number of hit wires are counted, even while it is possible that they are wire hits from multiple clusters.
- (3) From the distribution in Fig. 2.29 we can safely set maximum size for cluster spans in the analyzer database file to 8, which coincides with the design of the wire chambers (see section 4.2.2 in Part II). (Here we use pairs with energy range from 10 to 50 MeV as in this simulation)

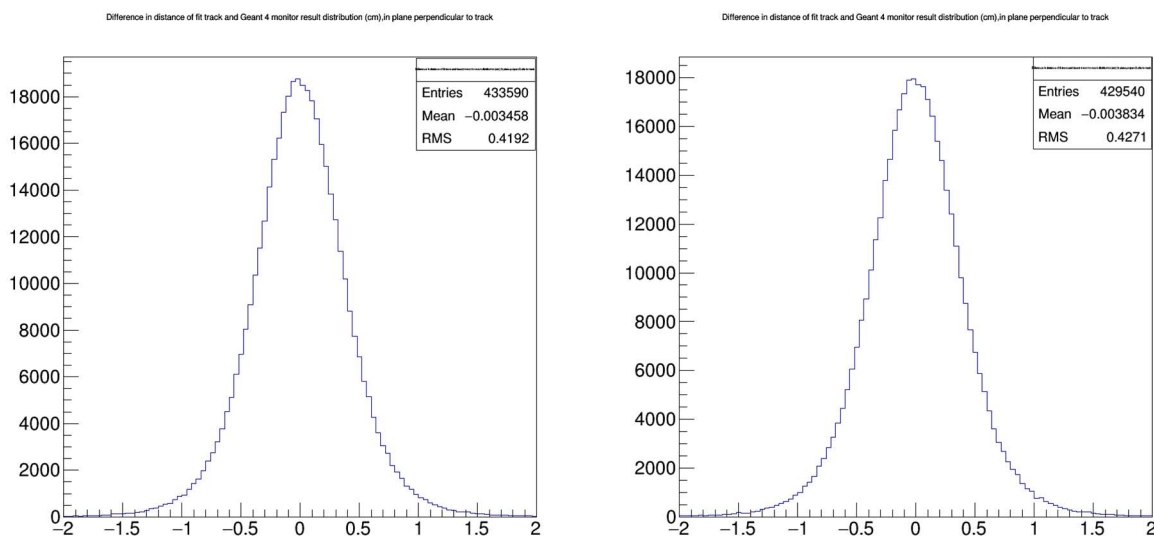
#### 4) Difference between fit track and monitor track extrapolation

Here we show some results reflecting the quality and efficiency of track finding and fitting. We have two sets of fitted track results, one from linking  $(x_0, y_0)$  and  $(x_2, y_2)$ , the other from linking  $(x_1, y_1)$  and  $(x_3, y_3)$ . These tracks are compared with tracks from the monitor, which uses the location and direction of the track intersection as the monitor. From the result we can see the combined effect of both multiple scattering of track starts from the monitor and the precision of track finding and fitting.



IV Fig 2. 31 Difference between fit track and Geant 4 monitor track  $x$  projection ( $x$  is the beam axis) angles. Ordinate: count, no unit, abscissa: angular difference between fit track and Geant 4 monitor track extrapolation in  $x$  projection ( $x$  is the beam axis) direction in *degrees*.

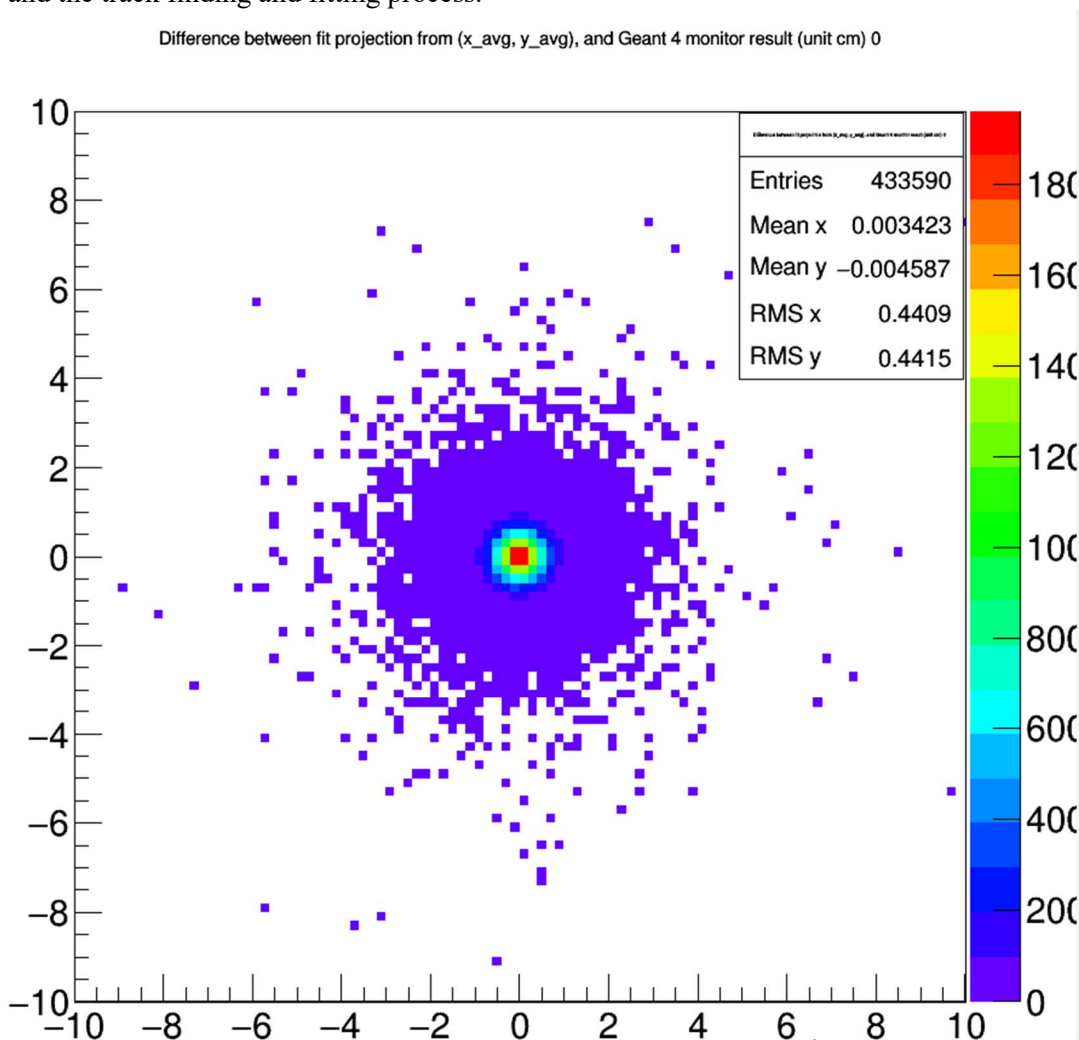
The horizontal projection angle is defined as  $\tan\theta = \frac{(y_0 + \Delta z) - y_2}{\Delta z}$  from formula (2.27), there are  $y$ 's because it uses wire chamber local coordinates), in *degrees*. Left: compare fit of track from linking intersections between wire plane 0 and 2:  $(x_0, y_0)$  and  $(x_2, y_2)$ . Right: compare the fit of tracks from linking intersections between wire plane 1 and 3:  $(x_1, y_1)$  and  $(x_3, y_3)$ . The mean is almost 0, while the RMS is about  $0.9^\circ$  due to the random fluctuations from the effects explained above.



IV Fig 2. 32 Difference between fit track and Geant 4 monitor track  $x$  projection. Ordinate: count, no unit, abscissa: coordinate difference between fit track and Geant 4 monitor track extrapolation in  $x$  projection ( $x$  is the beam axis) direction in *degrees*.

Plotted at the vertical plane 1 meter away from beam, in *cm*. Left: compare fit of track from linking intersections between wire plane 0 and 2:  $(x_0, y_0)$  and  $(x_2, y_2)$ . Right: compare the fit of track from linking intersections between wire plane 1 and 3:  $(x_1, y_1)$  and  $(x_3, y_3)$ . The mean is

almost 0, while the RMS is about  $0.9^\circ$  due to the random fluctuations from multiple scattering and the track finding and fitting process.



IV Fig 2. 33 Difference between fit tracks and tracks extrapolate from monitor data. Ordinate: vertical coordinate difference in *cm*, abscissa: horizontal coordinate difference in *cm*.

Intersections on the plane which is vertical and parallel to beam and 100 *cm* from the beam. The fitted track results are from linking track intersections on wire planes 0 and 2. The monitor track means the straight line through intersection at the monitor, with particle direction at monitor. This result uses same Geant 4 simulation ROOT file, 500k events. Thus, when applying the two cuts in section 2.4.2 2) the efficiency is  $433590/500000=86.7\%$  and we can get a fitted track with  $\sigma_x = 0.48 \text{ cm}$ ,  $\sigma_y = 0.46 \text{ cm}$ . The uncertainty is due to a combination of cluster finding and track fitting algorithm errors, and the multiple scatter effects after monitor.

## 2.5 Additional transformations of wire chambers

### 2.5.1 Motivation

The results of Geant 4 simulations show the track projections on wire planes with different initial kinematics. In order to successfully measure this kinematics, we need to investigate the position and direction resolution from wire chamber data. In section 2.3.3 3) and Fig. 2.24, there are some preliminary results. As mentioned before, the resolution of energy (or polar angle) are composed of two parts:

- (1) How much magnet separates track of electron or positron with different energy.
- (2) How much is the effect of multiple scattering of electron or positron with a certain energy.

After investigating the distributions of hits on wire chambers in different mono-energy beam simulations (same format as Fig 2.24), we found effects reducing the energy resolution:

- (1) Low energy particles with the same initial angles, have large deviation on intersection on wire chamber due to multiple scattering.
- (2) High energy particles with the same initial angles, under small change in energy, while being less susceptible to multiple scattering effects, have much less separation from magnetic field.

Thus, we're trying to adjust some of the simulation settings to achieve the following goal, reduce both multiple scatter effect of low energy particles and the focusing effect on higher energy particles. There are two major parameters we can make change:

- (1) The magnitude of the magnetic field.
- (2) The locations of wire chambers.

As for how can we change these:

- (1) For magnetic field, 0.45 T is about the maximum our magnet can get (see Part II, Fig 3.2), thus a smaller magnetic field is possible but not a higher one.
- (2) For the location of wire chamber, either their distance to magnet center and orientation can be changed, or both.
  - 1) The further the distance, the larger the separation at the wire chamber, the better the resolution. However, we cannot indefinitely increase the distance by the constraint of wire chamber and hodoscope acceptance. Since the current setting is a balance between multiple scatter and acceptance, we keep the default value.
  - 2) For orientation of the wire chambers, we can rotate them about a vertical axis to make low energy intersection side of wire chamber closer to magnet to reduce multiple scattering while increase high energy track distance to wire chamber to increase spatial separation at the same time.
- (3) An additional freedom, that is to change the beam energy. It requires rerun of the BH pair generation.

The rotation of wire chambers is about vertical axis through center of front wire chamber, not rotate about magnet center (Geant 4 simulation global coordinate system origin). Care should be taken for this, and the math prerequisite is in Appendix 2.5. For choices of simulation runs with



different setups, we chose beam energies of  $60 \text{ MeV}$  or  $80 \text{ MeV}$ , magnetic field strength  $0.35\text{T}$  or  $0.45\text{T}$ , and rotation angle of wire chambers about vertical axis within  $-30^\circ$  to  $15^\circ$ .

## 2.5.2 Determine transformation of electron side wire chambers in Geant 4 simulation

As Geant 4 simulation required, we need to provide the combined rotation and translation to specify transformation of the wire chamber. The illustration on the next page shows how the wire chamber holder (see Fig. 2.2 and section 2.2.3 2) (6)) has been transformed from its initial location and orientation. Using the same convention in Appendix 2.5, we denote all transformations below (all in Geant 4 global coordinate system, see Fig. 2.1) as:

Rotations (All rotation are about axis through origin, or the center of magnet):

- (1)  $A_0$  rotate about  $z$  axis by  $180^\circ$  (rotate wire chamber holder from  $e+$  configuration to  $e-$  configuration)
- (2)  $A_1$  rotate about  $x$  axis by  $-45^\circ$  (rotate to make chamber holder tilt  $45^\circ$ , to  $e+$  configuration)
- (3)  $B$  rotate  $z$  axis by  $\varphi$ . (This is the additional rotation of wire chambers discussed in section 2.5.1)

Translations:

- (1)  $\xi$  translates from center of the magnet to the center of wire chambers holder in  $e-$  side  $\xi = (0, -y_0 - \Delta y/2, 0)$ .  $y_0 = 85\text{cm}$  is the distance between magnet center and center of front wire plane.
- (2)  $\Delta y$ : distance between front wire plane center to back wire plane centered in horizontal plane.  $\Delta y = \sqrt{2} \times 15.5'' \cong 55.68\text{cm}$ .
- (3)  $\eta$ : the translation that makes  $r \rightarrow Br + \eta$  the rotation about vertical axis through center of front chamber  $\eta_0 = (0, -y_0, 0)$ . Here  $r = (x, y, z)$  is any point in wire chamber holder volume of the simulation.
- (4)  $\zeta$ : Additional translation vector along wire chamber long axis, after rotation  $r \rightarrow Br + \eta$ . It makes back chamber centered at middle point of max and min range of  $e-$  tracks. (Which should be determined by simulation result)

Combination of all transformations in following steps (see Fig 5.1 in next page):

1. Making transformations equivalent to default transformation (making wire chambers tilted in desired orientation, then translate the wire chamber holder to default location), by applying formula (A5.2):

$$(1, \xi) \cdot (A_1, 0) \cdot (A_0, 0) = (A_1 A_0, \xi) = (A, \xi) \quad A = A_1 A_0 \quad (2.28)$$

2. (see remark at the end of Appendix A5.2.2 and eq. (A5.15)). Set  $\eta_0 = (0, -y_0, 0)$  to be the coordinate of center of the front wire chamber and as the fixed point of rotation  $Br + \eta$ , then:

$$\begin{aligned} \eta_0 &= B\eta_0 + \eta \\ \eta &= (1 - B)\eta_0 = \begin{pmatrix} 1 - \cos\varphi & \sin\varphi & 0 \\ -\sin\varphi & 1 - \cos\varphi & 0 \\ 0 & 0 & 0 \end{pmatrix} \begin{pmatrix} 0 \\ -y_0 \\ 0 \end{pmatrix} \\ &= \begin{pmatrix} -y_0 \sin\varphi \\ -y_0(1 - \cos\varphi) \\ 0 \end{pmatrix} \end{aligned} \quad (2.29)$$

3. Combine steps 1 and 2:

$$(B, \eta) \cdot (A, \xi) = (BA, \eta + B\xi) \quad (2.30)$$

4. Combine the last translation,  $\zeta$ :

$$(1, \zeta) \cdot (BA, \eta + B\xi) = (BA, \zeta + \eta + B\xi) \quad (2.31)$$

Explicit forms of translations and rotations:

$$B = \begin{pmatrix} \cos\varphi & -\sin\varphi & 0 \\ \sin\varphi & \cos\varphi & 0 \\ 0 & 0 & 1 \end{pmatrix}$$

$$\eta = (-y_0 \sin\varphi, -y_0(1 - \cos\varphi), 0)^T$$

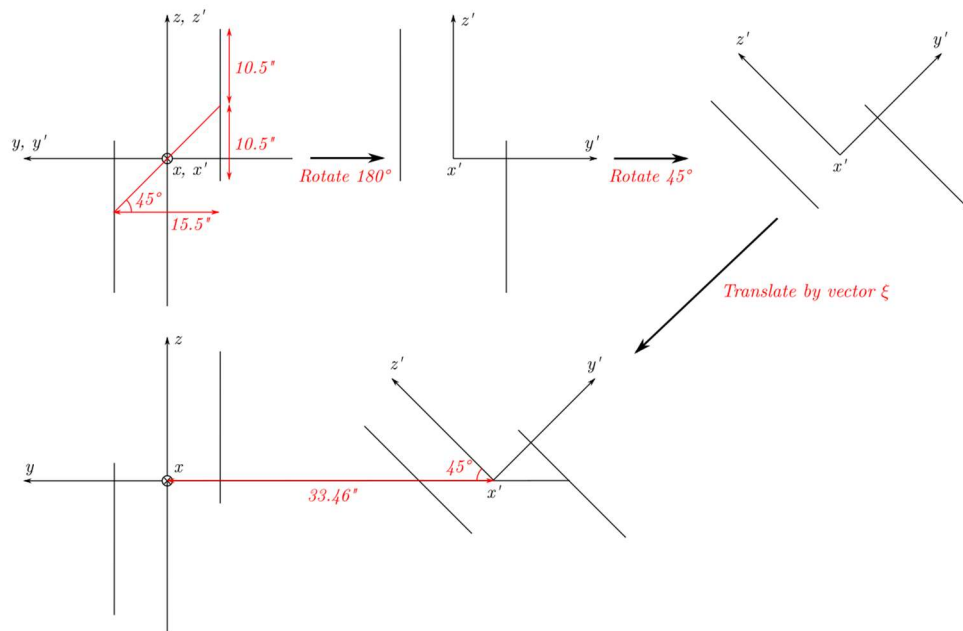
$$B\xi = \left( \left( y_0 + \frac{\Delta y}{2} \right) \sin\varphi, -\left( y_0 + \frac{\Delta y}{2} \right) \cos\varphi \right)^T$$

$$\zeta = l(\cos\varphi, \sin\varphi, 0)^T$$

Let  $l$  be the length of the final translation along long axis of wire chambers with the convention:  $l > 0$  and  $|\varphi| < 90^\circ$  means moving downstream. So the combined translation is:

$$\zeta + \eta + B\xi = \left( l\cos\varphi + \frac{\Delta y}{2} \sin\varphi, l\sin\varphi - \left( y_0 + \frac{\Delta y}{2} \right) \cos\varphi, 0 \right)^T \quad (2.32)$$

Formula (2.31) is the transformation we are using in the Geant4 simulation, instead of default transformation (2.28).



IV Fig 2. 34 All transformations in sequence and transformation  $(B, \eta)$ .

(1) (Updated Fig 2.2) All transformations in the sequence of making wire chambers till the placement in formula (2.28) in  $yz$  projection, only the active area of the center plane of each wire plane is drawn as line segment in the illustration. The notations of the transforms are as  $(A_0, 0)$   $(A_1, 0)$   $(1, \xi)$  are indicated in the plot.

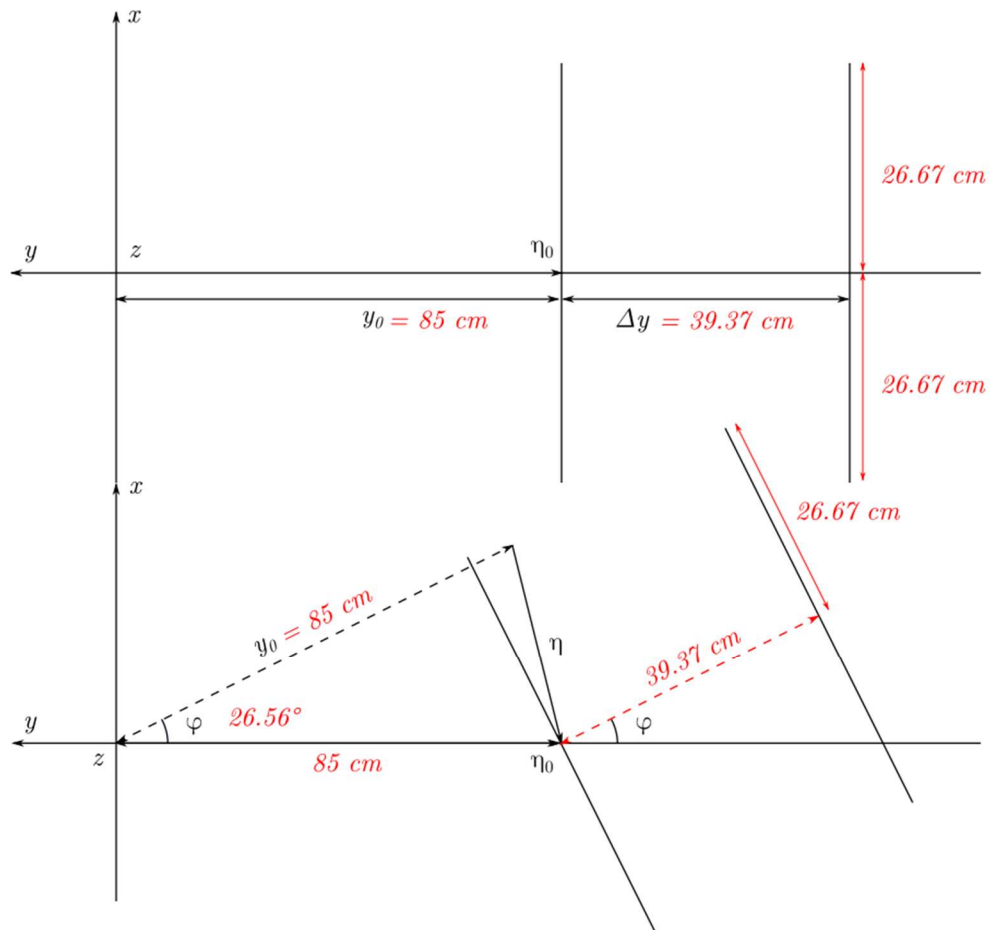


Fig 2.34 (2) Transformation  $(B, \eta)$  in (2.30) moving the wire chambers from the placement in formula (2.28) to formula (2.30) or the placement of wire chambers before final translation  $(1, \zeta)$ , in  $xy$  horizontal projection. Note the graph is in  $xy$  projection rather than  $yz$  projection in Fig. 2.34(1). Scaler  $y_0$ ,  $\Delta y$ , angle  $\varphi$ , and vector  $\eta_0$ ,  $\eta$  are marked. In this illustration, the convention is  $\varphi > 0$ ; if back chamber rotates to the other side of  $y$  axis,  $\varphi < 0$ .

Remark:

Remarks:

1) Extract track info from Geant 4 simulation ROOT file:

We are still aiming to compare the fitted track and monitor track results in Geant 4 global coordinate system, just as in section 2.4 *Track finding and fitting using Geant 4 results*. The wire chamber positions data in the ROOT file stored as local coordinate in each wire plane, but monitor position data are in global coordinate system. In order to compare them in the same frame, the global coordinate system has been chosen. We first convert wire chamber position data in the ROOT file from wire plane local coordinates, into the chamber holder coordinate system. Then we use the coordinate transformations in eq. (2.30) to transform all the coordinates of wire hits to positions in global coordinate system. To compare the fit track and monitor track,

we can check their angle and position differences in  $x, y$  projections on the wire chamber, which is the same as in section 2.4.3 4).

### 2.5.3 Results

There are some results which are counterparts to those in Section 2.4. Since our goal is to get better resolution for both high and low energy particles, we adjust the simulation settings (in 2.5.1) to achieve it. To reduce multiple scattering, there are two ways: either increase particle energies, or reduce distance from the magnet to the wire chambers. For the latter, it will reduce wire chamber track angular resolution, so it's not optimal. In order to increase particle energies, all we have to do is to increase beam energy. Besides the reduction of multiple scattering, there're some major change if we alter the beam energy:

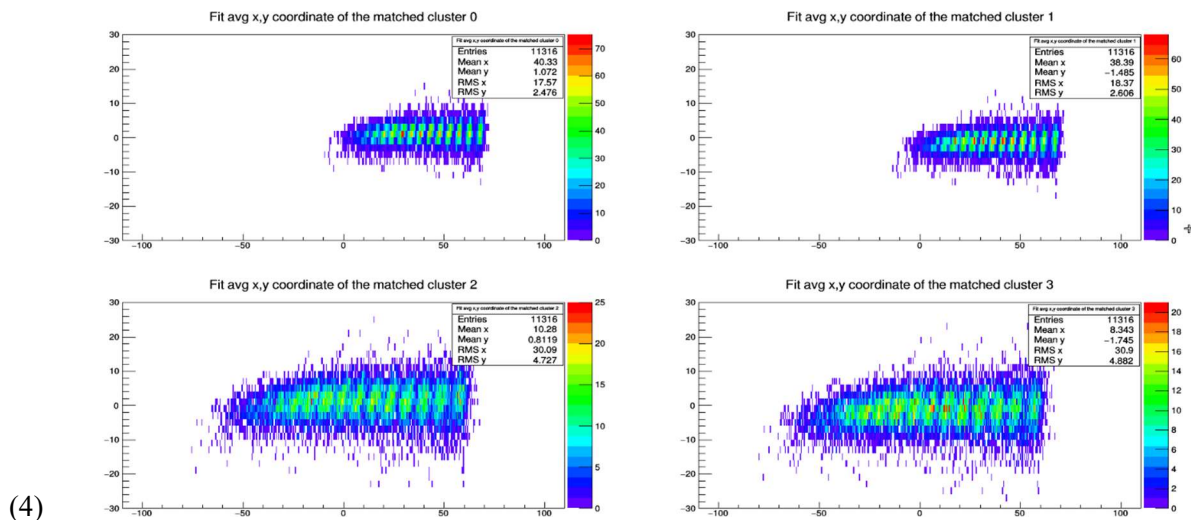
- (1) The cross section of the BH process is changed, and the asymmetry changed accordingly. In addition, the BH pair data file obeying the cross section must be re-generated, with the new beam energy setting. The new measurable asymmetry must be recalculated in order to find the energy range in which we can measure the asymmetry (see Fig. 2.18)
- (2) The bending effect of the magnetic field is reduced so the radius of particle trajectories are increased (Proportional to total energy of the particle, see formula (3.5) in next chapter). The particles in general will hit the wire chamber towards the downstream direction, thus the orientation of wire chambers must be changed accordingly. This is the reason we introduced the additional rotation  $(B(\varphi), \eta)$  and translation  $(1, \zeta)$  earlier to make tracks go through the center area of the chambers.
- (3) As for magnetic field, since the beam energy is increased, we need to keep the current maximum magnetic field strength (0.45 T) to prevent higher energy particles from hitting the magnet pole or side frame.

Every time we change the beam energy  $E_\gamma$ , the magnetic field strength  $|\mathbf{B}|$ , or the additional chamber rotation angle  $\varphi$  we need to rerun the Geant 4 simulation, so there are many ROOT files and results. Due to the limited space, we only show results of simulations with the following conditions:

- (1) electron energy ranges from 24 to 56 MeV (or 30% to 70% the 80MeV beam energy), with discrete energy values 24, 26, ..., 56 MeV. With fixed initial spherical angles  $\theta_0 = 5^\circ$ ,  $\varphi_0 = 0^\circ$ . 1000 events per energy, a total of 17k events.
- (2) 0.45 T Magnetic field.
- (3) Wire chamber rotation angles  $\varphi = -15^\circ, 0^\circ, 15^\circ, 30^\circ$ . This is the only factor changed between different simulations.

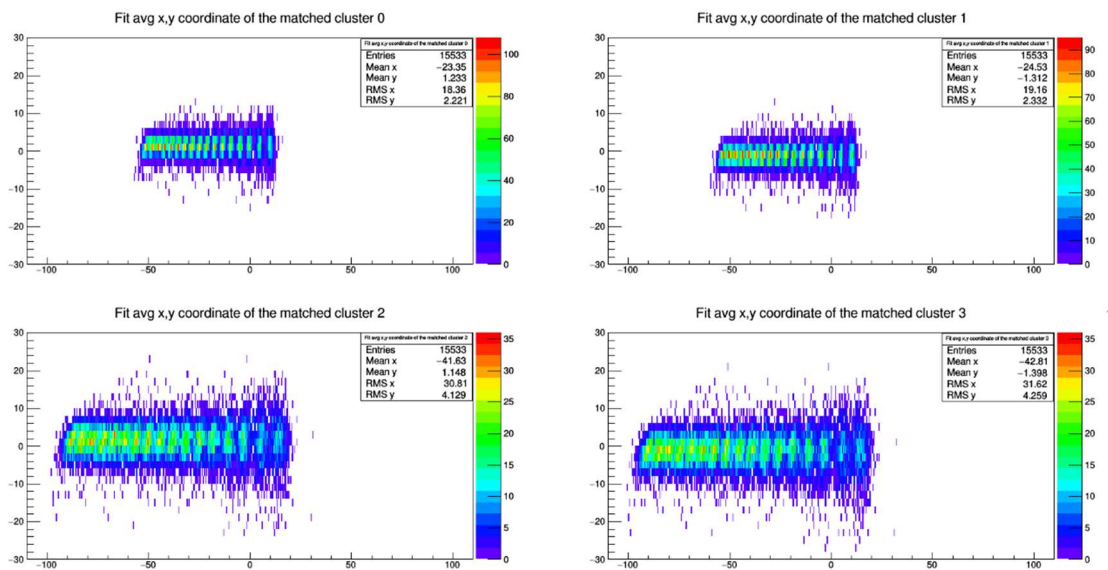
1) Track intersections on wire chambers.

These are the results which are counterparts of those in Fig. 2.28. We found and fitted tracks using the same procedure as in Section 2.4 and applied the same cuts as described in 2.4.2 2) below formula (2.26). We also required both  $u, v$  wire planes have matched clusters.

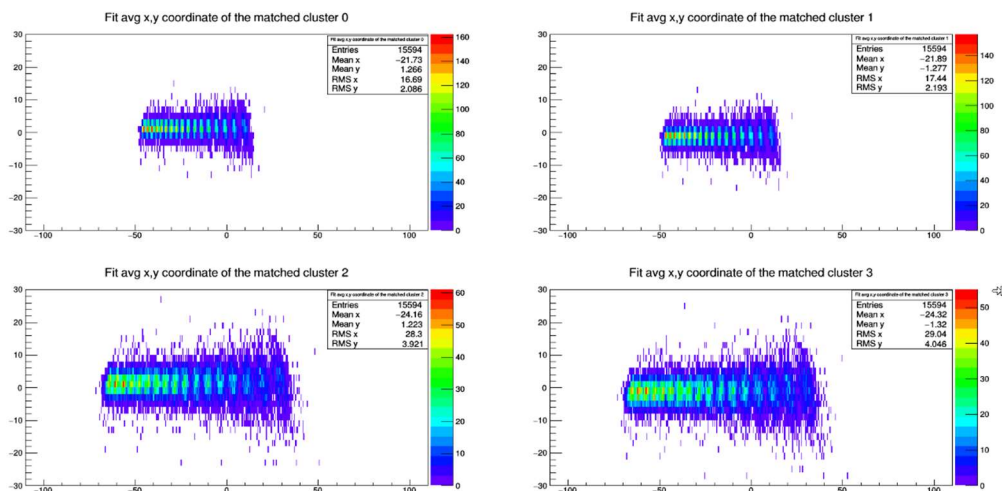


IV Fig 2. 35 Fitted track intersections on wire chambers with rotation angle  $\varphi = -15^\circ, 0^\circ, 15^\circ$ . Ordinate: vertical coordinate in *cm*, abscissa: horizontal coordinate in *cm*.

(1) Fitted track intersections on wire chambers with rotation angle  $\varphi = -15^\circ$  (convention of sign of  $\varphi$  in Fig 2.34 (2)), in *cm*. We also translate the wire chambers downstream along the long axis of the wire chambers after the rotation, to keep the center of back wire plane coincident with the average of 24 and 56 MeV particle track intersections.



IV Fig 2.35(2) Fitted track intersections on wire chambers with rotation angle  $\varphi = 0^\circ$ . Ordinate: vertical coordinate in *cm*, abscissa: horizontal coordinate in *cm*.



IV Fig 2.35(3) Fitted track intersections on wire chambers with rotation angle  $\varphi = 15^\circ$ . Ordinate: vertical coordinate in *cm*, abscissa: horizontal coordinate in *cm*.

Observations:

- (1) As  $\varphi$  increases (Fig 2.35(3)), the lower energy particles tracks will travel through longer distances to reach the wire chamber, and the effect of multiple scattering makes resolution worse.
- (2) For lower  $\varphi$  the first benefit is reduced multiple scattering for lower energy particles, also their tracks are more perpendicular to wire chambers, making much less spread on the wire chamber.
- (3) Second benefits for lower  $\varphi$  is that higher energy particles now make larger angles with the wire chamber, which means their intersections are more separated for smaller increments of energy (2 MeV change in these histograms). This improves the resolution.
- (4) However, there's a major defect of lower  $\varphi$  (Fig 2.35(1)): the angle between high energy track and wire chamber increased accordingly, which makes tracks through one of the *u, v* wire planes to not have enough wires to be identified as a cluster. This results in no tracks being found for such events. Out of 17k events, the total number of events with found tracks at  $\varphi = -15^\circ$  is much less than the other two  $\varphi$  values, with the most efficiency loss being suffered by high energy tracks.

$\varphi$	Events have track	Total track reconstruction efficiency
$-15^\circ$	11316	66.6%
$0^\circ$	15533	91.4%
$15^\circ$	15594	91.7%

We also ran simulations with fixed energy but changed  $\theta_0$ . The resolution was much worse, especially for low energy electrons. Bad angular resolution was observed in Fig 4.8 and Fig 4.9. Due to space, it won't be shown here. Also, 60 MeV beam simulations with 0.45T or 0.35T were conducted.

## 3 Simple acceptance simulation

### 3.1 Introduction

The Geant 4 simulation provides us results on detectors response of Bethe-Heitler electron, positron pairs through the magnet. However, there are some drawbacks for this simulation. It takes quite a long time to simulate the large number of events the experiment estimated to gather, so any changes in setup lead to a delay in getting results. The ROOT files storing the resulting data need customized code to analyze. Any change in the data structure in ROOT files results in changes to the analyzing code, usually making the old version obsolete. In addition, the simulation result is lacking reference, thus mistakes sometimes are very hard to be identified by checking the resulting data alone.

A simple simulation code was written to overcome some of the shortcomings of the Geant 4 simulation. It exploits the fact that our experimental setup has a very simple spectrometer; only one dipole magnet is used. Thus, under some plausible approximations, the tracks of electrons and positrons are also very easy to calculate. This code calculates particle tracks, applies cuts on each place which is not air and can block particles. The position and direction of particles at any time can be analytically solved and corresponding numerical results solved. Almost all data in the Geant 4 simulation regarding track info and acceptance of detectors have their correspondence in this code.

The code is very fast: it simulates 1 million events in about 10 seconds. Desired analysis results show up on each run, so there is no data storage issue and handling of ROOT files. Although it contains some approximation, the simulation results are reasonably close to Geant 4 simulation results. It can be used as a half quantitative prediction before running a full Geant 4 simulation, and a cross check of most Geant 4 simulation tracking results.

The next sections include following contents:

In section 3.2 calculation of tracks: it explained the approximation been used in the calculation, and how main analytic formulas obtained. There are also a few parameters are calibrated by comparing Geant 4 simulation results.

In section 3.3 basic results: it shows the basic distribution of energy, momentum directions, and particle local positions on detectors results from the simple simulation.

In section 3.4 application: The most direct application of the code is to compare results with Geant 4 simulation. Besides the basic results, some results need additional computation are also been compared, such as asymmetry.

## 3.2 Calculation of tracks

Topics are discussed in following order in this section: the approximations used, calculation of track: three segments and calculation of each one, the calibration of parameters.

### 3.2.1 Approximations

A few approximations have been used to make analytic form formula available, fast computing speed while keeping the result as close to Geant 4 simulation result as possible.

1) The background materials are vacuum, thus there is no multiple scattering effect. Multiple scatter affects tracks in following manner: It randomize direction of the particle. Particles loses energy, and will be bent more inside magnetic field. This effect is energy dependent, lower energy particles are more susceptible.

To justify the approximation, we compare Geant 4 simulation results. We found that by changing vacuum into air (approximated as 70% N and 30% O) in Geant 4 simulation as background the detector response are close. In simulation with about 1 million Bethe-Heitler pairs from theory calculation, the distribution of interactions of track on wire planes are very similar: average of horizontal intersection coordinates on front wire chamber only has about 1 mm difference between air and vacuum simulation, while root mean square difference is about 0.1 mm. The air simulation has 6.4% less counts, due to the multiple scatter of particles near the boundary of spectrometer acceptance, which is acceptable.

It should note that losing energy always result in smaller radius in magnetic field, and average of all tracks using air as background will be bent more than case in vacuum, results in shift of horizontal coordinate of intersection on wire chamber to opposite beam direction.

2) The magnetic field of the dipole magnet is approximated to be a uniform field within a cylinder. The magnet to be used in experiment has close to uniform magnetic field in between poles.

It has two main consequences, first the track under uniform magnetic field is a helix, which makes track very easy to compute. Second is that the fringe field is not completely described in this simple simulation, which is replaced by an effective radius of the uniform field other than pole radius. This effective radius has to be calibrated by comparing results of this simulation to Geant 4's vacuum simulation, which will be explained later in this section. In addition, the effect of fringe field on track making it different from helix cannot be simulated in this simulation.

3) If the particle hits any solid material, it will be considered unable to reach any object behind. Since if the particle has reached solid material, it requires a large change of direction to reach objects behind, and track reconstruction of these tracks will result in violation of energy conservation to make two particles trace back to target.

Another small approximation is when calculate time of flight, the speed of particles is approximated to speed of light. Since the lowest energy electron or positron in simulation will be over 10 MeV, or about 20 rest mass, this is plausible.



### 3.2.2 Calculation of track

Combining these approximations, we now can compute the track by divide it into 3 segments: (1) Straight line before particles enters uniform magnetic field. (2) Helix inside the uniform magnetic field. (3) Straight line after particle exits the field. All of which can be calculated using analytic formula, we will describe them below.

1) Position and velocity at a few key points on the track:

Points along the track have been denoted in alphabetic order:

A: target center, primary vertex.

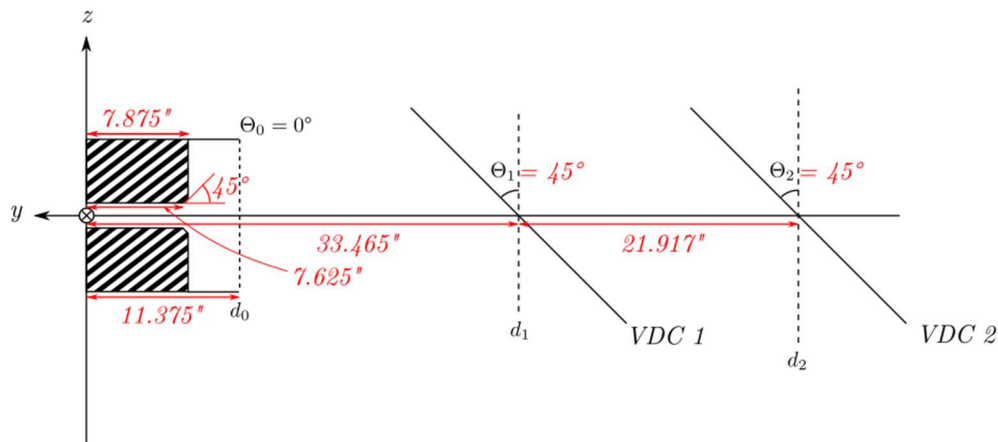
B: particle enters uniform magnetic field

C: particle exits magnetic field

CP: particle horizontal projection reaches the edge of poles of magnet

D, E,F,G: particle at side frame of magnet, 1<sup>st</sup> wire chamber, 2<sup>nd</sup> wire chamber, and hodoscope.

3 segments of the track are (1) A to B, straight line. (2) B to C, helix. (3) C and beyond, straight line. The acceptance of the spectrometer has been checked at point CP, D, E, F, and G. Since the effective radius of magnetic field is different from radius of pole, C and CP are different point. It can be deduced that radius of magnetic field is larger than the radius of the pole by the existence of fringe field, and CP is the intersection of the helix and edge circle of the pole in horizontal projection. In addition, position of the center of helix H is also been used.



IV Fig 3. 1 Coordinate system of the simple simulation.

Location of the magnet, wire chambers (y-z projection). (*Xy* axes were wrong here.)

## 2) Coordinate system

See Fig 3.1 above. Due to the symmetry of the magnetic field, origin is placed at its center. *x* direction is opposite beam direction. *y* direction is horizontal right direction, perpendicular to *x*. *z* direction is vertical up. So *x* and *y* directions are opposite to Geant 4 global coordinate system counterparts.

## 3) Calculation of each key point of the track

For reference, the track from point A to C is illustrated in Fig 3.2.

A: Target center. Denote  $D = 42.26 \text{ cm}$ , the distance between target center and magnet center.  $R_B$  the radius of the uniform magnetic field.  $\theta$  initial polar angle of the track,  $\varphi$  initial azimuthal angle of the track. Thus, the direction vector of the track at A is  $\mathbf{d}$  (scaled that *x* component is 1):

$$\mathbf{d} = (-1, \tan\theta\cos\varphi, \tan\theta\sin\varphi) = (-1, K, K\tan\varphi) \quad (3.1)$$

$K = \tan\theta\cos\varphi$  is the *y* component of  $\mathbf{d}$ , which makes representation of point B simpler.

$\mathbf{r}_A$ , the target center:

$$\mathbf{r}_A = (D, 0, 0) \quad (3.2)$$

B: where particle enters magnetic field. Before the calculation of point B, a cut is made to block any particle hits the magnet yoke hole. The particle direction at B is the same as A. Denote  $\mathbf{r}_B = (R_B\cos\vartheta, R_B\sin\vartheta, z)$  (here  $R_B$  is the radius of the uniform magnetic field) and solve equation:

$$\mathbf{r}_A + \mathbf{d}t = \mathbf{r}_B$$

We have (solved parameter *t* here is not time):

$$t = \frac{D - \sqrt{R_B^2(1+K^2) - K^2D^2}}{1+K^2} \quad (3.3)$$

$$\mathbf{r}_B = (x_B, y_B, z_B) = (D - t, Kt, y_B\tan\varphi) = \left( \frac{DK^2 + \sqrt{R_B^2(1+K^2) - K^2D^2}}{1+K^2}, K(D - x_B), y_B\tan\varphi \right) \quad (3.4)$$

Since  $K$  is not depend on particle energy  $E$ ,  $\mathbf{r}_B$  is only  $\theta, \varphi$  dependent, and with  $R_B, D$  as parameters.

C: Where particle exits magnetic field. From B to C, particle track is helix, and this is the most complicated part of calculation. Only results are shown here, the main part of the calculation includes: finding the projected radius of helix in horizontal plane, find circle center of projected helix, and solve intersections of magnetic field circle and circle of projected helix. More details in appendix.

Radius of the helix projection (circle in horizontal plane):

$$R_H = 10^6 E \sqrt{1 - (\sin\theta \sin\varphi)^2} / (cB) \quad (3.5)$$

See the appendix at the end of this chapter for the derivation of  $R_H$ . Here  $E$  is particle (denotes either electron or positron energy here) total energy, in unit MeV, the electron charge  $e$  has been canceled by  $e$  in MeV.  $\theta$ ,  $\varphi$  are initial polar and azimuthal angle of particle at target as in calculation of point A and B.  $\sqrt{1 - (\sin\theta \sin\varphi)^2}$  is the amplitude of the projection of unit direction vector  $\hat{\mathbf{d}} = (-\cos\theta, \sin\theta \cos\varphi, \sin\theta \sin\varphi)$  on to horizontal plane ( $xy$  plane).  $c = 299792458$  (m/s) as speed of light,  $B = 0.45T$  the magnetic field strength. Result  $R_H$  in (3.5) has unit cm. Electron/positron charge  $e$  is already canceled by using MeV included in this formula. Note, this result is computed by solving equations of motion of 4-vector under Lorentz force using special relativity.

Center of the circle of projected helix when particles enter magnetic field:

$$\mathbf{r}_H = (x_H, y_H, z_H) = (x_B + R_H \sin\alpha, y_B + R_H \cos\alpha, z_B) \quad (3.6)$$

The angle  $\alpha = \text{atan}(\tan\theta \cos\varphi) = \text{atan}(K)$ ,  $K$  defined below (3.1).  $\alpha$  is the angle between initial track projected direction  $\mathbf{d}$  to  $x$  axis in  $xy$  plane.

Exit point C: Using the assumption that the particles traveled near speed of light when computing time of flight, solve intersection of magnetic field circle and circle of projected helix to get point C. The angular velocity:

$$\omega = \frac{c^2 B}{10^6 E} \text{ (rad/s)} \quad (3.7)$$

Total angle bent in  $xy$  plane by uniform magnetic field is (by laws of cosines):

$$\omega t_c = 2\beta \equiv 2 \cdot \text{acos} \left( \frac{x_H^2 + y_H^2 + R_H^2 - R_B^2}{2R_H \sqrt{x_H^2 + y_H^2}} \right) = 2 \cdot \text{acos} \left( \frac{d_H^2 + R_H^2 - R_B^2}{2R_H d_H} \right) \quad (3.8)$$

$d_H$  is the distance between center of helix and center of magnetic field in  $xy$  plane projection.

Finally, the solution of point C:

$$\mathbf{r}_c = (x_H - R_H \sin(\omega t_c + \alpha), y_H - R_H \cos(\omega t_c + \alpha), z_H + (c \sin\theta \sin\varphi) t_c) \quad (3.9)$$

Here  $R_H$  can be found in (3.5),  $x_H, y_H, z_H$  can be found in (3.6),  $\omega t_c$  in (3.8),  $t_c = \omega t_c / \omega$  from (3.7), (3.8). And  $c \sin \theta \sin \varphi$  is the  $z$  component of particle velocity (by approximating particle velocity as speed of light). Since the  $xy$  plane projection velocity at point C is the derivative of  $t$  for formula (3.9) at  $t_c$ , it's easy:

$$\begin{aligned} \mathbf{v}_c &= (-\omega R_H \cos(\omega t_c + \alpha), \omega R_H \sin(\omega t_c + \alpha), c \sin \theta \sin \varphi) \\ &= c(-\sqrt{1 - (\sin \theta \sin \varphi)^2} \cos(\omega t_c \\ &\quad + \alpha), \sqrt{1 - (\sin \theta \sin \varphi)^2} \sin(\omega t_c + \alpha), c \sin \theta \sin \varphi) \end{aligned} \quad (3.10)$$

The identity  $\omega R_H = v_{xy} = c \sqrt{1 - (\sin \theta \sin \varphi)^2}$  the particle projected speed in  $xy$  plane is intuitive, also can be deduced from (3.5) and (3.7).

CP: Where the particle reaches boundary of projected circle in  $xy$  plane of magnet pole. As seen before the angle bent inside magnetic field is (3.8)  $\omega t_c = 2\beta = 2 \cdot \arccos\left(\frac{d_H^2 + R_H^2 - R_B^2}{2R_H d_H}\right)$ , now the later side of the track till reach CP is bent with angle  $\gamma \equiv \arccos\left(\frac{d_H^2 + R_H^2 - R_P^2}{2R_H d_H}\right)$  (by replacing  $R_B$  by  $R_P$  for the 2<sup>nd</sup> triangle). Then time it takes from point B (particle enters magnetic field) to CP is:

$$t_{CP} = \frac{\beta + \gamma}{\omega} = \frac{\left[ \arccos\left(\frac{d_H^2 + R_H^2 - R_B^2}{2R_H d_H}\right) + \arccos\left(\frac{d_H^2 + R_H^2 - R_P^2}{2R_H d_H}\right) \right]}{\omega} \quad (3.11)$$

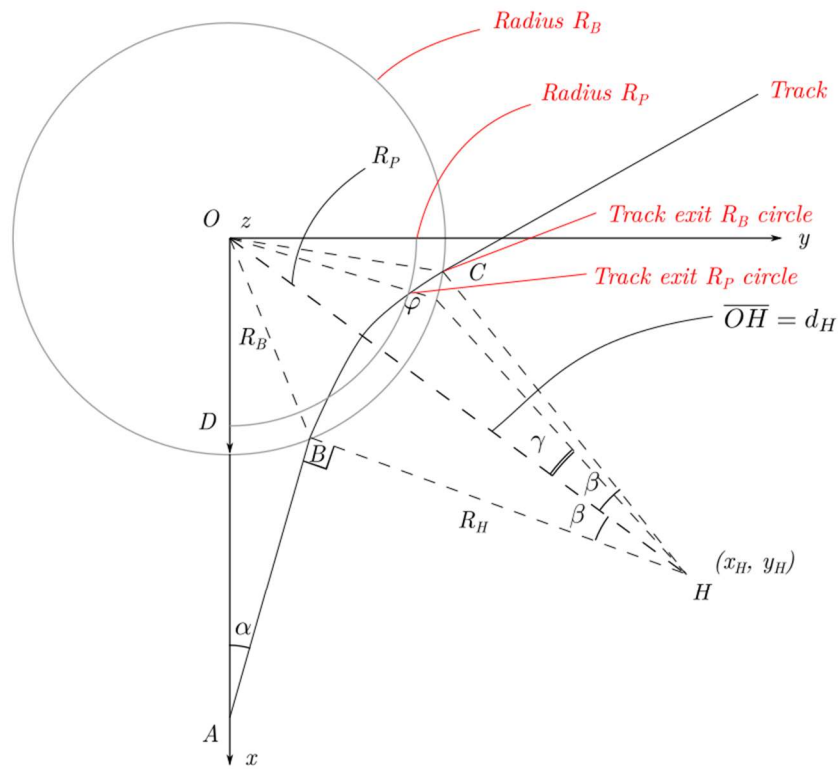
And thus, in order to check if particle hits magnet pole, compute position of CP by replacing  $t_c$  to  $t_{CP}$ :

$$\begin{aligned} \mathbf{r}_{CP} &= (x_H - R_H \sin(\omega t_{CP} + \alpha), y_H - R_H \cos(\omega t_{CP} + \alpha), z_H + (c \sin \theta \sin \varphi) t_{CP}) \\ &= (x_H - R_H \sin(\alpha + \beta + \gamma), y_H - R_H \cos(\alpha + \beta + \gamma), z_H + (c \sin \theta \sin \varphi) t_{CP}) \end{aligned} \quad (3.12)$$

Here  $\alpha$  is defined below (3.6). Check condition:

$$|z_H + (c \sin \theta \sin \varphi) t_{CP}| < PoleGap/2 \quad (3.13)$$

Will give cut if particle pass point CP.



IV Fig 3. 2 Geometry of particle tracks till it exits uniform magnetic field, in  $xy$  projection.

Point A,B,C,CP are defined in previous pages.  $R_B$  as effective magnetic field radius,  $R_P$  as radius of magnet pole,  $R_H$  as radius of projected helix circle in  $xy$  plane,  $d_H$  is the projected distance between center of helix to origin (center of magnet). Angle  $\alpha$  is the acute  $xy$  projected angle between track and  $x$  axis,  $\beta$  is half arc angle of projected helix circle from B (particle enters magnetic field) to C (particle exits magnetic field),  $\gamma$  is arc angle of projected helix circle from half way of BC to point CP (where particle  $xy$  projection exits magnet pole circle)

Remark: (1) The computation of CP above is based on assumption that Point CP is inside circle of magnetic field, or  $R_P < R_B$ . This is true since magnetic field radius is larger than pole radius. However, the code also calculates  $R_P > R_B$  case, here particle already exits magnetic field and travel as a straight line, the problem of finding CP turns to solve intersection of straight-line track from point C to circle centered at origin with radius  $R_P$ .

(2) If the radius  $R_P$  is small enough till triangle cannot be formed from  $R_H, d_H, R_P$  anymore, then particle simply misses the whole magnet pole and travel onward, (3.11) to (3.13) becomes invalid. However, since particle enters magnetic field with maximum polar angle about  $15^\circ$ , this won't happen since our pole radius is  $R_P = 15.25''/2$ .

(3) Angle in formula (3.8) and (3.11):

$$\beta = \text{acos}\left(\frac{d_H^2 + R_H^2 - R_B^2}{2R_H d_H}\right) \quad (3.14)$$

It can be shown that  $\beta$  is also equals to (or use this as replacement in (3.8) and (3.11)):

$$\beta = \text{atan}\left(\frac{x_H}{y_H}\right) - \text{atan}(\tan\theta\cos\varphi) = \text{atan}\left(\frac{x_H}{y_H}\right) - \alpha \quad (3.15)$$

While  $\alpha = \text{atan}(\tan\theta\cos\varphi) = \text{atan}(K)$ . All these geometry relations are shown in Fig 3.2.

(4) The value of  $R_B$  is still left to be calibrated. Since the calibration needs comparison between this result and Geant 4 simulation result, it's left to be solved in next section.

Point D,E,F,G: particle reaches side frame of magnet, 1<sup>st</sup> wire chamber, 2<sup>nd</sup> wire chamber, and hodoscope.

For the rest of the points, it's easy to compute since they're all intersections of a straight line and a plane. The condition of particle passing the frame of the detectors are checking if local coordinate of the particle inside those planes are within the rectangular window (i.e., side frame of magnet, wire chamber's wire plane active area ... are all as rectangle in shape) Thus a unified formula is used to compute those intersections, only difference is the location of those planes and the angle of how much they tilt. Solve linear equations:

$$\mathbf{r}_c + \mathbf{v}_c t_i = \mathbf{r}_i \quad (3.16)$$

$i$  can be any of D,E,F,G.  $\mathbf{r}_c$  and  $\mathbf{v}_c$  are position and velocity of particle exiting magnetic field. The equation of planes is:

$$\mathbf{r}_i = (x_i, y_i, z_i) = \left(x_i, d_i + \delta y_i, -\frac{\delta y_i}{\tan\theta_i}\right) \quad (3.17)$$

It's parameterized by two parameters  $x_i$  global and also local  $x$  coordinate of the intersection inside the plane, and  $d_i + \delta y_i$  the global  $y$  coordinate.  $\theta_i$  is the tilt angle of plane  $i$ . Solving equation (3.16) we get:

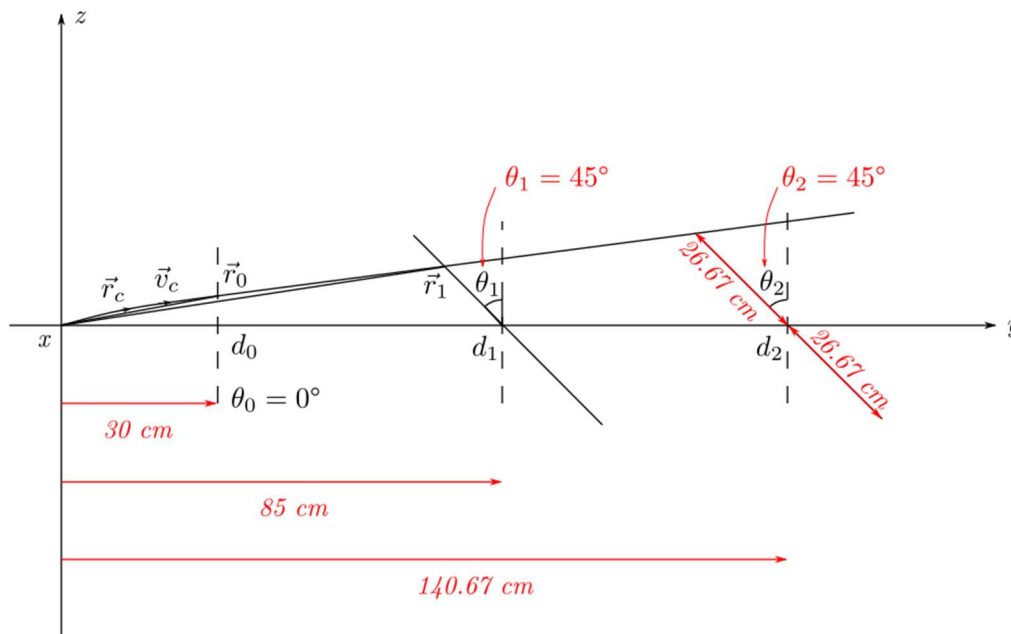
$$t_i = \frac{d_i - (y_c + z_c \tan\theta_i)}{v_{cy} + v_{cz} \tan\theta_i} \quad (3.18)$$

Global coordinate  $\mathbf{r}_i$  is consequentially computed by (3.16) and (3.18). While if the local coordinate is the goal, following is the conversion from global coordinate to local coordinate in the planes:

$$\begin{aligned} x'_i &= x_i \\ y'_i &= -(y_i - d_i)/\sin\theta_i \end{aligned} \quad (3.19)$$

All above formula works for electron, and in order to apply all these formula for positron only one modification needs to be made: the only difference in all the discussion above for positron is

the sign of its charge, and we only need to change initial azimuthal angle  $\varphi$  for positron to make it mirror image to  $xz$  plane. Then all formulas in this chapter for electron can be applied for positron.



IV Fig 3. 3  $yz$  projection view of track after it exits magnetic field.

$r_c$ ,  $v_c$ ,  $r_i$ ,  $d_i$ ,  $\theta_i$  are defined last page, solve the time needed from point C to intersections of later planes to get  $r_i$  s.

### 3.3 Basic results

The simple acceptance code is initially written for cross check Geant 4 simulation result, and checking acceptance of each physical boundary of magnet and detectors. The information we get from the simple simulation includes energy of the particles, position, velocity of particles at each surface been checked (can be represented in both global or local coordinate), and if the particles pass cut that they're inside boundaries of surfaces been checked.

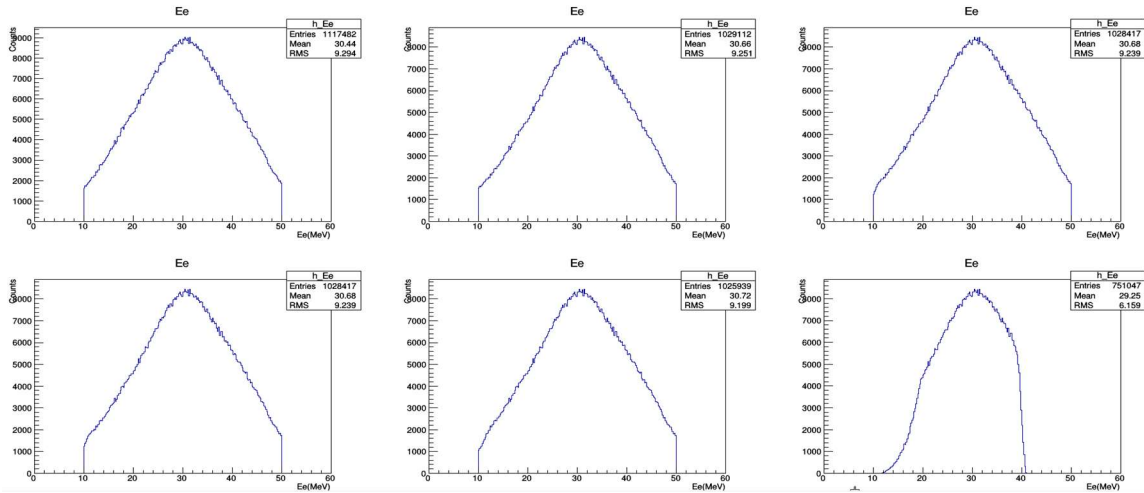
In this chapter all of this basic information has been shown, and some of them has been compared with Geant 4 simulation. It's been shown that the main difference of the result of this code to Geant 4 simulation is z coordinate component (or local y coordinate) on detectors. The reason will be explained in 3.3.3.

#### 3.3.1 Results

1) Energy distribution and counts at each check point. There're 6 points in the simulation can cause loss of particle counts: 1) downstream side of yoke hole, 2) where particle horizontal projection reaches magnet pole boundary or point CP computed at last chapter, 3) where particle reaches magnet side frame or point D, 4) intersection of track and the center plane of front wire chamber or point E, 5) intersection of track and the center plane of back wire chamber or point F, 6) intersection of track and hodoscope point G.

The energy distribution has been plotted at each of those points, it serves two main purposes: 1) Counts at each energy and its complement of photon energy will be used in asymmetry calculation, thus we know how many events can we used for asymmetry measurement. 2) Total counts at each check point give us idea of which geometry constraint block particle the most, and guidance of any change of individual component location of the spectrometer improving acceptance.

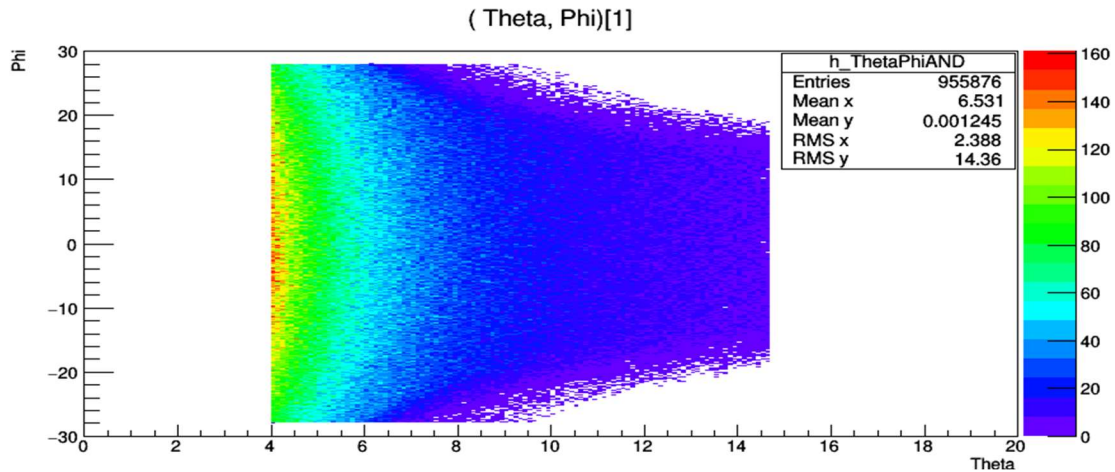




IV Fig 3. 4 Electron energy distribution at each check point. Ordinate: counts, no unit, abscissa: electron energy in  $MeV$ .

(c.f. last page) There're 1131114 events at primary vertex, the pairs obey BH process cross section distribution. Cuts used to generate pairs are described in Chapter 1 "Generate BH Pairs", including polar angle  $\theta$  in range  $[4^\circ, 15^\circ]$ , electron azimuthal angle  $\varphi_e$  in range  $[-28^\circ, 28^\circ]$ , positron azimuthal angle  $\varphi_p$  in range  $[180^\circ - 28^\circ, 180^\circ + 28^\circ]$ . While horizontal projection angle  $\theta'$  in range  $[0^\circ, 15^\circ]$  or electron and  $[-15^\circ, 0^\circ]$ , vertical projection angle  $\varphi'$  in range  $[-4^\circ, 4^\circ]$ . Except the last one, cut at old hodoscope dimension all distribution till back wire chamber retains most of electrons. In Geant 4 simulation, the results will be worse, since the effect of fringe field that we will discuss later. Note: 1) the geometry cut applied only on electron side, regardless how many positrons been blocked on the other side of the magnet. 2) a small effect but can be seen from the distributions is: detectors on the back blocks more particles with lower energies, this results from lower energy particle are more susceptible to change direction from magnetic field. Since a measurable event requires the pair of particles detected from both sides, those pairs will be lost. Thus, pure geometry acceptance leads to lower efficiency of detecting pairs with one low energy particle.

2) Target solid angle  $(\theta, \varphi)$  distribution after wire chamber acceptance cut.



IV Fig 3. 5 Electron primary vertex polar angle vs azimuthal angle  $(\theta, \varphi)$  distribution. Ordinate: azimuthal angle  $\varphi$  in *degrees*, abscissa: polar angle  $\theta$  in *degrees*.

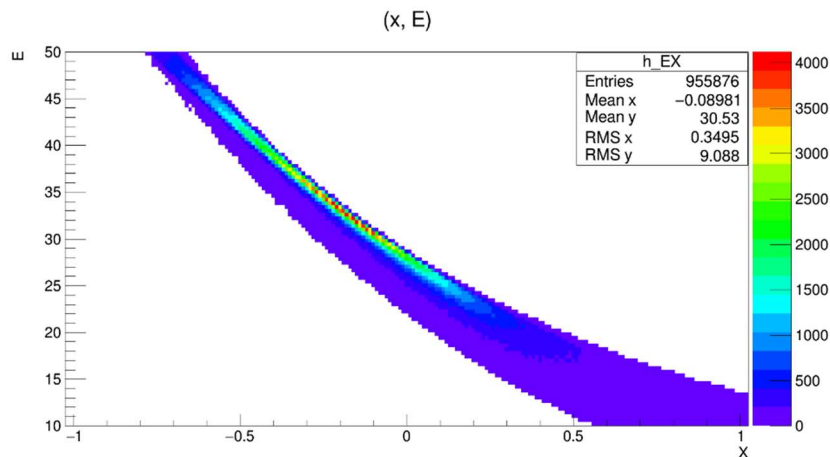
Unit degrees. Distribution of all events both particles of the pair reach back wire chamber. The  $\theta$  is cut off at  $4^\circ$  on the lower side, since it's the minimum value for generation of pair data file. On the higher side, the particles with  $\theta$  larger than  $\sim 14.67^\circ$  degrees are blocked by yoke hole. The silhouette of the distribution “shrinks” on larger  $\theta$  describes mainly the effect of magnet pole blocking particles. The  $\theta$  distribution counts drop quickly as  $\theta$  value increase, due to the BH cross section drops quickly.  $\varphi$  distribution remains largely uniform, while too large or small  $\varphi$  has lower counts, due to both larger  $\varphi$  particle is more prone to be blocked by magnet pole and an artificial effect of pair generation. That is for example  $\varphi_e$  generated at  $28^\circ$ , and  $\varphi_p$  will be generated with peak probability at  $180^\circ + 28^\circ$  (which is the set upper bound in pair generation), but only lower than  $180^\circ + 28^\circ$  side will be generated since the other side do not pass cut for  $\varphi_p$ . Meanwhile if  $\varphi_e$  generated at  $0^\circ$ ,  $\varphi_p$  will be generated with peak probability at  $180^\circ$ , but it can be generated freely on either side  $\varphi_p > 180^\circ$  or  $\varphi_p < 180^\circ$ .

### 3) Energy $E$ vs detectors local horizontal coordinate $x'$ distribution.

The reason we choose this relation is because  $x'$  has the most correlation to energy, and this relation somehow relates to reconstruct energy of particles at primary vertex using the measured particle positions on wire chambers. This distribution will give us idea of range of  $x'$  under certain energy  $E$ , and sanity check for the simulation results. There are some effects we can see from the results:

- (1) Since the  $x'$  is not only depend on energy, but also polar angle  $\theta$  and azimuthal angle  $\varphi$  at primary vertex, the correspondence is not 1 to 1 and each energy  $E$  will have a range of  $x'$  distributed.
- (2) If we fix  $\theta$  and  $\varphi$ , the higher the energy  $E$ , the larger the helix circle radius will be (Formula (3.5),  $R_H \propto E$ ), and  $x'$  will shift to downstream coordinates. This will result in certain measured  $x'$  can only possibly from certain range of  $E$ . This is the basics for initial attempt to fit  $E$  from only  $x'$  using Bayes' theorem.
- (3) Because of the relation  $R_H \propto E$ , the total (absolute) angle of the track deviate from  $x$  axis in  $xy$  plane is (combine Fig 3.2, and formula (3.15)):  $\delta = 2\beta + \alpha = 2 \left[ \text{atan} \left( \frac{x_H}{y_H} \right) - \alpha \right] + \alpha$  (3.20), while  $x_H, y_H$  can be represented by (3.4), (3.5) and (3.6). Even at  $\varphi = 0$  and thus  $\alpha = \theta$  the angle is quite complicated, while as observed low fixed  $E$  results in monotonic dependence of  $\delta$  on  $\theta$ , but high  $E$  is not. Results in less deviation of  $\delta$  and  $x'$  at higher energy.

Effect (2), (3) are clearly shown on Fig 3.6 below.



IV Fig 3. 6 Energy  $E$  vs detectors local horizontal coordinate  $x'$  distribution. Ordinate: electron energy  $E$ , abscissa: local horizontal coordinate in  $cm$ .

$E$  uses 0.5 MeV per bin,  $x'$  1cm per bin.

### 3.3.2 $xy$ distribution at front chamber, and calibration of $R_B$

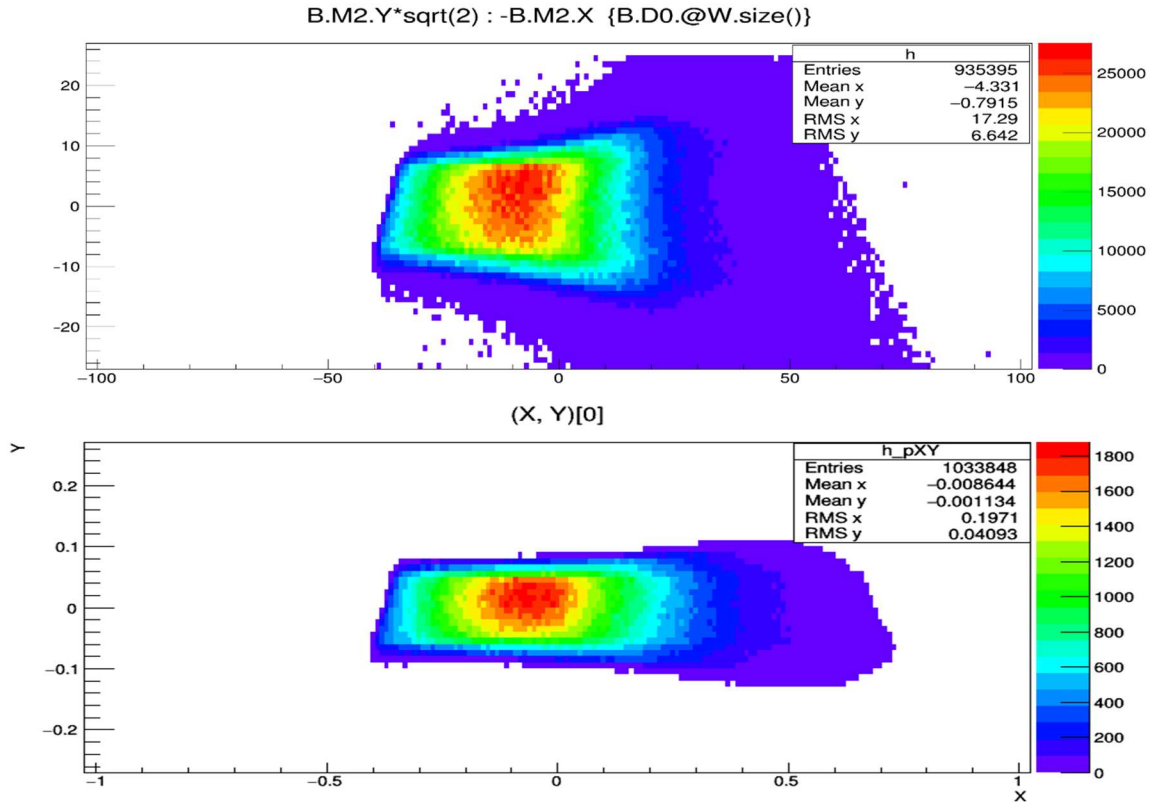
$xy$  distribution histograms show the local  $xy$  2D distribution on front wire chamber, its application includes:

- 1) It will give us an estimation of the actual area particles intersects the wire chamber.
- 2) Front wire chamber is significantly closer to the magnet compared to the back chamber, there will be a large area of the front chamber won't needed to be activated to collect data from the same electron or positron as the back chamber. This will reduce the amount of electronics and thus easier analyzation of real experiment data.
- 3) The effect of tilted detectors: the detectors are all tilted 45 degrees, upper side of them are closer to magnet. It will make upper side detector hits distributed in a smaller region, since any tracks which are not perpendicular to beam direction will travel shorter distance to upper side of the detectors, resulting in less shift in beam direction (or coordinate  $x'$ ).
- 4) Calibration of  $R_B$ , the effective radius of magnetic field is the only parameter in this simple simulation requires calibration. The process is simple, run a Geant 4 simulation with vacuum background and at same location (using front wire chamber) and compare the horizontal coordinate between its result and the result from simple simulation, change  $R_B$  value to match Geant 4 simulation result. Remarks: (1) Due to the approximation made, there is always difference, due to the fringe field is not uniform. (2) It's easier to check horizontal (beam or  $x$ ) coordinate for a few certain energies. And since higher energy particle tracks are more focused for varying angles. (3) To prevent effect in 3), it's even better to constraint  $\varphi$  near 0 when calibrate.

Condition	$2R_B$ (inch)	$\bar{x}$ (29<E< 31MeV) (cm)	$\bar{x}$ (48<E< 50MeV) (cm)
Geant 4	N/A	-3.34	-35.04
	17.35	-3.354	-35.55
	17.40	-3.13	-35.32
	17.46	-3.09	-35.27

Table 3.1. Average  $x$  value for different  $R_B$  in simulation and Geant 4 simulation, cut under two different energies. It's seen that the sum of absolute difference between Geant 4 and simple simulation for these two energies is about 0.4 cm, while the separation is about 30 cm. Thus, using uniform  $R_B$  is a good approximation to represent  $x$  distribution.  $2R_B = 17.35$  inches makes closest  $\bar{x}$  near 30 MeV,  $2R_B = 17.46$  inches make closest  $\bar{x}$  at 49 MeV, while  $2R_B = 17.40$  inches make balance of differences on both energies, and will be applied.

Next page shows the distribution of  $xy$  distribution at front chamber from both simulations, it's found that  $y$  distribution for Geant 4 simulation has a lot more spread than this. Will be explained in the next section.



IV Fig 3. 7 Comparison of  $xy$  distribution of electron intersection at front chamber between simple and Geant4 simulation. Both figures ordinate: short axis coordinate of wire plane in  $m$ , abscissa: long axis coordinate of wire plane in  $m$ .

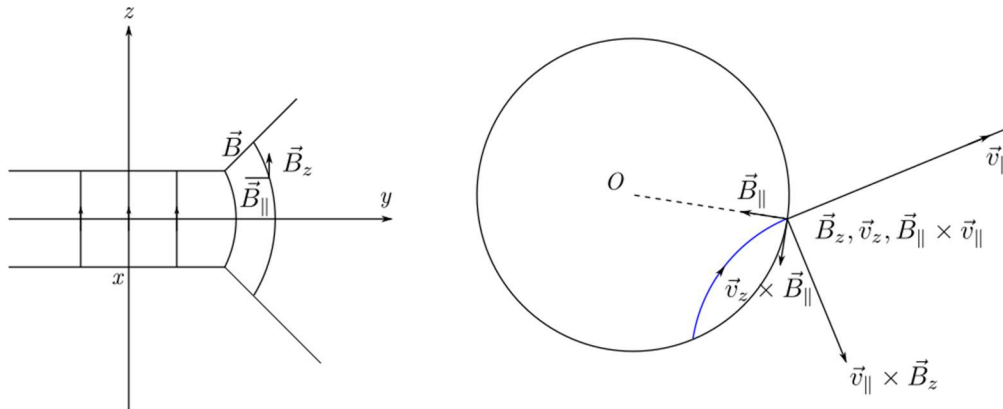
Upper, from simple simulation, unit  $m$ . Lower, from Geant 4 simulation, unit  $cm$ .  $\sqrt{2}$  of  $y$  coordinate in Geant 4 simulation plot come from changing the global coordinate to local coordinate of the wire plane.

### 3.3.3 Effect of fringe field

The effect of fringe field is twofold:

- 1) The varying amplitude of the field cannot make a uniform magnetic field approximation having precise horizontal intersection coordinate for all different target energy and angle. However, as seen from Table 3.1 and Fig 3.7, this approximation is very close to the Geant 4 vacuum simulation result.

- 2) When compare the two  $xy$  distribution at front chamber, the Geant 4 simulation has much larger deviation on  $y$  coordinate distribution. The reason is the horizontal component of the fringe field, it will make the particle track bending more, away from the center horizontal plane. As illustrated below in Fig 3.8.



IV Fig 3. 8 Effect of Fringe field on tracks.

Left figure, we assume magnetic field majorly directed upward, so positive charged particles are bent clockwise when look from above. Assume we have a positive charged particle has upward component  $v_z$ , and its horizontal component  $v_{\parallel}$ , which is the major part of the velocity. For magnetic field, its major part is upward  $B_z$  and horizontal part  $B_{\parallel}$ , which is along pole radius direction.

Right figure: The Lorentz force on the positive charge has the same direction of:

$$\mathbf{v} \times \mathbf{B} = (\mathbf{v}_z + \mathbf{v}_{\parallel}) \times (\mathbf{B}_z + \mathbf{B}_{\parallel}) = \mathbf{0} + \mathbf{v}_z \times \mathbf{B}_{\parallel} + \mathbf{v}_{\parallel} \times \mathbf{B}_z + \mathbf{v}_{\parallel} \times \mathbf{B}_{\parallel}$$

The component  $\mathbf{v}_{\parallel} \times \mathbf{B}_{\parallel}$  has upward direction, as long as angle between  $\mathbf{v}_{\parallel}$  and  $\mathbf{B}_{\parallel}$  is less than  $180^\circ$ . This will always be the case, (c.f. Fig 3.2) two circles in the figure are symmetric about line OH, and by symmetry of the particle track, the angle between  $\mathbf{v}_{\parallel}$  and  $\mathbf{B}_{\parallel}$  is equal to:

$$180^\circ - \alpha - \angle AOB < 180^\circ$$

At point C (where particle exits magnetic field).

### 3.4 Applications

#### 3.4.1 Energy asymmetry (for all angles, and $\varphi_{p-q}$ near $180^\circ$ )

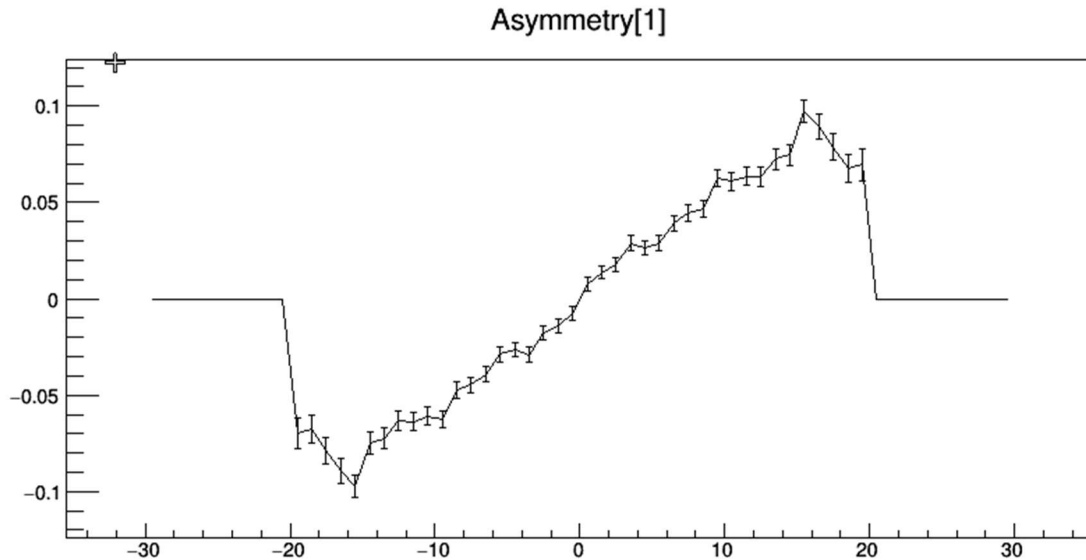
The cross sections are depended on energies  $E_e, E_p$  or  $\delta = E_e - E_p$  since  $E_e + E_p = E_\gamma$ , polar angles  $\theta_e, \theta_p$  and difference of azimuthal angles  $\varphi_{e-p}$ , the energy asymmetry is defined as:

$$\varepsilon(\delta) = \frac{d\sigma(\delta) - d\sigma(-\delta)}{d\sigma(\delta) + d\sigma(-\delta)} \quad (3.21)$$

While all  $\theta_e, \theta_p$  and  $\varphi_{e-p}$  are integrated out. For asymmetry extracted from this simulation, counts are used instead of differential cross sections:

$$\varepsilon(\delta) = \frac{N(\delta) - N(-\delta)}{N(\delta) + N(-\delta)} \quad (3.22)$$

Because the finite nature of the simulation,  $N(\delta)$  are counts of pairs when  $\delta = E_e - E_p$  as bin center and a specified width (1 MeV is used). The result we can measure is not only depends on the pairs generated from Monte-Carlo selection using  $d\sigma$  from theory and binning, but also depends on the acceptance of the pairs. For certain angles  $\theta_e, \theta_p, \varphi_e, \varphi_p$  will be blocked till they reach detectors, and the part of the differential cross sections  $d\sigma(\delta, \theta_e, \theta_p, \varphi_{e-p})$  will be omitted from the  $\varepsilon(\delta)$  calculation. So  $\varepsilon(\delta)$  measured is not  $\varepsilon(\delta)$  at primary vertex directly from theory. One other issue needs to be noted is this result is only an approximation to Geant 4 simulation since it's lacking effect of fringe field and multiple scatter.



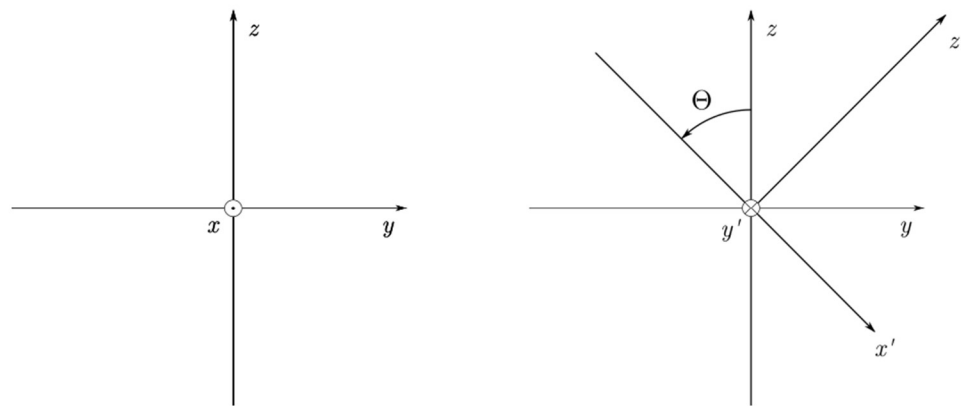
IV Fig 3. 9 Energy asymmetry as a function of  $E_e - E_p$  summing over all solid angles. Ordinate: asymmetry, no unit, abscissa: energy difference  $E_e - E_p$  in  $MeV$ .

From all pairs reaches both sides wire chambers.

### 3.4.2 Wire span ( $n_u, n_v$ ) distribution

Wire span  $n_u, n_v$  are defined as the number of intervals of wires the particle tracks inside gas layer of wire chamber, they're closely related to number of hit wires for the wire plane, which is used for track fitting in analyzer. The number of wires hit should be equal or larger than 3 so the analyzer can identify a cluster for track fitting. The wire spans calculated here are purely from geometry follow the steps:

- (1) Converting track direction into wire chamber coordinate system in analyzer.
- (2) Projecting track in analyzer coordinate system into plane perpendicular to sense wires.
- (3) Calculate wire span using angle between line linking wires and track inside the projected plane. Step (1) is a rotation, result of step (2) (3) are explained in Part III section 3.4 cluster fitting and Appendix.



IV Fig 3. 10 Conversion of e- direction in simulation coordinates ( $x, y, z$ ) to analyzer VDC coordinates ( $x', y', z'$ ).

$x'$  direction is the short axis direction of wire chamber,  $z'$  direction is perpendicular to wire chamber from front to back,  $y'$  makes  $x'y'z'$  right hand coordinate system.  $\theta$  is the tilt angle of wire chambers. Note: since the offset on  $x'$  direction from front wire chamber to back,  $\theta = 45^\circ$  is used as default setting. At  $\theta = 45^\circ$  the line linking centers of both wire chamber is horizontal.  $\theta$  can be changed in the simple simulation and the line will no longer be horizontal. The track direction will only depend on rotation about y axis with single parameter  $\theta$ .



Step (1): From the coordinate system shown in Fig 3.10, once we calculated velocity of particles when they exit magnetic field  $\mathbf{v}_c = (v_x, v_y, v_z)$ , rotate its unit vector to get  $\mathbf{v}_c'$  in local coordinate:

$$\begin{aligned} v_x' &= v_y \sin\theta - v_z \cos\theta \\ v_y' &= -v_x \\ v_z' &= v_y \cos\theta + v_z \sin\theta \end{aligned} \quad (3.23)$$

Step (2): The projection angles in VDC coordinate system  $\theta', \varphi'$  are defined as shift in  $x', y'$  direction over shifts in  $z'$  direction. Thus:

$$\tan\theta' = \frac{v_x'}{v_z'}, \quad \tan\varphi' = \frac{v_y'}{v_z'} \quad (3.24)$$

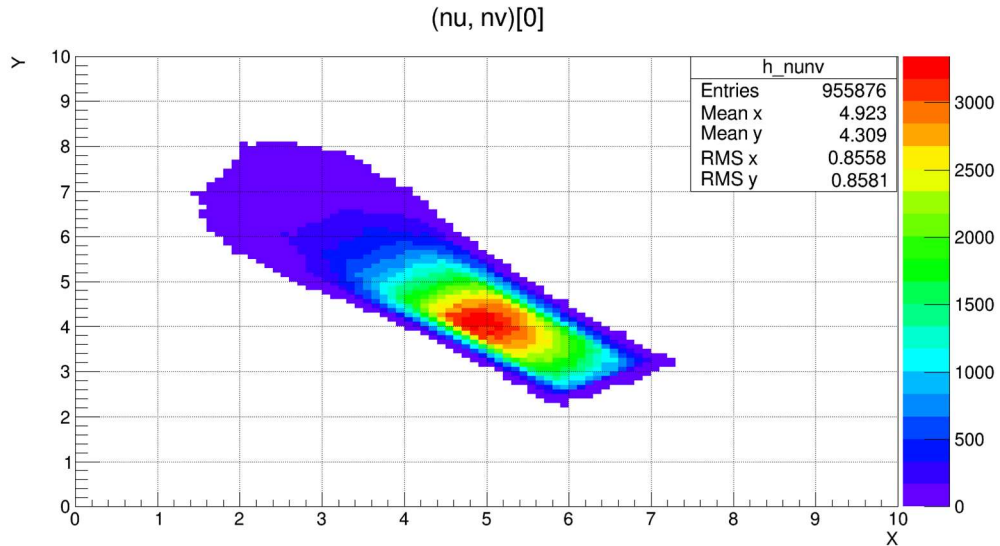
Step (3): Then after finding e- velocity direction in VDC coordinate  $(\tan\theta', \tan\varphi', 1)$ , see Appendix A1.3 in Part III formula (4)(5):

$$\begin{aligned} \tan\alpha_u &= \frac{1}{\sqrt{5}}(2\tan\theta + \tan\varphi) \\ \tan\alpha_v &= \frac{1}{\sqrt{5}}(2\tan\theta - \tan\varphi) \end{aligned} \quad (3.25)$$

Where  $\alpha_u, \alpha_v$  are the angles between track and line linking wires in the projected plane perpendicular to all wires. Then apply formula (3.3)  $n_{u/v} = \frac{h}{|s \times \tan\delta_{u/v}|}$  in section 3.4 of Part III:

$$n_{u/v} = \tan\alpha_{u/v} \frac{\text{wire plane thickness}}{\text{wire spacing}} = \tan\alpha_{u/v} \frac{2.54\text{cm}}{0.493\text{cm}} \quad (3.26)$$

To get wire spans. The result of all electron tracks is shown in below Fig 3.11.



IV Fig 3. 11 Wire span ( $n_u, n_v$ ) distribution with tilt angle  $45^\circ$ . Ordinate: wire span  $n_v$ , no unit, abscissa: wire span  $n_u$ , no unit.

Under cut: particle pairs reach both sides front wire chambers.

### 3.4.3 Results from different wire chamber tilt angle

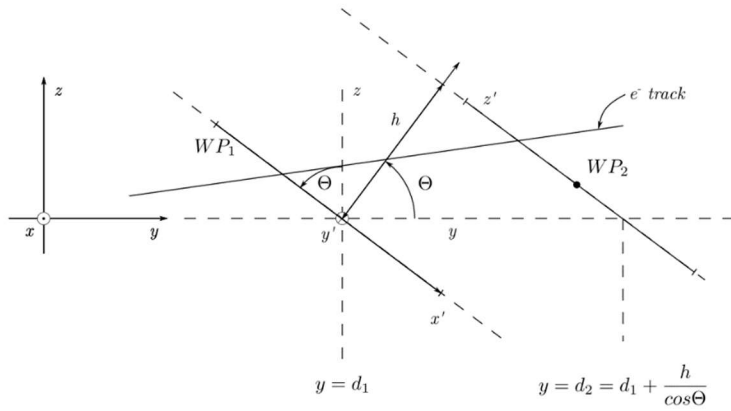
The wire chambers are default to tilt at 45 degrees from vertical position, the reason is wire chambers on each side are bolted together with z plates on sides of wire chambers, with the same amount of shift along short axis of wire chamber and along direction perpendicular to wire chamber (Part III Fig 2.4 side view). Thus 45 degrees tilt will make both centers of wire chambers in the same horizontal plane.

As we can see Fig 3.7, active area of wire chambers is not fully utilized, especially in short axis (local y axis) direction, so we can choose different tilt angle than 45 degrees if it has the benefit for measurement. One of the big benefits is the both larger wire span  $n_u$  and  $n_v$  values, we need both  $n_u$  and  $n_v$  of track larger that some track with smaller wire spans will improve (since track cross wire chambers with shallower angle, which decreases both  $\delta_u$  and  $\delta_v$ , and by  $n_{u/v} = \frac{h}{|s \times \tan \delta_{u/v}|}$ , cluster span increases) and thus the cluster finding and track fitting efficiency while using analyzer will improve. For track already with large enough wire spans on both u and v wire planes, the increase  $n_u$  and  $n_v$  values will not have big benefit since track fitting result of intersection between track and wire plane will not improve by much. We will check the result of wire spans with different wire chamber tilt angle next.

There are some constraints prohibiting we increasing the wire chamber tilt angle from vertical position indefinitely

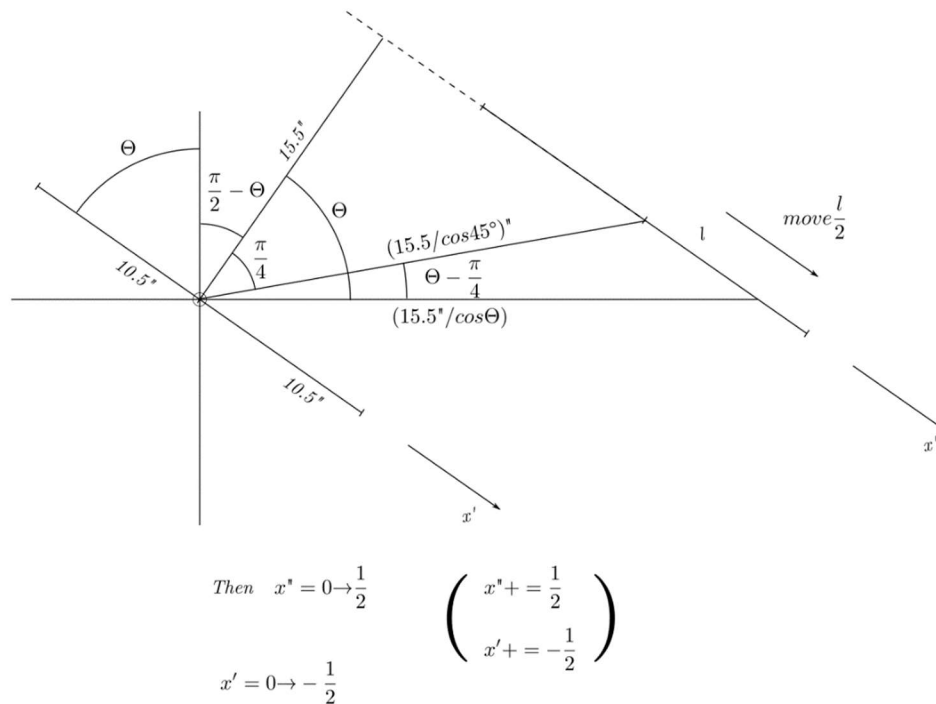
- (1) As the tilt angle increases, the wire chambers will have less area in vertical projection (area  $\propto \cos\theta$ ), while the same set of tracks will occupy larger area on wire chamber.
- (2) Since wire chambers are bolted together with z plates and relative angle fixed at 45 degrees. Increasing tilt angle will rotate front chamber down and back chamber up, tracks projected on lower side of back chamber will start to miss the chamber.
- (3) Possibly less efficiency on sides of wire chambers since the filling gas having less flow near the edges.

The additional shift to make the center of mass of both wire chambers at the same horizontal plane as the beam is illustrated below in Fig 3.12 and Fig 3.13.



IV Fig 3. 12 Intersection of e- track with wire planes.

$xyz$  is global coordinate system,  $x'y'z'$  is analyzer wire chamber coordinate system. Rotate about center of front wire chamber to increase tilt angle  $\theta$  we see 2<sup>nd</sup> wire chamber tilted up, and the acceptance loses on the lower part of the 2<sup>nd</sup> chamber. We need to translate both wire chambers along  $+x'$  direction to make center of mass of both wire chambers to the same horizontal plane as magnet center to increase acceptance.



IV Fig 3. 13 Calculation of amount of translation in  $+x'$  direction.

Using laws of cosine, the amount of translation  $l$  along  $x'$  axis is:

$$l^2 = h^2 \left( \frac{1}{\cos^2 \frac{\pi}{4}} + \frac{1}{\cos^2 \theta} - 2 \frac{\cos(\theta - \frac{\pi}{4})}{\cos \theta \cos \frac{\pi}{4}} \right) \quad (3.27)$$

$h = 15.5 \text{ inches}$  is the distance between wire chambers. Effectively front wire plane  $x'$  coordinate add by amount  $-l/2$ , and back wire plane  $x'$  add by amount  $l/2$ .

For determining track direction and wire spans  $n_u$  and  $n_v$  we can still use formula (3.23) to (3.26) with any chamber tilt angle  $\theta$  from vertical position.

For determining track intersections on wire chambers local coordinate system:

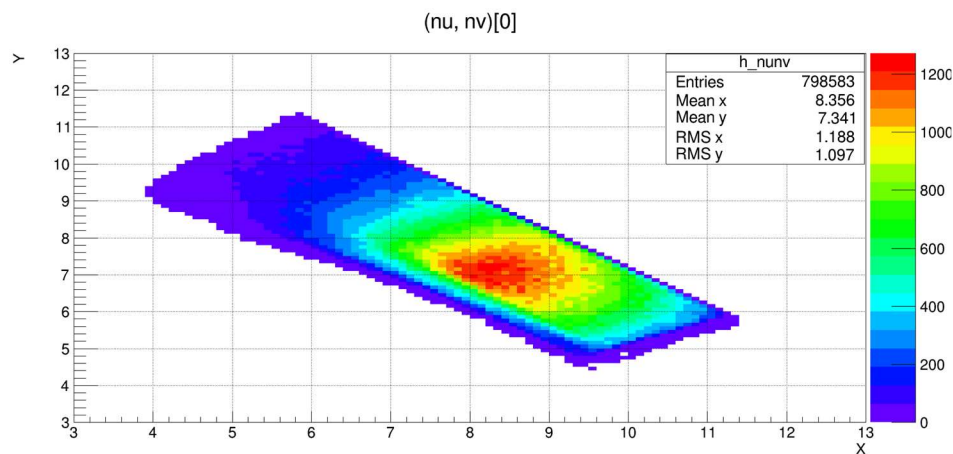
- 1) Find intersections of tracks and wire planes by formula (3.16) to (3.18), that is the global coordinate system result.
- 2) Rotate global coordinate to local, similar to (3.23), but has shift since the origin of local coordinate system is shift to intersection of wire planes and global  $y$  axis:

$$\begin{aligned} x' &= (y - d_i) \sin \theta - z \cos \theta \\ y' &= -x \\ z' &= (y - d_i) \cos \theta + z \sin \theta \end{aligned} \quad (3.28)$$

Here  $d_1 = 85 \text{ cm}$  is distance from center of magnet to horizontal intersection of front wire chamber to back, unchanged from 45 degrees case, from Fig 3.12 distance to back chamber  $d_2 = d_1 + h/\cos \theta$  has changed if  $\theta \neq 45^\circ$ .

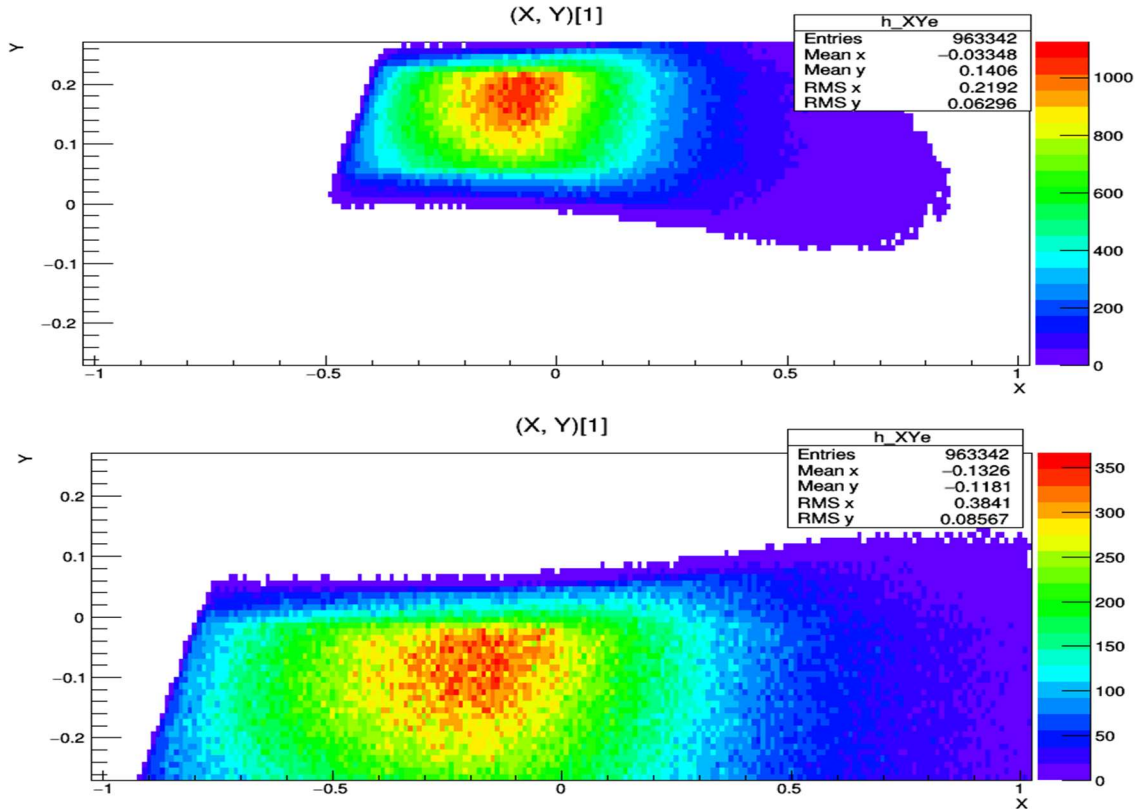
- 3) Change  $x'$  value by the description in Fig 3.13, with front chamber by  $-l/2$ , and back for  $l/2$ .
- 4) For plots, interchange axis:  $x'' = -y'$ ,  $y'' = -x'$

Result of tilt angle  $\theta = 60^\circ$  is shown below:



IV Fig 3. 14 Wire span ( $n_u, n_v$ ) distribution with tilt angle  $60^\circ$ . Ordinate: wire span  $n_v$ , no unit, abscissa: wire span  $n_u$ , no unit.

Only when electron positron pairs hits both sides back wire chamber the back ( $n_u, n_v$ ) values are filled. Compared to  $45^\circ$  case (Fig 3.11), the wire spans on both wire planes are increased by significant amount and much better cluster finding efficiency for tracks with either  $n_u$  or  $n_v$  low. If analyzer is used to find and fit tracks if 100% hardware efficiency is assumed. The acceptance of wire chamber starts to drop when track hits outside of upper, lower side of the wire chamber (as shown on the straight upper right boundary in Fig 3.14, also see Fig 3.15 below).



IV Fig 3. 15 Electron track intersections on wire chambers at  $60^\circ$  tilt angle. Ordinate: short axis coordinate, unit  $m$ , abscissa: long axis coordinate, unit  $m$ .

Upper figure: front chamber, lower figure: back chamber. Tracks miss the wire chambers on upper side of front chamber and lower side of back chamber.

As we can see above, following effects comes from increasing tilt angle:

- (1) For wire spans, both  $n_u, n_v$  values increase and will result in better cluster finding and local (for each wire plane) track fitting result.
- (2) For wire chamber acceptance, after solving global coordinate of intersection of track and wire planes, the chamber short axis coordinate will be stretched (increased absolute value of  $x'$ ) because of increased  $\theta$  value in (3.28) then translated to the upper side for front

chamber and lower side for back chamber. While the local  $x$  (horizontal) coordinate remains the same.

- (3) For track finding and fitting efficiency if we use analyzer track fitting code, the increased  $n_u, n_v$  values will make cluster finding easier and local track fitting more accurate, thus improve efficiency. Meanwhile, as tilt angle increases, the intersection of track on wire planes will eventually hits upper or lower bound of wire plane, thus reduce acceptance. The optimum value should be between 45 degrees and 60 degrees.

#### 3.4.4. Detector resolution on $E, \theta, \varphi$

Here we trying to answer the question: for small change of energy  $E$ , or change of initial spherical angle  $\theta, \varphi$ , how much shift in coordinates on wire chamber?

This can be answered easily using the simulation: in addition to the base simulation result, for each initial condition, change energy  $E$ , or initial spherical angle  $\theta, \varphi$  by a small amount and compare the change in track intersection coordinates on wire chamber with base result. It should be expected that change of  $E$  and  $\theta$  will mainly change horizontal coordinate. Change of  $\varphi$  (note it's azimuthal angle at target) will change mainly local vertical coordinate especially for larger  $\theta$ .

The real resolution of these quantities is much worse because multiple scatter. For wire chambers as hardware, the resolution is expressed in terms of wire plane u or v coordinate, which according to HallA NIM paper ([38] p. 334), the value is  $225\mu\text{m}$  or  $0.0225\text{cm}$ . It's expected be much better for the change of  $E, \theta, \varphi$  values  $\delta E, \delta\theta, \delta\varphi$  we set for the check.

Using the resolution of wire coordinates in NIM paper  $0.0225\text{ cm}$  in u or v direction, expressing unit vectors  $\hat{x}, \hat{y}$  in terms of unit vectors  $\hat{u}, \hat{v}$ :

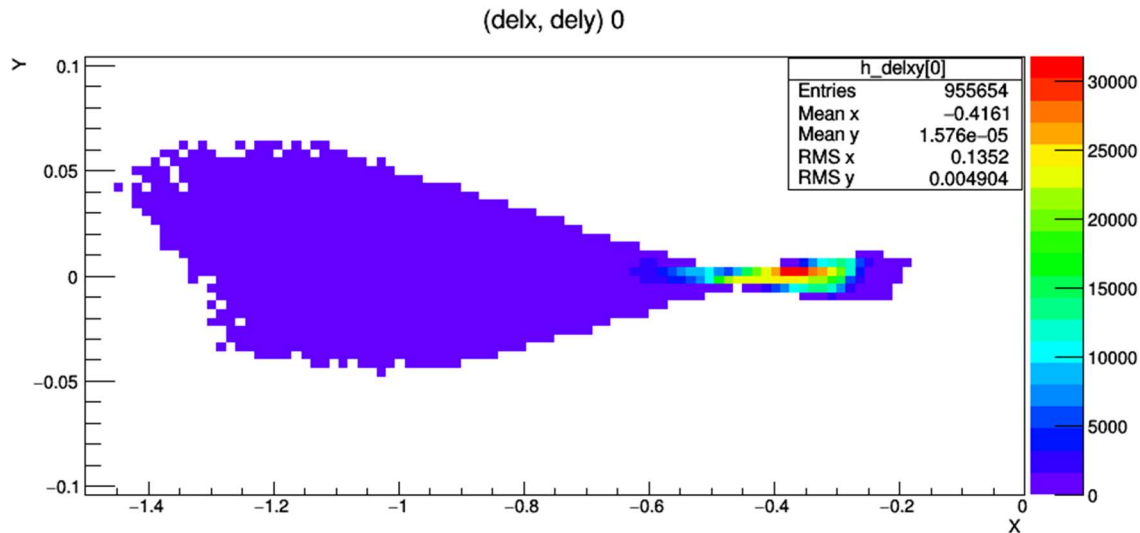
$$\begin{aligned}\hat{x} &= (\hat{u} - \hat{v})/2\sin\alpha \\ \hat{y} &= (\hat{u} + \hat{v})/2\cos\alpha \quad (3.29)\end{aligned}$$

$\alpha$  is the angle between wires and long axis of wire plane, with  $\tan\alpha = 1/2$ ,  $\sin\alpha = 1/\sqrt{5}$ , and  $\cos\alpha = 2/\sqrt{5}$ .

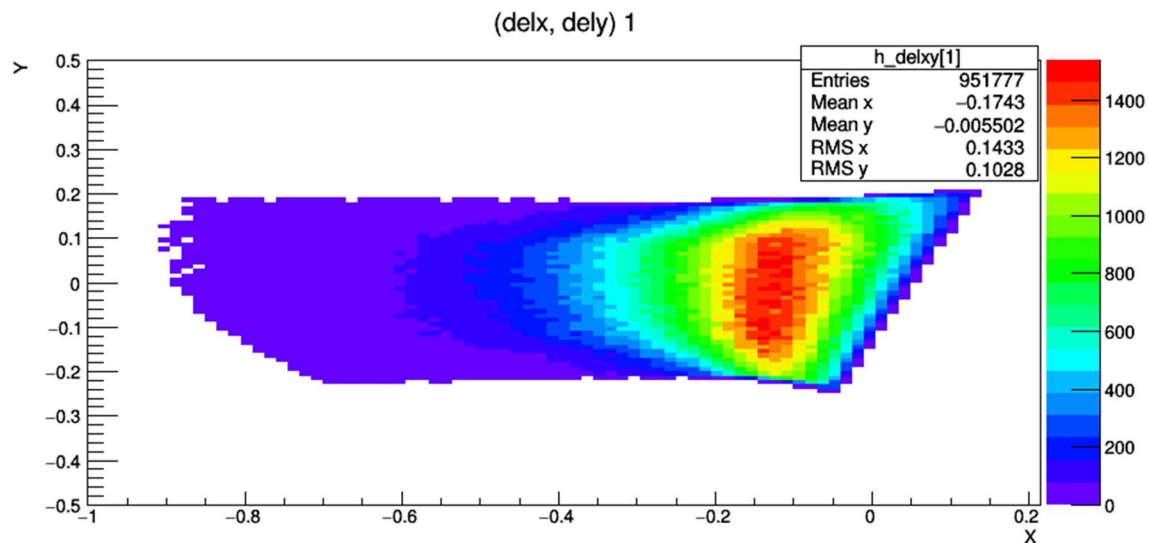
For example, in Fig 3.16 below, change energy  $E$  by  $0.1\text{ MeV}$ , average change in  $x$  is  $0.416\text{cm}$ , while change in  $y$  is negligible. then from (3.29), set  $\delta x = 0.416\text{cm}$ ,  $\delta y = 0$ :

$$\begin{pmatrix} \delta u \\ \delta v \end{pmatrix} = \begin{pmatrix} 1/2\sin\alpha & 1/2\cos\alpha \\ -1/2\sin\alpha & 1/2\cos\alpha \end{pmatrix} \begin{pmatrix} \delta x \\ \delta y \end{pmatrix} = \begin{pmatrix} 0.465\text{cm} \\ -0.465\text{cm} \end{pmatrix}$$

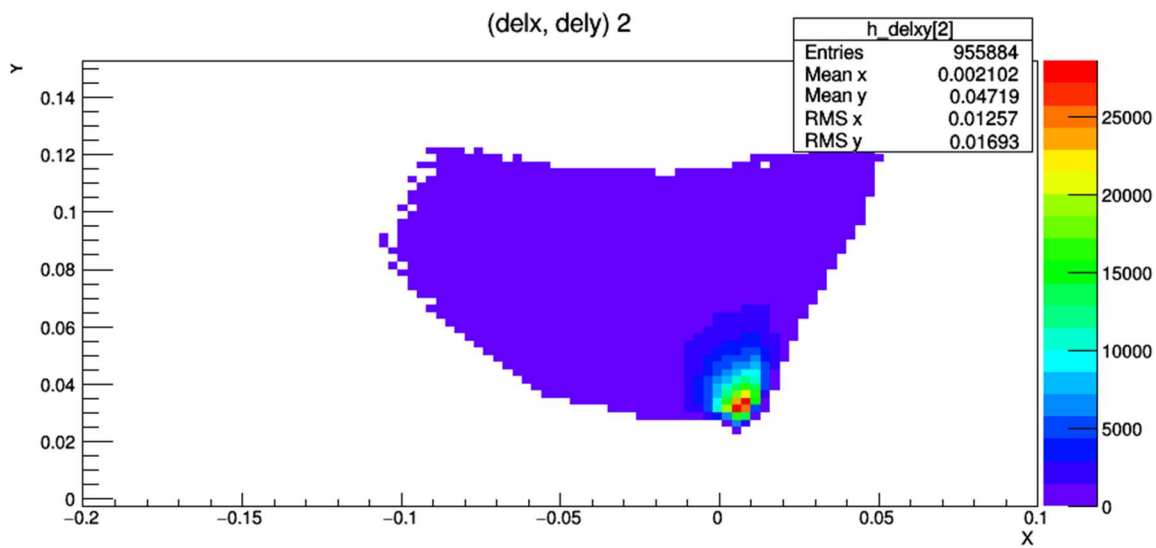
Change in u v coordinates is about  $0.465\text{cm}$  which is much larger than  $0.0225\text{cm}$ . Thus, without multiple scatter, wire chambers is having much better resolution than  $0.1\text{MeV}$ .



IV Fig 3. 16 Difference of  $xy$  coordinates of track on back chamber by changing  $E$  by  $0.1\text{MeV}$ . Ordinate: vertical change in track coordinate, in unit  $cm$ , abscissa: horizontal change in track coordinate, in unit  $cm$ .



IV Fig 3. 17 Difference of  $xy$  coordinates of track on back chamber by changing  $\theta$  by  $0.1^\circ$ . Ordinate: vertical change in track coordinate, in unit  $cm$ , abscissa: horizontal change in track coordinate, in unit  $cm$ .



IV Fig 3. 18 Difference of  $xy$  coordinates of track on back chamber by changing  $\varphi$  by  $0.1^\circ$ . Ordinate: vertical change in track coordinate, in unit  $cm$ , abscissa: horizontal change in track coordinate, in unit  $cm$ .



## 4 Reduce data dimension by principal component analysis

### 4.1 Introduction

As we already applied Bayes' theorem to infer probability of target energy distribution under condition of horizontal coordinate  $x$  measured at detector (or monitor in the Geant 4 simulation). By the following formula:

$$P(E|x) = \frac{P(x|E)P(E)}{P(x)}$$

That's for one side (either e- or e+) data.  $P(x|E)$  could be measured from calibration process,  $P(E)$  could use theory prediction,  $P(x)$  could also be measured through wire chamber. None the less, all terms on the left can be initially set by simulation result as starting point to compute the left side, which  $P(E|x)$  can be computed from. Thus, an iteration algorithm can be used to determine energy distribution  $P(E)$ .

However, even  $E$  and  $x$  has strong correlation, at lower energy side the  $x$  distribution under fixed  $E$  has large standard deviation since  $x$  is also largely depend on  $\theta_t$  (horizontal projection angle of particle direction at target). The fully formulated the conditional probability of target kinematics under the condition of certain measured position and angle value at wire chamber will be:

$$\begin{aligned} & P(E_e, \tan\theta_{et}, \tan\varphi_{et}, \tan\theta_{pt}, \tan\varphi_{pt} | x_e, y_e, \tan\theta_{ed}, \tan\varphi_{ed}, x_p, y_p, \tan\theta_{pd}, \tan\varphi_{pd}) \\ &= \frac{P(x_e, y_e, \tan\theta_{ed}, \tan\varphi_{ed} | E_e, \tan\theta_{et}, \tan\varphi_{et}) P(E_e, \tan\theta_{et}, \tan\varphi_{et})}{P(x_e, y_e, \tan\theta_{ed}, \tan\varphi_{ed})} \\ &\times \frac{P(x_p, y_p, \tan\theta_{pd}, \tan\varphi_{pd} | E_\gamma - E_e, \tan\theta_{pt}, \tan\varphi_{pt}) P(E_\gamma - E_e, \tan\theta_{pt}, \tan\varphi_{pt})}{P(x_p, y_p, \tan\theta_{pd}, \tan\varphi_{pd})} \quad (4.1) \end{aligned}$$

In above formula:  $E_e$  is the electron energy at target.  $\tan\theta_{et}, \tan\varphi_{et}, \tan\theta_{pt}, \tan\varphi_{pt}$  are tangents of electron and positron track projection angles (horizontal and vertical change of coordinates over beam direction change of coordinates of electron) out of target.  $x_e, y_e$  and  $x_p, y_p$  are positions of electron and positron tracks intersection coordinates at front wire chamber.  $\tan\theta_{ed}, \tan\varphi_{ed}$  and  $\tan\theta_{pd}, \tan\varphi_{pd}$  are tangents of electron and positron track horizontal ( $\theta$ ) and vertical ( $\varphi$ ) projection angles with respect to horizontal right (for electron) and left (for positron) perpendicular to beam direction.

Some simplifications of the terms are already been made: We utilized the constraint that  $E_e + E_p = E_\gamma$  so only one energy needs to be determined. In addition, after primary vertex, the e- e+ trajectory is independent, and results in probability independence of above formula on the right side.

Although with the simplification, we could already see the issue here: there're too many dimensions in the formula. A term like

$$P(x_e, y_e, \tan\theta_{ed}, \tan\varphi_{ed} | E_e, \tan\theta_{et}, \tan\varphi_{et})$$

Needs to be specified by 7-dimension data points, which makes: (1) computation like normalization (multiple sums, or multiple integral) difficult (2) hard to interpret and visualize data (3) storage (for example, tabulation) of data expensive.

However, high-dimensional data often has properties we can exploit. (1) In most case, they're overcomplete, i.e., many dimensions can be represented as combination of other dimensions. (2) Certain dimensions are correlated and data possess a lower-dimension structure. By using structure and correlations between dimensions of the data we can reduce dimension, and allow us to work with more compact data, ideally without losing information. The method we choose to reduce data dimension is principal component analysis, an algorithm for linear dimensionality reduction.

## 4.2 Principal component analysis (PCA)

### 4.2.1 Introduction

The purpose of PCA is to find projections  $\tilde{\mathbf{x}}_n$  of data point  $\mathbf{x}_n$  (data from  $n$ th event),  $n = 1, \dots, N$  that is similar to  $\mathbf{x}_n$  as possible, while might have significantly lower intrinsic dimensions. [58]

To be more precise, suppose we have dataset  $\{\mathbf{x}_1, \dots, \mathbf{x}_N\}$ ,  $\mathbf{x}_n \in \mathbb{R}^D$ ,  $N$  is the total number of data,  $D$  is the dimension of each data point. In our context  $\mathbf{x} = (x_e, y_e, \tan\theta_{ed}, \tan\varphi_{ed})^T$  (the transverse means  $\mathbf{x}$  is represented as a column vector/matrix) is the data, so  $D = 4$  (Also there is  $\mathbf{x}$  for the positron side, will be computed independently). We have covariance matrix:

$$S = \frac{1}{N} \sum_{n=1}^N \mathbf{x}_n \mathbf{x}_n^T = \frac{1}{N} X X^T \in \mathbb{R}^{D \times D} \quad (4.2)$$

Matrix  $X = [\mathbf{x}_1, \dots, \mathbf{x}_N] \in \mathbb{R}^{N \times D}$  represents entire dataset, with each individual data point as its column. First, we use a set of orthonormal vectors  $\{\mathbf{b}_1, \dots, \mathbf{b}_M\}$ ,  $\mathbf{b}_i \in \mathbb{R}^D$  as basis of a  $M$  dimensional subspace inside the vector space  $\mathbb{R}^D$ , to construct a matrix  $B = [\mathbf{b}_1, \dots, \mathbf{b}_M] \in \mathbb{R}^{D \times M}$  that represent point  $\mathbf{x}_n$  in the  $M$  dimensional space:

$$\mathbf{z}_n = B^T \mathbf{x}_n \in \mathbb{R}^M \quad (4.3)$$

While projection matrix  $BB^T$  projects each data point  $\mathbf{x}_n$  to  $M$  dimensional subspace  $U$  of  $\mathbb{R}^D$ :

$$\tilde{\mathbf{x}}_n = B \mathbf{z}_n = BB^T \mathbf{x}_n \in U \quad (4.4)$$

Where  $U \subset \mathbb{R}^D$  and  $\dim(U) = M < D$ , so from (4.3) and (4.4) we can see  $\mathbf{z}_n$  is the intrinsic coordinates of projected data, with dimension  $M$ .

To make  $\tilde{\mathbf{x}}_n$  similar to  $\mathbf{x}_n$  as possible we require: (1) variance of projected data  $\mathbf{z}$  (or equivalently variance  $\tilde{\mathbf{x}}$ ) to be as large as possible, to retain as much information as possible. Or equivalently (2) the average squared Euclidean distance (reconstruction error)  $J_M \equiv \frac{1}{N} \sum_{n=1}^N \|\mathbf{x}_n - \tilde{\mathbf{x}}_n\|^2$  is minimized. The goal of PCA is to find a set of orthonormal vectors  $\{\mathbf{b}_1, \dots, \mathbf{b}_M\}$  that satisfy condition (1) or (2), then intrinsic coordinate vector under basis  $\mathbf{b}_1, \dots, \mathbf{b}_M$  is  $\mathbf{z}_n = B^T \mathbf{x}_n$  and projected coordinate with essentially  $M$  dimension is  $\tilde{\mathbf{x}}_n = B \mathbf{z}_n = BB^T \mathbf{x}_n$ .

### 4.2.2 Derivation of PCA

As the purpose of PCA, to retain as much information as possible when we project our data into an intrinsic lower dimension space we choose to maximize the variance of projected intrinsic coordinates  $\mathbf{z}$  since variance is an indicator of spread of the data.

Before the derivation there are two subjects to be clarified:

1) We assume the mean of data  $\mathbf{x}$  is  $\mathbf{0}$ , without loss of generality:

( [58] p. 289) Let's assume the mean of data  $\mathbf{x}$  is  $\boldsymbol{\mu}$  instead of  $\mathbf{0}$ , using the property of variance we have the variance for  $\mathbf{z}$ :

$$V(\mathbf{z}) = V(B^T(\mathbf{x} - \boldsymbol{\mu})) = V(B^T\mathbf{x} - B^T\boldsymbol{\mu}) = V(B^T\mathbf{x}) \quad (4.5)$$

i.e., the variance of the low-dimensional data  $\mathbf{z}$  does not depend on the mean of the data  $\boldsymbol{\mu}$ . With the assumption, the expectation value of  $\mathbf{z}$  is also  $\mathbf{0}$ :

$$E(\mathbf{z}) = E(B^T\mathbf{x}) = B^TE(\mathbf{x}) = \mathbf{0} \quad (4.6)$$

Note: each individual coordinate component of data is indicated by index of its component and the index of amount of data. Random variable  $\mathbf{x}$  has  $N$  number of data and the  $n$ th data is indicate as  $\mathbf{x}_n = (x_{1n}, x_{2n}, \dots, x_{Dn})^T$  (column vector), where the projected coordinate  $\mathbf{z}_n = (z_{1n}, z_{2n}, \dots, z_{Mn})^T$

### 2) Review of (orthogonal) projection as linear transformation

(Many linear algebra literatures have derivation of projection transformation, here is a video [59])

Discarding the index of number of data, in formula (4.3) and (4.4) we use  $\mathbf{z} = B^T\mathbf{x}$  and  $\tilde{\mathbf{x}} = BB^T\mathbf{z}$  without confirming they're indeed the projection of  $\mathbf{x}$  onto the subspace  $U \subset \mathbb{R}^D$  spanned by orthonormal vectors  $\mathbf{b}_1, \dots, \mathbf{b}_M$ . A projection  $P$  is defined as a linear transformation that  $P^2 = P$ . Below is a quick recap.

(1) For simplest case, project vector  $\mathbf{x}$  onto a straight line (1D subspace) specified by vector  $\mathbf{b} \in \mathbb{R}^D$ . Since the projection has the same direction as  $\mathbf{b}$ , we can denote it as  $P\mathbf{x} = \lambda\mathbf{b}$ . In addition,  $\mathbf{x} - \lambda\mathbf{b}$  is perpendicular to  $\mathbf{b}$  (see Fig 4.1):

$$(\mathbf{x} - \lambda\mathbf{b}) \cdot \mathbf{b} = 0$$

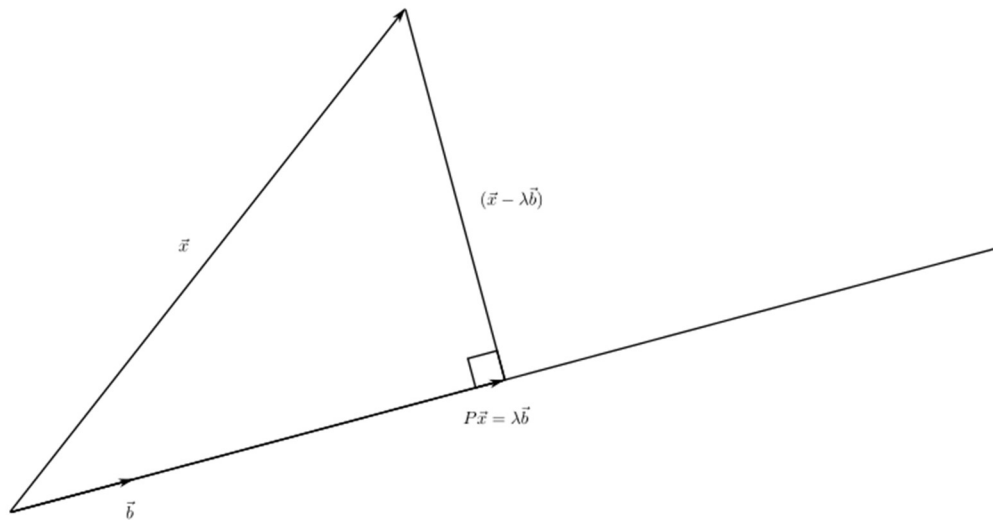
Solve  $\lambda$ , we have:

$$\lambda = \frac{\mathbf{b} \cdot \mathbf{x}}{\mathbf{b} \cdot \mathbf{b}} = \frac{\mathbf{b}^T \mathbf{x}}{\mathbf{b}^T \mathbf{b}} \quad (4.7)$$

For the 2<sup>nd</sup> equal sign, we notice  $\mathbf{b} = (b_1, \dots, b_D)^T$  and  $\mathbf{x} = (x_1, \dots, x_D)^T$  are column vectors, and uses definition of scalar product  $\mathbf{b} \cdot \mathbf{x} = \sum_{i=1}^D b_i x_i = \mathbf{b}^T \mathbf{x}$ . Thus, the projection of vector  $\mathbf{x}$  onto  $\mathbf{b}$  is:

$$P\mathbf{x} = \lambda\mathbf{b} = \frac{\mathbf{b}^T\mathbf{x}}{\mathbf{b}^T\mathbf{b}}\mathbf{b} = \mathbf{b}\frac{\mathbf{b}^T\mathbf{x}}{\mathbf{b}^T\mathbf{b}} = \frac{\mathbf{b}\mathbf{b}^T}{\mathbf{b}^T\mathbf{b}}\mathbf{x} = \mathbf{b}(\mathbf{b}^T\mathbf{b})^{-1}\mathbf{b}^T\mathbf{x} \quad (4.8)$$

Since  $\mathbf{b}^T\mathbf{b} = \sum_{i=1}^D b_i^2$  is a number,  $(\mathbf{b}^T\mathbf{b})^{-1}$  can be placed in between  $\mathbf{b}$  and  $\mathbf{b}^T$ .



IV Fig 4. 1 Projection  $P\mathbf{x}$  of vector  $\mathbf{x}$  onto 1D subspace spanned by vector  $\mathbf{b}$ .

It's easy to see the relation  $(\mathbf{x} - \lambda\mathbf{b}) \cdot \mathbf{b} = 0$ .

(2) For general case, project vector  $\mathbf{x}$  onto a subspace  $U \in \mathbb{R}^D$ ,  $\dim(U) = M$  spanned by vectors  $\mathbf{b}_1, \dots, \mathbf{b}_M, \mathbf{b}_i \in U \subset \mathbb{R}^D$  (Note: here we do not require  $\mathbf{b}_1, \dots, \mathbf{b}_M$  to be orthonormal). We denote matrix  $B = [\mathbf{b}_1, \dots, \mathbf{b}_M]$  with each vector  $\mathbf{b}_i$  as its column vector. Since the projection is in subspace  $U$ , it can be denoted as linear combination of vectors  $\mathbf{b}_1, \dots, \mathbf{b}_M$ :

$$P\mathbf{x} = \sum_{i=1}^M \lambda_i \mathbf{b}_i = B\boldsymbol{\lambda} \quad (4.9)$$

Where  $\boldsymbol{\lambda} = (\lambda_1, \lambda_2, \dots, \lambda_M)^T$ . Similar to 1 dimensional projection,  $\mathbf{x} - P\mathbf{x}$  is perpendicular to the subspace  $U$ , or any vector  $\mathbf{b}_i \in U$ :

$$(\mathbf{x} - P\mathbf{x}) \cdot \mathbf{b}_i = (\mathbf{x} - B\boldsymbol{\lambda}) \cdot \mathbf{b}_i = \mathbf{b}_i^T (\mathbf{x} - B\boldsymbol{\lambda}) = 0, i = 1 \dots, M$$

Concatenate all  $M$  equations above:

$$B^T(\mathbf{x} - B\boldsymbol{\lambda}) = \mathbf{0}, \text{ or } B^T\mathbf{x} = B^TB\boldsymbol{\lambda}$$

Solve vector  $\boldsymbol{\lambda}$ :

$$\boldsymbol{\lambda} = (B^T B)^{-1} B^T \mathbf{x} \quad (4.10)$$

Back to equation (4.9) (2.8) we have:

$$P\mathbf{x} = B\boldsymbol{\lambda} = B(B^T B)^{-1} B^T \mathbf{x} \quad (4.11)$$

Note: (1) For 1 dimensional case  $P\mathbf{x} = \mathbf{b}(\mathbf{b}^T \mathbf{b})^{-1} \mathbf{b}^T \mathbf{x}$ , which is a special case above. (2)  $P^2 = B(B^T B)^{-1} B^T \cdot B(B^T B)^{-1} B^T = B(B^T B)^{-1} B^T = P$ , so  $P$  is a projection.

Now back to our problem setting of PCA, which require  $\mathbf{b}_1, \dots, \mathbf{b}_M$  orthonormal, or  $\mathbf{b}_i \cdot \mathbf{b}_j = \delta_{ij} = (B^T B)_{ij}$ , we have  $B^T B = I$  the identity matrix in (4.10)(2.9) and (4.11)(2.10), change notation  $\boldsymbol{\lambda}$  by  $\mathbf{z}$  and  $(B^T B)^{-1} = I$ , we have:

$$\mathbf{z} = B^T \mathbf{x} \quad (4.12)$$

$$\tilde{\mathbf{x}} = P\mathbf{x} = B\mathbf{z} = BB^T \mathbf{x} = \sum_{i=1}^M \mathbf{b}_i \mathbf{b}_i^T \mathbf{x} \quad (4.13)$$

These are the formulas (4.3) and (4.4) once the subscript  $n$  is added.

### 3) Derivation of PCA

[58] pp. 289-293. We project all data points  $\mathbf{x}_1, \dots, \mathbf{x}_N$  onto a subspace  $U$  spanned by orthonormal basis  $\mathbf{b}_1, \dots, \mathbf{b}_M$ . Under basis  $\mathbf{b}_1, \dots, \mathbf{b}_M$  the projection coordinate vector is  $\mathbf{z}_n = B^T \mathbf{x}_n \in \mathbb{R}^M$ , and projected data is  $\tilde{\mathbf{x}}_n = B\mathbf{z}_n = BB^T \mathbf{x}_n \in U \subset \mathbb{R}^D$ . Our goal is to maximize variance of intrinsic coordinates  $\mathbf{z}(z_1, \dots, z_M)^T: V(\mathbf{z}) = V(B^T \mathbf{x})$ . Since we require the lower dimension projection subspace  $U$  spanned by orthonormal basis  $\mathbf{b}_1, \dots, \mathbf{b}_M$ , this property of  $\mathbf{b}_i$  will simplify our derivation by sequentially finding  $\mathbf{b}_1, \dots, \mathbf{b}_M$  and corresponding variance  $V(z_1), \dots, V(z_M)$ . We start with finding the 1<sup>st</sup> unit vector  $\mathbf{b}_1$ , or the principal component in 1 dimensional case:

1. Finding  $\mathbf{b}_1$  and variance of  $z_1$ : The definition of variance of  $z_1$  is

$$V(z_1) = V(\mathbf{b}_1^T \mathbf{x}) = \frac{1}{N} \sum_{n=1}^N (\mathbf{b}_1^T \mathbf{x}_n)(\mathbf{b}_1^T \mathbf{x}_n)^T = \frac{1}{N} \sum_{n=1}^N \mathbf{b}_1^T \mathbf{x}_n \mathbf{x}_n^T \mathbf{b}_1 = \mathbf{b}_1^T S \mathbf{b}_1 \quad (4.14)$$

Where  $S = \frac{1}{N} \sum_{n=1}^N \mathbf{x}_n \mathbf{x}_n^T$  is the covariance matrix of data. Under constraint  $\|\mathbf{b}_1\|^2 = \mathbf{b}_1^T \mathbf{b}_1 = 1$  we solve the maximum value problem by applying Lagrange multiplier, the problem is equivalent to solve the un-constraint maximum value of function:

$$L(\mathbf{b}_1, \lambda_1) = \mathbf{b}_1^T S \mathbf{b}_1 + \lambda_1 (1 - \mathbf{b}_1^T \mathbf{b}_1) \quad (4.15)$$

Solve (4.15) by taking partial derivatives with respect to  $\mathbf{b}_1, \lambda_1$ :

$$\frac{\partial L}{\partial \mathbf{b}_1} \equiv \left( \frac{\partial L}{\partial b_{11}}, \frac{\partial L}{\partial b_{12}}, \dots, \frac{\partial L}{\partial b_{1D}} \right) = 2(\mathbf{b}_1^T S - \lambda_1 \mathbf{b}_1^T) = 0 \quad (4.16)$$

$$\frac{\partial L}{\partial \lambda_1} = 1 - \mathbf{b}_1^T \mathbf{b}_1 = 0 \quad (4.17)$$

We have the solution:  $\mathbf{b}_1^T S = \lambda_1 \mathbf{b}_1^T$ , taking transpose and note covariance matrix  $S$  is symmetric. We have:

$$S \mathbf{b}_1 = \lambda_1 \mathbf{b}_1 \quad (4.18)$$

Thus  $\mathbf{b}_1$  is an eigen vector of  $S$  and  $\lambda_1$  is the corresponding eigen value. In order to maximize variance of coordinate  $z_1$ , we rewrite (4.14) using (4.18):

$$V(z_1) = \mathbf{b}_1^T S \mathbf{b}_1 = \mathbf{b}_1^T \lambda_1 \mathbf{b}_1 = \lambda_1 \quad (4.19)$$

If we choose  $\lambda_1$  to be the largest eigen value of data covariance matrix  $S$ , we solve the 1-dimension PCA problem. Eigen vector  $\mathbf{b}_1$  is called the 1<sup>st</sup> principal component. The coordinate of projected subspace  $U = \text{span}(\mathbf{b}_1)$  is  $z_{1n} = \mathbf{b}_1^T \mathbf{x}_n$  by (4.3), and representation of original data  $\mathbf{x}_n$ ,  $n = 1, \dots, N$  is  $\tilde{\mathbf{x}}_n = B \mathbf{z}_n = B B^T \mathbf{x}_n$  by (4.4).

2. We generalize the problem to finding the  $m$  dimensions principal subspace by induction:

Assume we have already found the first  $m-1$  principal components  $\mathbf{b}_i$ ,  $i = 1, \dots, m-1$ . Recall the original data matrix  $X = [\mathbf{x}_1, \dots, \mathbf{x}_N]$ , we subtract each data point by its projection onto subspace spanned by  $\mathbf{b}_1, \mathbf{b}_2, \dots, \mathbf{b}_{m-1}$  to get the reduced data matrix  $\hat{X}$ :

$$\hat{X} = X - P_{m-1} X = X - \sum_{i=1}^{m-1} \mathbf{b}_i \mathbf{b}_i^T X \quad (4.20)$$

From  $\hat{X}$ , we can construct the reduced covariance matrix  $\hat{S}$  as in (4.2):

$$\hat{S} = \frac{1}{N} \hat{X} \hat{X}^T \quad (4.21)$$

Following the same procedure as in 1 dimensional case, we find the largest eigen value of  $\hat{S}$ , denote by  $\lambda_m$  and its eigen vector  $\mathbf{b}_m$ , which is the 1-dimension solution of PCA for reduced data  $\hat{X}$ . If  $\lambda_m$  and its eigen vector  $\mathbf{b}_m$  also be the eigen value and eigen vector of original covariance matrix  $S$ , then maximizes the variance of  $z_m$  and will be the next solution for original data  $X$  in our iteration. Proof is shown below:

We need to shown  $S = \frac{1}{N} X X^T$  and  $\hat{S} = \frac{1}{N} \hat{X} \hat{X}^T$  has same eigen vectors: assume  $\mathbf{b}_i$  is the eigen vector correspond to  $m$  th largest eigen value of  $S$ :  $S \mathbf{b}_i = \lambda_i \mathbf{b}_i$  consider  $\hat{S} \mathbf{b}_i$ :

$$\begin{aligned} \hat{S} \mathbf{b}_i &= \frac{1}{N} \hat{X} \hat{X}^T = \frac{1}{N} (X - P_{m-1} X)(X - P_{m-1} X)^T \mathbf{b}_i \\ &= \frac{1}{N} (X X^T - X X^T P_{m-1}^T - P_{m-1} X X^T - P_{m-1} X X^T P_{m-1}^T) \mathbf{b}_i \\ &= (S - S P_{m-1} - P_{m-1} S - P_{m-1} S P_{m-1}) \mathbf{b}_i \end{aligned} \quad (4.22)$$

Since  $P_{m-1} \mathbf{b}_i = \sum_{j=1}^{m-1} \mathbf{b}_j \mathbf{b}_j^T \mathbf{b}_i = \sum_{j=1}^{m-1} \mathbf{b}_j \delta_{ij} = \mathbf{b}_i$  if  $i < m$ ;  $P_{m-1} \mathbf{b}_i = \mathbf{0}$  if  $i \geq m$ . So:

$$\hat{S}\mathbf{b}_i = \mathbf{0} \quad \text{if } i < m$$

$$\hat{S}\mathbf{b}_i = (S - P_{m-1}S)\mathbf{b}_i = \lambda_i\mathbf{b}_i - P_{m-1}\lambda_i\mathbf{b}_i = \lambda_i\mathbf{b}_i \quad \text{if } i \geq m \quad (4.23)$$

Thus, for any  $i = 1, \dots, D$ , eigen vector  $\mathbf{b}_i$  of  $S$  is also eigen vector of  $\hat{S}$ . If  $i < m$ , eigen value of  $\hat{S}$  is 0; if  $i \geq m$ , the eigen value is  $\lambda_i$ , the same as  $S$ .

### 3. Captured variance (information) after dimension reduction

Similar to the case of  $\mathbf{z}_1$ , the variance of  $\mathbf{z}_m$  is:

$$V(\mathbf{z}_m) = \mathbf{b}_m^T S \mathbf{b}_m = \mathbf{b}_m^T \lambda_m \mathbf{b}_m = \lambda_m \quad (4.24)$$

If we reduce dimension  $D$  of data using PCA to  $M$ , we pick the  $M$  eigen vectors with the largest eigen values of the variance matrix  $S$ . Variance of  $\mathbf{z}$  from (4.5) is:

$$\begin{aligned} V(\mathbf{z}) &= V(B^T \mathbf{x}) = \frac{1}{N} (B^T X)(B^T X)^T = B^T S B = B^T S [\mathbf{b}_1, \mathbf{b}_2, \dots, \mathbf{b}_M] \\ &= B^T [\lambda_1 \mathbf{b}_1, \lambda_2 \mathbf{b}_2, \dots, \lambda_M \mathbf{b}_M] = \begin{bmatrix} \mathbf{b}_1^T \\ \vdots \\ \mathbf{b}_M^T \end{bmatrix} [\lambda_1 \mathbf{b}_1, \lambda_2 \mathbf{b}_2, \dots, \lambda_M \mathbf{b}_M] = \begin{bmatrix} \lambda_1 & \dots & 0 \\ \vdots & \ddots & \vdots \\ 0 & \dots & \lambda_M \end{bmatrix} \quad (4.25) \end{aligned}$$

We denote  $V_M = \sum_{i=1}^M \lambda_i = \text{tr}(V(\mathbf{z}))$  (trace of variance matrix  $V(\mathbf{z})$ ) as captured variance by PCA, and  $V_D = \sum_{i=1}^D \lambda_i = \text{tr}(S)$  is the total variance dataset contains. And relative variance captured is  $V_M/V_D$ .

#### 4.2.3 Summary

Overall, to apply PCA for a given set of data  $\{\mathbf{x}_1, \dots, \mathbf{x}_N\}$ , follow steps:

- (1) From data matrix  $X = [\mathbf{x}_1, \dots, \mathbf{x}_N]$  calculate covariance matrix  $S = \frac{1}{N} X X^T$
- (2) To reduce dimension from  $D$  to  $M$ . Find the  $M$  largest eigen values of  $S$ :  $\lambda_i$ ,  $i = 1, \dots, M$  and corresponding eigen vectors  $\mathbf{b}_i$ .
- (3) The intrinsic coordinate under basis  $\mathbf{b}_1, \mathbf{b}_2, \dots, \mathbf{b}_M$  is  $\mathbf{z}_n = B^T \mathbf{x}_n \in \mathbb{R}^M$  and reduced (compressed) data point under the original basis is  $\tilde{\mathbf{x}}_n = B \mathbf{z}_n = B B^T \mathbf{x}_n$ .

## 4.3 Application of PCA to Geant 4 simulation data

### 4.3.1 Introduction

( [58] pp. 303-305) There is a change of convention since computer use indices from 0, all the discussion in this chapter uses the same convention. Our plan is to reduce the dimension of measured data  $\mathbf{x} = (x_0, x_1, x_2, x_3)^T = (x_e, y_e, \tan\theta_{ed}, \tan\varphi_{ed})^T$  from 4 to 2 or 3, since the obvious correlation between  $x_e$  and  $\tan\theta_{ed}$ , or  $y_e$  and  $\tan\varphi_{ed}$  to reduce dimension to 1 is not a option.

In addition to the standard PCA procedure discussed in last chapter. There is a few modifications needs to be made to reduce computation error:

1) Before applying PCA directly to data  $\mathbf{x}$ , instead we change  $\mathbf{x}$  to  $\mathbf{x}'$  by both mean subtraction, that is subtract each component  $x_i$  by its mean  $\mu_i$ . Since the variance matrix  $S$  is independent of mean  $\boldsymbol{\mu}$ , this won't change the variance of  $S$ , but can reduce the risk of numerical problems. Then standardize the data by dividing standard deviation  $\sigma_i$ . Summarized as below:

$$x'_i = \frac{x_i - \mu_i}{\sigma_i} \quad (4.26)$$

This makes standardize coordinate  $x'_i$  with mean 0, dimensionless, with standard deviation 1. The variance matrix  $S'$  of data  $\mathbf{x}'$  is essentially the correlation matrix of data  $\mathbf{x}$ :

$$\begin{aligned} S'_{ij} &= \frac{1}{N} (X'X'^T)_{ij} = \frac{1}{N} \sum_{n=1}^N (\mathbf{x}'_n \mathbf{x}'_n{}^T)_{ij} = \text{Cov}\left(\frac{x_i - \mu_i}{\sigma_i}, \frac{x_j - \mu_j}{\sigma_j}\right) = \frac{\text{Cov}(x_i, x_j)}{\sqrt{V(x_i)V(x_j)}} \\ &= \text{Corr}(x_i, x_j) \quad (4.27) \end{aligned}$$

2) Apply PCA on  $S'$ , i.e., find the first  $M$  largest eigen values  $\lambda_i$  and their eigen vectors  $\mathbf{b}_i$  of  $S'$ . Construct matrix  $\mathbf{B} = [\mathbf{b}_1, \mathbf{b}_2, \dots, \mathbf{b}_M]$ , then coordinate under basis  $\mathbf{b}$  is  $\mathbf{z}_n = \mathbf{B}^T \mathbf{x}'_n \in \mathbb{R}^M$  and reduced (compressed) data point  $\widetilde{\mathbf{x}}'_n = \mathbf{B} \mathbf{z}_n = \mathbf{B} \mathbf{B}^T \mathbf{x}'_n$ .

3) Transform compressed data  $\widetilde{\mathbf{x}}'_n$  back to  $\widetilde{\mathbf{x}}_n$  using the relation (4.26):

$$\widetilde{x}_{in} = \sigma_i \widetilde{x}'_{in} + \mu_i \quad (4.28)$$

### 4.3.2 Application

In this section, we apply PCA to one of our Geant 4 simulation. The settings of the simulation are:

(1) We generate Bethe-Heitler pair, which has been specified by

$$E_e, E_p = E_\gamma - E_e, \tan\theta_{et}, \tan\varphi_{et}, \tan\theta_{pt}, \tan\varphi_{pt}$$



at each event. We want to include energies and solid angles that a bit beyond what we want to measure since the pairs from these energies and solid angles will also have probability to render similar  $e^+ e^-$  position and angle data measured at wire chambers.

For projection angles  $\theta_{et}, \varphi_{et}, \theta_{pt}, \varphi_{pt}$  the constraints are: (1) since the maximum polar angle from target center to edge of yoke hole of the magnet is about  $14.7^\circ$ , we choose maximum  $\theta_{et}, \varphi_{et}, \theta_{pt}, \varphi_{pt}$  to  $15^\circ$ , that is a “square” with side length  $2\tan 15^\circ$  covers the “circle” with radius  $\tan 14.7^\circ$ . (2) pairs  $(\theta_{et}, \varphi_{et})$  and  $(\theta_{pt}, \varphi_{pt})$  are randomized so that the polar angle is between  $4^\circ$  (a little less than cone shaped baffle between pole of the magnets) to  $15^\circ$ . In addition, they’re chosen that the azimuthal angle is in range  $[-28^\circ, 28^\circ]$  for  $e^-$  and  $[(180 - 28)^\circ, (180 + 28)^\circ]$  for  $e^+$  since beyond this region  $e^-$  or  $e^+$  will obviously hit either poles of the magnet, or its side frame. Total number of events is more than 1.13 million.

(2) Geant 4 simulation setup, all geometry is the same as previous simulations. It should be noted that for choice of material: All backgrounds include target has been set to air. The measured position and angle at wire chambers  $x_e, y_e, \tan\theta_{ed}, \tan\varphi_{ed}$  are replaced by *values at monitor just in front of front wire chamber*. It’s a valid approximation at the moment since multiple scattering effect is much larger than the wire chamber resolution, which is  $\sim 100 \mu m$ . In addition,  $\tan\theta_{ed}, \tan\varphi_{ed}$  are measured projection angles along horizontal axis perpendicular to beam direction. Although the wire chambers are tilted and Jlab Hall A analyzer will produce track projection angle tangents in local frame of wire chamber at front wire plane, it’s a easy rotation to transform these angles to  $\tan\theta_{ed}, \tan\varphi_{ed}$ . Same procedure is applied for positron side wire chambers.

The following shows the result of each PCA step. They’re either represented in table or histogram, and since the original data  $\mathbf{x} = (x_0, x_1, x_2, x_3)^T = (x_e, y_e, \tan\theta_{ed}, \tan\varphi_{ed})^T$  at wire chamber has dimension 4, it’s impossible to visualize, instead we can select 2 of the 4 dimensions for visualization. As for the projected coordinate vector  $\mathbf{z}$ , in addition to histogram of each of 4 principal component coordinates, the 2D histogram of the largest two component  $(z_0, z_1)$  is a good choice since most information are contained in these 2 dimensions.

All the following histograms and tables are subjected to two cuts:

- (1) Require both sides monitor have hits (thus front wire chamber will be hit assuming efficiency 100%). In other word, if there is only one side has signal during experiment, there will be no coincidence detected from hodoscopes and those events will be discarded. In addition, the simulation require case the hit on left be  $e^+$  and hit on right be  $e^-$ .
- (2) Since air is background, and the simulation has probability that the hits on monitor has unreasonably large projection angle  $\theta_{ed}$  and/or  $\varphi_{ed}$ . As seen from next page the variance of  $\tan\varphi_{ed}$  is 0.01139, while its value was over 80 due to an event with  $\theta, \varphi$  very close to  $90^\circ$ . These isolated data can have huge impact on variance of  $\tan\theta_{ed}, \tan\varphi_{ed}$ , thus a cut is made to ensure track reaches back wire chamber.

Out of 1.13 million simulated events 823,290 events pass the cuts and shown below.

	$\mu_i$ (cm)	$V(x_i)$ (cm <sup>2</sup> )
$x_0 = x_e$	-1.91	344.8
$x_1 = y_e$	-0.207	40.11
$x_2 = \tan\theta_{ed}$	-0.0859	0.06151
$x_3 = \tan\varphi_{ed}$	0.00794	0.01139

Table 4.1 Mean and variance of original data  $\mathbf{x} = (x_0, x_1, x_2, x_3)^T = (x_e, y_e, \tan\theta_{ed}, \tan\varphi_{ed})^T$  Which are computed by formula  $\mu_i = \frac{1}{N} \sum_{i=0}^N x_i$ ,  $V(x_i) = \frac{1}{N} \sum_{i=0}^N x_i^2 - \mu_i^2$ .

$$S' = \begin{pmatrix} 1 & -0.0398 & 0.974 & 0.0494 \\ -0.0398 & 1 & 0.00437 & 0.894 \\ 0.974 & 0.00437 & 1 & 0.0970 \\ 0.0494 & 0.894 & 0.0970 & 1 \end{pmatrix}$$

Covariance matrix  $S'$  of data  $\mathbf{x}'$  of e-, with  $x'_i = \frac{x_i - \mu_i}{\sigma_i}$  and  $\mathbf{x} = (x_0, x_1, x_2, x_3)^T = (x_e, y_e, \tan\theta_{ed}, \tan\varphi_{ed})^T$  be the data measured from monitor. The diagonal terms are all 1, since the covariance matrix is essentially correlation matrix of  $\mathbf{x}$ , from (4.27)  $S'_{ii} = \frac{\text{Cov}(x_i, x_i)}{\sqrt{V(x_i)V(x_i)}} = \frac{V(x_i)}{V(x_i)} = 1$ . The largest off diagonal terms indications strong correlation between corresponding dimensions:

- (1)  $S'_{02} = S'_{20} = 0.974$  correspond to  $x_e$  and  $\tan\theta_{ed}$ , which are horizontal wire plane coordinate and horizontal projection angle. (See illustration below, check,  $x_e$   $y_e$  are local coordinates at monitor parallel to chambers?  $\tan\theta_{ed}$ ,  $\tan\varphi_{ed}$  are projection angles in global coordinate system.)
- (2)  $S'_{13} = 0.894$  correspond to  $y_e$  and  $\tan\varphi_{ed}$ , which are local coordinate perpendicular to horizontal axis (with 45° tilt) and vertical projection angle.

$$B_4 = (\mathbf{b}_0, \mathbf{b}_1, \mathbf{b}_2, \mathbf{b}_3) = \begin{pmatrix} 0.625 & 0.331 & -0.0508 & -0.705 \\ 0.285 & -0.649 & -0.705 & 0.000976 \\ 0.639 & 0.300 & -0.0178 & 0.708 \\ 0.346 & -0.616 & 0.707 & -0.0338 \end{pmatrix}$$

Above, full eigen vector matrix includes all 4 dimensions on e- side. If we want to reduce dimension to 1,2, or 3, use first 1,2, or 3 columns of this matrix.

$$(\lambda_0, \lambda_1, \lambda_2, \lambda_3) = (2.006 \quad 1.868 \quad 0.1013 \quad 0.02445)$$

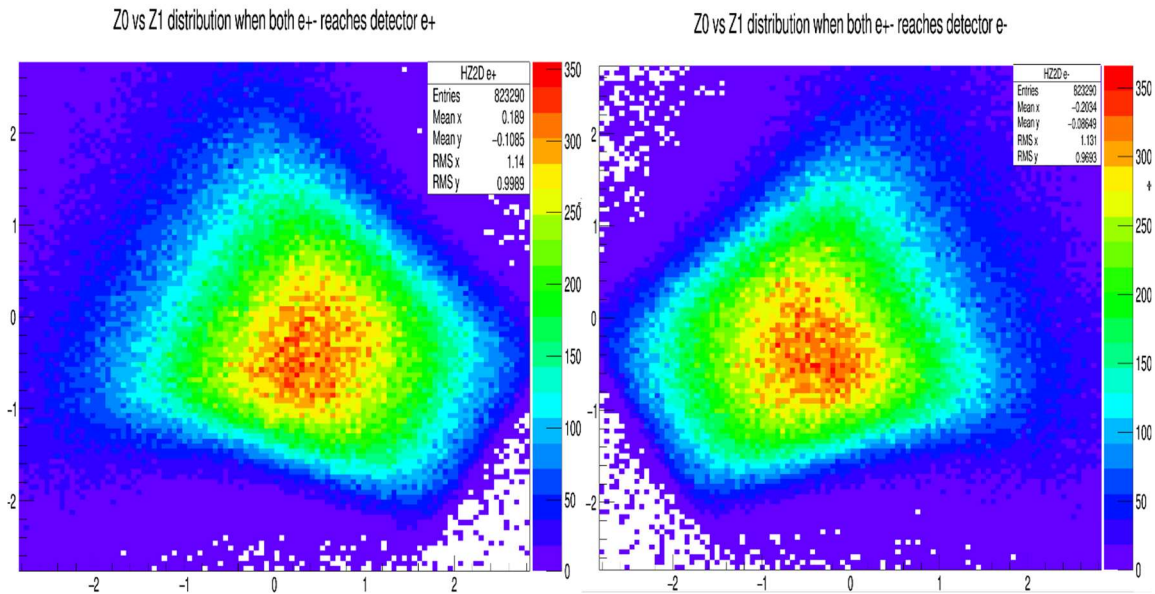
$$\frac{V_M}{V_D} = \frac{\sum_{i=0}^{M-1} \lambda_i}{\sum_{i=0}^{D-1} \lambda_i}, \quad \left( \frac{V_1}{V_4}, \frac{V_2}{V_4}, \frac{V_3}{V_4}, \frac{V_4}{V_4} \right) = (50.16\%, 96.86\%, 99.39\%, 100\%)$$

Above, eigen values of each principal component and percentage of information (variance) captured from 1,2,3,4 principal components. It's easy to see that the variance is mainly contributed by the first 2 principal components. This is understandable since from original data due to (1)  $x_e$  and  $\tan\theta_{ed}$ ,  $y_e$  and  $\tan\varphi_{ed}$  are strongly correlated, while (2)  $x_e$  and  $y_e$  both has significant spread (variance).

Remark: Instead of each component  $x_i'$ ,  $i = 0,1,2,3$  of  $\mathbf{x}'$  has variance exactly be 1, variance of  $z_0, z_1$  are larger than 1. As we can see from formula in paragraph below (4.25):

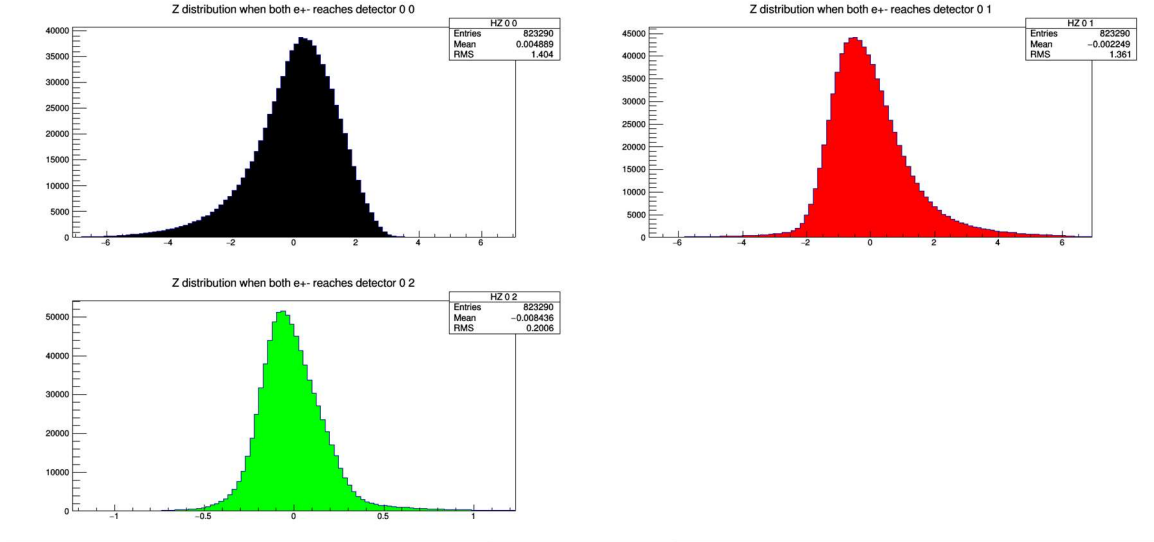
$$V_D = \sum_{i=0}^{D-1} \lambda_i = \text{tr}(S)$$

Replace dimension  $D$  by 4 and  $S$  by  $S'$ , since  $\text{tr}(S') = 1 + 1 + 1 + 1 = 4 = \sum_{i=0}^3 \lambda_i = 2.006 + 1.868 + 0.1013 + 0.02445$ , when all  $\lambda_i$  s are unequal, we must have sum of 1<sup>st</sup> two eigen values  $> 2$ .

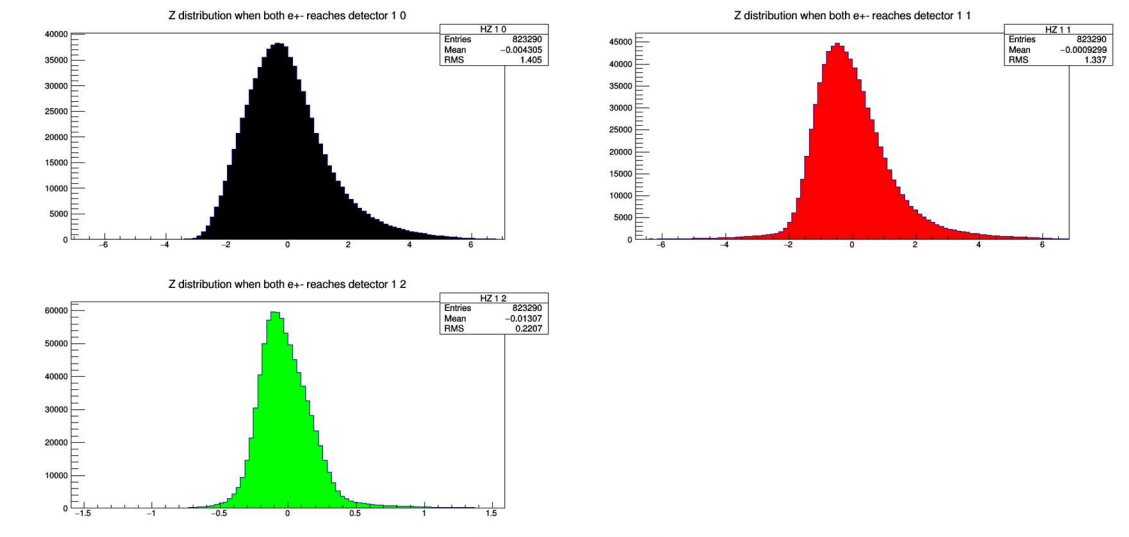


IV Fig 4. 2 Intrinsic projection coordinates (on standardized data  $\mathbf{x}'$ ) ( $z_0, z_1$ ) distribution by PCA. Ordinate:  $z_1$ , no unit, abscissa:  $z_0$ , no unit.

Left plots distribution of  $e^+$ , right  $e^-$ . The mirror image in plot between each 2D histogram is due to the opposite sign of horizontal coordinate  $x_e$  and  $x_p$ . Since the standardized data  $\mathbf{x}'$  is dimensionless, so does  $\mathbf{z} = B^T \mathbf{x}'$ . The range of axis  $z_i$  in above plots are  $[-2\sigma_i, 2\sigma_i]$ .



IV Fig 4. 3 Distribution of  $z_0, z_1, z_2$  of  $e^+$ . Ordinate: count, no unit, abscissa:  $z_0, z_1$ , or  $z_2$ , no unit.



IV Fig 4. 4 Distribution of  $z_0, z_1, z_2$  of  $e^-$ . Ordinate: count, no unit, abscissa:  $z_0, z_1$ , or  $z_2$ , no unit.

Data  $\mathbf{x}$  and standardized data  $\mathbf{x}'$  before and after projection has shown in the following pages. We recall the flow of data through PCA:

$$\mathbf{x} \rightarrow \mathbf{x}', x'_i = \frac{x_i - \mu_i}{\sigma_i} \rightarrow \mathbf{z} = B^T \mathbf{x}' \rightarrow \tilde{\mathbf{x}}' = B\mathbf{z} = BB^T \mathbf{x}' \rightarrow \tilde{\mathbf{x}}, \tilde{x}_i = \sigma_i \tilde{x}'_i + \mu_i, i = 0, \dots, M-1 \quad (4.29)$$

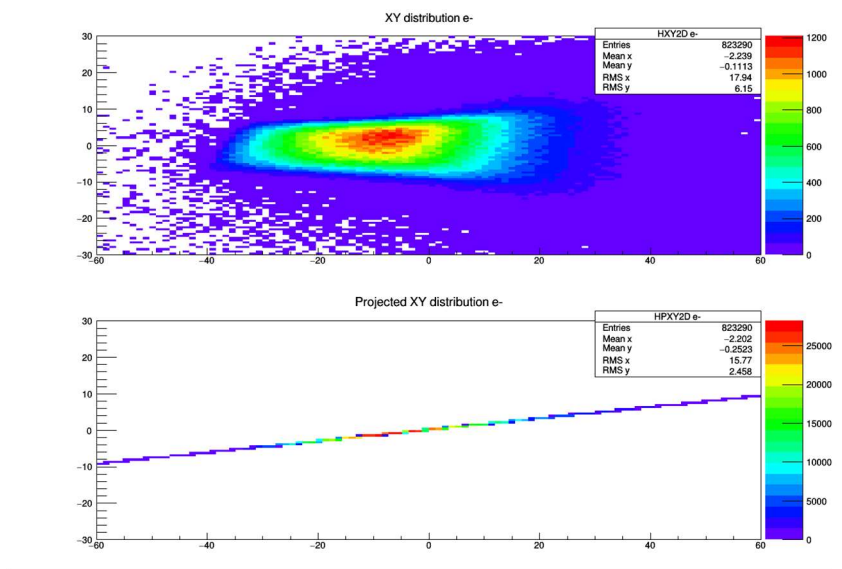
The subscript  $n$  (index of event) is omitted above. The matrix  $B = [\mathbf{b}_0, \mathbf{b}_1, \dots, \mathbf{b}_{M-1}]$  is also depends on number of principle components  $M$  we choose. The larger the  $M$ , the more information is captured, and the resulting  $\tilde{\mathbf{x}}'$  or  $\tilde{\mathbf{x}}$  will be closer to  $\mathbf{x}'$  or  $\mathbf{x}$ . Since issue of

visualization, only  $(x_0, x_1)^T = (x_e, y_e)^T$  2D histograms have been plotted in the next pages. For positron the distributions are similar and will be omitted here.

Remark: RMS of  $x_e', y_e'$  (before projection) should be 1, however the following plots are not due to the axes range of the histograms. If we expand the range of plot in either direction from  $[-3,3]$  to  $[5,5]$  those RMS will be larger than 0.996.

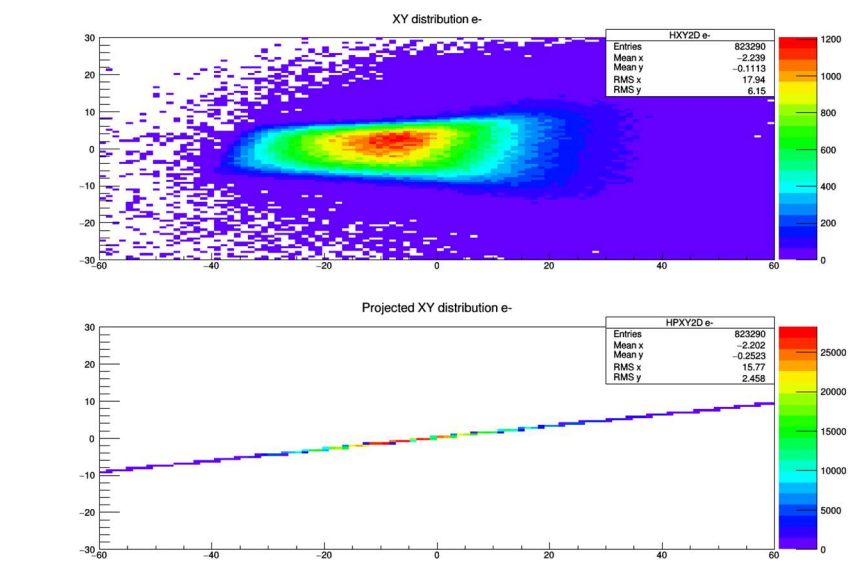
Number of PC equals 1: 4-dimension data has been projected onto 1 dimension subspace, so in  $(x_e, y_e)$  plot it also shows a straight line containing projected data. Even  $(x_e, y_e)$  before projection has significant spread on either  $x_e$  or  $y_e$  dimension and 1 dimension is not enough.

Number of PC equals 2: as we see from previous page, 96.86% of the information is retained when 2 principal components are chosen. The  $(x_e, y_e)$  distribution after projection looks a lot more similar to original data, albeit there is some obvious change in distribution.



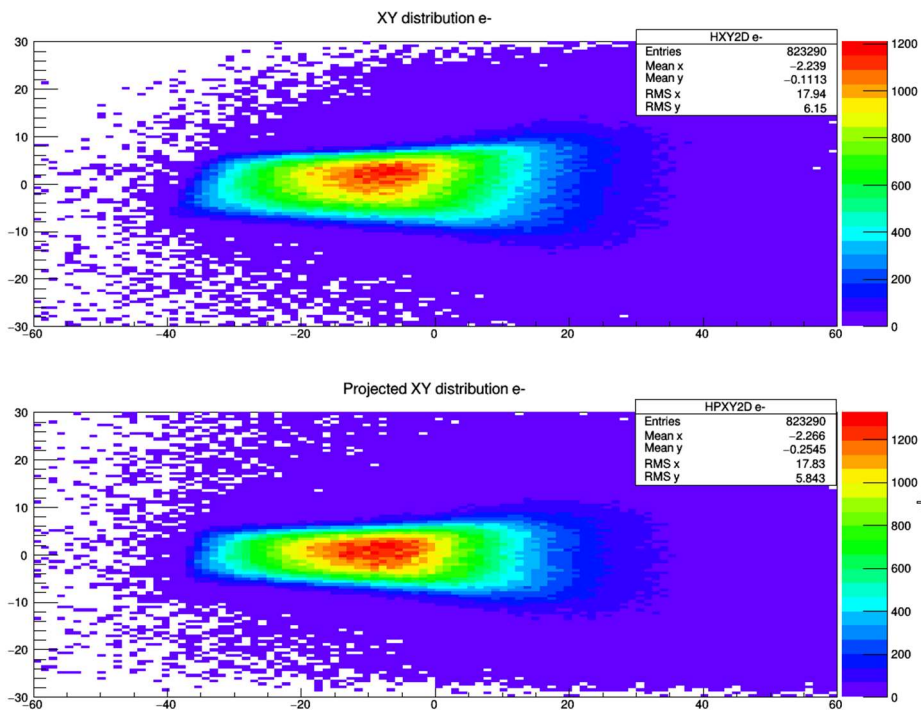
IV Fig 4. 5 Data  $x$  before and after projection with number of principal components 1,2,3. For all 4.5 figures, ordinate: vertical coordiante of electron intersection on detector in  $cm$ , abscissa: horizontal coordiante of electron intersection on detector in  $cm$ .

Fig 4.5 (1) Data  $x$  before and after projection. Only  $(x_0, x_1)^T = (x_e, y_e)^T$  has been plot, number of principal components equals 1.

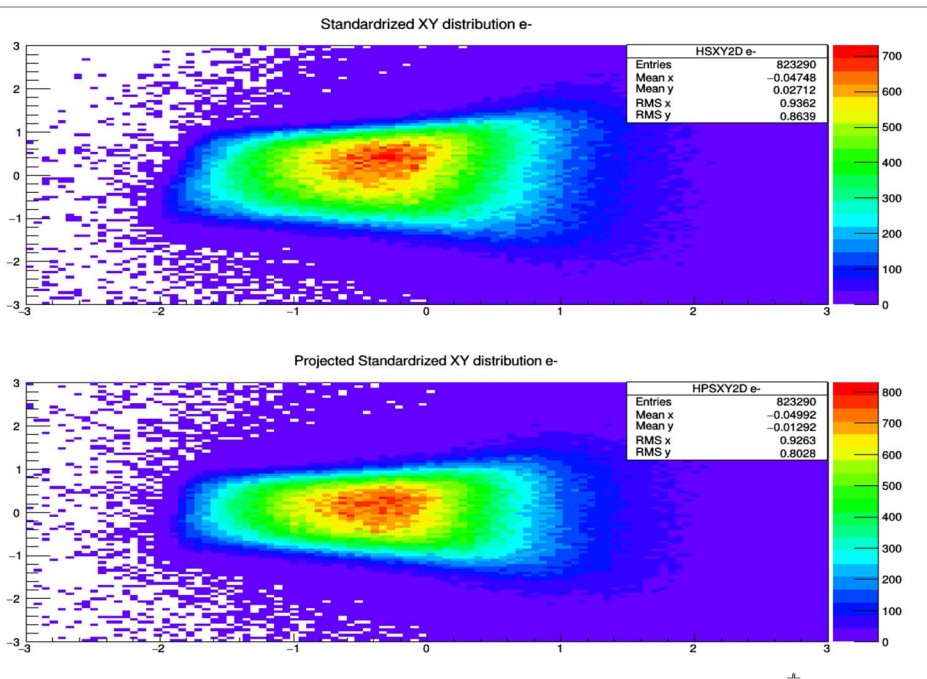


IV Fig 4. 6 Standardized data  $x'$  before and after projection with number of principal components 1,2,3. ordinate: standarized vertical coordiante of electron intersection on detector, no unit, abscissa: standarized horizontal coordiante of electron intersection on detector, no unit.

(1) Standardized data  $x'$  before and after projection. Only  $(x'_0, x'_1)^T = (x'_e, y'_e)^T$  has been plot, number of principal components equals 1.

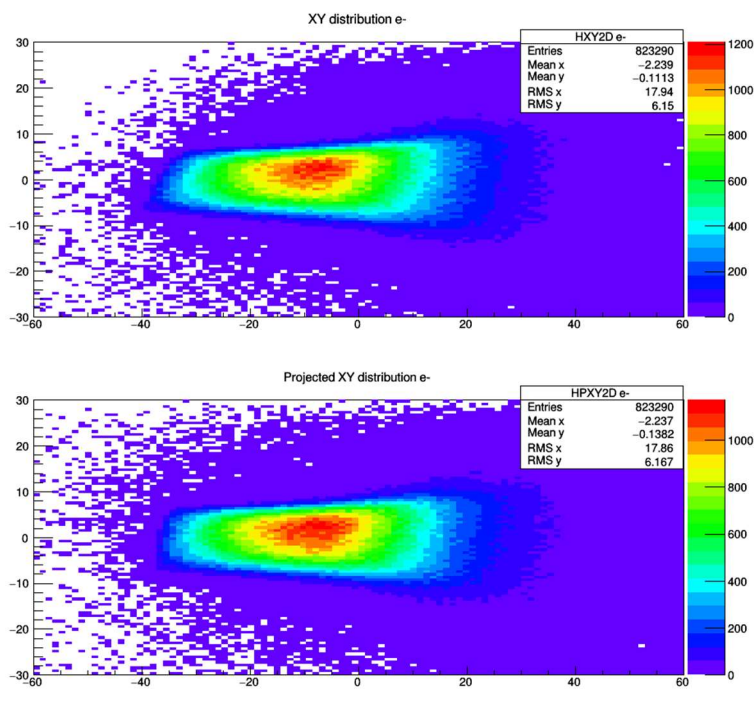


IV Fig 4.5 (2) Data  $\mathbf{x}$  before and after projection. Only  $(x_0, x_1)^T = (x_e, y_e)^T$  has been plot, number of principal components equals 2.

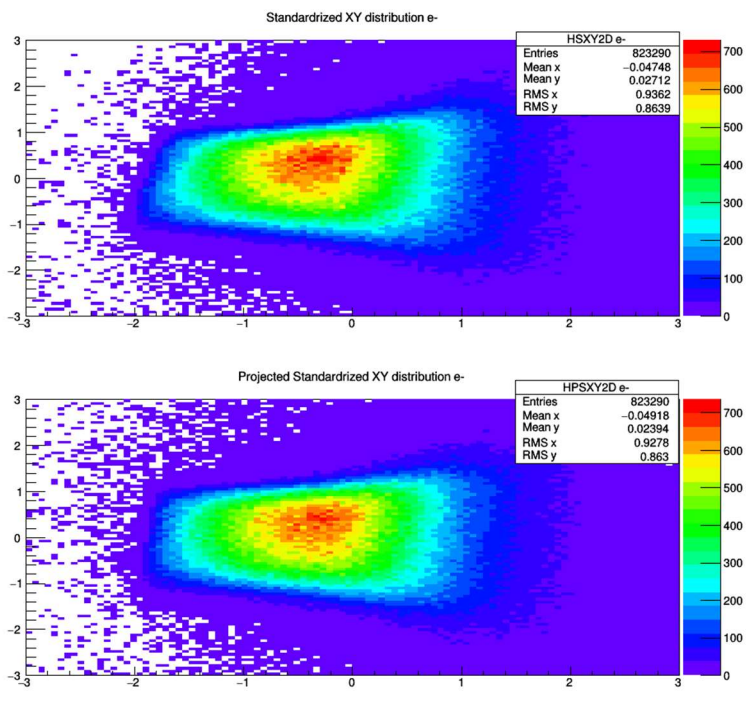


IV Fig 4.6 (2) Standardized data  $\mathbf{x}'$  before and after projection. Only  $(x'_0, x'_1)^T = (x'_e, y'_e)^T$  has been plot, number of principal components equals 2.





IV Fig 4.5 (3) Data  $x$  before and after projection. Only  $(x_0, x_1)^T = (x_e, y_e)^T$  has been plot, number of principal components equals 3.



IV Fig 4.6(3) Standardized data  $x'$  before and after projection. Only  $(x'_0, x'_1)^T = (x'_e, y'_e)^T$  has been plot, number of principal components equals 3.



### 4.3.3 Additional discussion and modifications

#### 1) Scheme of fitting Bethe-Heitler pair distribution

From formula (4.1), originally our way to fit Bethe-Heitler pair energy and angles distribution under the condition of certain measurement  $x_e, y_e, \tan\theta_{ed}, \tan\varphi_{ed}, x_p, y_p, \tan\theta_{pd}, \tan\varphi_{pd}$  at wire chambers includes conditional probability of these measurements under the condition of certain measurement of the Bethe-Heitler pair energy and angles

$P(x_e, y_e, \tan\theta_{ed}, \tan\varphi_{ed} | E_e, \tan\theta_{et}, \tan\varphi_{et})$  and

$P(x_p, y_p, \tan\theta_{pd}, \tan\varphi_{pd} | E_\gamma - E_e, \tan\theta_{pt}, \tan\varphi_{pt})$ , which can be estimated from Geant 4 simulation.

Through dimension reduction, we transform data point  $\mathbf{x} = (x_e, y_e, \tan\theta_{ed}, \tan\varphi_{ed})^T$  to  $\mathbf{z} = B^T \mathbf{x}$  with arbitrary lower dimension. Ideally, we want  $\mathbf{z}$  has significantly lower dimension than  $\mathbf{x}$  to facilitate analysis, while lose as little information as possible. Once we have distribution of  $\mathbf{x}$ , we transform it into distribution of  $\mathbf{z}$ , then instead of consider terms

$P(x_e, y_e, \tan\theta_{ed}, \tan\varphi_{ed} | E_e, \tan\theta_{et}, \tan\varphi_{et})$  on the right side of formula (4.1), we extract  $P(\mathbf{z} | E_e, \tan\theta_{et}, \tan\varphi_{et})$  from Geant 4 simulation. Formula (4.1) turns into:

$$\begin{aligned} & P(E_e, \tan\theta_{et}, \tan\varphi_{et}, \tan\theta_{pt}, \tan\varphi_{pt} | \mathbf{z}_e, \mathbf{z}_p) \\ &= \frac{P(\mathbf{z}_e | E_e, \tan\theta_{et}, \tan\varphi_{et}) P(E_e, \tan\theta_{et}, \tan\varphi_{et})}{P(\mathbf{z}_e)} \\ &\times \frac{P(\mathbf{z}_p | E_\gamma - E_e, \tan\theta_{pt}, \tan\varphi_{pt}) P(E_\gamma - E_e, \tan\theta_{pt}, \tan\varphi_{pt})}{P(\mathbf{z}_p)} \quad (4.30) \end{aligned}$$

Which simplifies the computation a lot. In this section, we will develop the scheme to properly getting  $P(\mathbf{z} | E_e, \tan\theta_{et}, \tan\varphi_{et})$ .

#### 2) Conditional probability of $P(\mathbf{z}_e | E_e)$ and $P(\mathbf{z}_e | \tan\theta_{et})$

We consider  $P(\mathbf{z}_e | E_e)$  and  $P(\mathbf{z}_e | \tan\theta_{et})$  as starting point. Before showing the probability distributions, there are things to be noted:

(1)  $\varphi$  is ignored at the moment. Since (1) Only  $\varphi_{et} - \varphi_{pt}$  has physical significance. However, without detector acceptance,  $\varphi_{et}$  distribution would be uniform and  $\varphi_{et} - \varphi_{pt}$  cannot be extracted from single side data. (2)  $\varphi_{et}$  only has strong correlation with  $y_e$  and  $\tan\varphi_{ep}$ , it doesn't play a big role of finding energy  $E_e$ , which are mainly correlated  $x_e$  and  $\tan\theta_{ep}$ .

(2)  $E_e$  and  $\theta_{et}$  affects the e- track in different way. For energy  $E_e$ , if  $\theta_{et}$  and  $\varphi_{et}$  unchanged, the larger the  $E_e$  the more  $x_e$  value shift to downstream direction (or the mapping from  $E_e$  to  $x_e$  without considering multiple scatter should be monotonic). This results from e- track inside magnet is helix, and its radius is proportional to  $E_e$ , it also means change same amount of  $E_e$  will change e- track direction more in low energy range.

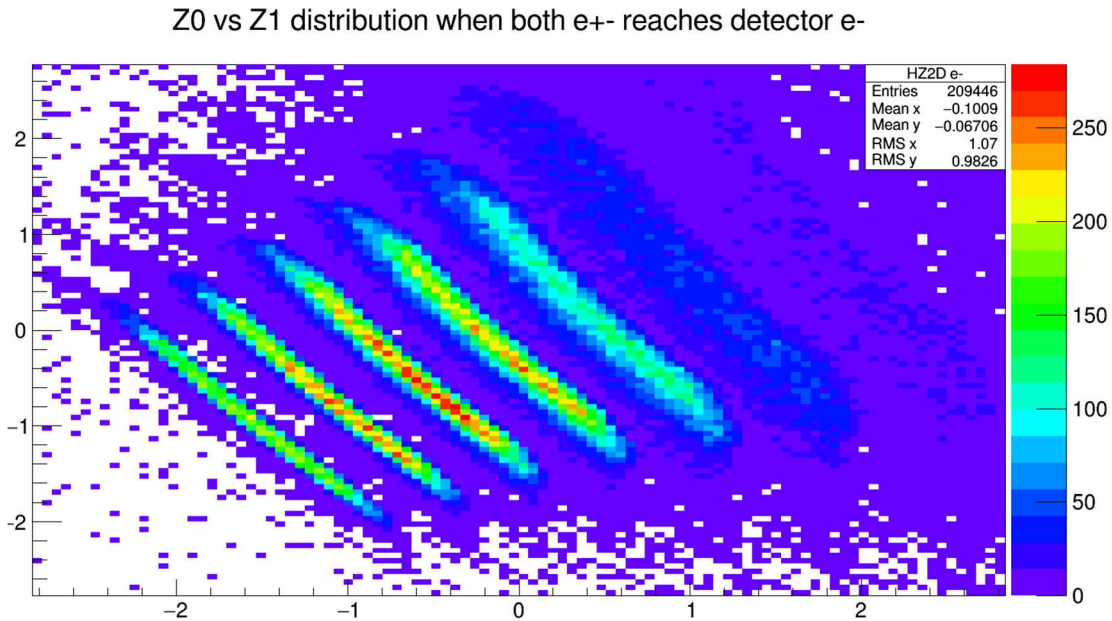
On the other hand, e- horizontal projection angle  $\theta_{et}$  alters e- track by changing the angle and position of the intersection of e- track enters the magnetic field. To first approximation, the magnetic field is uniform and shaped as a circle, under special relativity, e- track is a helix inside magnetic field with radius proportional to  $E_e$ . For this approximation, the angle between e- track exiting magnetic field and beam direction (total bent angle) is

$$\theta_{et} + \omega t$$

Here  $\omega$  is the angular velocity,  $\omega \propto 1/E_e$  and do not depend on  $\theta_{et}$ ; while  $t$  is the time of e- inside magnetic field, which depends on both  $\theta_{et}$  and  $E_e$ .  $\theta_{et}$  and  $\omega t$  contributions are competing each other, results in different total bent angle.

The lower  $E_e$  with much smaller circle intersect with circle of magnetic field in such manner: the smaller  $\theta_{et}$  would have much larger  $\omega t$  since the e- track enters magnetic field in direction close to magnetic circle's radius direction, having longer track inside magnetic field due to small radius.  $\omega t$  overwhelms  $\theta_{et}$  and  $\theta_{et} + \omega t$  is monotonic decreasing function of  $\theta_{et}$ . While in  $E_e \rightarrow \infty$  limit  $\omega \rightarrow 0$ ,  $\omega t \rightarrow 0$  and  $\theta_{et} + \omega t$  is monotonic increasing function of  $\theta_{et}$ , which is also the case of high  $E_e$  end of our experiment setting. In  $E_e$  somewhere in between  $\theta_{et} + \omega t$  first decreasing then increasing, result in a lot more focused group of e- tracks. In summary, with low  $E_e$  change of  $\theta_{et}$  will result in large change of total bent angle  $\theta_{et} + \omega t$  and thus large variance in  $\mathbf{z}_e$ , while the variance of  $\mathbf{z}_e$  is a lot smaller due to  $\theta_{et}$  change with higher  $E_e$ .

Below histogram that reflects the conditional probability of  $P(\mathbf{z}_e|E_e)$  and  $P(\mathbf{z}_e|\tan\theta_{et})$  are shown.



IV Fig 4. 7 ( $z_0, z_1$ ) of e+ distribution, under  $E_e$  cut. Ordinate:  $z_1$ , no unit, abscissa:  $z_0$ , no unit.

( $z_0, z_1$ ) of e+ distribution, under cut  $10MeV < E_e < 11MeV, 14MeV < E_e < 15MeV, \dots, 46MeV < E_e < 47MeV$  i.e., 1MeV bin width, with 4MeV change between bin centers. Strips of ( $z_0, z_1$ ) are clearly separated.

As we can see from the histogram above, strips of  $(z_0, z_1)$  are clearly separated under cut of  $E_e$ . In other word  $P(z_0, z_1|E_e)$  conditional probability distribution won't have much overlap on  $z_0, z_1$  for different  $E_e$ . This makes  $E_e$  clearly identifiable by using equation (4.30) under the condition of certain  $z_0, z_1$  value. In addition, all these strips are almost parallel to each other, thus perpendicular to the parallel direction,  $E_e$  can almost be identified under coordinate under this direction.

The strips of  $(z_0, z_1)$  under cut of  $E_e$  is not parallel to any of the  $z_0, z_1$  axis can be explained: when we applying PCA to find eigen vectors of covariance matrix of measured data. All those data are measured from detectors, which are  $x_e, y_e, \tan\theta_{ed}, \tan\varphi_{ed}$ . As we seen from the values of covariance matrix  $S'$  in 4.3.2, there are strong correlation between  $x_e$  and  $\tan\theta_{ed}$ , also between  $y_e$  and  $\tan\varphi_{ed}$ . PCA projects the detector data mainly onto  $z_0, z_1$  to maximize their variance from information of  $(x_e, \tan\theta_{ed})$  pair (to  $z_0$ ) and  $(y_e, \tan\varphi_{ed})$  pair (to  $z_1$ ) (as we can see from  $x$  verses  $y$  distribution, it's insufficient to use only one principle component projection to describe detector data, two dimensional subspace is minimum). This entire procedure (finding principal components of data at detectors) does not reflect any information (variance) of data from energy  $E_e$ , which carries information at target, nor correlation between  $E_e$  and detector data such as  $x_e$  and  $\tan\theta_{ed}$ .

The very good property of  $z_0, z_1$  is as described above,  $P(z_0, z_1|E_e)$  conditional probability distribution are strips which are separated by different  $E_e$  and almost parallel to each other. Which means the correlation between  $E_e$  and a linear combination of  $z_0, z_1$  is very strong, intuitively the correlation is mainly between  $E_e$  and  $(x_e, \tan\theta_{ed})$  pair. In next section 4.3.3 3) we rotate  $z_0, z_1$  to  $z_0', z_1'$  to make strips of  $P(z_0, z_1|E_e)$  distribution parallel to one of the  $z_0', z_1'$  coordinate axis to simplify  $P(z_0, z_1|E_e)$  fitting further.

In order to see the correlation between  $E_e$  and  $(x_e, \tan\theta_{ed})$  pair, we approximate correlation 1 between  $E_e$  and  $(x_e, \tan\theta_{ed})$  pair, which also has correlation 1 between  $x_e$  and  $\tan\theta_{ed}$ :

(1) Also, assuming correlation 1 between  $y_e$  and  $\tan\varphi_{ed}$  and from previous result

$$B_4 = (\mathbf{b}_0, \mathbf{b}_1, \mathbf{b}_2, \mathbf{b}_3) = \begin{pmatrix} 0.625 & 0.331 & -0.0508 & -0.705 \\ 0.285 & -0.649 & -0.705 & 0.000976 \\ 0.639 & 0.300 & -0.0178 & 0.708 \\ 0.346 & -0.616 & 0.707 & -0.0338 \end{pmatrix}$$

$$\mathbf{z} = B^T \mathbf{x}'$$

We see  $z_0 \cong 0.632((x_e' + (\tan\theta_{ed})') + 0.316(y_e' + (\tan\varphi_{ed})')$ ,  $z_1 \cong 0.315(x_e' + (\tan\theta_{ed})') - 0.633(y_e' + (\tan\varphi_{ed})')$ . (Here  $0.632 = (0.625 + 0.639)/2$  to approximate  $x_e'$  and  $(\tan\theta_{ed})'$  components of  $\mathbf{b}_0$ ,  $0.316 = (0.285 + 0.346)/2$  to to approximate  $y_e'$  and  $(\tan\varphi_{ed})'$  components of  $\mathbf{b}_0$ . Similar treatment for  $\mathbf{b}_1$ )

Try to cancel out  $(y_e' + (\tan\varphi_{ed})')$  in linear combination of  $z_0$  and  $z_1$ . We find

$$E_e \cong 1.41(0.633z_0 + 0.316z_1) = 0.895z_0 + 0.456z_1$$

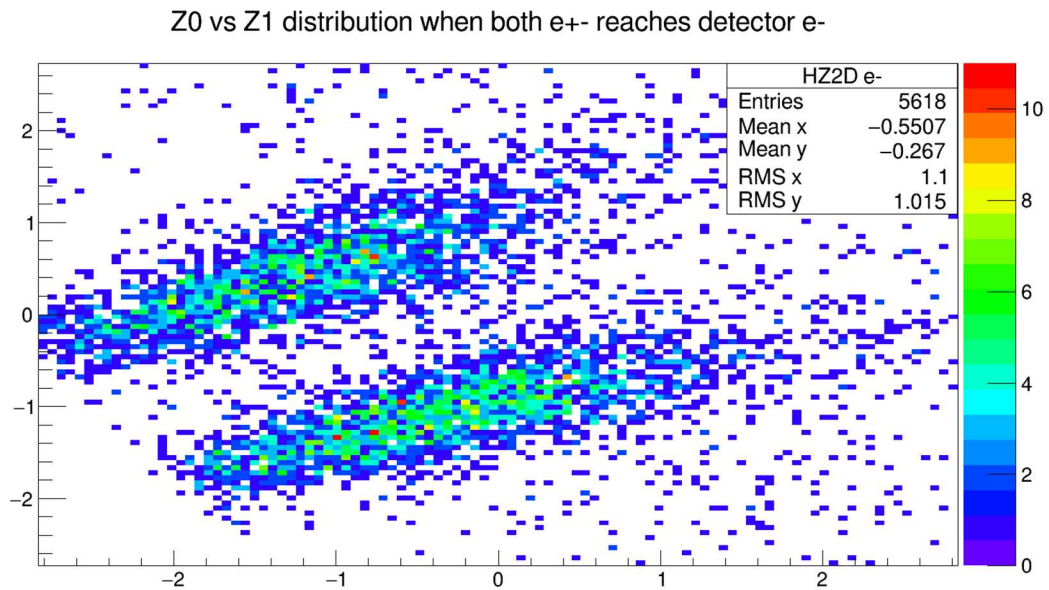
We will see later (section 4.3.3 3)) after a rotation in  $(z_0, z_1)$  plane,  $z_1'$  coordinate for e- which correspond to  $E_e$  dependence, is

$$z'_1 = -(0.861z_0 + 0.508z_1)$$

Which is quite close to the  $E_e$  expression.

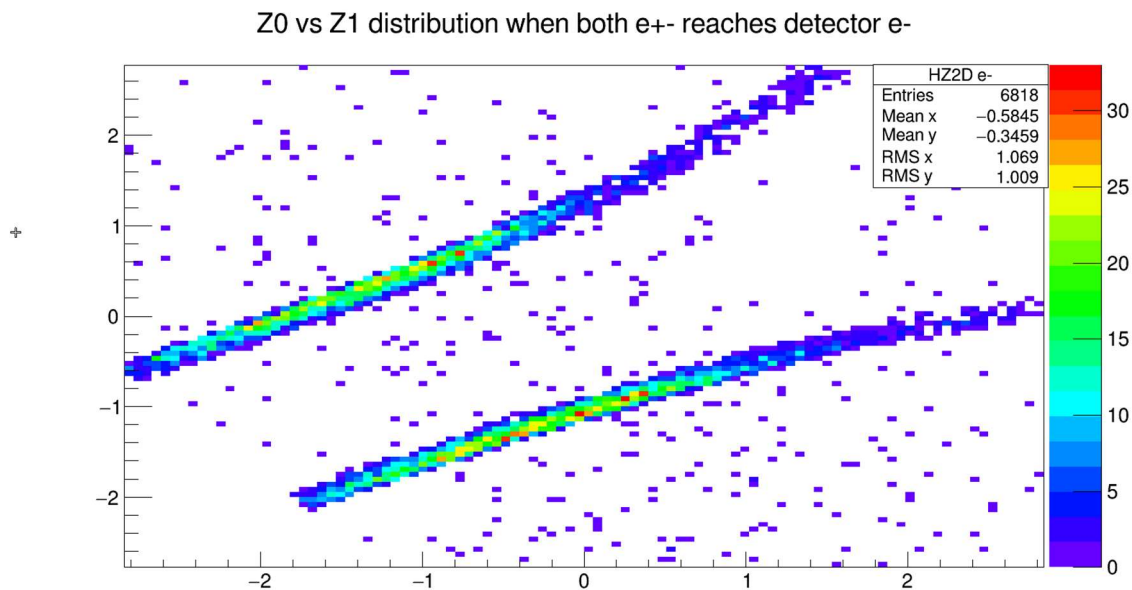
(2) If we apply PCA for data  $\mathbf{x} = (x_0, x_1, x_2, x_3, x_4)^T = (E_e, x_e, y_e, \tan\theta_{ed}, \tan\varphi_{ed})^T$  instead of  $(x_0, x_1, x_2, x_3)^T = (x_e, y_e, \tan\theta_{ed}, \tan\varphi_{ed})^T$ , the first principle component is  $z_0 = -0.567E'_e + 0.5834x'_e + 0.0174y'_e + 0.577\tan\theta'_{ed} + 0.0700\tan\varphi'_{ed}$  again reflects the correlation between  $E_e$  and  $(x_e, \tan\theta_{ed})$  pair .

$P(\mathbf{z}_e | \tan\theta_{et})$  results are less promising to be used:



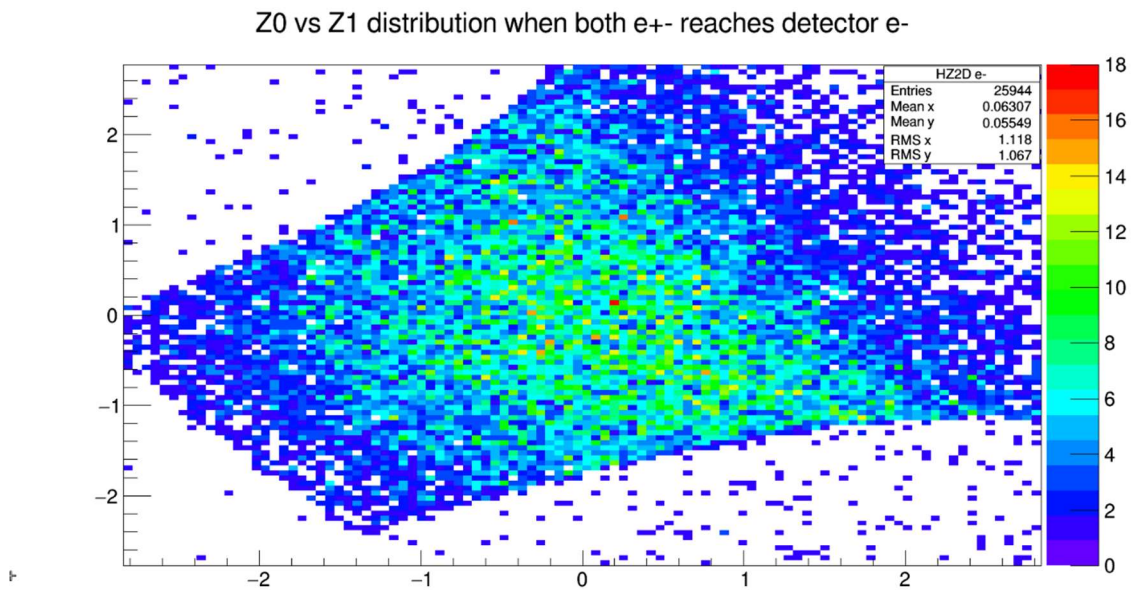
IV Fig 4. 8 ( $z_0, z_1$ ) of e+ distribution, under  $\tan\theta_{et}$  cut. Ordinate:  $z_1$ , no unit, abscissa:  $z_0$ , no unit.

$0.06 < \tan\theta_{et} < 0.065$  ( $6.84^\circ < \theta_{et} < 7.13^\circ$ ),  $0.26 < \tan\theta_{et} < 0.265$  ( $14.57^\circ < \theta_{et} < 14.84^\circ$ ).



IV Fig 4. 9 (1) ( $z_0, z_1$ ) of  $e^+$  distribution, under  $\tan\theta_{et}$  cut, vacuum background. Ordinate:  $z_1$ , no unit, abscissa:  $z_0$ , no unit.

$0.06 < \tan\theta_{et} < 0.065$  ( $3.43^\circ < \theta_{et} < 3.72^\circ$ ),  $0.26 < \tan\theta_{et} < 0.265$  ( $14.57^\circ < \theta_{et} < 14.84^\circ$ ).  
From analyzing vacuum background simulation result.



IV Fig 4.9(2) ( $z_0, z_1$ ) of  $e^+$  distribution, under cut  $0.12 < \tan\theta_{et} < 0.125$  ( $6.84^\circ < \theta_{et} < 7.13^\circ$ ).  
From analyzing vacuum background simulation result. Ordinate:  $z_1$ , no unit, abscissa:  $z_0$ , no unit.

As seen above, the conditional probability  $P(\mathbf{z}_e|\tan\theta_{et})$  results are less promising to be used. Unlike  $P(\mathbf{z}_e|E_e)$  distribution the  $P(\mathbf{z}_e|E_e)$  with separate  $E_e$  results in separate  $\mathbf{z}_e$  distribution, which makes  $E_e$  fit result reliable when applying Bayes' theorem to find  $P(E_e|\mathbf{z}_e)$ .

Even in vacuum background, the  $P(z_0, z_1|\tan\theta_{et})$  value are hard to be determined in certain  $\tan\theta_{et}$  region: at low or high  $\tan\theta_{et}$  value,  $P(z_0, z_1|\tan\theta_{et})$  has distinct strip distribution, while at  $\tan\theta_{et}$  somewhere in between  $P(z_0, z_1|\tan\theta_{et})$  will be spread throughout major region of  $(z_0, z_1)$  distribution.

### 3) Additional modification

As discussed in last section, the  $P(z_0, z_1|E_e)$  has good behavior so that we can rely on distributions  $P(z_0, z_1|E_e)$  under various  $E_e$  to construct  $P(E_e|z_0, z_1)$  distribution from Bayes' theorem. In other word, term in (4.30) such as

$$\frac{P(\mathbf{z}_e|E_e, \tan\theta_{et}, \tan\varphi_{et})P(E_e, \tan\theta_{et}, \tan\varphi_{et})}{P(\mathbf{z}_e)}$$

Will be simplified to:

$$\frac{P(\mathbf{z}_e|E_e)P(E_e)}{P(\mathbf{z}_e)}$$

Remark: c.f. (4.30) we need full distribution terms like  $P(\mathbf{z}_e|E_e, \tan\theta_{et}, \tan\varphi_{et})$  instead of  $P(z_0, z_1|E_e)$  for applying Bayes' theorem, even if we choose  $\mathbf{z}_e = (z_0, z_1)$  and drop  $\tan\varphi_{et}$  as discussed, it still has 4 dimensions. There is an assumption to make, that if:

$$P(\mathbf{z}_e|E_e, \tan\theta_{et}) = P(\mathbf{z}_e|E_e) \quad (4.31)$$

Then additional 1 dimension drop and numerical tabulation and fitting became much easier. This property is called *conditional independence*, which means choosing different value of  $\tan\theta_{et}$  won't affect  $P(\mathbf{z}_e|E_e)$  distribution.

If we denote  $\mathbf{z}_e \rightarrow \mathbf{x}$ ,  $\tan\theta_{et} \rightarrow y$ ,  $E_e \rightarrow z$ , (4.31)(3.6) is rewrite as:

$$P(\mathbf{x}|y, z) = P(\mathbf{x}|z) \quad (4.31)'$$

In order to understand the meaning of (4.31)', from chain rule of conditional probability (page 173 in [60]):

$$P(\mathbf{x}, y, z) = P(\mathbf{x}|y, z)P(y, z) = P(\mathbf{x}|y, z)P(y|z)P(z)$$

Divide both sides by  $P(z)$ :

$$P(\mathbf{x}, y|z) = P(\mathbf{x}|y, z)P(y|z)$$

Apply (4.31)' to right side:

$$P(\mathbf{x}, y|z) = P(\mathbf{x}|z)P(y|z) \quad (4.32)$$

The equivalent form (4.32) of (4.31)' is similar to unconditioned probability independence:  
 $P(\mathbf{x}, y) = P(\mathbf{x})P(y)$

Thus, the flow of data now become:

$$\mathbf{x} \rightarrow \mathbf{x}' \rightarrow \mathbf{z}_e \rightarrow \mathbf{z}_e'$$

$$\mathbf{z}_e = B^T \mathbf{x}'$$

$$\mathbf{z}_e' = R\mathbf{z}_e$$

The purpose of the additional rotation  $R$  is to make strips of  $P(z_{e0}', z_{e1}'|E_e)$  parallel to one of  $\mathbf{z}_e' = (z_{e0}', z_{e1}')$  coordinate axis. The condition for computing  $R$  is that its column vectors are the orthonormal eigen vectors of the covariance matrix of random variable  $\mathbf{z}_e$  under cut  $29MeV < E_e < 31MeV$ . Note strips with other e- energy cut will be parallel to this cut to a good approximation, we choose this cut since it has more data at 30MeV than other energies. In addition, we rotate  $\mathbf{z}_e = (z_0, z_1)$  by matrix  $R$  rather than standardize  $\mathbf{z}_e$  (that is  $z_{ei} \rightarrow \frac{z_{ei} - \mu_{ei}}{\sigma_{ei}}$ ) before the rotation.

Remark: This rotation also keeps total variance in  $z_0, z_1$  plane unchanged as from definition of variance captured in first  $M$  principal components  $V_M = \sum_{i=1}^M \lambda_i = tr(V(\mathbf{z}))$ , and now:

$$V(R\mathbf{z}) = \frac{1}{N} \sum_{n=1}^N (R\mathbf{z})(R\mathbf{z})^T = RSR^T$$

$S = \frac{1}{N} \sum_{n=1}^N (\mathbf{z})(\mathbf{z})^T$  is the covariance matrix of  $\mathbf{z}$ , using the property of trace of matrix?

$$tr(V(R\mathbf{z})) = tr(RSR^T) = tr(SR^T R) = tr(S) = tr(V(\mathbf{z})) = V_M$$

The procedure of fitting energy becomes:  $\mathbf{x} \rightarrow \mathbf{x}' \rightarrow \mathbf{z}_e \rightarrow \mathbf{z}_e' = (z_0', z_1')$ , then filling histograms to approximate  $P(\mathbf{z}_e'|E_e)$ . This discussion will be elaborated in next section 4.4.



## 4.4 Energy reconstruction results via applying PCA to data

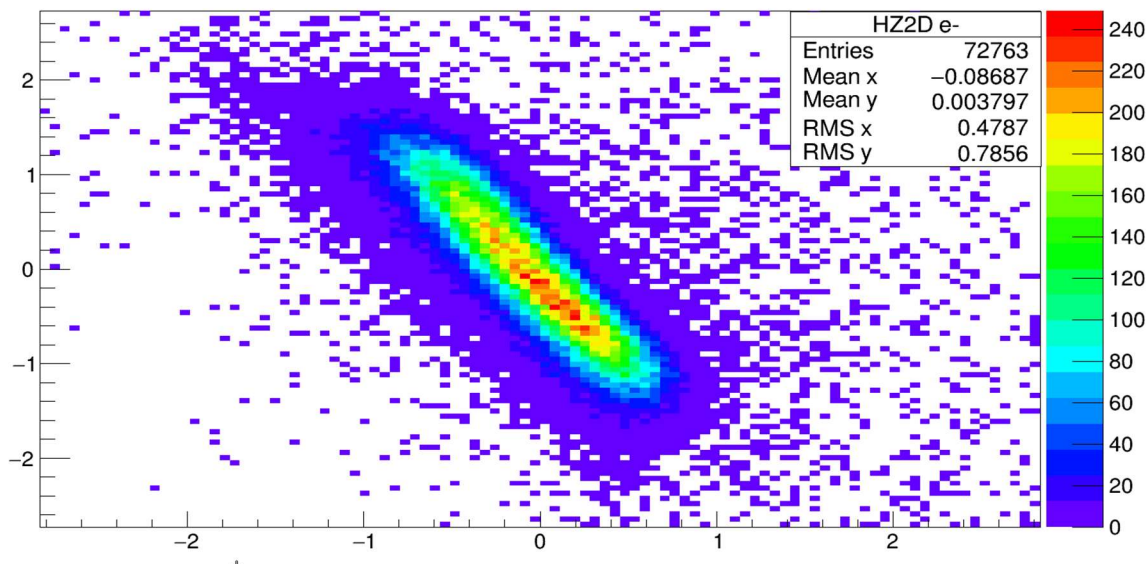
### 4.4.1 Additional rotation

Continuing the discussion in 4.3.3 3), we rotate  $\mathbf{z}_e$  by the rotation  $R$  which column vectors are eigen vectors of covariance matrix of  $\mathbf{z}_e = (z_{e0}, z_{e1})$  under conditional distribution  $P(z_{e0}, z_{e1} | 29\text{MeV} < E_e < 31\text{MeV})$ .

Convention of notation:

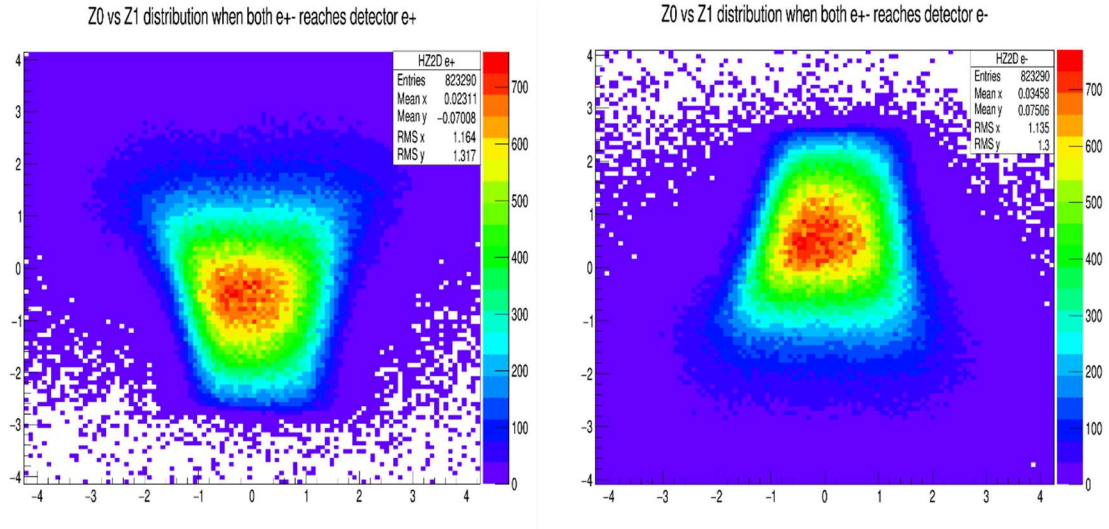
1. Since we are analyzing data after rotation  $R$  in this whole chapter, we drop ' from  $z_{e0}, z_{e1}$ ' to make formulas cleaner to read.
2. Since all algorithms applied to  $e^-$  is also applicable to  $e^+$ , thus if only discuss results on one side of the detectors, the subscript  $e$  or  $p$  is dropped.

Z0 vs Z1 distribution when both  $e^+$ - reaches detector  $e^-$



IV Fig 4. 10 Conditional distribution of  $e^-$   $P(z_0, z_1 | 29\text{MeV} < E < 31\text{MeV})$ . Ordinate:  $z_1$ , no unit, abscissa:  $z_0$ , no unit.

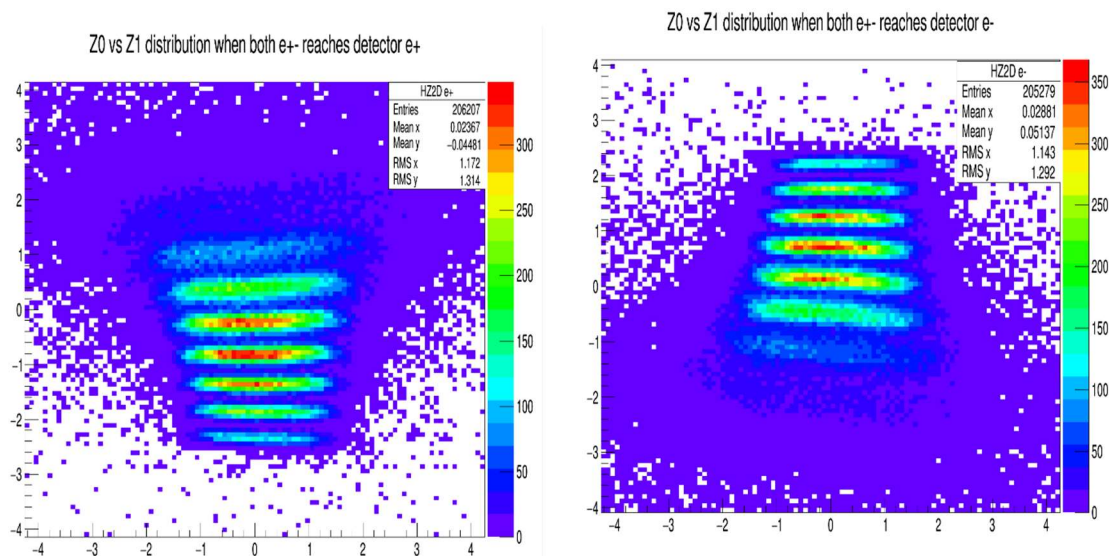




IV Fig 4. 11  $P(z_0, z_1)$ , after rotation  $R$ . Ordinate:  $z_1$ , no unit, abscissa:  $z_0$ , no unit.

Left e+ distribution, right e- distribution. Unit free.

Note: the rotation  $R$  for e+ and e- are different, since distribution  $P(z_{p0}, z_{p1} | 29\text{MeV} < E_p < 31\text{MeV})$  and  $P(z_{e0}, z_{e1} | 29\text{MeV} < E_e < 31\text{MeV})$  are different. Rotation matrices  $R$  are computed separately for different sides.



IV Fig 4. 12  $P(z_0, z_1 | E)$ , after rotation  $R$ , under energy  $E$  cut. Ordinate:  $z_1$ , no unit, abscissa:  $z_0$ , no unit.

Left figure e+ distribution under cut  $E_p \in ([10,11]\text{MeV}, [14,15]\text{MeV}, \dots)$ , right figure e- distribution  $E_e \in ([10,11]\text{MeV}, [14,15]\text{MeV}, \dots)$ . By checking figures above, it's easy to see:

1. The separation between  $(z_0, z_1)$  probability distributions under different energy cuts, thus the resulting  $P(E_e|z_{e0}, z_{e1})$  distribution computed from Bayes' theorem should also be well separated by different  $z_0, z_1$  value.
2. In addition, the energy  $E$  is majorly depended on coordinate  $z_1$ , and the dependence is monotonic. The lower the  $z_1$ , the higher the energy  $E$ .

#### 4.4.2 Analyzing and fitting $P(z_{e0}, z_{e1}|E_e)$

We want to apply following formula derived from Bayes' theorem (as a simpler version of (4.30)):

$$P(E_e|\mathbf{z}_e, \mathbf{z}_p) = \frac{P(\mathbf{z}_e|E_e)P(E_e)}{P(\mathbf{z}_e)} \frac{P(\mathbf{z}_p|E_p = E_\gamma - E_e)P(E_p = E_\gamma - E_e)}{P(\mathbf{z}_p)} \quad (4.33)$$

Here  $\mathbf{z}_{e/p} = (z_{e/p0}, z_{e/p1})$  are dimensionally reduced measured data by PCA. Find the energy  $E_e$  to maximize  $P(E_e|\mathbf{z}_e, \mathbf{z}_p)$  when the measurement on wire chamber correspond to  $\mathbf{z}_e, \mathbf{z}_p$ , and use it as input for Bethe-Heitler asymmetry computation.

For terms  $P(E)$  (c.f. convention of notation in 4.4.1,  $P(E)$  means either  $P(E_e)$  or  $P(E_p)$ ), they can be estimated by Geant 4 simulation. Applying BH pairs generated from theoretic calculation which has uncut energy distribution  $P'(E_e)$  and  $P'(E_p)$ , run the Geant 4 simulation, applying cut that requires both sides detectors having data  $\mathbf{x}_e, \mathbf{x}_p$  (and thus both  $\mathbf{z}_e, \mathbf{z}_p$  are measured) and corresponding  $E_e, E_p$  distribution are the terms  $P(E_e), P(E_p)$ . We already obtained the rotated post-PCA distributions  $P(\mathbf{z}|E)$  in last section, now fit each  $P(\mathbf{z}|E)$  then maximize (4.33).

Based on  $P(z_0, z_1|E)$  plots Fig 4.12, for single energy cut, the shape of the  $P(z_0, z_1|E)$  distribution is close to a strip parallel to  $z_0$  axis. If we make assumption  $P(z_0, z_1|E) \cong P(z_0|E)P(z_1|E)$  (c.f. (4.32) it means random variables  $z_0$  and  $z_1$  are conditional independent) and note that terms in denominator of (4.33) is independent of  $E_e$ . (4.33) is simplified to:

$$P(E_e|\mathbf{z}_e, \mathbf{z}_p) \propto P_e(z_{e0}|E_e)P_e(z_{e1}|E_e)P_e(E_e)P_p(z_{p0}|E_\gamma - E_e)P_p(z_{p1}|E_\gamma - E_e)P_p(E_\gamma - E_e) \quad (4.34)$$

All  $P(z_i|E)$  terms in (4.34) is then approximated by fitted functions  $F(z_i|E)$  and each function (specified by particle  $e^+$  or  $e^-$  and energy) has been represented by its entire fit parameters. Suffixes  $e$  and  $p$  are added in (4.34) since  $P_e$  are distribution for electrons, and  $P_p$  are distribution for positrons. The  $E_e$  which maximizes right side of (4.34) is the reconstructed energy.

Before applying (4.34) for the energy  $E_e$  reconstruction, we have terms on the right-hand side to be calculated:

(1)  $P_e(z_{e0}|E_e), P_e(z_{e1}|E_e), P_p(z_{p0}|E_p)P_p(z_{p1}|E_p)$  are represented by normalized fit function  $F(z_i|E)$ , for example  $P_e(z_{e0}|35MeV < E_e < 36MeV)$  will taken value  $F_e(z_{e0}; p_0, \dots, p_4)$ ,

where  $p_0, \dots, p_4$  are fit parameters for the function and all depend on the energy cut  $35MeV < E_e \leq 36MeV$ .

(2)  $P_e(E_e), P_p(E_p)$  are replaced by counts  $C_e(E_e), C_p(E_p)$ , instead of probability under the cut with the energy for reason will be discussed later, below Fig 4.14. Since,  $C_e(E_e) \propto P_e(E_e), C_p(E_p) \propto P_p(E_p)$  now maximizing right side of:

$$P(E_e | \mathbf{z}_e, \mathbf{z}_p) \propto P_e(z_{e0} | E_e) P_e(z_{e1} | E_e) C_e(E_e) P_p(z_{p0} | E_\gamma - E_e) P_p(z_{p1} | E_\gamma - E_e) C_p(E_\gamma - E_e) \quad (4.35)$$

will not change the value of reconstructed energy  $E_e$ . Procedure of computing (1), (2) are discussed below:

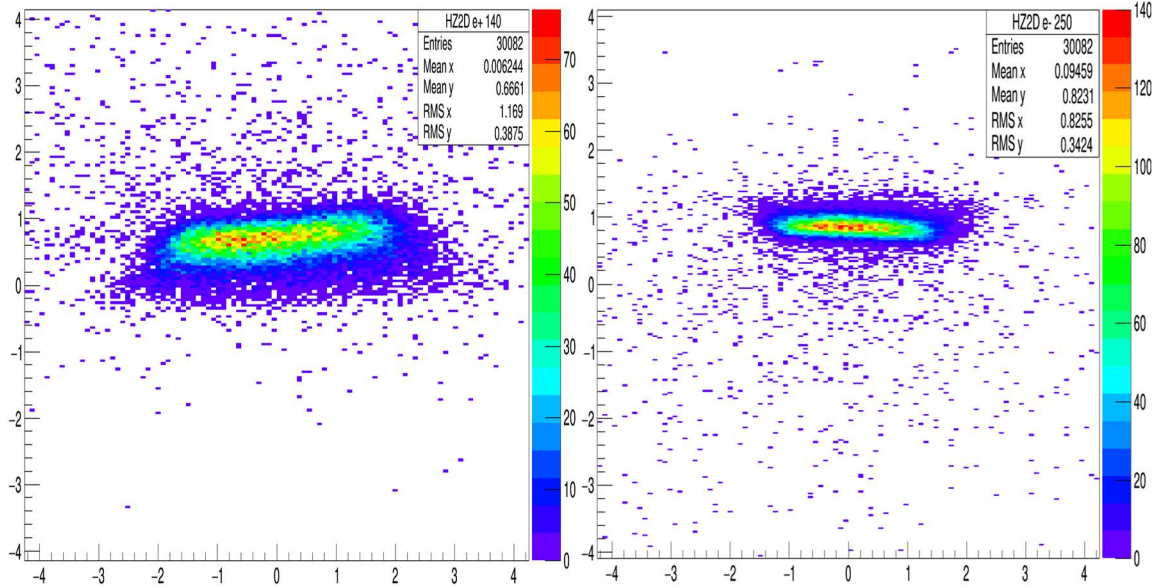
### 1) Finding $z_i$ bounds for each $E$ and particle type. Finding $C_e(E_e), C_p(E_p)$

For single energy cut, e.g.,  $35MeV < E \leq 36MeV$ , lower and upper bounds  $ZL$  and  $ZU$  for each component of  $\mathbf{z} = (z_0, z_1)$  in distribution  $P(\mathbf{z} | E) = P(z_0 | E) P(z_1 | E)$  are calculated. Reasons to apply bounds for  $z_i$  are:

- (1) Better and more believable fitting result, since most abnormal  $\mathbf{z}_e$  or  $\mathbf{z}_p$  data points are out of bounds and discarded.
- (2) Normalization result could be more accurate. Since bounded instead of unbounded range while computing normalization integration, divergent behavior can be avoided.
- (3) Faster energy reconstruction, since for a given  $\mathbf{z}_e$  data, only  $E_e$ s with associated  $\mathbf{z}_e$  bounds  $ZL_{e0}, ZU_{e0}$  and  $ZL_{e1}, ZU_{e1}$  satisfying  $ZL_{e0} \leq z_{e0} \leq ZU_{e0}$  and  $ZL_{e1} \leq z_{e1} \leq ZU_{e1}$  are the possible reconstruction energies.

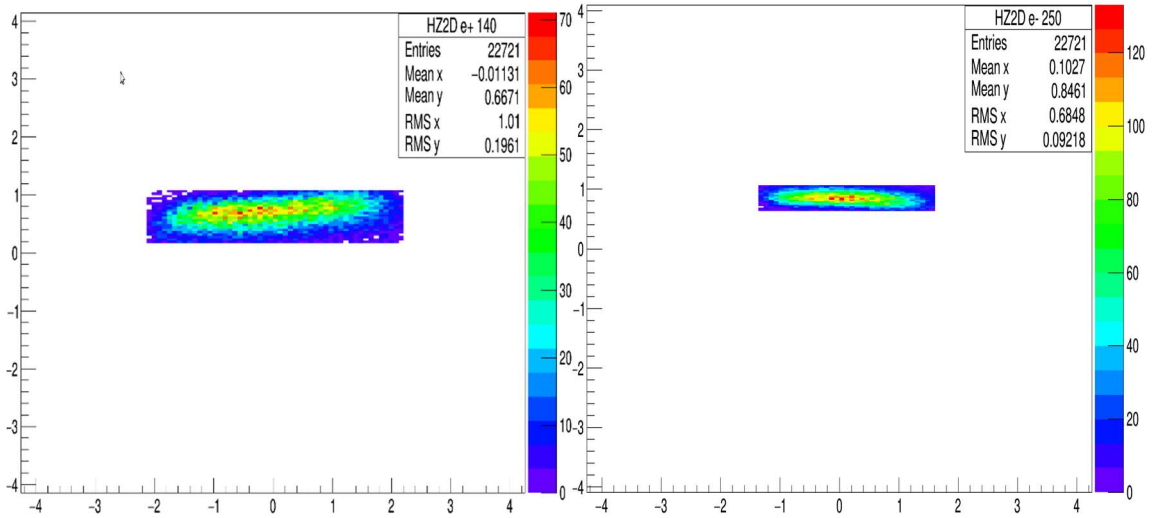
Bounds are determined as follow, for example:

- (1) For electron, under energy cut  $35MeV < E_e \leq 36MeV$ , reduced data  $\mathbf{z}_e$  are stored in histograms:  $H(z_{e0} | 35MeV < E_e \leq 36MeV, e^-)$  and  $H(z_{e1} | 35MeV < E_e \leq 36MeV, e^-)$  (these histograms can be simply denoted by  $H_0, H_1$ ).
- (2) Finding the bin with maximum number of counts for each histogram  $H_{0max}, H_{1max}$ , and bin indices.
- (3) Set a percentage limit  $\alpha$ , searching from the max valued bins  $H_{0max}, H_{1max}$  to left and right, the 1<sup>st</sup> bins reach value below  $\alpha H_{0max}$  or  $\alpha H_{1max}$  are bounds  $ZL_{e0}, ZU_{e0}$  and  $ZL_{e1}, ZU_{e1}$ .



IV Fig 4. 13  $(z_0, z_1)$  distribution under energy cut. Ordinate:  $z_1$ , no unit, abscissa:  $z_0$ , no unit.

Left figure plots positron, under cut  $24\text{MeV} < E_p \leq 25\text{MeV}$ , right for electron, under cut  $35\text{MeV} < E_e \leq 36\text{MeV}$ . Note both histograms have same number of entries, since for the specified cuts  $E_e + E_p = 60\text{MeV}$ .



IV Fig 4. 14  $(z_0, z_1)$  distribution under energy cut and cut  $(ZL_{e0} \leq z_{e0} \leq ZU_{e0}$  AND  $ZL_{e1} \leq z_{e1} \leq ZU_{e1}$  AND  $ZL_{p0} \leq z_{p0} \leq ZU_{p0}$  AND  $ZL_{p1} \leq z_{p1} \leq ZU_{p1})$ . Ordinate:  $z_1$ , no unit, abscissa:  $z_0$ , no unit.

AND inside () means logical AND, calling this cut as  $z$  cut. Left histogram is for positron,  $24\text{MeV} < E_p \leq 25\text{MeV}$ , right histogram for electron,  $35\text{MeV} < E_e \leq 36\text{MeV}$ .  $z$  cut is applied to both electron and positron side, while bounds  $ZL_{ei}, ZU_{ei}$  for electron is bound for

$35\text{MeV} < E_e \leq 36\text{MeV}$  and bounds  $ZL_{pi}, ZU_{pi}$  for electron is bound for  $24\text{MeV} < E_e \leq 35\text{MeV}$ . Note both histograms have same number of entries.

For these energy cuts,  $C_e(35\text{MeV} < E_e \leq 36\text{MeV}) = C_p(24\text{MeV} < E_e \leq 35\text{MeV}) = 22721$  in (4.35) are found by checking the entries of above histograms. The reason that counts instead of probability (to be precise, frequency) being stored is that there are overlaps in energy cuts during the whole tabulation of terms for formula (4.35): 1<sup>st</sup> cut  $10\text{MeV} < E_e \leq 11\text{MeV}$ , 2<sup>nd</sup> cut  $10.1\text{MeV} < E_e \leq 11.1\text{MeV}$  and so on. This procedure essentially improves the resolution of  $E_e$ , without the hassle of interpolation or fitting to find  $E_e$  maximizing the right-hand side of (4.35). Thus, the sum of counts from all energy cuts are mostly multi-counted, which prevents proper probability definition by dividing this sum.

## 2) Fit $P(z_i|E)$

Based on the shapes of  $P(z_0|E)$  and  $P(z_1|E)$  (Fig 4.15 4.6), following function forms are used in fitting:

$$P(z_0|E) \cong F(z_0|E) = p_0 \exp[-p_2(z_0 - p_1)^2 - p_3(z_0 - p_1)^2 - p_4(z_0 - p_1)^2] \quad (4.36)$$

$$P(z_1|E) \cong F(z_1|E) = p_0 \exp\left[-\frac{0.5(z_1 - p_1)^2}{p_2^2} - p_3(z_1 - p_1)^2\right] \quad (4.37)$$

For  $F(z_0|E)$ , 3<sup>rd</sup> order term reflects the asymmetry of the distribution, 4<sup>th</sup> order term deal with fast drop of probability on each side  $z_0$ . Choosing the same “most probable” location  $p_1$  for all orders to deal with overfitting. For  $F(z_1|E)$ , it’s very close to Gaussian with small asymmetry, thus 3<sup>rd</sup> order term is added.

The initial parameters are essential finding the correct fitting result and should be set. Finding those parameters are very situational, viable choices being used:

For  $F(z_0|E)$ , initial  $p_0 = 0.9H_{0max}$ , other parameters are using the result from previous  $E$  cut fitting result.

For  $F(z_1|E)$ ,  $p_0 = H_{1ma}$ ,  $p_1 = \{\text{bin center which correspond to } H_{1max}\}$ ,  $p_2 = \{\text{Root mean squared of histogram } H_1\}$ .  $p_1, p_2$  values are taken after histogram  $H_1$  removed data points outside the  $z$  cuts (as shown in Fig 4.14) since root mean squared are overestimated if those data points are kept in calculation.

Additional requirements for the fit functions  $F(z_i|E) \cong P(z_i|E)$ :

- (1) The  $P(z_i|E)$  with too small or large  $z$  values should not be fitted, since most of those  $z$  values are results from abnormal events, e.g., with large multiple scatter, and low counts (thus low error) of those data points will distort the shape of fit curve in  $z$  region we interested in. Thus, for each  $E$  and particle type, lower and higher bound of each  $z_i$   $ZL$  and  $ZU$  are used to limit  $z_{e0}, z_{e1}$  range need to be determined before fit.

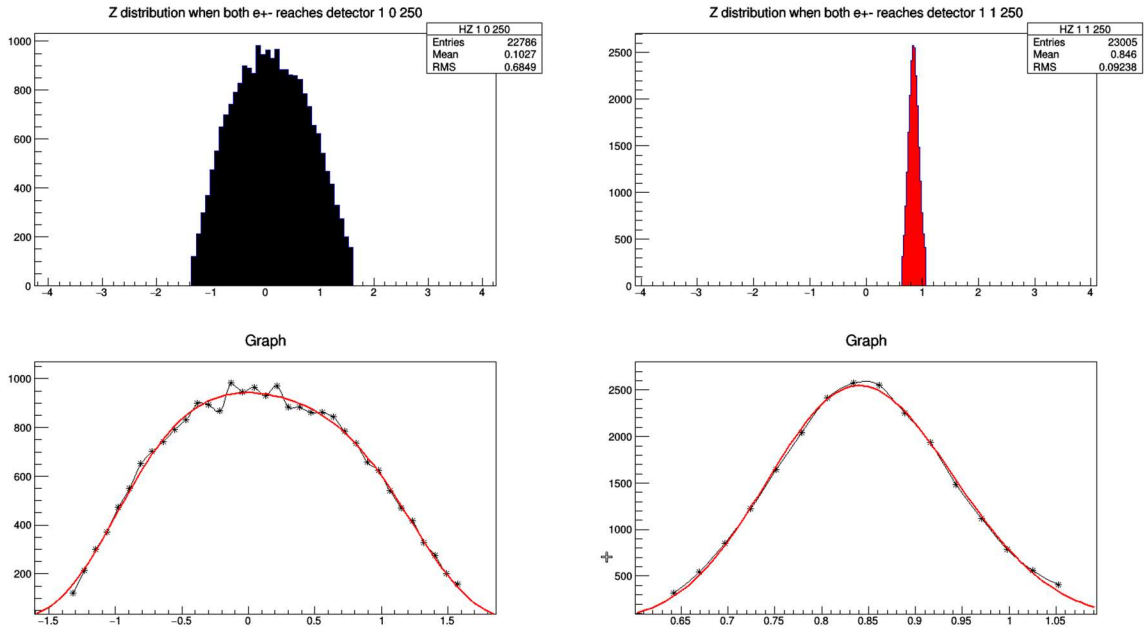
(2) The curves we fit is  $C(z_i|E)$ , thus additional normalization is needed. In addition, the difference between continuous function and discrete nature of numerical integration will appear in the normalization result. The normalization is conducted after initial fitting. The normalization condition is, while fixing all parameters except  $p_0$  :

$$1 = \int_{ZL_{ei}}^{ZH_{ei}} F(z_i|E) dz \cong \sum_{ZL_{ei} < z_i \leq ZH_{ei}} F(z_i|E) \Delta z_i \quad (4.38)$$

The sum is summing at bin centers of  $z_i$  only in range  $[ZL_{ei}, ZH_{ei}]$  of the histogram  $H_i$ , solving equation (4.38) will determine  $p_0$  in either (4.36) or (4.37).

Tabulated data file stores fit function data in such format (electron and positron data stored in separate file):

$E, p_0, \dots, p_4$  for  $F(z_0|E)$  and  $ZL_0, ZU_0, p_0, \dots, p_3$  for  $F(z_1|E)ZL_1, ZU_1$



IV Fig 4. 15 Electron's  $P(z_0|E)$  (upper left) and  $P(z_1|E)$  distribution (upper right), and fit function  $F(z_0|E)$  (lower left) and  $F(z_1|E)$  (lower right). Ordinate: count, no unit, abscissa:  $z_0$  for left figures  $z_1$  for right figures, no unit.

The energy cut is  $35MeV < E_e \leq 36MeV$ , the  $z$  cut  $ZL_{e0} \leq z_{e0} \leq ZU_{e0}$  and  $ZL_{e1} \leq z_{e1} \leq ZU_{e1}$  for this  $E_e$  cut range, and  $ZL_{p0} \leq z_{p0} \leq ZU_{p0}$  and  $ZL_{p1} \leq z_{p1} \leq ZU_{p1}$  for  $24MeV < E_p \leq 25MeV$  is applied. (Or the cuts are exactly the same as Fig 4.14) After this, normalization for both fits are conducted to find  $p_0$ .

### 4.4.3 Reconstruct energy $E_e$

Maximizing right hand side of equation (4.35):  $P(E_e | \mathbf{z}_e, \mathbf{z}_p) \propto$

$P_e(z_{e0} | E_e) P_e(z_{e1} | E_e) C_e(E_e) P_p(z_{p0} | E_\gamma - E_e) P_p(z_{p1} | E_\gamma - E_e) C_p(E_\gamma - E_e)$  to find reconstructed  $E_e$ . Procedure is below:

- (1) Convert detector measured data  $\mathbf{x}_e \rightarrow \mathbf{z}_e, \mathbf{x}_p \rightarrow \mathbf{z}_p$  ( $\mathbf{z}$  refer to dimension reduced data after additional rotation)
- (2) (c.f. 4.4.2 2)) Finding all possible  $E_e$  values.

Read the table storing electron fit function:

$E_e, p_0, \dots, p_4$  for  $F(z_{e0} | E_e)$  and  $ZL_{e0}, ZU_{e0}, p_0, \dots, p_3$  for  $F(z_{e1} | E_e) ZL_{e1}, ZU_{e1}$

Check if the data for the event  $(z_{e0}, z_{e1})$  satisfy  $ZL_{e0} \leq z_{e0} \leq ZU_{e0}$  and  $ZL_{e1} \leq z_{e1} \leq ZU_{e1}$  for the energy  $E_e$  in the current iteration (Note  $z$  lower and upper bounds  $ZL, ZU$  are energy dependent). If is, check positron fit function corresponding line satisfying condition  $E_p = E_\gamma - E_e$ :

$E_\gamma - E_e, p_0, \dots, p_4$  for  $F(z_{p0} | E_\gamma - E_e)$  and  $ZL_{e0}, ZU_{e0}, p_0, \dots, p_3$  for  $F(z_{p1} | E_\gamma - E_e) ZL_{p1}, ZU_{p1}$

Check if  $ZL_{p0} \leq z_{p0} \leq ZU_{p0}$  and  $ZL_{p1} \leq z_{p1} \leq ZU_{p1}$  is also satisfied. If is, this  $E_e$  is one of the possible values.

(3) Find  $E_e$  maximizing  $P'(E_e | \mathbf{z}_e, \mathbf{z}_p) =$

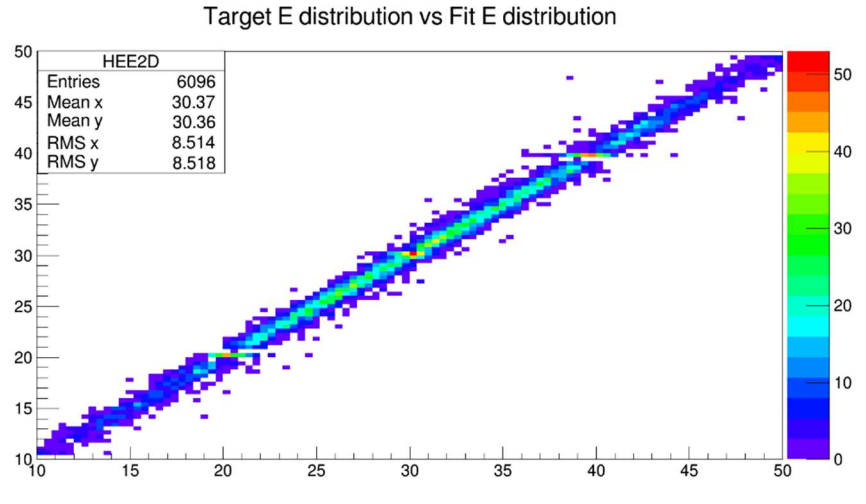
$P_e(z_{e0} | E_e) P_e(z_{e1} | E_e) C_e(E_e) P_p(z_{p0} | E_\gamma - E_e) P_p(z_{p1} | E_\gamma - E_e) C_p(E_\gamma - E_e)$ :

For each possible value of  $E_e$  found in (2). Retrieve  $C_e(E_e) = C_p(E_\gamma - E_e)$  from corresponding data file (last paragraph of 4.4.21), below Fig 4.14, described how  $C_e(E_e), C_p(E_\gamma - E_e)$  are found). And  $P_e(z_{e0} | E_e), P_e(z_{e1} | E_e), P_p(z_{p0} | E_\gamma - E_e), P_p(z_{p1} | E_\gamma - E_e)$  are calculated by replacing them by fit functions  $F_e(z_{e0} | E_e), F_e(z_{e1} | E_e), F_p(z_{p0} | E_\gamma - E_e), F_p(z_{p1} | E_\gamma - E_e)$  using the fit parameters in (2). Direct search within all the possible  $E_e$ s found in step (2) to find the  $E_e$  that maximize  $P'(E_e | \mathbf{z}_e, \mathbf{z}_p)$ .

Remarks:

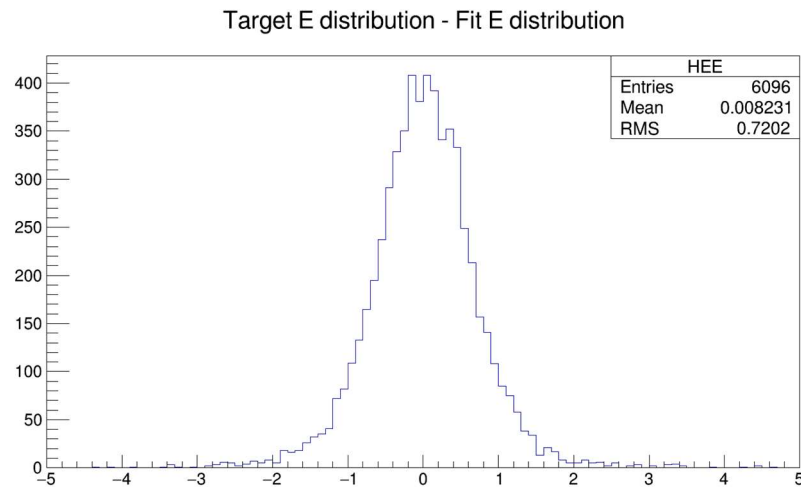
- (1) Above step (3) shows the benefits of overlapping  $E$  cut (e.g.  $35MeV < E_e \leq 36MeV$ , then next entry in data file stores  $35.1MeV < E_e \leq 36.1MeV$  in current setup) It makes a lot more possible  $E_e$  value satisfying cuts in step (2), thus much better energy resolution than storing data with not overlapped energy cut (e.g.  $35MeV < E_e \leq 36MeV$ , then next entry in data file stores  $36MeV < E_e \leq 37MeV$ ).
- (2) Another effect of overlapping  $E$  is more possible  $E_e$ , and thus more computation time of search, evaluating fit function values, and maximizing.

- (3) The efficiency (ratio of number of events with  $E_e$  reconstructed to total number of events) is affected by the choice of percentage limit  $\alpha$  determining  $ZL$  and  $ZU$ . The smaller the  $\alpha$ , the larger the range  $[ZL, ZU]$ , and more  $E_e$  values as candidates.



IV Fig 4. 16 Electron energy  $E_e$  at primary vertex (from generated pair data file as input for Geant4 simulation) vs reconstructed  $E_e$ . Ordinate: reconstructed  $E_e$  in  $MeV$ , abscissa: electron energy  $E_e$  at primary vertex in  $MeV$ .

This result is obtained by applying last page procedure. Using data from the same simulation data file as the plots in section 4.4.2, but only for 1<sup>st</sup> 10k events.



IV Fig 4. 17 Electron energy  $E_e$  at primary vertex (from generated pair data file as input for Geant4 simulation) minus reconstructed  $E_e$ . Ordinate: count, no unit, abscissa: difference between electron energy  $E_e$  at primary vertex and reconstructed  $E_e$ , in  $MeV$ .

Using data from the same simulation data file as the plots in section 4.4.2, but only for 1<sup>st</sup> 10k events. Thus, the energy reconstruction result has error about 0.7MeV by current fitting procedure. Multiple scattering and bending of magnet effects were taken into account.



## Part V Conclusion

Different aspects of the BH experiment have been prepared, besides scintillators all others are tested and experiment ready. Completed preparations are listed below:

For hardware, the photon beam is provided by HI $\gamma$ S at Duke Univ. The spectrometer we will use is constructed at Saskatchewan Accelerator Laboratory, and the field has been mapped at Jefferson Lab, while a tungsten cone shaped baffle is yet to be built for blocking small scattering angle pairs. Two pairs of vertical drift chambers from Q-weak experiment will be used to detect BH pairs' track out of magnet. The data acquisition code is provided by Brad Sawatzky at JLAB. Discriminator cards are installed, gas and voltage supplies for the chambers are provided, and scintillators has setup as telescope trigger for cosmic ray test runs. Efficiency plateaus of high voltage and threshold voltage are measured. The drift time data for track reconstruction were analyzed using modified JLAB Hall A analyzer. We have the scintillators, but need PMTs and light guide to prepare hodoscopes for the experiment.

JLAB Hall A analyzer wire chamber classes are used for track reconstruction from wire chamber drift time data. Database file entries are modified mainly for our wire chamber geometry, parameters of drift process, and channel mapping. Two most important sets of parameters: TDC time offset and time to distance conversion parameters are refitted based on the test run data. The analyzer track results are compared with the geometry constraints from the scintillator telescope setup of the test runs for single track events, resulting phase space region are matched with a simple simulation based on the trigger geometry. The track reconstruction efficiency is calculated for these geometrically constraint events, including multi-track events the efficiency is about 80%, different gas mixture will be used to achieve higher efficiency for the experiment. Misc. topics like track reconstruction resolution and effect of bad wire are also investigated.

For simulation, the theorists provided the program for numerical differential cross section calculation of BH process. A Monte-Carlo simulation written by Rob Pywell is used to generate BH pairs as primary particles for Geant 4 simulation. Since the differential cross section has very sensitive dependence on energy and directions, efficiency of pair generation is very low and modifications are made to improve about 20 times in rate. Units of the cross-section code are confirmed by comparing numerically integrated total cross section and standard values. In addition, data rate at detectors in real experiment is estimated by considering beam rate, (calculated) cross section at front window and detector acceptance.

The Geant 4 simulation has been setup for the geometry of the experiment. Distributions of variables in phase space are obtained at each (sensitive) detectors. The charge asymmetries as function of energy difference are computed through binning, from pairs within detector acceptance, with close polar angles, near 180° difference between azimuthal angles. The asymmetry with polar angle around 5° to 8°, energy difference ~9MeV to 15MeV is above 10%. Following investigations are conducted: (1) Effect of placing a tungsten cone baffle inside the magnet at beam line, which is used for blocking high rate BH pairs at small polar angle, along with other constraints affecting acceptance. (2) Resolution, accuracy and efficiency of track reconstruction. (3) Optimization of magnetic field strength and placement of wire chambers in order to balance multiple scattering effect on BH pairs with different energies. A simple but much

faster simulation with the same geometry setup as Geant 4, with approximation of vacuum as background and uniform circle shaped magnetic field was written for crosscheck of the Geant 4 results.

The main goal of Geant 4 simulation is to reconstruct the kinematics of BH pairs at primary vertices by detector data, Bayes' theorem is applied. Due to the high dimensions of detector data (4 for each side representing position and direction, dimension of 8 in total), principal component analysis is used to reduce dimension of the data by half. With the help of assuming conditional independence of the other dimensions at primary vertex to simplify calculation, the reduced data has good energy resolution and the difference between reconstructed energy and initial energy has near 0 MeV mean, and 0.7 MeV standard deviation.

## Appendices

### Part III Appendix A 4.3.1 Determine number of divisions for each iteration

Once all the data from a test run has been fixed, each drift distance  $d$  is dependent on parameter  $C$  in (4.5), and the statistics of  $d$  are also  $C$  dependent. We devised an algorithm to find minimum of single variable function below:

1. Assumption: The function is convex and continuous, thus having only one minimum.
2. Algorithm:

1) Assume we locate the upper and lower bound for each iteration, divide the interval of minimum searching into  $2n$  equal divisions. Compute the function value at end points of each division  $f(x_0), f(x_1), \dots, f(x_{2n})$ . Here we don't have to compute all values, the search of current sets of divisions will end when:

$$f(x_i) \geq f(x_{i+1}) \text{ and } f(x_{i+2}) \geq f(x_{i+1}) \quad (1)$$

2) Since the function can only have one minimum, then the minimum point of the function  $g$  (below) will lie in interval  $[x_i, x_{i+2}]$ . We choose the new interval  $[x_i, x_{i+2}]$  above, divide it again into into  $2n$  equal divisions, and search for the numerical solution of the minimum. Thus after each iteration, the interval size for the solution is shrunk into  $1/n$  of previous iteration.

3. Find optimum number of divisions  $n$ :

- 1) Assuming on average we can find end points  $x_i, x_{i+1}, x_{i+2}$  after  $n + 1$  function evaluations out of  $2n + 1$  that satisfies inequality (1).
- 2) After  $N(n + 1)$  evaluation, the interval will shrink to  $(\frac{1}{n})^N$  of initial size. Thus, the rate of convergence (average shrink in interval over number of function evaluation) is:

$$3) g(n; N) = \frac{(\frac{1}{n})^N}{N(n+1)} \quad (2)$$

4) We want to minimize expression (2) which means faster rate of convergence. For convenience now we treat number  $n$  and  $N$  as real number, and thus  $f(n; N)$  is a continuous function.

5) The function  $f(n; N)$  is of two variables. We change variable  $N$  into  $\varepsilon = (\frac{1}{n})^N$ , here  $\varepsilon$  is a small fixed number that is the ratio between the length final interval and initial interval, which depends on the final precision we want to achieve.

$$6) N = -\ln \varepsilon / \ln n$$

$$7) g(n; N) = \frac{(\frac{1}{n})^N}{N(n+1)} = -\frac{\varepsilon}{\ln} \cdot \frac{\ln n}{(n+1)} \quad (3)$$

8) Take derivative and minimize (3), the result is:

$$n = \frac{1}{W(\frac{1}{e})} \approx 3.59 \quad (4)$$

where  $W$  is product log function. We revert  $n$  to an integer, set  $n = 4$ , and  $2n = 8$  is number of divisions for each iteration.

## Part III Appendix A 4.6 Quick sort algorithm

### A 4.6.1 Introduction

As introduced in Section 4.6.3, given a drift time distribution, we want to find a sequence of times  $t_0, t_1, t_2, \dots, t_n$  that have equal integration values:

$$\int_{t_0}^{t_1} f(t)dt = \dots = \int_{t_{i+1}}^{t_i} f(t)dt = \dots = \int_{t_{n-1}}^{t_n} f(t)dt.$$

Note that  $\text{Prob}(t_i < t < t_{i+1}) = \int_{t_{i+1}}^{t_i} f(t)dt$ , which will be proportional to the counts from the drift time histogram within interval  $[t_i, t_{i+1}]$ . For example, for certain numbers of events, we measured 1 million drift times. If then we divide the distribution into  $n = 100$  equal sets of counts with the last drift time in each identified as  $t_i$ , it forms a sequence  $t_0 < t_1 < t_2, \dots < t_{100}$ , and for the  $i$  th set the time data  $t$  satisfies  $t_i \leq t \leq t_{i+1}$ . In order words, the time sequence  $t_0, t_1, t_2, \dots, t_n$  is the  $\frac{10^6}{100} = 10000^{th}$  smallest time and  $10^6 \times \left(\frac{2}{100}\right) = 20,000^{th}$  smallest time .... A good analogy is finding median of a set of data which in this example is  $\frac{10^6}{2} = 500,000^{th}$  smallest number in the time data set, but here it is arbitrary rather than the midpoint of the bin. Thus, the question is about *specifying an index, and find corresponding value in a set of data*.

Although the ordinary sorting algorithm can fill the role of finding the time sequence required, it's too time consuming based on the number of comparisons needed to be conducted for a large number of time data. For example, in Fig. 4.20 there're about 4.69 million drift time data in the wire plane  $u_1$  for this test run. On the other hand, the quick sort algorithm does not require the sorting of numbers within each subset, which greatly improve the efficiency.

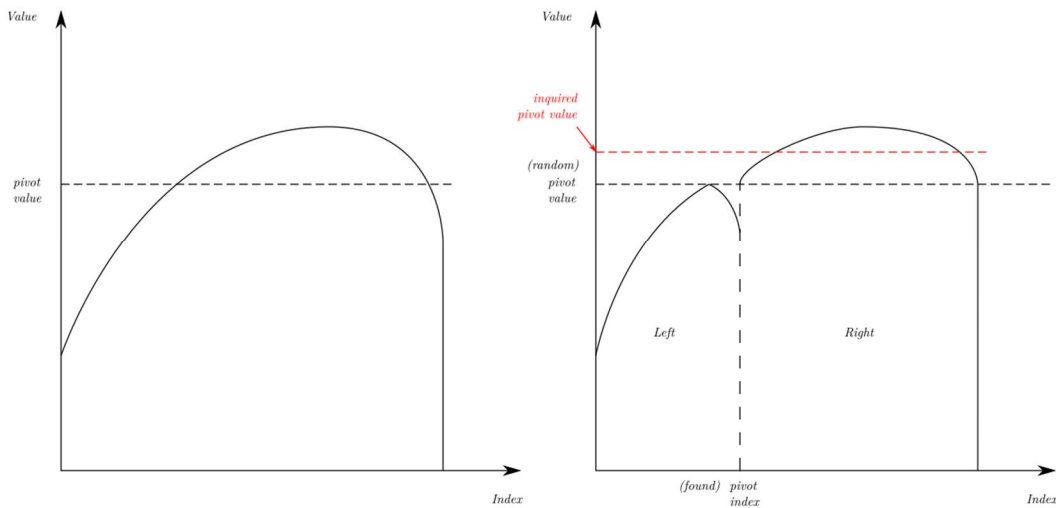
### A 4.6.2 The algorithm

The goal of the algorithm is to find the pivot value corresponding to the pivot index (the index of order of the pivot value, counting from smallest value in the set) from a data set. The scheme we applied here is attributed to Nico Lomuto, in his book *Programming Pearls*. [61] It includes two steps: 1) Find the pivot index corresponding to a pivot value. 2) Use recursion of the 1<sup>st</sup> function to find pivot value corresponding to the pivot index.

Step 1): (1) Iterate through all data in the data set, if the value from data is less than the pivot value, the index count is increased by 1. (2) In addition, all numbers less than the pivot value are stored in "left" set, the rest are stored in the "right" set. (3) The final index count after iterating through all data is the pivot index corresponding to the specified value.

Step 2): (1) Randomly pick a value from the data set, use function 1) to find its pivot index. (2) If the found index is less than the inquired pivot index, search in "right" set. If found index is equal to the inquired pivot index, the pivot value is found and end the recursion. If the found index is larger than the inquired pivot index, search the "left" set.

A simple graphic illustration below shows the algorithm. Fig 4.24.



III Fig 4. 24 Quick sort algorithm

Illustration of function 1).

Left illustration: a set of data is represented by a curve before quick sorting, with the abscissa being index of data set, and the ordinate being values of each datum. A horizontal dashed line shows the pivot value. Right illustration: after quick sorting by step 1) the original data set has been separated by the pivot index into a “Left” set and a “Right” set, with all values in the left set less than pivot value, and vice versa for the right set. The difference to ordinary sorting algorithm is that the quick sort didn’t sort numbers inside Left set and Right set. There is also a hint for the step 2). If we generated a random pivot value, then found its pivot index and the found pivot index (Right illustration) is less than inquired pivot index, it indicates that the random pivot value is also less than the inquired pivot value. This means we should search for the inquired pivot value in the Right set.

### Part III Appendix A5.2.1 Track reconstruction derivation from geometry point of view

The track propagates through all 4 wire planes and has a set of coordinates  $(u_1, v_1, u_2, v_2)$  on each wire plane. In order to reconstruct the track, we investigate the measurements of  $u_1, v_1, u_2, v_2$ . The measurement  $u_1, u_2$  indicates that the track is inside the plane containing a straight line, parallel to  $u$  wires with coordinate  $u_1$  in  $u_1$  plane and another straight line, parallel to  $u$  wires with coordinate  $u_2$  in  $u_2$  plane. The same argument also applies to measurement  $v_1, v_2$ . Thus, we have two planes containing the track, so the track must be the intersection of two planes. We only need to solve two linear equations to find the track as intersection of these two planes. First, from the standard plane equation:

$$\hat{n} \cdot \mathbf{r} = \hat{n} \cdot \mathbf{r}_0 \quad (1)$$

Where  $\hat{n}$  is the unit vector normal to the plane,  $\mathbf{r} = (x, y, z)$  is an arbitrary point on the plane,  $\mathbf{r}_0$  is a fixed point in the plane. For the plane contains straight lines parallel to  $u$  wires with  $u_1, u_2$  coordinate and the plane contains straight lines parallel to  $v$  wires with  $v_1, v_2$  coordinate respectively, normal vector

$$\begin{aligned} \hat{n}_u &= (\sin(\alpha_u)\hat{u} + \cos(\alpha_u)\hat{z}) \times (\hat{u} \times \hat{z}) \\ &= (\cos(\alpha_u)\hat{u} - \sin(\alpha_u)\hat{z}) = (\cos(\alpha_u)\cos\alpha, \cos(\alpha_u)\sin\alpha, -\sin(\alpha_u)) \end{aligned} \quad (2)$$

$$\begin{aligned} \hat{n}_v &= (\sin(\alpha_v)\hat{v} + \cos(\alpha_v)\hat{z}) \times (\hat{v} \times \hat{z}) \\ &= (\cos(\alpha_v)\hat{v} - \sin(\alpha_v)\hat{z}) = (\cos(\alpha_v)\cos\alpha, -\cos(\alpha_v)\sin\alpha, -\sin(\alpha_v)) \end{aligned} \quad (3)$$

Here  $(\hat{u} \times \hat{z})$  is unit vector parallel to wires,  $\sin(\alpha_u)\hat{u} + \cos(\alpha_u)\hat{z}$  is unit vector perpendicular to wires inside these planes. The last equation in each line uses  $\hat{u} = (\cos\alpha, \sin\alpha, 0)$ ,  $\hat{v} = (\cos\alpha, -\sin\alpha, 0)$ , and  $\hat{z} = (0, 0, 1)$ .

Next we find fixed points  $\mathbf{r}_{0u}$  and  $\mathbf{r}_{0v}$ . We choose  $\mathbf{r}_{0u}$  as the point inside the  $u_1$  plane with coordinate  $u_1$ , on  $u$  axis:

$$\mathbf{r}_{0u} = u_1\hat{u} \quad (4)$$

$$\mathbf{r}_{0v} = v_1\hat{v} + d_{uv}\hat{z} \quad (5)$$

Similarly, for  $\mathbf{r}_{0v}$  as  $\mathbf{r}_{0u}$ , but note  $v_1$  is distance  $d_{uv}$  above  $u_1$  plane. Combining eqs. 2-5:

$$\hat{n}_u \cdot \mathbf{r}_{0u} = u_1\cos(\alpha_u) \quad (6)$$

$$\hat{n}_v \cdot \mathbf{r}_{0v} = v_1\cos(\alpha_v) - d_{uv}\sin\alpha_v \quad (7)$$

Replacing the terms in (1) by eqs. 2, 3, 6, 7, the equation to solve the track as intersection of two planes is:

$$\begin{pmatrix} \cos(\alpha_u)\cos\alpha & \cos(\alpha_u)\sin\alpha & -\sin(\alpha_u) \\ \cos(\alpha_v)\cos\alpha & -\cos(\alpha_v)\sin\alpha & -\sin(\alpha_v) \end{pmatrix} \begin{pmatrix} x \\ y \\ z \end{pmatrix} = \begin{pmatrix} u_1\cos(\alpha_u) \\ v_1\cos(\alpha_v) - d_{uv}\sin(\alpha_v) \end{pmatrix} \quad (8)$$

The solution for the homogenous equation is:

$$\mathbf{t} = \begin{pmatrix} \frac{1}{2\cos\alpha} (\tan(\alpha_u) + \tan(\alpha_v)) \\ \frac{1}{2\sin\alpha} (\tan(\alpha_u) - \tan(\alpha_v)) \\ 1 \end{pmatrix} = \begin{pmatrix} \tan\theta \\ \tan\varphi \\ 1 \end{pmatrix} \quad (9)$$

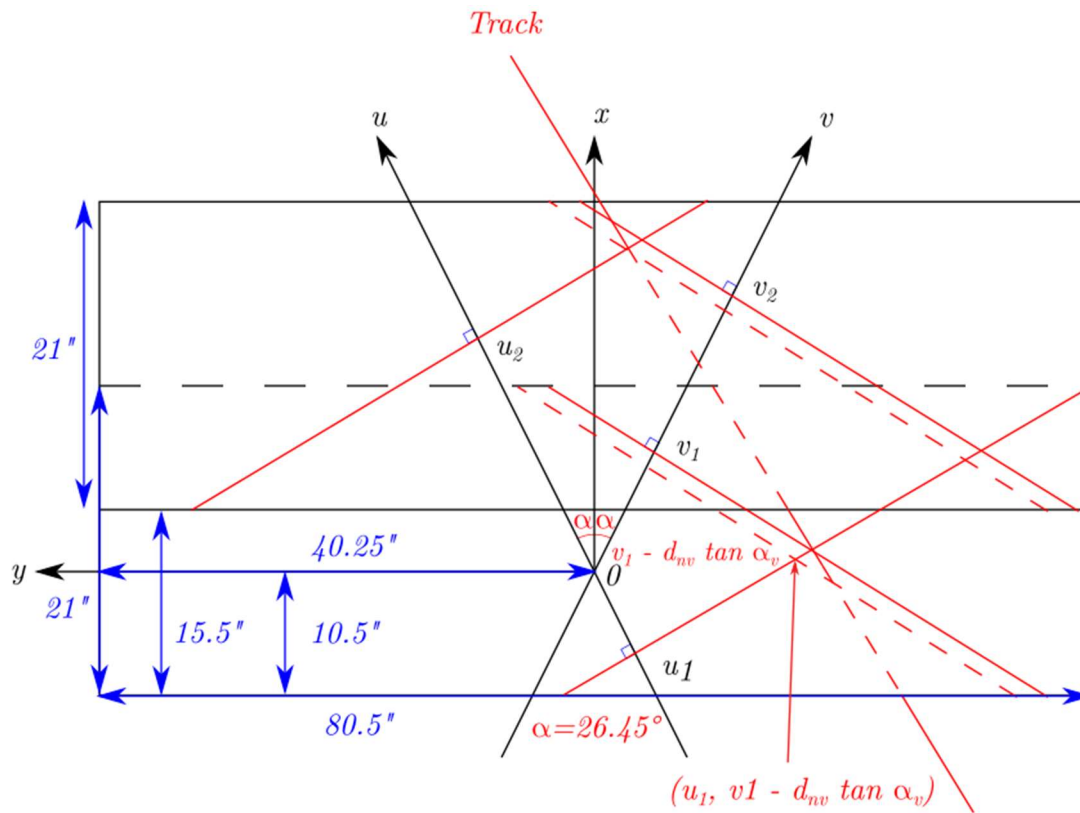
$\mathbf{t}$  is the track direction vector, and  $\tan\theta, \tan\varphi$  the same as (5.3) and (5.4). The special solution in the  $u_1$  plane (by set  $z = 0$  in equation (8)) is:

$$\begin{pmatrix} x \\ y \\ z \end{pmatrix} = \begin{pmatrix} \frac{1}{2\cos\alpha} (u + v) \\ \frac{1}{2\sin\alpha} (u - v) \\ 0 \end{pmatrix} \quad (10)$$

where  $u = u_1$ ,  $v = v_1 - d_{uv} \tan(\alpha_v)$  (see (5.7) and (5.8)) is the  $uv$  coordinate of the track intersection in  $u_1$  plane. Thus, the track info  $(x, y, \tan\theta, \tan\varphi)$  to be stored in ROOT file is calculated from (9) and (10). Remark: It's also easy to check that  $\mathbf{t}$  can be derived from normalizing z-component of

$$\hat{n}_u \times \hat{n}_v = \begin{pmatrix} -\sin(\alpha_u + \alpha_v) \sin\alpha, \\ -\sin(\alpha_u - \alpha_v) \cos\alpha, \\ -2\cos\alpha_u \cos\alpha_v \sin\alpha \cos\alpha \end{pmatrix} \quad (11)$$

to 1. It is easy to understand since  $\hat{n}_u \times \hat{n}_v$  is the only vector parallel to both planes under consideration (it's perpendicular to both  $\hat{n}_u$  and  $\hat{n}_v$ ). The illustration of the geometry is in Fig. 5.1.



III Fig 5. 30  $xy$  projection illustration of track reconstruction.

All notations comply with Appendix 5.5.1. The upper solid black-line rectangle represents the active area of wire planes in the upper chamber, and the lower black half-dash half-solid line rectangle represents the active area of the wire planes in the lower chamber. The track can be computed from the fact that it's the intersection of two planes, one through both  $u_1, u_2$  lines (in the  $u_1, u_2$  planes respectively, parallel to the  $u$  wires), and the other through both  $v_1, v_2$  lines as marked with red solid lines.

### Part III Appendix A5.2.2 Calculation of track $(x, y, \tan\theta, \tan\varphi)$ from crossover point coordinates $(u_1, v_1, u_2, v_2)$ .

Once we fit the associated clusters of each wire plane, we acquire a fit crossover point with coordinates  $(u_1, v_1, u_2, v_2)$ . The track should be represented in a more explicit form  $(x, y, \tan\theta, \tan\varphi)$ , but here  $(x, y)$  is the  $x, y$  coordinate of crossover points in the lowest wire plane  $u_1$ , and  $\vec{t} = (\tan\theta, \tan\varphi, 1)$  is the direction vector of the track in the analyzer coordinate system. Since  $u_1, v_1$  and  $u_2, v_2$  are not simply coplanar, we will establish a set of linear equations that solve  $(x, y, \tan\theta, \tan\varphi)$  from  $(u_1, v_1, u_2, v_2)$  below:

1. Geometry: the track is represented by a parameterized straight line, as do all 4 lines parallel to wire in each wire plane through each crossover point. Noting the track will intersect all 4 lines, this gives 4 equations to solve 4 coordinates  $x, y, \tan\theta, \tan\varphi$ . The track is represented by parameter  $p$ :

$$p\vec{t} + \vec{r} \quad (1)$$

Where  $\vec{t} = (\tan\theta, \tan\varphi, 1)$  is track direction vector, and  $\vec{r} = (x, y, 0)$  is the intersection of track and bottom most wire plane.

For A point on intersected line through crossover points and parallel to wires of  $i$ th wire plane can be represented by:

$$t_i\hat{w}_i + \vec{r}_i \quad (2)$$

where  $\hat{w}_i$  is the unit vector with direction parallel to wire direction of  $i$ th wire plane.

$$\hat{w}_i = \hat{u} = (\cos\alpha, \sin\alpha, 0) \text{ for } i = 0, 2 \text{ (u wire planes)} \quad (3)$$

$$\hat{w}_i = \hat{v} = (\cos\alpha, -\sin\alpha, 0) \text{ for } i = 1, 3 \text{ (v wire planes)} \quad (4)$$

$t_i$  is the parameter of the line,  $\vec{r}_i$  is any point on the intersected line through crossover point. The most convenient representation is:

$$\vec{r}_i = \vec{z}_i + \left(\frac{N-1}{2} - n_i\right)\vec{s}_i \quad (5)$$

where  $\vec{z}_i = (0, 0, z_i)$  indicates distance of the wire plane to bottommost wire plane,  $z_i = 0, 2.54 \text{ cm}, 39.4 \text{ cm}, 41.9 \text{ cm}$ , respectively,  $N = 279$  is total number of wires in each wire plane,  $\frac{(N-1)}{2}\vec{s}_i = 139\vec{s}_i$  is the location of wire with index 0 in each wire plane,  $\vec{s}_i = s\hat{w}_i$ ,  $s$  is the wire spacing,  $n_i$  is the fit crossover point wire index (see equation (3.4))

2) Equations to solve:

$\frac{(\vec{t} \times \hat{w}_i)}{|\vec{t} \times \hat{w}_i|}$  is the unit vector perpendicular to both track direction  $\vec{t}$  and wire direction  $\hat{w}_i$ , so the

distance between line  $p\vec{t} + \vec{r}$  and  $t_i\hat{w}_i + \vec{r}_i$  is:

$$\left| \frac{(\vec{t} \times \hat{w}_i)}{|\vec{t} \times \hat{w}_i|} \cdot (\vec{r} - \vec{r}_i) \right| \quad (6)$$

For  $i = 0, 1, 2, 3$ , the four wire planes from bottom to top, the distances are 0; or in other words the following three vectors  $\vec{t}, \hat{w}_i, \vec{r} - \vec{r}_i$  are coplanar. This gives 4 equations:

$$(\vec{t} \times \hat{w}_i) \cdot (\vec{r} - \vec{r}_i) = 0 \quad (7)$$

If indexing the 4 wire planes from bottom to top as  $i = 0, 1, 2, 3$ , then the equations are:

$$\begin{aligned} \cos\alpha(x - x_i) + (-1)^i \sin\alpha(y - y_i) \\ + (\cos\alpha \cdot \tan\theta + (-1)^i \sin\alpha \cdot \tan\varphi)z_i = 0 \end{aligned} \quad (8)$$

$$(x_i, y_i) = (\cos\alpha, \sin\alpha)w_i \quad (9)$$

where  $\vec{r}_i = (x_i, y_i, z_i)$  is the selected location of  $n_i$  th wire on  $i$ th wire plane in equation (5). And  $(w_0, w_1, w_2, w_3) = (u_1, v_1, u_2, v_2)$ .



Thus, 4 unknowns  $x, y, \tan\theta, \tan\varphi$  will be uniquely determined by these 4 simultaneous linear equations with known local cluster fit results  $n_i$ .

3) Summarized procedure:

- (1) Determine crossover point wire index  $n_i$  of each wire plane from cluster fitting. (see formulas (3.1) and (3.4))
- (2) Compute  $w_i = \left(\frac{N-1}{2} - n_i\right) \cdot s$  in equations (8) and (9).
- (3) Solve 4 simultaneous linear equations to determine  $(x, y, \tan\theta, \tan\varphi)$ .

It is expected that the solution  $(x, y, \tan\theta, \tan\varphi)$  should be the same as the one from Appendix A5.2.1 (9)(10).

## Part III Appendix A1 Angles in track reconstruction

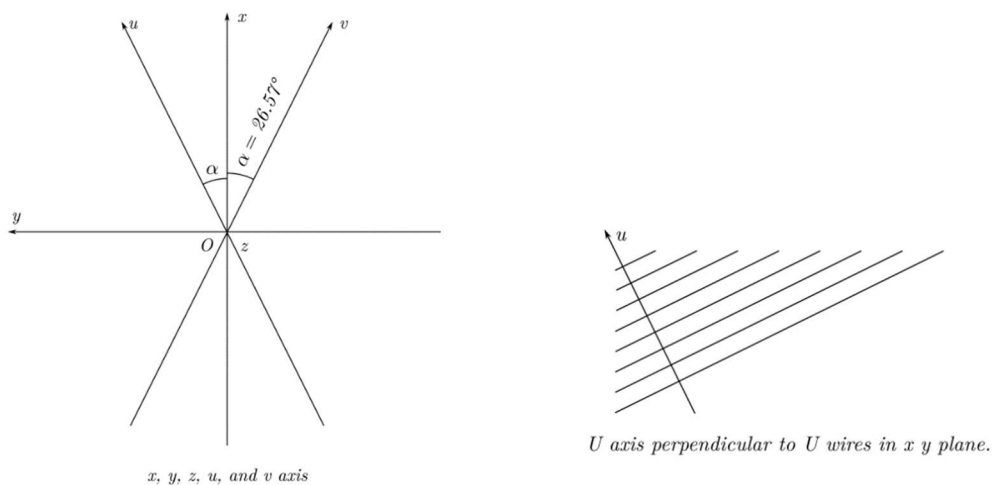
### A1.1 Coordinate system used in Hall A analyzer

#### Coordinate axes (Fig A1.1):

The  $XY$  plane is parallel to the wire planes. The  $X$ -axis is parallel to the short axis of the wire chamber; in a top view it is pointed from the center of the bottom wire chamber to the center of the top chamber. (In the HRS setup  $X$  is the primary dispersion axis of the wire chamber, but in the BH experiment the  $Y$  axis is the primary dispersion axis. However, since in the HRS setup the pair of wire chambers are also parallel, with a shift along  $X$  axis, our coordinate system matches in this way.) The  $Z$  axis is perpendicular to wire planes pointing from bottom to top. The  $Y$  axis makes the coordinate system right-handed.

#### Wire axes (Fig A1.2):

Wire axes  $U, V$  are inside wire planes and perpendicular to wires in the corresponding wire plane (i.e.  $U/V$  axis perpendicular to  $U/V$  wires). Their positive direction is chosen such that the acute angle is between  $U$  (or  $V$ ) axis to both  $X$  axis and  $Y$  axis.



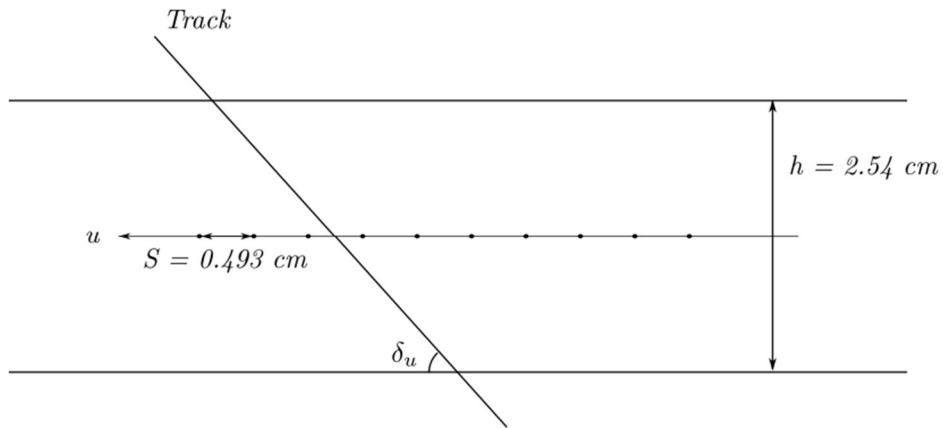
III Fig A1. 1 (Left)  $x, y, z, u, \text{ and } v$  axis.

The angle between  $u, v$  to the axis is  $\alpha = 26.57^\circ = \arctan(0.5)$ . In the database file the wire angle for the  $u$  plane is  $26.57^\circ$  and for the  $v$  plane is  $-26.57^\circ$  since the positive direction of increasing angle is counter-clockwise from  $x$ -axis.

III Fig A1. 2 (Right) Direction relation between  $u$  axis and  $u$  wires.

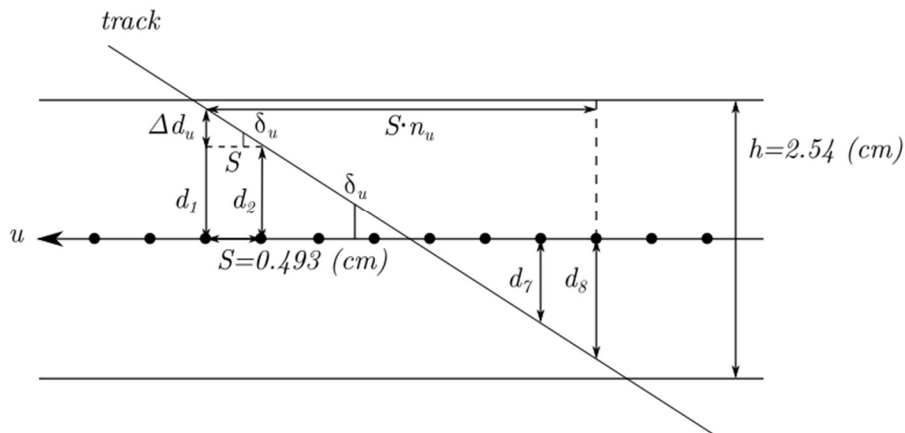
They're perpendicular to each other.

A1.2 Definitions of angles related to track reconstruction.



In projection plane  $UZ$ , define  $\delta_u$ , wire spacing  $S$  and wire plane height  $h$ .

III Fig A1. 3 Definition of  $\delta_u$  or  $\delta_v$ .



III Fig A1. 4 Relation between drift distance  $\Delta d$  and track projection angle  $\delta_u$ .  
 u plane has shown and  $\Delta d$  is suffixed as  $\Delta d_u$ .

### A1.3 Deriving relation from $(\theta, \varphi)$ to $(\delta_u, \delta_v)$ .

We directly compute  $(\delta_u, \delta_v)$  in terms of  $(\theta, \varphi)$  from their definitions in A1.2: (Fig. A1.5 shows all vectors)

The track direction is represented by the vector  $\vec{t} = (\tan\theta, \tan\varphi, 1)$ , and  $\delta_u$  or  $\delta_v$  can be computed by  $\cos(\delta_u) = \frac{\vec{t}_{u\parallel} \cdot \hat{u}}{|\vec{t}_{u\parallel}| \cdot |\hat{u}|}$  and  $\cos(\delta_v) = \frac{\vec{t}_{v\parallel} \cdot \hat{v}}{|\vec{t}_{v\parallel}| \cdot |\hat{v}|}$ . Here  $\vec{t}_{u\parallel}$  is the parallel component of  $\vec{t}$  in the  $uz$  plane, if we also define  $\vec{t}_{u\perp}$  as the component of  $\vec{t}$  that is orthogonal to  $uz$  plane. Then we can simplify the equation by:

$$\cos(\delta_u) = \frac{\vec{t}_{u\parallel} \cdot \hat{u}}{|\vec{t}_{u\parallel}| \cdot |\hat{u}|} = \frac{(\vec{t}_{u\parallel} + \vec{t}_{u\perp}) \cdot \hat{u}}{|\vec{t}_{u\parallel}|} = \frac{\vec{t} \cdot \hat{u}}{|\vec{t}_{u\parallel}|} \quad (1)$$

Note  $\vec{t}_{u\perp} \cdot \hat{u} = 0$  and  $|\hat{u}|=1$ . The easiest way to continue our computation is to decompose  $\vec{t}$  by

$$\vec{t} = (\vec{t} \cdot \hat{u})\hat{u} + (\vec{t} \cdot \hat{z})\hat{z} + [\vec{t} \cdot (\hat{u} \times \hat{z})](\hat{u} \times \hat{z}) \quad (2)$$

And it's easy to see

$$\vec{t}_{u\parallel} = (\vec{t} \cdot \hat{u})\hat{u} + (\vec{t} \cdot \hat{z})\hat{z} \text{ and } \vec{t}_{u\perp} = [\vec{t} \cdot (\hat{u} \times \hat{z})](\hat{u} \times \hat{z})$$

Note:  $\vec{t} = (\tan\theta, \tan\varphi, 1)$ ,  $\hat{u} = (\cos\alpha, \sin\alpha, 0)$ , and  $\alpha = \text{atan}1/2$  is the angle between the  $u$ -axis and the  $x$ -axis, and  $\hat{z} = (0,0,1)$ . We have  $\vec{t} \cdot \hat{z} = 1$  and  $|\hat{z}|=1$ . Then

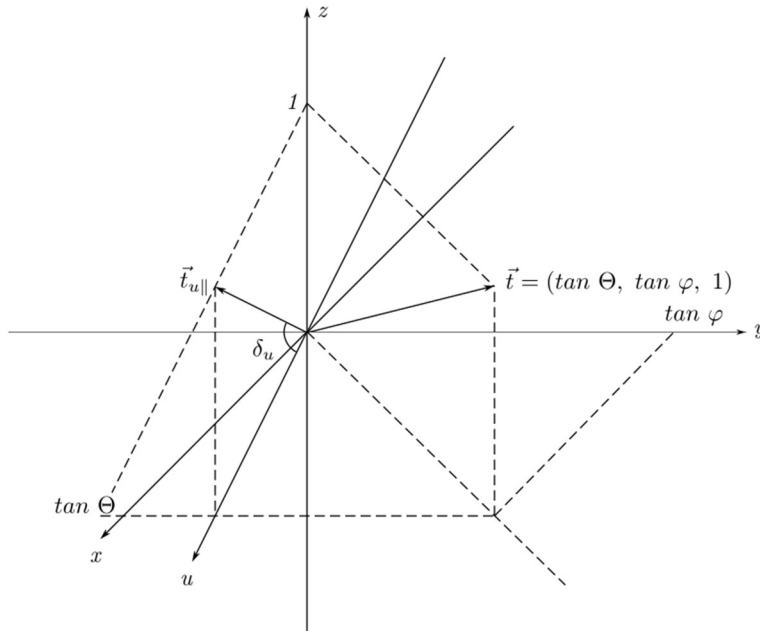
$$\cos(\delta_u) = \frac{\vec{t} \cdot \hat{u}}{|\vec{t}_{u\parallel}|} = \frac{\vec{t} \cdot \hat{u}}{\sqrt{(\vec{t} \cdot \hat{u})^2 + 1}} = \frac{k(\alpha)}{\sqrt{(k(\alpha))^2 + 1}} \quad (3)$$

where  $\vec{t} \cdot \hat{u} = \tan\theta \cdot \cos\alpha + \tan\varphi \cdot \sin\alpha \equiv k(\alpha)$ , and a simpler way to express  $\delta_u$  is

$$\cot(\delta_u) = k(\alpha) = \tan\theta \cdot \cos\alpha + \tan\varphi \cdot \sin\alpha = \frac{1}{\sqrt{5}}(2\tan\theta + \tan\varphi) \quad (4)$$

$$\cot(\delta_v) = k(-\alpha) = \tan\theta \cdot \cos\alpha - \tan\varphi \cdot \sin\alpha = \frac{1}{\sqrt{5}}(2\tan\theta - \tan\varphi) \quad (5)$$

( $\tan\alpha = 1/2$  applied in last equality in (4) and (5)) If we notice  $\hat{v} = (\cos(-\alpha), \sin(-\alpha), 0) = (\cos\alpha, -\sin\alpha, 0)$ .



Definition of  $\Theta, \varphi, \vec{t}, \vec{t}_{u\parallel}$  and  $\delta_u$

III Fig A1. 5 All vectors in section A1.3 computation.

### A1.4 Deriving relation from $(\delta_u, \delta_v)$ to $(\theta, \varphi)$

Knowing  $\delta_u$ , the track is spanned by two vectors:  $\cos\delta_u\hat{u} + \sin\delta_u\hat{z}$  and  $\hat{u} \times \hat{z}$ , the first vector is the unit projection of track vector in  $u$ - $z$  plane (it is parallel to  $\vec{t}_{u\parallel}$ ), and the second vector is the unit vector orthogonal to  $u$ - $z$  plane (it parallels  $\vec{t}_{u\perp}$ ). Tracks through the  $v$  plane are also in the plane spanned by two vectors:  $\cos(\delta_v)\hat{v} + \sin(\delta_v)\hat{z}$  and  $\hat{v} \times \hat{z}$ .

The direction of track  $\vec{t} = (\tan\theta, \tan\varphi, 1)$ , and  $\vec{t}$  is parallel to the intersection of the two planes (each spanned by two vectors) defined above. By establishing the equation of this relationship we can find  $\tan\theta$  and  $\tan\varphi$  in terms of  $\delta_u, \delta_v$ :  $\hat{u} = (\cos\alpha, \sin\alpha, 0)$ , and  $\hat{z} = (0,0,1)$ . Then

$$\begin{aligned}\cos\delta_u\hat{u} + \sin\delta_u\hat{z} &= (\cos\delta_u\cos\alpha, \cos\delta_u\sin\alpha, \sin\delta_u) \\ \hat{u} \times \hat{z} &= (\sin\alpha, -\cos\alpha, 0)\end{aligned}$$

Since only  $\cos(\delta_u)\hat{u} + \sin(\delta_u)\hat{z} = \cos(\delta_u)(\cot(\delta_u)\hat{u} + \hat{z})$  has a non-zero  $z$  component, we can write:

$$\begin{aligned}\vec{t} &= (\cot(\delta_u)\hat{u} + \hat{z}) + a(\hat{u} \times \hat{z}) \\ &= (\cot(\delta_u)\cos\alpha, \cot(\delta_u)\sin\alpha, 1) + a(\sin\alpha, -\cos\alpha, 0)\end{aligned}\quad (1)$$

For the  $v$  plane:

$$\begin{aligned}\vec{t} &= (\cot(\delta_v)\hat{v} + \hat{z}) + b(\hat{v} \times \hat{z}) \\ &= (\cot(\delta_v)\cos\alpha, -\cot(\delta_v)\sin\alpha, 1) + b(-\sin\alpha, -\cos\alpha, 0)\end{aligned}\quad (2)$$

Where  $a, b$  in (1), (2) are to be solved for. Equate (1), (2)  $x, y$  components with  $\vec{t} = (\tan\theta, \tan\varphi, 1)$  and we have equations:

$$\tan\theta = \cot(\delta_u)\cos\alpha + a\sin\alpha = \cot(\delta_u)\cos\alpha - b\sin\alpha \quad (3)$$

$$\tan\varphi = \cot(\delta_u)\sin\alpha - a\cos\alpha = -\cot(\delta_u)\sin\alpha - b\cos\alpha \quad (4)$$

Solve (3)(4) we get values for  $a, b$  and then  $\tan\theta, \tan\varphi$  in terms of  $\delta_u, \delta_v$ :

$$\tan\theta = \frac{1}{2\cos\alpha} (\cot(\delta_u) + \cot(\delta_v)) = \frac{\sqrt{5}}{4} (\cot(\delta_u) + \cot(\delta_v)) \quad (5)$$

$$\tan\varphi = \frac{1}{2\sin\alpha} (\cot(\delta_u) - \cot(\delta_v)) = \frac{\sqrt{5}}{2} (\cot(\delta_u) - \cot(\delta_v)) \quad (6)$$

where  $\tan\alpha = 1/2$  was used to obtain the last equations in each line. When solved for  $\cot\delta_u$  and  $\cot\delta_v$  in above equations, we can get result (4) (5) in A1.3.

## A1.5 Applications

### A1.5.1 Finding range of $\varphi$ when $\theta = 45^\circ$

(In this case, track is horizontal, when chambers are tilted  $45^\circ$  in BH experiment setup.)

Combining formulas:

$$\begin{aligned}\tan\theta &= \frac{\sqrt{5}}{4} (\cot(\delta_u) + \cot(\delta_v)) \\ \tan\varphi &= \frac{\sqrt{5}}{2} (\cot(\delta_u) - \cot(\delta_v))\end{aligned}$$

From A 1.4.

$$\begin{aligned}\cot(\delta_u) &= \frac{s}{\Delta d_u} \\ \cot(\delta_v) &= \frac{s}{\Delta d_v}\end{aligned}$$

From A 1.2.

See Fig A1.4.  $s$  is wire spacing (distance between two adjacent wires) and  $\Delta d_u, \Delta d_v$  are drift distance difference between adjacent wires. If in addition we denote  $\Delta d_u = \frac{h}{n_u}, \Delta d_v = \frac{h}{n_v}$ , where  $h$  is thickness of gas volume in a wire plane,  $n_u$  and  $n_v$  are number of wire span of a cluster used for fit the track defined in Fig A1.4. For the wire chamber we're using  $s = 0.497\text{cm}, h = 2.54\text{ cm}$ . We have (choosing  $\theta = 45^\circ$ ):

$$9.14 \tan\theta = 9.14 \tan 45^\circ = n_u + n_v \quad (1)$$

$$4.57 \tan\varphi = n_u - n_v \quad (2)$$

where  $n_u$  and  $n_v$  are not necessarily integers, and are signed (the convention is if  $\cot(\delta_u) > 0$ , or the projection of a track in  $u$ - $z$  plane and  $+u$  direction has an acute angle, then  $n_u$  is positive. If the angle is obtuse,  $\cot(\delta_u) < 0$  then  $n_u < 0$ .)

In order to obtain the range of  $\varphi$  or  $\tan\varphi$ , we notice  $n_{max} \geq |n_u|, |n_v| \geq n_{min}$ , where  $n_{max}$  and  $n_{min}$  are maximum and minimum spans of wires for a cluster (They're set in VDC database file, see section 2.2 VDC database file setup). For example, if we choose  $n_{min} = 3, n_{max} = 12$ . Then  $(n_u, n_v)$  pair will range from (3.00, 6.14) to (6.14, 3.00) which corresponds to (from equation (2) above)

$$|\varphi| < 34.5^\circ$$

Or, the  $(n_u, n_v)$  pair can choose (-3.00, 12.00) and (12.00, -3.00) and  $\varphi = \pm 73.1^\circ$ . We discard the solution with  $\varphi = \pm 73.1^\circ$  since the angle subtended from the center of magnet to the wire chamber further away from magnet in our experiment setup is about  $36^\circ$ , which is much less than  $73.1^\circ$ .

### A1.5.2 Number of wires hit when $\theta = 45^\circ$

From the range of  $(n_u, n_v)$  pair in A1.5.1, we choose possible integer values:  $(n_u, n_v) = (3,6), (4,5), (5,4), (6,3)$  which span the wire clusters. The actual hit wires could be either  $n_{u/v}$  or  $n_{u/v} + 1$ . Then, for a single cluster from each wire plane, all from the same track, the pair of integers (number of hit wires in  $u$  plane, the number of hit wires in  $v$  plane) can be  $(3,6), (4,6), (3,7), (4,7), (4,5), (5,5), (4,6), (5,6)$  and also pairs with the 1<sup>st</sup> and 2<sup>nd</sup> numbers swapped. (Assuming there is no broken wires with no signals or low efficiency issues in any of the clusters for each wire plane). Any other combination number of wires hits in  $u, v$  planes is invalid for  $\theta = 45^\circ$ .

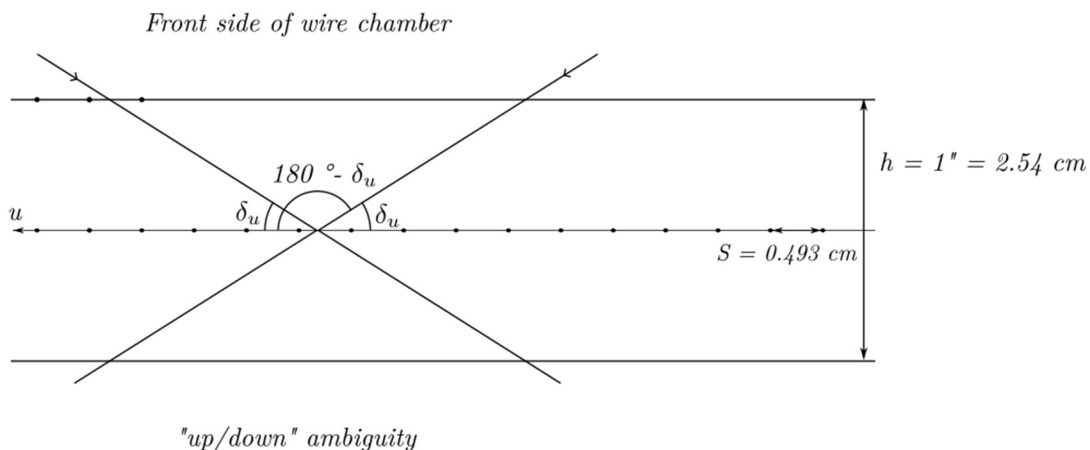
### A1.5.3 up/down ambiguity and it's relation to $(n_u, n_v)$

Since the following three conditions are met for

- 1) the speed of charged particles (almost the speed of light) are about 4 orders of magnitude higher than drift speed of ions in wire chamber, which make negligible offsets in drift time between wires.
- 2) the distance between wires to both sides of the anode planes from the wire planes are the same.
- 3) the drift time, which is always positive, contains no information of which side of wire plane the track is coming from.

Even if we know a particle propagates from one side of the wire plane, for a cluster of (hit wire, drift time) pairs, the track could still be coming from the side corresponding to either wire with highest or lowest index of the cluster. The two possible track candidates are mirror images of each other about the plane where the wires lie. This is known as the “*up/down ambiguity*”. Thus, we cannot determine track direction solely from drift time info. In the previous context, the drift time could only determine  $\delta_u$  or  $\delta_v$  to the degree that a possible angle between a track

projection and wires is either  $\delta$  or  $180^\circ - \delta$ . By the combination of 2 possible  $\delta$ 's in each wire plane, we can determine the 4 possible directions from a pair of  $u$ - $v$  planes (or a wire chamber). To resolve this ambiguity: the analyzer takes clusters in both wire chambers, and finds the best matching clusters with closest fitted absolute track slopes (but still contains a sign ambiguity) from  $u$  planes and  $v$  planes (that a pair of clusters of  $u_1$  plane and  $u_2$  plane with closest slope, and same for  $v$  planes). Use the absolute slope to draw the four possible tracks described above, from fitted the intersection of track in the first wire chamber to the second wire chamber, only the real track will intersect second wire chamber within acceptable error to the fitted intersection in the second wire chamber.



III Fig A1. 6 “Up/down” ambiguity of a wire plane.

Two possible tracks can be extracted from one set of TDC time data since they have same drift distances.

## Part IV Appendix 2.5 Coordinate transformations

In this appendix we derive the form of transformations used in section 2.5.2. The transformations of wire chambers are combinations of translation and rotation, whose properties have been stated in A 2.5.1. Eq. (A2.2) has been repeatedly used to get analytic forms of the composite transformations. Their categorization is discussed in A 2.5.2, and eq. (A2.18) is used to find the translational component (feq. (2.29)) of the additional rotation. [62]

### A 2.5.1 Coordinate transformations with translations

Conventions on notations: Denote non-degenerate linear transformations by upper case letters  $A, B, \dots$ . Denote translations by contravariant vectors (not bold Greek letters)  $\xi, \eta, \zeta$  etc. The vectors are transformed by a combination of a linear transformation  $A$  prior to translation  $\xi$ . The transformation is represented as  $(A, \xi)$ , and corresponding coordinate transformation of the vector  $z$  (here  $z$  is a vector, not  $z$  component of the vector) is:

$$z \rightarrow Az + \xi \quad (\text{A2.1})$$

1. Product rule of (A2.1) can be verified as

$$(A, \xi) \cdot (B, \eta) = (AB, \xi + A\eta) \quad (\text{A2.2})$$

(1) Product can also be represented by matrix  $\begin{pmatrix} A & \xi \\ 0 & 1 \end{pmatrix}$ , and it can be verified that:

$$\begin{pmatrix} A & \xi \\ 0 & 1 \end{pmatrix} \cdot \begin{pmatrix} B & \eta \\ 0 & 1 \end{pmatrix} = \begin{pmatrix} AB & \xi + A\eta \\ 0 & 1 \end{pmatrix}$$

(1) The transformation  $(A, \xi)$  represents a rotation  $A$  first, then a translation  $\xi$ . If translation first then rotation, should regard as product of two transformations (as  $(A, A\xi)$  below).

$$(A, 0) \cdot (1, \xi) = (A, A\xi) \neq (1, \xi) \cdot (A, 0) = (A, \xi) \quad (\text{A2.3})$$

2. The totality of these transformations form a group (Affine transformation group). With identity  $(1, 0)$ , and inverse

$$(A, \xi)^{-1} = (A^{-1}, -A^{-1}\xi) \quad (\text{A2.4})$$

3. We are only considering “normal motion”, where  $A$  is rotation:

$$A^T A = 1, \det A = 1 \quad (\text{A2.5})$$

Thus,  $(A, \xi)$  forms a subgroup of affine transformation group.

4. Pure rotation is of the form  $(A, 0)$ . All pure rotations form a subgroup of “normal motion” group, it is non-Abelian. Pure translation is of form  $(1, \xi)$ . All pure translations also form a subgroup of the “normal motion” group and is Abelian. In addition, the conjugate of translation is still translation:

$$(A, \xi) \cdot (1, \eta) \cdot (A, \xi)^{-1} = (1, A\eta) \quad (\text{A2.6})$$

Thus, all translations form a normal subgroup of “normal motion”. And the quotient group of “normal motion” to translation group is isomorphic to the rotation group.

Remark: The reason that normal motion group discussed right here is that it's implemented in Geant 4 simulation to represent the transformation of a daughter volume inside a mother volume as `G4Tranform3D(G4RotationMatrix, G4ThreeVector)`.

### A 2.5.2 Categorize normal motion in 2D and 3D cases

1) Normal motion in 2D:

1. By (A2.5)  $A \in SO(2)$ , has the form:

$$A = \begin{pmatrix} \cos\theta & -\sin\theta \\ \sin\theta & \cos\theta \end{pmatrix}$$



2. Any planar “normal motion” is a rotation about some point or translation:

$$z \rightarrow Az + \xi, A = \begin{pmatrix} \cos\theta & -\sin\theta \\ \sin\theta & \cos\theta \end{pmatrix} \quad (\text{A2.7})$$

To confirm the statement:

(1)  $A = 1$ ,  $z \rightarrow Az + \xi = z + \xi$  is translation.

(2)  $A \neq 1$ , suppose the rotation center  $z_0$  is the fixed point of above transformation:

$$\begin{aligned} z_0 &= Az_0 + \xi \\ (1 - A)z_0 &= \xi \end{aligned} \quad (\text{A2.8})$$

Since  $A \neq 1$ ,  $(1 - A)$  is non-degenerate and there is a unique solution  $z_0$  as the center of rotation.

3. In the case of rotation, change coordinate system to make  $z_0$  as the new origin, under this coordinate system vector transformed under pure rotation is denote as  $y$  (coordinate which use the fixed point  $z_0$  as its origin):

$$y = z - z_0 \quad (\text{A2.9})$$

$$\begin{aligned} z \rightarrow Az + \xi \text{ is equivalent to } y + z_0 \rightarrow A(y + z_0) + \xi &= Ay + (Az_0 + \xi) = Ay + z_0, \\ \text{or transformation in } y: y \rightarrow Ay \end{aligned} \quad (\text{A2.10})$$

## 2) Normal motion in 3D:

We 1<sup>st</sup> consider only rotations:

1. Consider pure rotation first. Transformation  $A \in SO(3)$  has a fixed axis, which is not moving under transformation of  $A$ . Solving the eigen equation:

$$Av = \lambda v, \lambda \text{ real number, is the root of equation } \det(A - \lambda \cdot 1) = 0 \quad (\text{A2.11})$$

(A2.11) is equation of order  $\lambda$  being 3, it has one at least real solution  $\lambda_0$ . Computing the inner product:

$$\langle v_0, v_0 \rangle = \langle Av_0, Av_0 \rangle = \lambda_0^2 \langle v_0, v_0 \rangle \quad (\text{A2.12})$$

We find  $\lambda_0 = \pm 1$ , for rotation  $\lambda_0 = 1$ .

2. If a vector  $w$  is perpendicular to  $v_0$ , then  $Aw$  also perpendicular to  $v_0$ :

$$\langle v_0, Aw \rangle = \pm \langle Av_0, Aw \rangle = \pm \langle v_0, w \rangle = 0.$$

Equivalently, we can say that the plane through origin and perpendicular to  $v_0$  is invariant under rotation  $A$ .

3.  $A \in SO(3)$  explicit form: set  $v_0$  along coordinate axis  $x^3$ ,  $A$  has form

$$A = \begin{pmatrix} \cos\theta & -\sin\theta & 0 \\ \sin\theta & \cos\theta & 0 \\ 0 & 0 & 1 \end{pmatrix} \quad (\text{A2.13})$$

$SO(3)$  consists of all rotation with axis through the origin.

Now add translation and consider “Normal motion” in 3D:

1. It has form:  $z \rightarrow Az + \xi$ . If origin is translated by  $z = y + y_0$ , that is the origin of the coordinate system  $y$  being translated from the origin of the coordinate system  $z$  by  $y_0$ . Then “motion” in  $y$  coordinate is  $y + y_0 \rightarrow A(y + y_0) + \xi$ , or equivalently:

$$y \rightarrow Ay + (A - 1)y_0 + \xi \quad (\text{A2.14})$$

2. To reduce the translation  $(A - 1)y_0 + \xi$  as much as possible, such that the transformation is as close to  $y \rightarrow Ay$  as possible. Here:

$$A = \begin{pmatrix} \cos\theta & -\sin\theta & 0 \\ \sin\theta & \cos\theta & 0 \\ 0 & 0 & 1 \end{pmatrix} \text{ and } \xi = \begin{pmatrix} \xi^1 \\ \xi^2 \\ \xi^3 \end{pmatrix}$$

Suppose  $A(\theta)$  with non-zero  $\theta$ , then transformation  $(A - 1)$  is degenerate. Equation:

$$(1 - A)y_0 = \xi \text{ with explicit form } \begin{cases} (1 - \cos\theta)y_0^1 - \sin\theta y_0^2 = \xi^1 \\ \sin\theta y_0^1 + (1 - \cos\theta)y_0^2 = \xi^2 \\ 0 = \xi^3 \end{cases} \quad (\text{A2.15})$$

Note: the first two equations of (A2.15) are exactly same as the 2D case with  $(1 - A)z_0 = \xi$ .

If  $\xi^3 \neq 0$ , the above equation has no solution. But the first two equations have unique solutions.

Substitute  $y_0 = (y_0^1, y_0^2, y_0^3)$  with  $y_0^1, y_0^2$  as the unique solution,  $y_0^3$  arbitrary number. Then:

$$\begin{aligned} (1 - A)y_0 &= (\xi^1, \xi^2, 0) \\ (A - 1)y_0 + \xi &= (0, 0, \xi^3) \end{aligned} \quad (\text{A2.16})$$

Transformation of  $y$  has the form (inserting (A2.16) into (A2.14)):

$$\begin{aligned} y &\rightarrow Ay + (A - 1)y_0 + \xi = Ay + (0, 0, \xi^3) = Ay + \eta \\ \eta &= (0, 0, \xi^3), \text{ and } A\eta = \eta. \end{aligned} \quad (\text{A2.17})$$

Thus, after coordinate transformation  $z = y + y_0$ ,  $y_0 = (y_0^1, y_0^2, y_0^3)$  with  $y_0^1, y_0^2$  as the unique solution of the first two equations of (A2.15) and  $y_0^3$  an arbitrary number:

- (1) if  $\xi^3 = 0$  the normal motion is rotation  $y \rightarrow Ay$ ;
- (2) if  $\xi^3 \neq 0$  the normal motion is helix motion  $y \rightarrow Ay + \eta$  (Rotate 1<sup>st</sup>, then translate along rotation axis by  $\xi^3$ ).

This completes the Categorization of normal motion in 3D case.

To end this appendix, here are two remarks:

- (1) In Geant 4 simulation wire chamber placement, we have a sequence of transformations of rotation and translation. In order to calculate the composite transformation in form  $(A, \xi)$ , formula (A2.2) is repeatedly used.
- (2) In order to calculate the form of  $(A, \xi)$  of the rotation about vertical axis through front wire chamber center, which is not the origin (magnet center) of the Geant 4 simulation. This is categorized as case (1) if  $\xi^3 = 0$  the normal motion is rotation  $y \rightarrow Ay$  above, since the translation  $\xi$  here has no 0 component in vertical axis or the rotation axis of  $A$ . In this case we want to do the reverse in (A2.15), that is instead of solving the fixed point  $y_0$ , we know  $y_0$  but want to find the translation  $\xi$  in the normal motion  $(A, \xi)$ . This is complete by directly applying (A2.15):  $\xi = (1 - A)y_0$  (A2.18). This is used in (2.29).

### Part IV Appendix 3.2: Derivation of projected radius $R_H$

The derivation can be found in most field theory books, here the reference is [63]. Different unit system is used here.

Constant magnetic field:

$$F^{0i} = 0$$

$$F^{ij} = \varepsilon^{ijk} B_k, \quad i = 1,2,3$$

Time component of equation of motion is:

$$\frac{dE}{cd\tau} = qF^{0i}u_i = 0$$

Energy of the particle is constant. Spatial components:

$$\gamma \frac{dp^i}{dt} = q\varepsilon^{ijk} B_k \gamma v_j$$

Or in 3-vector form:

$$\frac{d\mathbf{p}}{dt} = m\gamma \frac{d\mathbf{v}}{dt} = q\mathbf{v} \times \mathbf{B} \quad (\text{A1})$$

The 1<sup>st</sup> equality results from constant energy and thus  $\frac{d\gamma}{dt} = 0$ . Reorder (A1)

$$\frac{d\mathbf{v}}{dt} = \frac{q\mathbf{v} \times \mathbf{B}}{m\gamma} = \mathbf{v} \times \boldsymbol{\omega}_B \quad (\text{A2})$$

If we denote  $\boldsymbol{\omega}_B = \omega \hat{\mathbf{k}}$ , where  $\omega = \frac{qB}{m\gamma}$ , as in non-relativistic case, solution of equation (A2) turns into helix motion of the particle. It has constant speed circular motion in  $xy$  plane, direction changed by  $\mathbf{B}$ .  $z$  direction motion is constant speed motion. And the radius of the circle in  $xy$  plane is:

$$R_H = \frac{v_{xy}}{\omega} = \frac{m\gamma c \sqrt{1 - (\sin\theta \sin\varphi)^2}}{qB} = \frac{E \sqrt{1 - (\sin\theta \sin\varphi)^2}}{ecB} \quad (\text{A3})$$

When energy unit using MeV, cancel out  $e$  and turns  $M$  into  $10^6$ :

$$R_H = 10^6 E \sqrt{1 - (\sin\theta \sin\varphi)^2} / (cB) \quad (\text{A4})$$

That is the formula (3.5)

## References

- [1 G. Ron and et al., "Proposal to the High Intensity Gamma-Ray Source (HI- $\gamma$ S) PAC-12: A  
] Measurement of the Bethe-Heitler Pair Production Asymmetries".
- [2 S. D. Drell and A. C. Hearn, "Exact Sum Rule For Nucleon Magnetic Moments," *Phys. Rev.  
] Lett.*, vol. 16, p. 908, 1966.
- [3 S. B. Gerasimov, "A sum rule for magnetic moments and the damping of the nucleon  
] magnetic moment in nuclei," *Sov. J. Nucl. Phys.*, vol. 2, p. 430, 1966.
- [4 H. Bethe and W. Heitler, "On the Stopping of fast particles and on the creation of positive  
] electrons," *Proc. Roy. Soc. Lond. A*, vol. 83, p. 146, 1934.
- [5 H. A. Bethe and L. C. Maximon, "Theory of Bremsstrahlung and Pair Production. 1.  
] Differential Cross Section," *Phys. Rev.*, vol. 93, p. 768, 1954.
- [6 H. Davies, H. A. Bethe and L. C. Maximon, "Theory of Bremsstrahlung and Pair Production.  
] 2. Integral Cross Section for Pair Production," *Phys. Rev.*, vol. 93, p. 788, 1954.
- [7 J. G. Asbury and et al., "Validity of Quantum Electrodynamics at Small Distances," *Phys.  
] Rev. Lett.*, vol. 18, p. 65, 1967.
- [8 S. J. Brodsky and J. Gillespie, "Second Born Corrections To Wide Angle Electron Pair  
] Production and Bremsstrahlung," *Phys. Rev.*, vol. 173, p. 1011, 1968.
- [9 F. E. Low, "Scattering of Light of Very Low Frequency by Systems of Spin 1/2," *Phys. Rev.*,  
] vol. 96, p. 1428, 1954.
- [1 M. Gell-Mann and M. L. Goldberger, "Scattering of Low-Energy Photons by Particle of Spin  
0] 1/2," *Phys. Rev.*, vol. 96, p. 1433, 1954.
- [1 S. J. Brodsky and J. R. Primack, "The Electromagnetic Interactions of Composite Systems,"  
1] *Annals Phys.*, vol. 52, p. 315, 1969.
- [1 S. J. Brodsky and I. Schmidt, "Classical photoabsorption sum rules," *Phys. Lett. B*, vol. 351,  
2] pp. 344-348, 1995.
- [1 P. A. M. Guichon and M. Vanderhaeghen, "How to reconcile the Rosenbluth and the  
3] polarization transfer method in the measurement of the proton form-factors," *Phys. Rev. Lett.*,  
vol. 91, p. 142303, 2003.
- [1 A. V. Afanasev, S. J. Brodsky, C. E. Carlson, Y. C. Chen and M. Vanderhaeghen, "The two-  
4] photon exchange contribution to elastic electron nucleon scattering at large momentum  
transfer," *Phys. Rev. D*, vol. 013008, p. 72, 2005.

- [1 A. Afanasev, S. J. Brodsky, C. E. Carlson and A. Mukherjee, "Timelike Virtual Compton  
5] Scattering from Electron-Positron Radiative Annihilation," *Phys. Rev. D*, vol. 81, p. 034014,  
2010.
- [1 S. J. Brodsky, F. E. Close and J. F. Gunion, "Compton Scattering and Fixed Poles in Parton  
6] Field Theoretic Models," *Phys. Rev. D*, vol. 5, p. 1384, 1972.
- [1 M. Damashek and F. J. Gilman, "Forward Compton Scattering," *Phys. Rev. D*, vol. 1, p.  
7] 1319, 1970.
- [1 S. J. Brodsky, F. J. Llanes-Estrada and A. P. Szczepaniak, "Local Two-Photon Couplings and  
8] the  $J=0$  Fixed Pole in Real and Virtual Compton Scattering," *Phys. Rev. D*, vol. 79, p.  
033012, 2009.
- [1 J. C. Collins and A. Freund, "Proof of factorization for deeply virtual Compton scattering in  
9] {QCD}," *Phys. Rev. D*, vol. 59, p. 074009, 1999.
- [2 R. N. Lee, A. I. Milstein and V. M. Strakhovenko, "Charge asymmetry in the differential  
0] cross section of high-energy  $e^+e^-$  photo-production in the field of a heavy atom," *Phys. Rev. A*  
85, p. 042104, 2012.
- [2 V. B. Berestetski, E. M. Lifshits and L. P. Pitayevsky, Quantum electrodynamics, Oxford:  
1] Pergamon, 1982.
- [2 J. Feldhaus, J. Arthur and J. B. Hastings, "X-ray free-electron lasers," *Journal of Physics B*.  
2] 38(9), p. S799, 2005.
- [2 V. N. Litvinenko and et. al., "Gamma-Ray Production in a Storage Ring Free-Electron  
3] Laser," *Physical Review Letters*, vol. 78, no. 24, pp. 4569-4572, 1997.
- [2 G. Ron and et al., "Proposal to the High Intensity Gamma-Ray Source (HI- $\gamma$ S) PAC-12: A  
4] Measurement of the Bethe-Heitler Pair Production Asymmetries".
- [2 G. Ron and et al., "Proposal to the High Intensity Gamma-Ray Source (HI- $\gamma$ S) PAC-12: A  
5] Measurement of the Bethe-Heitler Pair Production Asymmetries".
- [2 J. R. Sigurdson, "A Magnetic Pair Spectrometer to Detect Photon Splitting, MSc thesis,"  
6] University of Saskatchewan, 1994.
- [2 R. V. Servranckx and et al., "Users Guide to the Program DIMAD," SLAC Report, 1999.  
7]
- [2 W. R. Leo, in *Techniques for Nuclear and Particle Physics Experiments*, Springer-Verlag,  
8] 1993, pp. 127-141.
- [2 J. P. Leckey, "The First Direct Measurement of The Weak Charge of the Proton, PhD.  
9] Thesis, chap. 4," College of William and Mary, 2012.

- [3 R. Veenhof, "Garfield, a drift chamber simulation program," *CERN program library W*, vol. 0] 5050, 1984.
- [3 S. Agostinelli, J. Allison, K. Amako, J. Apostolakis, H. Araujo, P. Arce, M. Asai, D. Axen,  
1] S. Banerjee and G. Barrand, "Geant4-a simulation toolkit," *Nucl. Instr. and Meth. A*, vol. 506, no. 3, p. 250303, 2003.
- [3 K. Grimm, "Update on the Region III Drift Chambers," College of William and Mary, 2007.  
2]
- [3 W. R. Leo, in *Techniques for Nuclear and Particle Physics Experiments*, Springer-Verlag,  
3] 1993, pp. 157-214.
- [3 "BC400-404-408-412-416 Data Sheet," [Online]. Available: <https://www.crystals.saint-gobain.com/sites/hps-mac3-cma-crystals/files/2021-10/BC400-404-408-412-416-Data-Sheet.pdf>.  
4]
- [3 H. Handbook, in *Photomultiplier Tubes Basics an Application*, 2017, p. 45.  
5]
- [3 Hamamatsu, "Photomultiplier Tube R7723, R7724, R7725 Data Sheet," Aug. 2009. [Online].  
6] Available:  
[http://hamamatsu.com.cn/UserFiles/DownFile/Product/R7723\\_TPMH1315E01.pdf](http://hamamatsu.com.cn/UserFiles/DownFile/Product/R7723_TPMH1315E01.pdf).
- [3 "Care Instructions Plastics & Scintillating Fiber," 2005. [Online]. Available:  
7] <https://vepp2k.inp.nsk.su/~inest/halometer/SGC%20Handling%20and%20Cleaning%20Plastic%20Scintillators%20Information%20Sheet.pdf>.
- [3 J. Alcorn and et al., "Basic instrumentation for Hall A at Jefferson Lab," *Nuclear Instruments  
8] and Methods in Physics Research A* 522, pp. 294-346, 2004.
- [3 J. Alcorn and et al., "Basic instrumentation for Hall A at Jefferson Lab," *Nuclear Instruments  
9] and Methods in Physics Research A* 522, pp. 333-339, 2004.
- [4 O. Hansen, "THaVDCPlane-source file," 2015. [Online]. Available:  
0] [https://hallaweb.jlab.org/podd/doc/html\\_v16/src/THaVDCPlane.cxx.html](https://hallaweb.jlab.org/podd/doc/html_v16/src/THaVDCPlane.cxx.html).
- [4 S. Riordan, "APEX High Rate VDC Analysis," 2010.  
1]
- [4 "THaVDCCluster-source file," 2015. [Online]. Available:  
2] [https://hallaweb.jlab.org/podd/doc/html\\_v16/src/THaVDCCluster.cxx.html](https://hallaweb.jlab.org/podd/doc/html_v16/src/THaVDCCluster.cxx.html).
- [4 "THaVDCAnalyticTTDCConv-source file," 2015. [Online]. Available:  
3] [https://hallaweb.jlab.org/podd/doc/html\\_v16/src/THaVDCAnalyticTTDCConv.cxx.html](https://hallaweb.jlab.org/podd/doc/html_v16/src/THaVDCAnalyticTTDCConv.cxx.html).

- [4 in *An Introduction To Error Analysis: The Study of Uncertainties in Physical Measurements*  
4] *2nd Edition*, University Science Books, 1996, pp. 215-220, 290-291.
- [4 in *Basic Probability Theory*, Dover Publications, 2008, pp. 59-61.  
5]
- [4 *Engauge Digitizer 12.1*.  
6]
- [4 Wikipedia, "Bilinear interpolation," [Online]. Available:  
7] [https://en.wikipedia.org/wiki/Bilinear\\_interpolation](https://en.wikipedia.org/wiki/Bilinear_interpolation).
- [4 "THaVDCPlane-source file," no.  
8] [https://hallaweb.jlab.org/podd/doc/html\\_v16/src/THaVDCPlane.cxx.html](https://hallaweb.jlab.org/podd/doc/html_v16/src/THaVDCPlane.cxx.html), 2015.
- [4 in *Basic Probability Theory*, Dover Publications, 2008, pp. 33-36.  
9]
- [5 R. Pywell, "Bethe-Heitler Measurable Asymmetry, Subatomic Physics Internal Report SPIR-  
0] 150," University of Saskatchewan.
- [5 in *Basic Probability Theory*, Dover Publications, 2008, pp. 59-61.  
1]
- [5 R. Pywell, "Bethe-Heitler Measurable Asymmetry, Subatomic Physics Internal Report  
2] SPIR-150," University of Saskatchewan.
- [5 M. Asai and S. Incerti, "Geant4 Geometry, KIT tutorial," 2011. [Online]. Available:  
3] [http://geant4.in2p3.fr/IMG/pdf\\_Lecture-Geometry.pdf](http://geant4.in2p3.fr/IMG/pdf_Lecture-Geometry.pdf).
- [5 "ROOT users guide," [Online]. Available: [https://root.cern.ch/root/html534/guides/users-](https://root.cern.ch/root/html534/guides/users-4)  
4] [guide/AddingaClass.html#adding-a-class](https://root.cern.ch/root/html534/guides/users-4/guide/AddingaClass.html#adding-a-class).
- [5 "ROOT users guide, section 14.20," [Online]. Available:  
5] <https://root.cern.ch/root/html534/guides/users-guide/Trees.html>.
- [5 in *Techniques for Nuclear and Particle Physics Experiments*, Springer-Verlag, 1993, p. 103.  
6]
- [5 "k-means clustering-Wikipedia," [Online]. Available: [https://en.wikipedia.org/wiki/K-](https://en.wikipedia.org/wiki/K-means_clustering)  
7] [means\\_clustering](https://en.wikipedia.org/wiki/K-means_clustering).
- [5 in *Mathematics for Machine Learning, 1st ed.*, Cambridge University Press, 2020, pp. 286-  
8] 293.

- [5 Khan Academy, "A projection onto a subspace is a linear transformation," 2009. [Online].  
9] Available:  
[https://www.youtube.com/watch?v=cTyNpXB92bQ&ab\\_channel=KhanAcademy](https://www.youtube.com/watch?v=cTyNpXB92bQ&ab_channel=KhanAcademy).
- [6 in *Mathematics for Machine Learning, 1st ed.*, Cambridge University Press, 2020, p. 173.  
0]
- [6 J. Bentley, *Programming Pearls*, Addison-Wesley Professional, 1999.  
1]
- [6 in *Modern Geometry — Methods and Applications: Part I: The Geometry of Surfaces,*  
2] *Transformation Groups, and Fields 2nd edition*, Springer, 1991, pp. 23-38.
- [6 "Motion in a constant uniform magnetic field," in *The Classical Theory of Fields 4th ed.*,  
3] Elsevier, 1975, p. section 21.
- [6 J. Alcorn and et al., "Basic instrumentation for Hall A at Jefferson Lab," *Nuclear Instruments*  
4] *and Methods in Physics Research A 522*, p. 334, 2004.
- [6 S. J. Brodsky, J. Rathsman and C. Merino, "Odderon-pomeron interference," *Phys. Lett. B*,  
5] vol. 461, p. 114, 1999.



## Acknowledgements

I have received a lot of help from many people over the years directly and indirectly here at UVA and JLAB. First and foremost, I give my thanks to my advisor Prof. Blaine Norum. He gave me the freedom to travel weekly to JLAB from 2016 to 2020. He is interesting, kind, and a good story teller. It is always been very relaxed to talk with him and learn something at the same time. His knowledge on physics is expansive and always has tricks up his sleeve when answering my questions.

Secondly, huge thanks to Dr. Brad Sawatzky at JLAB, he advised me on the commissioning of the Q-weak drift chambers from 2015 to 2020. He is very efficient and on point when doing the job. He is always without hesitation to help anything on every task, with keen insights on the details.

A lot of thanks to Prof. Rob Pywell from the University of Saskatchewan. He built up the framework of the Geant4 simulation and helped me to understand it when he traveled to Duke University, which is the foundation of my work on the simulations. Thanks to many JLAB staff members, Prof. Ole-Hansen for clarifying wire chamber geometries in the analyzer and modified the analyzer for our TDC application. Thanks to Jack Seagal and Chuck Long for the help on the hardware.

Thanks to Prof. Michael Fowler, Prof. Richard Lindgren and Prof. Ken Paschke as my research committee members over the years. Thanks Prof. Richard Lindgren, Prof. Donald Day, and Prof. Karen Schmidt for reading the dissertation and giving valuable suggestions.

Thanks to other students of Blaine, Peng Peng for helping me travel to JLAB during 2014 to 2015. Ryan Duve, Matt Roberts and Thomas Krahulik for the company at the office.

Thanks to fellow students at UVA: Xinzhan Bai and Danning Di, they let me have free lodging in their house during 2016 to 2017 and sharing the office at JLAB; Kai Jin as roommate and lunchmate at JLAB since 2017. Huangxin Li as a friend I probably talked with most in the US. Puhan Zhang, a late acquaintance from my hometown for the fun time spent the last years when old friends graduated, and the suggestion on the quick-sort algorithm.

Lastly, thanks to my family. They came to US to see me yearly since 2015 until Covid and were always fully supporting me on every aspect, letting me focus on the work and study.